# **Tsunami** and Its Hazards in the Indian and Pacific Oceans

Edited by
Kenji Satake
Emile A. Okal
José C. Borrero

BIRKHÄUSER

**pageoph topical volumes**

BIRKHÄUSER

# **Tsunami** and Its Hazards in the Indian and Pacific Oceans

Edited by
Kenji Satake
Emile A. Okal
José C. Borrero

Birkhäuser
Basel · Boston · Berlin

Reprint from Pure and Applied Geophysics
(PAGEOPH), Volume 164 (2007) No. 2 - 3

Editors:

Kenji Satake
Geological Survey of Japan
National Institute of Advanced Industrial
Science and Technology
Tsukuba, 305-8567
Japan
kenji.satake@aist.go.jp

José C. Borrero
University of Southern California
Viterbi School of Engineering
Civil and Environmental Engineering
USA
jborrero@usc.edu

Emile A. Okal
Northwestern University
Department of Earth and Planetary Sciences
Evanston, Illinois 60208-2150
USA
emile@earth.northwestern.edu

Library of Congress Control Number: 2007921304

Bibliographic information published by Die Deutsche Bibliothek. Die Deutsche Bibliothek lists this publication in the Deutsche Nationalbibliografie; detailed bibliographic data is available in the Internet at <http://dnb.ddb.de>

ISBN 978-3-7643-8363-3 Birkhäuser Verlag AG, Basel · Boston · Berlin



ISBN 978-3-7643-8363-3
9 8 7 6 5 4 3 2 1

e-ISBN 978-3-7643-8364-0
www.birkhauser.ch

PURE AND APPLIED GEOPHYSICS
Vol. 164, No. 2–3, 2007

Contents

Pure appl. geophys. 164 (2007) 249–259
0033–4553/07/030249–11
DOI 10.1007/s00024-006-0172-5



Pure and Applied Geophysics

# Tsunami and its Hazard in the Indian and Pacific Oceans: Introduction

K. SATAKE,[1] E. A. OKAL,[2] and J. C. BORRERO[3]

*Abstract*—The 2004 Indian Ocean tsunami caused an estimated 230,000 casualties, the worst tsunami disaster in history. A similar-sized tsunami in the Pacific Ocean, generated by the 1960 Chilean earthquake, commenced international collaborations on tsunami warning systems, and in the tsunami research community through the Tsunami Commission of International Union of Geodesy and Geophysics. The IUGG Tsunami Commission, established in 1960, has been holding the biannual International Tsunami Symposium (ITS). This volume contains selected papers mostly presented at the 22nd ITS, held in the summer of 2005. This introduction briefly summarizes the progress of tsunami and earthquake research as well as international cooperation on tsunami warning systems and the impact of the 2004 tsunami. Brief summaries of each paper are also presented.

**Key words:** Tsunami, Sumatra-Andaman earthquake, Indian Ocean, Pacific Ocean, seismology, tsunami warning system, IUGG Tsunami Commission.

## 1. Introduction

The 2004 Indian Ocean tsunami was the worst tsunami disaster in history. The tsunami, caused by the giant Sumatra-Andaman earthquake ($M_w$ 9.3; STEIN and OKAL, 2005) on December 26, 2004, devastated the shores of the Indian Ocean. The total number of victims, dead and missing together, is estimated as 230,000 (INTERNATIONAL FEDERATION OF RED CROSS AND RED CRESCENT SOCIETIES, 2005); the largest in Indonesia (163,795), followed by Sri Lanka (35,399), India (16,389), Thailand (8,345), and Somalia (298).

In the Pacific Ocean, a similar, basin-wide tsunami occurred in 1960. This tsunami was generated by the giant Chilean earthquake, which remains the largest instrumentally-recorded earthquake on record ($M_w$ 9.5). The tsunami caused more than 1,000 casualties along the Chilean coast, then propagated across the Pacific

[1] Geological Survey of Japan, National Institute of Advanced Industrial Science and Technology, Tsukuba, 305-8567, Japan.
[2] Department of Geological Sciences, Northwestern University, Evanston, IL 60208-2150, USA.
[3] Tsunami Research Center, University of Southern California, Los Angeles, CA 90089-2531, USA.

Ocean, taking 61 lives in Hawaii 15 hours later, and reaching the coast of Japan in 23 hours and claiming 142 more casualties. Following this Pacific-wide tsunami, international collaborations started on operational tsunami warning systems and scientific studies of tsunamis.

The Tsunami Commission of IUGG (International Union of Geodesy and Geophysics) was established immediately after the 1960 tsunami. The Tsunami Commission organizes the biannual International Tsunami Symposium (ITS). The 22nd ITS was held in Chania, Greece, from July 27 to 29, 2005, with approximately 90 participants from 20 countries. This volume contains selected papers presented at the meeting and a few other papers, and reflects tsunami research after the 2004 Indian Ocean tsunami.

In this introductory paper, Section 2 reviews international cooperation and progress on earthquake and tsunami research in the last half century. Section 3 describes the impacts of the 2004 Indian Ocean tsunami. Finally in Section 4 we briefly introduce the papers in the following categories; survey and research results on the 2004 and other recent tsunamis, geological studies of older tsunamis, and studies on tsunami hazard analysis.

## 2. Status Before the 2004 Tsunami

### 2.1. International Coordination on Tsunami Warning Systems

After the 1960 tsunami, which affected many countries around the Pacific Ocean, international coordination was initiated by the IOC (Intergovernmental Oceanographic Commission) under UNESCO (United Nations Educational, Scientific and Cultural Organization). In 1965, IOC set up ITIC (International Tsunami Information Center) in Hawaii with support from the USA NOAA (National Oceanic and Atmospheric Administration). With the mission of mitigating tsunami hazards around the Pacific, ITIC coordinates international activities on tsunami warning systems, helps countries to establish national warning and mitigation systems, collects publications and other materials on tsunami events, develops educational and awareness materials, and serves as an information resource on tsunamis. The ICG/ITSU (International Coordination Group for the Tsunami Warning System in the Pacific) was also established under the auspices of IOC, and first convened in 1968. The ICG/ITSU as of 2006 has 30 member countries and holds a biannual meeting to exchange information and coordinate international activities in the Pacific.

For operational tsunami monitoring and warning activities in the Pacific, three tsunami warning centers have been established. The PTWC (Pacific Tsunami Warning Center), established in 1949 following the 1946 Aleutian tsunami, serves as the international warning center for the Pacific. The WC/ATWC (West Coast/Alaska

Tsunami Warning Center), established in 1967 following the 1964 Alaska earthquake tsunami, serves as a sub-regional center for the western USA and Canada. In 2006, Japan commenced operation of the Northwest Pacific Tsunami Advisory Center to provide advisories to the northwest Pacific. These centers, operated by USA NOAA and Japan Meteorological Agency, monitor seismic activity around the Pacific, and issue tsunami warnings for the Pacific countries. All the centers share information and coordinate message content before issuing advisories.

### *2.2. International Collaboration in Research Community*

The Tsunami Commission was established at the 12th general assembly of International Union of Geodesy and Geophysics (IUGG). The Tsunami Commission is closely related to three associations of the IUGG, IASPEI (International Association of Seismology and Physics of the Earth's Interior), IAVCEI (International Association of Volcanology and Chemistry of the Earth's Interior) and IAPSO (International Association for the Physical Sciences of the Oceans). The Tsunami Commission also organizes the biannual International Tsunami Symposium and publishes Proceedings with selected papers presented at the Symposium.

Since 1992, many tsunamis have occurred in the world. The development of the internet has accelerated international collaboration through the 1990s. Immediately after the 1992 Nicaragua tsunami, an e-mail list, then called Nicaragua Bulletin Board, was set up, and has been used ever since as a forum for international collaboration and exchange of information. Now called the Tsunami Bulletin Board (TBB), this service is maintained by ITIC.

The Tsunami Commission has also performed successful international projects. The Tsunami Inundation Modeling Exchange (TIME) project distributed computer software, a support manual and conducted training programs to teach tsunami inundation modeling techniques using a numerical model developed at Tohoku University in Japan. Under the Historical Tsunami Data Base project, a repository of tsunami data has been established and is maintained through the joint efforts of the Institute of Computational Mathematics and Mathematical Geophysics, in Novosibirsk, Russia and the National Geophysical Data Center, Boulder, Colorado, USA, which also serves as the World Data Center – Solid Earth Geophysics – Tsunamis.

### *2.3. Scientific Developments*

In 1960, when the giant Chilean earthquake generated a Pacific-wide tsunami, little was known about tsunami generation. Most of the current seismological concepts have been developed since the 1960s. Plate tectonic theory was introduced in the 1960s and now explains the mechanism of great or giant earthquakes. Mathematical models of earthquake source were developed in the 1960s to relate

seismic moment and size of fault. On the observational side, the World Wide Standard Seismic Network was deployed in the 1960s.

In the 1970s, using these theories and observed data, fault parameters of many large earthquakes in the world were determined. The moment magnitude ($M_w$) scale, based on seismic moment, was also introduced. It took more than a decade to accurately estimate the size of the 1960 Chilean earthquake. Theoretical and computational developments made it possible to compute seafloor deformation from fault models and the tsunami propagation on actual bathymetry.

Since the 1980s, seismograms have been recorded digitally, which has improved data quality and reduced processing times. As a result, basic earthquake source parameters can be estimated quickly and almost automatically. Heterogeneous slip distributions (asperities) on the fault also have been studied. Large-scale numerical simulations of tsunamis also became popular in the 1980s.

In the 1990s, developments in computer networking have made it possible to share the results of seismic wave analysis and tsunami numerical simulations in real time through the internet. In addition to instrumental seismology, historical and geological studies of past earthquakes and tsunamis have made important discoveries around the Pacific, advancing our understanding of tsunami hazards and recurrence intervals.

At present, after a large earthquake, globally observed seismological and sea-level data, as well as initial estimation of earthquake source parameters, are available within minutes through the internet. Based on these data and information, more seismological and tsunami studies are made and the results are also shared in real time. The development of the internet thus made positive feedback and accelerated tsunami research.

## *3. Impacts of the 2004 Tsunami*

### *3.1. International Activities*

The lack of a tsunami warning system in the Indian Ocean contributed to the severity of the 2004 Indian Ocean tsunami. At the 2005 IOC general assembly, it was proposed and adopted to organize ICGs (Intergovernmental Coordination Groups) in oceans and basins other than the Pacific. They are ICG/IOTWS (ICG for the Indian Ocean Tsunami Warning and Mitigation System), ICG/NEAMTWC (ICG for the Tsunami Early Warning and Mitigation System in the northeastern Atlantic, the Mediterranean and connected seas), and ICG/CARIBE-EWS (ICG for Tsunami and Coastal Hazards Warning System for the Caribbean and Adjacent Regions). The ICG/ITSU for the Pacific has been renamed as ICG/PTWS (ICG for the Pacific Tsunami Warning and Mitigation System). ICG/PTWC performed the first

international tsunami drill for issuing and transmitting tsunami warning messages in May 2006.

Among the scientific community, information on tsunami damage, survey plans and obtained data or research results have been exchanged and discussed through Tsunami Bulletin Board (TBB). Within a month after December 26, about 500 mails were posted to the TBB. Through such coordination, hundreds of tsunami scientists around the world participated in tsunami surveys, most of them consisting of international teams, to document the 2004 tsunami. The survey data were also shared through the Tsunami Bulletin Board and individual websites. The surveys showed that tsunami heights were very large around Band Aceh (maximum 30 m) on Sumatra Island. They were 5 to 15 m along Thailand and Sri Lanka coast, but much smaller in Myanmar ($< 3$ m) or the Andaman Islands ($< 5$ m).

At the business meeting held during the 22nd ITS, the Tsunami Commission decided to publish collections of selected papers presented at the Symposium. The Commission also organized Working Groups to collect field data, survey results, tide gauges and satellite data on the 2004 Indian Ocean tsunami.

### *3.2. Scientific Impacts*

There are several new lines of scientific progress resulting from the 2004 Indian Ocean tsunami. Numerical simulations were made immediately; with several groups performing the numerical simulations within hours after the event and posting the results on websites.

Sea-level monitoring stations, namely GLOSS (Global Sea Level Observation System) stations and stations in Australia, the Pacific and Atlantic Oceans recorded the 2004 tsunami (RABINOVICH and THOMSON, 2007). For tsunami recording, higher sampling interval (1 min) than ordinary tide (typically 6 min) is required. Such digital data were provided to researchers through websites in real- or semi-real-time.

High-resolution satellite images, taken before and after the tsunami, made it possible to estimate the tsunami damage in the hardest-hit areas such as Banda Aceh (e.g., BORRERO, 2005). Snapshots of nearshore tsunamis (e.g., on Sri Lanka coasts) were recorded in high-resolution satellite images. Tsunami propagation across the Indian Ocean was also captured by satellite altimeter (JASON-1) data (e.g., FUJII and SATAKE, 2007).

Numerous reports and papers have been published regarding the 2004 earthquake and tsunami, and it is almost impossible to list all of them. Here we only refer to special issues of other scientific journals. A special section in *Science* on May 20, 2005 (BILHAM, 2005) contains papers mostly on the seismological aspects. The special issue of *Earth, Planets and Space* (vol. 58, no. 2) contains 20 papers on various aspects such as GPS measurements or tsunami surveys (TANIOKA *et al.*, 2006). The June 2006 issue of *Earthquake Spectra* contains 44 reports, mostly on tsunami field surveys and societal responses (IWAN, 2006). A special issue of *Bulletin*

*of Seismological Society of America* contains 22 papers on seismological and tsunami analysis (BILEK *et al.*, 2007).

### *3.3. Future Improvements*

Despite the advances mentioned in the previous subsection, we still need to improve our scientific understanding of tsunamis. We are still unable to accurately forecast coastal tsunami heights in real time. Initial numerical simulations made after the Sumatra earthquakes in December 2004 and March 2005 assumed a generalized source mechanism and computed tsunami propagation over the relatively coarse ETOPO2, 2 min gridded bathymetry data (SMITH and SANDWELL, 1997). Although these data are accurate for deep oceans, shallow bathymetry is not accurate enough to be used for reliable tsunami forecasting. Hence the numerical simulations reproduce the overall features of tsunami propagation but cannot predict accurate arrival times and amplitudes. Nearshore tsunami effects can be accurately reproduced using available numerical codes for tsunami generation, propagation and inundation, however the results depend heavily on detailed information on the source mechanism as well as on local bathymetric and topographic features.

Since it is unlikely that the detailed analysis of the seismic signals will accelerate significantly nor will there ever be established a comprehensive database of detailed bathymetry for every coast in the world, it is important that we develop the technology to continuously monitor the tsunamigenic regions of the world and directly observe tsunami generation and propagation. Offshore tsunameters (buoys) capable of relaying real-time information to warning centers are essential for determining whether or not a tsunami has been generated and how big the wave will be when it reaches the coast. Dense networks of costal sea-level gauges in tsunami-prone areas provide important confirmation of a tsunami's generation, so that more distant communities can be warned. All of these will enable more informed evacuation decisions, as well as eliminate costly and potentially dangerous false evacuations. Satellite technology should also be improved to allow for targeted tsunami observation and rapid damage assessment for remote or inaccessible locations. Of course, the real-time availability and exchange of these data are essential to improving our understanding of a tsunami event as it unfolds and for saving lives and property. It is also important to urge port and harbor officials to install or upgrade tide measuring stations to record water levels at a higher sampling rate (1-minute or shorter) on a continuous or event-triggerred basis.

For long-term forecast of future tsunamis, probabilistic estimation can be made based on the study of past tsunamis, using historical and geological data. Paleoseismological work in the Nicobar and Andaman Islands would help us to understand the occurrence and recurrence of great earthquakes in the Indian Ocean since prehistoric time.

## 4. Contents of this Issue

### 4.1. On the 2004 Indian Ocean Tsunami

As a part of the Tsunami Commission Working Group on tide gauge data, RABINOVICH and THOMSON (2007) collected and compiled about 50 tide gauge records around the Indian Ocean and provided analysis such as arrival times, maximum amplitude and spectral components.

Tsunami was also recorded on hydrophones or seismometers. OKAL *et al.* (2007) analyzed the hydrophone records at Diego Garcia and showed that the tsunami signal is detected in a very wide period range (about 90 s to 3000 s), beyond the shallow-water approximation. The dispersion character was modeled by normal mode theory. OKAL (2007) shows that the 2004 Indian Ocean tsunami and other recent tsunamis are recorded on horizontal components of seismometers. The seismic detection of a tsunami can be modeled by using normal mode theory of the Earth including the tsunami mode, thus leading to estimate the seismic moment of parent earthquake from tsunami records.

OKAL and TITOV (2007) proposed a new magnitude scale, $M_{TSU}$, from spectral amplitude of tsunami. Similar to the mantle magnitude, $M_m$, the method is based on normal-mode theory and uses variable frequency, hence it is free from saturation. They demonstrate that the new magnitude scale recovers the seismic moment within a factor of two (0.2 in magnitude scale) from DART tsunameter records, and from satellite sea-surface data obtained for the 2004 tsunami in the Indian Ocean.

The 2004 tsunami was also detected in the Atlantic and Pacific Oceans. KOWALIK *et al.* (2007) carried out a tsunami simulation on the global ocean while monitoring energy flux. They found many important features of the tsunami. Reflection from the coasts of Sri Lanka and Maldives were larger than the direct wave; the tsunami entered the Pacific Ocean through various routes; the amplified tsunami energy arrived much later than the first arrival.

INOUE *et al.* (2007) reports tsunami heights, arrival times and damage along the Sri Lankan coast. A damaging tsunami had never been observed on this island country, and then the 2004 tsunami resulted in about 36,000 victims. KELLETAT *et al.* (2007) examined the geological effects of the 2004 tsunami on the Thai coast. They found minimal geomorphological changes and tsunami traces in their survey immediately after the tsunami. Based on their observations, they concluded that the 2004 tsunami was considerably smaller than the paleo-tsunami events in the Atlantic Ocean or Caribbean Sea that transported boulders.

### 4.2. Analysis and Simulations for other Tsunamis

The last disastrous tsunami prior to the 2004 tsunami was the 1998 tsunami in Papua New Guinea. This event generated tsunami waves as large as 15 m around

Sissano Lagoon near the epicenter and casualties estimated at 2,200. JOKU *et al.* (2007) report on their follow-up surveys of eyewitness accounts of this tsunami on the coast west of the tsunami source region. They also summarize the experiences of coastal residents from historical tsunamis since 1940.

Large tsunamis, including the 2004 event, demonstrate strong directivity; the largest tsunami heights were in directions perpendicular to the source, e.g., Sumatra, Thai and Sri Lankan coasts. ABE (2007) found that in the direction of the long axis of the tsunami source, or in the direction where the smallest tsunami amplitudes are observed, the source length is represented well by the period of the initial tsunami wave. Through examinations of tide gauge records from four large Japanese earthquakes in the last few decades, he measured the periods of the initial tsunami wave, estimated the source length assuming that the observed period is equal to the tsunami travel time across the source, and found that they are well correlated with the earthquake magnitudes.

CHERNIAWSKY *et al.* (2007) carried out numerical simulations of tsunamis in the southern Vancouver Islands from possible scenario earthquakes in the Cascadia region of the Pacific Northwest. A very fine bathymetry grid, as small as 10 m, is used in their simulation, and tsunami run-up on land is considered. The computed coastal tsunami heights are mostly 5–8 m, with the maximum of 16 m, and larger than those inferred from paleoseismological studies. The simulation also predicts very fast current velocity up to 17 m/s (33 knots).

### *4.3. Geological Studies of old Tsunamis*

Geological records or tsunami deposits have been studied around the Pacific Ocean for the last two decades. KOMATSUBARA and FUJIWARA (2007) provide an overview of such studies carried out in southwestern Japan along Nankai, Suruga and Sagami troughs. Many studies of tsunami deposits have been carried out in the last 15 years but most of them were reported in Japanese language and not known to the international community. The geological records cover a much longer time range than the historical records. The inferred recurrence interval is variable; the shortest ones are similar to those estimated from historical records.

In the Cascadia subduction zone, off the Pacific Northwest of the USA and Canada, the recurrence of giant earthquakes similar in size to the 2004 event has been inferred from geological and historical records. KILFEATHER *et al.* (2007) extended such studies on tsunami deposits by examining micro-structures in thin sections. They found millimeter-scale stratigraphic features indicating multiple waves of tsunamis, that are not visible on a macro-scale in the field.

FREUNDT *et al.* (2007) examined geological traces of past tsunamis around two lakes in Nicaragua, Lake Nicaragua and Lake Managua. These tsunamis were of volcanic origin, generated by pyroclastic flows or debris avalanches from flank

collapse of nearby volcanoes. They emphasize that the tsunamis in shallow lakes can be highly disastrous, not only in Nicaragua but also in other countries.

### *4.4. Tsunami Hazard Analysis*

Probabilistic models have been developed to estimate coastal tsunami heights from future earthquakes. Such methods have been widely used for seismic hazard (Probabilistic Seismic Hazard Analysis), but only recently applied to tsunamis. POWER *et al.* (2007) developed a Probabilistic Tsunami Hazard Analysis (PTHA) method and applied it for estimating probabilistic tsunami heights from distant earthquakes. The end result is a map showing expected maximum tsunami heights in the next 500 years around New Zealand from earthquakes off South America.

A method for evaluating tsunami risk at nuclear power facilities in Japan is proposed by YANAGISAWA *et al.* (2007). Their method is based on a parametric study, in which numerical simulations are repeated for element tsunamis with various fault parameters, and the element tsunami with the greatest influence is selected as the design tsunami. The design tsunami is further compared with the historical data to ensure that it produces tsunami heights larger than those historically recorded. ANNAKA *et al.* (2007) proposed a logic-tree approach for PTHA. Their end product is a hazard curve, a relationship between coastal tsunami heights and the probability of exceedance at a particular site. The hazard curve is obtained by integration over the aleatory uncertainties, whereas a large number of hazard curves are obtained for different branches of logic-trees representing epistemic uncertainty, such as tsunami sources, size and frequency of tsunamigenic earthquakes, standard errors of estimated tsunami heights.

ORFANOGIANNAKI and PAPADOPOULOS (2007) examined the stochastic methods to compute the probability of tsunami generation from historical data of tsunami and earthquakes. Two methods, based on the conditional probability of tsunami occurrence and the total probability theorem, are compared to estimate the probabilities in three regions around the Pacific: South America, Kuril-Kamchatka and Japan.

FARRERAS *et al.* (2007) reports developments of the Mexican national program for tsunami hazard reduction. It consists of a sea-level monitoring system with real-time data access, deployment of a numerical simulation to construct tsunami inundation maps for coastal communities, and publication and distribution of educational material on tsunamis. These efforts cover the three important areas, warning guidance, hazard assessment and mitigation of tsunami hazard reduction on both national and international levels.

The coastal behavior of tsunamis, such as wave fission or wave breaking, can be studied by laboratory experiments. MATSUYAMA *et al.* (2007) report their experiments on tsunami wave fission and wave-breaking in large-scale undistorted experiments.

## References


Abe, K. (2007), *Phases representing source lengths of tsunamis in tide gauge records*, Pure Appl. Geophys. *164*, 453–463.

Annaka, T., Satake, K., Sakakiyama, T., Yanagisawa, K., and Shuto, N. (2007), *Logic-tree approach for probabilistic tsunami hazard analysis and its applications to the Japanese coasts*, Pure Appl. Geophys. *164*, 577–592.

Bilham, R. (2005), *A flying start, then a slow slip*, Science *308*, 1126–7.

Bilek, S.L., Satake. K., and Sieh, K. (2007), *Preface to the issue dedicated to the 2004 Sumatra-Andaman earthquake*, Bull. Seismol. Soc. Am. *97*, 1–5.

Borrero, J.C. (2005), *Field data and satellite imagery of tsunami effects in Banda Aceh*, Science *308*, 1596.

Cherniawsky, J.Y., Titov, V.V., Wang, K., and Li, J.-Y. (2007), *Numerical simulations of tsunami waves and currents for southern Vancouver Island from a Cascadia megathrust earthquake*, Pure Appl. Geophys. *164*, 465–492.

Fujii, Y. and Satake, K. (2007), *Tsunami source of the 2004 Sumatra-Andaman earthquake inferred from tide gauge and satellite data*, Bull. Seismol. Soc. Am. *97*, 192–207.

Farreras, S., Ortiz, M., and Gonzalez, J.I. (2007), *Steps towards the implementation of a tsunami detection, warning, mitigation and preparedness program for southwestern coastal areas of Mexico*, Pure Appl. Geophys. *164*, 605–616.

Freundt, A., Strauch, W., Kutterolf, S., and Schmincke, H.-U. (2007), *Volcanogenic tsunamis in lakes: examples from Nicaragua and general implications*, Pure Appl. Geophys. *164*, 527–545.

Inoue, S., Wijeyewickrema, A.C., Matsumoto, H., Miura, H., Gunaratna, P., Madurapperuma, M., and Sekiguchi, T. (2007), *Field survey of tsunami effects in Sri Lanka due to the Sumatra-Andaman earthquake of December 26, 2004*, Pure Appl. Geophys. *164*, 395–411.

International Federation of Red Cross and Red Crescent Societies, *World Disasters Report*. (Kumarian Press, 2005), 246 p.

Iwan, W.D. (2006), *Preface to the Issue dedicated to the 2004 Sumatra-Andaman earthquake*, Earthq. Spectra *22*, S3, xi.

Joku, G.N., Davies, J.M., and Davies, H.L. (2007), *Eye-witness accounts of the impact of the 1998 Aitape tsunami, and of other tsunamis in living memory, in the region from Jayapura, Indonesia, to Vanimo, Papua New Guinea*, Pure Appl. Geophys. *164*, 433–452.

Kelletat, D., Scheffers, S., and Scheffers, A. (2007), *Field signatures of the SE-Asian mega-tsunami along the West Coast of Thailand compared to holocene paleo-tsunami from the atlantic region*, Pure Appl. Geophys. *164*, 413–431.

Kilfeather, A.A., Blackford, J.J., and van der Meer, J.J.M. (2007), *Micromorphological analysis of coastal sediments from Willapa Bay, Washington, USA: A technique for analysing inferred tsunami deposits*, Pure Appl. Geophys. *164*, 509–525.

Komatsubara, J. and Fujiwara, O. (2007), *Overview of Holocene tsunami deposits along the nankai, Suruga, and Sagami Troughs, southwest Japan*, Pure Appl. Geophys. *164*, 493–507.

Kowalik, Z., Knight, W., Logan, T., and Whitmore, P. (2007), *The tsunami of 26 December 2004: Numerical modeling and energy considerations*, Pure Appl. Geophys. *164*, 379–393.

Matsuyama, M., Ikeno, M., Sakakiyama, T., and Takeda, T. (2007), *A study on tsunami wave fission in an undistorted experiment*, Pure Appl. Geophys. *164*, 617–631.

Okal, E.A. (2007), *Seismic records of the 2004 Sumatra and other tsunamis: A quantitative study*, Pure Appl. Geophys. *164*, 325–353.

Okal, E.A., Talandier, J., and Reymond, D. (2007), *Quantification of Hydrophone records of the 2004 Sumatra tsunami*, Pure Appl. Geophys. *164*, 309–323.

Okal, E.A. and Titov, V.V. (2007), $M_{TSU}$: *Recovering seismic moments from tsunameter records*, Pure Appl. Geophys. *164*, 355–378.

Orfanogiannaki, K. and Papadopoulos, G.A. (2007), *Conditional probability approach of the assessment of tsunami potential: application in three tsunamigenic regions of the Pacific Ocean*, Pure Appl. Geophys. *164*, 593–603.

Power, P., Downes, G., and Stirling, M. (2007), *Estimation of tsunami hazard in New Zealand due to South American earthquakes*, Pure Appl. Geophys. *164*, 547–564.

RABINOVICH, A.B. and THOMSON, R.E. (2007), *The 26 December 2004 Sumatra tsunami: analysis of tide gauge data from the World Ocean: Part 1. Indian Ocean and South Africa*, Pure Appl. Geophys. *164*, 261–308.

SMITH, W.H.F. and SANDWELL, D.T. (1997), *Global sea floor topography from satellite altimetry and ship depth soundings*, Science *277*, 1956–1962.

STEIN, S. and OKAL, E.A. (2005), *Speed and size of the Sumatra earthquake*, Nature *434*, 581–582.

TANIOKA, Y., GEIST, E.L., and PUSPITO, N.T. (2006), *Preface to special issue* "The 2004 great Sumatra earthquake and tsunami", Earth, Planet Space *58*, 111.

YANAGISAWA, K., IMAMURA, F., SAKAKIYAMA, T., ANNAKA, T., TAKEDA, T., and SHUTO, N. (2007), *Tsunami assessment for risk management at nuclear power facilities in Japan*, Pure Appl. Geophys *164*, 565–576.

Pure appl. geophys. 164 (2007) 261–308
0033–4553/07/030261–48
DOI 10.1007/s00024-006-0164-5



Pure and Applied Geophysics

# The 26 December 2004 Sumatra Tsunami: Analysis of Tide Gauge Data from the World Ocean Part 1. Indian Ocean and South Africa

Alexander B. Rabinovich,[1,2] and Richard E. Thomson[1]

*Abstract*—The $M_w$ = 9.3 megathrust earthquake of December 26, 2004 off the northwest coast of Sumatra in the Indian Ocean generated a catastrophic tsunami that was recorded by a large number of tide gauges throughout the World Ocean. Part 1 of our study of this event examines tide gauge measurements from the Indian Ocean region, at sites located from a few hundred to several thousand kilometers from the source area. Statistical characteristics of the tsunami waves, including wave height, duration, and arrival time, are determined, along with spectral properties of the tsunami records.

**Key words:** 2004 Sumatra tsunami, tide gauge records, Sumatra earthquake, Indian Ocean, tsunami travel time, spectral analysis.

## 1. Introduction

At 07:59 Local Indonesian Time (00:59 UTC) on December 26, 2004, a magnitude $M_w$ = 9.3 megathrust earthquake occurred along 1300 km of the oceanic subduction zone from northwestern Sumatra Island to the Andaman Islands in the eastern Indian Ocean (Stein and Okal, 2005; Lay *et al.*, 2005a). The earthquake generated highly destructive tsunami waves that severely damaged the coastal regions of the Indian Ocean and killed more than 226,000 people (International Federation of Red Cross and Red Crescent Societies, 2005). Because of international tourism, many countries far removed from the major disaster areas lost citizens, triggering the largest international aid and relief effort in history. Tsunami waves recorded around the world revealed the unprecedented global reach of the 2004 tsunami (Titov *et al.*, 2005).

The December 2004 tsunami is one of very few well documented global-scale tsunamis for which waves generated in one ocean propagate into other oceans. The first known global tsunami — that associated with the Krakatau Volcano explosion

[1] Department of Fisheries and Oceans, Ocean Sciences Division, Institute of Ocean Sciences, 9860 West Saanich Road, Sidney, B.C., V8L 4B2 Canada.
[2] Russian Academy of Sciences, P.P. Shirshov Institute of Oceanology, 36 Nakhimovsky Prosp., Moscow, 117997 Russia.

of 27 August 1883 (cf., MURTY, 1977) — was generated in the same region (the Indonesian Archipelago), demonstrating the potential of this region as a major source for worldwide catastrophic tsunamis. The 1883 Krakatau tsunami was recorded by 35 tide gauges, including gauges in Le Havre (France), Kodiak Island (Alaska) and San Francisco (SYMONS, 1888; PELINOVSKY *et al*., 2005). However, a common opinion (cf., EWING and PRESS, 1955; GARRETT, 1970) is that tsunami waves recorded at far-field sites originated from coupling between the ocean surface and the eruption-induced atmospheric waves (that circuited the globe three times, see MURTY, 1977) rather than from direct water waves propagated from the source area. The limited quality of the analog records available for the 1883 tsunami, and the sketchy information on the source characteristics for the waves, do not allow a thorough quantitative analysis of the tsunami wave properties and global propagation pattern. An interesting attempt to model the global effect of this tsunami is presented by CHOI *et al*. (2003).

The second known global tsunami was the Chilean tsunami of May 22, 1960. The $M_w$ = 9.5 earthquake off the coast of South Central Chile (the strongest ever recorded) generated one of the most destructive trans-Pacific tsunamis. The tsunami was measured by about 250 tide gauges in the Pacific Ocean (BERKMAN and SYMONS, 1960; WIGEN, 1960; TAKAHASHI and HATORI, 1961). Tsunami waves observed at many far-field sites (ten thousand kilometers from the source area) were very strong: For example, tsunami trough-to-crest of heights recorded at Attu Island (Alaska), Crescent City and Santa Monica (both California), were more than 3–4 m (BERKMAN and SYMONS, 1960). However, all these records were analog records in which the crests and troughs of the largest waves (i.e., those most important for analysis) were frequently chopped off because the instruments of the day were not designed to measure such strong oscillations. Moreover, it appears that no attention was paid to possible recordings of this tsunami outside of the Pacific Ocean; the single exception being the records at Fremantle and Port MacDonnell on the Indian Ocean coast of Australia (these records were assembled along with Australian records for the Pacific coast; cf., BERKMAN and SYMONS, 1960). Evidence that the 1960 Chilean tsunami was a global-scale event was provided over 25 years later when VAN DORN (1987) examined British and other hydrographic archives and located a few records of this tsunami at sites in the Indian Ocean (Bunbury, Australia; Mossel Bay, South Africa; and Mauritius Island) and Atlantic Ocean (Luderitz, South Africa; Newlyn, UK; and Bermuda).

The 2004 Sumatra tsunami was the third known global-scale tsunami, but the first to occur during the ''instrumental era,'' and it was clearly recorded by a large number of tide gauges throughout the World Ocean, including tide gauges located in the North Pacific and North Atlantic (RABINOVICH *et al*., 2006). Global tsunami propagation models (TITOV *et al*., 2005; KOWALIK *et al*., 2005) demonstrate that mid-ocean ridges served as waveguides to the 2004 event, efficiently transmitting tsunami energy from the source area to far-field regions of the Pacific and Atlantic coasts of North America. The 2004 Sumatra tsunami is now recognized as the most globally

distributed and accurately measured tsunami in recorded history. More than 200 digital records of this tsunami are available (cf., Institute of Ocean Sciences http://www-sci.pac.dfo-mpo.gc.ca/osap/projects/tsunami/tsunamiasia_e.htm) and months after the event, tsunami measurements were still being collected and archived. Some of these data have been previously examined (cf., MERRIFIELD *et al.*, 2005; WOODWORTH *et al.*, 2005; TITOV *et al.*, 2005; NAGARAJAN *et al.*, 2006; TSUJI *et al.*, 2006; RABINOVICH *et al.*, 2006; FUJII and SATAKE, 2007). However, most of the data remain unexamined and unpublished. The purpose of our three-part study is to provide an overview of all available records for the 2004 Sumatra tsunami and to present fundamental statistical characteristics of these records. This study was initiated by the Working Group on Tide Gauge Measurements of the 2004 Sumatra Tsunami, IUGG Tsunami Commission. This first part focuses on the Indian Ocean; the second part will deal with the Atlantic Ocean, and the third part, with the Pacific Ocean.

In general, our ability to detect tsunami waves in a tide gauge record depends strongly on the signal/noise ratio of the data. For example, for the North Pacific and North Atlantic records, the 2004 Sumatra tsunami signal-to-background noise ratio typically ranged from 4:1 to 1:1, and was even lower at some sites, making tsunami detection difficult (RABINOVICH *et al.*, 2006). In contrast, for the Indian Ocean this ratio ranged from 40:1 to 20:1, so detection was straightforward. The main problems with the Indian Ocean records are the inadequate quality of some instruments, the overly long sampling interval (up to 1 hour at Kerguelen and St. Paul islands), extensive gaps in the data due to instrument and transmission problems, and damage from tsunami waves (some of the gauges were totally destroyed). In the present study, we filled gaps in the residual (de-tided) series with zeros. Data processing is similar to that described by RABINOVICH *et al.* (2006), including: (1) preliminary analysis, verification and correction of the original data; (2) de-tiding; (3) tsunami detection and statistical analysis; (4) high-frequency filtering (only for plotting purposes); (5) spectral analysis (except for the poor quality records or records with a sampling interval $\geqslant$ 30 min); and (6) time-frequency (wavelet-type) analysis. Published material has been used for those sites (in Thailand and at Port Blair, Andaman Islands, India) for which we do not have the original time series records.

Because tide gauge records available for the various sites had markedly different durations, sampling intervals and quality (some series had numerous gaps), we were required to select series with differing lengths for statistical, spectral and time-frequency analysis. We also had to take into account the actual length of the "ringing" (the duration of tsunami oscillations with significant wave heights) which was of much shorter duration for sites located relatively close to the source area (e.g., for the Maldives stations) than for the distant sites (e.g., South African stations). Despite these constraints, we tried to be consistent in our analysis by keeping the same analysis format and by assembling stations into comparable groups.

Known tide gauge records of the 2004 Sumatra tsunami in the Indian Ocean were separated into five groups (Fig. 1). The first group (Section 2) included records from stations in the Tropical Indian Ocean, specifically ten digital GLOSS stations and two digital Australian stations (the Cocos Islands and Hillarys). These records were probably the best known and widely used (cf., MERRIFIELD *et al*., 2005; LAY *et al*., 2005a; FINE *et al*., 2005; FUJII and SATAKE, 2007). Most of the instruments for these sites were located on isolated islands. As a result, the records were not significantly affected by local topography and are, therefore, especially valuable for the analysis of the source parameters and for comparison with numerical modeling of the tsunami. The second group of records (Section 3) consists of records from nine Indian sites: eight from mainland tide gauges and one from Port Blair on the Andaman Islands. We do not have the Port Blair record, so the statistical information on this record is mainly from NEETU *et al*. (2005) and SINGH *et al*. (2006). Focus in Section 4 is on the near-field instruments located on the coasts of Indonesia and Thailand (Group 3).

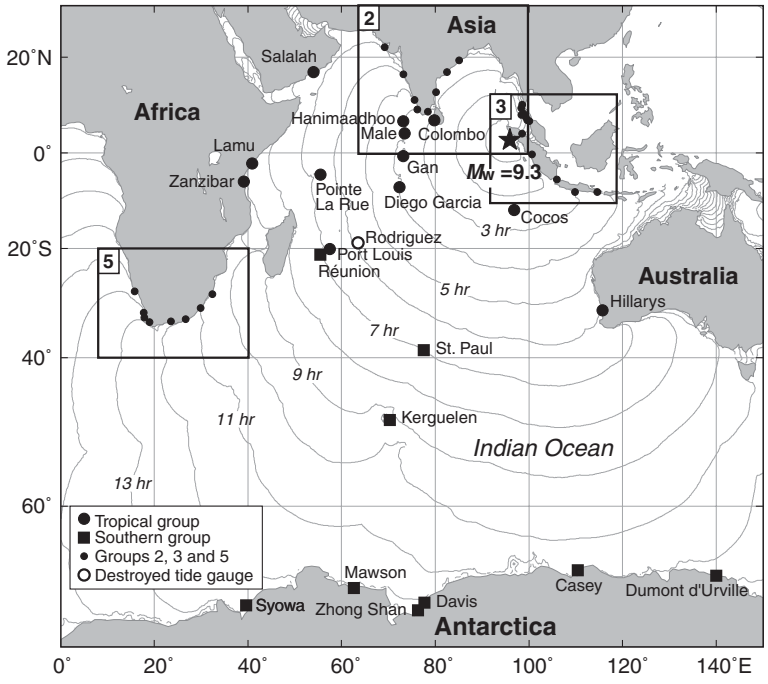


Figure 1

Map of the Indian Ocean showing the location of the $M_w$ = 9.3 earthquake epicenter (star) and positions of tide gauges. Also shown are locations of the "India" (2), "Thailand and Indonesia" (3), and "South Africa" (5) boxes and the approximate positions of tide gauges for the corresponding groups (Groups, 2, 3 and 5, respectively). The names of the stations for these groups and more exact positions are presented in Figures 5, 9, and 17. Solid thin lines are the hourly isochrones of the tsunami travel time from the source area.

A preliminary analysis of the analog records from these tide gauges was provided by MERRIFIELD *et al.* (2005), TSUJI *et al.* (2006) and TANIOKA *et al.* (2006). The Indonesian records have now been re-digitized and made available for processing. Section 5 describes the records from the southern part of the Indian Ocean and the Antarctic coast (Group 4), specifically from three French stations located on La Réunion, Kerguelen and St. Paul islands and the French Antarctic station Dumont d'Urville, and four stations from the Australian Antarctic Division (Casey, Davis, Zhong Shan, and Mawson). This section also examines the record from the Japanese Antarctic station Syowa (Showa). Finally, the records from eight South African stations (Group 5) are presented and analyzed in Section 6. Although four of these stations are actually located on the Atlantic coast of South Africa, we decided to include the South African records from all eight stations into one group and describe them in Part 1 of this study rather than separate them into Indian Ocean and Atlantic units. Section 7 provides a discussion of the main results and a comparison between different groups of stations.

## 2. Tropical Indian Ocean Stations

The 2004 Sumatra tsunami was accurately recorded by ten digital Global Sea Level Observing System (GLOSS) stations located in the central and western parts of the Tropical Indian Ocean; one other GLOSS station located at Rodriguez Island (Mauritius) was destroyed by the first tsunami wave that arrived. Most of these stations were float tide gauges in stilling wells located in harbors, bays and lagoons (MERRIFIELD *et al.*, 2005). Data for the GLOSS stations were obtained from the University of Hawaii's (Honolulu) Sea Level Center database http://ilikai.soest.hawaii.edu/uhslc/iotd. Three of the GLOSS gauges, Colombo (Sri Lanka), Hanimaadhoo (Maldives), and Port Louis (Mauritius), had sampling intervals $\Delta t = 2$ min; station Diego Garcia (UK) had 6 min sampling, and six other stations had 4 min sampling (Table 1). In this group, we have included two Australian stations: Hillarys (west coast of Australia) and the Cocos Islands (Fig. 1). The digital tide gauge data for these stations (with 1-min sampling) were provided by the Australian Bureau of Meteorology. The tsunami arrival times for the GLOSS stations and the Cocos Islands were used by LAY *et al.* (2005a), FINE *et al.* (2005) and FUJII and SATAKE (2007) in inverse wave-tracing algorithms to delineate the source region for the 2004 event; the estimates were in good agreement with geophysical delineations of the source region (cf., STEIN and OKAL, 2005; TSAI *et al.*, 2005). The 2004 tsunami was also recorded by several other tide gauges along the mainland coast of Australia, including tide gauges on the southern coast of Australia that are officially designated as Indian Ocean sites (stations west of 147°E). However, all mainland stations from the south, east and north coasts of Australia, except Hillarys, will be examined in Part 3 of our study for the Pacific Ocean.

Table 1

*Tsunami characteristics estimated from tide gauge records in the Tropical Indian Ocean. The number appearing in the brackets in column six denotes which wave in the sequence of incoming waves was highest*

| No | Station | Country | Coordinates | Sampling interval (min) | Maximum wave height (cm); number | First wave | |
|---|---|---|---|---|---|---|---|
| | | | | | | Sign, arrival time (UTC) | Travel time |
| 1 | Cocos Islands | Australia | 12.13°S; 96.88°E | 1 | 59 (1) | (+) 03:17 | 2hr 18min |
| 2 | Colombo | Sri Lanka | 06.93°N; 79.83°E | 2 | >300 (2?)* | (+) 03:49 | 2hr 50min |
| 3 | Hanimaadhoo | Maldives | 06.77°N; 73.18°E | 2 | 217 (1) | (+) 04:30 | 3hr 31min |
| 4 | Male | Maldives | 04.18°N; 73.52°E | 4 | 215 (1) | (+) 04:14 | 3hr 15min |
| 5 | Gan | Maldives | 00.68°S; 73.17°E | 4 | 139 (1) | (+) 04:16 | 3hr 17min |
| 6 | Diego Garcia | UK | 07.30°S; 72.38°E | 6 | 90 (1) | (+) 04:45 | 3hr 46min |
| 7 | Rodriguez I. | Mauritius | 19.67°S; 63.42°E | 2 | ? | (?) 06:40 | 5hr 41min |
| 8 | Port Louis | Mauritius | 20.15°S; 57.50°E | 2 | 195 (?) | (?) 07:46 | 6hr 47min |
| 9 | La Réunion | France | 20.92°S; 55.30°E | 0.5* | 70 (13) | (+) 07:55 | 6hr 56min |
| 10 | Hillarys | Australia | 31.82°S; 115.73°E | 1 | 108 (4) | (+) 07:14 | 6hr 15min |
| 11 | Salalah | Oman | 17.00°N; 54.00°E | 4 | 261 (3) | (+) 08:08 | 7hr 09min |
| 12 | Pointe La Rue | Seychelles | 04.68°S; 55.53°E | 4 | 278 (2) | (+) 08:16 | 7hr 17min |
| 13 | Lamu | Kenya | 02.27°S; 40.90°E | 4 | 100 (3) | (+) 09:52 | 8hr 53min |
| 14 | Zanzibar | Tanzania | 06.15°S; 39.18°E | 4 | 72 (4) | (+) 10:40 | 9hr 41min |

Comments: (1) The tide gauge at Colombo was damaged by the first tsunami wave and did not operate for 5 hr 40 min; eyewitnesses reported that the second wave was the highest.
(2) The "La Réunion" record was digitized from a float-type analog tide gauge (an analysis of this record is presented in Section 5).
(3) The sign in brackets indicates the sign of the first semi-wave: crest (+) or trough (–).
(4) The tide gauge at Port Louis ceased to operate for one hour; the sign of the first wave remains unknown.
(5) The tide gauge at Rodriguez Island was destroyed by the first arriving tsunami wave.

### *2.1. Statistical Characteristics*

Figure 2 presents de-tided records for the ten GLOSS and the two Australian stations. Due to technical problems, there were gaps in the Colombo, Hanimaadhoo, Gan and Port Louis records. These gaps prevented us from estimating exact statistical parameters for tsunami waves at these sites (Table 1). However, the general structure of the waves measured at each of these stations is well defined. MERRIFIELD *et al.* (2005) estimated the tsunami arrival times as the time of the first measured increase (or decrease) before the wave crest (or trough). In the present study, if there is a significant increase or decrease in water level between two successive observational samples, we have assumed that the actual arrival time is the time midway between the times of these samples; if the change is gradual, we take the first increase/decrease data point as the arrival time. This accounts for the small

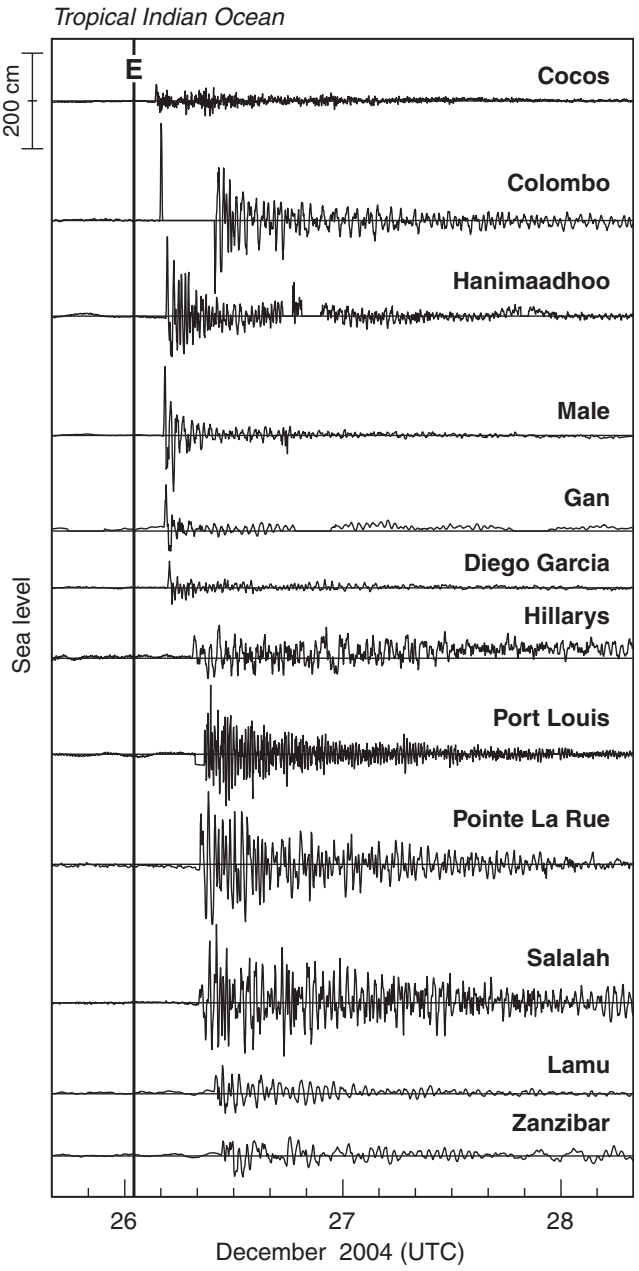


Figure 2
Tsunami records in the Indian Ocean for the 2004 Sumatra tsunami for 10 GLOSS and 2 Australian (Cocos and Hillarys) stations. Solid vertical line labelled ''E'' denotes the time of the main earthquake shock.

differences between our estimates (Table 1) and those of MERRIFIELD *et al.* (2005).[1] As noted above, the Rodriguez Island tide gauge (Mauritius) was destroyed by tsunami waves. In this case, the recording stop time is used to estimate the tsunami arrival and tsunami travel times (Table 1). For comparison, statistical characteristics of an analog record from La Réunion Island, France (a tropical island from the same group of the Mascarene Islands as Mauritius and Rodriguez — see Fig. 1) are also included in Table 1 (analysis of this record is presented in Section 5 together with other French records). Tsunami arrival times (TAT) estimated from direct observations are in good agreement with expected tsunami arrival times (ETA) obtained numerically (Fig. 1).

The main tsunami features evident in the records presented in Figure 2 are:

(a) Arrival times for tsunami waves at each site were abrupt and unambiguous;
(b) The first wave in most records was *positive* (wave crest);
(c) Maximum trough-to-crest wave heights ranged from 59 cm (Cocos Islands) to more than 2.5 m (Colombo, Salalah, and Pointe La Rue);
(d) Maximum waves occurred near the beginning of the first wave train; the first wave was maximum for the Cocos Islands, Hanimaadhoo, Male, Gan, and Diego Garcia; the second wave for Colombo (by eyewitness reports) and Pointe La Rue, the third wave for Salalah and Lamu; and the forth wave for Hillarys and Zanzibar. In general, the greater the distance and wave propagation time for the waves, the higher the sequence number (1st, 2nd, …) of the maximum wave (Table 1);
(e) The rate of tsunami energy decay was relatively fast for stations close to the source region (Cocos, Hanimaadhoo, Male, Gan and Colombo) and slowed with increasing station distance from the source (Hillarys, Port Louis, Pointe La Rue, Salalah, Lamu and Zanzibar);
(f) In general, the duration of tsunami ringing for distant sites increased with increasing distance from the source region, ranging from a few hours for Male and Gan to more than two days for Salalah and Pointe La Rue.
(g) The recorded oscillations were polychromatic, with different periods for different sites, but with clear dominance of 40–50 min waves at most sites. The exceptions are Port Louis (Mauritius) and the Cocos Islands, where 20-min waves prevailed.

The observational records and numerical simulations (TITOV *et al.*, 2005; KOWALIK *et al.*, 2005) indicate marked anisotropic spreading of tsunami energy from the source area. Most of the energy propagated toward the west and southwest, while only a fraction went toward the south and southeast. This aspect of energy spreading is mainly related to the orientation of the earthquake rupture. Most tsunami energy

[1] In Table 1 of MERRIFIELD *et al.* (2005), the tsunami arrival time for Diego Garcia was out by 1 hour and the tsunami arrival time for Port Louis was erroneously written as 7:42 instead of 7:46 (Mark Merrifield, Pers. Comm., 2006).

radiates normally (at 90°) to the direction of rupture; little energy radiates outward along the direction of the rupture. For this reason, tsunami waves at the Maldives, Seychelles and Salalah were considerably higher than those at the Cocos Islands, despite the fact that the latter are much closer to the source (~1650 km versus ~2500–5000 km).

### *2.2. Spectral Properties*

To determine the spectral properties of the tsunami waves at the twelve gauge sites (Table 1; Fig. 2), and to compare these properties with those of the background oscillations at the same sites, we separated the records into pre-tsunami and tsunami parts. The data from roughly 1-day period preceding the tsunami arrivals were selected for determination of the background oscillations. For the "tsunami" periods, we mainly used the leading 21.3 hours of each segment (1280 samples for 1-min data, 640 for 2-min, and 320 for 4-min data); for Diego Garcia, we used 25.6-hour segments (256 samples) for both background and tsunami periods. Our spectral analysis procedure is similar to that described by EMERY and THOMSON (2003). To improve the spectral estimates, we used a Kaiser-Bessel (KB) spectral window with half-window overlaps prior to the Fourier transform. The length of the window was chosen to be 768 min for Diego Garcia and 512 min for the eleven other stations, yielding 6 to 10 degrees of freedom per spectral estimate depending on the length of the data segment.

In general, the spectra of both tsunami and background (Fig. 3) are "red," with spectral energy decreasing with increasing frequency as roughly $\omega^{-2}$. This is typical for long-wave sea-level spectra (RABINOVICH, 1997). At most stations, tsunami spectra are two to three orders of magnitude greater than background spectra. The background spectra at most stations have a relatively "smooth" profile, probably because the majority of these stations are located on isolated open-ocean islands. On the other hand, background spectra at Port Louis (Mauritius) have prominent peaks at periods of 20 and 7.4 min (Fig. 3b, upper right). Near identical peaks are evident in the corresponding tsunami spectrum indicating that the local topography has a major effect on the longwave oscillations at this site. The dominance of relatively high-frequency oscillations at Port Louis compared to all other sites is clearly evident in the records (Fig. 2). The only other station with dominant high-frequency tsunami oscillations (periods of 21 and 14 min) is the Cocos Islands (the upper record in Fig. 2 and the upper left plot in Fig. 3a). At all other stations, low-frequency tsunami oscillations (with typical periods from 35 to 85 min) prevailed (Fig. 3). The dominance of strong low-frequency oscillations in the 2004 tsunami records is apparently associated with the large extent of the source area (approximately 1300 km according to recent estimates; cf., STEIN and OKAL, 2005; FUJII and SATAKE, 2007). At the same time, the specific tsunami spectral peaks observed at certain sites (73 min at Colombo, 45 min at Salalah, 64 min at Lamu, 51 min at

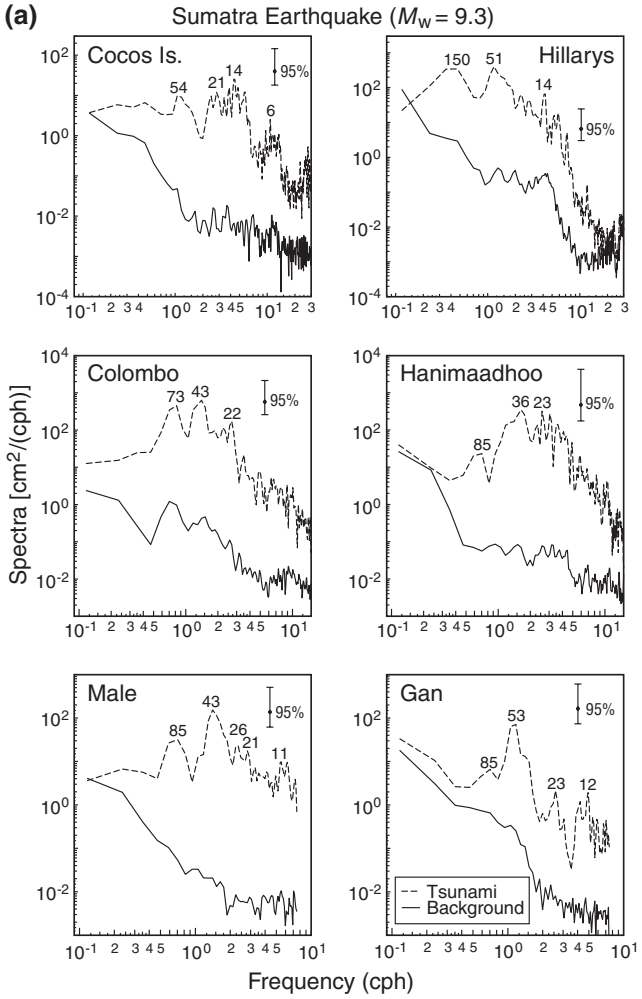


Figure 3
Computed spectra of background (pre-tsunami) and tsunami oscillations for the twelve tide gauge records shown in Figure 2. Periods (in min) of the main spectral peaks are indicated. Note differences in frequency scales for the various stations due to the differences in tide gauge sampling intervals.

Zanzibar) are similar to the background spectral peaks at the corresponding sites, indicating the pronounced influence of local topography.

### *2.3. Time-frequency Analysis*

To examine temporal variations in the frequency of the observed tsunami waves, we used a method developed by DZIEWONSKI *et al.* (1969) to study nonstationary

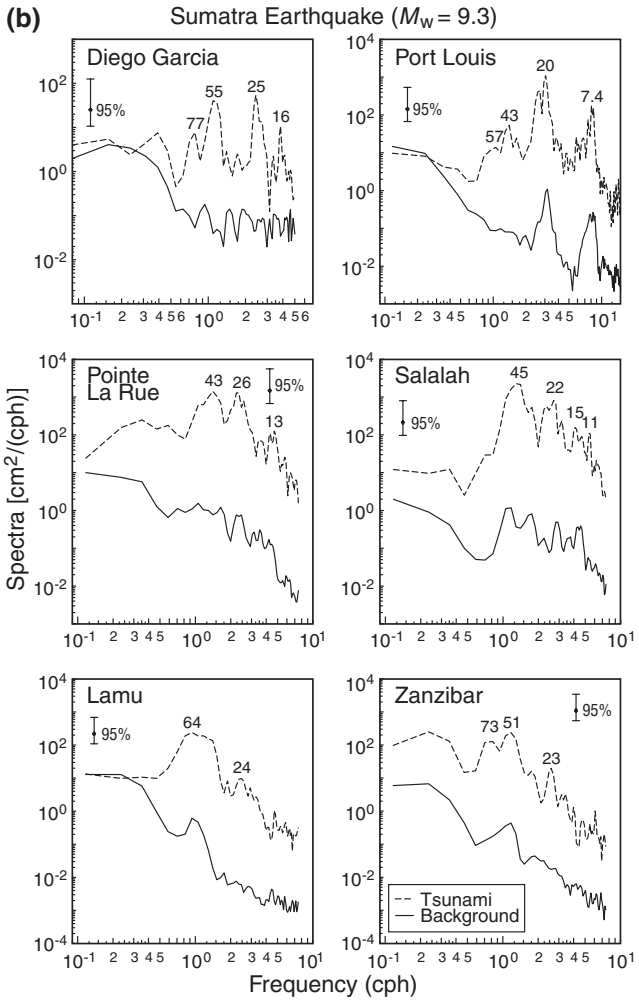


Figure 3
(Contd.)

seismic signals in which the time series displays rapid temporal changes in amplitude and/or phase. The method, which is similar to wavelet analysis (EMERY and THOMSON, 2003), is based on narrow-band filters, $H(\omega)$, with a Gaussian window that isolates a specific center frequency, $\omega_n = 2\pi f_n$:

$$H_n(\omega) = e^{-\alpha\left(\frac{\omega-\omega_n}{\omega}\right)^2}. \quad (1)$$

The frequency resolution is controlled by the parameter $\alpha$. The higher the value of $\alpha$, the better the resolution in the frequency domain but the poorer the resolution in the time domain (and *vice versa*.) We used $\alpha$ = 60–80 in our computations.

Demodulation of a sea-level time series, $\zeta(\omega_n; t)$, yields a matrix of amplitudes (phases) of wave motions with columns representing time and rows representing frequency (the so-called *f-t* diagrams). This method can be used effectively to indicate how the tsunami wave energy $E(f, t)$ changes as a function of frequency, $f$, and time, $t$ (GONZÁLEZ and KULIKOV, 1993; KULIKOV *et al.*, 1996; RABINOVICH *et al.*, 2006).

Figure 4 presents *f-t* diagrams for tide gauge records for twelve Tropical Indian Ocean stations. Blank bands correspond to data gaps. The tsunami wave arrival times are well defined at all stations and mutually consistent. There were no pronounced background oscillations prior to the tsunami arrival, which is an advantage for tsunami wave detection and estimation of exact arrival time. Overall, the range of periods having high energy concentration (20 to 85 min) with peak values at 35–60 min is roughly the same for the entire Indian Ocean and approximately the same as that observed in the North Pacific and North Atlantic oceans (RABINOVICH *et al.*, 2006). However, the *f-t* diagrams for Port Louis and the Cocos Islands are different from the others in that most of the observed tsunami energy is associated with short wave periods (<22 min), with little energy at periods of 35–60 min (see also Fig. 3). According to the *f-t* diagrams, the tsunami waves at most sites were mainly polychromatic with several dominant energy bands. There is an obvious difference between the *f-t* diagrams for stations located relatively close to the source area (i.e., Colombo, Hanimaadhoo, Male, Gan, and Diego Garcia, which lie within 3–4 hour travel distances from the source) and similar diagrams for far-field stations (Hillarys, Salalah, Pointe La Rue, Port Louis, Lamu, and Zanzibar). The former are characterized by high energy 6–12 hr after the tsunami arrival with negligible energy afterwards; the latter are remarkable for their long ringing times and clear wave-train structure with train durations from 8 to 18 hours. Once again, the Cocos record is different. Located closest to the source (2.3-hr travel time), this station is characterized by a long ringing time (~1.5 days) and many short-duration wave trains (~3–5 hr) (Fig. 4, top left). Apparently, the tsunami wave behavior at this site is attributable to the fact that the waves emanating from the source travelled in a parallel direction to the earthquake rupture and to the influence of tsunami waves reflected from the southwestern coasts of the Indonesian Islands and northwestern coast of Australia.

## 3. Indian Stations

The Survey of India (SOI) agency maintains a network of tide gauges along the coast of India (Fig. 5) that accurately recorded the 2004 Sumatra tsunami (Fig. 6). High-quality de-tided records for this region are available from the National Institute of Oceanography (NIO), Goa, India for seven tide gauges (see the NIO website: http://www.nio.org/jsp/tsunami.jsp): Paradip, Vishakhapatnam,

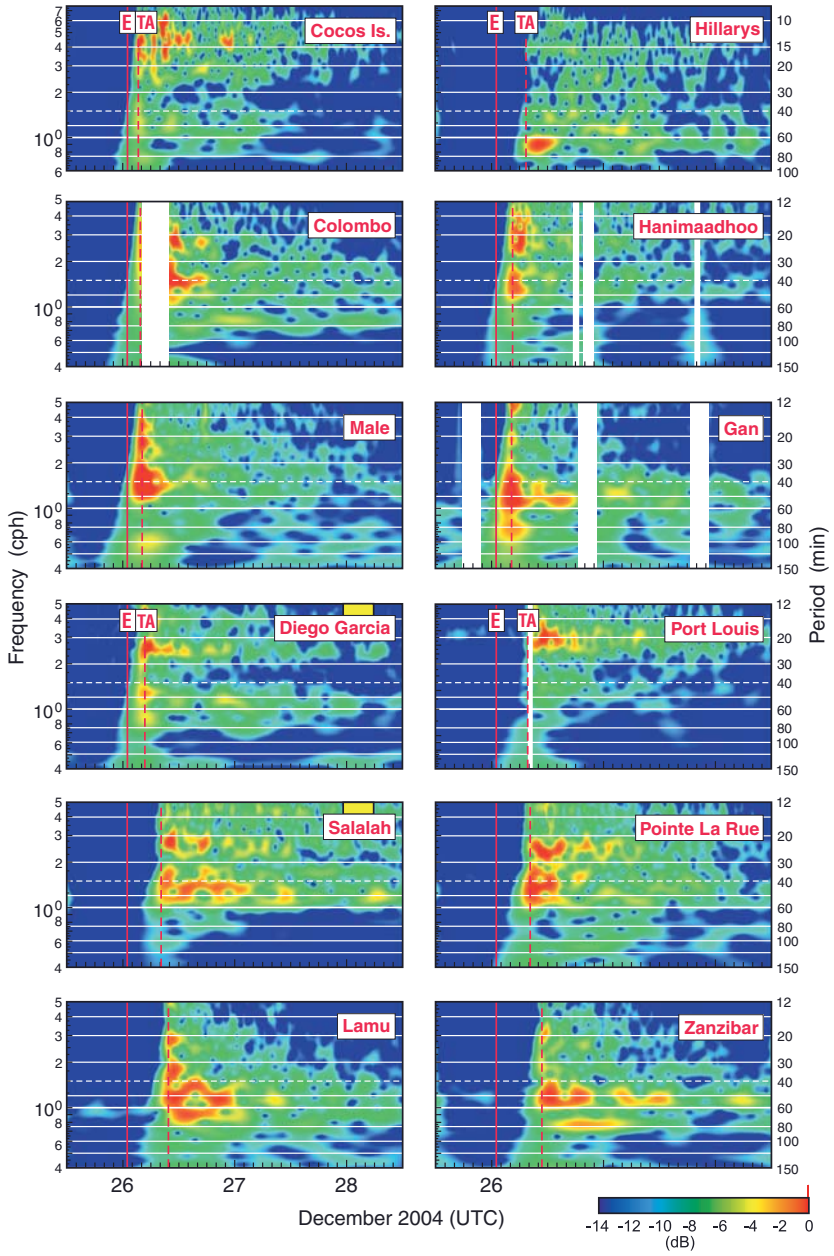


Figure 4

Frequency-time plots (*f-t* diagrams) for the 2004 Sumatra tsunami tide gauge records for twelve records shown in Figure 2 (station locations are shown in Figure 1) Blank bands correspond to the data gaps. The dashed white horizontal line indicates the 40-minute wave period; the solid red vertical line labelled "E" denotes the time of the main earthquake shock and the dashed red vertical line indicates tsunami arrival time ("TA").

Chennai, Tuticorin, Kochi (Cochin), Mormugao, and Okha (Table 2). Unfortunately, the tide gauge for Nagapattinam, located in the most strongly affected sector of the Indian coast (southward from Chennai; Fig. 5), was heavily damaged by the tsunami waves so that the 2004 tsunami record could not be retrieved (NAGARAJAN *et al.*, 2006).

SOI tide gauges were either mechanical float-type analog gauges or pressure-sensor gauges (NAGARAJAN *et al.*, 2006). The pressure-sensor gauges (Paradip, Tuticorin and Kochi) had sampling intervals of 6 min; the analog records were digitized by SOI at an interval of 5 min for Vishakhapatnam, Chennai, and Mormugao and at interval of 6 min for Okha (Table 2). We also used the 15-min sampled tsunami record (provided to us by K.A. Abdul Rasheed, NIO, Regional Centre, Kochi, India) from the tide gauge at Neendakara located on the southwestern coast of India southward from Kochi (Fig. 5). Pronounced tsunami oscillations were clearly recorded at this station (KURIAN *et al.*, 2006; RASHEED *et al.*, 2006). Figure 6 presents the de-tided records for all eight stations of Group 2. Due to instrumental problems, the Vishakhapatnam record had a gap of approximately two hours that was filled by zeros.

### *3.1. General Description and Statistical Characteristics*

Maximum tsunami wave heights (2.9–3.2 m) were recorded at Paradip, Vishakhapatnam and Chennai on the east coast of India. Tsunami waves arrived at these

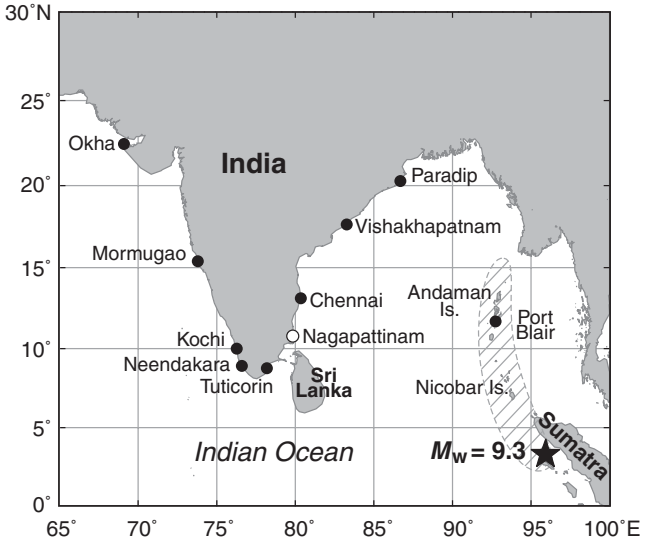


Figure 5
Map of the coast of India showing the location of the $M_w = 9.3$ earthquake epicenter (star), the aftershock zone (shaded area), and positions of Indian tide gauges where the 2004 Sumatra tsunami waves were recorded (solid circles) and the Nagapattinam tide gauge destroyed by the tsunami (empty circle).

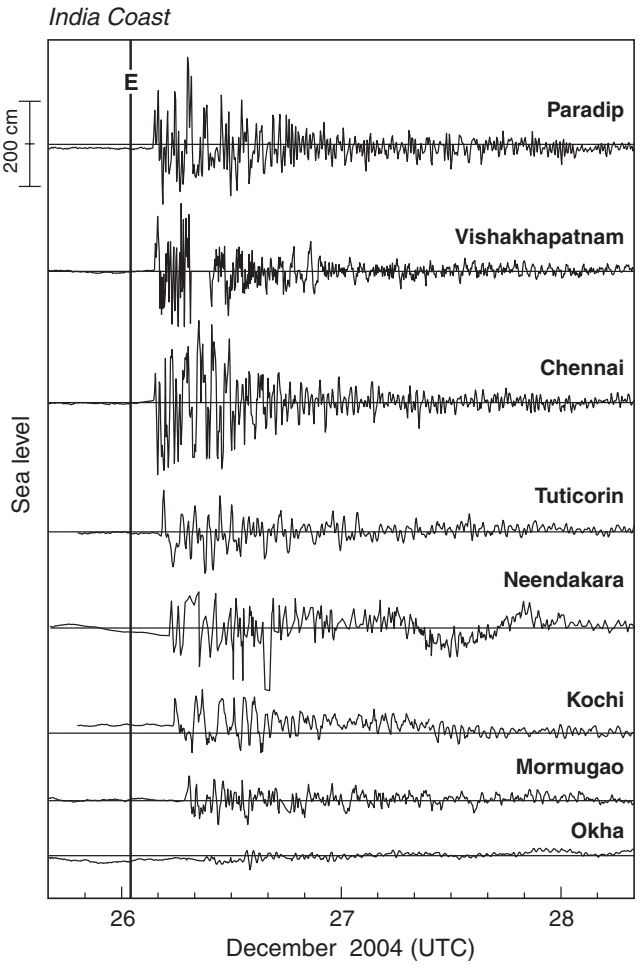


Figure 6
As in Figure 2 but for eight tide gauges on the coast of India (see Fig. 5 for tide gauge locations).

stations approximately 2.5 hr after the main shock (Table 2). As with the Tropical Indian Ocean stations (Section 2), we applied a mid-sampling time interpolation correction to define the arrival time of tsunami waves at the Indian stations if the first measured tsunami wave increase was significant; this adjustment is apparently the main reason for the small differences in timing between our estimates in Table 2 and those of NAGARAJAN *et al*. (2006). Defining the precise tsunami arrival times at the Indian coast is highly important for accurate delineation of the source area. LAY *et al*. (2005a) used an inverse wave-tracing (wave-retracing) algorithm and arrival times from a number of stations, including the Indian stations Vishakhapatnam and Chennai, to define a source region extending up to 600 km (to ~9°N) north of the

Table 2

*Tsunami characteristics estimated from the Indian tide gauge records*

| No | Station | Country | Coordinates | Sampling interval (min) | Maximum wave height (cm); number | First wave | |
|---|---|---|---|---|---|---|---|
| | | | | | | Sign, arrival time (UTC) | Travel time |
| 1 | Paradip | India | 20.26°N; 86.70°E | 6 | 318 (8) | (+) 03:27 | 2 hr 28 min |
| 2 | Vishakhapatnam | India | 17.65°N; 83.28°E | 5* | 291 (11) | (+) 03:35 | 2 hr 36 min |
| 3 | Chennai | India | 13.10°N; 80.32°E | 5* | 324 (8) | (+) 03:33 | 2 hr 34 min |
| 4 | Tuticorin | India | 08.75°N; 78.20°E | 6 | 181 (1) | (+) 04:24 | 3 hr 25 min |
| 5 | Neendakara | India | 08.93°N; 76.54°E | 15 | 217 (9) | (+) 05:08 | 4 hr 09 min |
| 6 | Kochi (Cochin) | India | 09.97°N; 76.27°E | 6 | 149 (3) | (+) 05:41 | 4 hr 42 min |
| 7 | Mormugao | India | 15.42°N; 73.80°E | 5* | 157 (4) | (+) 06:53 | 5 hr 54 min |
| 8 | Okha | India | 22.50°N; 69.10°E | 6* | 45.5 (8) | (+) 09:03 | 8 hr 04 min |
| 9 | Port Blair | India | 11.68°N; 92.77°E | 2 | 350 (4?) | (+) 01:14 | 0 hr 15 min |

* Analog digitized records from float-type tide gauges.

epicenter. Inverse wave-retracing by FINE *et al.* (2005) used the same Indian stations together with Tuticorin, but with more precise bathymetry (1-min GEBCO). Taking into account the finite rupture speed of 2 km·s$^{-1}$, FINE *et al.* (2005) find that the source region extends at least 1000 km northward to ~12°N. NEETU *et al.* (2005) came to the same conclusion based on additional information provided by the Paradip station. LAY *et al.* (2005a) and FINE *et al.* (2005) did not have information from this station.

Tsunami waves from the source area propagated around the Indian Peninsula and arrived at Tuticorin at 04:24, Neendakara at 05:08, Kochi at 05:41, Mormugao at 06:53, and Okha at 09:03 UTC, in good agreement with predicted tsunami arrival times (Fig. 1). As the tsunami waves rounded India, wave heights decreased from 3.24 m at Chennai to 1.81 m at Tuticorin, 1.49 m at Kochi and 0.45 m at Okha. The relative amplification of tsunami wave heights at Neendakara (for which the observed trough-to-crest wave height of 2.17 m would probably be even greater if the sampling interval for this station had been shorter than 15 min) appears to have had been due to local resonance; this suggestion is supported by the fact that the maximum wave occurred several hours after the first wave arrival (Table 2 and KURIAN *et al.*, 2006). At all stations, the first wave was positive (crest) supporting the notion that the first positive wave traveled westward and southwestward, while the first negative tsunami wave traveled eastward (cf., LAY *et al.*, 2005a; TITOV *et al.*, 2005). Only at Tuticorin was the first wave the highest; at all other sites the maximum wave occurred later in the wave sequence (see Fig. 6, Table 2 and NAGARAJAN *et al.*, 2006).

The station of most interest was Port Blair in the Andaman Islands (Fig. 5). This was the only station in the tsunami source region and a station for which the instrumental record could hopefully provide constraints on the temporal evolution of

the slip (SINGH *et al.*, 2006). There were two tide gauges operating in the same well at Port Blair: One was a conventional stilling-well float-type gauge deployed by the Survey of India (SOI) and the other was an acoustic tide gauge deployed by the National Institute of Ocean Technology (NIOT), Chennai. The existence of two tide gauges at the same site resulted in some confusion in published papers (LAY *et al.*, 2006a; NAGARAJAN *et al.*, 2006; SINGH *et al.*, 2006). At the time of the 2004 Sumatra tsunami, the SOI tide gauge was not operational. NAGARAJAN *et al.* (2006), who dealt only with the data supplied by SOI, reported that data for the 2004 tsunami for the Andaman Islands were not available because the Port Blair tide gauge "*was under repair at the time of the tsunami*." Fortunately, the NIOT tide gauge was working at the time of the 2004 Sumatra tsunami. The instrument was an acoustic gauge with a 2-min sampling interval and was designed so that it collected data for 36 min and then stopped for 24 min for processing and storage (SINGH *et al.*, 2006). As discovered later, the clock in the NIOT gauge at Port Blair at the time of the tsunami was 46 min ahead of actual time (NEETU *et al.*, 2005; SINGH *et al.*, 2006). As a consequence, the record was initially taken as evidence for a delay in the subsidence below the Andaman Islands and sited as an indication of slow slip (cf., AMMON *et al.*, 2005; BILHAM *et al.*, 2005; LAY *et al.*, 2005a). Moreover, LAY *et al.* (2005a) used this erroneous timing to constrain the northern extent of the 2004 tsunami source region. This was later corrected (NEETU *et al.*, 2005; LAY *et al.*, 2005b; FUJII and SATAKE, 2007). SINGH *et al.* (2006) corrected timing errors and tried to fill the 24-min data gap from 35 to 59 min after the earthquake associated with the data storage period. The residual time series for the restored record yielded a mean sea-level change of +95 cm after the earthquake, consistent with GPS and field observations which reported a subsidence of 80 to 120 cm (cf., BILHAM *et al.*, 2005).

The increase in sea level at the Port Blair tide gauge began at 01:14 UTC, within ~15 min of the first shock at 00:58:53 UTC. Assuming an average rupture speed of 2.5 km/s, the expected rupture arrival time at Port Blair is ~01:05:30 UTC. This means that the change in sea level occurred ~8.5 min after the passage of the rupture (SINGH *et al.*, 2006). The fourth, rather than the first, wave appears to have been the highest (~3.5 m), although it should be noted that the data gaps create problems in precise detection of tsunami wave parameters.

### *3.2. Spectral Properties*

The spectral analysis applied to the eight Indian mainland records (Fig. 7) is similar to that applied for the twelve Tropical Indian Ocean records (Section 2.2). The available data for all series except Neendakara enabled us to use 256-sampling segments for tsunami and 384-sampling segments for background oscillations (i.e., 32.0–21.3-hour segments for 5-min data and 38.4–25.6-hour segments for 6-min data). The length of the KB window (using half-window overlaps prior to the Fourier transform) was 128 points, yielding 6 (10) degrees of freedom for tsunami

(background) spectra. For Neendakara (15-min sampling), we used 160-sampling segments for both the tsunami and background oscillations. The 64-point length of the KB window, yielded 8 degrees of freedom.

As with the wave spectra for the Tropical Indian Ocean stations (Fig. 3), tsunami spectra at almost all of the Indian coastal sites (except Okha) are three to four orders of magnitude higher than the corresponding background spectra (Fig. 7). Again, the background spectra have relatively smooth "profiles," with no well-defined peaks. The sole exception is Paradip which has a prominent peak at 1.8 hr in both the background and tsunami spectra. A spectacular feature of the coastal Indian tsunami spectra is the dominance of long-period oscillations (Fig. 7) which are: 1.5 hr at Chennai; 1.8 hr at Paradip and Vishakhapatnam; 2.0 hr at Neendakara; 2.2 hr at Mormugao; 2.8 hr at Kochi; and 3.2 hr at Tuticorin. In part, this feature is undoubtedly associated with the very large extent of the tsunami source area ($L$). The maximum periods of generated tsunami waves ($T$) may be estimated as

$$T \sim L/\bar{c}, \tag{2}$$

where $\bar{c} = \sqrt{g\bar{H}}$ is the long-wave speed in the tsunami source area, $g$ is the gravity acceleration, and $\bar{H}$ is the mean ocean depth in the source area. For $\bar{H} = 3000$ m (a typical depth along the 2004 Sumatra source rupture zone), we obtain $\bar{c} \approx 172$ m/s, which for $L = 1300$ km in (2) gives $T \sim 2.1$ hr, in good agreement with the long-period oscillations in this region. However, it is also likely that these motions are partly related to the eigen oscillations of specific sectors of the Indian Ocean (e.g., the Bay of Bengal or the Gulf of Mannar). Oscillations in the range 35 to 70 min form another band of high tsunami energy. We also observe mutual spectral peaks at a number of stations: For example, a peak at 74–77 min is observed at Tuticorin, Kochi, and Okha. The most common spectral peak, at periods of 43–50 min, is observed at Paradip, Chennai, Neendakara, Kochi, Mormugao, and Okha (Fig. 7). The same peak is observed at several Indian Ocean stations (Fig. 3) and at many stations in the North Pacific and North Atlantic (RABINOVICH *et al.*, 2006). We assume that spectral peaks that are common to sites in different parts of the World Ocean arise from specific features of the tsunami source, including its "dual" or "multiple-source" structure (cf., FINE *et al.*, 2005; FUJII and SATAKE, 2007).

### *3.3. Time-frequency Analysis*

The observed changes over time in the frequency content of the tsunami records for the Indian coast were examined in the same manner as for the Tropical Indian Ocean records (Section 2.3). Figure 8 presents *f-t* diagrams for eight Indian tide gauge records; the blank band for Vishakhapatnam corresponds to the data gap. As for the first group of stations (Tropical Indian Ocean), there were no pronounced background oscillations prior to the tsunami arrivals. Thus, the

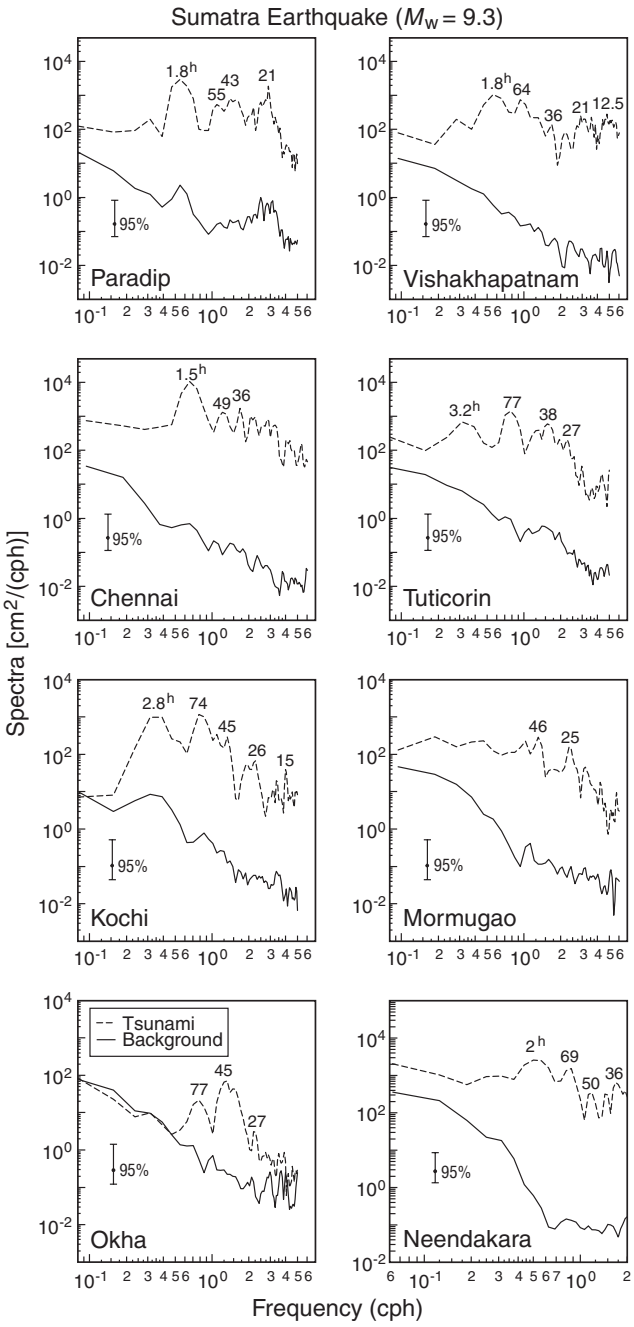


Figure 7
As in Figure 3 but for the eight tide gauge records shown in Figure 6. The Neendakara spectrum has a different frequency scale than other Indian stations because of its 15-min sampling interval compared to 5 or 6 min for the other stations.

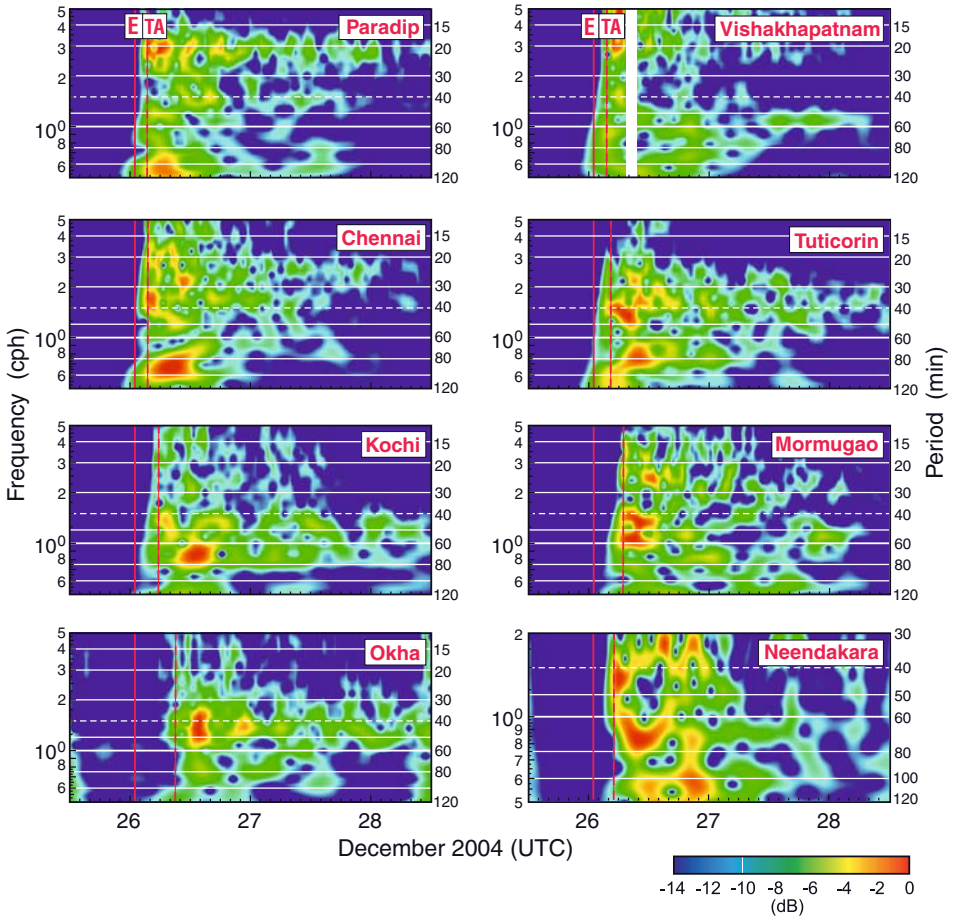


Figure 8
As in Figure 4 but for the eight Indian records in Figure 6. Note that the *f-t* plot for Neendakara has different frequency (period) ranges than the other seven plots.

tsunami wave arrival times at all stations were very distinct and consistent with the direct estimates of these times made from the record analyses (Table 2). For almost all stations, major tsunami energy was observed within the first 8–12 hours after the tsunami arrival; the only exception was Neendakara where highly-energetic oscillations persisted for 18 hours (Fig. 8). At the same time, long "tails" of prominent oscillations associated with the dominant local frequencies (1.5 and 3 cpd at Paradip; 1.1 cpd at Vishakhapatnam; 1.5 and 2.5 cpd at Chennai; 1.5 cpd at Tuticorin; 0.8–1.3 cpd at Kochi; and 1.2–1.5 cpd at Okha, etc.) were observed for more than two days. The range of periods which had high energy concentration (20 to 85 min) was roughly the same as that for stations in the Tropical Indian Ocean

and those in the North Pacific and North Atlantic Oceans (RABINOVICH *et al.*, 2006). Similarly to what we observed in other regions, the tsunami waves at most sites were mainly polychromatic with several dominant energy bands that were slightly different for different sites.

In general, the *f-t* diagrams for the Indian stations (Group 2) were more similar to corresponding diagrams for stations in the Central Indian Ocean located within 3–4 hour travel distances from the source (Colombo, Hanimaadhoo, Male, Gan, and Diego Garcia). There was considerably greater difference between *f-t* diagrams from the stations on the coast of India and those from far-field Indian Ocean stations (Hillarys, Salalah, Pointe La Rue, Port Louis, Lamu, and Zanzibar). As noted above, high energy tsunami oscillations at most of the Indian stations were observed 8–12 hr after the tsunami arrival; waves arriving after this time had much smaller energy. Unlike the far-field Tropical Indian Ocean stations (from Group 1), the Indian stations did not have a clear wave-train structure.

## *4. Thailand and Indonesian Stations*

The devastating tsunami waves struck the coasts of Indonesia and Thailand two to four hours after the December 2004 earthquake and surged far inland, causing unprecedented destruction and death. About 170,000 were killed on the coasts of Indonesia and Thailand alone. To prevent and mitigate such catastrophes in the future, it is important to assemble all available observational information for this event. The data from tide gauges in these regions are crucial for the tsunami source reconstruction and determination of tsunami wave characteristics (LAY *et al.*, 2005a; FINE *et al.*, 2005; TANIOKA *et al.*, 2006; FUJII and SATAKE, 2007). Although tsunami waves were recorded by several tide gauges along the coasts of Thailand and Indonesia, most gauges were archaic analog devices which are not designed to measure tsunami waves. For this reason, derived wave characteristics, in particular, arrival times, are not fully reliable. Nevertheless, the gauges provide essential information for tsunami research.

Regrettably, we could not find the original records for Thailand stations. For this reason, we were unable to show the tsunami records (and the results of spectral and time-frequency analysis of tsunami waves) for these stations; the general statistical characteristics of the 2004 tsunami waves for these sites were mainly taken from TSUJI *et al.* (2006) or estimated from the plots of tide gauge records presented in this paper and at some websites. In contrast, the situation with the Indonesian tide gauges has improved considerably as records from five Indonesian tide gauges (Sibolga, Belawan, Panjang, Prigi, and Lembar) have been recently re-digitized with a sampling interval of 3 min. These data are thoroughly examined in the present study.

### *4.1. General Description and Statistical Features of the Thailand Records*

TSUJI *et al.* (2006) provide an overview and preliminary analysis of the Thailand tide gauge records. There were eight gauges along the west (Andaman Sea) coast of Thailand (Fig. 9). Five of these gauges, Satun (Tummarkarg), Kantrang (Trang), Krabi, Kuraburi (Phangnga), and Ranong (Ban Pak Nam) were operated by the Thai Marine Department; three others, Phuket (Taphaonoi), Ban Leen Po, and Tarutao, were operated by the Hydrographic Department of the Thai Navy. The Ban Laen Po tide gauge did not work during the 2004 Sumatra tsunami; however, the seven others successfully recorded the tsunami waves. TSUJI *et al.* (2006) published the images of analog records from five of the instruments (excluding Phuket and Tarutao, which may be found at www.navy.mi.th/hydro/tsunami.htm.). Table 3 presents the main tsunami characteristics estimated for all seven Thai records.

In contrast to what we observed in the records for the Tropical Indian Ocean stations (Group 1, Fig. 2) and Indian stations (Group 2, Fig. 6), the first wave at all Thai stations was negative, indicating that the trough wave propagated eastward from the source area. Also, at all sites except Kuraburi, the first wave was the highest. It was this wave which was responsible for most of the casualties on the coast of Thailand. At Kuraburi, the third wave was the highest wave, although the first three waves at this site had almost the same trough-to-crest height of 135–140 cm. The first coastal region of Thailand to be impacted by the tsunami waves was the Phuket Peninsula. Based on the analog record, the tsunami struck the Phuket tide gauge at

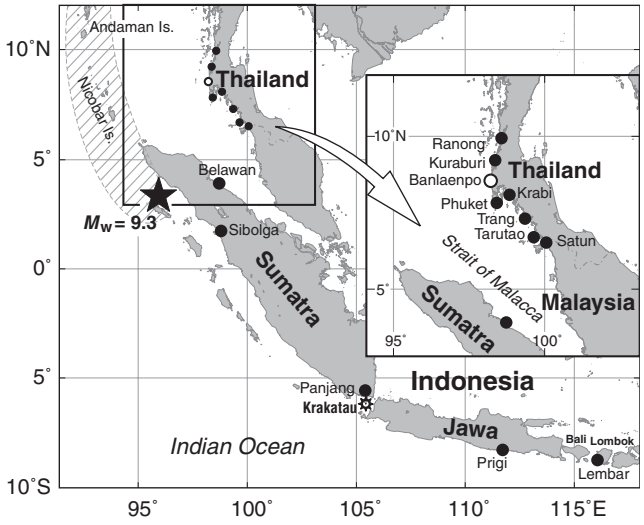


Figure 9
Map of Indonesia and Thailand with location of the $M_w = 9.3$ earthquake epicenter (star) and positions of tide gauges where the 2004 Sumatra tsunami waves were recorded (solid circles). The Banlaenpo tide gauge in Thailand (empty circle) was not operating during the tsunami. Also shown is the location of the Volcano Krakatau that exploded in 1883 and generated a catastrophic tsunami.

Table 3

*Tsunami characteristics estimated from the Thailand and Indonesian tide gauge records*

| No | Station | Country | Coordinates | Sampling interval (min) | Maximum wave height (cm); number | First wave | |
|---|---|---|---|---|---|---|---|
| | | | | | | Sign, arrival time (UTC) | Travel time |
| 1 | Ranong | Thailand | 09.95°N; 98.60°E | – | 141 (1) | (–) 04:00 | 3 hr 01 min |
| 2 | Kuraburi | Thailand | 09.23°N; 98.38°E | – | 140 (3) | (–) 03:32 | 2 hr 33 min |
| 3 | Phuket | Thailand | 07.83°N; 98.42°E | – | 221 (1) | (–) 02:55 | 1 hr 56 min |
| 4 | Krabi | Thailand | 08.07°N; 98.87°E | – | 168 (1) | (–) 03:45 | 2 hr 46 min |
| 5 | Trang | Thailand | 07.50°N; 99.30°E | – | 125 (1) | (–) 04:40 | 3 hr 41 min |
| 6 | Tarutao | Thailand | 06.70°N; 99.65°E | – | 178 (1) | (–) 03:27 | 2 hr 28 min |
| 7 | Satun | Thailand | 06.65°N; 100.02°E | – | 57 (1)? | (–) 05:15 | 4 hr 16 min |
| 8 | Sibolga | Indonesia | 01.75°N; 98.75°E | 3* | 246 (4) | (+) 02:46 | 1 hr 47 min |
| 9 | Belawan | Indonesia | 03.78°N; 98.72°E | 3* | 93 (4) | (–) 04:24 | 3 hr 25 min |
| 10 | Panjang | Indonesia | 05.51°S; 105.35°E | 3* | 129 (5) | (+) 04:02 | 3 hr 03 min |
| 11 | Prigi | Indonesia | 08.29°S; 111.73°E | 3* | 102 (25) | (+) 04:30 | 3 hr 31 min |
| 12 | Lembar | Indonesia | 08.73°S; 116.07°E | 3* | 185 (30) | (+) 05:27 | 4 hr 28 min |

* Digitized analog records from float-type tide gauges.

02:55 UTC (09:55 local Thai time), i.e., 1 hr 56 min after the earthquake (Table 3). The maximum wave height of 2.21 m was recorded at Phuket, where much of the destruction and most of the casualties (especially among foreign tourists) took place. Empirically, it is commonly accepted that tsunami runups are about 2.5–3 times higher than the corresponding waves recorded by tide gauges. As found by TSUJI *et al.* (2006), typical 2004 Sumatra runup heights on the coast of central Thailand (between 7.5°N and 9.5°N) were 5–6.5 m, with a maximum runup height of 19.6 m at Ban Thung Dap (9.028°N; 98.257°E) located about 22 km south from Kuraburi.

Additional important tsunami information was provided by the Belgian yacht ''Mercator'' anchored about 1.6 km off the Phuket coast (07.715°N; 98.28°E). By chance, the yacht's ''fishfinder'' (depth gauge) was turned on and measured changing wave heights during the tsunami (SIFFER, 2005). Based on these measurements, the three main tsunami waves had trough-to-crest wave heights of 6.6, 2.2, and 5.5 m. The first wave (trough) struck the ''Mercator'' area at 02:38 UTC, roughly 1 hr 39 min after the earthquake, or 17 min earlier than the Phuket tide gauge.

We remark that the first wave arrival time estimated from the ''Mercator'' is more reliable than that from the tide gauges: Because ship's clocks tend to be highly precise, the fishfinder on the vessel recorded the arrival tsunami waves with an accuracy of a few tens of seconds. Tide gauge clocks are imprecise by comparison. Moreover, it is difficult to recognize an accurate time from low-speed analog paper records. TSUJI *et al.* (2006) checked the time for the Phuket tide gauge on 26 February, 2005 and found that the time recorded on the sheet is 11 min earlier than

the correct time. A similar discrepancy probably applies for 26 December, 2004. The authors also used predicted astronomical tides at Kuraburi for 26 December, 2004 to estimate the accuracy of the gauge and found that the record was shifted 12 min earlier than the exact time. So, it is possible that the tide gauge detected arrival times in Table 3 will need future adjustment. It was for this reason that FINE *et al.* (2005) used the "Mercator" time for the source delineation but did not use arrival times from the Thailand tide gauges.

Maximum wave heights of $1.5 \pm 0.3$ m recorded at most of the Thailand stations are in close mutual agreement. There are two exceptions: Phuket with a maximum height of 2.21 m, and Satun with a maximum height of only 0.57 m. The considerably much lower wave height at Satun likely occurred because the site is sheltered from incoming tsunami waves by the Butang Group Islands.

### *4.2. Indonesian Tide Gauges*

The initial information available for the Indonesian tide gauges and measurements of the 2004 Sumatra tsunami by these gauges were scarce and contradictive. MERRIFIELD *et al.* (2005) indicated that five Indonesian tide gauges recorded the tsunami waves: Sibolga, Belawan, Panjang, Prigi, and Lembar (Fig. 9). The stations were operated by the Geodesy and Geodynamic Center in Indonesia (GGCI). Records from these gauges consisted of short, 20 to 23 hr, segments of analog records digitized for the tsunami event. The Panjang tide gauge record had a sampling interval of 30 min; the four others had sampling intervals of 10 min. MERRIFIELD *et al.* (2005) are the only authors to report on the records for all five tide gauges, including Prigi, Panjang, and Lembar. However, the preliminary data from the two other stations, Sibolga and Belawan, were used by several authors (LAY *et al.*, 2005a; TANIOKA *et al.*, 2006; FUJII and SATAKE, 2007), who attempted to reconstruct the source area based on tide gauge data. FINE *et al.* (2005) tried also to use these draft data for a similar purpose but found the data imprecise and dubious. In particular, the differences between the computed tsunami travel times and those from the tide gauges were too large to be explained by some physical factors or inaccuracy in bathymetry.

Recently, the Indonesian Gravity and Tide Division, GGCI, re-digitized the 2004 Sumatra tsunami records for Indonesian analog tide gauges. Digitized records for Sibolga, Belawan, Panjang, Prigi and Lembar were kindly provided to us by Dr. Parluhutan Manurung, Head of the Division. These re-digitized 2 to 3 day records had 3-min sampling interval and were of much higher quality than previous records for these sites. As a result, the statistical parameters estimated for these stations (Table 3) became considerably more accurate and precise; the arrival/travel times now agree with estimates calculated numerically (Fig. 1).

The first wave (positive) arrived at Sibolga located on the western coast of Sumatra Island (Fig. 9) at 02:46 UTC; i.e., 1 hr 47 min after the earthquake. This compares with the previous travel-time estimate of 1 hr 21 min for Sibolga by

MERRIFIELD *et al*. (2005) based on the preliminary wave data; the maximum wave of 246 cm was wave #4 that arrived approximately 4 hours after the first wave arrival (Table 3, Fig. 10a). At Belawan, located on the eastern coast of Sumatra (Fig. 9), the first wave was clearly negative (Fig. 10b). It arrived at 04:24 UTC, or 3 hr 25 min after the main earthquake shock (Table 3). This time is markedly different than the time of 0 hr 41 min given by MERRIFIELD *et al*. (2005). The reason for this large time difference was the problem faced by MERRIFIELD *et al*. in identifying the exact arrival times of tsunami waves from short records that also contained tides and local seiches. Regrettably, this offset created major problems for reconstruction of the southern and southeastern sectors of the source area (cf., FINE *et al*., 2005). Similarly to what was observed at Sibolga, the maximum wave at Belawan (93 cm) arrived several hours after the first wave (Fig. 10b).

The Panjang tide gauge is located on the southern end of Sumatra Island, close to Krakatau Island (Fig. 9). The first wave (positive) arrived at this site at approximately 04:02 UTC or 3 hr 03 min after the earthquake (a preliminary estimate of 3 hr 00 min for this site given by MERRIFIELD *et al*., 2005 was, therefore, quite precise). The maximum trough-to-crest wave height was associated with the fifth wave, observed approximately 10 hours after the first wave arrival (Table 3, Fig. 10c). A highly noteworthy feature of the tsunami oscillations observed at Panjang during the first 15 hours were their very low frequencies. The fundamental period of these regular and consistent oscillations was 2.6 hr (see the *f-t* diagram in Fig. 10c and the spectrum of the Panjang record in Fig. 11). This is a distinct property of the oscillations at this site that has not been observed elsewhere. Although low-frequency spectral peaks with periods of 1 to 3 hours are relatively common in the 2004 tsunami spectra (cf., the spectra of the Indian stations shown in Fig. 7), at no other site are the low-frequency oscillations so clear and persistent than at Panjang. One of the key factors undoubtedly responsible for these oscillations is the regional topography (the background spectrum at this site shown in Fig. 11 has the same peak). However, the oscillations are also apparently strongly influenced by specific source parameters.

The record for Prigi on the southeastern coast of Jawa (Fig. 9) is quite different from the Panjang record in that it contains almost monochromatic oscillations with a period of about 40 min (Fig. 10d). The first wave (a positive wave) arrived at this site at 04:30 UTC, or 3 hr 31 min after the main earthquake shock (this is significantly different from the estimate 2 hr 21 min given by MERRIFIELD *et al*., 2005). The noteworthy features of this record are the gradual amplification of the observed wave heights with time and the delayed arrival of the maximum wave (wave #25) which came approximately 16 hours after the first wave (Fig. 10d) and had a height of 102 cm (Table 3). About 12 hours later, another wave arrived which had almost the same height (96.5 cm) (Fig. 10d). From this point of view, the record for Prigi is markedly different from other stations of Group 3 (Thaliand and Indonesian) considered above. More specifically, at the latter stations the first wave was the highest (Table 3) whereas at Prigi the highest waves occurred 16–28 hours after the

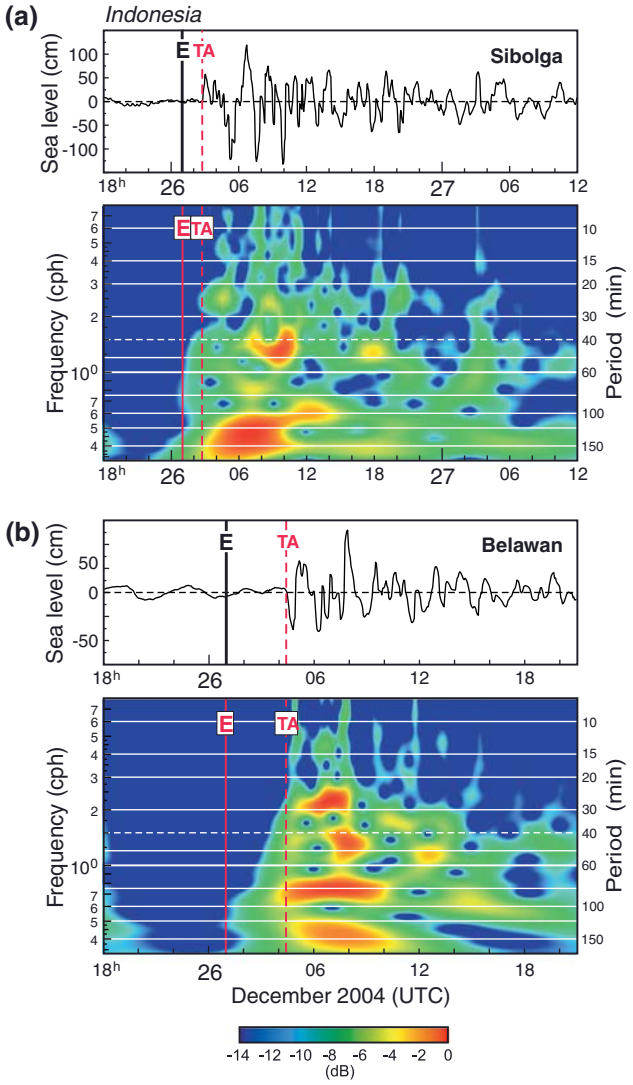


Figure 10
Tsunami records at the Indonesian tide gauges (a) Sibolga, (b) Belawan, (c) Panjang, (d) Prigi, and (e) Lembar and their *f-t diagrams*. The dashed vertical line indicates the tsunami arrival time ("TA"); the solid red vertical line "E" denotes the time of the main earthquake shock.

first arrival. It is obvious that there were different physical mechanisms responsible for formation of the maximum waves at Prigi and those on the coasts of Thailand and northwestern Sumatra. Apparently, the local and regional topography played an important role in the formation of the oscillations observed at Prigi. The spectrum of the tsunami record at Prigi has two peaks with neighboring periods of 40 and 34 min

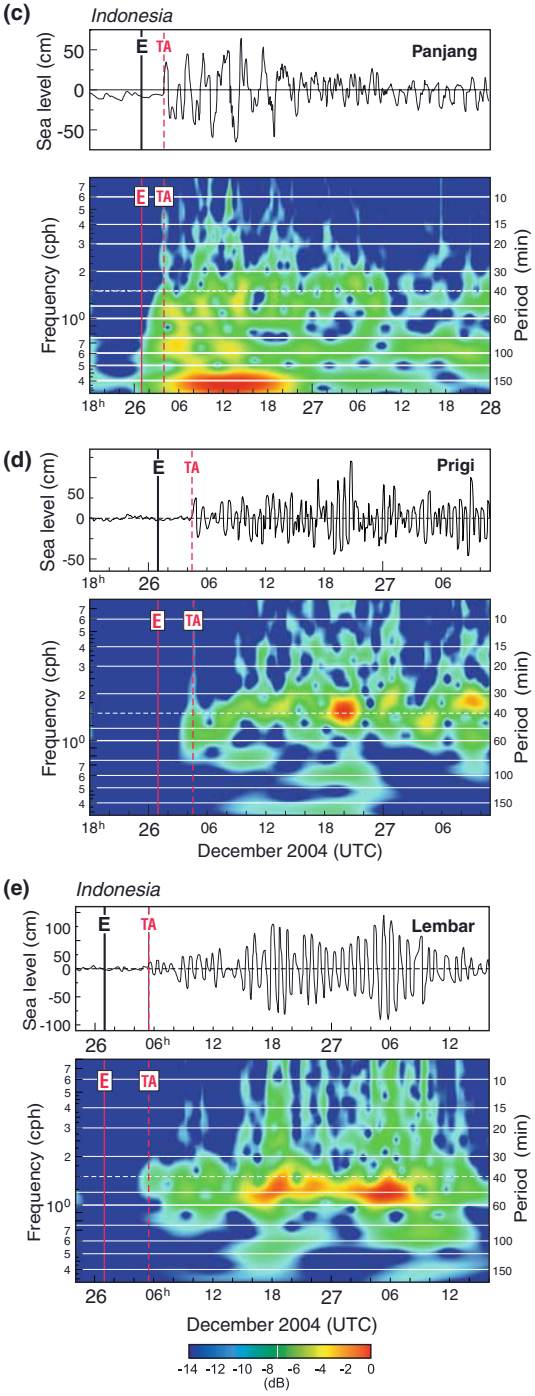


Figure 10
(Contd.)

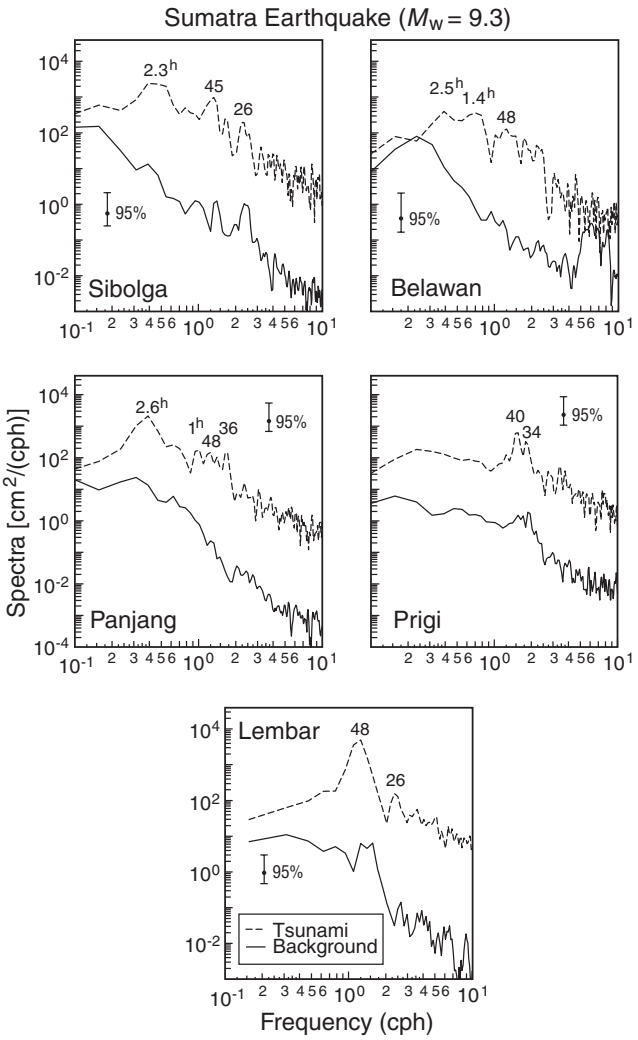


Figure 11
As in Figure 3 but for the five Indonesian tide gauge records: Sibolga, Belawan, Panjang, Prigi and Lembar.

and the same peaks are evident in the background spectrum (Fig. 11), indicating that both peaks have a topographic origin.

The Indonesian tide gauge station farthest from the source is Lembar located on the west coast of Lombok Island (east from Jawa, close to the Island of Bali; see Fig. 9). The record at this site (Fig. 10e) is distinct in that the oscillations were highly regular and monochromatic with a dominant period of 48 min (see *f-t* diagram in Fig. 10c and the spectrum of tsunami waves in Lembar in Fig. 11). In contrast, the

tsunami waves recorded at Sibolga and Belawan were irregular and polychromatic (see the *f-t* diagrams in Figs. 10a and 10b). Consequently, the tsunami record at Lembar is similar to the record at Prigi (Fig. 10d) and remarkably similar to the tsunami record at Manzanillo, the Mexican tide gauge which recorded the maximum tsunami waves in the Pacific Ocean associated with the 2004 Sumatra earthquake (see Fig. 13, RABINOVICH *et al*., 2006). Another specific feature of the Lembar record is very clear wave-train structure. The first train containing four waves (first semi-wave was positive) arrived at this site at 05:27 UTC, 4 hr 28 min after the earthquake (tsunami travel time to this station was erroneously estimated as 1 hr 51 min by MERRIFIELD *et al*., 2005). The maximum trough-to-crest wave in this train was 26 cm (Fig. 10c). At about 08:00 UTC (i.e., $\sim$ 7 hours after the earthquake), the second wave train arrived, including six high waves with maximum height of 69 cm. Then, at about 14:00, UTC the third wave train arrived, with a maximum wave of 157 cm. Finally, around 00:30 UTC on December 27, the fourth and the highest wave train arrived. The maximum wave height in this train (and in the record ) of 185 cm was observed at 05:18 UTC; i.e., 28 hr 19 min after the earthquake and 23 hr 51 min after the first tsunami arrival. This record clearly demonstrates problems for tsunami warning for some sites: it is quite difficult to raise the alarm about approaching destructive tsunami waves a full day after the first arrival. Clearly, the tsunami behavior at Lembar (as well as at Manzanillo) is due to local resonance. In fact, the background spectrum at Lembar has the same resonant peak of 48 min as did the tsunami spectrum at this site (Fig. 11). It is apparent that the 48-min resonant oscillation at this site matched the dominant frequency band of the source.

The newly digitized records for Sibolga, Belawan, Panjang, Prigi and Lembar had different start times and durations. Consequently, the constructed *f-t* plots for these stations also had different lengths. For this reason, instead of combining all these plots (as we did for the stations from Groups 1 and 2; see Figs. 4 and 8), we created separate *f-t* diagrams for each of the records (Fig. 10). This better illustrates specific details of the frequency bands for individual wave trains. In particular, the *f-t* diagram for Panjang indicates that the first low-frequency train of tsunami waves had a characteristic period of 160 min and duration of 16 hours, while at Prigi the 34–40 min period tsunami oscillations were observed throughout the entire period of observation. The *f-t* plots for Sibolga and Belawan look similar, indicating the irregular chaotic character of the observed tsunami oscillations and the considerable energy at low frequencies (periods 80–150 min) and at periods 30–50 min. The spectra of these records (Fig. 11) give similar results and, unlike the single dominant period observed at Lembar, show a variety of long-period oscillations.

Arrival times for the Indonesian stations presented in Table 3 demonstrate that the wave front propagated along the south-southwestern coasts of the islands of Sumatra, Jawa and Bali with an approximate speed of 540 km/h. The arrival times at different sites were in good agreement with each other and with the calculated tsunami propagation time (Fig. 1). At all stations located on this side of the island

chain (Sibolga, Panjang, Prigi and Lembar) the first semi-wave was positive. It would appear that at least part of the tsunami wave energy had propagated from the source area along the island chain as trapped waves. It is likely that these trapped waves (edge Stokes waves) were responsible for the *maximum waves* observed at Sibolga, Panjang, Prigi and Lembar. In contrast, the first observed waves were non-trapped tsunami waves that had arrived from the open ocean (see Fig. 1).

## 5. Southern and Antarctic Stations

Most tide gauges in the Indian Ocean are located in the northern or central parts of the ocean. There are only a few tide gauges located in the southern part of the ocean (at some French islands) and a few more on the Antarctic coast, including the French station at Dumont d'Urville, the Japanese station at Syowa and four Australian Antarctic stations. These stations (Group 4) are examined in this section (see Fig. 1 for exact positions of the stations).

### 5.1. French Southern and Antarctic Territories

Service d'Observations ROSAME, LEGOS/OMP, France provided us with data for three stations for the French Southern and Antarctic Territories: Kerguelen, Saint Paul and Dumont d'Urville (Fig. 1). Unfortunately, detailed interpretation of the waves was limited by the inadequate (for tsunami recording purposes) sampling intervals of 60 min for Kerguelen and Saint-Paul, and 30 min for Dumont d'Urville (Table 4). Despite the long sampling interval, tsunami waves are evident in the records (Fig. 12). Estimated parameters of the waves are presented in Table 4. Here, the slightly diminished wave heights in Figure 12 compared to estimates presented in Table 4 arise from high-frequency filtering of the tsunami oscillations presented in the plots. Ideally, we should take into account the low resolution of these height estimates due to the inadequate sampling step. More specifically, the true wave height (the tsunami oscillations that would have been recorded, for example, with 1-min sampling) is likely 2 to 3 times higher, so the estimates in Table 4 should be considered as qualitative rather than quantitative. On the other hand, the observed tsunami travel times are in good agreement with the predicted travel times (Fig. 1). An interesting aspect of this group of southern tsunami records is the factor of 4.5 greater wave heights measured at Kerguelen compared to those measured at Saint Paul. According to the numerical model of the 2004 Sumatra tsunami by TITOV *et al.* (2005), this effect is due to local amplification of tsunami waves that impinged on the Kerguelen Ridge. The first semi-wave at all three stations is positive; the small negative waves in Figure 12 at the tsunami arrival times are artifacts of the high-frequency filtering.

Table 4

*Tsunami characteristics estimated from southern and Antarctic tide gauge records*

| No | Station | Country | Coordinates | Sampling interval (min) | Maximum wave height (cm); number | First wave | |
|---|---|---|---|---|---|---|---|
| | | | | | | Sign, arrival time (UTC) | Travel time |
| 1 | St. Paul | France | 38.72°S; 77.54°E | 60 | 15 (1) | (+) 07:30 | 6 hr 30 min |
| 2 | Kerguelen | France | 49.35°S; 70.22°E | 60 | 68 (3) | (+) 10:00 | 9 hr |
| 3 | Dumont d'Urville | France | 66.63°S; 140.01°E | 30 | 31 (4) | (+) 13:48 | 12 hr 49 min |
| 4 | Syowa | Japan | 69.00°S; 39.57°E | 0.5 | 78 (5) | (+) 13:40 | 12 hr 41 min |
| 5 | Casey | Australia | 66.27°S; 110.52°E | 10 | 88 (10) | (+) 12:00 | 11 hr 01 min |
| 6 | Davis | Australia | 68.57°S; 77.97°E | 10 | 94 (16) | (+) 13:10 | 12 hr 11 min |
| 7 | Zhong Shan | Australia | 69.38°S; 76.37°E | 10 | 56 (13) | (+) 13:20 | 12 hr 21 min |
| 8 | Mawson | Australia | 67.60°S; 62.87°E | 10 | 85 (3) | (+) 13:10 | 12 hr 11 min |

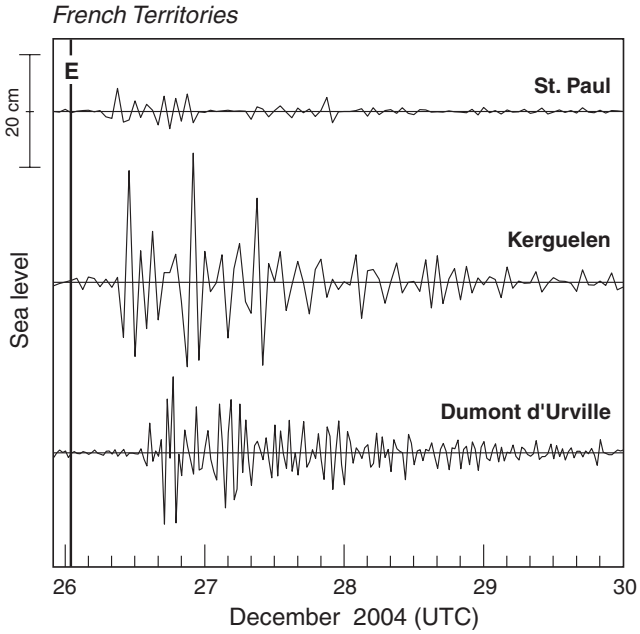


Figure 12
As in Figure 2 but for the three tide gauges from the French Southern and Antarctic territories (see Fig. 1 for tide gauge locations).

There is one more French island station in the Indian Ocean, La Réunion, which is not an island within the French Southern and Antarctic Territories but an overseas French department. In fact, this island is located in the tropical rather than in the southern part of the Indian Ocean (Fig. 1). For this reason, the statistical characteristics of the La Réunion tsunami record are included in Table 1 (for better comparison with the records from other tropical island stations located in the same region). A detailed analysis of this record (that only became available recently[2], i.e., much later than the GLOSS stations discussed in Section 2) is presented in this Section.

La Réunion, together with two other islands, Mauritius and Rodriguez (Fig. 1), form the Mascarene Islands group. The island from this group most affected by the 2004 tsunami was Rodriguez, at which the maximum tsunami runup was about 2.9 m (HÉBERT *et al.*, 2007). As mentioned in Section 2, the Rodriguez tide gauge was totally destroyed by the arriving tsunami waves; no tsunami record exists at this site. The Port Louis tide gauge located on Mauritius Island clearly recorded the 2004 tsunami waves; the corresponding digital record, which was examined in a few days after the event, was considered in Section 2 (see Table 1 and Figs. 2–4). The situation with the La Réunion record is quite different. As noticed by HÉBERT *et al.* (2007), the tsunami data from this site are a good illustration of recordings by an instrument that is poorly designed for tsunami measurements and even more poorly designed for tsunami alerts. An analog tide gauge located in the western harbor of La Pointe des Galets during three days continuously recorded a superimposed record of tsunami waves mixed with tides. Only recently has this record has been deciphered and digitized (HÉBERT *et al.*, 2007).

The first tsunami wave (a positive wave similar to those observed at most stations in the Central and West Indian Ocean) arrived at La Réunion at 07:55 UTC, in good agreement with tsunami arrivals at Rodriguez (06:40) and Port Louis, Mauritius (07:46) (Table 1). The estimated tsunami travel time (6 hr 56 min) closely matches the calculated tsunami travel time (Fig. 1). The maximum wave height at this site (70 cm) was smaller than at Port Louis (195 cm) probably because of a weak local response of the harbor of La Pointe des Galets; runup data along the coast of La Réunion ranged from 1 to 2 m with the maximum of 2.7 m measured at the east coast (HÉBERT *et al.*, 2007).

The La Réunion de-tided record and the corresponding *f-t* diagram are shown in Figure 13a. The plot clearly indicates that there were no noticeable background oscillations prior to the tsunami arrival. The first 12 hours after the arrival were the most energetic and mainly associated with two trains of waves: The first train was longer (~6-7 hours) and the second, shorter (~3 hours). As evident in the *f-t* diagram, the most intriguing feature of the tsunami waves at La Réunion are the

[2] The digitized record from the La Réunion tide was provided by Hélène Hébert (Laboratoire de Détection et de Géophysique, Bruyères-le-Châtel, France).

short-period (10–25 min) oscillations. Dominant oscillations with similar periods were also observed at Mauritius (Port Louis) but were not observed at other stations located in the West and Central Indian Ocean; e.g., at the Maldives or Seychelles

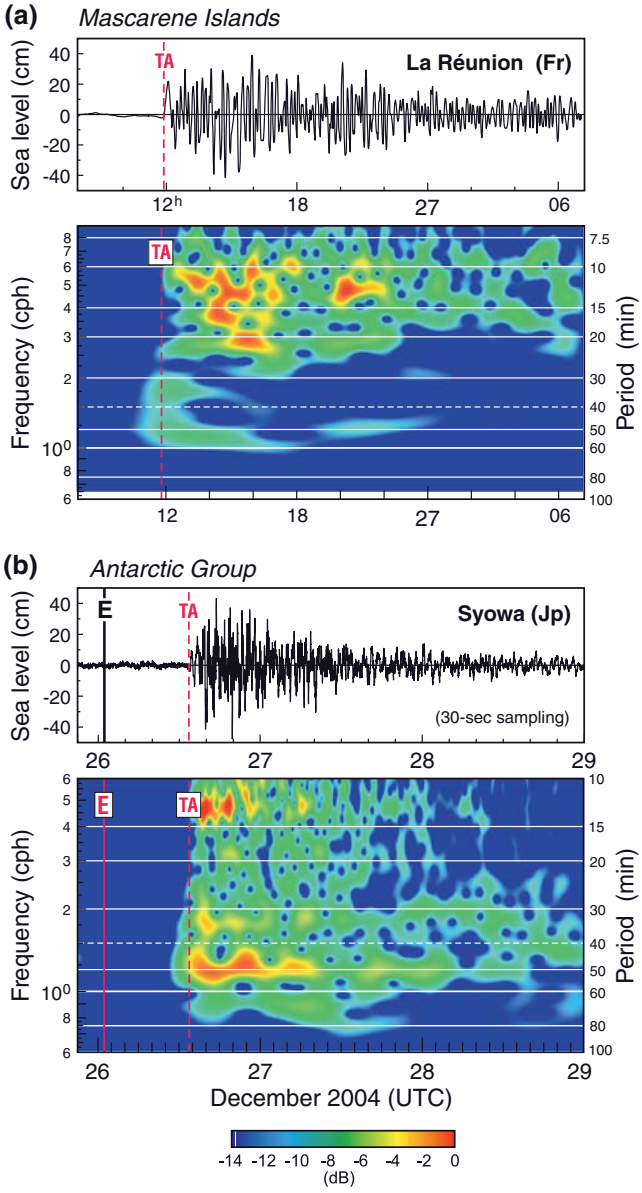


Figure 13
(a) Tsunami record at La Réunion Island and its *f-t diagram*; (b) as in (a) but for the Japanese Antarctic station Syowa. (See caption Fig. 10).

islands (see Section 2, Fig. 4). So the question is: Was this just a coincidence or a specific feature of the Mascarene Islands region?

### *5.2. Antarctic Japanese Station Syowa*

The Japanese Antarctic station Syowa (Showa), maintained by the Hydrographic and Oceanographic Department of the Japan Coast Guard has provided critical information regarding the 2004 Sumatra tsunami propagation in the southern region of the Indian Ocean (Fig. 1). The high-quality record at this station had a sampling interval of 30 sec, enabling us to undertake a detailed analysis of the tsunami waves. (The de-tided high-pass filtered tsunami record at this station is shown in Fig. 13b and the main features of the waves are given in Table 4). The tsunami waves arrived at Syowa at 13:40 UTC, yielding a tsunami travel time of 12 hr 41 min, consistent with the computed travel time (Fig. 1). The maximum observed tsunami wave height 78 cm was associated with the fifth wave that arrived about 4 hrs after the initial tsunami arrival. At this site, the tsunami record had a long (>3 days) ringing time with several wave trains evident in the record and in the corresponding *f-t* diagram (Fig. 13b). These trains apparently arrived at the site after multiple reflections from continental boundaries, thereby bringing additional energy that enhanced the local tsunami oscillations and supported the protracted ringing. Strong oscillations with slow energy decay were observed at Syowa over a period of 18–20 hours. These oscillations appear to be mainly associated with two ranges of periods having the highest energy concentration (see the *f-t* diagram in Fig. 13b): (a) ~48–58 min; and (b) 12–14 min. Pronounced oscillations were also observed at periods of 33 to 38 min. We note that the longer period oscillations (periods 48–58 and 33–38 min) have substantially longer ringing than the shorter period oscillations of 12–14 min: The latter became unrecognizable from the background noise after 1.5 days, while the former remained evident even after 2.5 days.

### *5.3. Australian Antarctic Stations*

The Australian Antarctic Division has four digital tide gauges on the Antarctic coast of the Indian Ocean: Casey, Davis, Mawson and Zhong Shan (Nella Fjord) (Fig. 1). The gauges are bottom-mounted instruments designed and constructed by Platypus Engineering (Hobart, Australia). The Paroscientific Digiquartz Transducer pressure sensor provides a sea-level resolution of 1.4 mm. The main purpose of these tide gauges was to measure tidal, seasonal and climatic variations (in particular, sea-level changes associated with the Antarctic Circumpolar Current). No one had anticipated that tsunamis could occur in this region and that these instruments could be used to examine characteristics of such waves. Because of this, all four instruments were set to a long sampling interval of 10 min. Nevertheless, all these tide gauges clearly recorded the 2004 Sumatra tsunami waves (Figure 14 presents the de-tided records for

the four instruments; the corresponding *f-t* diagrams are shown in Figure 15). Statistical characteristics of the observed tsunami waves are presented in Table 4.

A noteworthy feature of the four records is their mutual consistency (Fig. 14): the maximum observed trough-to-crest wave heights of 85 to 94 cm were similar (the only exception being Zhong Shan where the maximum wave height was only 56 cm apparently because the tide gauge was located deep within Nella Fjord), the records had > 2 days ringing, and the first waves were positive. Arrival times at Davis, Zhong Shan and Mawson were almost identical (13:10–13:20 UTC, i.e., 12 hr 11 min to 12 hr 21 min after the earthquake). At Casey, the waves arrived about 70 min earlier (at 12:00 UTC). In all cases, the observed times closely match the estimated arrival times (Fig. 1).

The *f-t* diagrams for the four Australian Antarctic stations "look" similar (Fig. 15) in the sense that diagrams indicate that significant tsunami oscillations

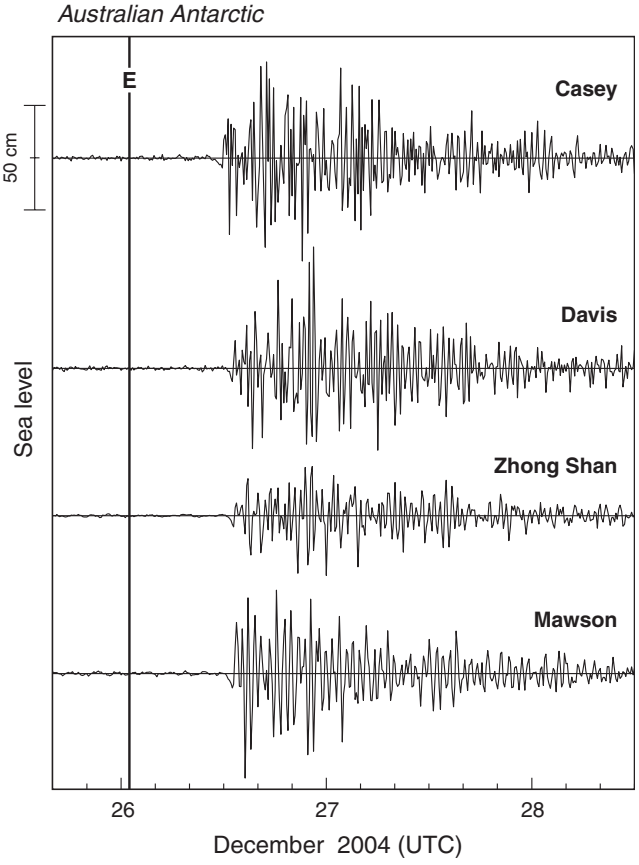


Figure 14
As in Figure 2 but for the four Australian Antarctic stations.

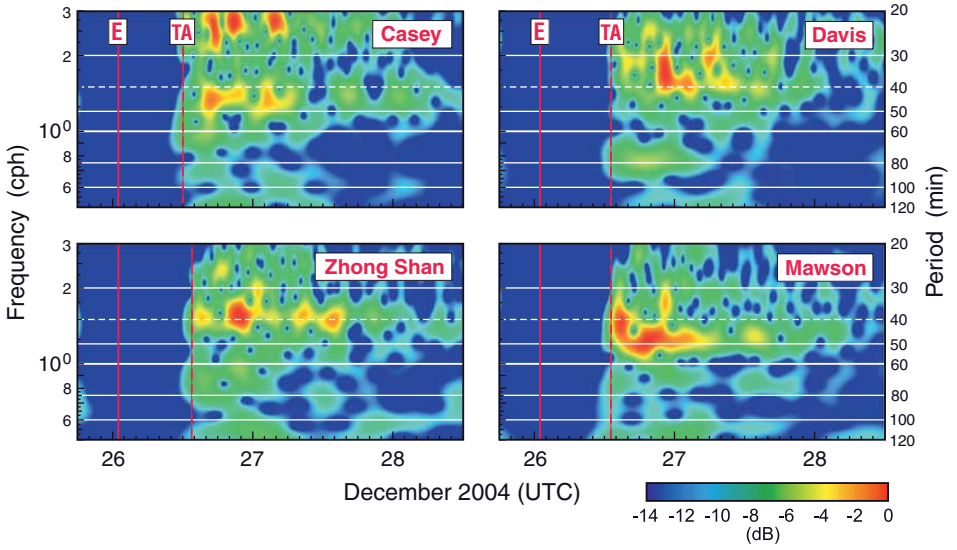


Figure 15
As in Figure 4 but for records of the four Australian Antarctic stations shown in Figure 14.

occurred at all stations during the first day, followed by at least one more day of detectable oscillations. However, the dominant periods of tsunami oscillations at different stations were clearly distinct, apparently because of the influence of local resonant responses (approximately 45 and 23–24 min at Casey; 30–40 min at Davis; 35–40 min at Zhong Shan; and 45–50 min at Mawson).

### *5.4. Spectral Analysis*

We again have used spectral analysis to more precisely estimate the dominant frequencies for waves observed at the Southern and Antarctic stations. The records for Kerguelen, Saint-Paul and Dumont d'Urville are not analyzed because the sampling interval at these stations (30–60 min) is too long, preventing analysis of waves with periods less than 1–2 hours.

The spectra of the background and tsunami oscillations for stations of Group 4 are shown in Figure 16 (La Réunion background spectrum cannot be estimated since the digitized segment of the record preceding the tsunami arrival is too short). The periods of spectral peaks are indicated. The tsunami spectra for all sites are approximately two orders of magnitude greater than the background spectra. In general, the main frequency band of increased sea-level energy associated with the arriving tsunami waves, is approximately the same for all stations (with certain limitations related to different sampling interval and, consequently, different Nyquist frequencies; see EMERY and THOMSON, 2003): $\sim$ 0.3 to 3.0 cph (20 cph for Syowa). However, the frequencies of individual peaks are different at each site. For example,

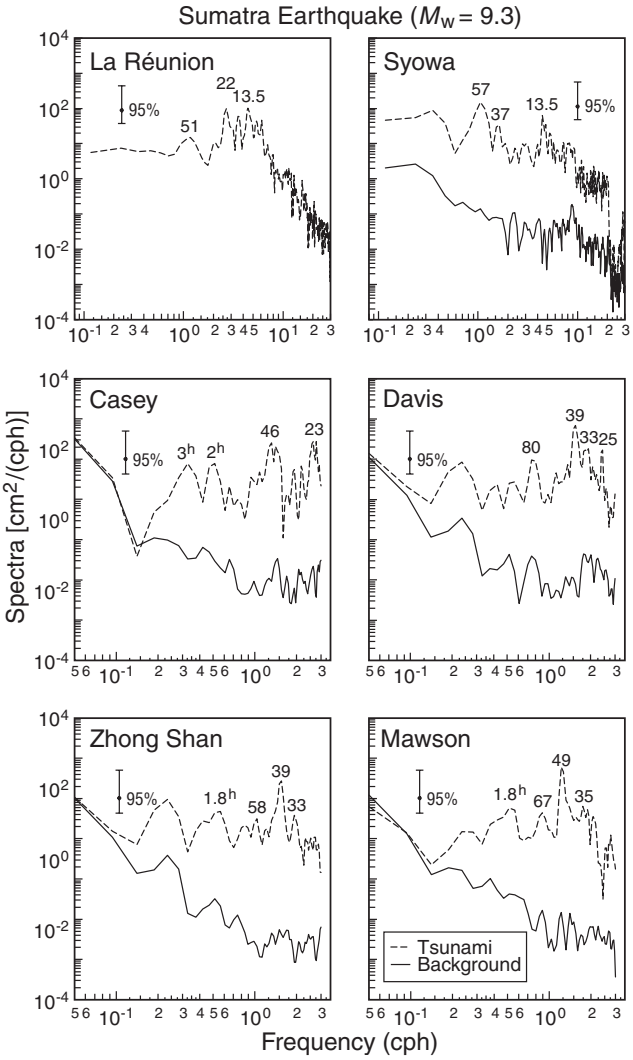


Figure 16
As in Figure 3 but for six stations of Group 4 (La Réunion, Syowa and four Australian Antarctic).

the main peaks for the La Réunion spectrum are at 22 and 13.5 min, with a weaker peak at 51 min. At Syowa, we find prominent peaks at periods of 57 and 13.5 min, and a much weaker peak at 37 min (in good agreement with the *f*-*t* diagrams in Fig. 13). The principal peaks in the tsunami spectra of the Australian Antarctic stations are 3 hr, 2 hr, 46 min, and 23 min (Casey); 80, 39, 33 and 25 min (Davis); 1.8 hr, 58, 39 and 33 min (Zhong Shan); and 1.8 hr, 67, 49 and 35 min (Mawson). These peaks likely reflect interaction of the arriving tsunami waves with the local topography. From this point of view, it is interesting to compare the tsunami spectra

for Davis and Zhong Shan, two stations located relatively close together (within 110 km). The spectral peaks at 39 and 33 min are at almost the same periods and are likely related to shared resonant characteristics of the shelf in the Amery Basin of the Antarctic coast, while other peaks are probably associated with individual topographic features. Despite differences in the tsunami spectra at each site, the overall range of periods with the highest energy at all stations (except La Réunion) lies within the 30 to 60 min band, which is approximately the same as for tsunami spectra at other sites in the Indian (Figs. 3 and 7), Atlantic, and Pacific oceans (cf., RABINOVICH *et al.*, 2006).

## 6. South African Stations

There were eight tide gauges on the coast of the Republic of South Africa (RSA) operating at the time of the 2004 Sumatra earthquake (Fig. 17, Table 5) and all of them recorded the tsunami waves quite clearly. (Data from these gauges were provided by the Hydrographic Office of the RSA). Two of the instruments (for Richards Bay and Port Nolloth) were Kalesto radar gauges; the six others were SRD acoustic tide gauges. All gauges had 3 min sampling intervals, but the data collection procedure was different for the different types of gauges. The SRD gauge takes one reading every minute and averages it over 3 min, whereas the radar gauge takes 40 readings and averages them over 17 sec; the 17 sec readings are then averaged over 3 min. For this reason, the data from the SRD gauges tend to be ''spiky'' while those from the radar sites are much smoother (Ruth Farre, Pers. Comm., 2005). Our preliminary analysis of the RSA tide gauge data consisted of editing the records, correcting the data for spikes, interpolating the gaps, and calculating and subtracting

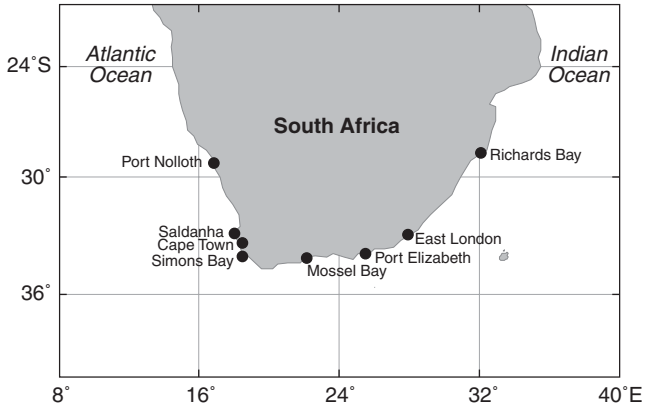


Figure 17
Map of the South African coast with positions of tide gauges.

Table 5

*Tsunami characteristics estimated from South African tide gauge records*

| No | Station | Country | Coordinates | Sampling interval (min) | Maximum wave height (cm); number | First wave | |
|---|---|---|---|---|---|---|---|
| | | | | | | Sign, arrival time (UTC) | Travel time |
| 1 | Richards Bay | RSA | 28.80°S; 32.08°E | 3 | 152 (24) | (+) 12:06 | 11 hr 07 min |
| 2 | East London | RSA | 33.02°S; 27.92°E | 3 | 128 (2) | (+) 12:28 | 11 hr 29 min |
| 3 | Port Elizabeth | RSA | 33.97°S; 25.47°E | 3 | 268[2] (4?) | (+) 13:12 | 12 hr 13 min |
| 4 | Mossel Bay | RSA | 34.18°S; 22.08°E | 3 | 156 (6) | (+) 14:01 | 13 hr 02 min |
| 5 | Simmons Bay[1] | RSA | 34.19°S, 18.44°E | 3 | 85 (29) | (+) 14:18 | 13 hr 19 min |
| 6 | Cape Town[1] | RSA | 33.07°S, 18.43°E | 3 | 88 (32) | (−) 15:00 | 14 hr 01 min |
| 7 | Saldanha[1] | RSA | 33.02°S, 18.97°E | 3 | 74 (12) | (−) 15.28 | 14 hr 29 min |
| 8 | Port Nolloth[1] | RSA | 29.25°S, 16.87°E | 3 | 49 (19) | (+) 16:01 | 15 hr 02 min |

[1] Atlantic Ocean stations.
[2] The crest of the largest wave was chopped off.

the tides. The subsequent de-tided series (Fig. 18) were of sufficiently high quality to permit a detailed tsunami analysis. Although four of the eight stations (Port Nolloth, Saldanha, Cape Town, and Simmons Bay) are officially located in the Atlantic Ocean (Fig. 17), we have included all RSA records in our present analysis instead of separating them between the Indian (Part 1) and Atlantic (Part 2) Oceans.

As shown in Table 5, the tsunami waves arrived at the east coast of South Africa at approximately 12:00–12:30 UTC (11–11.5 hours after the earthquake). The waves then hit the south coast at ~13:00–14:00 (12–13 hours after the earthquake) and the west (Atlantic) coast at ~14:20–16.00 (13hr 20min — 15 hrs after the earthquake). All times are in good agreement with calculated tsunami travel times (Fig. 1). At all sites, the first tsunami wave was positive. The maximum wave height (2.7 m) was recorded at Port Elizabeth. Apparently, the actual wave height was even higher but the wave crest wave was chopped off due to an instrumental problem (Fig. 18). The furthest recorded death associated with the 2004 Sumatra tsunami occurred in Port Elizabeth, about 8000 km from the earthquake epicenter (INTERNATIONAL FEDERATION OF RED CROSS and RED CRESCENT SOCIETIES, 2005).

Significant waves were recorded by the RSA tide gauges on the Indian Ocean coast. Specifically, 1.5 m at Richards Bay; 1.3 m at East London; and 1.6 m at Mossel Bay. Maximum wave heights on the Atlantic coast (Table 5) were much smaller, diminishing to 0.75–0.9 m at Simmons Bay, Cape Town and Saldanha, and 0.5 m at Port Nolloth. At East London, the second wave was the highest, while at Port Elizabeth and Mossel Bay, the fourth and sixth waves were the highest, respectively. At all other sites, the maximum waves were observed long after (8 to 26 hrs) the first wave arrival. A noteworthy feature of all records was the very long (>4 days) ringing time (Fig. 18). Several distinct wave trains with typical durations of 12 to 24 hrs

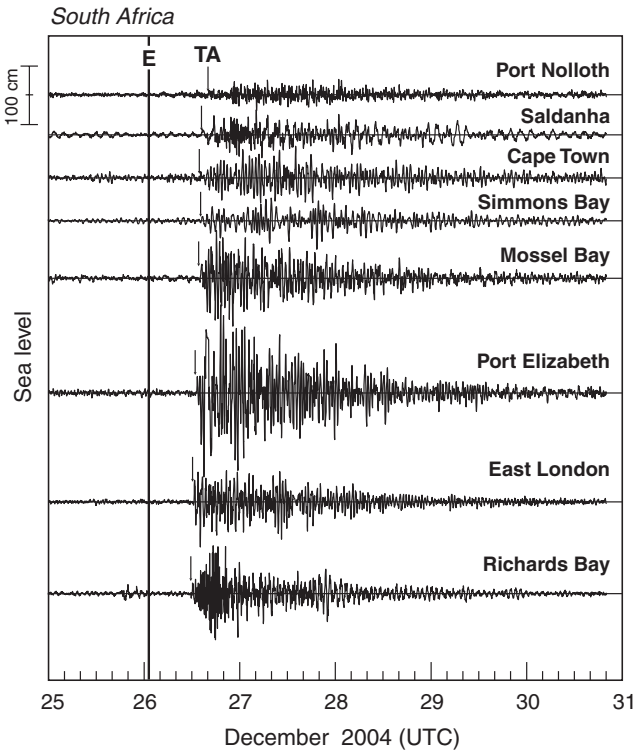


Figure 18
As in Figure 2, but for eight tide gauges on the coast of South Africa (see Fig. 17 for tide gauge locations).

appear in the records. Apparently the wave trains and long ringing times were due to multiple wave reflections from continental boundaries, including the Antarctic coast, the coasts of south and southeast Asia, and Western Australia.

Spectral analysis of the South African records (Fig. 19) followed the same procedure used for the other records (Figs. 3, 7, and 16). Because of their long tsunami ringing times and slow energy decay, the South African records required longer data segments. For these records, we have used 1024 samples (i.e., 3072 min $\approx$51 hr) for the background spectra and 640 samples (32 hr) for the tsunami spectra, yielding 14 and 8 degrees of freedom, respectively.

In general, the spectra for the South African records (Fig. 19) are similar to those for the Tropical stations (Group 1, Fig. 3), Indian coastal stations (Group 2, Fig. 7) and Southern stations (Group 4, Fig. 16). The main difference is the frequency range over which the tsunami wave energy significantly exceeds the background wave energy, which for the South African records is 0.3 to 5 cph (periods of 3.3 hr to 12 min). The most common spectral peaks, observed at several sites and most likely related to the source properties, are: 13–14 min; 37–38 min; 40–43 min; and 48–55 min. Low-frequency peaks are evident at some sites, specifically, 1.8 hr at Cape Town

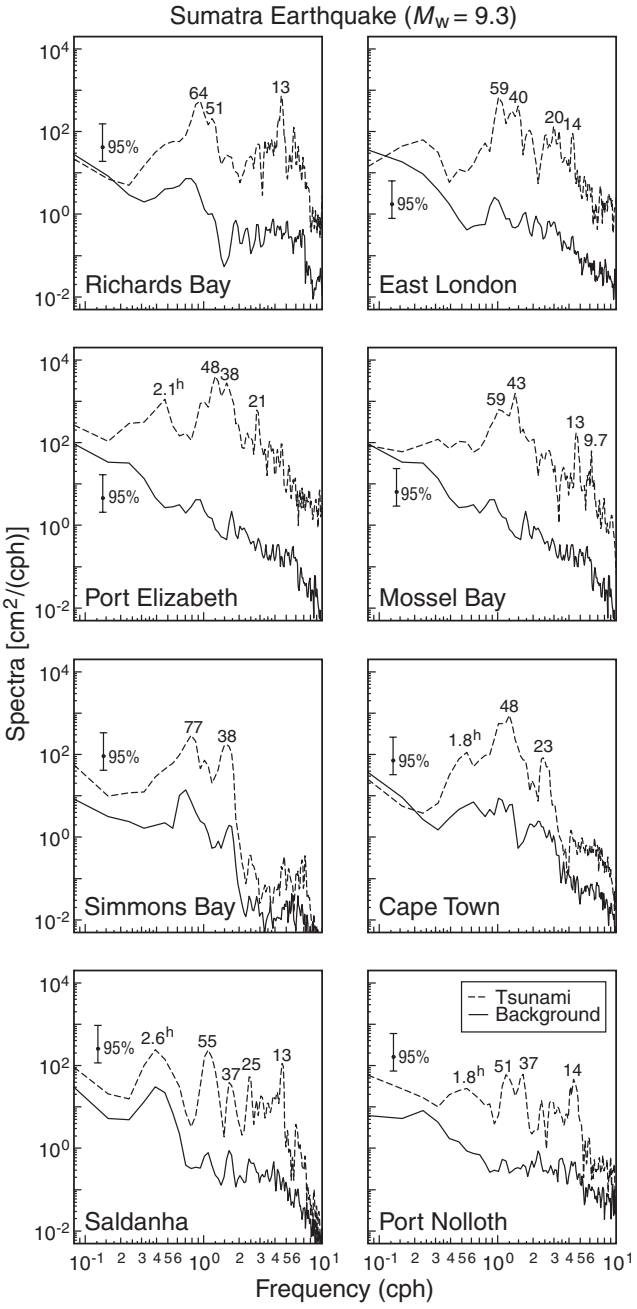


Figure 19
As in Figure 3 but for stations on the coast of South Africa (see Fig. 18 for the eight tide gauge records).

and Port Nolloth, 2.1 hr at Port Elizabeth, and 2.6 hr at Saldanha. Similar low-frequency peaks were observed at the Indian coastal stations (Fig. 7).

The time-frequency *f-t* diagrams for the eight South African stations (Fig. 20) clearly indicate that the tsunami arrivals (TA) times are close to the theoretical estimates (see Fig. 1). The dominant frequency oscillations in the *f-t* diagrams match those in the spectral estimates (Fig. 19). In general, the *f-t* diagrams for the South African stations are similar to those for other stations in the Indian Ocean (Figs. 4, 8, 13, and 15). However, the SA records have some distinct features:

(1) *Very long* (*~2.5 days*) *high-energy ringing* of broad-band tsunami oscillations for all stations located on the southern (Indian Ocean) and western (Atlantic) coasts. The only station with relatively short energetic ringing (~1.5 days) is Richards Bay, the station located on the eastern (Indian Ocean) coast and closest of the Southern African stations to the source area.
(2) *Strongly polychromatic tsunami oscillations*: The oscillations span a wide range of frequencies (0.5–8.0 cph) with several dominant frequency bands. The two exceptions are Simmons Bay and Cape Town, which are located close to one another. At both sites there is a definite cut-off frequency — 2.0 cph at Simmons Bay and 3.0 cph at Cape Town — with no oscillations above this frequency (cf., standard spectra in Fig. 19).
(3) *Distinct periodic train structure* at periods of approximately 12 hrs that is especially evident at the three stations located at the southwestern corner of South Africa: Simmons Bay, Cape Town and Saldanha. Apparently, these trains arise from tsunami wave reflection from the Antarctic coast.

## 7. Discussion and Conclusions

The 2004 Sumatra tsunami was the first global-scale tsunami in the instrumental era and the most extensively observed tsunami in history. The tsunami was recorded throughout the World Ocean, including the North Pacific and North Atlantic Oceans (RABINOVICH *et al.*, 2006). Because the coastal areas of the Indian Ocean received the brunt of the destruction and loss of life, the Indian Ocean is of prime importance in any study of the 2004 Sumatra tsunami. It was in the Indian Ocean that the tsunami waves were highest and where tide gauges, located relatively near the earthquake epicenter, can yield the most reliable and complete information about the source. In the present study, we have attempted to summarize the basic properties of all available tsunami records in the Indian Ocean. In total, we have located and analyzed 45 Indian Ocean records from the 2004 event, excluding the four South African records from tide gauges located on the Atlantic coast.

Despite our best effort, we cannot be certain that we have located all existing wave records for the Indian Ocean. Also, there are additional records from the South Australian coast, geographically located in the Indian Ocean, that have not been

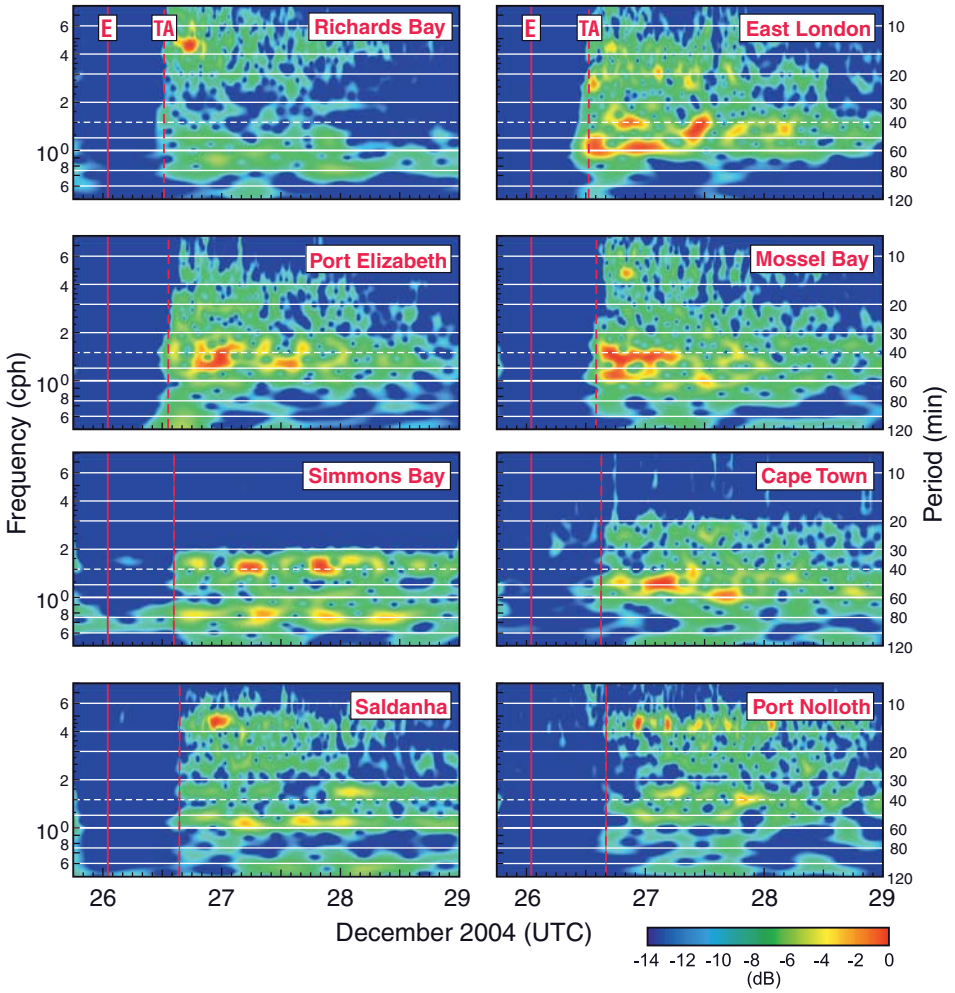


Figure 20
As in Figure 4 but for records for the eight South African stations in Figure 18.

analyzed in the present study. We suspect that there are a few more records that may eventually be found, for example from Pakistan, Bangladesh, and Malaysia. Digital or analog tide gauges probably do exist for these coasts and they likely were operating during the 2004 event. We may also have missed a few records from the coasts of India and Indonesia. Our experience for some other regions of the World Ocean is that it is quite difficult to find such records when there are independent tide gauge systems belonging to different owners (for example, in many countries, Port and Harbor authorities have their own instruments). Additional records for these regions are essential. Fortunately, the known records provide critical information concerning the propagation of the 2004 tsunami that can be used for source analysis

and reconstruction, and for formulation of an effective Indian Ocean Tsunami Warning System (IOTWS).

The present study enables us to formulate crucial questions for future tsunami analysis:

(*1*) *Island and continental stations*

Isolated, open-ocean islands are considerably less affected by topographic effects and normally have much lower background noise than mainland stations. For this reason, island stations could form the backbone of a future IOTWS. Island stations are especially important for examining tsunami source characteristics. In contrast, tsunami wave properties (particularly wave height and period) in continental coastal regions are strongly affected by the resonant characteristics of the shelf and coastline. Due to topographic trapping effects, tsunamis at continental coastal stations have much longer ringing times than isolated island stations. Our comparison of island and continental responses allows us to estimate the resonant influence of local topography and, therefore, tsunami risk for individual coastal areas.

(*2*) *Tsunami evolution with distance*

The tide gauge records for the Indian Ocean make it possible to examine the transformation and evolution of the 2004 Sumatra tsunami as a function of distance. The amplitudes of the tsunami waves emanating from the source area diminish, and the wave structure changes substantially, as the waves propagate across the Indian Ocean. Although the 2004 records reveal no simple relationship between observed wave heights and distance from the source (cf., RABINOVICH *et al.,* 2006), there are definite changes in wave property. For example, at sites nearest to the source area, the first wave was the highest (e.g., at almost all Thai stations, except Kuraburi, and at the Maldives and Cocos Islands) whereas at more distant stations, later waves were highest, depending on distance from the source. In particular, the second wave was highest at Colombo and Pointe La Rue, the third wave at Salalah, Lamu, and Kerguelen, and the forth wave at the Hillarys, Zanzibar, Port Elizabeth, and Dumont d'Urville. At far-field stations, such as most of the South African stations and at stations located in the Pacific and Atlantic oceans (RABINOVICH *et al.*, 2006), maximum waves were observed 8–30 hr after the first wave arrival. However, this effect is not limited to far-field waves. The Indian stations of Paradip, Vishakhapatnam, and Chennai, located on the eastern coast relatively near the source area, or the Indonesian stations Lembar and Prigi, also observed maximum waves long after the arrival of the first wave (Tables 2 and 3), an effect we attribute to multiple wave reflections from the east and west coasts of the Bay of Bengal for the Indian stations and to coastal trapping and local resonance effects for Lembar and Prigi. Other distant-dependent changes in the observed tsunami waves include an increase in wave ringing durations and the appearance of multiple wave trains.

''Train structure'' is one of the more spectacular properties of the far-field records for the 2004 event. Observations show that individual trains of incoming waves ''pump'' additional energy into the coastal regions, augmenting the local oscillations generated by preceding tsunami wave trains (the Lembar record in Fig. 10c is a spectacular example of such an effect). Global tsunami propagations models (TITOV *et al.*, 2005; KOWALIK *et al.*, 2005) demonstrate that these wave trains are associated with wave refraction by sea-floor features and reflections from continental margins. These oceanic features are responsible for the ever-evolving properties of the wave trains during their inter-ocean propagation. Thus, global and regional topography play major roles in formation of far-field tsunami features, leading to their convoluted wave structure and persistent ringing. On the other hand, in near-field regions, it is mainly the source configuration that determines the energy redistribution. The paucity of multiple tsunami pathways and reflections accounts for the relatively simple structure of tsunami records in near-field regions.

### (*3*) *Directional distribution of wave energy*

Both observations and global propagation models for the 2004 Sumatra tsunami confirm that the highly directional redistribution of tsunami energy by the mid-ocean ridge wave guide and regional topographic features are the primary factors determining the tsunami wave behavior in the far-field regions. Mid-ocean ridges played a major role as wave guides that transferred the tsunami energy to far-field regions outside the source area in the Indian Ocean (TITOV *et al.*, 2005; KOWALIK *et al.*, 2005).

There are, however, other major factors influencing the directivity of the tsunami wave energy. Tide gauge data clearly indicate that the source properties and the general geometry of the fault area and coastal boundaries in the source region effectively determined energy distribution and specific focusing effects for the 2004 event. The dominant energy flux propagated normally to the seismic rupture orientation (i.e., in the western and southwestern directions), whereas little energy radiated parallel to the direction of rupture (i.e., southeastward toward Australia and northward toward the coast of Bangladesh). It is for this reason that the 2004 tsunami amplitudes on the coasts of India, Sri Lanka, Maldives, East and South Africa were much higher than at the Cocos Islands, the coasts of North and West Australia or Mynmar and Bangladesh. There were no tide gauges available for the northern part of Bengal Bay, but it is known that the wave destruction was much weaker for the coasts of Mynmar (SATAKE *et al.*, 2006) and Bangladesh than for the coasts of Indonesia, Thailand, India and Sri Lanka. ABE (2006) suggested that, due to differences in length and width of the source region, the tsunami waves for the 2004 event would have significantly different dominant frequencies in the longitudinal and latitudinal directions. This is an interesting suggestion that needs to be carefully tested using both observational and simulated records that take into account the regional topographic effects.

In summary, our results reveal that the tsunami wave trains formed through wave refraction by sea-floor irregularities and reflections from continental margins are the primarily mechanism by which individual wave trains pump energy into local tsunami oscillations and create prolonged tsunami ringing at far-field coastal sites. Seismic source features determine major tsunami characteristics near the generation region, while topographic features determine wave characteristics for more distant regions.

When this paper was in press, three more analog records of the 2004 Sumatra tsunami were found for the Indian Ocean region. These records are from the following tide gauges: Djibouti (Republic of Djibouti, Northeastern Africa); Chah Bahar and Kangan (both Republic of Iran). These records will be examined separately.

## *Acknowledgements*

We gratefully acknowledge the following organizations for providing us with sea-level records for the 2004 Sumatra tsunami: The University of Hawaii Sea Level Center, Honolulu, Hawaii; the Survey of India, Delhi, and the National Institute of Oceanography, Goa, India; the Service d'Observations ROSAME, LEGOS/OMP, Toulouse, France; the National Tidal Centre and Australian Antarctic Division, Australian Bureau of Meteorology, Kent Town, South Australia; the Hydrographic and Oceanographic Department, Japan Coast Guard; the Hydrographic Office, Republic of South Africa; the Thai Marine Department and Hydrographic Department of Thai Navy, Thailand; and the Geodesy and Geodynamic Center in Indonesia. We also thank several people who helped us obtain, assemble and verify these data: Mark Merrifield (Honolulu, HI); S. I. Iwasaki (Tsukuba, Japan); Ruth Farre (Tokai, South Africa); K.A. Abdul Rasheed (Kochi, India), Hélène Hébert (Bruyères-le-Châtel, France), Laurent Testut (Toulouse, France), Bill Mitchell (Adelaide, Australia), Mike Davis and Paul Davill (Kent Town, Australia) and Parluhutan Manurung (Cibinong, Indonesia). We further thank Fred Stephenson (Sidney, BC) for his constant support and interest, Isaac Fine (Minsk, Belarus) for calculating tsunami travel times for the Indian Ocean and Maxim Krassovski (Victoria, BC) for helping construct maps for the study regions, and Patricia Kimber (Sidney, BC) for drawing the figures. Lastly, we thank the two reviewers for their thorough and constructive criticism of the manuscript. Partial financial support was provided by the Russian Federation through RFBR Grant 05-05-64585.

## References

Abe, K. (2006), *Dominant periods of the 2004 Sumatra tsunami and the estimated source size*, Earth Planets Space *58*, 217–221.

Ammon, C. J. *et al.* (2005), *Rupture process of the 2004 Sumatra-Andaman earthquake*, Science *308*, 1133–1138.

BERKMAN, S.C., and SYMONS, J.M. (1960), *The tsunami of May 22, 1960 as recorded at tide gauge stations*, U.S. Department of Commerce, Coast and Geodetic Survey, Washington, D.C., 79 pp.

BILHAM, R., ENGDAHL, R, FELDL, N., and SATUYABALA, S.P. (2005), *Partial and complete rupture of the Indo-Andaman plate boundary 1847–2004*, Seism. Res. Lett. *76*, 299–311.

CHOI, B.H., PELINOVSKY, E., KIM, K.O., and LEE, J.S. (2003), *Simulation of trans-oceanic tsunami propagation due to the 1883 Krakatau volcanic eruption*, Natural Hazards Earth Syst. Sci. *3*, 321–332.

DZIEWONSKI, A., BLOCH, S., and LANDISMAN, M. (1969), *Technique for the analysis of transient seismic signals*, Bull. Seism. Soc. Am. *59*, 427–444.

EMERY, W.J., and THOMSON, R.E., *Data Analysis Methods in Physical Oceanography*, Second and revised edition (Elsevier, New York 2003), 638 pp.

EWING, M., and PRESS, F. (1955), *Tide gauge disturbances from the great eruption of Krakatoa*, Trans. Amer. Geophys. Un. *36*(1), 53–60.

FINE, I.V., RABINOVICH, A.B., and THOMSON, R.E. (2005), *The dual source region for the 2004 Sumatra tsunami*, Geophys. Res. Lett. *32*, L16602, doi: 10.1029/ 2005GL023521.

FUJII, Y., and SATAKE, K. (2007), *Tsunami source of the 2004 Sumatra-Andaman Earthquake inferred from tide gauge and satellite data*, Bull. Seismol. Soc. Amer. 97(1A), S192–S207.

GARRETT, C.J.R. (1970), *A theory of the Krakatoa tide gauge disturbances*, Tellus *22*(1), 43–52.

GONZÁLEZ, F.I., and KULIKOV, E.A., *Tsunami dispersion observed in the deep ocean*. In *Tsunamis in the World* (ed. S. Tinti) (Kluwer Acad. Publ., Dordrecht 1993), pp. 7–16.

HÉBERT, H., SLADEN, A., and SCHINDELÉ, F. (2007), *Numerical modeling of the Great 2004 Indian Ocean tsunami: Focus on the Mascarene Islands,* Bull. Seismol. Soc. Amer. 97(1A), S208–S222.

International Federation of Red Cross and Red Crescent Societies (2005), *World Disasters Report*, Kumarian Press, 246 pp.

KOWALIK, Z., KNIGHT, W., and WHITMORE, P. (2005), *Numerical modeling of the global tsunami: Indonesian tsunami of 26 December 2004*, Sci. Tsunami Hazards *23*(1), 40–56.

KULIKOV, E.A., RABINOVICH, A.B., THOMSON, R.E., and BORNHOLD B.D. (1996), *The landslide tsunami of November 3, 1994, Skagway Harbor, Alaska*, J. Geophys. Res. *101*(C3), 6609–6615.

KURIAN, N.P., PILLAI, A.P., RAJITH, K., KRISHNAN, B.T.M., and KALAIARASAN, P. (2006), *Inundation characteristics and geomorphological impacts of December 2004 tsunami on Kerala coast*, Current Science *90*(2), 240–249.

LAY, T. *et al*. (2005a), *The Great Sumatra-Andaman earthquake of 26 December 2004*, Science *308*, 1127–1133.

LAY, T. *et al*. (2005b), *Response to Comment on "The Great Sumatra-Andaman earthquake of 26 December 2004"*, Science *310*, 1431b.

MERRIFIELD, M.A. *et al*. (2005), *Tide gage observations of the Indian Ocean tsunami, December 26, 2004*, Geophys. Res. Lett. *32*, L09603, doi:10.1029/2005GL022610.

MURTY, T.S. (1977), *Seismic Sea Waves - Tsunamis,* Bull. Fish. Res. Board Canada *198*, 337 pp.

NAGARAJAN, B., SURESH, I., SUNDAR, D. SHARMA, R., LAL, A.K., NEETU, S., SHENOI, S.S.C. and, SHETYE, S.R., and SHANKAR, D. (2006), *The great tsunami of 26 December 2004: A description based on tide-gauge data from the Indian subcontinent and surrounding areas*, Earth Planets Space *58*, 211–215.

NEETU, S., SURESH, I., SHANKAR, R., SHANKAR, D., SHENOI, S.S.C. and, SHETYE, S.R., SUNDAR, D. and NAGARAJAN, B. (2005), *Comment on "The Great Sumatra-Andaman earthquake of 26 December 2004"*, Science *310*, 1431a.

PELINOVSKY, E., CHOI, B.H., STROMKOV, A., DIDENKULOVA, I., and KIM, H.S., *Analysis of tide-gauge records of the 1883 Krakatau tsunami*. In *Tsunamis: Case Studies and Recent Developments* (ed. K. Satake) (Springer, Dordrecht 2005), pp. 57–77.

RABINOVICH, A.B. (1997), *Spectral analysis of tsunami waves: Separation of source and topography effects*, J. Geophys. Res. *102*(C6), 12, 663–12, 676.

RABINOVICH, A.B., THOMSON, R.E., and STEPHENSON, F.E. (2006), *The Sumatra tsunami of 26 December 2004 as observed in the North Pacific and North Atlantic oceans*, Surveys in Geophysics *27*, 647–677.

RASHEED, K.A.A. and, DAS, V.K., REVICHANDRAN, C., VIJAYAN, P.R., and THOTTAM, T.J. (2006), *Tsunami impacts on morphology of beaches along south Kerala coast, west coast of India*, Sci. Tsunami Hazards *24*(1), 24–34.

SATAKE, K. *et al*. (2006), *Tsunami heights and damage along the Myanmar coast from the December 2004 Sumatra-Andaman earthquake,* Earth Planets Space *58*, 243–252.

SIFFER, T. (2005), "Mercator" depth gauge recording of 26 December 2004 tsunami. (http://www.knmi.nl/onderzk/seismo).

SINGH, S.K., ORTIZ, M., GUPTA, H.K., and RAMADASS, D.G.A. (2006), *Slow slip below Port Blair, Andaman, during the great Sumatra-Andaman earthquake of 26 December 2004*, Geophys. Res. Lett. *33,* L03313, doi:10.1029/2005GL025025.

STEIN, S., and OKAL, E.A. (2005), *Speed and size of the Sumatra earthquake*, Nature *434*, 581–582.

SYMONS, G.J., *The Eruption of Krakatoa and Subsequent Phenomena* (Triibner and Co., London, 1888), 494 pp.

TAKAHASHI, R., and HATORI, T. (1961), *A Summary Report on the Chilean Tsunami of May 1960*, in *Report on the Chilean Tsunami*, Comm. Field Investigation on Chilean Tsunami, Tokyo, 23–34.

TANIOKA, Y., YUDHICARA, KUSUSOSE, T., KATHIROLI, S., NISHIMURA, Y., IWASAKI S.-I., and SATAKE, K. (2006), *Rupture process of the 2004 Great Sumatra-Andaman earthquake estimated from tsunami waveforms,* Earth Planets Space *58*, 203–209.

TITOV, V.V., RABINOVICH, A.B., MOFJELD, H., THOMSON, R.E., and GONZÁLEZ, F.I. (2005), *The global reach of the 26 December 2004 Sumatra tsunami*, Science *309*, 2045–2048.

TSAI, V.C., NETTLES, M., EKSTRÖM, G., and DZIEWONSKI, A.M. (2005), *Multiple CMT source analysis of the 2004 Sumatra earthquake*, Geophys. Res. Lett. *32*, L17304, doi:10.1029/2005GL023813.

TSUJI, Y., NAMEGAYA, Y., MATSUMOTO, H., IWASAKI, S.-I., KANBUA, W., SRIWICHAI, M., and MEESUK, V. (2006), *The 2004 Indian tsunami in Thailand: Surveyed runup heights and tide gauge records,* Earth Planets Space *58*, 223–232.

VAN DORN, W.G. (1984), *Some tsunami characteristics deducible from tide records*, J. Phys. Oceanogr. *14*, 353–363.

VAN DORN, W.G. (1987), *Tide gauge response to tsunamis. Part II: Other oceans and smaller seas*, J. Phys. Oceanogr. *17*, 1507–1516.

WIGEN, S.O. (1960), *Tsunami of May 22, 1960. West Coast of Canada*. Unpublished Report, Canadian Hydrographic Service, Sidney, BC.

WOODWORTH, P.L., BLACKMAN, D.L., FODEN, P., HOLGATE, S., HORSBURGH, K., KNIGHT, P.L., SMITH, D.E., MACLEOD, E.A., and BRADSHAW, E. (2005), *Evidence for the Indonesian tsunami in British tidal records*, Weather *60*(9), 263–267.

(Received May 5, 2006, accepted October 9, 2006)
Published Online First: January 30, 2007

Pure appl. geophys. 164 (2007) 309–323
0033–4553/07/030309–15
DOI 10.1007/s00024-006-0165-4



Pure and Applied Geophysics

# Quantification of Hydrophone Records of the 2004 Sumatra Tsunami

EMILE A. OKAL,[1] JACQUES TALANDIER,[2] and DOMINIQUE REYMOND[3]

*Abstract*—The 2004 Sumatra-Andaman tsunami was recorded by hydrophones of the International Monitoring System at Site H08 near Diego Garcia, notably in frequency bands extending outside the range of the Shallow Water Approximation. Despite the severe high-pass filtering involved in this instrumentation, we show that the spectral amplitudes recovered around $T = 87$ s can be successfully explained by generation from the seismic source, in the framework of the normal mode theory of tsunami excitation. At the lower frequencies characteristic of more conventional tsunami waves (800 to 3200 s), the signal is probably present in the hydrophone records, but reliable deconvolution of its spectral amplitude is precluded by the fact that the instrumental filters lowered the tsunami signal to the level of resolution of the instrument digitizer. In the context of distant tsunami warning, hydrophone records could provide useful insight into high-frequency tsunami components, and even at lower, more conventional, frequencies, provided that an unfiltered channel could be recorded routinely.

**Key words:** Tsunami, *T* waves, hydroacoustics, normal mode theory.

## *Introduction*

The catastrophic tsunami generated by the 2004 Sumatra earthquake was recorded not only by traditional tidal gauges (RABINOVICH, 2005), but also by a number of ancillary instruments using a wide variety of technologies, most of which had not been designed for such recording. Actually, some of these techniques had previously detected smaller tsunamis; these include satellite altimetry (SCHARROO *et al*., 2005), which had identified the 1992 Nicaragua tsunami (OKAL *et al*., 1999), and the use of GPS receiver arrays to infer variations in the electron content of ionospheric layers affected by the upwards continuation of the tsunami eigenfunction (OCCHIPINTI *et al*., 2005), as pioneered by ARTRU *et al*. (2005) in the case of the 2001 Peruvian event. Both techniques lend themselves well to the measurement of the

[1] Department of Geological Sciences, Northwestern University, Evanston, IL 60201, USA.
[2] Département Analyse et Surveillance de l'Environnement, Commissarviat à l'Energie Atomique, Boîte Postale 12, F-91680, Bruyères-le-Châtel, France.
[3] Laboratoire de Géophysique, Commissariat à l'Energie Atomique, Boîte Postale 640, F-98713 Papeete, Tahiti, French Polynesia.

tsunami on the high seas, unaffected by the complex, site-dependent and often nonlinear process of shoaling and runup which strongly deforms the waves before they can be recorded by tidal gauges.

In the wake of the Indonesian event, LE PICHON *et al.* (2005) also reported for the first time the detection of tsunami-generated signals at infrasound stations of the International Monitoring System (IMS) of the Comprehensive Nuclear-Test Ban Treaty Organization (CTBTO), although the exact mechanism of their generation remains unclear. In addition, YUAN *et al.* (2005), and later HANSON and BOWMAN (2005) reported detections of the arrival of the tsunami wave on horizontal seismometers at several stations on island and continental shores around the Indian Ocean, and suggested that such records may be related to a component of tilt at the relevant stations.

Finally, the 2004 Sumatra tsunami was recorded by hydrophones of the IMS (HANSON and BOWMAN, 2005), notably at Site H08 near Diego Garcia, approximately 2750 km from the epicenter (Fig. 1). These instruments are pressure sensors deployed in the SOFAR channel, at a depth of 1300 m. They are somewhat comparable in concept to the ocean-bottom "tsunameter" sensors of the DART project (TITOV *et al.*, 2005a) in that they capture subtle variations in pressure inside the oceanic water column; however the IMS hydrophones' primary mandate is to detect explosive sources in the ocean, and as such they have been designed as

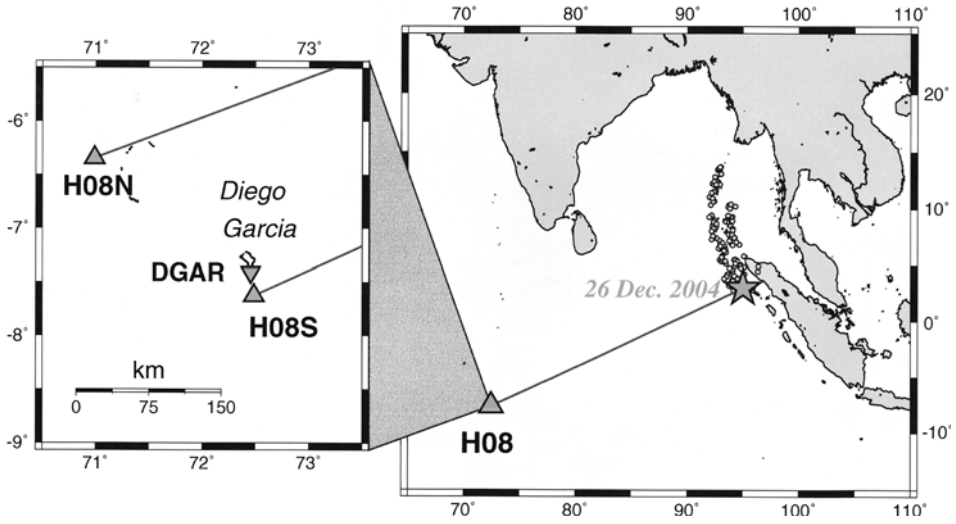


Figure 1
Location of the IMS station H08 at Diego Garcia (triangle), in relation to the 2004 Sumatra earthquake. The star shows the epicentral location of the initiation of rupture, and the smaller symbols the same-day aftershocks, illustrative of the dimension of the fault zone. The inset details the location of the Northern and Southern hydrophone triads, H08N and H08S respectively, relative to the atoll of Diego Garcia, and of the IRIS broadband seismic station (DGAR, inverted triangle), on the atoll itself.

high-frequency instruments, operating at very high sampling rates (250 Hz) and featuring strong high-pass filters in order to eliminate tidal and meteorological sources of noise. Nevertheless, the Sumatra tsunami was so large that it was well recorded even outside the designated frequency band of the instrument.

The purpose of this paper is to analyze quantitatively hydrophone records of the tsunami at Diego Garcia, and to show that order-of-magnitude quantifications of these records can yield acceptable results for the seismic moment $M_0$ of the parent earthquake in a range of frequencies where far-field tsunamis had not been previously studied, let alone quantified.

## *The Hydrophone Record at H08S1*

As part of the IMS, the hydroacoustic station H08 consists of two triads of instruments tethered to the island of Diego Garcia, BIOT. The Northern group (H08N) is located approximately 200 km to the Northwest of the island, while the Southern group (H08S) is only 25 km due South of the island (Figure 1). In this section, we concentrate on the record from Hydrophone H08S1, part of the Southern triad. The time series under consideration, shown on Figure 2a, starts at 04:00:00 GMT on 26 December, 2004, i.e., 3 hours after the Sumatra event, and runs for 9 hours. It is dominated by acoustic signals, most of which are *T* phases from large and small Sumatra aftershocks. However, as shown on Figure 2b, conventional surface waves are also recorded in the 30-to-100 mHz frequency band from the major aftershocks; the figure also shows energy around 10 mHz, arriving over a window of some 8 hours. This portion of the spectrogram is detailed in Figure 2c which clearly illustrates a strong dispersion. As reported by HANSON and BOWMAN (2005), this is interpreted as the arrival of the tsunami wave, since it matches perfectly the group time predicted by the linear approximation to the Navier-Stokes equations outside the range of validity of the shallow-water approximation (SWA), which predict a dispersion relation between angular frequency $\omega$ and wavenumber $k$ of the form

$$\omega^2 = g \cdot k \ \tanh(kH), \tag{1}$$

where $g$ is the Earth's gravity and $H$ the thickness of the water column. The corresponding times, computed for an ocean of depth $H = 4$ km and a source placed at the origin of rupture, as given by the USGS epicentral parameters (3.30°N; 95.98°E; origin time 00:58:53 GMT), are shown as the solid line on Figure 2c.

The spectrogram on Figure 2c documents the presence of substantial amounts of tsunami energy at frequencies significantly higher than for conventional tsunami waves, in particular in the 5 to 13 mHz frequency range. High-frequency tsunami components had been previously described in the gulf of Alaska using early prototypes of tsunameters (GONZÁLEZ and KULIKOV, 1993), and are particularly important to document and study, if possible quantitatively, in view of the

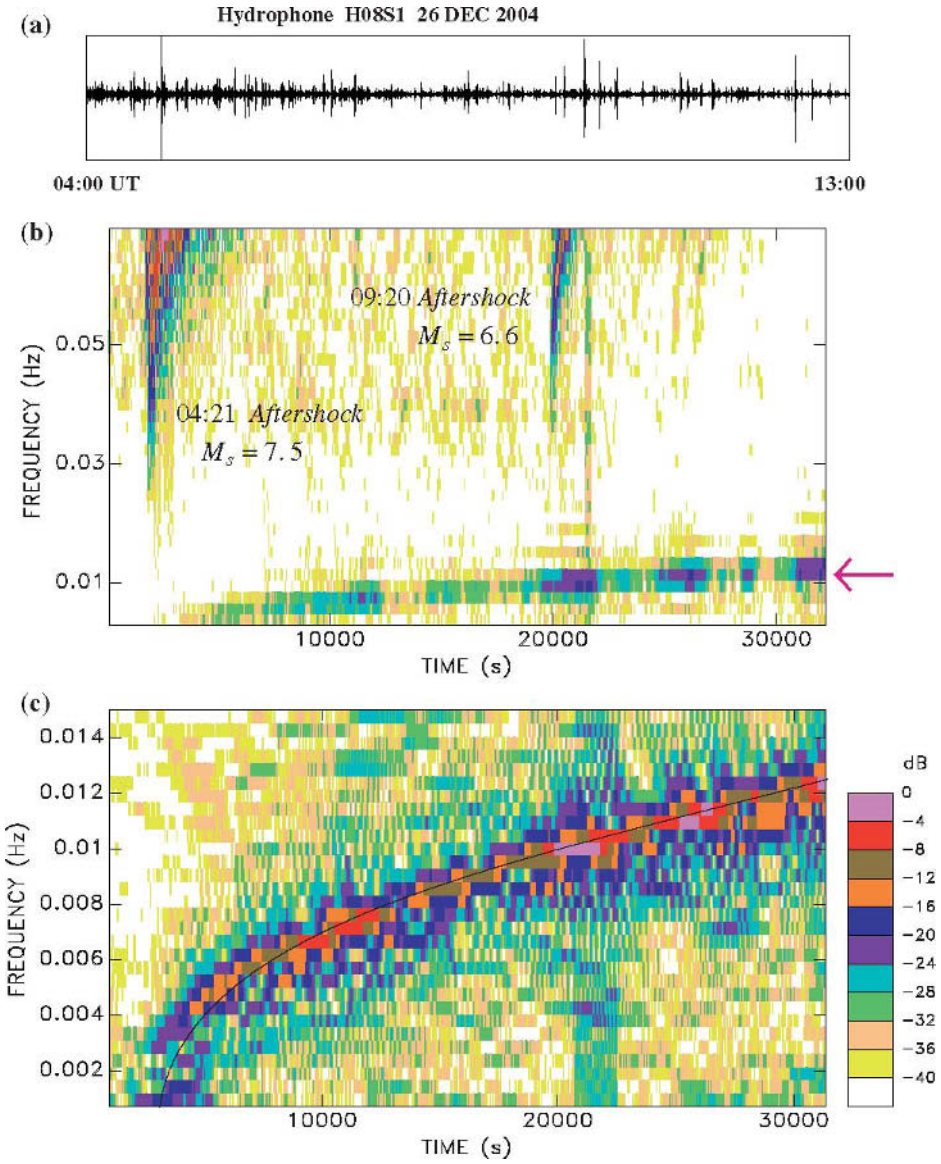


Figure 2

(**a**): Raw time series of the hydrophone record at H08S1, starting 04:00 GMT, i.e., approximately 3 hours after the Sumatra earthquake. (**b**): Spectrogram of the hydrophone record between frequencies of 2.9 and 70 mHz . The diagram is dominated by the Rayleigh waves of two major aftershocks, featuring classic dispersion. The tsunami wave appears as the strongly dispersed branch at $f \leq 0.01$ Hz (red arrow). (**c**): Close-up of the tsunami branch between frequencies of 0.7 and 15 mHz . Note the perfect agreement with the dispersion predicted by (1) (black line). Each pixel is colored according to the palette at right, relative to the maximum spectral amplitude for the spectrogram considered.

observation of anomalous activity in harbors, during which large vessels broke their moorings, up to four hours after the passage of the tsunami waves of reported maximum amplitude (OKAL *et al.*, 2006*a,b,c*). This phenomenon was tentatively interpreted as involving harbor resonances upon the arrival of higher-frequency spectral components of the wavetrain.

In order to quantify the tsunami record at H08S1, it is necessary to first deconvolve the instrument response, outside its designated range of frequencies. As response characteristics are available from the IMS data center only for $f \geq 0.1$ Hz (R. Bowman, pers. comm., 2005), we proceeded to verify the applicability of extending the computation of the response from available poles and zeroes to the frequency range (10 mHz) of the maximum recorded tsunami energy (Fig. 3a). This can be achieved by noting that the hydrophone also recorded conventional Rayleigh waves of the Sumatra earthquake in the same range of frequencies (Fig. 2b). These can be compared directly to the recording at the IRIS seismic station DGAR, on Diego Garcia Atoll, located 25 km from the hydrophone, i.e., considerably less than a wavelength away (Fig. 1). As detailed in the Appendix, a pressure sensor inside the oceanic column will record a long-period Rayleigh wave as an accelerometer whose sensitivity is proportional to the depth of the sensor. Based on this remark, we compare on Figure 3b the spectral amplitudes of the vertical displacements of the

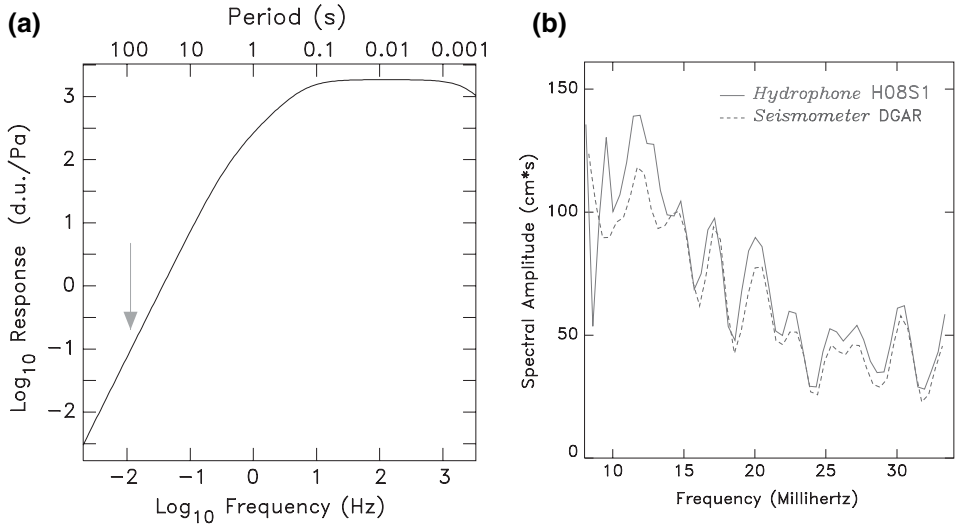


Figure 3

(**a**): Response to pressure of the H08S1 hydrophone, expressed as digital units (d.u.) per Pascal. Note the rapid $\omega^2$ fall-off at low frequencies (e.g., by a factor of 19000 from its nominal value at 100 Hz, for $T = 87$ s; arrow). (**b**): Deconvolved spectra of Rayleigh wave recordings of the Sumatra main shock on the H08S1 hydrophone (solid line) and at the nearby IRIS station DGAR (dashed trace). The former is expressed as equivalent vertical displacement of the ocean floor; see text and appendix for details.

Rayleigh wave trains recorded at H08S1 and DGAR, after appropriate deconvolution of the instrument responses. The agreement between the two spectra is excellent down to 15 mHz, and remains acceptable (within 20%) down to 10 mHz. This means that the calculation of the instrument response using published poles and zeroes can be safely extended to 10 mHz, which is three orders of magnitude or 10 octaves below the cut-off frequency of the main high-pass filters.

With this observation in mind, we elect to quantify the tsunami signal at H08S1 around the local maximum observed at 11.5 mHz ($T = 87$ s), for a group time of 11:17 GMT. We prefer this frequency to the principal signal around 10 mHz at 09:40 GMT, since the instrument response may be less well controlled, and the signal may also be altered by spurious energy in the wake of the large aftershock of 09:20 GMT (Fig. 2*b*). We then isolate a 6000–s window centered on the arrival (note that because of the extreme dispersion, this corresponds to very narrow band-pass filtering, between 81 and 95 s in period), and recover an average spectral amplitude of $2 \times 10^5$ Pa*s in this period range, with a peak value of $3.2 \times 10^5$ Pa*s (Fig. 4).

We proceed to convert this measurement to that of an equivalent vertical displacement of the ocean surface by computing the eigenfunction of the tsunami at 87 s in the normal mode formalism introduced by WARD (1980). For a 4–km deep ocean, we find that the equivalent normal mode has an orbital number $l = 3450$, a

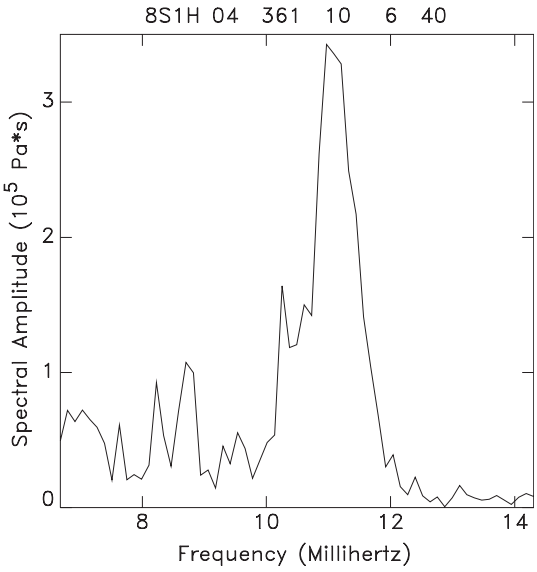


Figure 4
Spectral amplitude of the pressure signal of the tsunami wave deconvolved from the H08S1 trace. The window processed starts at 10:40 GMT and lasts 6000 s. The rapid fall-off of spectral amplitude is due to the extreme dispersion of the branch, under which windowing in the time domain amounts to narrow band-pass filtering.

phase velocity $C = 133$ m/s, and a group velocity $U = 74$ m/s. Figure 5 shows the variation with depth in the ocean column of the vertical displacement and overpressure components of the eigenfunction, respectively $y_1$ and $-y_2$ in the notation of SAITO (1967) and OKAL (1982) (note that the surface value of $y_1$ is usually written as $\eta$ in hydrodynamic applications). The breakdown of the SWA is expressed both by the curvature of these functions (which would otherwise vary linearly with depth), and by the much reduced value of $p$ at the ocean floor (22.2 Pa for $\eta = 1$ cm as opposed to 101 Pa under the SWA). At the sensor depth of 1300 m, we find that the impedance ratio of overpressure to vertical displacement at the surface is 3.95 Pa/cm (solid dot on Fig. 5). Thus, the measured pressure spectral amplitudes convert to spectral amplitudes of equivalent displacement at the surface, $\eta(\omega)$, of $5.1 \times 10^4$ cm*s (average) and $8.1 \times 10^4$ cm*s (peak value).

In turn, $\eta(\omega)$ is given directly by the classic surface wave excitation formula

$$|\eta(\omega)| = \frac{M_0}{\sqrt{\sin \Delta}} \sqrt{\frac{\pi}{2l}} \frac{a}{U} \left| s_R K_0 - i q_R l K_1 - p_R l^2 K_2 \right| \tag{2}$$

simply adapted from KANAMORI and STEWART (1976) by neglecting anelastic attenuation in the case of tsunamis. For a shallow crustal source, we take $K_0 = 0.12$, $K_1 = 0.5 \times 10^{-5}$ and $K_2 = -0.25 \times 10^{-8}$, in units of $10^{-27}\text{dyn}^{-1}$. Using a distance $\Delta = 25\,^\circ$, and the initial Harvard CMT focal geometry ($\phi = 329\,^\circ$; $\delta = 8\,^\circ$; $\lambda = 110^\circ$), we find $s_R = p_R = 0.13$; $q_R = 0.92$. The term between vertical bars in (2) is then

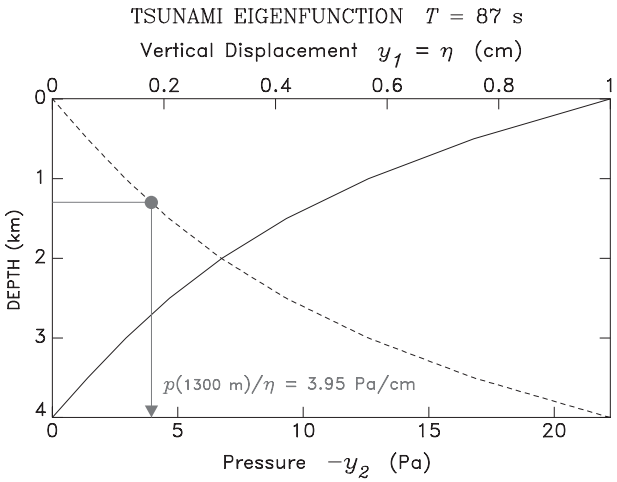


Figure 5
Structure of the eigenfunction of the tsunami in the water column at a period of 87 s. The solid line represents the vertical displacement $y_1$, normalized to $\eta = 1$ cm at the surface (top scale). The dashed line shows the overpressure $-y_2$ (bottom scale), reaching 22.2 Pa at the ocean floor. The projection of the solid dot (arrow) gives the impedance between the overpressure measured by the hydrophone at a depth of 1300 m and the equivalent wave height on the surface.

$2.7 \times 10^{-29}$dyn$^{-1}$. This finally leads to $M_0 = 6.7 \times 10^{29}$ dyn-cm from the average recorded spectral amplitude and $M_0 = 1.1 \times 10^{30}$ dyn-cm from the peak value.

Note that this computation was performed under many drastic approximations, such as the assumption of a homogeneous ocean layer with a constant depth $H = 4$ km, and of a point source double-couple, rather than of the generally accepted model of a 1200–km long rupture (ISHII *et al.*, 2005; GUILBERT *et al.*, 2005; TOLSTOY and BOHNENSTIEHL, 2005). In particular, because of the heterogeneous nature of the distribution of strain release along the fault (e.g., ISHII *et al.*, 2005), it is impractical to attempt to use directivity formulae such as BEN-MENAHEM and ROSENMAN'S (1972), which assume a smooth propagation of the rupture. Note also the jagged nature of the spectrum (Fig. 4), which is reflected in the difference between average and peak spectral values. Under such conditions, the above estimates of $M_0$ cannot pretend to represent more than an order of magnitude of the size of the seismic source, and the results are, perhaps surprisingly, excellent, as $M_0$ fits between the initial Harvard CMT solution ($3.95 \times 10^{29}$ dyn-cm), and the larger values later obtained either in the composite Harvard model ($1.2 \times 10^{30}$ dyn-cm; (TSAI *et al.*, 2005)) or by fitting the Earth's gravest normal modes ($1.0 \times 10^{30}$ dyn-cm; (STEIN and OKAL, 2005)).

### *Hydroacoustic Records of the Main Tsunami Components*

In this section, we explore the possibility of detecting, in hydroacoustic records, the main low-frequency components of the tsunami wave, in the period range of their conventional far-field observation (1/2 to 1 hour, or 2000 to 4000 s). We show that a signal is most probably present in the records at H08S1, H08S2 and H08N3, but that the filters applied to the instruments preclude a quantitative interpretation of the recordings.

On Figure 6a, we examine the record of Hydrophone H08N3, part of the Northern triad (Fig. 1), starting 6 hours before the Sumatra earthquake (19:00 UT on 25 December), and lasting 2000 minutes (33.3 hr). After decimation to $\delta t = 1$ s, the record was simply low-pass filtered for $T > 200$ s. Note the distortion of the wavetrain shortly after the predicted arrival of the low-frequency components of the tsunami at 04:37 UT. On the corresponding spectrogram (Fig. 6b), the signal features a maximum of energy around 0.35 mHz at that time. This, and the continuity of the spectrogram along the dispersion curve predicted from (1), warrant the association of this signal with the tsunami. This interpretation is further supported by the agreement between the period of maximum energy (3200 s) and estimates obtained from eyewitness reports in the far field (40 mn to 1 hour) and from the analysis of satellite altimetry data (e.g., OKAL and TITOV, 2007).

Figure 6c presents an attempt to deconvolve the instrument response in the range 0.2–1.25 mHz. This procedure extracts a reasonable signal at the time expected for the tsunami, with a maximum of spectral amplitude at the frequency noted on the

spectrogram (0.35 mHz). However, its interpretation runs into several difficulties. First and foremost, the amplitude of the signal is in excess of 50 kPa peak-to-peak. At such frequencies, the SWA holds, and it predicts an overpressure growing linearly with depth $d$, $p = \eta\rho_w g d/H$, so that the signal would in turn predict a peak-to-peak wave amplitude on the order of 15 m, which is clearly unacceptable on the high seas, being one order of magnitude greater than measured nearby on the JASON trace (SCHARROO *et al.*, 2005). Note that the latter, being obtained along the track of a fast-moving satellite, constitutes neither a time- nor a space-series (OKAL *et al.*, 1999), and as such does not lend itself to a direct spectral comparison with the hydrophone. The proposed deconvolved amplitude (15 m peak-to-peak) is also one order of magnitude greater than simulated by TITOV *et al.* (2005*b*) in their global numerical model of the propagation of the tsunami on the high seas. Similarly, we cannot envision a meaningful comparison with the tidal gauge record of the tsunami at Diego Garcia (90 cm peak-to-peak), which is not directly interpretable in terms of tsunami height on the high seas, and is sampled at a time step (360 s) sending its Nyquist frequency in the domain of unreliability of the instrumental response of the hydrophones.

In addition, it is clear from the examination of the various frames in Figure 6 that the signal-to-noise characteristics of this putative tsunami signal are weak: Oscillations of nearly comparable amplitude (40 kPa peak-to-peak) and somewhat lower frequency (0.25 mHz) are present both before and after the predicted arrival of the tsunami, the former in the hours preceding the earthquake, their non-causality classifying them irrevocably as noise. On the other hand, similar results are obtained at the hydrophones of the Southern triad, located 220 km away from the Northern group; however, as shown on Figure 7, the maximum spectral amplitude is displaced to 1.25 mHz, and the overpressure amplitudes, while somewhat reduced (to 15 kPa peak-to-peak) remain unacceptably large.

There could be *a priori* several explanations to the unrealistic values obtained when attempting to quantify the relevant spectral amplitudes. They fall in three general categories: (i) signals such as those on Figures 6 and 7 may not be associated with the tsunami; (ii) the hydrophones may be responding to tsunami-induced signals other than the strict overpressure component of the tsunami eigenfunction; and (iii), which we favor, the instrument response used to deconvolve the signal is simply not applicable in the relevant range of frequencies. We reject (i) on the basis of the similarity between the filtered wave shapes at the two groups of hydrophones, as well as the good agreement with the expected arrival times of the tsunami (arrows on Figs. 6 and 7). In addition, the spectrogram shown on Figure 7b is clearly continuous with the higher-frequency one on Figure 2c, the latter lending itself well to quantification. Thus we believe that the signals on Figures 6 and 7 are indeed the principal (low-frequency) components of the tsunami, in the 0.3 to 1.25 mHz frequency range. Regarding (ii), we have assumed that the hydrophone sensors respond to the overpressure $p = -y_2$, neglecting the dynamic pressure $p_{\mathrm{dyn}} = 1/2\rho_w v^2$,

Figure 6
(**a**): Hydrophone record at Site H08N3, starting at 19:00 on 25 December 2004, 6 hours before the Sumatra earthquake. The record was simply low-pass filtered for $f \geq 5$ mHz . Note the deformation of the waveform about the time predicted for the tsunami arrival under the SWA (red arrow), the generally noisy character of the record, including before the earthquake, and the very low digit count after filtering. (**b**): Spectrogram of (**a**) between frequencies of 0.1 and 5 mHz. Note the strong energy present at 0.3 mHz at the time of predicted arrival, and the general agreement of the main energy train with the dispersed group times (white line). (**c**): Pressure signal $p$ deconvolved from (**a**) in the frequency band 0.2–1.25 mHz , using available instrument response characteristics. Note the excessive resulting amplitudes.

where $v$ is the particle motion of the water in the wave. Under the SWA, we expect the velocity to be mostly horizontal, $v = \eta C/H$, where $C$ is phase velocity, leading to $p_{\mathrm{dyn}}/p = (1/2)\eta/d$, on the order of $10^{-3}$ in the present case ($\eta \approx 1$ m; $d = 1300$ m), and thus totally negligible; we have verified from normal mode computations that $p_{\mathrm{dyn}}$ is similarly negligible at the higher frequencies featured on Figure 2c.

We are therefore left with hypothesis (iii), namely that it becomes impossible, at the low frequencies involved, to properly deconvolve the instrument response. We note that such frequencies are up to 32000 times lower than the corner frequency of the filter (10 Hz; Fig. 3), and it is unlikely that the published instrumental response remains reliable over 15 octaves. Even if it were, a simple calculation shows that a signal of the amplitude of the JASON trace (1.2 m peak-to-peak) with a period of 3200 s would be reduced to a recorded amplitude of less than 1 digital count. This clearly introduces digitizing noise and makes any quantitative interpretation impossible. We have independently verified that a similar result is obtained when attempting to extract the Earth's free oscillations in the 1–2 mHz range from short-period seismometers: while the gross shape of their spectrum can be recovered, their amplitude becomes unreliable (often times too large) when the instrument response reduces the corresponding signal to a time-domain amplitude of no more than a few digital counts.

## *Conclusion and Recommendations*

The 2004 Sumatra tsunami was recorded by the hydrophones of the IMS at station H08 (Diego Garcia), well outside the frequency range of their designated characteristics. The exceptionally clear dispersion revealed by spectrograms (HANSON and BOWMAN, 2005) is to our knowledge the first documented observation of high-frequency tsunami waves ($f \geq 10$ mHz) in the far field. Our results show that such high-frequency spectral components can be interpreted (within an order of magnitude) in terms of the excitation of the tsunami by the seismic source, in the framework of normal mode theory (WARD, 1980; OKAL, 1988). Thus, the present instrumentation of the IMS hydrophones can provide reliable information regarding the amplitude of such spectral components, which have been documented to pose

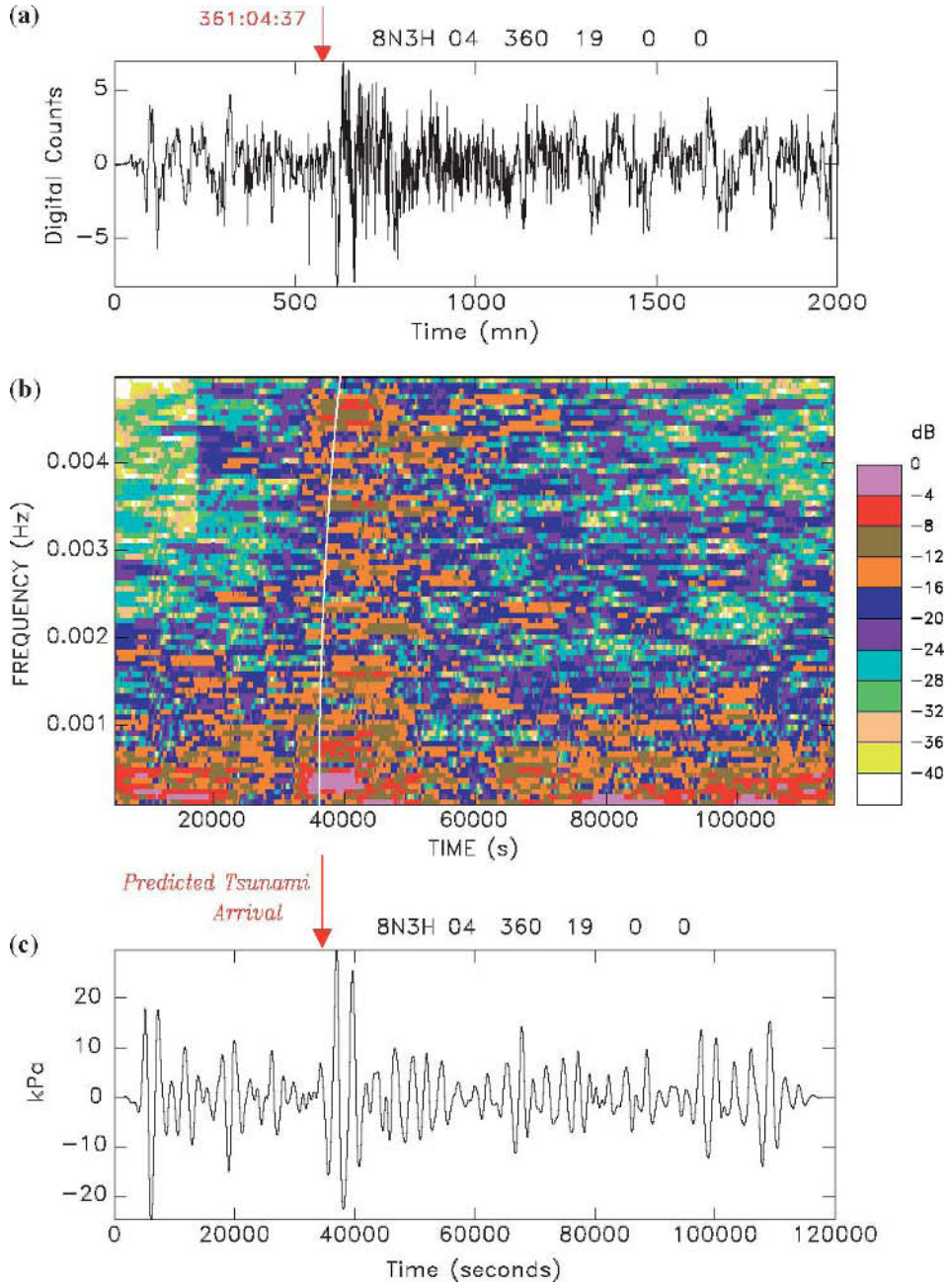


significant hazard in harbors (with the potential for damage to port infrastructures) in the far field (OKAL *et al.*, 2006a,b,c). Because of the strong dispersion involved at those frequencies, such effects can be substantially delayed with respect to tsunami

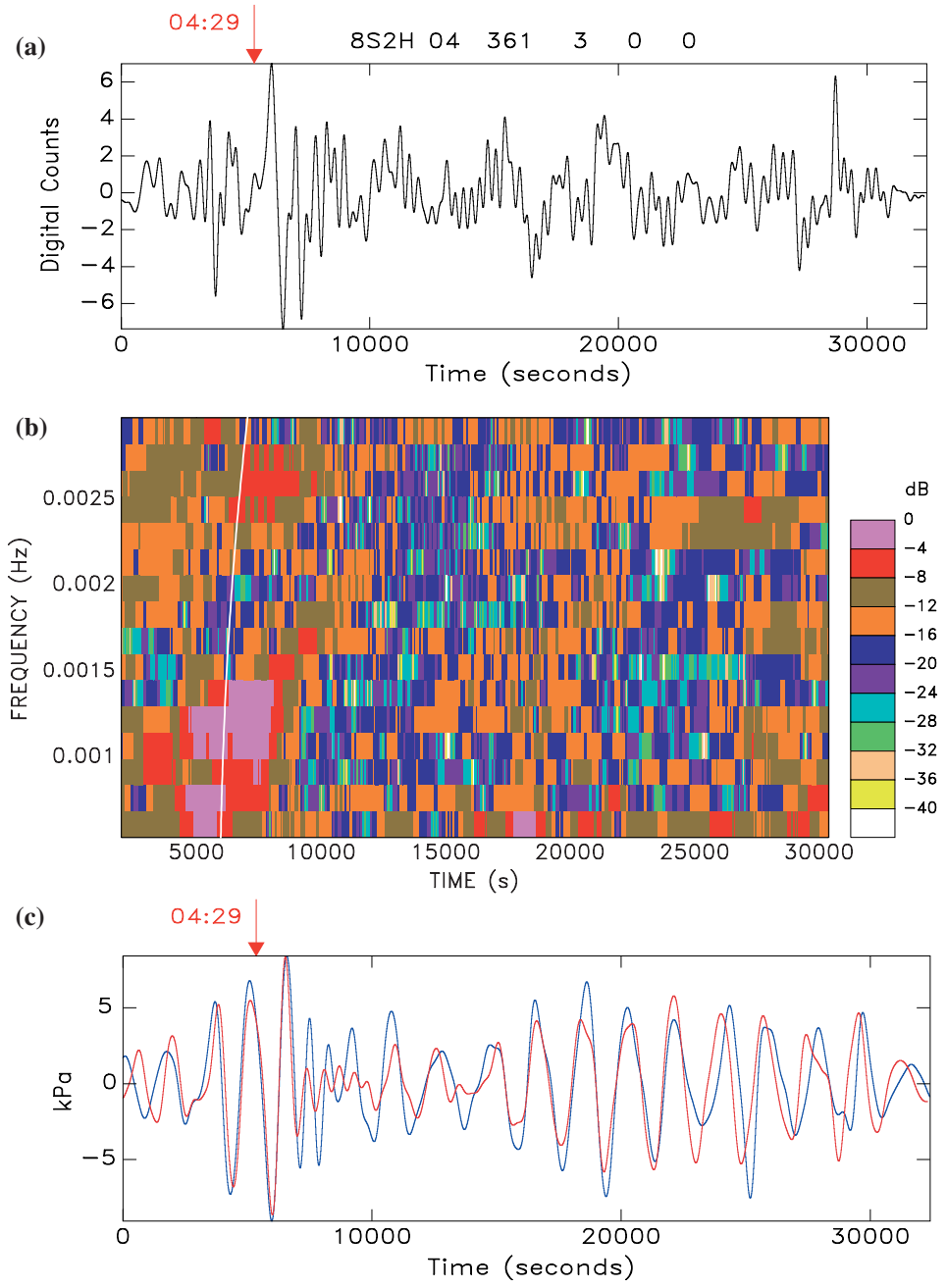


Figure 7

Same as Figure 6 for Hydrophone H08S2 from the Southern triad. The record starts at 03:00 on 26 December, and lasts only 11 hours. The frequency range of the spectrogram (**b**) extends from 0.5 to 3 mHz. On Frame (**c**), records are filtered between 0.5 and 2 mHz , to emphasize the prominent energy present at 1.25 mHz ; the H08S2 record is shown in red, with H08S1 superimposed in blue.

first arrivals, and thus the IMS hydrophones have the potential to contribute significant information for the purpose of transoceanic tsunami warning.

At the lower frequencies ($\approx$ 0.3 mHz) typical of conventional tsunami waves associated with more brutal far-field destruction, we argue that the IMS hydrophones can detect the signal, but that the nature of their present instrumentation (as mandated under the CTBT for the purpose of detecting explosions of much higher frequency content) precludes the deconvolution of a quantitative estimate of the surface amplitude of the tsunami. As the sensors use essentially the same technology as the DART ocean-bottom pressure recorders (TITOV *et al.*, 2005a), this situation evolves entirely from the characteristics of the high-pass filters integrated upstream of recording (in terms of data flow) into the IMS hydrophone systems. We would recommend that, in the future, the original pressure signal be recorded before filtering, so that these instruments could have the possibility of contributing the detection and quantification of a conventional tsunami wave on the high seas, unaffected by shoaling and coastal interaction, to oceanwide tsunami warning algorithms.

## *Acknowledgments*

This research was supported by the National Science Foundation, under Grant CMS-03-01054 and by Commissariat à 1'Energie Atomique. We thank Roger Bowman for information on the frequency responses at H08. Several figures were drafted using the GMT software (WESSEL and SMITH, 1991).

## *Appendix*

### *Response of a Hydrophone to the Passage of a Rayleigh Wave*

We consider a Rayleigh wave propagating along the surface of the Earth with a phase factor $\exp i(\omega t - kx)$. Under the shallow water approximation, i.e., if the depth $H$ of the water column satisfies $k \cdot H \ll 1$, we can assume that the dispersion of the Rayleigh wave is unaffected by the ocean. Then, according to Snell's law, the surface wave will be prolonged into the water layer in the form of two progressive waves, one upgoing, the other downgoing, with potentials

$$\phi_1 = A \exp i(\omega t - kx) \exp(-i\gamma z); \qquad \phi_2 = B \exp i(\omega t - kx) \exp(+i\gamma z),$$

where the coordinate $z$ is taken positive upwards and vanishing at the surface of the ocean ($z = -H$ at the bottom), $\gamma^2 = \omega^2/\alpha^2 - k^2$, and $\alpha$ is the velocity of sound in water (1.5 km/s). Boundary conditions impose a zero pressure at the surface ($z = 0$), hence $A + B = 0$, which quickly leads to a vertical displacement field in the water column

$$u_z = -2i\gamma A \cos(\gamma z)$$

and to a pressure

$$p = -\sigma_{zz} = -K\frac{\omega^2}{\alpha^2} A\, 2i \sin \gamma z = -\rho_w \omega^2 2i\, A \sin(\gamma z),$$

where $\rho_w$ is the density of salt water (1.03 g/cm$^3$), $K = \rho_w \alpha^2$, and we have omitted the common propagation factor $\exp i(\omega t - kx)$. The ratio of the pressure at depth $-z$ to the vertical displacement at the ocean bottom is thus

$$\frac{p}{u_z|_{z=-H}} = \rho_w \omega^2 \frac{\sin(\gamma z)}{\gamma \cdot \cos(\gamma H)}.$$

In the shallow water approximation ($k \cdot H << 1$ and $\gamma \cdot H << 1$), $\sin(\gamma z) = \gamma z$ and $\cos(\gamma H) = 1$, hence

$$\frac{p}{u_z|_{z=-H}} = \rho_w \omega^2 z \qquad (z < 0).$$

Under these conditions, the hydrophone functions as an accelerometer with a sensitivity proportional to its depth $-z$ in the water layer.

## References


Artru, J., Dučić, V., Kanamori, H., Lognonné, P., and Murakami, M. (2005), *Ionospheric detection of gravity waves induced by tsunamis*, Geophys. J. Intl. *160*, 840–848.

Ben-menahem, A. and Rosenman, M. (1972), *Amplitude patterns of tsunami waves from submarine earthquakes*, J. Geophys. Res. *77*, 3097–3128.

Hanson, J.A. and Bowman, J.R. (2005), *Dispersive and reflected tsunami signals from the 2004 Indian Ocean tsunami observed on hydrophones and seismic stations*, Geophys. Res. Letts. *32*(17), L17608, 5 pp.

González, F.I. and Kulikov, Ye. A., *Tsunami dispersion observed in the deep ocean. In Tsunamis in the World* (ed. S. Tinti), pp. 7–16, (Kluwer, 1993).

Guilbert, J., Vergoz, J., Schisselé, A., Roueff, E., and Cansi, Y. (2005), *Use of hydroacoustic and seismic arrays to observe rupture propagation and source extent of the $M_w = 9.0$ Sumatra earthquake*, Geophys. Res. Letts. *32*(15), L15310, 5 pp.

Ishii, M., Shearer, P., Houston, H., and Vidale, J. (2005), *Rupture extent, duration and speed of the 2004 Sumatra-Andaman earthquake image by the Hi-Net array*, Nature *435*, 933–936.

Kanamori, H. and Stewart, G.S. (1976), *Mode of the strain release along the Gibbs fracture zone, Mid-Atlantic Ridge*, Phys. Earth Planet Inter. *11*, 312–332.

Le Pichon, A., Herry, P., Mialle, P., Vergoz, J., Brachet, N., Garcés, M., Drob, D., and Ceranna, L. (2005), *Infrasound associated with 2004–2005 large Sumatra earthquakes and tsunami*, Geophys. Res. Letts. *32*(19), L19802, 5 pp.

Occhipinti, G., Lognonné, P., Kherami, A., and Hébert, H. (2005), *Modelling and detection of the ionospheric perturbation associated with the Sumatra tsunami of December 26th, 2004*, Eos, Trans. Amer. Geophys. Un. *86*(52), U11A–0829, [abstract].

Okal, E.A. (1982), *Mode-wave equivalence and other asymptotic problems in tsunami theory*, Phys. Earth Planet. Inter. *30*, 1–11.

Okal, E.A. (1988), *Seismic parameters controlling far-field tsunami amplitudes: A review*, Natural Hazards *1*, 67–96.

OKAL, E.A. and TITOV V.V. (2007), $M_{TSU}$: *Recovering seismic moments from tsunameter records*, Pure Appl. Geophys. *164*, 309–323.

OKAL, E.A., PIATANESI, A., and HEINRICH, P. (1999), *Tsunami detection by satellite altimetry*, J. Geophys. Res. *104*, 599–615.

OKAL, E.A., FRITZ, H.M., RAVELOSON, R., JOELSON, G., PANČOŠKOVÁ P., and RAMBOLAMANANA, G. (2006*a*), *Field survey of the 2004 Indonesian tsunami in Madagascar*, Earthquake Spectra, *22*, S263–S283.

OKAL, E.A., FRITZ, H.M., RAAD, P.E., SYNOLAKIS, C.E., AL-SHIJBI, Y., and AL-SAIFI, M., (2006b), *Field survey of the 2004 Indonesian tsunami in Oman*, Earthquake Spectra, *22*, S203–S218.

OKAL, E.A., SLADEN, A., and OKAL, E.A.-S. (2006c), *Field survey of the 2004 Indonesian tsunami on Rodrigues, Mauritius and Réunion Islands*, Earthquake Spectra, *22*, S241–S261.

RABINOVICH, A.B. (2005), *The Great Sumatra tsunami of December 26, 2004: Observation and analysis*, Geophys. Res. Abstr. *7*, 05-A-11061, [abstract].

SAITO, M. (1967), *Excitation of free oscillations and surface waves by a point source in a vertically heterogeneous Earth*, J. Geophys. Res. *72*, 3689–3699.

SCHARROO, R., SMITH, W.H.F., TITOV, V.V., and ARCAS, D. (2005), *Observing the Indian Ocean tsunami with satellite altimetry*, Geophys. Res. Abstr. *7*, 230, [abstract].

STEIN, S. and OKAL, E.A. (2005), *Size and speed of the Sumatra earthquake*, Nature *434*, 581–582.

TITOV, V.V., GONZÁLEZ, F.I., BERNARD, E.N., EBLE, M.C., MOFJELD, H.O., NEWMAN, J.C., and VENTURATO, A.J. (2005*a*), *Real-time tsunami forecasting: Challenges and solutions*, Natural Hazards *35*, 41–58.

TITOV, V.V., RABINOVICH, A.B., MOFJELD, H.O., THOMSON, R.E., and GONZÁLEZ, F.I. (2005b), *The global reach of the 26 December 2004 Sumatra tsunami*, Science *309*, 2045–2048.

TOLSTOY, M. and BOHNENSTIEHL, D.R. (2005), *Hydroacoustic constraints on the rupture duration, length and speed of the great Sumatra-Andaman earthquake*, Seismol. Res. Letts. *76*, 419–425.

TSAI, V.C., NETTLES, M., EKSTRÖM, G., and DZIEWOŃSKI, A.M. (2005), *Multiple CMT source analysis of the 2004 Sumatra earthquake*, Geophys. Res. Letts. *32*(17), L17304, 4 pp.

WARD, S.N. (1980), *Relationships of tsunami generation and an earthquake source*, J. Phys. Earth *28*, 441–474.

WESSEL, P. and SMITH, W.H.F. (1991), *Free software helps map and display data*, Eos, Trans. Amer. Geophys. Un. *72*, 441 and 445–446.

YUAN, X., KIND, R., and PEDERSEN, H.A. (2005), *Seismic monitoring of the Indian Ocean tsunami*, Geophys. Res. Lett. *32*(15), L15308, 4 pp.

(Received May 6, 2006, accepted June 15, 2006)

Pure appl. geophys. 164 (2007) 325–353
0033–4553/07/030325–29
DOI 10.1007/s00024-006-0181-4



Pure and Applied Geophysics

# Seismic Records of the 2004 Sumatra and Other Tsunamis: A Quantitative Study

EMILE A. OKAL

*Abstract*—Following the recent reports by YUAN *et al.* (2005) of recordings of the 2004 Sumatra tsunami on the horizontal components of coastal seismometers in the Indian Ocean basin, we build a much enhanced dataset extending into the Atlantic and Pacific Oceans, as far away as Bermuda and Hawaii, and also expanded to five additional events in the years 1995–2006. In order to interpret these records quantitatively, we propose that the instruments are responding to the combination of horizontal displacement, tilt and perturbation in gravity described by GILBERT (1980), and induced by the passage of the progressive tsunami wave over the ocean basin. In this crude approximation, we simply ignore the island or continent structure, and assume that the seismometer functions *de facto* as an ocean-bottom instrument. The records can then be interpreted in the framework of tsunami normal mode theory,and lead to acceptable estimates of the seismic moment of the parent earthquakes. We further demonstrate the feasibility of deconvolving the response of the ocean floor in order to reconstruct the time series of the tsunami wave height at the surface of the ocean, suggesting that island or coastal continental seismometers could complement the function of tsunameters.

**Key words:** Tsunami, seismic recording, 2004 Sumatra earthquake.

## *Introduction*

In the aftermath of the 2004 Sumatra tsunami, YUAN *et al.* (2005) reported that seven seismic stations located on islands and continental shores of the Indian Ocean had recorded on their horizontal components the actual impact of the tsunami on the nearby shores. These signals were generally polarized perpendicular to the shoreline and featured energy in the 1 to 2 mHz range and amplitudes, expressed as accelerations, on the order of $10^{-4}$ cm/s$^2$. Following the landslides at Stromboli in 2002, LA ROCCA *et al.* (2004) had similarly reported low-frequency signals at the seismic station on the nearby island of Panarea (21 km away from the source), but Yuan *et al.*'s remarkable observations constitute the first such report in the far field. They were also briefly confirmed by HANSON and BOWMAN (2005).

Department of Geological Sciences, Northwestern University, Evanston, IL 60201, USA.

In this context, the purpose of the present paper is to expand on YUAN *et al.*'s (2005) work in several directions, by showing that such recordings were detectable worldwide; that the signals extend, at least in the regional field, to high frequencies in the 10 mHz range; that such signals are justifiable quantitatively using normal mode theory; that similar signals from smaller tsunamis are also identifiable in the seismic record, with their spectral amplitudes correlating well with the seismic moment of the parent earthquake; that acceptable time series of the tsunami on the high seas can be reconstructed from seismic records; and finally that seismic records of tsunami waves can also be obtained on vertical seismometers, albeit at a lower amplitude.

## *2. The Universal Character of the Seismic Recordings*

Following in the footsteps of YUAN *et al.* (2005), we conducted a systematic worldwide search for similar records, including at stations located outside the Indian Ocean. At each targeted station, we extracted the long-period horizontal channels, and proceeded to deconvolve the instrument and bandpass filter the resulting ground motion between 0.1 and 10 mHz. Table 1 lists the stations at which the tsunami was detected, with relevant information such as dominant frequency and equivalent amplitude; their location is shown on Figure 1. Figure 2 provides representative examples of typical time series, after deconvolution of the instrument response to ground displacement and bandpass filtering in the 0.1–10 mHz range. The association of the signals with the tsunami was made on the basis of its arrival time, as predicted by the global simulation of TITOV *et al.* (2005). Among the most remarkable results, we note that the tsunami is well recorded seismically as far as Bermuda (29 hours after origin time and at a distance of 20,800 km around the Cape of Good Hope), and Kipapa, Hawaii (31.5 hours after origin time). The latter site is reached after a westward path estimated at 26,700 km, through the Atlantic Ocean and the Drake Passage (the eastward path going south of Australia being about 8 hours shorter). This is an expression of the strong directivity of the source towards the Western Indian Ocean, at right angles to the direction of faulting (BEN-MENAHEM and ROSENMAN, 1972), and of the efficient focusing of the wave by the shallow bathymetry along the Southwest Indian Ridge (TITOV *et al.*, 2005) as previously observed for Pacific Ocean tsunamis by WOODS and OKAL (1987) and SATAKE (1988). These effects also probably contribute to the spectacular quality of the recording at Hope, South Georgia, where the tsunami is clearly discernible on the raw record, without the need for filtering or instrument deconvolution (Fig. 3); they may be compounded by local resonance effects in the Bays of Cumberland. The tsunami is also well recorded at station SBA (Scott Base, Antarctica), following a somewhat convoluted path around Australia and into McMurdo Sound.

Table 1

*List and properties of seismic records of the 2004 Sumatra tsunami*

| Station | | Epicentral distance (km) | Distance from shore (km) | Arrival date and time | Spectral peak | | | Peak-to-peak amplitude (cm) | | |
|---|---|---|---|---|---|---|---|---|---|---|
| Code | Location | | | | Prominent component | Amplitude (cm*s) | Period (s) | Apparent ground motion | Deconvolved $\eta$ | Virtual gauge (Titov *et al.*, 2005) |
| COCO | Cocos Island, IOTA | 1721 | < 1 | | N141E | | | 20 | 210 | 46 |
| DGAR | Diego Garcia, BIOT | 2748 | < 1 | (361) 04:40 | EW | 3500 | 800 | 14 | 370 | 135 |
| MSEY | Mahé, Seychelles | 4564 | 2; 120 ¶¶ | (361) 08:00 | N247E | 700 | 800 | 6.3 | 133 | 42 |
| AIS | Ile Amsterdam, TAAF | 4930 | < 4 | (361) 07:48 | EW | 2000 | 800 | 4 | 170 | 54 |
| RER | Rivière de l'Est, Réunion | 5133 | 7 | (361) 07:46 | EW | 17000 | 3000 | 1.6 | 42 | 45 |
| PAF | Port-aux-Français, Kerguelen, TAAF | 6340 | < 2; 20 † | (361) 10:20 | NS | 5500 | 1000 | 7 | 186 | 93 |
| CRZF | Ile de la Possession, Crozet, TAAF | 7009 | < 2 | (361) 10:50 | EW | 2700 | 800 | 18 | 107 | 36 |
| CASY | Casey, Antarctica | 7818 | < 1 | (361) 12:18 | NS | 4000 | 800 | 10 | 208 | 99 |
| DRV | Dumont d'Urville, Antarctica | 8519 | < 1; 30 ¶ | (361) 14:24 | NS | 1000 | 800 | 4 | 43 | 40 |
| HOPE | Hope, South Georgia | 12906 | < 1; 8 † | (361) 20:07 | NS | 6000 | 800 | 13 | 291 | 15 |
| TRIS | Edinburgh, Tristan da Cunha, BOT | 9700 (*) | < 1 | (361) 14:13 | EW | 18000 | 3000 | 21 | 31 | 10 |
| SBA | Scott Base, Antarctica | 11300 (*) | | (361) 19:02 | NS | 500 | 800 | 1.5 | 27 | 7 |
| DZM | Dzoumac, New Caledonia | 12000 (*) | 15 | (361) 20:29 | NS | 3500 | 950 | 9 | 127 | 4.5 |
| ASCN | Ascension Island, BOT | 13900 (*) | 3 | (362) 00:48 | NS | 10000 | 3000 | 3 | 10 | 8.5 |
| BBSR | Hamilton, Bermuda | 20800(*) | 4 | (362) 05:52 | N126E | 2200 | 1500 | 0.6 | 16 | 2.5 |
| KIP | Kipapa, Hawaii, USA | 26700 (*) | 10 | (362) 08:33 | NS | 7000 | 3000 | 0.5 | 10 | 1.5 |

(*) Distances to these stations are estimated along a path deviating from the great circle in order to avoid continental masses. Consequently, they are not used in the source retrieval computations.

† For stations located in strongly indented bays, we give the distance to the nearest shore point followed by the distance to a more regular coastline.

¶ For stations involving a broad continental shelf, we give first the distance to the nearest shoreline, and then to the continental slope.

BIOT: British Indian Ocean Territory; BOT: British Overseas Territory; IOTA: Indian Ocean Territories of Australia; TAAF: Terres Australes et Antarctiques Françaises.

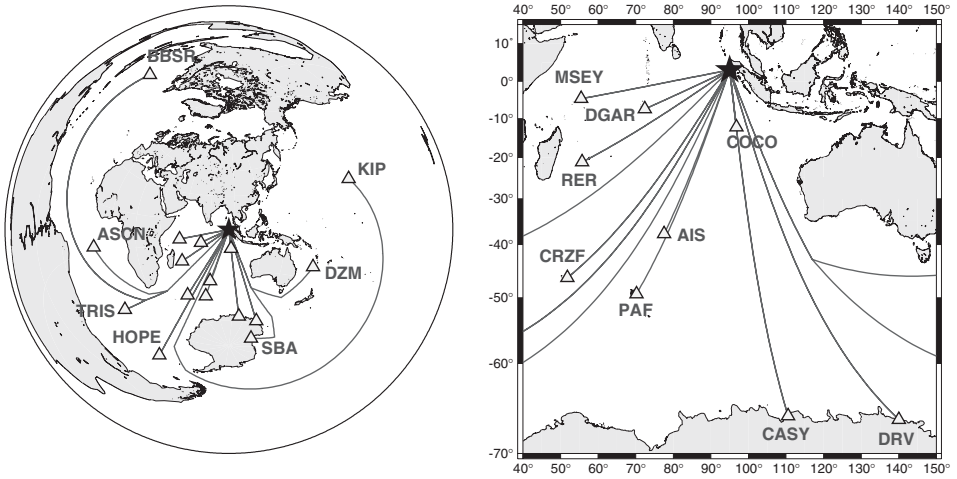


Figure 1
Maps of seismic stations (triangles) having recorded the 2004 Sumatra tsunami. *Left*: Azimuthal equidistant projection centered on the epicenter of the earthquake (star). Segmented lines correspond to paths departing from great circles to avoid continental masses. *Right*: Mercator projection close-up of the Indian Ocean Basin.

As a whole, we were able to make observations at 16 stations, including nine not described by YUAN *et al.* (2005). Of the latter, two are in the Indian Ocean Basin (MSEY and DRV), four in the Atlantic (HOPE, TRIS, ASCN and BBSR), and three in the Pacific (DZM, SBA and KIP). By contrast, we failed to observe detectable signals at the stations listed in Table 2. We confirm the observation by YUAN *et al.* (2005) that only coastal stations can record seismic signals of impacting tsunamis. This is best demonstrated by the case of the two Hawaiian stations: the tsunami is recorded at KIP on Oahu, only 10 km from the coastline, while it is not at POHA, on the saddle of the Big Island, 55 km from the receiving shore. An examination of the datasets of Tables 1 and 2 suggests an empirical threshold of ˜35 km for the detection of the Indonesian tsunami in both the near and far fields. In addition, a station deployed near the shore at the toe of a large gulf or bay (e.g., Arta Grotte, Djibouti) may not record the tsunami; furthermore, in the presence of an extended continental shelf, even a coastal station (e.g., Montagne des Pères, French Guyana, only 10 km from the shore) will not record the tsunami. The absence of record at Rarotonga (less than 3 km from the shore line) probably reflects the low amplitude of the wavefield in that part of the Central Pacific, but the situation at Easter Island (RPN) is more intriguing, since the stations lies practically on the path to KIP, where the tsunami is well recorded.

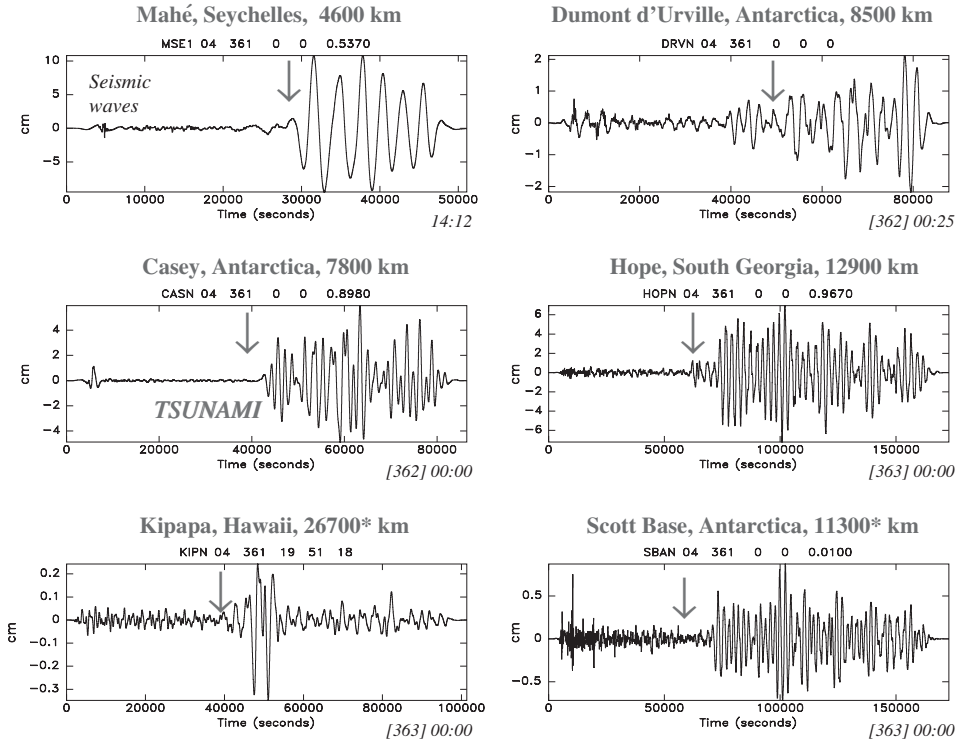


Figure 2
Representative examples of seismic recordings of the 2004 Sumatra tsunami. On each frame, the instrument response was deconvolved, and the record bandpass filtered, to obtain the equivalent ground motion between 0.1 and 10 mHz. Note the different time and displacement scales on each frame. All records start at 00:00 UTC (except KIP; 19:51 UTC), on 26 December 2004. The numbers in italics at the bottom right of each frame show the time at the end of each record (including Julian Day in brackets). The vertical arrows point to the arrival time of the tsunami, computed along the great circle to the station or, at Kipapa and Scott Base, using an estimated distance around continental masses (flagged by a star, as in Table 1).

## 3. High-frequency Components of the Tsunami

On Figure 4, we document that energy is present on the seismic record of the tsunami at Amsterdam Island (AIS) at the higher frequencies detected on hydrophones by HANSON and BOWMAN (2005) and OKAL *et al.* (2007). These spectral components, which fall outside the range of conventional observations of tsunamis, are characterized by significant dispersion, as they do not follow the shallow-water approximation. Rather, the black solid line on Figure 4 shows the group arrival times predicted by the classical dispersion relation

$$\omega^2 = g\, k \cdot \tanh\,(kH) \tag{1}$$

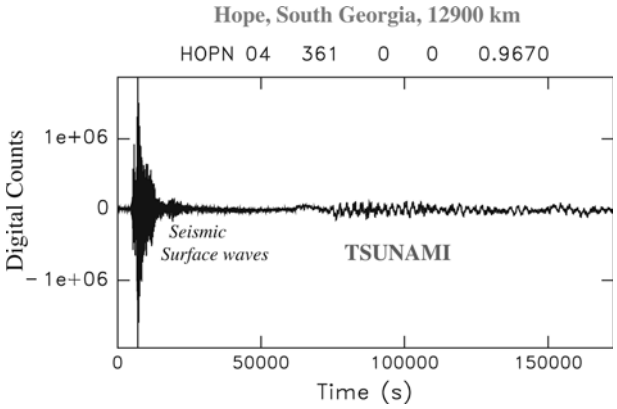


Figure 3
Original North-South Long-Period (LHN) record at Hope, South Georgia. This unprocessed raw seismogram starts at 00:00 UTC on 26 December and lasts 48 hours. Note the clear recording of the tsunami.

Table 2

*Seismic stations at which the 2004 Sumatra tsunami was not detectable*

| Code | Location | Distance (km) from | | |
|---|---|---|---|---|
| | | Shore | high seas (†) | continental slope (¶) |
| ATD | Arta Grotte, Djibouti | 7 | 60 | |
| EFI | East Falklands, Falkland Is. | 25 | | 45 |
| MPG | Montagne des Pères, French Guyana | 10 | | 135 |
| NWA | Narrogin, Western Australia | 150 | | |
| PALK | Pallekele, Sri Lanka | 120 | | |
| POHA | Pohakuloa, Hawaii, USA | 55 | | |
| RAR | Rarotonga, Cook Islands | < 3 | | |
| RPN | RapaNui, Easter Island, Chile | 3 | | |
| TAU | Hobart, Tasmania, Australia | 3 | 45 | 75 |

The symbols (†; ¶) refer to the conventions of Table 1.

between angular frequency $\omega$, acceleration of gravity $g$ and wave number $k$, for an average basin depth $H = 4$ km, and using the epicentral parameters (3.30°N; 95.98°E; origin time 00:58:50 UT) corresponding to the nucleation of the rupture; the white line uses an average depth of 3.5 km, and a centroid of rupture at 7°N, 93°E, with an origin time of 01:03:00 UT. At each frequency, the first arrival of tsunami energy at AIS coincides with the former, and the maximum of energy generally

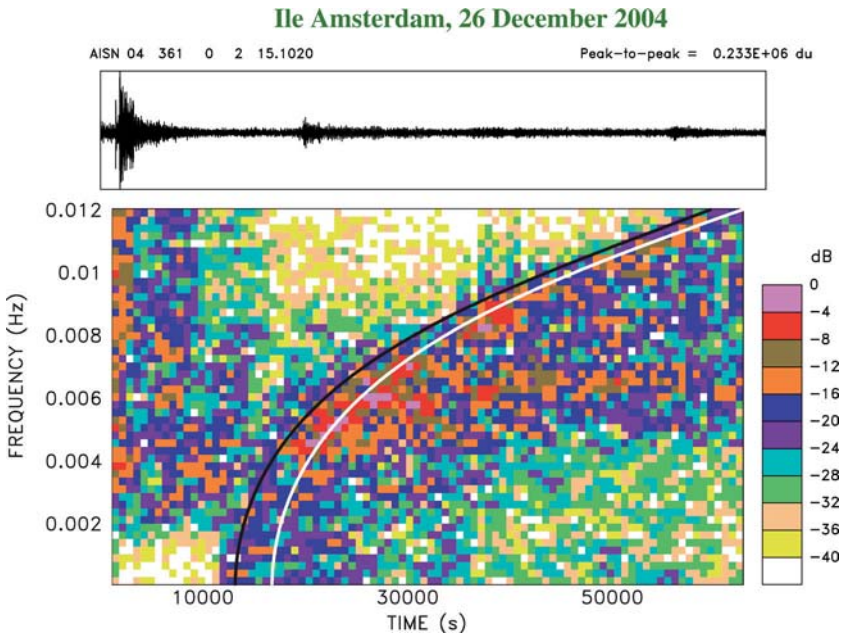


Figure 4
Spectrogram of the tsunami recording at AIS (Ile Amsterdam). The individual pixels identify the spectral amplitude present in the wave train as a function of time (abscissa) and frequency (ordinate), according to the logarithmic scale at right. In order to emphasize the high frequencies in the record, we processed the raw seismogram, without deconvolution of the instrument response. The black curve is the dispersion expected from equation (1) for a 4-km deep ocean basin and a source at the epicenter of rupture. The white curve uses a 3.5-km basin and places the source at the centroid of rupture (TSAI *et al.*, 2005).

follows the latter. The signals then last for many hours. High-frequency components of the tsunami wave are of particular concern in the framework of civil defense as OKAL *et al.* (2006a,b) have suggested that they are responsible for setting distant harbors in resonance long after the passage of the main wavetrains observed at lower frequencies.

When attempting to generalize this result to other stations, we obtained only mediocre results. In the near field (COCO, DGAR), the high-frequency components of the tsunami interfere with seismic mantle waves from the large aftershock at 04:21 in the Nicobar Islands. At larger distances, the amplitudes decay rapidly, as a result of the strong dispersion under the deep water regime. Even at CRZF, a volcanic island generally similar in structure to Amsterdam, little energy is present above 2.5 mHz. At the continental coastal station CASY, most of the energy is concentrated below 2 mHz, and the large continental shelves probably act as low-pass filters at MSEY and DRV, where the energy in the tsunami signals falls off rapidly above 1.5 mHz.

### 4. Quantification of the Seismic Records of the Tsunami

In order to interpret the seismic records of the tsunami, we concentrate on their low-frequency components, typically in the 0.3–1.5 mHz range, and note that at such periods, the receiving stations are generally within one wavelength of the abyssal plain where most of the propagation takes place. We then make the extreme simplifying assumption that the shoreline seismometer actually functions as a horizontal Ocean-Bottom Seismometer (OBS), simply attached to the solid Earth structure underlying the water column in an unperturbed abyssal plain. Following the seminal work of WARD (1980), it has long been known that the tsunami eigenfunction is not limited to the oceanic layer, but is prolonged into any substratum with finite rigidity $\mu$ in the form of a pseudo-Rayleigh wave in which potential energy is mostly elastic, as opposed to gravitational in the fluid (OKAL, 2003). While boundary conditions predict a discontinuity of the horizontal component of particle displacement at the ocean bottom, the latter does not vanish in the elastic medium, where its expression can be obtained in the limit $\omega \rightarrow 0$ as

$$l\, y_3 = \frac{1}{4} \cdot \frac{\eta \rho_w g}{\mu k} \tag{2}$$

using the formalism of OKAL (1988, 1991, 2003) and the notation of SAITO (1967); $\eta$ is the vertical amplitude of the eigenfunction $y_1$ at the surface of the ocean, and $\rho_w$ the density of the ocean water.

In addition, we note following GILBERT (1980) that a horizontal seismometer responds to a spheroidal mode of the Earth through the combination of its horizontal displacement, of the tilt component of the strain induced by the passage of the equivalent wave, and of a component of gravity anomaly. As fully discussed in the Appendix, the effect of the latter two is usually negligible, at most marginal, for seismic modes, but will become primordial for a tsunami mode.

We rewrite GILBERT's (1980) equation (4.13)

$$AV = \omega^2 V - r^{-1} l\, (gU + \Phi) \tag{3}$$

in the formalism of SAITO (1967) as an apparent horizontal component $y_3^{app}$ of the tsunami eigenfunction by noting that $ly_3 = V$; $y_1 = U$; and $y_5 = -\Phi$, and obtain

$$y_3^{app} = y_3 - \frac{1}{r\omega^2} \cdot (g y_1 - y_5), \tag{4}$$

where the $\{y_i\}$ make up the solution's eigenvector, $l = ka$ is the angular order of the equivalent normal mode ($a$ being the radius of the Earth), and $r \approx a$ the radius at the recorder.

We further assume that the tsunami is simply excited by a point source double-couple, of seismic moment $M_0$ with strike, dip and slip angles $\phi_f$, $\delta$ and $\lambda$, with the receiver at distance $\Delta$ and azimuth $\phi_s$, and detail the computation in the

case of the record at Casey, Antarctica (CASY) shown on Figure 2. After deconvolution of the instrument response, we measure spectral amplitude peaks $X(\omega) = 4000$ cm*s at $T = 840$ s and $X(\omega) = 4700$ cm*s at $T = 1175$ s (Fig. 5). We present below a detailed analysis of the former measurement. Note that such spectral amplitudes are at least one order of magnitude greater than those expected from the Earth's free oscillations in a corresponding range of frequencies (STEIN and OKAL, 2005).

We first proceed to compute the eigenfunction of the equivalent tsunami normal mode at this period, using an Earth model derived from PREM (DZIEWONSKI and ANDERSON, 1981) and featuring an ocean of depth $H = 4$ km, the corresponding angular order being $l = 242$. Using $\eta = 1$ cm as a normalization of the vertical displacement at the free surface, we obtain a vertical displacement of the ocean bottom $y_1 = -3.12 \times 10^{-2}$ cm, an overpressure at the sea floor $-y_2 = 974$ dyn/cm$^2$, a horizontal component of the eigenfunction at the sea floor $y_3 = 4.12 \times 10^{-6}$ cm in the solid Earth and $2.72 \times 10^{-2}$ cm in the fluid column, and a potential component of the eigenfunction, $y_5 = 0.946$ cm$^2$s$^{-2}$. The values of $y_1$ and $y_3$ are also in good agreement with those predicted ($-2.77 \times 10^{-3}$ and $3.81 \times 10^{-6}$ cm, respectively) under the asymptotic approximations derived for an ocean layer over a homogeneous half

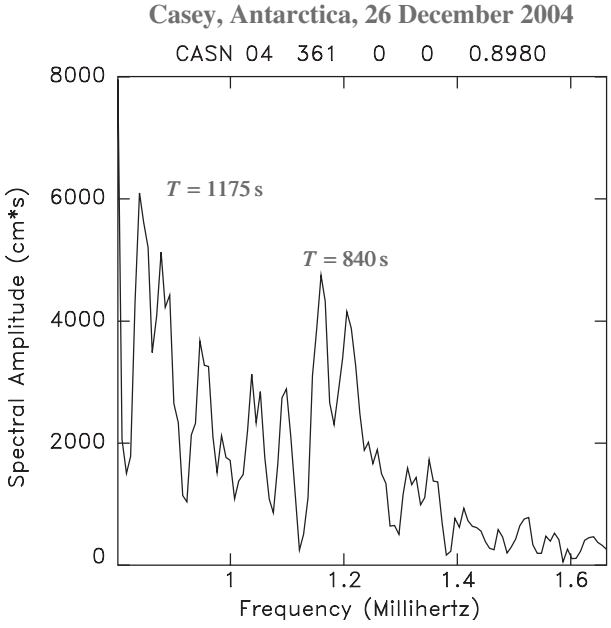


Figure 5
Spectral amplitude of the deconvolved apparent ground motion at CASY.The measurement of the spectral peaks allows the resolution of the seismic moment of the source. See text for details.

space by OKAL (2003). These numbers combine to an apparent horizontal eigenfunction $y_3^{app} = 1.17 \times 10^{-4}$ cm in (3), where the tilt term ($0.85 \times 10^{-4}$ cm) is predominant. Conversely, this suggests, for the CASY record, a spectral amplitude of the vertical displacement of the tsunami wave at the surface $\eta(\omega) = X(\omega)/(l \times y_3^{app}) = 1.42 \times 10^5$ cm*s.

From this spectral amplitude $\eta(\omega)$, we can obtain an estimate of the seismic moment $M_0$ of the earthquake using the $M_{TSU}$ algorithm introduced by OKAL and TITOV (2007). We recall that this procedure parallels that of the mantle magnitude $M_m$ developed by OKAL and TALANDIER (1989), and is derived from the representation of the tsunami wave as a branch of normal modes of the Earth (WARD, 1980). In this formalism, for $T = 840$ s, the source correction is $C_S^{TSU} = 2.201$, and at $\Delta = 74.2$ degrees, the distance correction is $C_D = -0.008$. We then obtain $M_{TSU} = \log_{10} \eta(\omega) + C_D + C_S^{TSU} + 3.10 = 10.44$, equivalent to a seismic moment $M_0 = 2.75 \times 10^{30}$ dyn*cm. A more rigorous calculation correcting for the exact excitation of the mode for the particular focal geometry and azimuth of the receiver, rather than using $C_S^{TSU}$, leads to $M_0 = 1.56 \times 10^{30}$ dyn*cm for the Harvard CMT centroid depth $h = 29$ km. For the second spectral peak ($T = 1175$ s; $l = 172$; $X(\omega) = 4700$ cm*s, one finds similarly $M_{TSU} = 10.30$, and $M_0 = 1.21 \times 10^{30}$ dyn*cm when using the exact source geometry.

Given the many approximations involved in this computation, namely that the seismometer functions as an OBS in the absence of the continental structure, and that the rupture can be modeled as a point source double-couple, we regard the agreement between our estimates and those resulting from seismological inversions ($M_0 = 1.0 \times 10^{30}$ dyn*cm (STEIN and OKAL, 2005); $M_0 = 1.15 \times 10^{30}$ dyn*cm (TSAI *et al.*, 2005) as remarkable. Certainly, these calculations reproduce an excellent order of magnitude of the exceptional size of the earthquake. In Table 1

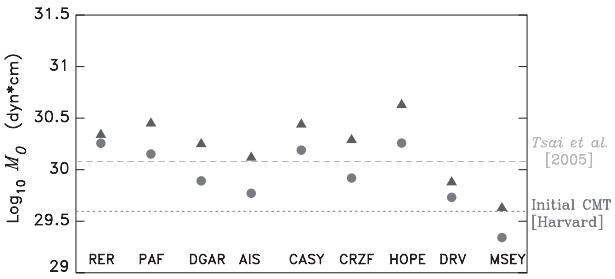


Figure 6

Estimates of the seismic moment of the 2004 Sumatra earthquake obtained from spectral amplitudes recorded at nine seismic stations, using the $M_{TSU}$ algorithm (triangles) or a more exact correction for source geometry (circles). The dotted line represents the moment initially inverted by the Harvard CMT project, and the dashed one the full moment of the composite source inverted by TSAI *et al.* (2005). The deficient values at DRV and MSEY express the effect of their extended continental shelves.

and Figure 6, we extend our measurements to eight additional stations. At each station, the moment is measured at the period featuring the spectral amplitude of horizontal ground displacement with highest signal-to-noise ratio in the range 500–5000 s; in practice these periods vary from 800 to 3000 seconds. We exclude stations such as Bermuda and Scott Base for which the tsunami path around continental masses departs significantly from a great circle. We also do not process the record at Cocos Island, on which the timing of the arrivals is difficult to reconcile with a definitive path, as already noted by YUAN *et al.* (2005). If we further exclude the clearly deficient results at MSEY (Mahé, Seychelles) and DRV (Dumont d'Urville, Antarctica), the geometrically averaged values of the moments are 2.29 and $1.16 \times 10^{30}$ dyn*cm, using the $M_{TSU}$ and full correction algorithms, respectively, or only $0.30 \pm 0.15$ and $0.00 \pm 0.18$ logarithmic units over TSAI *et al.*'s (2005) solution (dashed line on Fig. 6). In particular, all these measurements suggest a moment several times larger than the original Harvard CMT solution of $3.95 \times 10^{29}$ dyn*cm (dotted line on Fig. 6). They also confirm that the amplitude of the tsunami in the far field is well accounted for by conventional mechanisms of generation (once the exceptional size of the seismic moment is recognized), and discount the need for ancillary mechanisms of excitation (influence of steep slopes in the epicentral area; contribution of splay faults; large landslides).

We interpret the significant deficiencies of the solutions at MSEY, and to a lesser extent at DRV, as site effects. Even though MSEY is within 2 km of the shoreline, the Seychelles Islands have a continental structure (WEGENER, 1915; DU TOIT, 1937; DAVIES, 1968), whose shelf extends about 120 km at sea in the direction of arrival of the tsunami. Thus, the station cannot be regarded as coastal, let alone as functioning as an OBS. Similarly, the extended continental shelf seaward of DRV is probably responsible for the damping of the tsunami signal at this otherwise coastal station.

We similarly attempted to invert a seismic moment from the spectral amplitudes of the high-frequency components of the tsunami recorded at AIS, and described in Section 2. We use the full source correction, since the the $M_{TSU}$ algorithm should not be used at such periods, as the modeling of the correction $C_{TSU}$ was carried out only in the 0.3–4 mHz frequency range (OKAL and TITOV, 2006). For amplitudes $X(\omega) \approx 500$ and 1000 cm*s at the principal spectral peaks ($T = 160$ and 200 s), we obtain $M_0 = 6.2$ and $3.4 \times 10^{29}$ dyn*cm, respectively. These values, especially the second one, underestimate the moment of the event. We attribute this deficiency to the significant depth extent of the source, for which the model of a point source, legitimate at low frequencies ($\sim$1 mHz), becomes increasingly simplistic at 5–10 mHz, this effect being directly comparable to the deficiency affecting conventional surface wave magnitudes $M_S$ when the source depth becomes comparable to the wavelength.

## 5. Application to Other Events

The purpose of this section is to apply the above formalisms to a selection of other tsunamigenic earthquakes, in order to confirm the universal character of seismic recordings of tsunamis, and to explore any possible quantitative correlation between their amplitudes and the size of the parent earthquakes. All relevant information is summarized in Table 3.

• *The "Second" Sumatra (Nias) Earthquake of 28 March 2005*

Although damaging in the near field, the tsunami generated by this earthquake was deceptively small in the far field, a reflection of the shallow waters and large islands present in the rupture area (SYNOLAKIS and ARCAS, quoted by KERR, 2005). Nevertheless, YUAN *et al.* (2005) did mention a seismic recording at DGAR. We were able to detect the tsunami on seismic records at at least eight stations, listed in Table 3, and to make spectral measurements at DGAR and CRZF (at the other stations, the spectrum does not exhibit an appropriate signal-to-noise ratio). While the seismic moment inverted from these records remains large, it definitely characterizes the Nias earthquake as smaller than the 2004 Sumatra-Andaman one.

There are, however, significant differences between the seismic recordings of the two Sumatra tsunamis. The 2005 tsunami was not recorded above noise level at the Antarctic stations (CASY, DRV, SBA), and its record featured prominent ultra-long period instabilities at MSEY. High-frequency components are not detected at Amsterdam Island. Perhaps most astonishing is the timing of the signal at KIP, around 15:20 on 29 March, or only 23 hours after origin time (Fig. 7), which would correspond to eastward propagation, south of Australia, into the Tasman Sea and the Southwest Pacific, rather than westward through the Drake Passage on 26 December, 2004. We have no explanation for this difference in routing between the two tsunamis.

• *The Peruvian Tsunami of 23 June 2001*

This tsunami was damaging in the near field (OKAL *et al.*, 2002), while its parent earthquake was at the time the largest in the CMT catalogue ($M_0 = 4.7 \times 10^{28}$ dyn-cm), which it remained until the 2004 Sumatra earthquake. As shown on Figure 7a, the tsunami is well recorded in the South central Pacific, from Pitcairn to Rarotonga. Spectral measurements at RAR and PPT give an average moment only 11% larger than the Harvard CMT solution.

The 2001 Peruvian tsunami was also recorded by the H2O observatory (CHAVE *et al.*, 2002) which operated on the ocean bottom about half way between Hawaii and the Pacific Coast of the US from 1999 to 2003. The tsunami can be identified in the spectrogram of the horizontal long-period component oriented N168°E

Table 3

*Characteristics of seismic records from other tsunamis, 1995–2006*

| Station | | Epicentral distance (km) | Arrival date and time | Prominent component | Prominent period (s) | Apparent ground motion | | Inverted seismic moment $M_0$ (dyn*cm) |
|---|---|---|---|---|---|---|---|---|
| Code | Location | | | | | Peak-to-peak (cm) | Spectral amplitude $X(\omega)$ (cm*s) | |
| **Nias (Indonesia), 28 MAR (087) 2005;** 16:10:32 UT; 1.67°N; 97.07°E; $M_0 = 1.05 \times 10^{29}$ dyn*cm | | | | | | | | |
| DGAR | Diego Garcia, BIOT | 2911 | (087) 20:16 | EW | 800 | 9.2 | 800 | $1.99 \times 10^{29}$ |
| MSEY | Mahé, Seychelles | 4674 | (087) 23:12 | N247E | 2500 | 1.0 | | |
| AIS | Ile Amsterdam, TAAF | 4815 | (087) 22:43 | EW | 2500 | 1.7 | | |
| RER | Rivière de l'Est, Réunion Is. | 5157 | (087) 22:25 | EW | 2900 | 0.5 | | |
| PAF | Port-aux-Français, Kerguelen, TAAF | 6220 | (088) 01:20 | NS | 2600 | 1.8 | | |
| CRZF | Ile de la Possession, Crozet Is., TAAF | 6925 | (088) 01:52 | EW | 1000 | 1.0 | 800 | $1.81 \times 10^{29}$ |
| | | | | | 1250 | | 1100 | $1.97 \times 10^{29}$ |
| HOPE | Hope, South Georgia | 12815 | (088) 10:10 | NS | 3200 | 2.2 | | |
| KIP | Kipapa, Hawaii, USA | 17000 (*) | (088) 15:20 | NS | 3000 | 0.16 | | |
| **Peru, 23 JUN (174) 2001;** 20:33:14 UT; 17.28°S; 72.71°W; $M_0 = 4.7 \times 10^{28}$ dyn*cm | | | | | | | | |
| PTCN | Pitcairn Is., B.C.C. | 5917 | (175) 04:57 | EW | 800 | 1 | | |
| PPT | Papeete, Tahiti, Fr. Polynesia | 8092 | (175) 07:56 | N5E | 1100 | 0.3 | | |
| RAR | Rarotonga, Cook Is. | 8977 | (175) 09:01 | N335E | 800 | 0.3 | 200 | $6.05 \times 10^{28}$ |
| | | | | | 1000 | | 300 | $6.72 \times 10^{28}$ |
| | | | | | 1550 | | 250 | $3.50 \times 10^{28}$ |
| H2O | Hawaii-2 Observatory | 8978 | (175) 09:13 | N168E | | | | |
| **Antofagasta (Chile), 30 JUL (211) 1995;** 05:11:57 UT; 24.17°S; 70.74°W; $M_0 = 1.2 \times 10^{28}$ dyn*cm | | | | | | | | |
| RPN | Easter Island, Chile | 3870 | (211) 10:35 | NS | 690 | 0.3 | 100 | $2.87 \times 10^{28}$ |

Table 3

*(Contd.)*

| Station | | Epicentral distance (km) | Arrival date and time | Prominent component | Prominent period (s) | Apparent ground motion | | Inverted seismic moment $M_0$ (dyn*cm) |
|---|---|---|---|---|---|---|---|---|
| Code | Location | | | | | Peak-to-peak (cm) | Spectral amplitude $X(\omega)$ (cm*s) | |
| RAR | Rarotonga, Cook Is. | 8972 | (211) 17:45 | NS | 800 | 0.3 | 70 | $2.18 \times 10^{28}$ |
| KIP | Kipapa, Hawaii, USA | 10699 | (211) 20:09 | NS | 1750 | 0.2 | 250 | $3.37 \times 10^{28}$ |
| **Biak (Indonesia), 17 FEB (048) 1996;** 05:59:30 UT; 0.67°S; 136.62°E; $M_0 = 2.4 \times 10^{28}$ dyn*cm | | | | | | | | |
| GUMO | Agaña, Guam | 1823 | (048) 08:31 | NS | 1000 | 0.3 | 150 | $2.08 \times 10^{28}$ |
| ERM | Erimo, Japan | 4781 | (048) 12:43 | NS | 1000 | 0.9 | | |
| **Tonga, 03 MAY (123) 2006;** 15:27:09 UT; 20.33°S; 174.03°W; $M_0 = 9.6 \times 10^{27}$ dyn*cm | | | | | | | | |
| PTCN | Pitcairn Is., B.C.C. | 6564 | (123) 21:29 | NS | 690 | 1.4 | | |
| KIP | Kipapa, Hawaii, USA | 4944 | (123) 22:23 | NS | 1400 | 0.07 | 200 | $4.27 \times 10^{28}$ |
| RPN | Easter Island, Chile | 6564 | (124) 00:37 | NS | 690 | 0.2 | 125 | $3.57 \times 10^{28}$ |

(*) Distance estimated along off-great circle path going south of Australia.

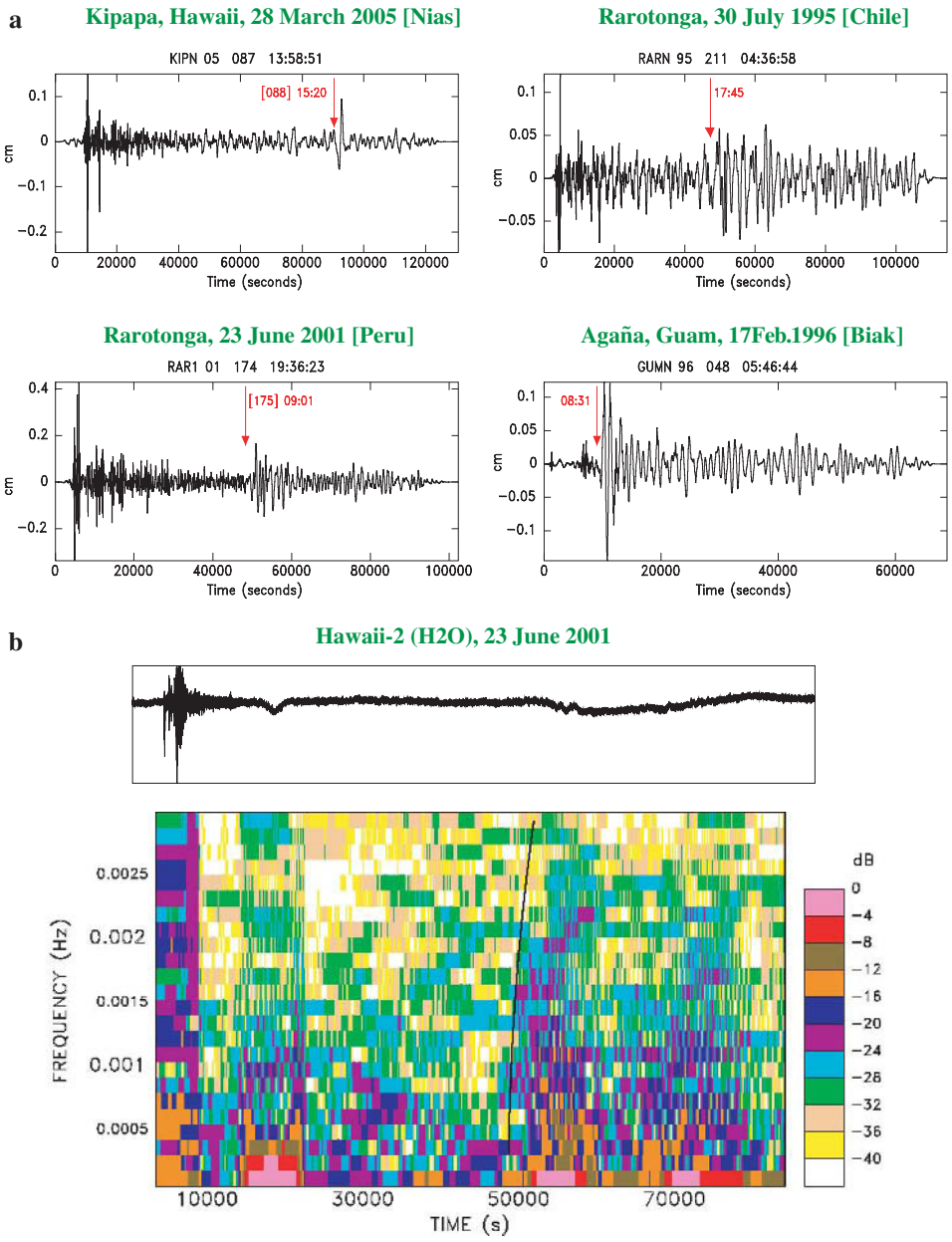


Figure 7

(**a**) Examples of seismic recordings of tsunamis from smaller earthquakes. The arrows identify the arrival of the tsunami at selected stations. These records represent apparent ground motion (in cm) after instrument deconvolution and bandpass filtering between 0.1 and 10 mHz. (**b**) Time series and spectrogram at the ocean-bottom observatory H2O following the 2001 Peruvian earthquake. The black line across the spectrogram shows the expected arrival of the tsunami, dispersed according to (1); note the coherent increase in spectral density, but the following nonlinearity in the record, probably triggered by the passage of the tsunami.

(Fig. 7b), on the basis of the coherent rise in spectral density between 0.3 and 2 mHz at the group arrival times predicted by the dispersion relation (1). However, the record suffers from obvious nonlinearity following this arrival and cannot be processed quantitatively; it is possible that this instability was triggered by the tsunami. Under the shallow water approximation, the ratio of velocity of horizontal flow $V$ in the water column to vertical surface displacement $\eta$ is simply $V/\eta = \sqrt{g/H}$, which predicts $V$ on the order of a few mm/s. It is unclear whether this would suffice to disturb the loose sedimentary structure in which the instrument at H2O was deployed. Also, we note another occurrence of similar instability much earlier in the time series.

• *The Antofagasta, Chile Tsunami of 30 July 1995*

This was the last Pacific tsunami with reported damage in the far field, as it rocked a supply ship against the bottom of the harbor of Hakahau on Ua Pou in the Marquesas Islands (GUIBOURG *et al.*, 1997). The tsunami is well recorded on seismic instruments from Easter Island to Western Samoa; however the record at AFI is affected by strong nonlinearity. The average moment measured from spectral amplitudes, $M_0 = 2.7 \times 10^{28}$ dyn-cm, is about 2.3 times the CMT solution.

• *The Biak, Indonesia Tsunami of 17 February 1996*

This large earthquake ($M_0 = 2.4 \times 10^{28}$ dyn*cm) generated a locally devastating tsunami which caused at least 120 deaths (MATSUTOMI *et al.*, 2001), but was recorded only marginally in the far field. We were able to identify a seismic recording of the tsunami at Station GUMO (Agaña, Guam), where the spectral amplitude (150 cm*s at 1 mHz) leads to an excellent value of the seismic moment ($2.08 \times 10^{28}$ dyn*cm). Unfortunately, Station KIP in Hawaii was down at that time.

• *The Tonga Tsunami of 03 May 2006*

We also consider the case of this recent event, reminiscent of the 1977 intraslab Tonga earthquake (TALANDIER and OKAL, 1979; LUNDGREN and OKAL, 1988), 300 km to the South. Despite a relatively deep focus (65 km), the tsunami is detectable at seismic stations PTCN, RPN and KIP (at the time of writing, not all South Pacific stations are available), and spectral amplitudes could be quantified at the latter two.

These results are summarized on Figure 8, which compares seismic moments inverted from spectral amplitudes of seismic recordings of the tsunamis to the Harvard CMT solutions. This figure suggests a remarkable correlation, at least for $M_0 \geq 2 \times 10^{28}$ dyn*cm, which serves to justify *a posteriori* the many assumptions used in the present approach. It also confirms that the 2004 Sumatra earthquake was not

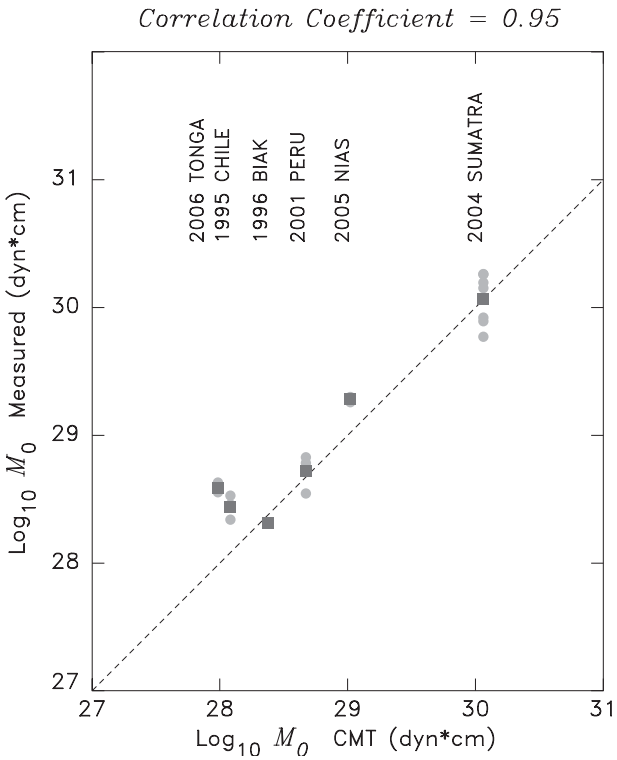


Figure 8
Comparison of moments retrieved from spectral amplitudes of seismic records of six tsunamis with published CMT solutions. For each earthquake, the gray circles are measurements at individual stations (analogous to the circles on Fig. 6), and the squares the resulting geometrical average of the moments. In the case of the 2004 Sumatra event, the deficient values at MSEY and DRV have been excluded.

anomalously tsunamigenic, and reconciles the amplitude of its tsunami with its seismic source.

Finally, we examined the case of the Papua New Guinea tsunami of 17 July 1998. The tsunami was catastrophic in the near field, with run-up reaching 15 m and causing 2200 deaths, and is generally interpreted as resulting from an underwater landslide triggered by the earthquake with a delay of 13 minutes (SYNOLAKIS *et al.*, 2002). Figure 9 shows that the tsunami is detectable on the EW component of the regional station GUMO, between 1.5 and 3.5 mHz, with a dispersion of group times suggesting propagation over an average water depth of 3 km, generally compatible with the bathymetry of the shallow Eauripik Rise separating the East and West Caroline Basins. However, the peak spectral amplitudes on this record ($X(\omega)$ = 30 cm*s at $T$ = 690 s and 2.5 cm*s at $T$ = 330 s) lead to seismic moments of $6.1 \times 10^{27}$ and $1.29 \times 10^{28}$ dyn*cm, or 16 and 35 times the Harvard CMT solution,

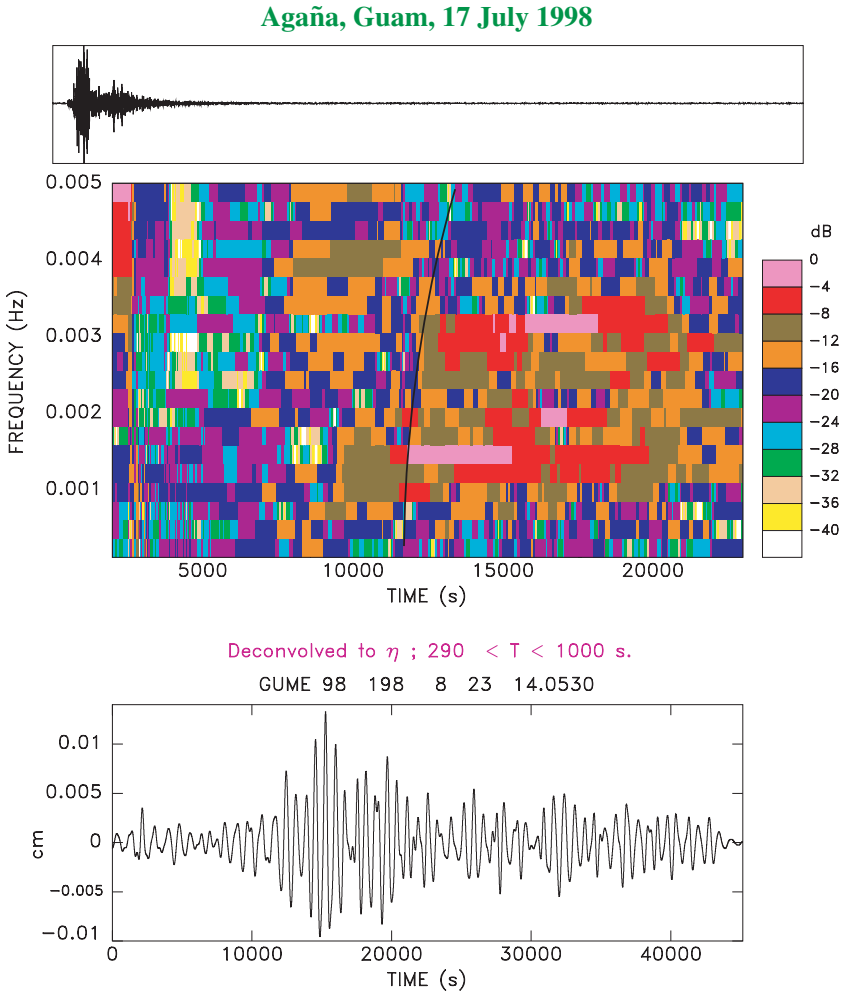


Figure 9

*Top*: Time series of the EW long-period channel at Agaña, Guam (GUMO) following the Papua New Guinea earthquake of 17 July, 1998. The record is 25,000 s (≈ 7 hr) long. Center: Corresponding spectrogram, showing arrival of tsunami ~12,000 s into the time series with energy concentrated in the 1.2 to 3.5 mHz range. The black curve is the theoretical dispersion for propagation over a 3-km deep basin from a source located at the Sissano amphitheater and and activated at 09:02 UTC (SYNOLAKIS *et al.*, 2002). *Bottom*: Equivalent surface wave amplitude $\eta$ deconvolved from the top trace following the procedure in Section 6, but bandpass filtered between 290 and 1000 s.

respectively. This confirms, if need be, that the 1998 Papua New Guinea tsunami could not have been generated directly by the main shock. These observations represent to our knowledge the first detection of the 1998 Papua New Guinea

tsunami at a distance (1809 km) falling outside the near field domain, which can be used to support this conclusion.

## 6. Deconvolution of the Seismic Records

In this section, we explore the possibility of deconvolving the response of the seismometer to the tsunami in order to reconstruct the time series of the surface displacement of the tsunami wave, $\eta(t)$. For this purpose we define at each frequency a so-called "Gilbert Response Factor" $GRF(\omega) = ly_3{}^{app}$, which is just the ratio between the apparent ground motion "felt" by the seismometer (still supposed to reside on the ocean bottom) and the vertical displacement of the surface of the ocean (normalized to unity in our computations of eigenfunctions). This function is simply

$$GRF(\omega) = l \cdot y_3^{app} \approx ly_3 - \frac{1}{C\,\omega}(gy_1 - y_5), \tag{5}$$

where $C$ is the phase velocity of the wave, and we have further assumed that the depth of the ocean column is negligible with respect to the Earth's radius $a$. $GRF(\omega)$ is readily computed from normal mode theory, and Figure 10 shows its variation over a wide range of frequencies both within and outside the shallow-water approximation ($lH/a \ll 1$). We verified (see Appendix) that for a given frequency, $GRF(\omega)$ depends only marginally on the depth of the ocean column. We then simply divide, in the Fourier domain, the apparent seismic amplitude $X(\omega)$ by

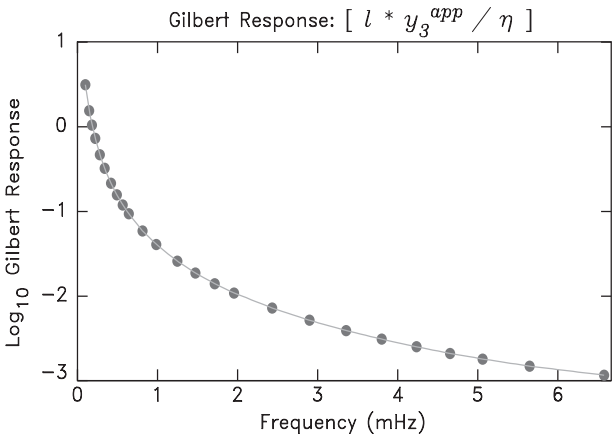


Figure 10
"Gilbert Response Factor" as a function of frequency computed for a 5-km deep ocean. At each frequency, *GRF*, defined by (5), represents the ratio between the apparent displacement to which a horizontal seismometer on the ocean bottom responds and the vertical amplitude of the tsunami wave on the surface of the ocean.

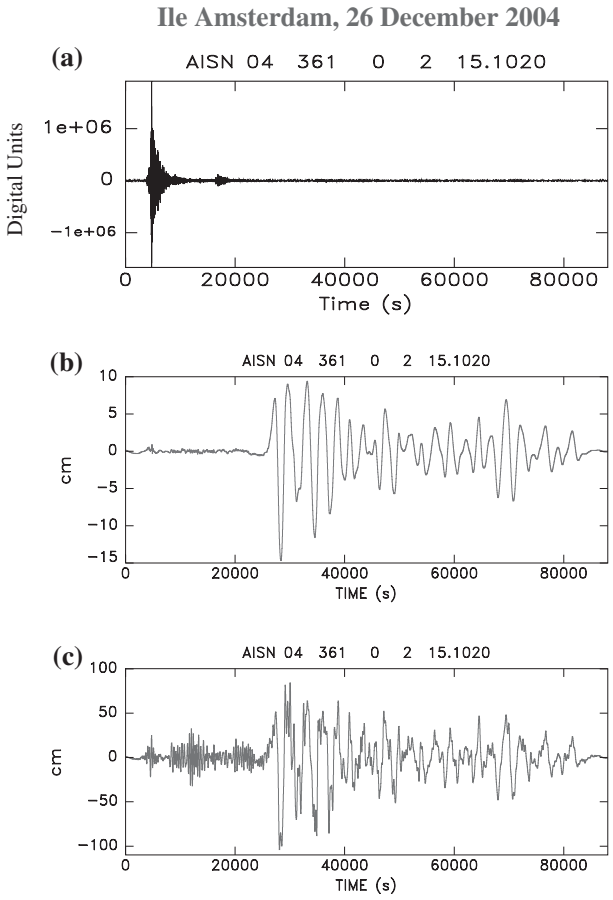


Figure 11
Reconstruction of the tsunami wave time series from a seismogram by deconvolution of the Gilbert Response Factor *GRF*, illustrated on the example of Station AIS (2004 Sumatra event). (*a*): Raw Long-period NS seismogram at AIS; (*b*): Apparent horizontal ground motion after instrument deconvolution and bandpass filtering between 0.1 and 10 mHz; (*c*): Reconstructed time series of the sea surface deformation, $\eta$.

$GRF(\omega)$ before returning to the time domain to reconstruct the time series $\eta(t)$ of the tsunami at the surface. This procedure is illustrated on Figure 11 in the case of the record at Amsterdam Island (AIS). The top frame shows the raw record, the middle one the time series of the apparent ground displacement after removing the instrument response and bandpass filtering between 100 and 10000 s, and the bottom one the time series resulting from the deconvolution of the Gilbert Response Factor, and further filtering between 300 and 5000 s. In the framework of our admittedly crude assumptions, this record should in principle represent the

time series of the wave elevation $\eta(t)$ of the surface of the ocean at the location, but in the absence, of Amsterdam Island. Obviously, the high-frequency signal to the left of the tsunami in the deconvolved trace should be ignored, as it represents the result of processing the seismic surface waves from the earthquake through an algorithm which is not applicable to them. This procedure was carried out for all 16 seismic records of the tsunami and the results, expressed as peak-to-peak $\eta$, are listed in Table 1.

Unfortunately, no instruments capable of directly recording the 2004 Sumatra tsunami on the high seas were operating at the time in the Indian Ocean, and thus it is impossible to compare the results of our deconvolution to the actual height of the tsunami. We nevertheless validate our algorithm in three different ways. First, we use the record of the tsunami obtained by the JASON satellite altimeter which featured a zero-to-peak amplitude of ~70 cm (SCHARROO *et al.*, 2005), on the same order of magnitude as the deconvolved time series $\eta$ on Figure 11 (85 cm). We emphasize, however, the strong limitations of this comparison, given that the JASON trace is neither a time nor a space series, and that it samples the tsunami several thousand km to the north of AIS.

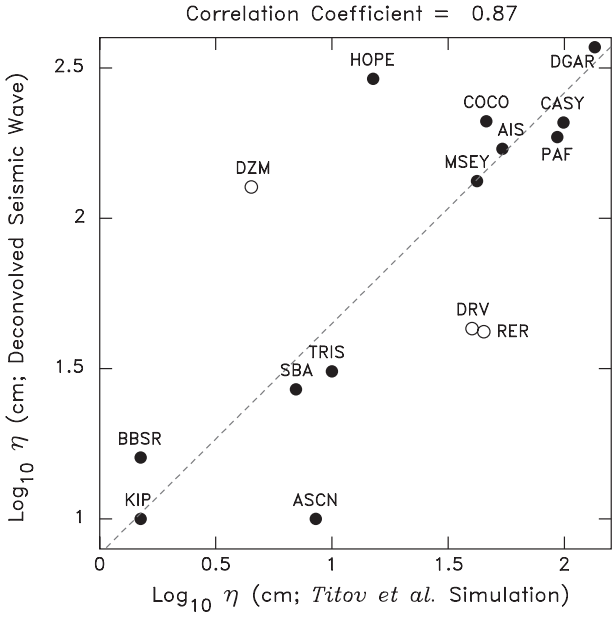


Figure 12
Equivalent tsunami wave height $\eta$ deconvolved from seismic records (ordinate) plotted against the wave height computed from TITOV *et al.*'s (2005) global simulation of the 2004 Sumatra tsunami. The open symbols are outliers excluded from the regression; see text for details. The dashed line is the best-fitting regression to the dataset.

▶

Figure 13

Analysis of the seismic record of the 2006 Tonga tsunami at Kipapa, Hawaii. (*a*): Raw record of the North-South Long-Period channel; the record starts at 14:58:29 UTC. (*b*): Spectrogram of (a), identifying the tsunami arrival, about 25,000 s into the signal. The black trace is the dispersion expected from propagation over a 4.5-km deep ocean basin. (*c*): Apparent ground motion recorded by the instrument, after deconvolution of its response. The red arrow points to the arrival of the tsunami, barely discernible above noise level, but clearly present in the spectrogram. The time scale is common to (a), (b) and (c). (*d*): Surface wave height, $\eta$, reconstructed by deconvolution of the Gilbert Response Factor. (*e*): Tsunami waveforms recorded at tsunameters of the DARTprogram deployed off the islands of Oahu (DART-ETD; red trace) and Hawaii (DART-II; black trace); the scale in cm at left corresponds to equivalent tsunami height at the sea surface (Courtesy V.V. Titov).

Second, we compare in Figure 12 the peak-to-peak amplitudes of our deconvolved traces (listed in Table 1) to those computed as part of TITOV *et al.*'s (2005) global simulation of the 2004 tsunami. Specifically, for each station, we extracted from these authors' database a time series at a ''virtual gauge'' located on the high seas in the neighborhood of the station (typically 50 km out at sea, but with allowances made for exceptional structures), and retained its peak-to-peak amplitude, which we list as the last column of Table 1. The dataset is well correlated, except for a number of intriguing outliers. Among them is Dumont d'Urville (DRV), where we have already noted the deficient amplitude of the tsunami signal, possibly due to the large continental shelf bordering the continent; the virtual gauge is located seaward of the shelf. Both DZM in New Caledonia and RER in Réunion are the only stations at substantial altitude (in both cases $\sim$800 m), which may affect their response; we note however that one of them (DZM) has an enhanced response, the other (RER) a deficient one. Excluding those three stations, we find a very strong correlation (87%) between our deconvolved amplitudes and those simulated by TITOV *et al.* (2005). However, we have no interpretation for the extreme amplitude deconvolved at HOPE (although it may express some form of resonance of the strongly indented Cumberland Bays where the station is located), nor for the extreme deficiency at Ascension Island (ASCN). Also, we note that, while the deconvolved amplitudes correlate with the simulated ones, the former remain generally several times larger than the latter.

Finally, we take advantage of the recent deployment of many tsunameters (GONZÁLEZ *et al.*, 2005), notably in the Pacific Basin, to compare the deconvolved wave height of the Tonga tsunami of 03 May 2006 recorded at Kipapa, Hawaii, with time series obtained at two nearby tsunameters. As shown in Figure 13, and while significant differences remain between the waveshapes involved, the peak-to-peak amplitude deconvolved in our experiment, 1.6 cm, is comparable to that (2.1 cm) recorded at the offshore site DART-ETD, approximately 110 km from Station KIP, the ratio of these amplitudes (0.76), being itself comparable to the scatter (0.79) between the amplitudes at the two tsunameters.

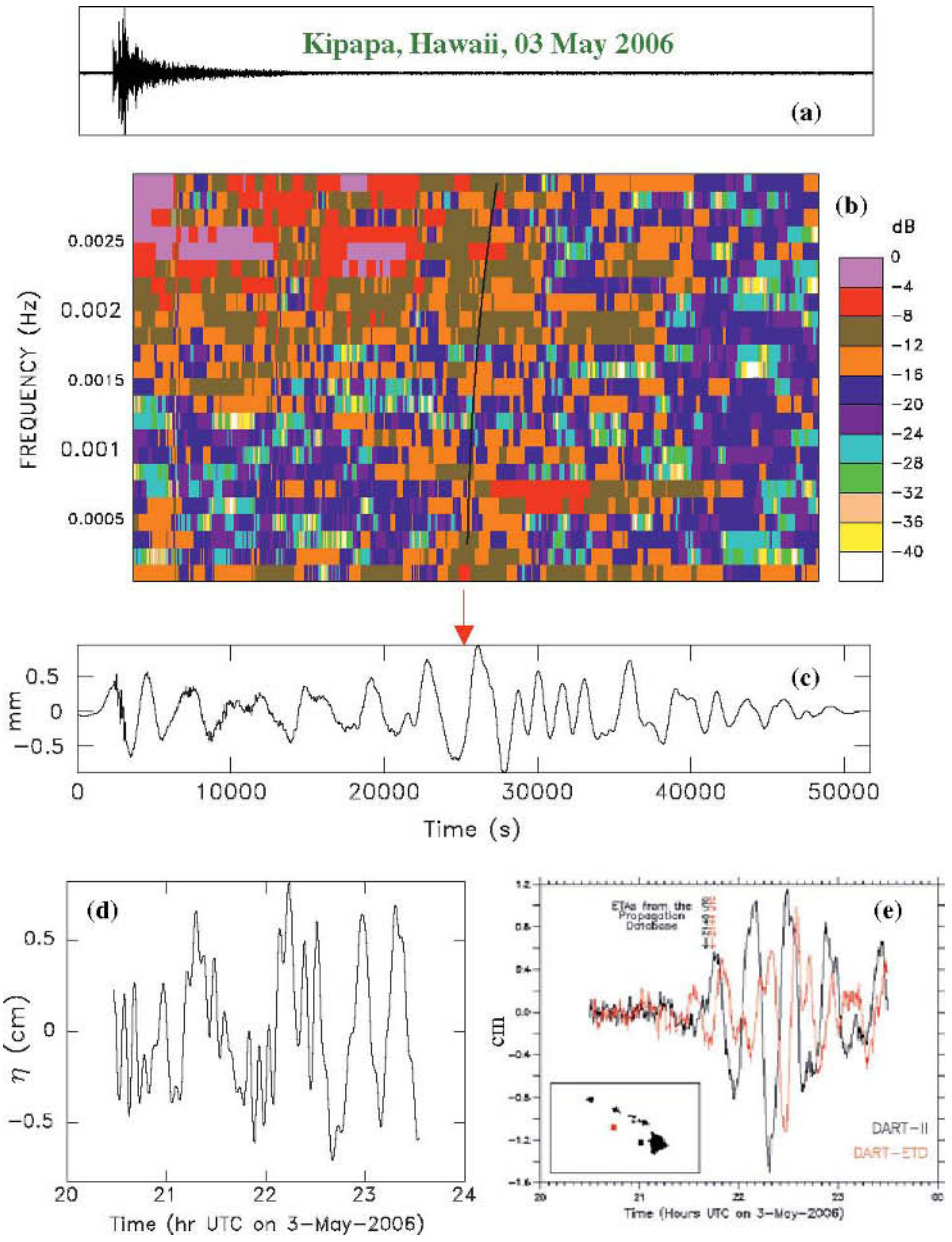


## 7. Conclusion and Perspective

We have expanded the observations of YUAN *et al.* (2005) and HANSON and BOWMAN (2005), and established that the 2004 Sumatra earthquake was recorded

essentially worldwide on the horizontal long-period channels of seismic stations located in the vicinity (within ~35 km) of shorelines. However, the recording can be affected by site effects such as the presence of an extended continental shelf; large bays can apparently enhance the signal (as at HOPE), or suppress it (as at ATD). At intermediate ranges of distance (~4000 km), we show that seismometers can detect the full spectrum of a tsunami branch, including their higher-frequency component up to 10 mHz, which are strongly affected by dispersion outside the domain of applicability of the shallow water approximation.

We have shown that it is possible to interpret seismic recordings of the tsunami as representing the response of the seismometer to a deformation of the ocean floor involving lateral displacement, tilt and gravitational potential, as derived theoretically by GILBERT (1980). In this model, it is assumed that, for stations located much closer to the shoreline than one wavelength, the progressive wave is essentially unaltered from its structure on the high seas, with the result that the instrument functions as an Ocean-Bottom Seismometer responding to the tsunami in a deep basin. Estimates of the seismic moment of the parent earthquake obtained in this framework and using standard normal mode theory (WARD, 1980; OKAL, 1988, 2003) are in excellent agreement with published values, which serves to justify the model, however outrageous the approximations involved may sound.

In addition, we show that tsunami signals are present in the seismic recordings of at least five more earthquakes, and that the seismic moments derived from our algorithm scale remarkably well with published centroid-moment tensor values.

The technique can be extended to a formal deconvolution of the seismic records by removal of the Gilbert Response Function. On Figures 12 and 13, we found a clear correlation between the amplitudes of the resulting time series and those obtained from TITOV *et al.*'s [2005] global simulation (and in one case with a genuine tsunameter record). This further confirms that such deconvolved signals are representations of the tsunami wavefields on the high seas, and hence supports the validity of the interpretation of the seismic recordings of the tsunamis. While this requires a number of drastic simplifying assumptions, and notwithstanding the potential importance of site effects at individual locations, the seismic instruments have the great advantage of being for the most part already deployed on many oceanic islands and continental shores, and in any case of coming at a fraction of the deployment and above all maintenance costs of a network of bottom pressure recorders linked to their open-seas buoys. The present study suggests that existing or future broadband horizontal seismometers located near shore on oceanic islands or continents could complement advantageously a network of buoy-based instruments of the DART type.

*Acknowledgments*

This research was supported by the National Science Foundation, under Grant CMS-03-0154. I thank Rainer Kind for many discussions on this and other topics in Potsdam in the Fall of 2005. I am grateful to Vasily Titov for access to the database of global simulations of the Sumatra tsunami (TITOV *et al.*, 2005), and for the DART tsunameter records included in Figure 13. I thank Steve Ward for his review of the original version of the paper, and in particular for his suggestion to look at vertical records. Figure 1 was plotted using the GMT software (WESSEL and SMITH, 1991).

## *Appendix*

### *Tilt and Gravity Terms Compared for Seismic and Tsunami Modes*

We compare here the various contributions from displacement, tilt and gravity to the recording by long-period seismometers, of conventional seismic and tsunami modes.

In addition to the response of a horizontal seismometer, given by equations (3) or (4), we consider GILBERT'S (1980) expression for the response of a vertical seismometer (his equation (4.12) p. 66):

$$AU = \left(\omega^2 + \frac{2g}{r}\right)U + \frac{l+1}{r}\Phi, \tag{A-1}$$

which we rewrite in the formalism of SAITO (1967) as equivalent to the recording of an apparent vertical displacement $y_1^{app}$

$$y_1^{app} = y_1 + \frac{2g}{r\omega^2}y_1 - \frac{l+1}{r\omega^2}y_5. \tag{A-2}$$

- For conventional seismic spheroidal modes, the second terms in (4) and (A-2) are negligible as long as their period $T$ remains less than $2\pi\sqrt{a/2g} \approx 1$ hr, which is the case of all mantle waves. As the latter carry very little gravitational energy, the third terms are also negligible and for all practical purposes, $y_1^{app} = y_1$; $y_3^{app} = y_3$; the seismometer responds to ground motion. For the lowest frequency modes, whose period approaches one hour, the contributions of the second and third terms in (A-2) become important; however, because their signs are generally opposite, the departure of $y_1^{app}$ from $y_1$ does not exceed 20% (for ${}_0S_2$), as

documented in GILBERT'S (1980) Table 1 (p. 66) or DAHLEN and TROMP'S (1998) Table 10.1 (p. 375); the horizontal response would be affected more significantly for the four gravest spheroidal modes, down to ${}_0S_5$. Since few studies of the fundamental spheroidal modes are conducted on horizontal instruments, and toroidal modes are unaffected by such terms (GILBERT, 1980), the conclusion is that tilt and gravity terms contribute marginally if at all to the recording of conventional seismic modes. They do not affect the *order of magnitude* of the recorded amplitude (this would happen only in the case of the yet-to-be observed Slichter mode ${}_1S_1$).

- We illustrate the case of tsunami modes by considering a typical period of 1014 seconds, corresponding to $l = 200$ for an ocean depth of 4 km, overlying a solid Earth inspired from PREM (DZIEWONSKI and ANDERSON, 1981). For a normalization of the eigenfunction $\eta = 1$ cm at the surface of the ocean, we compute at the ocean bottom $y_1 = -0.0037$ cm; $y_3 = 5.96 \times 10^{-6}$ cm in the solid; and $y_5 = 0.0117$ (cm/s)$^2$. (Note that a negative value of $y_1$ is expected, as it expresses the downward vertical response of the elastic Earth to the overpressure accompanying an upwards vertical displacement of the ocean surface.) In turn, these numbers lead to a free air contribution (second term in (A-2)) of $-2.98 \times 10^{-4}$ cm (or only 8% of $y_1$), and to a potential contribution (third term in (A-2)) of $-9.66 \times 10^{-3}$ cm (or 2.6 times $y_1$), the apparent displacement for a vertical seismometer being $y_1^{app} = -0.0137$ cm. For the horizontal component, the tilt contribution to $y_3^{app}$ (second term in (4)) is $1.49 \times 10^{-4}$ cm (25 times $y_3$) and the potential contribution (third term in (4)) is $4.81 \times 10^{-5}$ cm (8 times $y_3$), for a total $y_3 = 2.03 \times 10^{-4}$ cm, and an apparent displacement $l\ y_3^{app} = 4.06 \times 10^{-2}$ cm, i.e., three times the amplitude of the vertical signal. This factor of three is further found to vary little with frequency.

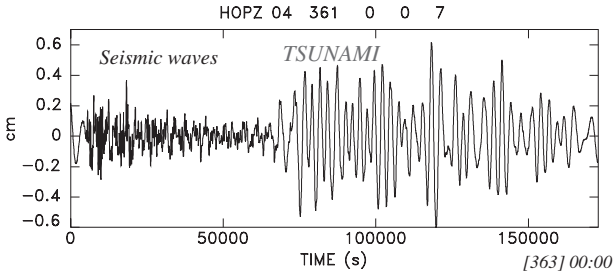


Figure A1
Deconvolved vertical record at HOPE, showing recording of the tsunami by the vertical instrument. The time window (48 hours starting at 00:00 on 26 December 2004), deconvolution and filtering are exactly analogous to those used on Figure 2 for the NS component. Note, however, that the amplitude is reduced by a factor of 10.

On Figure A1, we plot the vertical long-period seismogram at Hope, processed in exactly the same fashion as the horizontal component on Figure 2. Note that the tsunami is very prominent in this high-quality record, but that its amplitude is only 1/10 of its north-south counterpart, as opposed to the predicted 1/3. We cannot explain this discrepancy by a factor of about three, but suspect that it may be rooted in the different nature of the terms controlling the horizontal and vertical responses. The former is completely governed by the tilt term, which depends only on the wavelength of the tsunami mode, and as such may be more robust under the extreme approximation made in assuming that the island seismometer behaves as an OBS, while the vertical response is controlled principally by the potential term, for which the approximation may not hold; note in particular that the missing factor of three represents essentially the ratio $y_1^{app}/y_1$ at the bottom of the ocean (3.78). For this reason, we elect not to further study and attempt to quantify the vertical records of the tsunami. However, we stress that they are indeed present.

Finally, we address the question of the sensitivity of the Gilbert Response Function *GRF* to the height *H* of the ocean column. Under the Linear Shallow Water Approximation, we have shown in OKAL (1982, 1988) that the eigenstress $y_2$ at the fluid-solid interface can be taken as $y_2 = -\eta\rho_w g$, and that in turn the vertical displacement at the interface is $y_1 = y_2/Z$ with the impedance $Z = 4/3\ \mu k$ where $\mu$ is the rigidity of the substratum and $k$ the wavenumber. As we discussed above, the *GRF* is controlled by the tilt term in (4), leading to

$$GRF = \frac{l y_3^{app}}{\eta} \approx \frac{lg}{r\omega^2} \cdot \frac{3}{4} \frac{\rho_w g}{\mu k} \approx \frac{3}{4} \cdot \frac{\rho_w g^2}{\mu} \cdot \frac{1}{\omega^2}. \tag{A-3}$$

This expression is expected to be independent of *H*, which we verified by recomputing all the contributions to $y_1^{app}$ and $y_3^{app}$ for an ocean depth $H = 5$ km, for which the new value of $l$ at 1014 s is 179, as opposed to ($H = 4$ km; $l = 200$) used above. We find that $y_3^{app}$ becomes $2.23 \times 10^{-4}$ cm, and thus $l\, y_3^{app} = 3.99 \times 10^{-2}$ cm, a decrease of 1.7%, and for the vertical component, $y_1^{app} = -0.0139$ cm, an absolute increase of 1.3% with respect to the case of the shallower ocean. Similar numbers are also found across the frequency spectrum, and so we conclude that the effect of *H* on the Gilbert Response Function *GRF* is negligible given the other approximations made in this study.

## REFERENCES

BEN-MENAHEM, A. and ROSENMAN, M. (1972), *Amplitude patterns of tsunami waves from submarine earthquakes*, J. Geophys. Res. *77*, 3097–3128.

CHAVE, A.D., DUENNEBIER, F.K., BUTLER, R., PETITT, R.A., Jr., WOODING, F.B., HARRIS, D., BAILEY, J.W., HOBART, E., JOLLY, J., BOWEN, A.D. and YOERGER, D.R., H2O: *The Hawaii-2 Observatory*. *In*

*Science-technology Synergy for Research in the Marine Environment: Challenges for the XXIst Century* (eds. L. Beranzoli, P. Favali, and G. Smriglio), Devel. Mar. Tech. Ser., *12*, pp. 83–92 (Elsevier, Amsterdam, 2002).

DAHLEN, F.A. and TROMP, J. *Theoretical Seismology* (Princeton Univ. Press, 1998, 1025 pp.)

DAVIES, D. (1968), *When did the Seychelles leave India*? Nature *220*, 1225–1226.

DU TOIT, A.L., *Our Wandering Continents*, 366 pp. (Oliver & Boyd, London, 1937).

DZIEWONSKI, A.M. and ANDERSON, D.L. (1981), *Preliminary Earth Reference Model*, Phys. Earth Planet. Inter. *25*, 297–356.

GILBERT, F., *An introduction to low-frequency seismology*. *In Proc. Intl. School Phys. "Enrico Fermi"*, *78* (eds. A.M. Dziewonski and E. Boschi), pp. 41–81 (North Holland, Amsterdam, 1980).

GONZÁLEZ, F.I., BERNARD, E.N., MEINIG, C., EBLE, M.C., MOFJELD, H.O. and STALIN, S. (2005), *The NTHMP Tsunameter network*, Natural Hazards *35*, 25–39.

GUIBOURG, S., HEINRICH, P., and ROCHE, R. (1997), *Numerical modeling of the 1995 Chilean tsunami. Impact on French Polynesia*, Geophys. Res. Lett. *24*, 775–778.

HANSON J.A. and BOWMAN, J.R. (2005), *Dispersive and reflected tsunami signals from the 2004 Indian Ocean tsunami observed on hydrophones and seismic stations*, Geophys. Res. Lett. *32*(17), L17606, 5 pp.

KERR, R.A. (2005), *Model shows islands muted tsunami after latest Indonesian earthquake*, Science *308*, 341.

LA ROCCA, M., GALLUZZO, D., SACCOROTTI, G., TINTI, S., CIMINI, G.B., and DEL PEZZO E. (2004), *Seismic signals associated with landslides and with a tsunami at Stromboli Volcano, Italy,* Bull. Seismol. Soc. Amer. *94*, 1850–1867.

LUNDGREN, P.R. and OKAL, E.A. (1988), *Slab decoupling in the Tonga arc: the June 22, 1977 earthquake*, J. Geophys. Res. *93*, 13355–13366.

MATSUTOMI, H., SHUTO, N., IMAMURA, F., and TAKAHASHI, T. (2001), *Filed survey of the 1996 Irian Jaya earthquake tsunami on Biak Island*, Nat. Haz. *24*, 199–212.

OKAL, E.A. (1982), *Mode-wave equivalence and other asymptotic problems in tsunami theory*, Phys. Earth Planet. Inter. *30*, 1–11.

Okal, E.A. (1988), *Seismic parameters controlling far-field tsunami amplitudes: A review*, Natural Hazards *1*, 67–96.

OKAL, E.A. (1991), *Erratum [to "Seismic parameters controlling far-field tsunami amplitudes: A review"]*, Natural Hazards *4*, 433.

OKAL, E.A. (2003), *Normal modes energetics for far-field tsunamis generated by dislocations and landslides*, Pure Appl. Geophys. *160*, 2189–2221.

OKAL, E.A. and TALANDIER, J. (1989), $M_m$*: A variable period mantle magnitude*, J. Geophys. Res. *94*, 4169–4193.

OKAL, E.A. and TITOV, V.V. (2007), $M_{TSU}$: *Recovering seismic moments from tsunameter records*, Pure Appl. Geophys., *164*, 355–378.

OKAL, E.A., DENGLER, L., ARAYA, S., BORRERO, J.C., GOMER, B., KOSHIMURA, S., LAOS, G., OLCESE, D., ORTIZ, M., SWENSSON, M., TITOV, V.V., and Vegas, F. (2002), *A field survey of the Camana, Peru tsunami of June 23, 2001*, Seismol. Res. Lett. *73*, 904–917.

OKAL, E.A., FRITZ, H.M., RAVELOSON, R., JOELSON, G., PANČOŠKOVÁ, P., and RAMBOLAMANANA, G. (2006a), *Field survey of the 2004 Indonesian tsunami in Madagascar*, Earthquake Spectra *22*, S263–S283.

OKAL, E.A., SLADEN, A., and OKAL, E.A.-S. (2006b), *Field survey of the 2004 Indonesian tsunami on Rodrigues, Mauritius, and Réunion Islands*, Earthquake Spectra *22*, S241–S261.

OKAL, E.A., TALANDIER, J., and REYMOND, D. (2007) *Quantification of hydrophone records of the 2004 Sumatra tsunami*, Pure Appl. Geophys. *164*, 309–323.

SAITO, M. (1967), *Excitation of free oscillations and surface waves by a point source in a vertically heterogeneous Earth*, J. Geophys. Res. *72*, 3689–3699.

SATAKE, K. (1988), *Effects of bathymetry on tsunami propagation: Application of ray tracing to tsunamis*, Pure Appl. Geophys. *126*, 28–35.

SCHARROO, R., SMITH, W.H.F., TITOV, V.V., and ARCAS, D. (2005) *Observing the Indian Ocean tsunami with satellite altimetry*, Geophys. Res. Abstr. *7*, 230 (abstract).

STEIN, S. and OKAL, E.A. (2005), *Size and speed of the Sumatra earthquake*, Nature *434*, 581–582.

SYNOLAKIS, C.E., BARDET, J.-P., BORRERO, J.C., DAVIES, H.L., OKAL, E.A., SILVER, E.A., SWEET, S., and TAPPIN, D.R. (2002), *The slump origin of the 1998 Papua New Guinea tsunami*, Proc. Roy. Soc. (London), Ser. *A 458*, 763–789.

TALANDIER, J. and OKAL, E.A. (1979), *Human perception of T waves: the June 22, 1977 Tonga earthquake felt on Tahiti*, Bull. Seismol. Soc. Amer. *69*,1475–1486.

TITOV, V.V., RABINOVICH, A.B., MOFJELD, H.O., THOMSON, R.E., and GONZÁLEZ, F.I. (2005), *The global reach of the 26 December 2004 Sumatra tsunami*, Science *309*, 2045–2048.

TSAI, V.C., NETTLES, M., EKSTRÖM, G., and DZIEWOŃSKI, A.M. (2005), *Multiple CMT source analysis of the 2004 Sumatra earthquake*, Geophys. Res. Lett. *32*(17), L17304, 4 pp.

WARD, S.N. (1980), *Relationships of tsunami generation and an earthquake source*, J. Phys. Earth *28*, 441–474.

WEGENER, A.L., *Die Entstehung der Kontinente und Ozeane* (Vieweg, Braunschweig, 1915).

WOODS, M.T. and OKAL, E.A. (1987) *Effect of variable bathymetry on the amplitude of teleseismic tsunamis: a ray-tracing experiment*, Geophys. Res. Lett. *14*, 765–768.

WESSEL, P. and SMITH, W.H.F. (1991), *Free software helps map and display data, Eos*, Trans. Amer. Geophys. Un. *72*, 441 and 445–446.

YUAN, X., KIND, R., and PEDERSEN, H. (2005), *Seismic monitoring of the Indian Ocean tsunami*, Geophys. Res. Lett. *32*(15), L15308, 4 pp.

(Received May 29, 2006, accepted July 30, 2006)

Pure appl. geophys. 164 (2007) 355–378
0033–4553/07/030355–24
DOI 10.1007/s00024-006-0180-5



Pure and Applied Geophysics

# $M_{TSU}$ : Recovering Seismic Moments from Tsunameter Records

EMILE A. OKAL[1] and VASILY V. TITOV[2]

*Abstract*—We define a new magnitude scale, $M_{TSU}$, allowing the quantification of the seismic moment $M_0$ of an earthquake based on recordings of its tsunami in the far field by ocean-bottom pressure sensors (''tsunameters'') deployed in ocean basins, far from continental or island shores which are known to affect profoundly and in a nonlinear fashion the amplitude of the tsunami wave. The formula for $M_{TSU}$, $M_{TSU} = \log_{10} M_0 - 20 = \log_{10} X(\omega) + C_D^{TSU} + C_S^{TSU} + C_0$, where $X(\omega)$ is the spectral amplitude of the tsunami, $C_D^{TSU}$ a distance correction and $C_S^{TSU}$ a source correction, is directly adapted from the mantle magnitude $M_m$ introduced for seismic surface waves by OKAL and TALANDIER. Like $M_m$, its corrections are fully justified theoretically based on the representation of a tsunami wave as a branch of the Earth's normal modes. Even the locking constant $C_0$, which may depend on the nature of the recording (surface amplitude of the tsunami or overpressure at the ocean floor) and its units, is predicted theoretically. $M_{TSU}$ combines the power of a theoretically developed algorithm, with the robustness of a magnitude measurement that does not take into account such parameters as focal geometry and exact depth, which may not be available under operational conditions in the framework of tsunami warning. We verify the performance of the concept on simulations of the great 1946 Aleutian tsunami at two virtual gauges, and then apply the algorithm to 24 records of 7 tsunamis at DART tsunameters during the years 1994–2003. We find that $M_{TSU}$ generally recovers the seismic moment $M_0$ within 0.2 logarithmic units, even under unfavorable conditions such as excessive focal depth and refraction of the tsunami wave around continental masses. Finally, we apply the algorithm to the JASON satellite trace obtained over the Bay of Bengal during the 2004 Sumatra tsunami, after transforming the trace into a time series through a simple *ad hoc* procedure. Results are surprisingly good, with most estimates of the moment being over $10^{29}$ dyn-cm, and thus identifying the source as an exceptionally large earthquake.

**Key words:** Tsunami, magnitudes, normal mode theory, tsunami warning.

## *Introduction*

With the recent development and deployment of tsunameters under the DART project (GONZÁLEZ *et al.*, 2005), it has become possible, at least in the Pacific Ocean, to routinely record tsunami waves on the high seas, unaffected by the distortion they undergo during the complex, highly nonlinear, process of shoaling and run-up at continental and island shores. We recall that tsunameters consist of pressure sensors

[1] Department of Geological Sciences, Northwestern University, Evanston, IL 60208, USA.
[2] Pacific Marine Environmental Laboratories, NOAA, 7600 Sandpoint Way, Seattle, WA 98105, USA.

deployed on the ocean floor, capable of recording the overpressure accompanying the passage of the tsunami wave, and of relaying this information to a remote data center via satellite communication from a surface buoy which receives the signal acoustically from the nearby deep-water sensor (Fig. 1).

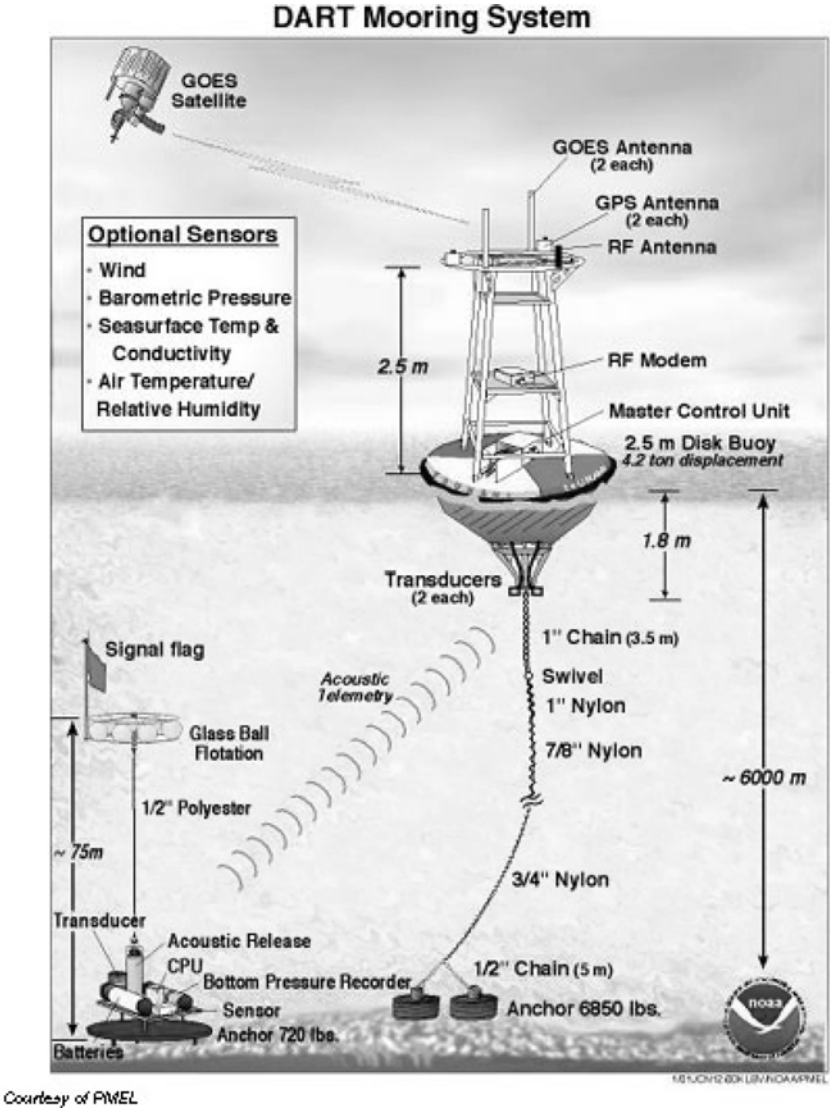


Figure 1
Schematic diagram of a DART tsunameter (González *et al.*, 2005). The pressure sensor (bottom left) is deployed on the ocean floor and its signal relayed acoustically to a buoy floating nearby, which in turn transmits the data to a central laboratory via satellite telemetry.

At least three other technologies have been used to detect tsunami waves on the high seas, some of which lend themselves to a quantitative measurement. (1) OKAL *et al.* (1999) analyzed satellite altimetry signals in the wake of several tsunamis in the 1990s, and claimed the detection of an 8-cm signal following the 1992 Nicaraguan event, and the tentative recognition of the 1995 Antofagasta, Chile tsunami. Satellite altimetry successfully detected the 2004 Sumatra tsunami, with an amplitude of 70 cm on the JASON satellite trace (SCHARROO *et al.*, 2005), which was successfully modeled by, among others, TITOV and ARCAS (2005) and SLADEN and HÉBERT (2005). (2) Following an idea originally proposed by WEAVER *et al.* (1970) and PELTIER and HINES (1976), ARTRU *et al.* (2005) used dense arrays of land-based GPS receivers to detect a disturbance in the electron density of the ionosphere, induced by the upwards continuation of the tsunami eigenfunction, first in the wake of a small earthquake south of Japan, then during the large Peruvian event of 2001. This technique also detected successfully the 2004 Sumatra tsunami (OCCHIPINTI *et al.*, 2005), leading to a preliminary quantitative interpretation in terms of an estimate of the vertical amplitude of the tsunami wave at the surface of the ocean. (3) More recently, HANSON and BOWMAN (2005) reported the detection of the 2004 Sumatra tsunami on hydrophones of the International Monitoring System. Such instruments are conceptually similar to tsunameters, in that they detect the pressure component of the tsunami wave in the oceanic water column, albeit at a different depth (1.3 km as opposed to the ocean floor for tsunameters); they also feature a drastically different instrumental response. These authors did not address the question of the amplitude of the reported signals. which OKAL *et al.* (2007) later interpreted quantitatively in the 10 mHz frequency range.

In the framework of far-field tsunami warning, signals from tsunameters can provide a crucial input to the rapid quantification of the source. In this respect, it should be possible to interpret the amplitude of tsunameter signals in terms of the lowest-frequency components of the seismic moment release. The purpose of the present paper is the development of an ultra-long period seismic magnitude scale, $M_{TSU}$, based on the measurement of far-field tsunami waves on the high seas. We wish to emphasize that it differs fundamentally from the ''tsunami magnitude'' $M_t$ introduced by ABE (1981), which, we recall, consists of interpreting maximum tidal gauge or run-up measurements, which by definition include the effects of shoaling and the responses of coastlines, bays and harbors. Furthermore, $M_t$ remains an empirical concept, which does not lend itself to a full theoretical justification of its algorithm, and in particular of its distance correction and locking constants. By contrast, our approach is to derive theoretically in Section 2 an algorithm for the retrieval of the seismic moment $M_0$ of an earthquake from a tsunameter record of its tsunami. In Section 3, we test the method on records obtained by numerical simulation, and in Section 4, we examine an actual dataset of 24 records from seven Pacific tsunami events in the years 1994–2003. We further illustrate that the concept may be applied to satellite altimetry by

processing the JASON trace recorded over the Bay of Bengal during the 2004 Sumatra tsunami.

## 2. Theory

Our theoretical approach for the development of $M_{TSU}$ closely follows that of the mantle magnitude $M_m$ introduced by OKAL and TALANDIER (1989). We recall that the $M_m$ algorithm consists of measuring the spectral amplitude $X(\omega)$ of long-period Rayleigh or Love mantle waves, and of calculating an estimate of the seismic moment $M_0$ of the source as

$$M_m = \log_{10} M_0 - 20 = \log_{10} X(\omega) + C_D + C_S + C_0. \quad (1)$$

In this formula, $M_0$ is in dyn*cm, $X(\omega)$ is expressed in $\mu$m*s, and the distance and source corrections, $C_D$ and $C_S$, as well as the locking constant $C_0$, are all derived theoretically from normal mode theory, under the surface wave asymptotic approximation. As detailed in OKAL and TALANDIER (1989), the power of the mantle magnitude algorithm resides in that it combines the practicality of the magnitude approach (a "quick-and-dirty" measurement ignoring details of focal mechanism geometry and exact source depth), with a modern theoretical approach, *i.e.*, the measurement of a *bona fide* physical quantity, namely the seismic moment $M_0$, in the framework of an established physical theory. Finally, because it uses a variable frequency, $M_m$ does not saturate, as do conventional magnitude scales (GELLER, 1976), even for the largest earthquakes ever recorded, such as the 1960 Chilean event (OKAL and TALANDIER, 1991).

We refer to the series of seminal papers by WARD (1980; 1981; 1982a,b), in which he describes tsunami waves as a particular branch of the spheroidal family of normal modes of the Earth. The power of this approach is that the analytical formalism developed for example by ALTERMAN *et al.* (1959) (actually traceable to LOVE'S (1911) famous monograph) for the computation of the eigenfunctions of the Earth's modes is directly applicable to the case of tsunamis, as long as the Earth model includes an oceanic layer and the computation is carried out in the full six-dimensional space allowing for the effect of gravity. This includes the computation of the excitation of an individual mode by a double-couple source located in the solid Earth (SAITO, 1967; GILBERT, 1970), for which the expression of the excitation coefficients ($K_0$, $K_1$, $K_2$ in the notation of KANAMORI and CIPAR 1974) can be directly transcribed to the case of the tsunami eigenfunction. As discussed by OKAL (1982; 1988; 1990), this allows the direct and seamless handling of the coupling between the ocean water layer and any vertically heterogeneous solid Earth structure, including sedimentary layers. In particular, the normal mode approach does not make any assumptions on the parameter $kH$ scaling the equivalent wavelength $2\pi/k$ to the depth of the ocean column $H$, and as such remains applicable outside the range of the shallow-water approximation.

However, normal mode theory is by nature linear and also requires, at least in the simpler application considered here, a spherically symmetric structure involving an ocean covering the entire planet with a uniform depth $H$, which we will take as 5 km. While these approximations may seem drastic, the robustness of the concept of magnitude for seismic waves (and normal modes, including tsunamis) is such that they do not significantly limit the applicability of our algorithm, as detailed below in Sections 3 and 4.

Accordingly, the spectral amplitude $X(\omega)$ of the vertical displacement $\eta(t)$ of the tsunami wave generated by a double-couple of moment $M_0$ at an epicentral distance $\Delta$ is given by the same formula as that of a Rayleigh wave

$$X(\omega) = M_0 \cdot a\sqrt{\frac{\pi}{2}} \cdot \frac{1}{\sqrt{\sin\Delta}} \cdot \left[\frac{1}{U}\left|s_R l^{-1/2} K_0 - p_R l^{3/2} K_2 - i q_R l^{1/2} K_1\right|\right], \tag{2}$$

so that in turn $M_{TSU}$ will be given by a formula similar to (1)

$$M_{TSU} = \log_{10} M_0 - 20 = \log_{10} X(\omega) + C_D^{TSU} + C_S^{TSU} + C_0. \tag{3}$$

In these formulæ, $a$ is the radius of the Earth, $l$ the orbital number of the spheroidal mode, related to the equivalent wavenumber through $l = ka - 1/2$, $U$ is the group velocity of the wave at angular frequency $\omega$, the excitation coefficients $K_i$ depend only on frequency and depth (KANAMORI and CIPAR, 1974), and the trigonometric coefficients $s_R$, $p_R$ and $q_R$ depend only on focal geometry and receiver azimuth.

- In (2), we have neglected any non-geometric attenuation of the wave, so that the new distance correction is simply

$$C_D^{TSU} = \frac{1}{2}\log_{10}\sin\Delta. \tag{4}$$

- As the locking constant $C_0$ simply compensates for the term $a \cdot \sqrt{\pi/2}$, it will take the same value as in the case of Rayleigh waves, $C_0 = 3.10$ if $X(\omega)$ is expressed in cm*s and all computations are carried out with traditional units, *i.e.*, the $K_i$'s are in $10^{-27}$ dyn$^{-1}$ and $U$ in km/s. ($C_0 = -0.90$ if $X(\omega)$ is in $\mu$m*s.)
- The source correction ${C_S}^{TSU}$ is designed to correct for the term in large brackets in (2), $E(\phi_f, \delta, \lambda; \phi_s; h; \omega)$, under the formalism of a magnitude measurement, *i.e.*, for average focal mechanism geometry (defined by the three angles $\phi_f$, $\delta$, $\lambda$), receiver azimuth $\phi_s$, and source depth $h$. Following OKAL and TALANDIER (1989), we derive an expression of ${C_S}^{TSU}$ by looping, for each source depth $h$, over a very large number $N$ of focal geometries, and computing the logarithmic average excitability

$$L_{av} = \log_{10} E_{av}(h, \omega) = \log_{10}\left[\frac{1}{N}\sum_{\delta,\lambda;\phi} E(\phi_f, \delta, \lambda; \phi_s; h; \omega)\right], \tag{5}$$

using the actual excitation coefficients computed from normal mode solutions. Figure 2 shows the results of these computations for $N = 49248$ source-receiver geometries and 10 source depths, from $h = 6$ km (1 km below the ocean floor; symbols "0") to 100 km (symbols "9"). It is equivalent to Figure 3 of OKAL and TALANDIER (1989). Note that, except for the greatest depths (80 km, "8"; and 100 km, "9"), the excitability features little dependence on depth at periods greater than 600 s, typical of far-field tsunamis generated by very large earthquakes, as predicted by WARD (1981) and OKAL (1988). As expected, at shorter periods, depth starts to play a role for increasingly shallow sources.

At each period, we average $L_{av}$ obtained from (5) over those depths for which $L_{av}$ remains in the pack (all depths for $T > 1000$ s; eliminating 100 km under 1000 s, 80 and 100 km under 820 s; etc. up to keeping only $h \leq 20$ km under 300 s). The resulting averages are plotted as the solid dots on Figure 2. We then regress these values using a cubic spline, as in OKAL and TALANDIER (1989). The result is

$$\langle L_{av} \rangle = -0.84526\,\theta^3 - 0.53189\,\theta^2 - 0.55748\,\theta - 2.2974, \tag{6}$$

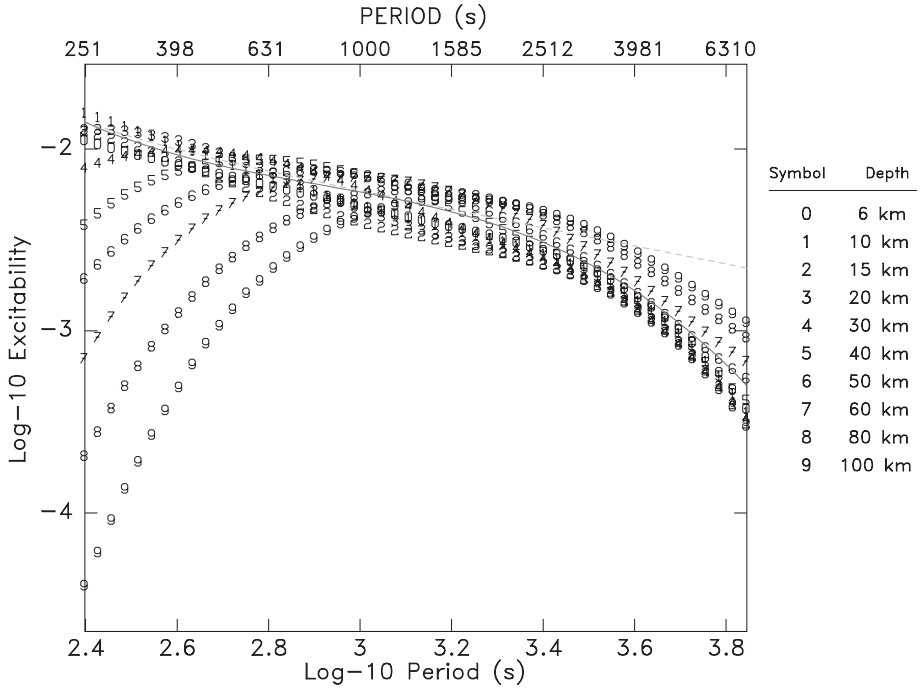


Figure 2

Logarithmic average excitability $L_{av}$ as a function of period $T$. At each depth $h$, $L_{av}$ is computed from (5), and the results plotted using symbols "0" ($h = 6$ km) to "9" ($h = 100$ km). The solid dots are average values of $L_{av}$ (see text for details), and the solid line their regression by a cubic spline (6). The dashed line is the excitability predicted by (10), using the asymptotic theory.

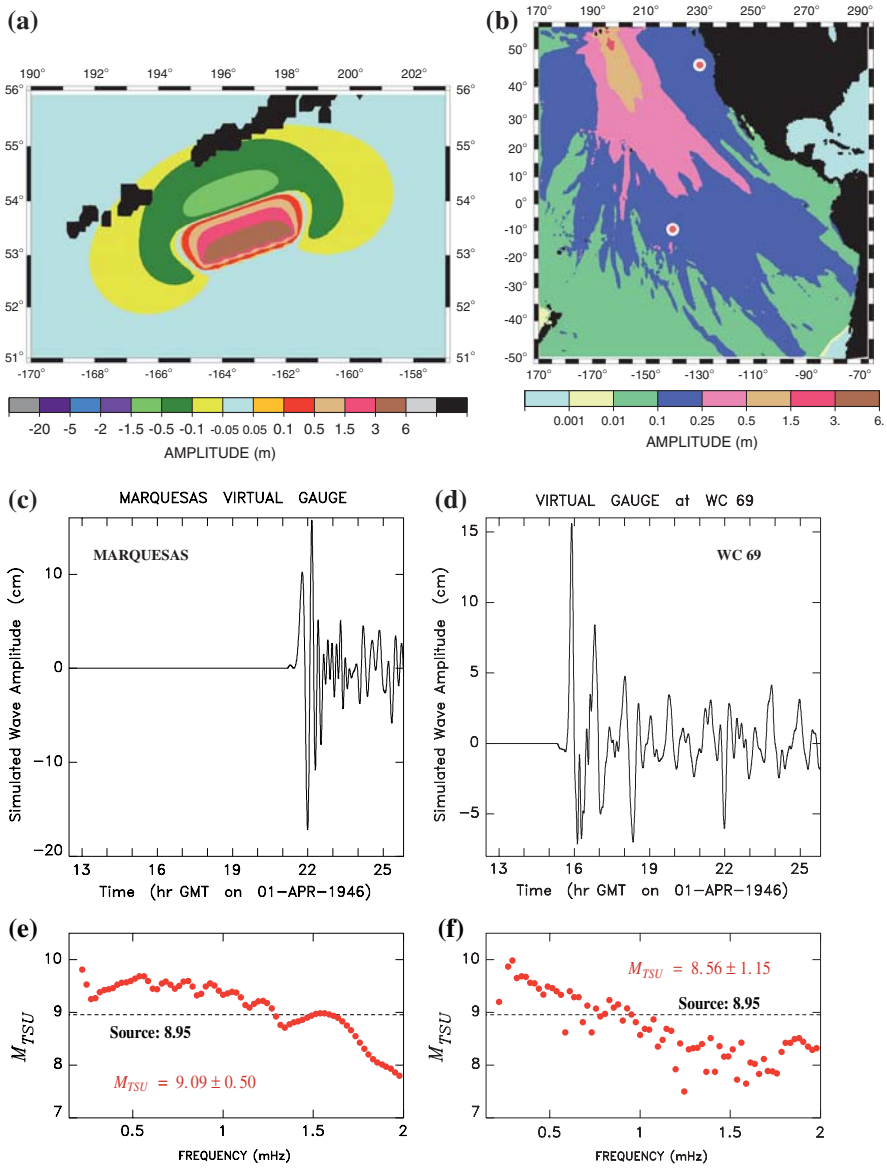


Figure 3

Test of the $M_{TSU}$ concept and algorithm on a simulation of the 1946 Aleutian earthquake. (*a*): Static displacement field of the source area used as an initial condition of the simulation. (*b*): Maximum sea-surface height obtained by simulating the first 18 hours of propagation in the Pacific Basin. Note the strong directivity in the resulting field of amplitudes. The two bull's eye symbols represent the virtual gauges at WC69 (next to the North American Coast) and in the Marquesas. (*c*) and (*d*): Synthetic sea-surface time series at the virtual gauges. The origin of the time axis is the source time of the earthquake, 12:29 GMT on 01 April, 1946. The results of applying the $M_{TSU}$ algorithm to these records are given in (*e*) (Marquesas) and (*f*) (WC69), and compared to the source value used in the synthetics (*dashed lines*).

where $\theta = \log_{10} T - 3.1215$ ($T$ being the period in seconds). This regression is shown as the solid curve on Figure 2, and provides an excellent match to the average values of $L_{av}$, as defined by the individual dots. Consequently, the correction $C_S{}^{TSU}$ can be taken as

$$C_S^{TSU} = -\langle L_{av} \rangle = 0.84526\,\theta^3 + 0.53189\,\theta^2 + 0.55748\,\theta + 2.2974 \quad (\theta = \log_{10} T - 3.1215) \tag{7}$$

We also verified that this formula is well predicted by the asymptotic expressions of the excitation coefficients defined by OKAL (2003), namely

$$K_2 = \frac{1}{8\pi\mu}\frac{Y^{-1}}{la^2}; \quad K_0 = l(l+1)K_2; \tag{8}$$

and $K_1 = 0$, the latter expressing the classical singularity of the excitation of a vertical dip-slip source at the top of the solid Earth, itself due to the vanishing of the traction $\sigma_{r\theta}$ at the bottom of the ocean. In (8), $\mu$ is the rigidity of the source region, $a$ the radius of the Earth, and $Y$ the normalization of the eigenfunction of vertical displacement at the ocean's surface (taken here as 1 cm). The expression predicted for $L_{av}$

$$L_{av} = \log_{10}\left[\frac{\langle |s_R - p_R| \rangle l^{1/2}}{8\pi\mu a^2 U}\right] \tag{9}$$

is shown as the dashed curve on Figure 2, where a mantle rigidity ($\mu = 7 \times 10^{11}$ dyn/cm$^2$)has been assumed. Note the generally good agreement with the previous computation, except for $T > 3000$ s, in principle beyond the typical period of transoceanic tsunamis. This asymptotic approach is particularly powerful, because it allows in principle a correction for variations in water depth $H$. In the shallow water approximation, $l = a\omega/C$, $C = (g\,H)^{1/2}$, and $U = C$. Then (9) leads to

$$C_S^{TSU} = -L_{av} = -\log_{10}\left[\frac{\langle |s_R - p_R| \rangle \omega^{1/2} g^{-3/4}}{8\pi\mu a^{3/2}} \cdot H^{-3/4}\right]. \tag{10}$$

Note, however that water depth is expected to vary significantly between source and receiver, and the question then arises as to which value of $H$ to use in (10). In this respect, the normal mode formalism does not lend itself well to such lateral heterogeneities in structure; nevertheless, we can make the following argument: at any given angular frequency $\omega$, the propagation terms of the Fourier integral under the asymptotic approximation of the Legendre polynomials in (2) will involve the average water depth along the path, $H_p$. These terms are proportional to $l^{-1/2}/U$ for the isotropic $m = 0$ term in (2), which will behave like $H_p{}^{-1/4}$ under the shallow-water approximation. For the clover-leaf $m = 2$ term, $l^{3/2}/U$ will behave like $H_p{}^{-5/4}$. By contrast, the expression of the excitation coefficients $K_0$ and $K_2$ will be controlled by the water depth at the source, $H_s$, with according to (8), $K_2 \sim l^{-1} \sim H_s{}^{1/2}$ and

$K_0 \sim l \sim H_s^{-1/2}$. Thus the term $H^{-3/4}$ in (10) should be split as $H_p^{-1/4} H_s^{-1/2}$ for the isotropic $m = 0$ terms and $H_p^{-5/4} H_s^{1/2}$ for the clover-leaf $m = 2$ ones.

Thus, one would expect that any difference between $H_p$ and $H_s$ would act in opposite ways on the two terms, suggesting an overall trade off. In addition, the situation will be made even more complex by the fact that a source water depth $H_s$ will be difficult to define, as the source region of most large tsunamis in subduction zones (integrated over the full extent of the fault width in the rupture area) is bound to feature significant variations in bathymetry, in the presence of the trench–arc system.

In the context of a magnitude scale, characterized by measurements necessarily averaged over a large number of parameters and by a logarithmic scale, it appears justified to remain with an average estimate $H$ in (10). In principle, one could further define a water depth correction to be added to (10) or (7):

$$C_{WD} = \frac{3}{4} \log_{10} \left[ \frac{H}{H_{5000}} \right], \tag{11}$$

where $H_{5000} = 5000$ m, and $H$ would be an appropriate measure of the average water depth at the source and along the path to the receiver. We note however that, for long transoceanic paths, $H$ will rarely be less than 3000 m, leading to a correction of less than 0.2 units of $M_{TSU}$, which we regard as negligible in view of the many other approximations made.

Next, we note that tsunameters record the overpressure at the bottom of the ocean, $p(t)$, rather than the displacement at the surface, $\eta(t)$, the relation between the two being simply (OKAL, 1982)

$$p(t) = \rho_w g \eta(t) \quad \text{or} \quad P(\omega) = \rho_w g X(\omega), \tag{12}$$

where $\rho_w$ is the density of water (1 g/cm$^3$) and $g$ the acceleration of gravity (981 cm/s$^2$). We can then rewrite (3) as

$$M_{TSU} = \log_{10} P(\omega) + C_D^{TSU} + C_S^{TSU} + C_0^P, \tag{13}$$

where the new locking constant is simply $C_0{}^P = C_0 - \log_{10}(\rho_w g) = 3.10 - 2.99 = 0.11$ if $p$ is measured in dyn/cm$^2$ (also called "baryes"), and hence $P(\omega)$ in barye*s, which is the cgs unit of kinematic viscosity, called a "poise".

NOAA sensors of the DART program actually output $p$ in British units, reportedly pounds per square inch, or "psi". These should actually be called "pounds–*force* per square inch" (pfsi) to be appropriate units of pressure. The relationship of pfsi to baryes involves the acceleration of gravity (going from psi to pfsi), and is

$$1 \text{ pfsi} = 981 \cdot \frac{453}{2.54^2} \text{ baryes} = 68881 \text{ baryes} = 10^{4.84} \text{ baryes}. \tag{14}$$

Accordingly, if $p$ is measured in pfsi, and hence $P(\omega)$ in pfsi*s, then ${C_0}^P = 4.84 + 0.11 = 4.95$ in (13).

In summary, the algorithm of $M_{TSU}$ proceeds as follows: Given a time series of overpressure measurements at the bottom of the ocean, obtain its spectral amplitude $P(\omega)$ at all periods between 600 and 3500 seconds, apply the distance and source corrections ${C_D}^{TSU}$ (4) and ${C_S}^{TSU}$ (7), and use the appropriate locking constant ${C_0}^P$ depending on recording units. Then the quantity (13) should be an approximation of $\log_{10} M_0 - 20$, where $M_0$ is in dyn*cm. $M_{TSU}$ can also be related to the so-called "moment magnitude" introduced by KANAMORI (1977) through $M_{TSU} = 1.5\, M_w - 3.9$.

## 3. Validation on Numerical Simulations

Before applying the concept of $M_{TSU}$ to actual data recorded on tsunameters, we proceed to validate the algorithm on synthetic data obtained by hydrodynamic simulation of the far-field tsunami of a very large earthquake. For this purpose, we use the geometry of the 1946 Aleutian tsunami, with a model inspired by the work of LÓPEZ and OKAL (2006), and featuring a seismic moment $M_0 = 9 \times 10^{28}$ dyn-cm, with a bilateral rupture totaling 200 km, and a slip reaching 10 m. This source was used successfully by OKAL and HÉBERT (2007) to model a dataset of 27 run-up values obtained in the far field by OKAL *et al.* (2002). The static displacement created by the earthquake source in the epicentral area was computed using MANSINHA and SMYLIE'S (1971) algorithm, and is shown in Figure 3*a*. It forms the initial condition of a simulation using the MOST code (TITOV and SYNOLAKIS, 1998), which solves the nonlinear equations of hydrodynamics, depth-averaged under the shallow water approximation, using a finite-difference algorithm and the method of splitting integration steps. Details are provided in SYNOLAKIS (2002). We compute virtual gauge records at two locations, one at a DART site WC69 off the coast of Oregon (45.933°N, 129.981°W; 2486 km from the source), and the other off the Marquesas Islands (9°S, 140°W; 7246 km from the source). Figure 3*b* shows that the former is located outside the main lobe of directivity of the tsunami wave, oriented perpendicular to the direction of rupture as predicted by BEN-MENAHEM and ROSENMAN (1972). As the algorithm for $M_{TSU}$, based on the concept of magnitude, ignores directivity, it is important to test its effect on the final result.

Figures 3c and 3d show time series of the simulated tide gauges at the two locations. The Marquesas record has a greater peak-to-peak amplitude, and is obviously richer in high frequencies, than its counterpart at WC69, even though it is located at greater distance; this illustrates the effect of source directivity. The time series were then processed through the $M_{TSU}$ algorithms, using Equation (3). The results are shown on the bottom frames (Figs. 3e and 3f), where the dots represent individual $M_{TSU}$ measurements and the dashed line the value (8.95) corresponding to

the seismic moment used. The agreement is generally good, and clearly better at the Marquesas receiver, located in the lobe of directivity than at the West Coast one, which suffers from destructive interference at frequencies above 1 mHz. Nevertheless, the algorithm still recovers an appropriate value of $M_0$ from the WC69 synthetic, using the lower frequencies (0.5–1.2 mHz).

## *4. Application to Real Data*

The algorithm $M_{TSU}$ was then applied to the case of seven Pacific Ocean tsunamis recorded by DART stations in the far field during the years 1994–2003. Tables 1 and 2 lists all relevant details of the experiment.

• *Event 1; Kurile Islands, 04 OCT 1994*

Figure 4 presents details of the methodology applied to all records, in the case of the 1994 Kurile Island tsunami, which was locally destructive in the Southern Kurile Islands (YEH *et al.*, 1995). This event was recorded by four tsunameters (AK 59 and 60 off the Alaskan Peninsula, and WC 61 and 62 off the West Coast of the US); note the coherence of signals at nearby locations. However, despite featuring the largest seismic moment of any event recorded by DART to date ($M_0 = 3 \times 10^{28}$ dyn*cm), the earthquake does not constitute an interplate thrust event, but rather a probable tear within the subducted lithosphere (TANIOKA *et al.*, 1995). As such, its depth (68 km) and focal mechanism (shown in Fig. 4*a*) are unfavorable to the generation of a distant tsunami, especially in the azimuth of the available tsunameters.

For each tsunameter signal, we define a 12-hour window, and simply apply (3) to its Fourier spectrum, within ranges of frequencies offering suitable signal-to-noise ratios, as defined by comparing with the spectra of similar windows on the preceding day (Fig. 4*c*). The results in Table 1 show that the two West Coast stations give values ($8.23 \pm 0.37$ and $8.25 \pm 0.39$) compatible with the expected value (8.48), if slightly underestimating it, whereas the Gulf of Alaska records are somewhat deficient ($7.98 \pm 0.24$ and $7.95 \pm 0.31$). This is probably due to the unfavorable geometry of the relevant paths, the great circle to the AK sites crossing substantially into the Bering Sea (Fig. 4*a*), in particular through its shallow eastern half, which consists of an extended continental shelf. By contrast, the West Coast records are apparently less affected by the passage of the great circle over the Aleutians; it is probable that the actual ray paths are slightly refracted around the arc. It remains remarkable that the moment of the earthquake is well recovered, within the error bars of the WC measurements, despite unfavorable centroid depth (68 km) and station azimuth for the particular mechanism involved.

Table 1

*$M_{TSU}$ measurements for seven Pacific tsunamigenic earthquakes, 1994–2003*

| Event Number and Region | Station | Date | Origin | CMT Solution | | | $M_{TSU}$ | |
|---|---|---|---|---|---|---|---|---|
| | | D M (J) Y | Time (GMT) | Lat.; Lon. (°N; °E) | Depth (km) | Moment ($10^{27}$ dyn*cm) | predicted | measured |
| **1.** Kurile Is. | | 04 OCT (277) 1994 | 13:23 | 43.6; 147.6 | 68 | 30 | 8.48 | |
| | AK 59 | | | | | | | 7.98 ± 0.24 |
| | AK 60 | | | | | | | 7.95 ± 0.31 |
| | WC 61 | | | | | | | 8.25 ± 0.39 |
| | WC 62 | | | | | | | 8.23 ± 0.37 |
| | **Average** | | | | | | | **8.08 ± 0.14** |
| **2.** Kurile Is. | | 03 DEC (337) 1995 | 18:01 | 44.82; 150.17 | 26 | 8.24 | 7.92 | |
| | AK 64 | | | | | | | 7.58 ± 0.35 |
| | WC 67 | | | | | | | 7.87 ± 0.28 |
| | WC 68 | | | | | | | 7.89 ± 0.25 |
| | WC 69 | | | | | | | 7.88 ± 0.24 |
| | **Average** | | | | | | | **7.81 ± 0.13** |
| **3.** Andreanof Is. | | 10 JUN (162) 1996 | 04:04 | 51.10; −177.41 | 29 | 8.05 | 7.91 | |
| | WC 67 | | | | | | | 7.84 ± 0.22 |
| | WC 68 | | | | | | | 7.86 ± 0.21 |
| | WC 69 | | | | | | | 7.75 ± 0.26 |
| | **Average** | | | | | | | **7.82 ± 0.05** |
| **4.** Biak | | 17 FEB (048) 1996 | 06:00 | −0.67; 136.62 | 15 | 24.1 | 8.38 | |
| | AK 64 | | | | | | | 8.13 ± 0.28 |
| | WC 67 | | | | | | | 8.29 ± 0.30 |
| | WC 68 | | | | | | | 8.39 ± 0.24 |
| | WC 69 | | | | | | | 8.32 ± 0.28 |
| | **Average** | | | | | | | **8.28 ± 0.10** |
| **5.** No. Chile | | 30 JUL (211) 1995 | 05:11 | −24.17; −70.74 | 29 | 12.1 | 8.08 | |
| | AK 64 | | | | | | | 8.08 ± 0.26 |
| | WC 67 | | | | | | | 8.00 ± 0.31 |
| | WC 68 | | | | | | | 8.08 ± 0.24 |
| | WC 69 | | | | | | | 8.04 ± 0.25 |
| | Average | | | | | | | **8.05 ± 0.03** |
| **6.** Mexico | | 09 OCT (282) 1995 | 15:36 | 19.34; −104.80 | 15 | 11.5 | 8.06 | |
| | AK 64 | | | | | | | 7.50 ± 0.29 |
| | WC 67 | | | | | | | 7.86 ± 0.29 |
| | WC 68 | | | | | | | 7.92 ± 0.24 |
| | WC 69 | | | | | | | 8.00 ± 0.20 |
| | **Average** | | | | | | | **7.82 ± 0.19** |
| **7.** Aleutian Is. | | 17 NOV (321) 2003 | 06:43 | 51.14; 177.86 | 22 | 5.3 | 7.71 | |
| | D171 | | | | | | | **7.70 ± 0.22** |

Table 2

*Tsunameters used in this study*

| Code | Region | Latitude °N | Longitude °E | Water depth (m) | Event(s) recorded |
|---|---|---|---|---|---|
| AK 59 | Gulf of Alaska | 54.044 | −158.749 | 5889 | 1 |
| AK 60 | Gulf of Alaska | 54.022 | −155.729 | 4553 | 1 |
| AK 64 | Gulf of Alaska | 53.430 | −157.290 | 4550 | 2,4,5,6 |
| WC 61 | Off West Coast of U.S. | 45.960 | −129.964 | 2420 | 1 |
| WC 62 | Off West Coast of U.S. | 45.953 | −129.999 | 2440 | 1 |
| WC 67 | Off West Coast of U.S. | 45.960 | −129.970 | 2420 | 2,3,4,5,6 |
| WC 68 | Off West Coast of U.S. | 45.960 | −130.000 | 2435 | 2,3,4,5,6 |
| WC 69 | Off West Coast of U.S. | 45.933 | −129.981 | 2447 | 2,3,4,5,6 |
| D 171 | Off Aleutian Islands | 46.630 | −170.790 | 5654 | 7 |

• *Event 2; Kurile Islands, 03 DEC 1995*

The situation is very similar in the case of the smaller Kurile Islands event of 03 December, 1995, which occurred about 250 km to the northeast, but was a *bona fide* interplate thrust event at a regular depth (26 km). As shown in Figure 5 (top panels), the three West Coast stations recover the earthquake's moment flawlessly, while Receiver AK64 remains deficient, probably again on account of the incursion of the path into the Bering Sea. The comparison with Event 2 shows that the variations in depth (as long as the source remains shallower than 60 km) and focal mechanism do not affect significantly the relationship between earthquake moment and far-field tsunami amplitude on the high seas. Even though this observation may seem paradoxical, it is in general agreement with the results of WARD (1981) and OKAL (1988); this justifies *a posteriori* the use a magnitude concept in which such details are ignored.

• *Event 3; Andreanof Islands, 10 JUN 1996*

The tsunami was recorded only at the West Coast sites, as the Gulf of Alaska tsunameters were not operational at the time. As shown on the central panels of Figure 5, the $M_{TSU}$ algorithm recovers the seismic moment of the event adequately at all three sites.

• *Event 4; Biak (Indonesia), 17 FEB 1996*

For this large earthquake in the Western Equatorial Pacific, great circle paths to both the Alaskan and West Coast locations should be unaffected by the Aleutian arc, and all four records yield adequate values of the moment, even though Station AK 64 still provides the lowest value (Fig. 5; lower panels).

• *Event 5; Antofagasta, Chile, 30 JUL 1995*

This earthquake generated a significant tsunami in the South Pacific, which knocked a supply ship to the bottom of the harbor at Ua Pou, in the Marquesas

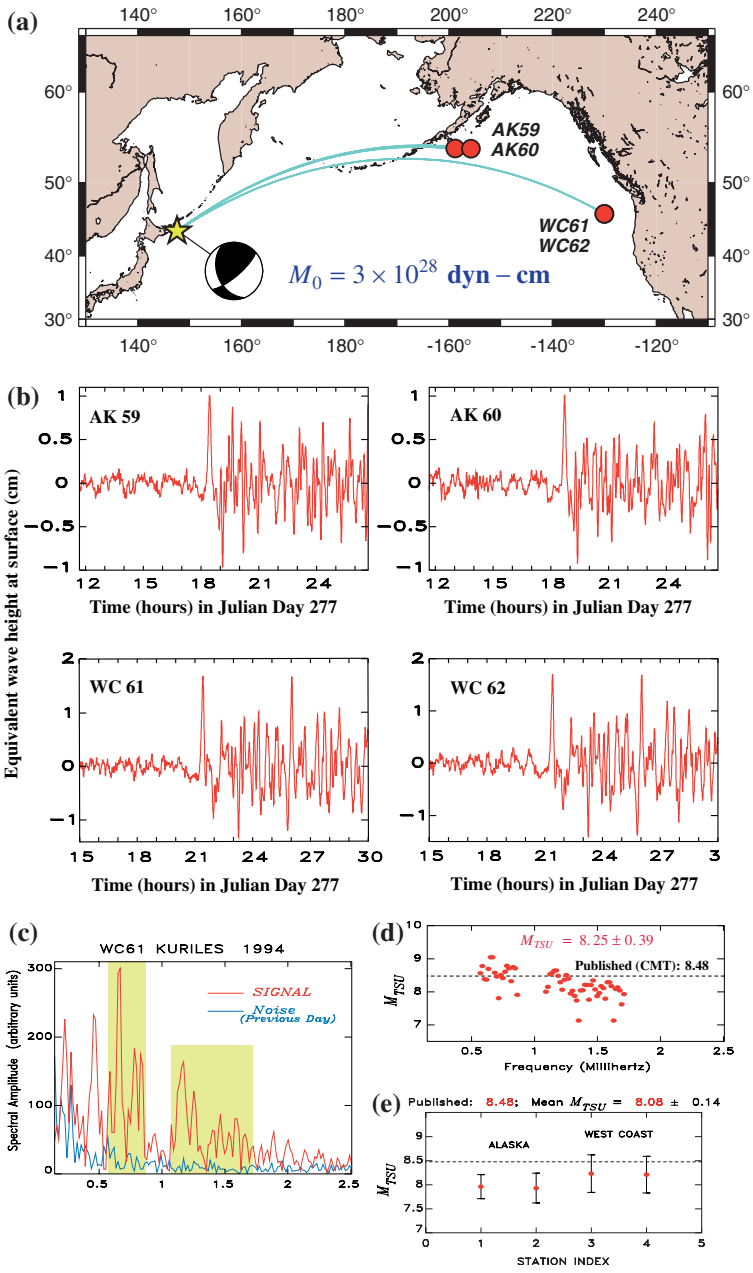


Islands (GUIBOURG *et al.*, 1997). We tested the algorithm in the case of this large earthquake, even though the geometry of the great circle paths from its source to the tsunameters involves significant land paths (Fig. 6a). This should in principle

◀

Figure 4
Computation of $M_{TSU}$ for the 1994 Kuriles earthquake. (*a*): Map of the Northern Pacific showing the location of the source (*star*) and receivers (*solid dots*). Note that the great circle paths to the tsunameters intersect the Aleutian chain. (*b*): Original records at the four tsunameter sites. The vertical axis has been converted to equivalent surface amplitude, using (12). Note the remarkable signal coherence at nearby sites AK59 and 60 and at WC61 and 62. (*c*): Optimization of frequency windows based on signal-to-noise ratios, illustrated on the WC61 record. Based on a comparison with spectra for the previous day, the two shaded frequency bands (in this case 0.55–0.86 mHz and 1.06–1.71 mHz) are retained in the computation. (*d*): Individual $M_{TSU}$ values (*solid dots*) computed inside the frequency bands, compared with the published value derived from the CMT solution (*dashed line*). (*e*): Summary of results for the four tsunameters.

invalidate the use of the $M_{TSU}$ algorithm, since WARD'S (1980) formalism, on which Equation (2) is based, is valid only for a laterally homogeneous ocean basin. Yet, the vigor of the signals recorded at all sites clearly indicates refraction around the coasts of Central and North America, and, remarkably, all four values of $M_{TSU}$ recover the seismic moment perfectly (Fig. 6*b*). Once again, this expresses the robustness of the concept of magnitude, which manages to override the nongeometrical propagation, which apparently affects only marginally the spectral amplitudes of the waves as recorded in the Northeastern Pacific.

• *Event 6; Mexico, 09 OCT 1995*

Bolstered by the Chilean results, we decided to process the tsunameter records of this large event, for which the great circles to the tsunameters similarly interfere with land masses over a large portion of their paths (Fig. 6c). The results are surprisingly good at the West Coast stations, but show a significant deficiency at the Gulf of Alaska instrument (Fig. 6d).

• *Event 7; Aleutian Islands, 17 NOV 2003*

This considerably smaller event ($M_0 = 5.2 \times 10^{27}$ dyn-cm) did not generate a tsunami in the far field and was not recorded above noise level on the tsunameters in the Gulf of Alaska and along the West Coast of the U.S. It was, however, recorded with an equivalent surface amplitude of 4 cm peak-to-peak by a newly installed instrument, D-171, only 900 km from the epicenter (Figs. 7a, b). The good agreement between $M_{TSU}$ and the published CMT moment (Fig. 7d) illustrates the feasibility of using the algorithm in the regional field ($\Delta \approx 1000$ km), in particular in the case of smaller events whose tsunamis may not be detectable in the far field. On the other hand, the absence of detectable signals in the far field suggests a lower bound of at least $M_0 \geq 6 \times 10^{27}$ dyn-cm for the method to be applicable. This estimate is confirmed by the absence of a usable signal during the Chimbote, Peru tsunami earthquake of 21 February 1996 ($M_0 = 2.2 \times 10^{27}$ dyn-cm).

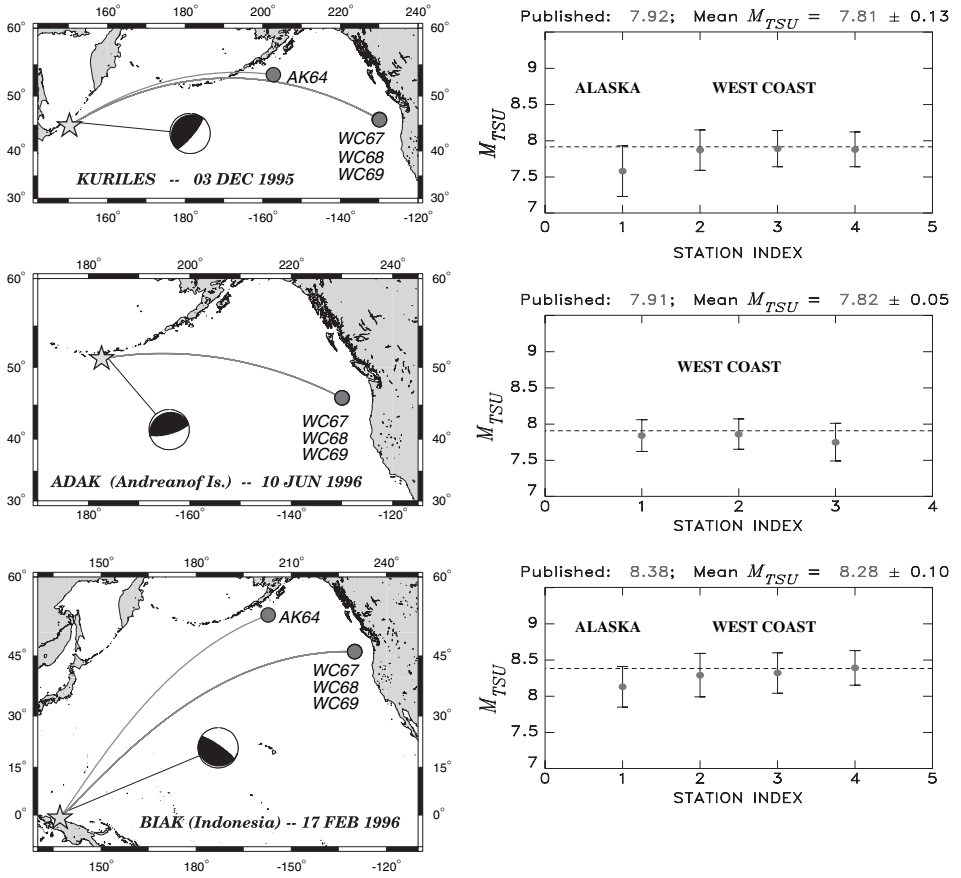


Figure 5
Results for events 2, 3, 4. Situation maps similar to Figure 4a are at *left* and summaries similar to Figure 4e at *right*. Note the generally excellent performance of the West Coast stations, but the remaining deficiency of the Gulf of Alaska tsunameter AK64.

Incidentally, the tsunameter record in Figure 7b was used in real time to estimate the moment of the event, by comparing its amplitude to those in a library of synthetic sea-surface height time series obtained by numerical simulation for a large number of earthquake scenarios along the subduction zones of the Pacific Basin (Titov *et al.*, 2005). The estimated source was then used to forecast expected tsunami heights, notably in the Hawaiian Islands, which were found not to exceed 25 cm.

While this episode did not specifically use the $M_{TSU}$ algorithm, it shares its philosophy and basic concept, and underlines the potential of the algorithm in the context of real-time tsunami warning.

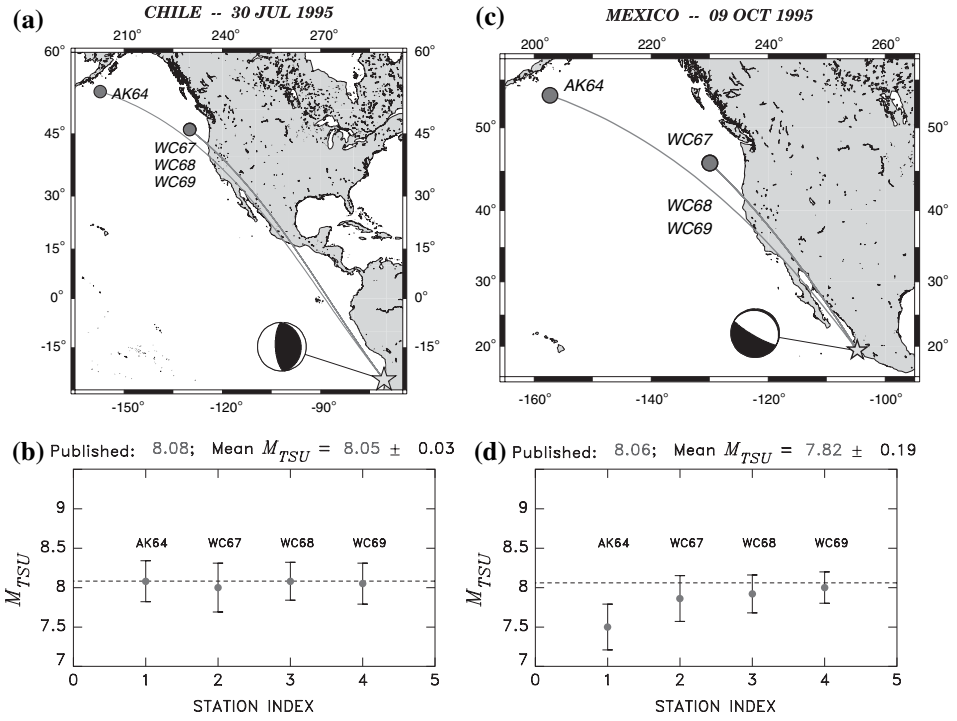


Figure 6
Results for events 5 (*a* and *b*) and 6 (*c* and *d*). In both instances, the great circle paths to the tsunameters intersect the Central and North American continental masses.

## 5. The Case of the JASON Trace

The catastrophic tsunami of 26 December 2004 in Sumatra was not recorded by tsunameters, since no such instruments were available in the Indian Ocean. However, there exist a number of direct observations of the deformation of the ocean surface under the passage of the tsunami from satellite altimetry traces (SCHARROO *et al.*, 2005; SLADEN and HÉBERT, 2005). We concentrate here on the so-called JASON trace, whose raw data are plotted in Figure 8b, and use it for a preliminary measurement of $M_{TSU}$.

As pointed out by OKAL *et al.* (1999), the interpretation of such profiles is made complex by the fact that they are neither time series (a record of the wave as a function of time at a fixed receiver), nor space series (a snapshot of the wave along a trace at a given time), because of the finite velocity of the satellite over the study area. In order to convert the JASON trace to a time series usable by the $M_{TSU}$ algorithm, we proceed as follows: Each point $i$ in the JASON trace, for which the sea height is $\eta_i$, corresponds to a particular position $P_i = [Lat_i; Lon_i]$ and time $t_i$. We correct the time

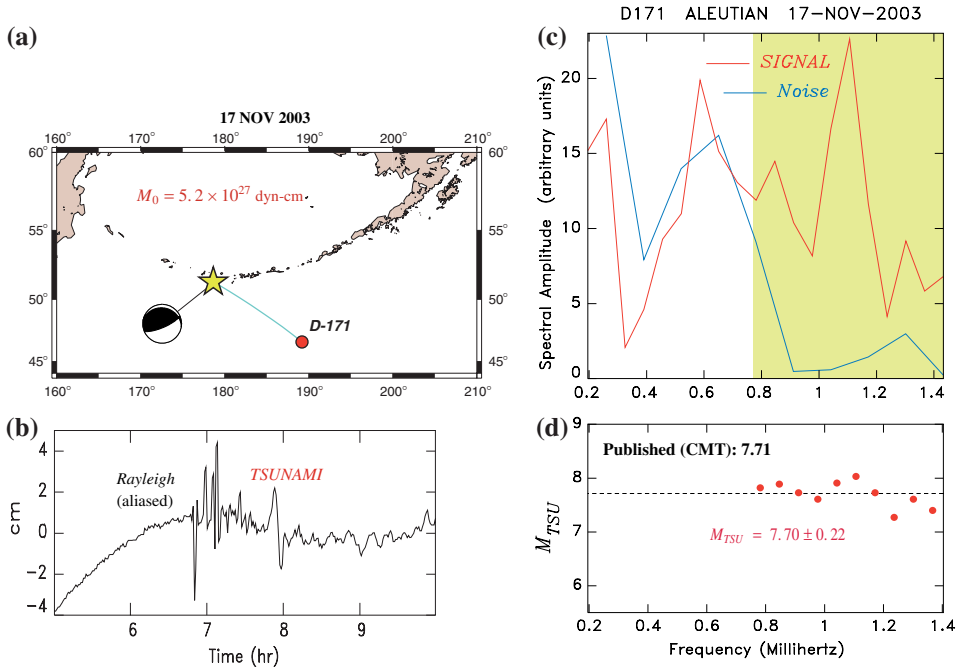


Figure 7
Case of the smaller Aleutian event of 17 November, 2003. (*a*): Location map of the epicenter and D-171 tsunameter. (*b*): Original tsunameter record at D-171. (*c*): Spectral amplitude of (*b*) defining adequate signal-to-noise ratios between 0.8 and 1.4 mHz. (*d*): Results of processing of (*b*) through the $M_{TSU}$ algorithm, showing excellent agreement with the CMT moment.

$t_i$ by the group time from the epicenter to $P_i$, assuming propagation at a constant velocity $U = 200$ m/s, to obtain

$$\tau_i = t_i - t_0 - \frac{\Delta_i}{U}, \tag{15}$$

where $\Delta_i$ is the distance separating $P_i$ from the epicenter and $t_0$ the origin time of the event. Then $\tau_i$ (which can be negative) represents the time elapsed at $P_i$ since the arrival of the first wave. We then interpret the set of $\eta_i$ values as representative of the sea surface deformation at the resulting times $\tau_i$ for an average point $P$ that we take as the location registering the maximum value of $\eta$ (−3.01°N; 84.68°E). We consider only the initial part of the JASON trace, for which $\Delta$ decreases monotonically along the trace to the point of closest approach of the epicenter by the satellite. The series $\eta_i$ are then re-interpolated at constant spacing $\delta\tau = 1$ s. The resulting time series is plotted on Figure 8c.

Additional approximations consist of using a point source rather than the true extent of some 1200 km of the Sumatra earthquake rupture, and of placing it at the

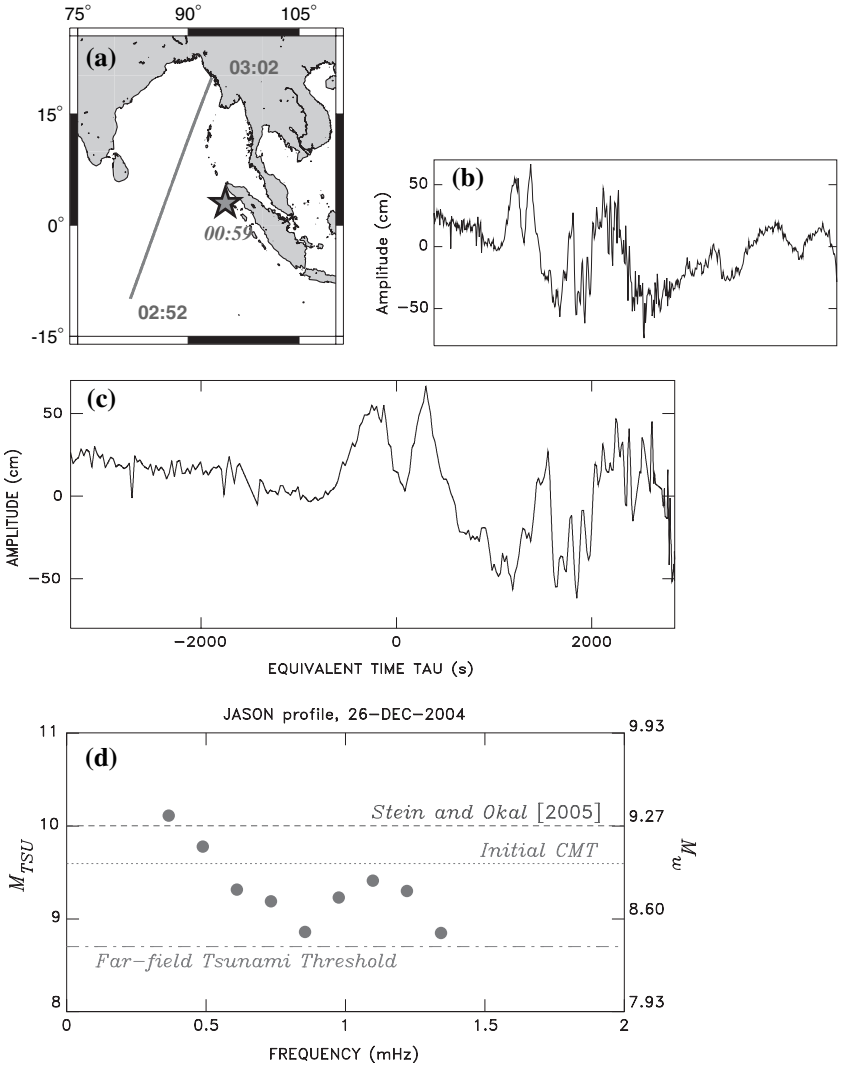


Figure 8

Processing of the JASON trace. (*a*): Map of the Bay of Bengal, showing the epicenter of the Sumatra earthquake (*star*), and the track of JASON. The satellite crosses the area from SSW to NNE approximately two hours after the occurrence of the main shock. Times at the source and at the extremities of the track are in GMT. (*b*): Original trace of sea-surface height along JASON. Both time and space vary along the abscissa. (*c*): Equivalent time series reconstructed from (b); see text for details. (*d*): Computation of $M_{TSU}$ from the JASON profile and comparison with the initial CMT inversion (*dotted line*), the definitive moment inverted from normal modes by STEIN and OKAL (2005) (*dashed line*), and the *ad hoc* threshold for far field tsunami risk (dash-dot line).

epicenter of the earthquake (3°N; 95°E) rather than at the centroid of rupture. We justify this approach in the context of the potential future use of satellite altimetry in real-time under operational conditions where only initial determinations of the source parameters are available. We have independently verified that moving the source to the centroid of the rupture (around 7°N; 93°E) only affects the second decimal point of the values of $M_{TSU}$.

The time series on Figure 8c was then run through the $M_{TSU}$ algorithm with results shown in Figure 8d, where they are compared both with the initial CMT inversion ($M_0 = 3.95 \times 10^{29}$ dyn-cm), and with the more definitive moment obtained by STEIN and OKAL (2005) from the modeling of the Earth's gravest normal modes ($1.0 \times 10^{30}$ dyn-cm), the latter value being also in agreement with the composite CMT inversion later proposed by TSAI *et al.* (2005). While the $M_{TSU}$ values are relatively scattered with a mean of $M_{TSU} = 9.34 \pm 0.38$, it is remarkable that the values at the lowest frequencies (0.5 mHz and below), which are characteristic of the main signal in the initial portion of the JASON trace, are in excellent agreement with the moment derived by STEIN and OKAL (2005). Furthermore, all $M_{TSU}$ measurements suggest $M_0 \geq 7 \times 10^{28}$ dyn-cm, is significantly larger than the *ad hoc* threshold ($M_0 = 5 \times 10^{28}$ dyn-cm) for generation of a tsunami posing substantial risk in the far field.

In view of the large number of approximations made, both in the definition of the $M_{TSU}$ algorithm, and more importantly in its application to the JASON profile, we regard the ability of $M_{TSU}$ to recover an estimate of the seismic moment of the Sumatra earthquake within bounds emphasizing its tsunamigenic potential in the far field as nothing short of spectacular. However, the JASON profile sampled a path located primarily in or near the lobes of directivity of the rupture. Thus, the only dataset available to date for processing the $M_{TSU}$ algorithm from a truly gigantic source with a source length greater than 1000 km was favorably located in this respect, and there remains the possibility that the algorithm would underestimate such sources if applied at an azimuth where the interference is highly destructive.

## 6. Discussion and Conclusion

We have shown that tsunameter records can be interpreted in terms of the seismic moment of the parent earthquake in the framework of a rigorous theory which justifies all terms in the expression of $M_{TSU}$ including its locking constant. The summary of our results, presented in Figure 9, shows that

* For events 2, 3, 4, 5 and 7, the average value of the mean $M_{TSU}$ computed at individual stations recovers the seismic moments within 0.12 logarithmic units.
* In most such cases, the performance of the instrument[s] located in the Gulf of Alaska is degraded, probably as a result of the passage of the wave trains over the Aleutian Islands and the Bering Sea continental shelf.

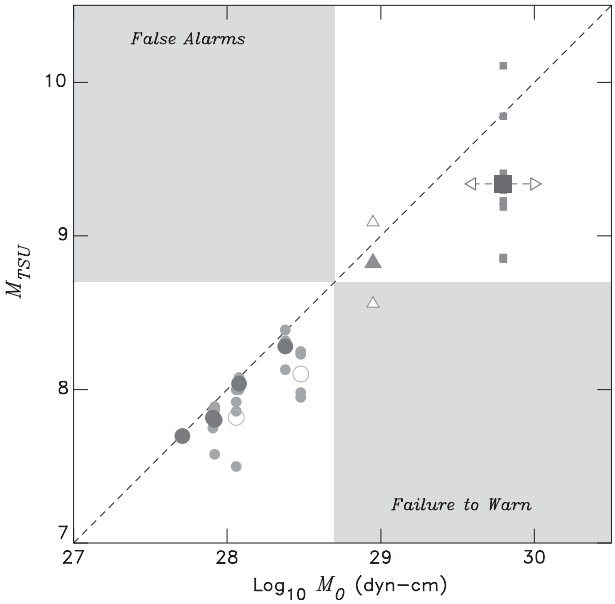


Figure 9

Summary of the performance of $M_{TSU}$ for seven earthquakes, the 1946 simulation and the JASON trace of the 2004 Sumatra tsunami. This figure plots values of $M_{TSU}$ obtained in the present study as a function of published seismic moment $M_0$. For the seven earthquakes recorded by tsunameters, the small shaded symbols are the mean values at each site, as listed in Table 1. For each event, their average over the various sites (shown in bold in Table 1) is plotted as a circle (events 1 and 5, showing deficiency in $M_{TSU}$ use an open symbol; see text for discussion). The triangles relate to the 1946 simulation: open symbols show the mean at the two virtual gauges, the solid one the average of the latter. Sumatra data from the JASON trace are shown as squares: shaded symbols are values at the individual frequencies, the larger symbol their average; the horizontal double arrow shows the range of published moments, from the initial CMT solution to the normal mode study by STEIN and OKAL (2005). The two shaded regions illustrate domains of false alarms or failure to warn, using a threshold of $5 \times 10^{28}$ dyn-cm for the source of a tsunami damaging in the far field. See text for details.

* In the case of event 1, the 1994 earthquake in the Kuriles, the deficiency of $M_{TSU}$ *vs.* $\log_{10} M_0$ at the West Coast tsunameters (0.25 unit) is probably due to the singular depth and focal mechanism of the event, which does not involve interplate thrusting.
* Even for event 6, the 1995 Mexican earthquake, the source is adequately recovered at the West Coast sites, despite severe refraction around the American continent, in a geometry where the $M_{TSU}$ algorithm would not be expected to work.
* The algorithm gives an adequate estimate of the moment of the great 2004 Sumatra earthquake from the JASON satellite altimeter dataset, even though the latter first had to be converted into a time series through a rather *ad hoc* procedure.

* Under the simplified assumption of a threshold of $M_0 \approx 5 \times 10^{28}$ dyn-cm for potential tsunami damage in the far field, the shaded quadrants in Figure 9 define schematically domains of false alarm (upper left) where the use of $M_{TSU}$ would overestimate the event beyond the threshold, and of failure to warn (bottom right), where a deficient $M_{TSU}$ would miss a potentially hazardous tsunami. It is noteworthy that only one point in the diagram falls into a shaded quadrant. In particular, all values measured on the JASON trace correctly predict a very large earthquake with $M_0 \geq 7 \times 10^{28}$ dyn-cm; measurements at the lowest frequencies ($f \leq 1$ mHz; average $M_{TSU} = 9.41$) define a truly gigantic event. The lone failure to warn is obtained at the West Coast virtual gauge for the 1946 simulation. This point represents an average of values featuring a regular decrease of $M_{TSU}$ with increasing frequency (Fig. 3*f*), which expresses the destructive effect of source directivity at an unfavorable azimuth. However, $M_{TSU}$ measured at the lowest frequencies ($f \leq 1$ mHz) does recover a correct estimate of the moment.

In conclusion, these observations suggest that $M_{TSU}$ is a particularly robust algorithm, which, being fully justified from a theoretical standpoint, can be expected to provide reliable estimates of the seismic moment of large earthquakes, with measurements taken at or below 1 mHz giving particularly reliable estimates. The case of event 7 shows that it can work in the regional field, and thus become a contributor to real-time tsunami warning procedures.

## *Acknowledgments*

This research was supported by the National Science Foundation, under Grant Number CMS-03-01054 to EAO.

## References

Abe, K. (1981), *A new scale of tsunami magnitude*, $M_t$, Phys. Earth Planet. Inter. *27*, 194–205.

Alterman, Z., Jarosch, H., and Pekeris, C.L. (1959), *Oscillations of the Earth*, Proc. Roy. Soc. Ser. *A*, *252*, 80–95.

Artru, J., Dučić, V., Kanamori, H., Lognonné, P., and Murakami, M. (2005), *Ionospheric detection of gravity waves induced by tsunamis*, Geophys. J. Intl. *160*, 840–848.

Ben-Menahem, A., and Rosenman, M. (1972), *Amplitude patterns of tsunami waves from submarine earthquakes*, J. Geophys. Res. *77*, 3097–3128.

Geller, R.J. (1976), *Scaling relations for earthquake source parameters and magnitudes*, Bull. Seismol. Soc. Amer. *66*, 1501–1523.

Gilbert, F. (1970), *Excitation of the normal modes of the Earth by earthquake sources*, Geophys. J. Roy. astr. Soc. *22*, 223–226.

González, F.I., Bernard, E.N., Meinig, C., Eble, M.C., Mofjeld, H.O., and Stalin, S. (2005), *The NTHMP Tsunameter network*, Natural Hazards *35*, 25–39.

Guibourg, S., Heinrich, P., and Roche, R. (1997), *Numerical modeling of the 1995 Chilean tsunami; impact on French Polynesia*, Geophys. Res. Letts. *24*, 775–778.

HANSON, J.A. and BOWMAN, J.R. (2005), *Dispersive and reflected tsunami signals from the 2004 Indian Ocean tsunami observed on hydrophones and seismic stations*, Geophys. Res. Letts. *32*(17), L17608, 5 pp.

KANAMORI, H. (1977), *The energy release in great earthquakes*, J. Geophys. Res. *82*, 2981–2987.

KANAMORI, H. and CIPAR, J.J. (1974), *Focal process of the great Chilean earthquake, May 22, 1960*, Phys. Earth Planet. Inter. *9*, 128–136.

LÓPEZ, A.M. and OKAL, E.A. (2006), *A seismological reassessment of the source of the 1946 Aleutian "tsunami" earthquake*, Geophys. J. Intl. *165*, 835–849.

LOVE, A.E.H., *Some Problems in Geodynamics* (Cambridge Univ. Press, 1911).

MANSINHA, L. and SMYLIE, D.E. (1971), *The displacement fields of inclined faults*, Bull. Seismol. Soc. Amer. *61*, 1433–1440.

OCCHIPINTI, G., LOGNONNÉ, P., KHERANI, A., and HÉBERT, H. (2005), *Modeling and detection of ionospheric perturbation associated with the Sumatra tsunami of December 26th, 2004*, Eos, Trans. Amer. Geophys. Un. *86*(52), U11A–0829 (abstract).

OKAL, E.A. (1982), *Mode-wave equivalence and other asymptotic problems in tsunami theory*, Phys. Earth Planet. Inter. *30*, 1–11.

OKAL, E.A. (1988), *Seismic parameters controlling far-field tsunami amplitudes: A review*, Natural Hazards *1*, 67–96.

OKAL, E.A. (1990), *Single forces and double-couples: A theoretical review of their relative efficiency for the excitation of seismic and tsunami waves*, J. Phys. Earth *38*, 445–474.

OKAL, E.A. (2003), *Normal mode energetics for far-field tsunamis generated by dislocations and landslides*, Pure Appl. Geophys. *160*, 2189–2221.

OKAL, E.A. and HÉBERT, H. (2007), *Far-field modeling of the 1946 Aleutian tsunami*, Geophys. J. Intl. in press.

OKAL, E.A. and TALANDIER, J. (1989), *$M_m$: Avariable period mantle magnitude*, J. Geophys. Res. *94*, 4169–4193.

OKAL, E.A. and TALANDIER, J. (1991), *Single-station estimates of the seismic moment of the 1960 Chilean and 1964 Alaskan earthquakes, using the mantle magnitude $M_m$*, Pure Appl. Geophys. *136*, 103–126.

OKAL, E.A., PIATANESI, A., and HEINRICH, P. (1999), *Tsunami detection by satellite altimetry*, J. Geophys. Res. *104*, 599–615.

OKAL, E.A., SYNOLAKIS, C.E., FRYER, G.J., HEINRICH, P., BORRERO, J.C., RUSCHER, C., ARCAS, D., GUILLE, G., and ROUSSEAU, D. (2002), *A field survey of the 1946 Aleutian tsunami in the far field*, Seismol. Res. Letts. *73*, 490–503.

OKAL, E.A., TALANDIER, J., and REYMOND, D. (2007), *Quantification of hydrophone records of the 2004 Sumatra tsunami*, Pure Appl. Geophys. *164*, 309–323.

PELTIER, W.P. and HINES, C.O. (1976), *On a possible ionospheric technique for tsunami detection*, Geophys. J. Roy. astr. Soc. *46*, 669–706.

SAITO, M. (1967), *Excitation of free oscillations and surface waves by a point source in a vertically heterogeneous Earth*, J. Geophys. Res. *72*, 3689–3699.

SCHARROO, R., SMITH, W.H.F., TITOV, V.V., and ARCAS, D. (2005), *Observing the Indian Ocean tsunami with satellite altimetry*, Geophys. Res. Abstr. *7*, 230, (abstract).

SLADEN, A. and HÉBERT, H., *Inversion of satellite altimetry to recover the Sumatra 2004 earthquake slip distribution*, Eos, Trans. Amer. Geophys. Un. *86*(52), U22A–07, (2005) (abstract).

STEIN, S. and OKAL, E.A. (2005), *Size and speed of the Sumatra earthquake*, Nature *434*, 581–582.

SYNOLAKIS, C.E., *Tsunami and seiche*, In *Earthquake Engineering Handbook* (eds.) W.-F. Chen and C. Scawthron pp. 9_1–9_90, (CRC Press, Boca Raton, 2002).

TANIOKA, Y., RUFF, L.J., and SATAKE, K. (1995), *The great Kurile earthquake of October 4, 1994 tore the slab*, Geophys. Res. Letts. *22*, 1661–1664.

TITOV, V.V. and ARCAS, D. (2005), *Indian Ocean tsunami generation and propagation from modeling and observations*, Geol. Soc. Amer. Abstr. with Programs *37*(7), p.93, (abstract).

TITOV, V.V. and SYNOLAKIS, C.E. (1998), *Numerical modeling of tidal wave run-up*, J. Waterw. Port, Coastal and Ocean Eng. *124*, 157–171.

TITOV, V.V., GONZÁLEZ, F.I., BERNARD, E.N., EBLE, M.C., MOFJELD, H.O., NEWMAN, J.C., and VENTURATO, A.J. (2005), *Real-time tsunami forecasting: Challenges and solutions*, Natural Hazards *35*, 41–58.

TSAI, V.C., NETTLES, M., EKSTRÖM, G., and DZIEWOŃSKI, A.M. (2005), *Multiple CMT source analysis of the 2004 Sumatra earthquake*, Geophys. Res. Letts. *32*(17), L17304, 4 pp.

WARD, S.N. (1980), *Relationships of tsunami generation and an earthquake source*, J. Phys. Earth *28*, 441–474.

WARD, S.N. (1981), *On tsunami nucleation: I. A point source*, J. Geophys. Res. *86*, 7895–7900.

WARD, S.N. (1982a), *On tsunami nucleation: II. An instantaneous modulated line source*, Phys. Earth Planet. Inter. *27*, 273–285.

WARD, S.N. (1982b), *Earthquake mechanism and tsunami generation: the Kurile Islands event of October 13, 1963*, Bull. Seismol. Soc. Amer. *72*, 759–777.

WEAVER, P.F., YUEN, P.C., PRÖLSS, G.W., and FURUMOTO, A.S. (1970), *Acoustic coupling into the ionosphere from seismic waves of the earthquake at Kurile Islands on August 11, 1969*, Nature *226*, 1239–1241.

YEH, H., TITOV, V.V., GUSIAKOV, V., PELINOVSKY, E., KHRAMUSHIN, V., and KAISTRENKO, V. (1995), *The 1994 Shikotan earthquake tsunamis*, Pure Appl. Geophys. *144*, 855–874.

(Received January 7, 2006, accepted May 6, 2006)

Pure appl. geophys. 164 (2007) 379–393
0033–4553/07/030379–15
DOI 10.1007/s00024-006-0162-7



Pure and Applied Geophysics

# The Tsunami of 26 December, 2004: Numerical Modeling and Energy Considerations

Zygmunt Kowalik,[1] William Knight,[2] Tom Logan,[3] and Paul Whitmore[2]

*Abstract*—A numerical model for the global tsunamis computation constructed by Kowalik *et al.* (2005), is applied to the tsunami of 26 December, 2004 in the World Ocean from 80°S to 69°N with spatial resolution of one minute. Because the computational domain includes close to 200 million grid points, a parallel version of the code was developed and run on a Cray X1 supercomputer. An energy flux function is used to investigate energy transfer from the tsunami source to the Atlantic and Pacific Oceans. Although the first energy input into the Pacific Ocean was the primary (direct) wave, reflections from the Sri Lankan and eastern shores of Maldives were a larger source. The tsunami traveled from Indonesia, around New Zealand, and into the Pacific Ocean by various routes. The direct path through the deep ocean to North America carried miniscule energy, while the stronger signal traveled a considerably longer distance via South Pacific ridges as these bathymetric features amplified the energy flux vectors. Travel times for these amplified energy fluxes are much longer than the arrival of the first wave. These large fluxes are organized in the wave-like form when propagating between Australia and Antarctica. The sources for the larger fluxes are multiple reflections from the Seychelles, Maldives and a slower direct signal from the Bay of Bengal. The energy flux into the Atlantic Ocean shows a different pattern since the energy is pumped into this domain through the directional properties of the source function. The energy flow into the Pacific Ocean is approximately 75% of the total flow to the Atlantic Ocean. In many locations along the Pacific and Atlantic coasts, the first arriving signal, or forerunner, has lower amplitude than the main signal which often is much delayed. Understanding this temporal distribution is important for an application to tsunami warning and prediction.

**Key words:** Indonesian tsunami, tsunami model, maximum amplitude, energy flux.

## 1. Introduction

This paper is a continuation of our research on the Indian Ocean Tsunami (Kowalik *et al.*, 2005). Above paper contains detailed information about earthquake, tsunami and numerical methods. To study tsunamis in the World Ocean, we have formulated the vertically integrated equations of motion in spherical polar coordinates. In this numerical approach the higher order of approximation in

[1] Institute of Marine Science, University of Alaska, Fairbanks, AK 99775, USA.
E-mail: ffzk@ims.uaf.edu
[2] NOAA/NWS/West Coast and Alaska Tsunami Warning Center, Palmer, Alaska, USA.
[3] Arctic Region Supercomputing Center, University of Alaska, Fairbanks, AK 99775, USA.

space for the continuity equation was achieved by expanding the upwind/downwind flux code originally proposed by MADER (2004). For large-scale computations an upwind/downwind scheme is essential as it displays strong stability. The integration domain extends from 80°S to 69°N. The boundaries include both wet and dry points. Along the coastal (dry points) the normal velocity is set to zero. At the wet boundary points (along 69°N) the radiation condition, established by REID and BODINE (1968) is used. The entire globe is cut along 20°E longitude, requiring a cyclic boundary condition for sea level and the E-W velocity on this meridian. It appears at first glance that the above boundary conditions are sufficient to derive a solution. Early numerical experiments however, show that even with the relatively large space step of 1′, new dry and wet points may be generated due to runup or run-down. A numerical scheme for wetting and drying needs to be introduced. The total water depth is the parameter usually tested to detect the presence of wet or dry points (FLATHER and HEAPS, 1975; IMAMURA, 1996; and KOWALIK and MURTY, 1993b). Wet and dry points are identified by setting the average (undisturbed) ocean depth as positive (wet points) and elevations (dry points) as negative values. The total water depth in the dry grid points is taken as zero.

The spatial grid step of numerical computation is 1' (1 minute equals 1.852 km at the equator), and its length changes along the circle of latitude. The total number of grid points is close to $2 \times 10^8$, therefore the simple time-stepping solution, even on a supercomputer, takes several weeks. The entire domain was split along meridians into 60 subdomains to apply 60 processors. With this parallelization, 50 h of tsunami propagation was reproduced in 9 h of a CRAY X1.

A small spatial step is important as short-period waves can be obliterated during large propagation distances when large spatial steps are used. Taking the average depth of the World Ocean as 4000 m, a wave with a 10-minute period has a wavelength close to 120 km. This wave length is discretized by a 1′ grid into about 64 mesh lengths. The amplitude of a sinusoidal wave propagating over 10,000 km will diminish only about 2% and some shorter dispersive waves will be generated as well (KOWALIK, 2003).

The details of the source function construction and geographical distribution are given in KOWALIK *et al.* (2005). Permanent, vertical sea-floor displacement is computed using the static dislocation formulae from OKADA (1985). The generation mechanism for the Indian Ocean tsunami is mainly the static sea-floor uplift caused by an abrupt slip at the India/Burma plate interface. To accommodate trench curvature, the fault plane is broken into two segments. Maximum uplift is 507 cm and maximum subsidence approximately 474 cm. The 3-D rendering of the source function is shown in Figure 1.

The major conclusion in KOWALIK *et al.* (2005) was that in the Pacific Ocean, those stations located in the Northern Pacific show the largest differences between calculated and observed travel time. This is caused either by a small tsunami signal-to-noise ratio or by multiple paths from the source to gauge locations. In the latter

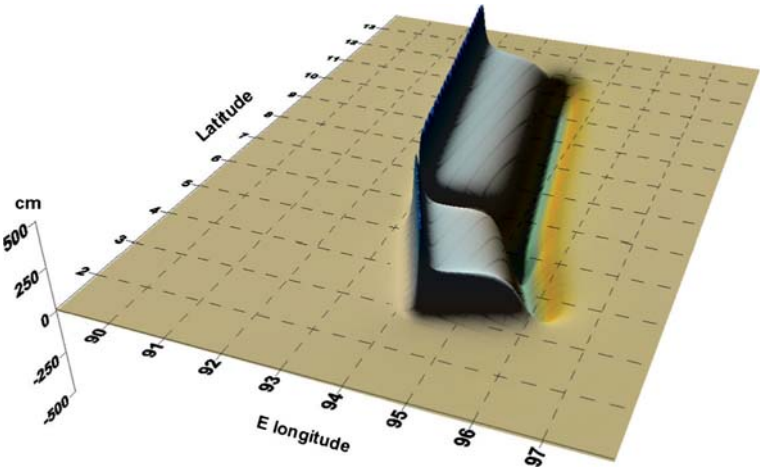


Figure 1
The source function for the tsunami of 26 December, 2004.

case, especially important is an interaction of the higher energy tsunami signals which travel slowly over the oceanic ridges and the lower energy signals which travel faster over the deep oceanic regions. In the present paper we follow the changes in the tsunami signal as it traveled from Indonesia to the Pacific Ocean. The tsunami energy flux is the investigative tool used for this purpose.

This paper has been prepared for the 22nd International Tsunami Symposium held in Greece, June 2005. From the time of the Symposium until the present time (April, 2006) a variety of modeling and observational data on the IOT has been gathered and investigated (see e.g. MEGURO, 2005). Numerical simulation of the IOT will be further improved through a comprehensive comparison with the new data. A large body of work has been directed towards establishing tsunami source model, e.g., LAY *et al*. (2005), HIRATA *et al*. (2005), and STEIN and OKAL (2005). The physics of the global IOT tsunami amplification has been further elucidated through the trapping effect of mid-ocean ridge topographic waveguides, e.g., TITOV *et al*. (2005) and by including the wave dispersion (WATTS *et al*., 2005).

## *2. Global Distribution of Maximum Amplitude*

Model computations using the above source were made for 50 hrs of propagation, allowing the tsunami signal to travel over the entire World Ocean. During this computation the maximum tsunami amplitude in every grid point was recorded. The amplitude here is defined as positive sea-level change from the mean sea level to the wave crest. The plot of maximum amplitude in the proximity of the generation

domain is shown in Figure 2 and the corresponding plot for the World Ocean is shown in Figure 3.

The strongly directional signal generated by the elongated source dominates the Indian Ocean domain. As the wave amplitude squared is proportional to the potential energy we can infer that the main energy lobe is directed towards Sri Lanka and the secondary lobe points towards South Africa, sending a strong signal into the Atlantic Ocean.

The global maximum amplitude distribution (Fig. 3) shows that the Indonesian tsunami traveled all over the World Ocean. Although the source directivity pushed most of the wave energy towards southern Africa, a strong signal is nonetheless

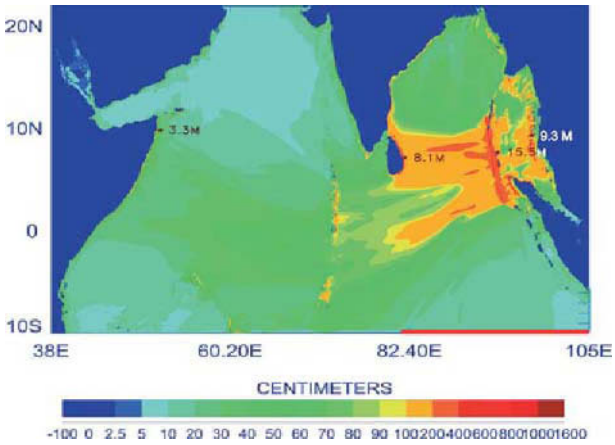


Figure 2
Maximum modeled tsunami amplitude in the Indian Ocean.

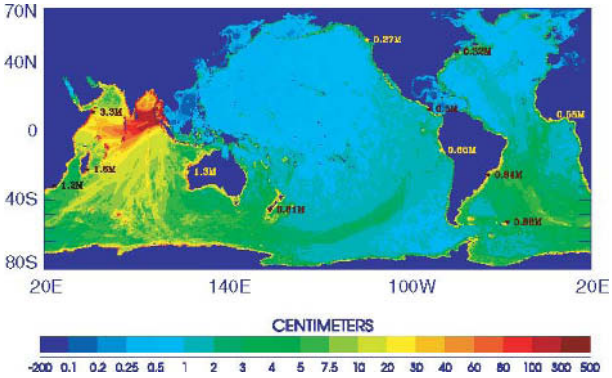


Figure 3
Maximum modeled tsunami amplitude in the World Ocean.

directed towards Antarctica. It is easy to see that the tsunami tended to propagate towards Antarctica along the oceanic ridges and subsequently continued to transfer higher energy along the South Pacific ridge towards South and Central America. This mode of propagation brings the modeled tsunami amplitude up to 65 cm along the Pacific coast of South America. A similar mode of energy transfer is observed in the Atlantic, where the Mid-Atlantic Ridge channels the tsunami to produce locally 30 cm amplitude as far north as Nova Scotia. This figure also depicts the amplitude enhancement in shallow water and especially in proximity to peninsulas and islands due to energy concentration through refraction.

An especially large energy flux is ducted from the South Atlantic Ridge towards Brazil and Argentina. The filaments of energy trapped along the South Pacific Ridges are most spectacular as they duct tsunami energy for many thousands of kilometers. A simple explanation of the energy trapping using the continuity equation leads us to conclude that amplitude should increase over the ridges due to shallower depth. At the same time, the role of bottom friction over the 3-km deep ridge is negligible and therefore the tsunami can travel a long distance without energy losses.

To demonstrate the pattern of the energy trapped over the various bathymetric features, the energy flux is introduced. In the rectangular system of coordinates, with the $x$ coordinate along E-W direction and $y$ along N-S direction, the $u$ component of velocity along $x$ direction can be combined with the sea level ($\zeta$) to define the E-W component of the energy flux vector (e.g., KOWALIK and MURTY, 1993a):

$$E_x = \rho g H u \zeta. \tag{1}$$

Similarly, the N-S component of the energy flux vector is defined (with $v$, the velocity component along the $y$ direction):

$$E_y = \rho g H v \zeta. \tag{2}$$

In the above: $\rho$ is the sea-water density, $g = 9.81\ \mathrm{ms}^{-2}$ is the Earth's gravity acceleration and $H$ is the ocean depth. The energy flux vector for the progressive wave is always propagating into the same direction as the sea level and velocity and its direction is perpendicular to the wave front. To preserve direction of the energy flux in the progressive wave the velocity and sea-level elevation remain in phase (HENRY and FOREMAN, 2001). Energy flux units are expressed as Joule/(s cm) so this is an energy flux per unit width and per unit time. To derive the total energy flux the above expressions should be multiplied by the length of a cross section and integrated over the time period.

In Figure 4 the energy flux vectors are shown in the southwestern part of the Pacific Ocean. The larger tsunami amplitudes are located above the oceanic ridge and the energy flux is directed along the ridge. This small group of higher amplitude waves does not belong to the first tsunami signal to arrive in this region. Its average wavelength is about 1350 km, as the depth of the ridge is close to 3 km the wave

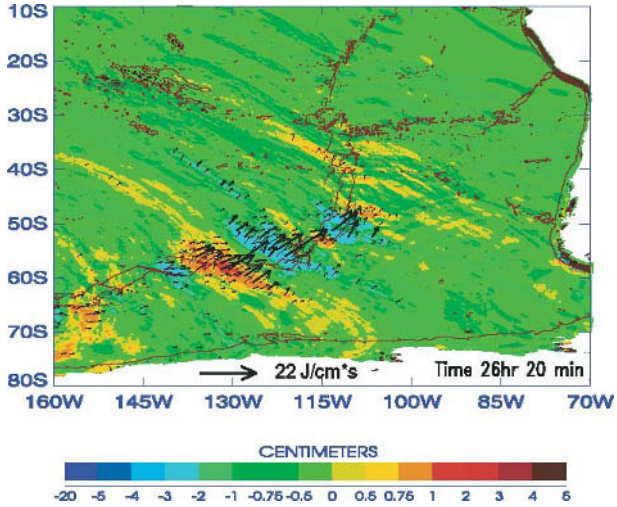


Figure 4
Energy flux vectors over the South Pacific Ridge at time 26 hr 20 min. The colors denote the sea level. The dark-brown lines denote the ridge depth – 3000 m depth contour.

period is about 2 hr. This is a somewhat long period for a tsunami. The wave pattern also shows that the waves over ridges are slower than the off-ridge waves, suggesting trapping due to refraction and focusing of off-ridge energy towards the ridge. Nonetheless we cannot exclude the possibility of a resonance interaction of the tsunami wave and ridge bathymetry since SNODGRASS *et al.* (1962) demonstrated the presence of discrete spectra in waves trapped over depth discontinuities. MEI (1989) showed that over a stepped bottom ridge the discrete spectra exist as well. If an incident wave can excite these trapped modes, an amplification of the tsunami signal due to resonance will follow.

## 3. Time-dependent Propagation

Although the maximum amplitude defines tsunami distribution in the World Ocean, it does not reveal the temporal development of tsunamis. To improve understanding of the large-scale temporal processes we use the temporal change of the tsunami energy fluxes passing through various cross sections. To obtain instantenous value of such flux, the energy fluxes flowing through all numerical lattices located along the cross section are added and afterwards the total energy flux is divided by the length of the cross section. The first cross section is considered in the Indian Ocean, located from 80°E to 105°E along 10°S (see red line in Fig. 2). The southward directed energy flux shown in Figure 5 is responsible for the tsunami signal propagating into the Pacific.

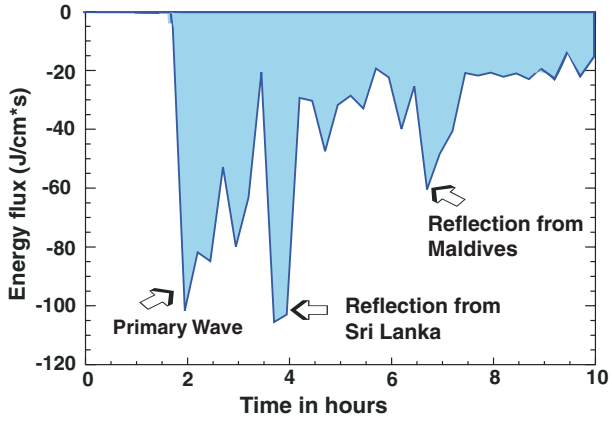


Figure 5
Southward directed energy flux through the E-W cross section located in the Indian Ocean along 10°S from 80°E to 105°E (see Fig. 2).

The first maximum in this figure has been associated with the direct wave passing through the latitude 10°S at 2 hr after the initial source motion. The next, even bigger energy influx arrives 2 hr later, and is caused by the reflection from Sri Lanka and the east coast of India. The reflection from the Maldives Islands generates a signal which passes the cross section at about 6.5 hr from the initial disturbance. This cross section is located quite close to the Bay of Bengal and therefore a large portion of the Maldives-reflected signal omits this route. Since the Bay of Bengal and entire Indian Ocean act as a parabolic mirror, they send many reflected signals of smaller amplitude southward. The conclusion from the above experiment is that the reflected signal may send more energy south than the direct signal.

With the major maxima in the southward directed signal identified, the task to associate them with the signal propagating into the Pacific Ocean remains. For this purpose an energy flux is considered through the three cross sections located between Antarctica and the major continents. The cross section (blue color in Figure 6) along the longitude 20°E from Antarctica to South Africa (AS) shows the time variation of the energy flux between the Indian and Atlantic Oceans. This flux remains negative for the entire period of 50 hr, thus confirming that the inflow is directed into the Atlantic Ocean. On the other hand the energy flow through a cross section along 140°E (green color in Fig. 6) from Antarctica to Australia (AA) is at all times positive (from the Indian to Pacific Oceans). The flux through the cross section located between South America and Antarctica at 70 W (red color in Fig. 6), reveals a small in-flow from the Atlantic into the Pacific. Figure 6 clearly demonstrates that the magnitude and the time variability of energy fluxes through cross sections AA and AS are quite different in character. The flux passing AS has a large value and the maximum energy inflow to the Atlantic is located close to the

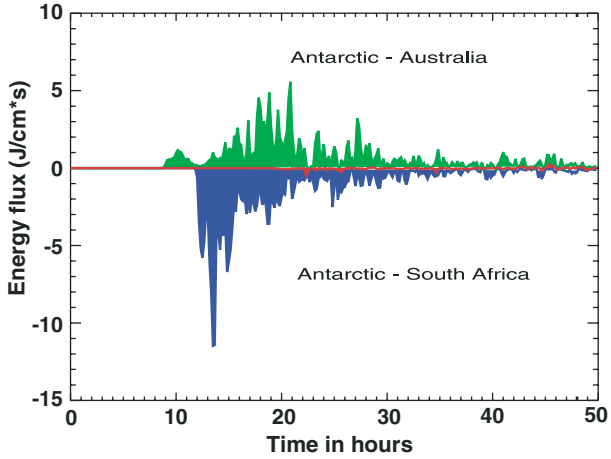


Figure 6
Energy flux through the cross sections located between Antarctic and major continents. Along 20°E from Antarctic to South Africa, blue color; along 140°E, from Antarctic to Australia, green color, along 70 W from South America to Antarctic, red color.

initial wave front, even though the first arriving signal is not related to the maximum energy. The energy flow into the Atlantic is a result of the source orientation as shown in Figure 2. The main energy maximum is slower to arrive than the initial signal because, as Figure 3 suggests, the maximum energy directed towards SA cross section is located along the oceanic ridge. Due to smaller depth over this ridge the more energetic signal propagates slower. The energy flow through AA demonstrates that the tsunami arrives about 10 hr from the onset of the earthquake; it initially has a small amplitude which slowly increases in time to achieve a few maxima from 18 to 21 hr. To understand the origin of this complicated temporal pattern of energy flux through AA we turn to Figure 5 and analyze the southward energy flux from the source area. The first signal arriving at the southern boundary in Figure 5 also crosses AA as the initial signal, since the travel time for this signal is close to 10 hr. The second signal arriving two hours later is caused by the reflection from the Sri Lanka and Indian coasts. The maxima in Figure 6 occurring from 18 to 21 hr are related to the energy flux arriving by the various routes from the Indian Ocean. The arrival time of these signals depends on the depth and on the traveled distance. It is useful to notice that the route from the generation domain to South America via passages between Australia and Antarctic is the great circle of a sphere. Signals which travel from the generation area to the section AA through the deep ocean travel faster, in about 10 hr, but they transfer less energy. The slower signal travels along oceanic ridges and transfers more energy as confirmed in Figure 4 by the energy flux vectors. This appears to be only a part of the story. Tracking through animations the signal shown in Figure 4

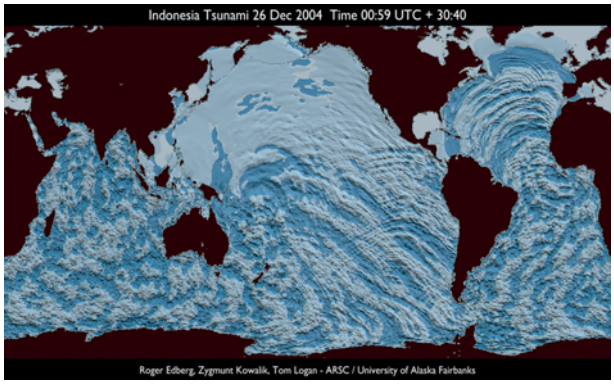


Figure 7
Sea-level pattern generated by the Indian Ocean Tsunami of 26 December, 2004 at 30 hr 40 min from the tsunami onset. Tsunami signals in the Northern Atlantic and Southern Pacific have been reorganized into coherent waves after passing through the narrows between Africa and South America, and Australia and Antarctica.

backwards, the tsunami passes between Australia and Antarctica, as depicted in cross section AA (Fig. 6) and then loses its identity going back into the southern Indian Ocean. The large inflow of energy shown in Figure 6 is related to the reflected signals off the Seychelles, Maldives and Africa and to a slowly traveling tsunami which originated in the Bay of Bengal.

To compare the total energy flux entering the Pacific and Atlantic Oceans over the 50 hr of process, the energy fluxes given in Figure 6 have been integrated in time. The total energy flowing into the Pacific Ocean is approximately 75% of the total energy inflow to the Atlantic Ocean.

The passage between Antarctica and Australia/New Zealand plays a large role in signal amplification. As the passage is wide on the Indian Ocean side and constrained on the Pacific side, the eastward moving signal is amplified and also reorganized into periodic wave-like structures (Fig. 7). A similar reorganization of a quasi-turbulent signal into oscillatory wave pattern can be observed in the passage between South America and Africa for the tsunami propagating from the Southern into the Northern Atlantic.

## *4. Observations versus Computations*

Although the 1' computational mesh resolves many coastal and bathymetric features, nonetheless it is too large to resolve the local dynamics such as runup. In Figure 8, four stations have been chosen from the Indian Ocean area and are compared with observations described by MERRIFIELD *et al.* (2005).

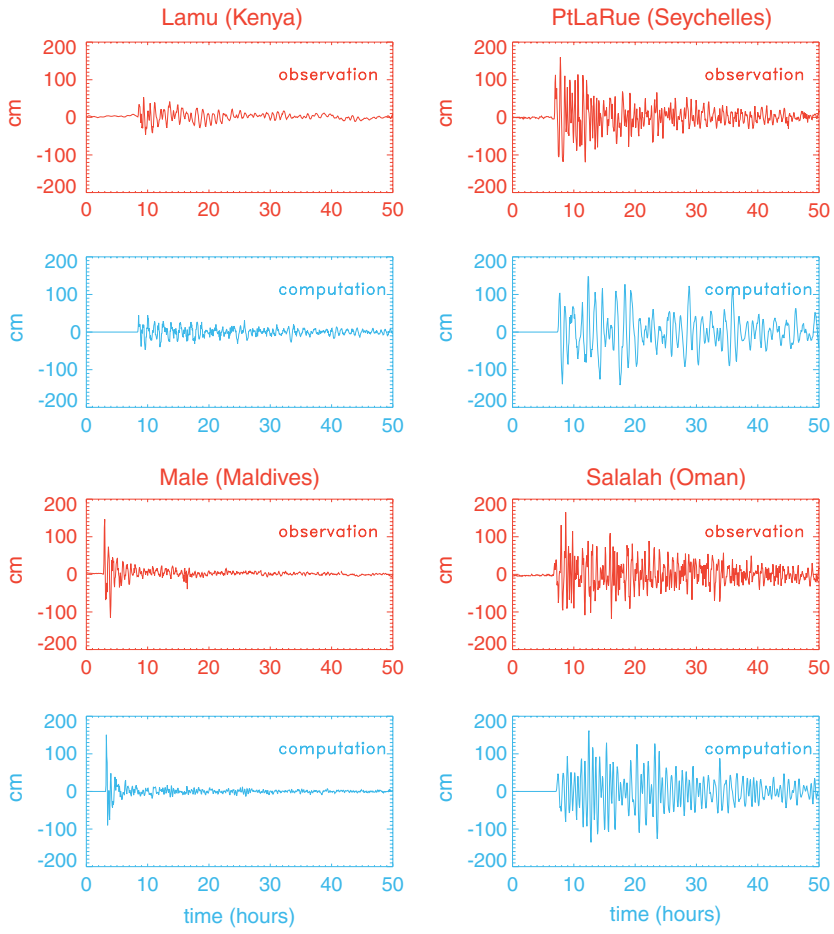


Figure 8
Observations and computations from the four stations in the Indian Ocean.

The stations are located on Maldives Island (Male), on the Seychelles Islands (Pt LaRue), on the African coast of Kenya (Lamu) and on the Arabian Peninsula coast of Oman (Salalah). The model reproduces quite well the maximum amplitude and the temporal behavior of the tsunami, indicating that with higher resolution bathymetry an even better comparison can be achieved. The fine resolution bathymetry around Maldives Island is very important for the distant propagation towards Seychelles, or Oman, as the signal observed at these locations depends on tsunami reflection, trapping and refocusing in the Maldives Island chain.

As luck would have it, Jason-I altimetry satellite traversed the Indian Ocean about 2 hr after the event origin time. It crossed the equator on a NNE path at 02:55

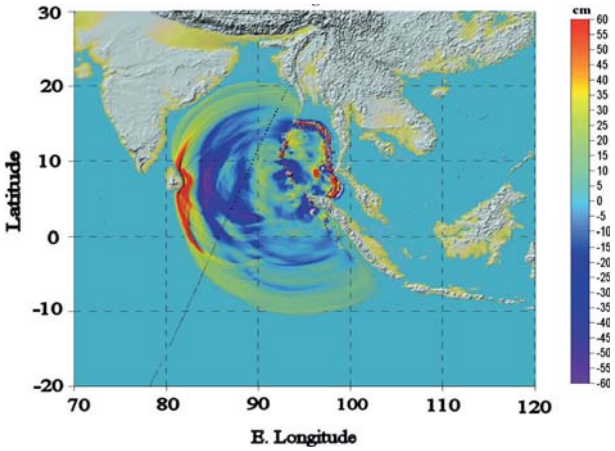


Figure 9
Ground track of Jason-I and computed tsunami amplitude at 2:55 UT on Dec. 26, 2004 in the Indian Ocean.

UTC on 12-26-2004 (Fig. 9). The non-validated altimetry data were downloaded from the JPL Physical Oceanography website at ftp: //podaac.jpl.nasa.gov/pub/sea_surface_height/jason/j1nrtssha/data/.

Altitude is sampled approximately once per second and is corrected for tides. In order to remove any background, the raw data from the "tsunami pass" were corrected by subtracting out an average of 4 "non-tsunami" passes. Jason-I repeats its track about once every ten days, so four repeat paths were averaged to generate the background. The corrected signal was then smoothed by removing fluctuations with wavelengths shorter than 20 km. The smoothed signal with background removed was compared against the model data. Note that Jason-I was above the tsunami for about ten minutes. During this time the tsunami was in motion, consequently the comparison is made to dynamic model predictions and not against a static snapshot.

The model wave heights at the moment of equatorial crossing are shown in Figure 9. Jason-I crosses the leading edge wave at a point on the wave front where the amplitude is rapidly increasing towards the NW. The comparison between observed data and model is therefore sensitive to small variations in source details. The final comparison is shown in Figure 10 (upper panel). The leading edge wave location is predicted accurately by the model, even if the amplitude is not. The modeled leading wave with the amplitude similar to the one recorded by satellite was in the satellite footprint 15 min earlier (see, Fig. 9). A closer amplitude/period match was obtained by rotating the source strike counterclockwise slightly, and by reducing the fault width from 200 km to 125 km. The comparison, given in Figure 10 (lower panel) shows that the model

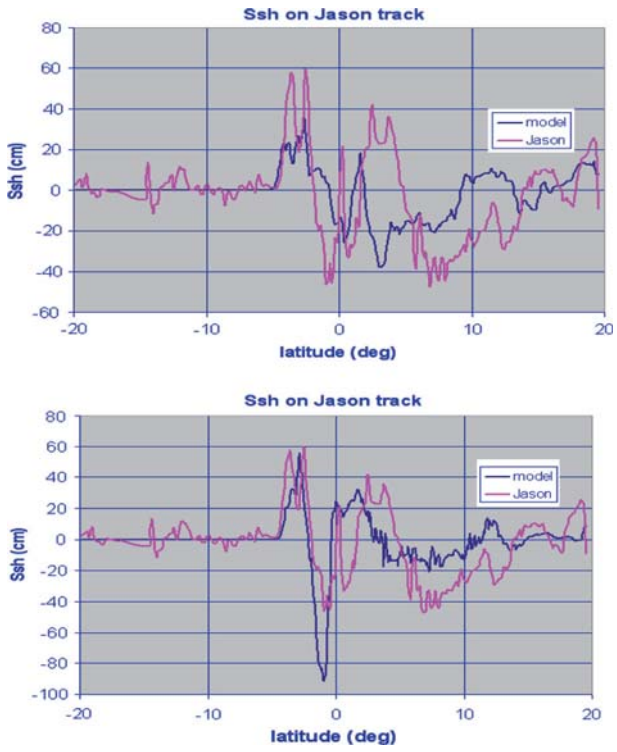


Figure 10
Computed and observed tsunami amplitude along the Jason-I track. Upper panel: Source function given in Figure 1. Lower panel: Source function orientation and width adjusted.

as driven by the adjusted source function reproduces more accurately the leading wave recorded by Jason-I.

## 5. *Discussions and Conclusions*

Based on the constructed computer model, we aim at a better understanding of the global propagation of the Indian Ocean tsunami. By comparison to the global observation we hope to identify major patterns of tsunami propagation. The preliminary model calibration against the December 26, 2004 Indian Ocean tsunami showed the following:

a) The chart of the maximum tsunami amplitude showed enhancement of the tsunami amplitude over the major oceanic ridges. Oceanic ridges acted as ducts for tsunami waves, transferring energy for many thousand kilometers without noticeable dissipation;

b) Travel-time computation based on the first wave arrival time may lead to errors in the prediction of tsunami arrival time as higher energy waves propagate slower along ridges; and
c) In passing through straits between continents, a tsunami signal is reorganized from noisy into coherent wave motion.

Computed distributions of the maximum amplitude compare well with observations analyzed by MERRIFIELD *et al.* (2005) and by RABINOVICH (2005). The observed and computed temporal variation of the tsunami at gauge stations in the Indian Ocean displays quite similar amplitude and variability, although the model resolution of about 2 km still needs to be refined for proper runup calculations. The comparison against satellite data (GOVER, 2005) shows that improvements in the source function are needed. The source location was constrained by tsunami travel times to tide gauge locations and by earthquake parameters computed from seismic data inversions (see, KOWALIK *et al.*, 2005). Further investigation through comparison to the magnitude and location of the satellite signal should also improve the source parameters. As the source function is one of the major building blocks of the tsunami model and, as new insight on the source function pattern and tsunami generation has been suggested by LAY *et al.* (2005) and HIRATA *et al.* (2005), it will be important to improve the global tsunami model using this new information. The model computations reveal peculiarities of the tsunami signal when it travels from the source over the entire World Ocean. The most interesting is ducting the tsunami energy along oceanic ridges which is so clearly shown in Figures 2 and 3. To demonstrate the pattern of energy trapping over the ridges, the energy flux function is used. The energy flux vectors show magnification over the South Pacific Ridge and their distribution suggests trapping due to refraction and focusing the off-ridge energy towards the ridge.

Further investigations of energy fluxes show more complicated temporal and spatial patterns in tsunami propagation. The primary signal traveling towards the Pacific Ocean depicted the low energy level, therefore it was not well observed at the sea-level gauges. The more energetic signal arrived with some delay. Comparison of the total energy flux entering the Pacific and Atlantic Oceans over the 50 hr of process, show that the total energy flowing into the Pacific Ocean is approximately 75% of the total energy inflow to the the Atlantic Ocean. Therefore, the energy inflow into the Pacific Ocean and into the Atlantic Ocean do not differ strongly as one would expect from the directional properties of the source as revealed by the maximum amplitude contours. A subtle process of multiple reflection and refocusing in the Indian Ocean was responsible for rerouting the tsunami energy into the Pacific Ocean. The southward directed energy fluxes in the Indian Ocean, given in Figure 5 are considerably larger than those outflowing from the Indian Ocean (Fig. 6). It seems from this comparison that the large portion of the tsunami energy was dissipated in the Indian Ocean.

The investigation of the energy flux along the South Pacific Ridge reveals a tsunami of approximately 2 hr period. Tracking (through animations) tsunamis passing between Australia and Antarctica we have found that the signal moving from west to east is amplified and also reorganized into periodic wave-like structures. Similar reorganization of the tsunami occurs between South America and Africa for the tsunami propagating from the Southern into the Northern Atlantic.

## *Acknowledgements*

We would like to thank both anonymous reviewers for their comments and suggestions which enhanced this manuscript.

## References

Flather, R. A. and Heaps, N. S. (1975), *Tidal computations for Morecambe Bay*, Geophys. J. Royal Astr. Soc. *42*, 489–517.

Gover, J. (2005), *Jason 1 detects the 26 December 2004 tsunami*, EOS, Trans. AGU *86*, 37–38.

Henry, R.F. and Foreman, M.G.G. (2001), *A representation of tidal currents based on energy flux*, Marine Geodesy, *2493*, 139–152.

Hirata, K., Satake, K., Tanioka, Y., Kuragano, T., Hasegawa, Y., Hayashi, Y., and Hamada, N. (2005), *The Indian Ocean Tsunami: Tsunami source model from satellite altimetry*. Proc. Internat. Tsunami Symp. (eds., G.A. Papadopoulos and K. Satake) (Chania, Greece, 2005), pp. 72–76.

Imamura, F., *Review of tsunami simulation with a finite difference method.* In: *Long-Wave Runup Models* (eds. H.Yeah, P. Liu, and C. Synolakis) (World Scientific (1996)), pp. 25–42.

Kowalik, Z. (2003), *Basic relations between tsunami calculation and their physics - II*, Science of Tsunami Hazards *21*(3), 154–173.

Kowalik, Z. and Murty, T. S., *Numerical Modeling of Ocean Dynamics* (World Scientific (1993a)), 481 p.

Kowalik, Z. and Murty, T. S. (1993b), *Numerical simulation of two-dimensional tsunami runup,* Marine Geodesy *16*, 87–100.

Kowalik, Z., Knight, W., Logan, T., and Whitmore, P. (2005), *Numerical Modeling of the Global Tsunami: Indonesian Tsunami of 26 December, 2004*, Science of Tsunami Hazards *23*(1), 40–56.

Lay, T., Kanamori, H., Ammon, C. J., Nettles, M., Ward, S. N., Aster, R. C., Beck, S. L., Bilek, S. L., Brudzinski, M. R., Butler, R., DeShon, H. R., Ekstrom, G., Satake, K., and Sipkin, S. (2005), *The Great Sumatra-Andaman Earthquake of 26 December, 2004*. Science *308*, 1127–1139.

Mader, C. L., *Numerical Modeling of Water Waves* (CRC Press (2004)), 274 p.

Meguro, K. (2005), *Report on the 2004 Sumatra Earthquake and Tsunami Disaster,* http://icus-incede.iis.u-tokyo.ac.jp/wwwe/publications/reports/report8.htm#top.

Mei, C. C., *The Applied Dynamics of Ocean Surface Waves,* (World Scientific (1989)), 740 p.

Merrifield, M. A., Firing, Y. L., Aarup, T., Agricole, W., Brundrit, G., Chang-Seng, D., Farre, R., Kilonsky, B., Knight, W., Kong, L., Magori, C., Manurung, P., McCreery, C., Mitchell, W., Pillay, S., Schindele, F., Shillington, F., Testut, L., Wijeratne, E. M. S., Caldwell, P., Jardin, J., Nakahara, S., Porter, F. -Y., and Turetsky, N. (2005), *Tide gauge observations of the Indian Ocean tsunami, December 26, 2004*, Geophys. Res. Lett. *32* L09603, doi:10.1029/2005GL022610.

Okada, Y. (1985), *Surface deformation due to shear and tensile faults in a half-space,* Bull. Seismol. Soc. Amer. *75*, 1135–1154.

Rabinovich, A. B. (2005), *Web compilation of tsunami amplitudes and arrival times.* http://www-sci.pac.dfo-mpo.gc.ca/osap/projects/tsunami/tsunamiasia_e.htm.

REID, R. O. and BODINE, R. O. (1968), *Numerical model for storm surges in Galveston Bay*, J. Waterway Harbor Div. *94(WWI)*, 33–57.

STEIN, S. and E. Okal, E. (2005), *Speed and size of the Sumatra earthquake*, Nature *434*, 581–582.

SNODGRASS, F. E., MUNK, W. H., and MILLER, G. R. (1962), *California's continental borderland. Part I. Background spectra,* J. Mar. Research *20*, 3–30.

TITOV, V., RABINOVICH, A. B., MOFJELD, H. O., THOMSON, R. E., and GONZÁLEZ, F. I. (2005), *The global reach of the 26 December, 2004 Sumatra tsunami,* Science *309*, 2045–2048.

WATTS, P., IOUALALEN, M., GRILLI, S., SHI, F., and KIRBY, J. T. (2005), *Numerical simulation of the December 26, 2004 Indian Ocean tsunami using high-order Boussinesq model,* Fifth Int. Symp. Waves 2005, July, 2005, Madrid Spain, 10 p.

(Received December 12, 2005, accepted May 5, 2006)
Published Online First: January 30, 2007

Pure appl. geophys. 164 (2007) 395–411
0033–4553/07/030395–17
DOI 10.1007/s00024-006-0161-8



Pure and Applied Geophysics

# Field Survey of Tsunami Effects in Sri Lanka due to the Sumatra-Andaman Earthquake of December 26, 2004

Shusaku Inoue,[1] Anil C. Wijeyewickrema,[2] Hiroyuki Matsumoto,[3]
Hiroyuki Miura,[1] Priyantha Gunaratna,[4]
Manoj Madurapperuma,[4,2] and Toru Sekiguchi[5]

*Abstract*—The December 26, 2004 Sumatra-Andaman earthquake that registered a moment magnitude ($M_w$) of 9.1 was one of the largest earthquakes in the world since 1900. The devastating tsunami that resulted from this earthquake caused more casualties than any previously reported tsunami. The number of fatalities and missing persons in the most seriously affected countries were Indonesia - 167,736, Sri Lanka - 35,322, India - 18,045 and Thailand - 8,212. This paper describes two field visits to assess tsunami effects in Sri Lanka by a combined team of Japanese and Sri Lankan researchers. The first field visit from December 30, 2004 – January 04, 2005 covered the western and southern coasts of Sri Lanka including the cities of Moratuwa, Beruwala, Bentota, Pereliya, Hikkaduwa, Galle, Talpe, Matara, Tangalla and Hambantota. The objectives of the first field visit were to investigate the damage caused by the tsunami and to obtain eyewitness information about wave arrival times. The second field visit from March 10–18, 2005 covered the eastern and southern coasts of Sri Lanka and included Trincomalee, Batticaloa, Arugam Bay, Yala National Park and Kirinda. The objectives of the second visit were mainly to obtain eyewitness information about wave arrival times and inundation data, and to take relevant measurements using GPS instruments.

**Key words:** Damage, field survey, inundation, Sri Lanka, Sumatra-Andaman earthquake, tsunami.

## 1. Introduction

At 07:58:53 December 26, 2004 (00:58:53 UTC) a great earthquake of moment magnitude ($M_w$) 9.1 struck northern Sumatra. The epicenter was located at 3.3° N, 9.9° E with a focal depth of 33 km (USGS, 2006). This event was one of only four events since 1900 with magnitude greater than or equal to 9.0. The other events are, the 1960 Great Chilean earthquake (9.5), the 1964 Prince William Sound, Alaska earthquake (9.2) and the 1952 Kamchatka earthquake (9.0), (USGS, 2006). The

[1] Department of Built Environment, Tokyo Institute of Technology, Japan.
[2] Department of Civil Engineering, Tokyo Institute of Technology, Japan. E-mail: anil@cv.titech.ac.jp
[3] Japan Agency for Marine-Earth Science and Technology, Japan.
[4] Department of Civil Engineering, University of Moratuwa, Sri Lanka.
[5] Department of Architecture and Building Engineering, Tokyo Institute of Technology, Japan.

tsunami generated by the Sumatra-Andaman earthquake resulted in more casualties than any previous tsunami in recorded history. Due to the earthquake and tsunami 167,736 people lost their lives or were reported missing in Indonesia. The other countries that reported a large number of fatalities or missing persons due to the tsunami were Sri Lanka – 35,322, India – 18,045 and Thailand – 8,212 (Appendix A). The location of the epicenter and the most seriously affected countries are shown in Figure 1.

This paper describes two field visits to assess tsunami effects in Sri Lanka by a combined team of Japanese and Sri Lankan researchers. The field visit routes and main cities covered by the field visits are shown in Figure 2. The first field visit from December 30, 2004 – January 04, 2005 covered the western and southern coasts of Sri Lanka and included the cities of Moratuwa, Beruwala, Bentota, Pereliya, Hikkaduwa, Galle, Talpe, Matara, Tangalla, and Hambantota. The objectives of the first field visit were to investigate the damage caused by the tsunami and to obtain eyewitness information about wave arrival times. One of the most tragic events due to the tsunami occurred at Pereliya on the SW coast, where a train that was stopped between stations was swept off the rail tracks when the tsunami struck, and around 1,000 people are estimated to have lost their lives due to this incident (Fig. 3). Most

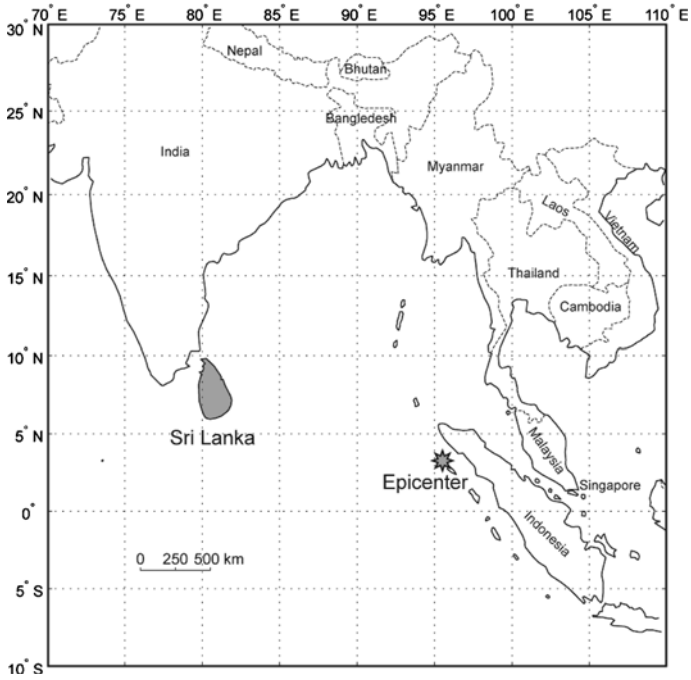


Figure 1
Epicenter of Sumatra-Andaman earthquake and surrounding countries. The most seriously affected countries were Indonesia, Sri Lanka, India and Thailand.

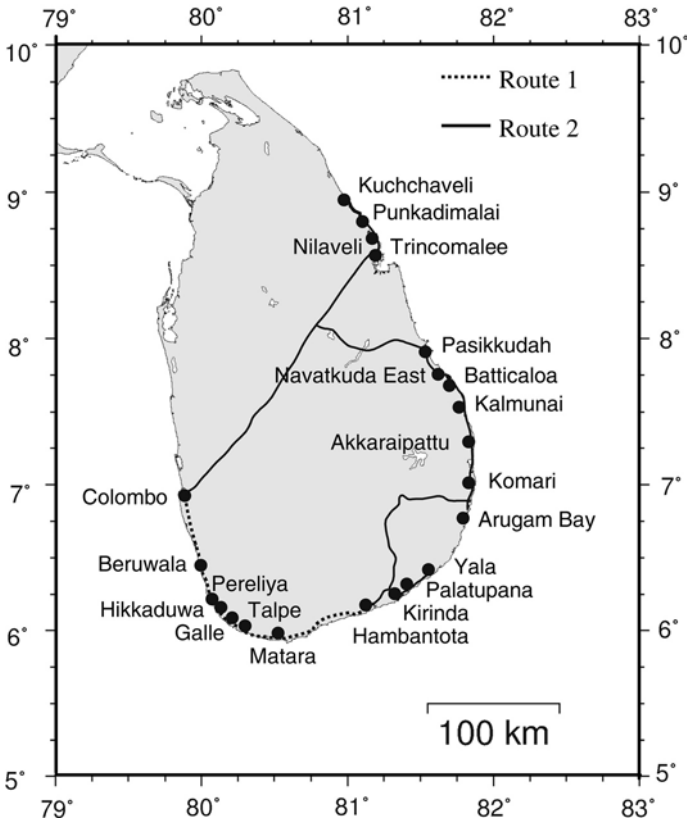


Figure 2
Field visit routes. 1st Route: Colombo, Moratuwa, Beruwala, Bentota, Pereliya, Hikkaduwa, Galle, Talpe, Matara, Tangalla, and Hambantota. 2nd Route: Colombo, Trincomalee, Kuchchaveli, Trincomalee, Polonnaruwa, Batticaloa, Arugam Bay, Yala National Park, and Kirinda.

of the low-cost masonry houses located in the coastal region were completely destroyed, while two story-buildings with concrete columns and beams sustained less damage. Figure 4 shows destroyed masonry houses near the Hambantota coast. More photographs of tsunami damage taken during the first field visit are given in WIJEYEWICKREMA *et al.* (2005). The second field visit from March 10–18, 2005 covered the NE, east, SE and south Sri Lanka and included Trincomalee, Kuchchaveli, Batticaloa, Arugam Bay, Yala National Park, and Kirinda. Some photographs taken during the second field visit are given in WIJEYEWICKREMA *et al.* (2006). The objectives of the second visit were mainly to obtain eyewitness information about wave arrival times and inundation data, and to take relevant measurements using GPS instruments.

In this paper tsunami arrival times are discussed in Section 2 and tsunami inundation heights and depths are discussed in Section 3. Remote sensing techniques,

Figure 3
Pereliya: Though this area is about 200 m from the coast, an express train was washed away by the tsunami and about 1,000 people lost their lives.

Figure 4
Hambantota: Masonry houses located within a few hundred meters from the coast were completely destroyed, a few more recently constructed houses had less damage.

especially the use of high resolution satellite images are quite useful to estimate tsunami damage, since the land surface of vast areas can be examined with high-resolution. In Section 4 inundation distances measured in the Batticaloa district are discussed and compared with the topography observed in IKONOS satellite images.

## *2. Tsunami Arrival Times*

Wave heights and wave arrival times recorded at tidal observation stations are very useful for calibrating numerical models of tsunamis. In the case of Sri Lanka, since there are very few tidal stations, eyewitness accounts of local people were

obtained to provide wave arrival times. The tsunami phenomenon is not limited to a single wave but a sequence of two or more main waves, including the maximum wave. Hence, in order to fully understand the tsunami, the wave arrival times of the main tsunami waves are very important.

Several eyewitnesses gave a similar account of the tsunami behavior at Bentota: The first wave came at 09:55 and inundated the land up to about 30 m from the shoreline. Part of the wave crest of this wave broke while approaching the coast and this happened at least four times. A few minutes later at approximately 10:00, the water then receded some 500 m exposing areas that are normally covered by the sea. A second wave arrived at approximately 10:30 with a height of about 3 m and crashed on the shore. Witnesses reported a foul odor when the second wave arrived. The third and largest wave arrived at 11:30 and had a height of about 5 m.

In addition to the eyewitness data, wave arrival times are also available from the following three sources:

(a) Data from the tidal observation station of the National Aquatic Resources Research and Development Agency (NARA) located in the Colombo Fisheries Harbor. The tidal record for December 25, 2004 – January 01, 2005 is shown in Figure 5. The tide record clearly shows the tsunami on December 26 and this unusual behavior continued until December 29. The detailed tidal record of December 26 is shown in Figure 5(b). The first wave of the tsunami is recorded at 09:48 with a water-surface elevation of 2.6 m above datum. Unfortunately, this tidal record does not contain the full time history and two time intervals are not properly recorded. It is possible that the maximum wave arrived around 12:00 consistent with eyewitness data.

(b) Time recorded on the clock tower located close to the Hambantota main bus station (Fig. 6). The clock had stopped due to the wave action at 09:22 and this time corresponds to the arrival time of the maximum wave according to an eyewitness who reported that the first wave was the biggest wave among the waves that attacked this area and the second wave was at 09:35.

(c) The arrival time reported by a seismologist (CHAPMAN, 2005) that the first wave arrived at 09:30, followed by the maximum wave at 10:10 and the third wave at 11:10.

The locations where tsunami arrival time data were obtained from eyewitnesses are shown in Figure 7, with the arrival times given in Table 1. We analyzed the reported wave arrival times to scan for obviously unreliable data that are inconsistent with other data and these are given in italics in Table 1. Some of the discrepancy in the eyewitness information may be due to residents who did not have watches during the tsunami and depended only on their sense of time. It is also possible that some eyewitnesses did not see all the waves as they escaped after the arrival of the first wave, and that some of them did not see the first wave

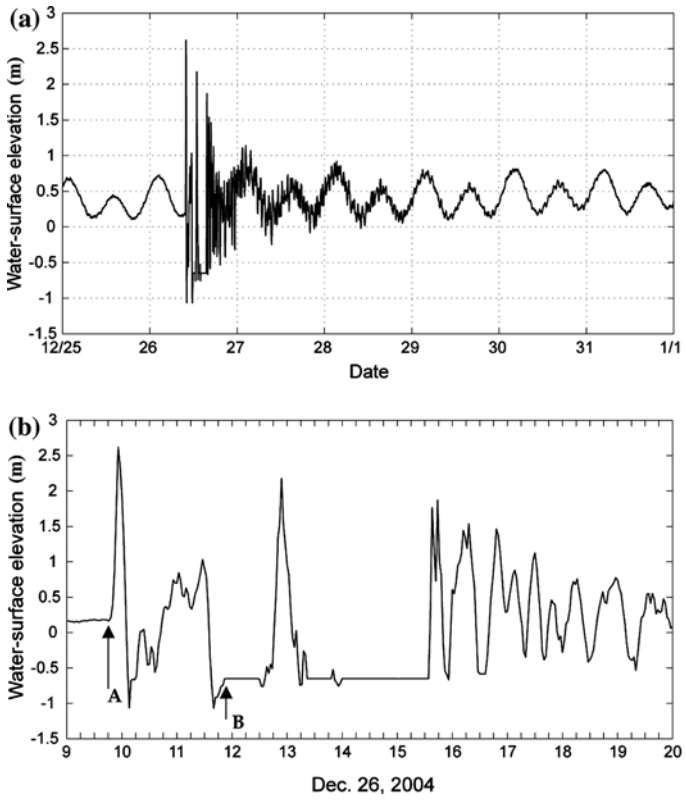


Figure 5
Tide-gauge record from Colombo Fisheries Harbor for (a) December 25, 2004–January 01, 2005, and (b) 09:00–20:00 December 26, 2004. The arrows in (b) indicate the first arrival recorded at 09:48 (A) and the probable arrival of the maximum wave at around 12:00 (B).

because they were not near the ocean at that time. For that reason, the first wave or maximum wave of an eyewitness does not necessarily correspond to the actual first wave or maximum wave.

Arrival times of the first wave and the maximum wave listed in Table 1 are shown in Figure 8. Here it can be seen that the first wave arrived at the eastern coast between 8:20–9:00, the southern coast between 9:00–9:22 and the western coast between 09:30–09:55. The maximum wave arrived at the eastern coast between 8:35–9:23, the southern coast between 9:13–9:50 and the western coast between 09:55–12:00. The velocity of the maximum wave along the western coast is observed to be slower than that of the first wave. It is most likely that at most locations, there were one or two waves before the maximum wave. The wave period on the western coast was greater than 30 min and on the eastern coast was less than 30 min. Before the maximum wave, the sea retreated for several hundred meters in some locations.

Figure 6
A broken clock close to the main bus station in Hambantota indicates 09:22. The Hambantota bay is on the left.

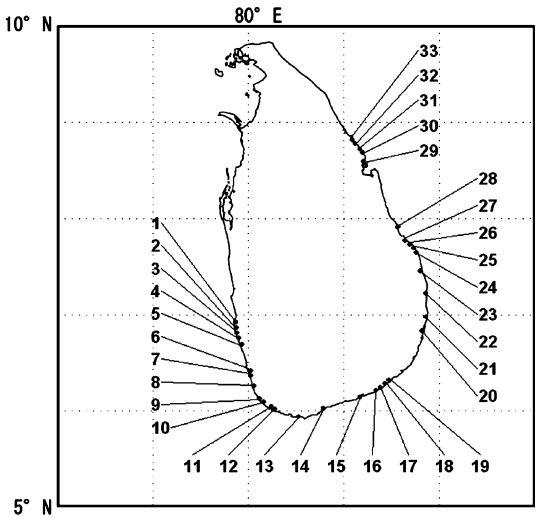


Figure 7
Locations of tsunami arrival time data obtained from eyewitnesses. The data is given in Table 1.

### *3. Tsunami Inundation Heights and Inundation Depths*

Tsunami height measurements are very important for many purposes such as tsunami modeling, tsunami disaster mitigation planning and tsunami education. During the second field visit from March 10–18, 2005, tsunami height measurements were carried out on the east and the SE coasts in Sri Lanka, based on tsunami evidence such as water marks, broken branches on trees, debris carried by the tsunami, dead vegetation and plants, and eyewitness accounts from tsunami survivors. The tsunami height measurements carried out were, tsunami inundation

Table 1

*Tsunami arrival times obtained from eyewitnesses*

| No. | Location | Date | Time (Local) | Tsunami arrival time | | |
|---|---|---|---|---|---|---|
| | | | | First wave | Second wave | Third wave |
| 1 | Colombo | 01/02/05 | 12:20 | 9:15-30 | **10:00-15** | - |
| 2 | Dehiwala | 01/02/05 | - | 9:45 | **11:45** | - |
| 3-a | Mt. Lavinia | 12/31/04 | 10:10 | *8:45* | 9:45 | - |
| 3-b | Mt. Lavinia | 12/31/04 | 10:10 | 9:45 | 10:15 | - |
| 3-c | Mt. Lavinia | 12/31/04 | 10:10 | 9:45 | **11:35** | - |
| 4 | Moratuwa | 12/31/04 | 10:45 | *10:30* | 11:00 | **11:05-10** |
| 5 | Panadura | 12/31/04 | 11:10 | *7:30* | 9:30 | **10:30-11:00** |
| 6 | Beruwala | 12/31/04 | 13:00 | 9:45 | 10:30-11:00 | - |
| 7 | Bentota | 12/31/04 | 14:20 | 9:55 | 10:30 | **11:30** |
| 8-a | Ahungalla | 03/17/05 | 12:00 | 9:20-35 | **10:15** | - |
| 8-b[1] | Ahungalla | 12/26/04 | - | 9:30 | **10:10** | 11:10 |
| 9 | Pereliya | 12/31/04 | 18:00 | 9:45 | **10:30** | - |
| 10 | Hikkaduwa | 12/31/04 | 17:10 | 9:30-35 | **9:50-10:00** | - |
| 11 | Galle Fort | 01/01/05 | 9:20 | 9:00-30 | 9:30-45 | **9:50** |
| 12 | Talpe | 01/01/05 | 10:30 | - | **9:45** | - |
| 13 | Matara | 01/01/05 | 11:55 | 9:15 | 9:25 | **9:40** |
| 14 | Tangalla | 01/01/05 | 13:40 | 8:45-9:15 | - | **9:20** |
| 15-a | Hambantota | 01/01/05 | 15:40 | **9:22** | 9:35 | - |
| 15-b | Hambantota | 01/01/05 | 16:20 | **9:10** | - | - |
| 16 | Kirinda | 03/16/05 | 14:30 | **9:15** | - | - |
| 17 | Palatupana | 03/15/05 | 14:45 | **9:14** | - | - |
| 18 | Palatupana | 03/15/05 | 16:00 | 9:15-20 | **9:18-23** | - |
| 19 | Yala | 03/16/05 | 10:24 | **9:10-15** | - | - |
| 20 | Arugam Bay | 03/15/05 | 6:45 | 8:20 | ***8:25*** | - |
| 21 | Komari | 03/14/05 | 18:10 | 8:45 | **9:20-25** | - |
| 22 | Akkaraipattu | 03/14/05 | 16:45 | 8:45 | **9:00** | - |
| 23 | Kalmunai | 03/14/05 | 15:30 | 8:45 | - | - |
| 24 | Kirittona | 03/14/05 | 9:10 | 8:30 | - | - |
| 25 | Kirittona | 03/14/05 | 7:30 | 9:00 | **9:05** | - |
| 26-a | Navatkuda East | 03/13/05 | 18:50 | 8:30-55 | **8:40-9:05** | - |
| 26-b | Navatkuda East | 03/13/05 | 18:50 | 8:15 | **8:45** | - |
| 27-a | Batticaloa | 03/13/05 | 16:50 | 8:30 | **8:31-32** | - |
| 27-b | Batticaloa | 03/13/05 | 16:50 | 8:30 | **8:35** | - |
| 28-a | Pasikkudah | 03/13/05 | 12:05 | 8:45 | **8:50** | - |
| 28-b | Pasikkudah | 03/13/05 | 12:05 | **9:00** | - | - |
| 28-c | Pasikkudah | 03/13/05 | 12:30 | 8:58 | **9:15** | - |
| 28-d | Pasikkudah | 03/13/05 | 12:45 | 9:05 | **9:20** | - |
| 29 | Trincomalee | 03/12/05 | 16:00 | 8:45-9:15 | **8:46-9:16** | - |
| 30 | Nilaveli | 03/12/05 | 10:00 | 8:55 | **9:00** | - |
| 31 | Nilaveli | 03/12/05 | 11:05 | 9:00 | **9:05** | - |
| 32 | Punkadimalai | 03/12/05 | 12:05 | 8:45 | **9:10-15** | - |
| 33 | Kuchchaveli | 03/12/05 | 15:00 | 8:45 | **8:52-53** | 8:58 |

Site Nos. correspond to locations given in Figure 7.
Arrival time of maximum wave shown in bold. Doubtful data in italics.
[1] CHAPMAN (2005).

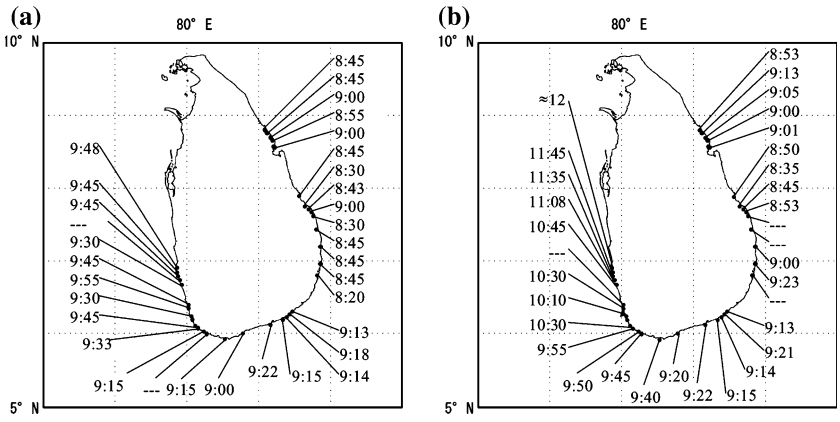


Figure 8
Arrival times of (a) first wave and (b) maximum wave, given in Table 1. When arrival times in Table 1 are given as a time range, the average is taken. For locations where data from multiple sources are available, the most consistent data was selected. Dashes indicate data is unavailable or inconsistent.

heights (heights measured from sea level), and tsunami inundation depths (heights measured from ground level) as defined by IUGG TSUNAMI COMMISSION (2005).

Tsunami inundation and inundation depths were measured using laser rangefinders and optical survey equipment. Position information was obtained by using a differential Global Positioning System (GPS). All tsunami height measurements were obtained by adopting the detailed guidelines given by INTERGOVERNMENTAL OCEANOGRAPHIC COMMISSION (1998). Because the sea-surface level at the time of tsunami arrival generally differs from that at the time of measurement, we corrected our observations using an astronomical tide table around the Indian Ocean given by TSUJI *et al.* (2005). Tsunami inundation heights and inundation depths are given in Table 2.

Corrected tsunami inundation heights measured at 17 locations (Table 2, 2nd column from right) are shown in Figure 9. On the east coast, the tsunami inundation height north of Trincomalee varies from 3.4–8.4 m, while south of Trincomalee it varies from 4.7–10.7 m. On the eastern and southeastern coast where the measured inundation height was greater than 5 m, most of the houses were swept away or severely damaged by the tsunami. Of the regions surveyed on the east coast, Kuchchaveli and Komari were the most severely affected areas. On the other hand, in the southeastern coast, in particular around Yala National Park, the inundation height is variable, which might be due to the local shallow coastal topographies. In Palatupana close to Yala National Park, the inundation height at the back of the lagoon is around 60% less than the inundation height at the front of the lagoon, indicating that the tsunami would be reduced by the lagoon.

Because of highly reliable information provided by CHAPMAN (2005), we recorded tsunami inundation data at Ahungalla on the west coast of Sri Lanka. CHAPMAN (2005) experienced the tsunami while a guest at a local hotel and reported details such

Table 2

*Tsunami inundation heights and inundation depths along the east and SE coasts of Sri Lanka*

| No. | Location | Date | Time (Local) | Latitude (N) | Longitude (E) | Descriptions | Rating | Rmax (m) | Corr. (m) | Corr. Rmax (m) | Inu. depth (m) |
|---|---|---|---|---|---|---|---|---|---|---|---|
| 1 | Nilaveli | 3/12/05 | 10:25 | 8° 41.542′ | 81° 11.674′ | coconut tree - EE | A | 8.6 | −0.2 | 8.4 | |
| 2 | Nilaveli | 3/12/05 | 11:10 | 8° 42.420′ | 81° 11.269′ | water mark on wall of house | B | | | | 2.0 |
| 3 | Nilaveli | 3/12/05 | 11:15 | 8° 42.437′ | 81° 11.361′ | coconut tree - EE | A | 5.6 | −0.2 | 5.4 | |
| 4 | Punkadimalai | 3/12/05 | 12:20 | 8° 47.421′ | 81° 07.265′ | top of the bridge | A | 3.5 | −0.1 | 3.4 | |
| 5 | Kuchchaveli | 3/12/05 | 15:00 | 8° 49.326′ | 81° 05.833′ | coconut tree - EE | A | | | | 6.7 |
| 6 | Kuchchaveli | 3/12/05 | 15:00 | 8° 49.315′ | 81° 05.827′ | water mark inside house | B | | | | 1.1 |
| 7 | Trincomalee | 3/12/05 | 16:55 | 8° 34.134′ | 81° 11.928′ | water mark on wall of NARA guest house | B | 3.3 | 0.5 | 3.8 | |
| 8 | Pasikkudah | 3/13/05 | 12:10 | 7° 55.442′ | 81° 34.064′ | broken branch on tree | B | 6.2 | −0.1 | 6.1 | |
| 9 | Pasikkudah | 3/13/05 | 12:45 | 7° 55.280′ | 81° 34.127′ | top of roof of hotel - EE | A | | | | 8.0 |
| 10 | Batticaloa | 3/13/05 | 17:30 | 7° 43.045′ | 81° 42.631′ | water mark on wall of house | B | | | | 0.8 |
| 11 | Batticaloa | 3/13/05 | 17:30 | 7° 43.060′ | 81° 42.636′ | water mark on wall of building | B | | | | 1.3 |
| 12 | Navatkuda East | 3/13/05 | 18:45 | 7° 41.129′ | 81° 44.452′ | death of the coconut tree - EE | A | 8.6 | 0.4 | 9.0 | |
| 13 | Kirittona | 3/14/05 | 8:20 | 7° 38.250′ | 81° 45.531′ | water mark on wall of house - EE | A | | | | 0.8 |
| 14 | Putukudiyiruppu | 3/14/05 | 10:05 | 7° 34.884′ | 81° 47.022′ | water mark on wall of house - EE | A | | | | 1.1 |
| 15 | Kalmunai | 3/14/05 | 15:35 | 7° 25.400′ | 81° 49.866′ | death of the coconut tree - EE | A | 7.2 | 0.4 | 7.6 | |
| 16 | Akkaraipattu | 3/14/05 | 17:00 | 7° 11.943′ | 81° 51.710′ | coconut tree - EE | A | 4.2 | 0.5 | 4.7 | |
| 17 | Komari | 3/14/05 | 18:15 | 6° 59.013′ | 81° 51.824′ | broken branch on the tree - EE | A | | | | 5.3 |
| 18 | Komari | 3/14/05 | 18:30 | 6° 59.001′ | 81° 51.888′ | coconut tree - EE | A | 10.3 | 0.4 | 10.7 | |
| 19 | Arugam Bay | 3/15/05 | 6:50 | 6° 50.489′ | 81° 49.966′ | cloth on tree - EE | A | 5.7 | 0.3 | 6.0 | |
| 20 | Palatupana | 3/15/05 | 15:20 | 6° 14.845′ | 81° 23.286′ | debris - EE | A | 4.9 | 0.2 | 5.1 | |
| 21 | Palatupana | 3/15/05 | 16:05 | 6° 14.796′ | 81° 22.774′ | coconut tree - EE | A | 3.2 | 0.3 | 3.5 | |
| 22 | Yala | 3/16/05 | 10:35 | 6° 20.459′ | 81° 29.829′ | broken branch on tree | B | 5.8 | −0.1 | 5.7 | |

| | | | | | | | | | | | | | |
|---|---|---|---|---|---|---|---|---|---|---|---|---|---|
| 23 | Yala | 3/16/05 | 11:20 | 6° | 20.657′ | 81° | 29.840′ | broken branch on tree - EE | A | 10.6 | −0.1 | 10.5 | |
| 24 | Palatupana | 3/16/05 | 13:40 | 6° | 16.523′ | 81° | 25.310′ | broken branch on tree | B | 5.9 | 0.1 | 6.0 | |
| 25 | Palatupana | 3/16/05 | 13:45 | 6° | 16.588′ | 81° | 25.233′ | roof of hotel broken by the water current | B | | | | 9.7 |
| 26 | Palatupana | 3/16/05 | 13:50 | 6° | 16.593′ | 81° | 25.240′ | debris on tree | B | | | | 11.0 |
| 27 | Kirinda | 3/16/05 | 14:55 | 6° | 13.071′ | 81° | 20.183′ | water mark on wall inside shelter | B | 8.5 | 0.2 | 8.7 | |
| 28 | Kirinda | 3/16/05 | 15:20 | 6° | 13.078′ | 81° | 20.157′ | water mark on wall of house | B | | | | 2.8 |
| 29 | Ahungalla | 3/17/05 | 12:05 | 6° | 18.687′ | 80° | 01.879′ | water mark on wall of Triton Hotel - EE | A | 4.3 | −0.1 | 4.2 | |

EE - eyewitness evidence.
Rating - A, very reliable physical evidence; B, moderately reliable, based on physical evidence and/or eyewitness.
Rmax - uncorrected tsunami inundation height.
Corr. - correction to account for tide difference between tsunami arrival time and measurement time.
Corr. Rmax - tsunami inudation height after tidal correction.
Inu. depth - inundation depth.
Location names taken from 1:50,000 topographical maps from Survey Dept., Sri Lanka.

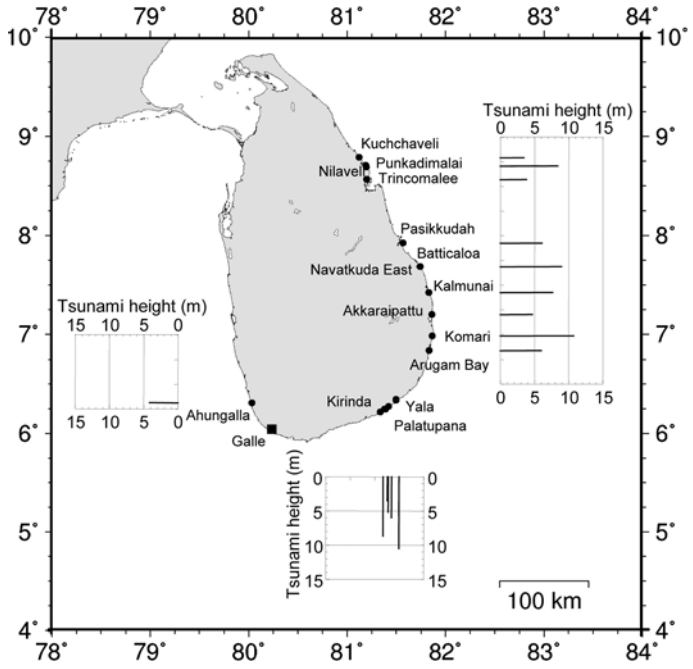


Figure 9
Corrected tsunami inundation heights along the east and SE coasts of Sri Lanka. The astronomical tide level at Galle was used as the reference site for the tide correction.

as the arrival time, the sequence of waves, and the response of the hotel guests and staff. A hotel staff member who had observed the tsunami was also interviewed. According to CHAPMAN (2005) and the hotel staff member, the biggest wave came at 10:10. The tsunami inundation height was estimated to be 4.2 m above sea level at the time of the event. The largest tsunami inundation height measured on the east coast was 10.7 m at Komari and on the southern coast was 10.5 m at Yala. LIU *et al.* (2005) have recorded the largest inundation heights of approximately 7.0 m at Kalmunai and Palatupana.

## *4. Investigation of Inundation Area in Batticaloa*

Batticaloa located on the east coast of Sri Lanka, was one of the districts that was severely affected by the tsunami. The number of deaths, missing people, completely damaged and partially damaged houses in the affected districts are given in Appendix B. In Batticaloa district 3,873 people were reported dead or missing while the number of completely damaged and partially damaged houses were 15,939 and 5,665, respectively. During the second field trip in March a GPS survey was carried out in the coastal region of Batticaloa.

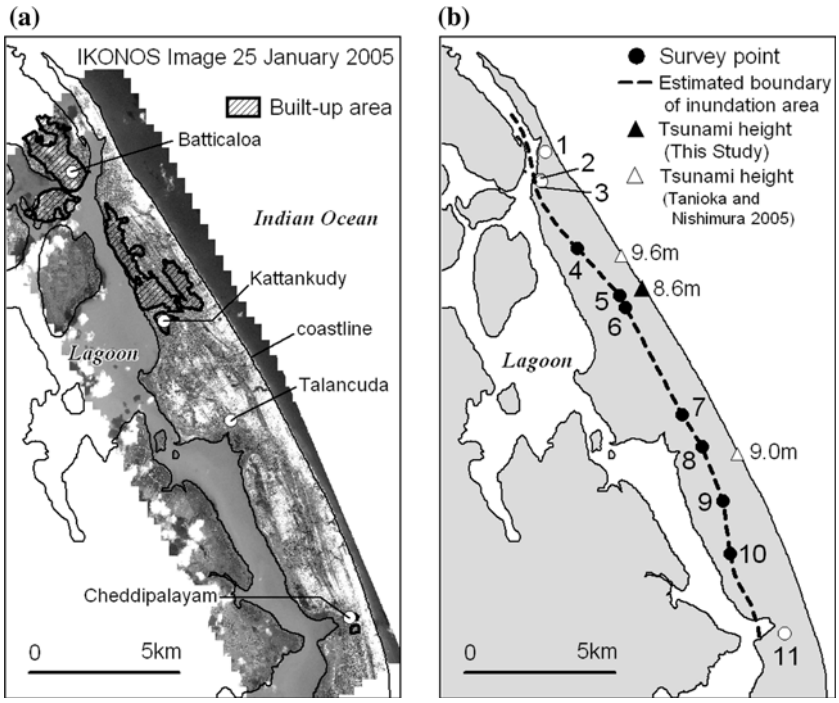


Figure 10
(a) IKONOS image with built-up areas in Batticaloa, (b) Locations of GPS survey points and estimated boundary of inundation area. Measured inundation depths and inundation distances are given in Table 3.

Figure 10(a) shows the map of the study area in Batticaloa with the IKONOS satellite image of 25 January, 2005. The hatched areas indicate the built-up areas taken from a land use map prepared in 1985. The survey was conducted in the spit area approximately 18 km by 10 km which is bordered by the Indian Ocean on the east and a lagoon on the west. Triangles in Figure 10(b) show the location of tsunami height measurements of TANIOKA and NISHIMURA (2005) and of this study, showing that tsunami waves with nearly 10 m heights attacked the region.

The boundary of the inundation area was determined based on the evidence of the tsunami eyewitness since it was difficult to detect the inundation boundary by using traces of the tsunami. The locations of the inundation boundary were measured by using a differential GPS (Ashtech ProMark2) which provides more accurate positions and elevations than stand-alone observations. One of the instruments was installed in Batticaloa Town as the reference site and the other was used for the observations. Horizontal locations and ground elevations are computed from the difference of the observation site and the reference site. Solid circles in Figure 10(b) show the locations of the inundation distance observations. Table 3 shows the measured inundation depth and the distance from the coastline at each site.

Table 3

*Tsunami inundation depths and inundation distances in Batticaloa District*

| No. | Latitude N (deg.) | Longitude E (deg.) | Ground elevation (m) | Inundation depth (m) | Distance from coastline (m) |
|---|---|---|---|---|---|
| 1* | 7.7263 | 81.7119 | - | - | 270 |
| 2 | 7.7177 | 81.7106 | - | 1.3 | 870 |
| 3 | 7.7173 | 81.7107 | - | 0.8 | 880 |
| 4 | 7.6971 | 81.7215 | 2.3 | 0 | 1,140 |
| 5 | 7.6828 | 81.7343 | 1.8 | 0 | 820 |
| 6 | 7.6793 | 81.7360 | 1.6 | 0 | 870 |
| 7 | 7.6471 | 81.7529 | 1.4 | 0 | 1,090 |
| 8 | 7.6375 | 81.7589 | 1.9 | 0 | 980 |
| 9 | 7.6213 | 81.7652 | 1.8 | 0 | 1,190 |
| 10 | 7.6053 | 81.7674 | 2.6 | 0 | 1,710 |
| 11* | 7.5814 | 81.7837 | 0.9 | 0.2–0.3 | 920 |

* The tsunami crossed over into the western lagoon.
Site numbers correspond to locations given in Figure 10.
Sites 4–10 yield inundation distance measured from the coastline.

According to the accounts of eyewitnesses, the tsunami crossed over into the western lagoon at sites 1 and 11 located in the northern and southern part of the survey area, respectively. Inundation depths were measured at sites 2 and 3 from tsunami traces left on the building walls. The depths at the sites were 1.3 m and 0.8 m, respectively. The dotted line in Figure 10(b) shows the extent of inundation estimated by taking into account the results of the GPS observations, the inundation depths and the accounts of the eyewitnesses. The result shows that the inundation distance from the coastline was between 800 and 1,800 m.

Inundation distances around sites 5 and 6 are approximately 800 m while at sites 9 and 10 the inundation distance was nearly double, some 1500 m. As shown in Figure 10(a), sites 5 and 6 are located in the center of a built-up area. Satellite images of sites 5 and 9 (Fig. 11) show how site 5 is surrounded by many buildings while site 9 is unpopulated and covered with sand and native bush. This suggests that inundation distances are lower in built-up areas because the momentum of tsunami would be weakened due to the collision with many buildings. It also indicates that inundation area would be wide in bare land, grassland or bushes because there are few obstacles to the propagation of the tsunami such as buildings or tall trees. More details of the inundation area in the Batticaloa region can be found in MIURA and MIDORIKAWA (2006).

## 5. Concluding Remarks

Measurements and observations of tsunami arrival times and inundation heights and depths were carried out on the western, southern and eastern coasts of Sri

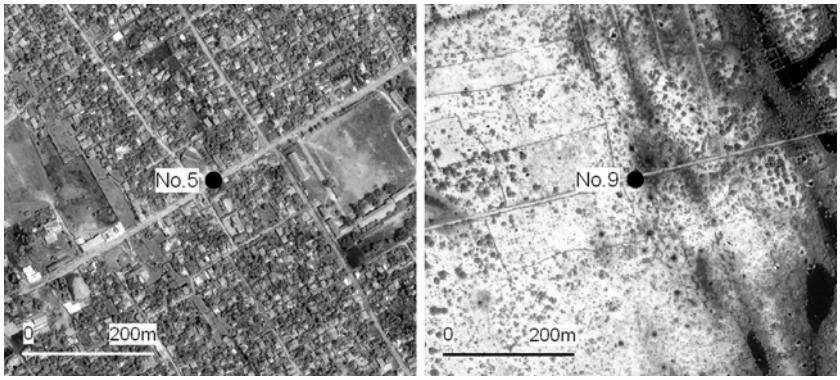


Figure 11
IKONOS images at sites 5 and 9.

Lanka. In addition a detailed survey of the inundation area was carried out in Batticaloa. In Sri Lanka the tsunami phenomenon was not limited to a single wave but a sequence of two or more main waves. The largest inundation heights were measured on the southeast coast and were greater than 10 m. The maximum inundation distance measured in Batticaloa was nearly 2 km.

This was the first time that a tsunami caused by an earthquake had affected Sri Lanka. The island nation had never anticipated a tsunami and consequent no contingency plans had been prepared. It is reported that although certain international tsunami monitoring agencies were aware of the tsunami before it reached Sri Lanka, no warning was conveyed to the Sri Lankan government, as no procedures to inform appropriate government officials were in place. Even if such a warning was received, it is doubtful that it would have been possible to inform the people living in the coastal areas, in a timely manner.

A question that was repeatedly asked by the people that were interviewed by the survey team was whether another tsunami would arrive again in the near future. It was explained that the probability of a similar magnitude earthquake triggering a tsunami from the same region was very low.

## *Acknowledgements*

The advice and support of Prof. Tatsuo Ohmachi, COE Program Leader of CUEE and Prof. Kohji Tokimatsu, COE Program Sub-Leader of CUEE, is gratefully acknowledged. Financial support for the tsunami field surveys in Sri Lanka from the Center for Urban Earthquake Engineering (CUEE), Tokyo Institute of Technology, is gratefully acknowledged. Shusaku Inoue and Hiroyuki Matsumoto acknowledge financial support for the second field visit from the Special Coordination Funds for Promoting Science and Technology from the

Ministry of Education, Sports, Culture, Science and Technology (MEXT). Tide gauge data recorded at Colombo were provided by the National Aquatic Resources Research and Development Agency.

## *Appendix A*

Table A

*Fatalities and missing persons due to the Sumatra-Andaman earthquake*

| Country | Fatalities | Missing[1] | Total |
|---|---|---|---|
| Indonesia | 130,736 | 37,000 | 167,736 |
| Sri Lanka | 35,322 | - | 35,322 |
| India | 12,405 | 5,640 | 18,045 |
| Thailand[2] | 8,212 | - | 8,212 |
| Somalia | 78 | 211 | 289 |
| Maldives | 82 | 26 | 108 |
| Malaysia | 69 | 6 | 75 |
| Myanmar | 61 | - | 61 |
| Tanzania | 13 | - | 13 |
| Seychelles | 2 | - | 2 |
| Bangladesh | 2 | - | 2 |
| Kenya | 1 | - | 1 |
| Total | 186,983 | 42,883 | 229,866 |

(UN Office of the Special Envoy for Tsunami Recovery, 2006).
[1] Some countries do not give separate figures for the deceased and the missing.
[2] In Thailand, fatalities include 2,448 foreign tourists from 37 other countries.

## *Appendix B*

Table B

*Casualties and Housing Damage in Sri Lanka*

| Province | District | Deaths | Missing people | Completely damaged houses | Partially damaged houses |
|---|---|---|---|---|---|
| Northern | Jaffna | 2,640 | 540 | 6,084 | 1,114 |
| | Killinochchi | 560 | 1 | 1,250 | 4,250 |
| | Mullativu | 3,000 | 552 | 3,400 | 600 |
| Eastern | Trincomalee | 1,078 | 337 | 5,974 | 10,394 |
| | Batticaloa | 2,840 | 1,033 | 15,939 | 5,665 |
| | Ampara | 10,436 | 876 | 29,077 | - |
| Southern | Hambantota | 4,500 | 963 | 2,303 | 1,744 |
| | Matara | 1,342 | 613 | 2,362 | 5,659 |
| | Galle | 4,216 | 554 | 5,525 | 5,966 |
| Western | Kalutara | 256 | 148 | 2,572 | 2,930 |
| | Colombo | 79 | 12 | 3,398 | 2,210 |
| | Gampaha | 6 | 5 | 292 | 307 |
| North Western | Puttalam | 4 | 3 | 23 | 72 |
| Total | | 30,957 | 5,637 | 78,199 | 40,911 |

Data as at 23/01/05 (National Disaster Management Center, 2005).

## References


CHAPMAN, C. (2005), *The Asian tsunami in Sri Lanka: A personal experience*, EOS *86*(2), 13–14.

INTERGOVERNMENTAL OCEANOGRAPHIC COMMISSION (1998), *Post-tsunami Survey Field Guide*, UNESCO Manuals and Guides *37*, 62 pp.

IUGG TSUNAMI COMMISSION (2005), *Compiling the trace height of Indian Ocean tsunami*, Internat. Un. Geod. Geophy. 8 pp.

LIU, P.L.-F., LYNETT, P., FERNANDO, H., JAFFE, B.E., FRITZ, H., HIGMAN, B., MORTON, R., GOFF, J., and SYNOLAKIS, C. (2005), *Observations by the International Tsunami Survey Team in Sri Lanka*, Science *308*(5728), 1595.

MIURA, M. and MIDORIKAWA, S. (2006), *Extraction of Tsunami inundation area in the eastern part of Sri Lanka due to the 2004 Sumatra earthquake using high-resolution satellite images*, Proc. *third internat. Conf. Urban Earthq. Engin.*, March 6–7, Tokyo, Japan, pp. 237–244.

NATIONAL DISASTER MANAGEMENT CENTER (2005), *Summary Report on Tsunami Disaster, Sri Lanka*, http://www.lankalibrary.com/news/summary.htm.

TANIOKA, Y. and NISHIMURA, Y. (2005), *Field Survey Result in Sri Lanka, The December 26, 2004 Earthquake Tsunami Disaster of Indian Ocean*, http://www.drs.dpri.kyoto-u.ac.jp/ sumatra/srilanka2/ (in Japanese).

TSUJI, Y., NAMEGAYA, Y., and ITO, J. (2005), *Astronomical tide levels along the coasts of the Indian Ocean*, http://www.eri.u-tokyo.ac.jp/namegaya/sumatera/tide.

UN OFFICE OF THE SPECIAL ENVOY FOR TSUNAMI RECOVERY (2006), http://www.tsunamispecialenvoy.org/country/humantoll.asp.

USGS (2006), *Largest Earthquakes in the World since 1900*, http://earthquake.usgs.gov/regional/world/10_largest_world.php.

WIJEYEWICKREMA, A.C., INOUE, S., and SEKIGUCHI, T. (2005), *Tsunami damage in Sri Lanka due to the Sumatra earthquake of December 26, 2004 – Preliminary reconnaissance*, Proc. *Second Internat. Conf. Urban Earthq. Engin.*, March 7–8, Tokyo, Japan, pp. 181–191.

WIJEYEWICKREMA, A.C., INOUE, S., MATSUMOTO, H., MIURA, H., GUNARATNA, P., MADURAPPERUMA, M., and SEKIGUCHI, T. (2006), *Report of two field visits to assess tsunami damage in Sri Lanka due to the Sumatra-Andaman earthquake of December 26, 2004*, Proc. *Third Internat. Conf. Urban Earthq. Engin.*, March 6–7, Tokyo, Japan, pp. 219–229.


(Received June 12, 2006, accepted October 18, 2006)
Published Online First: January 30, 2007

Pure appl. geophys. 164 (2007) 413–431
0033–4553/07/030413–19
DOI 10.1007/s00024-006-0171-6



Pure and Applied Geophysics

# Field Signatures of the SE-Asian Mega-Tsunami along the West Coast of Thailand Compared to Holocene Paleo-Tsunami from the Atlantic Region

DIETER KELLETAT, SANDER R. SCHEFFERS, and ANJA SCHEFFERS

*Abstract*—The Andaman-Sumatra Tsunami of Dec. 26, 2004, was by far the largest tsunami catastrophe in human history. An earthquake of 9 to 9.3 on the Richter scale, the extension of waves over more than 5000 km of ocean and run-ups up to 35 m are its key features. These characteristics suggest significant changes in coastal morphology and high sediment transport rates. A field survey along the west coast of Thailand (Phuket Island, Khao Lak region including some Similan Islands, Nang Pha mangrove areas and Phi Phi Don Islands) seven to nine weeks after the tsunami, however, discovered only small changes in coastal morphology and a limited amount of dislocated sediments, restricted to the lower meters of the tsunami waves. This is in striking contrast to many paleo-tsunami's events of the Atlantic region. Explanations for this discrepancy are sought in:
a. Mechanics of the earthquake. A rather slow shock impulse on the water masses over the very long earthquake zone,
b. Shallow water in the earthquake zone, and
c. Bathymetry of the foreshore zone at the impacted sites. Shallow water west of Thailand has diminished wave energy significantly.The differences in geomorphological and sedimentological signatures of this tsunami compared with many paleo-tsunami worldwide makes it unsuitable to be used as a model for old and future tsunami imprints by an event of this extreme energy and extension.

**Key words:** Tsunami, Thailand, run-up, sediment deposits, coral reef damage, comparison to paleo-tsunami.

## *Introduction*

During the last several years, new studies in paleo-tsunami research focusing on the sedimentological record in southern Europe and the Caribbean (SCHEFFERS, 2002a,b; 2004; 2005; SCHEFFERS and KELLETAT, 2003, 2005; KELLETAT and SCHEFFERS, 2004; SCHEFFERS *et al.*, 2005a,b), have turned up a treasure of novel information on tsunami characteristics. Significant tsunami relics, mostly as coarse sediments including large boulders up to 200 tons, have been discovered. Boulder ridges and ramparts, and often a bimodal setting of the sediment (floating boulders in

Dept. of Geography, University of Duisburg-Essen, Universitätsstrasse 15, D-45117, Essen, Germany.

sand) could be recognized. The sandy matrix was mostly chaotic without stratification. In 19 regions the tsunami impacts could be dated with radiocarbon and/or ESR, to dates between 250 BP and 4500 BP.

Some important questions regarding these paleo-tsunami deposits were left unsolved: Are all sedimentological characteristics of the tsunami events identified, or are some parts ignored due to post-tsunami weathering, storm wave impacts, washing out by heavy rain, or other processes? And: are the conclusions from the geological record on the tsunami energies more or less correct? Therefore we inspected the sedimentological imprints of the Sumatra-Andaman-Tsunami of 2004 (KOWALIK *et al.*, 2005; AMMON *et al.*, 2005; LAY *et al.*, 2005) shortly after the event and before vegetation could cover important aspects or monsoon rain would have washed out deposits. The fieldwork was focused on the west coast of Thailand comprising 150 km of coastline (Phuket, the Khao Lak area, central Similan Islands, the inner part of Phang Nga Bay, Ko Racha and both of the Phi Phi Islands in the south, see Fig. 1). The main aims were: (a) objectively documenting geomorpholog-

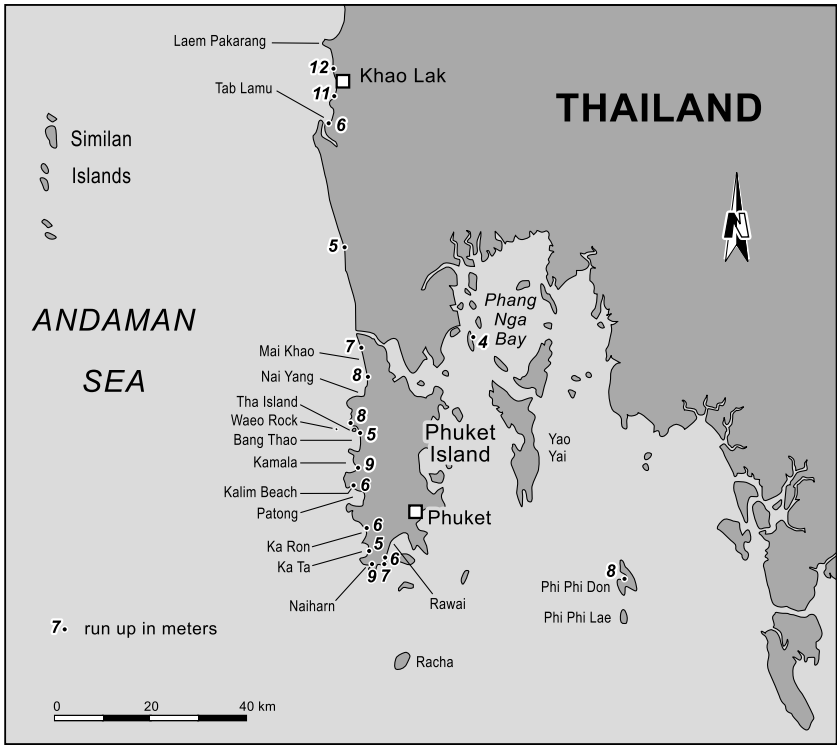


Figure 1
Regions visited along the west coast of Thailand in February, 2005, and heights of run-up identified in the field.

ical and sedimentological tsunami signatures (including at least a few spots of the coral reefs) along the special coastal setting of west Thailand, including tsunami heights as a measure of tsunami energy for sediment transport; (b) relation of the amount, setting and type of sediments left to the tsunami wave heights (and wave velocity, if possible); (c) developing an idea which of these tsunami signatures might be preserved in the geological record, and (d) which conclusions scientists long after will conclude from these signatures on the event itself, and whether these conclusions are in accordance with the event's category or not—keeping in mind similar conclusions from many other paleo-tsunami sites, where we use the relics to reconstruct the event's parameters.

## *Methods Used*

At all sites visited we took inundation widths from satellite images (Quick Bird and Ikonos) as a rough frame and measured the height of the waves by vertical reach of mechanical destruction at trees and buildings to judge the tsunami wave height at the coastline. The basis of the measurements has been the barnacle and oyster line as a rough measure for mean high water. Tsunami water height might have been 0.5 to 1 m higher than broken twigs, etc. because of grass or leaves left in trees. In fine tsunami sediments at a few sites we cut small trenches to see the base, thickness and character of setting. Additionally we took several sand samples for OSL inspection (i.e., testing to find the expected zero signal). The height of extended deposition was measured in the field and coarse tsunami deposits (in particular boulders of significant size) were determined for weight, height and place of origin. To determine these figures we took a conservative mean of the axes figures for volume, multiplying with mostly 2.5 for density to gain the weight. Calcium has a density of 2.7, granite normally 2.6, but the different corals may go down to about 2.0. The *Porites* sp., however, which are the largest coral boulders present, have a very dense skeleton which might have a density of around 2.3. In any case we took all figures very conservative to guarantee a minimum value of volume or weight. Video documents focusing on changes in reef structure and damage to scleractinean corals were taken by means of snorkeling and SCUBA diving. Very useful information could be gained from eyewitnesses of the waves, including original videotapes, the latter as well to identify the water flow velocity across the shoreline and the tsunami wave height before reaching the coastline.

## *Results and Discussion*

### *Inundation*

In determining inundation values, the best estimates can be obtained from high quality satellite images, although groundtruthing is a must. Vegetation debris like

Figure 2
Vegetation debris marks the inland inundation line near Tap Lamu south of Khao Lak.

leaves and twigs (Fig. 2), rubbish as well as a very thin, light colored, sand carpet mostly marks the inland reach of inundation. Its extension in Thailand showed the most extreme values north of Khao Lak (Laem Pakarang) where the tsunami reached 5 km land inwards (see also GHOSH *et al.*, 2005). In the center of Khao Lak values were mostly around 400 to 600 m on flat ground, and the highest values on Phuket Island were found in the south of Nai Yang Beach where the inundation reached about 400 m. In the southern bays of Phuke's west coast, inundation was not more than approximately 400 m, evidently restricted by the densely set buildings, and at the rocky promontories inundating values mostly did not surpass 10 to 20 m.

*Run-up Heights*

To determine run-up heights, i.e., the vertical reach of tsunami waves (in the December 26 tsunami case in Thailand, wave no. 4 rode on top of wave no. 3 and therefore was designated as the highest wave), it is difficult to measure the exact values after the event. What is left behind everywhere in the landscape is damaged at trees and buildings, but these marks document an impact not necessarily identical to the maximum water level. Therefore run-up heights gained by these observations are conservative estimates, maybe 0.5 to 1 m lower than the real maximum, because we found at several places grass or dead leaves attached to trees several decimeters higher than the highest broken twigs or bark incisions. Many of the older and higher trees (Coconut Palms, Casuarinas, *Pandanus sp.*, *Araucaria sp.*, etc.) have survived the tsunami (Fig. 3), therefore numerous trees with traces on them to determine impact heights could be found. These traces consist of severe damage with broken off branches (Fig. 4) or deep incisions in the stems (Fig. 5) as well as very tiny ones on

Figure 3
Kasuarina plantation at Mai Khao Beach on a 4-m high beach berm has survived a tsunami flow depth of 4-5 m.

Figure 4
Damage to branches of a Kasuarina tree at 10 m asl in Khao Lak.

Figure 5
Fresh scars on a coconut tree at 7 m asl inside Naiharn beach.

the bark. The vertical wave heights determined on trees are mostly consistent with heights determined from damage to buildings, in particular at lightly constructed roofs (Fig. 6). Values of tsunami wave height by these measures reach a maximum of 12 m above the high water mark (spring tide range is mostly around 1.5 m, and the tsunami waves came during nearly low tide) in Khao Lak, about 9 m at Kamala Beach and Naiharn Beach on Phuket island, 8 m on Phi Phi Don and Bang Thao Bay, but only around 5 m at Tap Lamu or in the southern Bays of Phuket. Waeo Rock about 1 km west of Tha Island in front of the northern part of Bang Thao Beach allows—regarding dead and green leaves on the trees—reconstruction of the contour of the highest tsunami wave (Fig. 7). Nearly without impeding at the small rock outcrop in deep water it has had a height of about +8m. Photos as well as videos from the arrival of the highest tsunami waves in this region allow a very good reconstruction of the condition: The tsunami wavefront, consisting of 2 parallel foam belts (i.e., wave no. 4 riding on wave no. 3), narrowed in a straight line from the west. The height of the double wave front could be estimated to be approximately 8 m by two Police Patrol Boats and smaller sail ships with masts at least 6-m high riding the wavefront. The green leaves at around +8 m coincide with these observations, and Waeo Rock nearly has not deformed the tsunami front wave significantly. More important to mention is the nearly perfect preservation even of tiny and fragile corals around the rock, which is a famous snorkeling and diving spot. It also should be

Figure 6
Damage up to a level of at least +9 m on roofs at Kamala Beach.

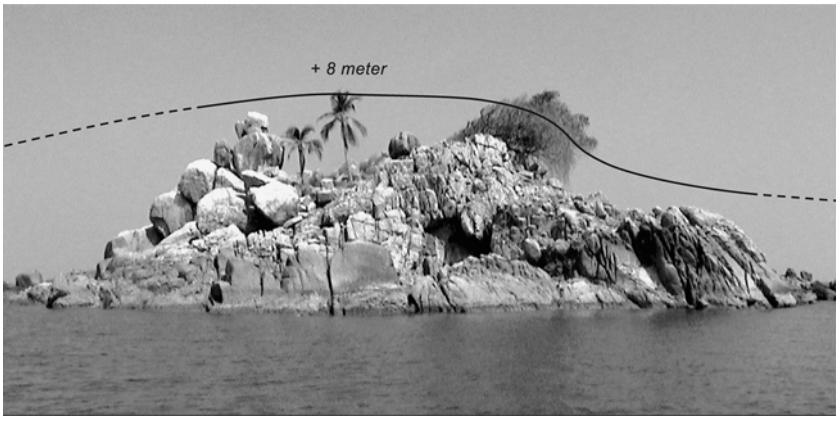


Figure 7
Contour of the highest tsunami wave at Waeo Rock.

stated that the most catastrophic tsunami in the history of mankind regarding the number of fatalities, the Sumatra-Andaman tsunami of 2004 does not fall within the category of wave events with the highest ranking run-ups during the last centuries (Fig. 8) or even the Holocene. Since the year 1600 AD at least 18 tsunami have had the same or much higher maximum run-up values, and from these several have had these heights for extended regions like that of Lisbon 1755, or the three Pacific Ocean mega-tsunami of 1946, 1960, and 1964.

The term, ''run-up'' gives the impression that the highest watermark can be found along rising land and slopes inland, i.e., at the landward end of inundation. At Khao Lak, Kamala Beach and other places this is not the case: The highest values were

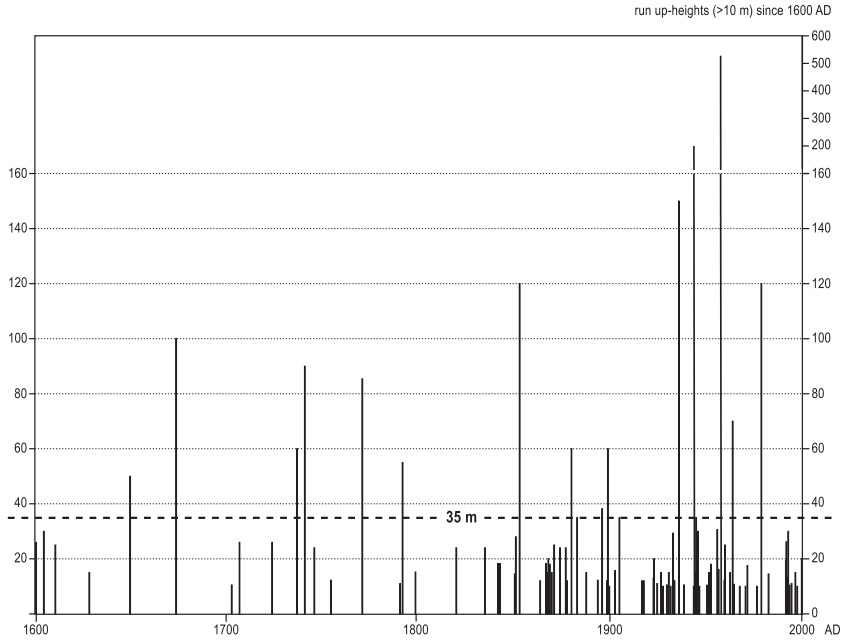


Figure 8
Maximum run-up values of strong tsunami since 1600 AD (acc. to NGDC, 2001).

found close to the shoreline, sinking down to inland because of friction on buildings and vegetation.

Run-up values are clearly determined by water depth in the foreshore area, which is even 20-30 km beyond the coast of western Thailand not more than 80 m. At steep obstacles as well as in bays with deeper water and where refraction of the tsunami waves from SW to E or even SE such as at Kamala or Patong occurred, values are higher than along open and straight shorelines.

Our knowledge of damage on corals or coral reefs is restricted to the southern and northern end of Similan Island no. 6, Ko Racha Noi, Waeo Rock, northern coast of the Phi Phi Don tombolo, the southern part of the Nai Yang Beach (Fig. 9) and Naiharn Beach area.

*Coral Reef Damage*

At all places significant physical damage to coral colonies could be found, but it is restricted to local points directly exposed to the tsunami waves as well as leeward ends of reefs where the waves converged. Reefs in between were spared. Most physical damage was concentrated in the first 10 m, although some deeper reefs were affected, due to gravitational downward transport of colonies. By far the most extensive and sustainable damage is the result of sediment deposition on the corals.

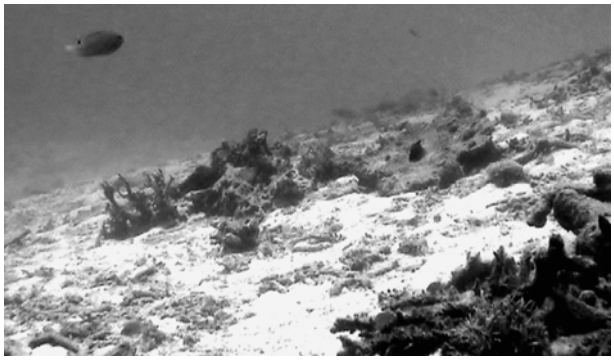

Figure 9
Damage on Reef no. 3 in front of Nai Yang Beach.Water depth is approximately 5 m.

Sand and mud transported by the tsunami covered nearly 90% of the coral (e.a. *Acropora clathrata*) directly in front of the mainland, shown exceptionally clear at reef no. 3 in front of southern Nai Yang Beach. All coral tissue under the fine sediment layer was deceased. Even 7 weeks after the tsunami, coastal waters were very turbid; sedimentation is expected to take its toll on the remaining live corals. Many large coral colonies (mostly *Porites lutea*) north of Phi Phi Don have been dislocated, but the coral tissue was still alive. The reefs around the Similan Islands were not covered with sediments and the water was clear. This is due to the fact that the Similan Islands are composed of granite with a very thin layer of soil and the tsunami could not dislocate large quantities of (anthropogenic-) sediments and saturate the water column.

*Fine Sediment Transport*

Dislocated sheets of sand onshore can be seen nearly everywhere, but they are thin (centimeters to decimeters) and only locally more than 2 m (restricted to the leeward side of steep beach ridges closing ephemeral streams at Patong Beach and Naiharn Beach). The tsunami waves washed the sand from the beaches (which are now at places much steeper) and the foreshore area land inwards. The latter mostly shows angular mineral fragments of quartz, feldspar and mica (Fig. 10) deriving from the chemical deep weathering of the granite rocks, however, the sorting is quite well, i.e., a medium fine sand. The brown mud, which could be seen on many of the eyewitness's videos, is mostly gone in suspension and now deposited in deeper water. On land the tsunami sand is settled on top of the soil and grass without any destruction or discordance a short distance to the shore zone, and this mostly sand composition is clearly stratified showing heavy mineral strata (Fig. 11). Both facts are in disagreement with a description of paleo-tsunami sand layer characteristics in the literature (DAWSON, 1994, 1996; DAWSON and SHI, 2000; DAWSON et al., 1991;

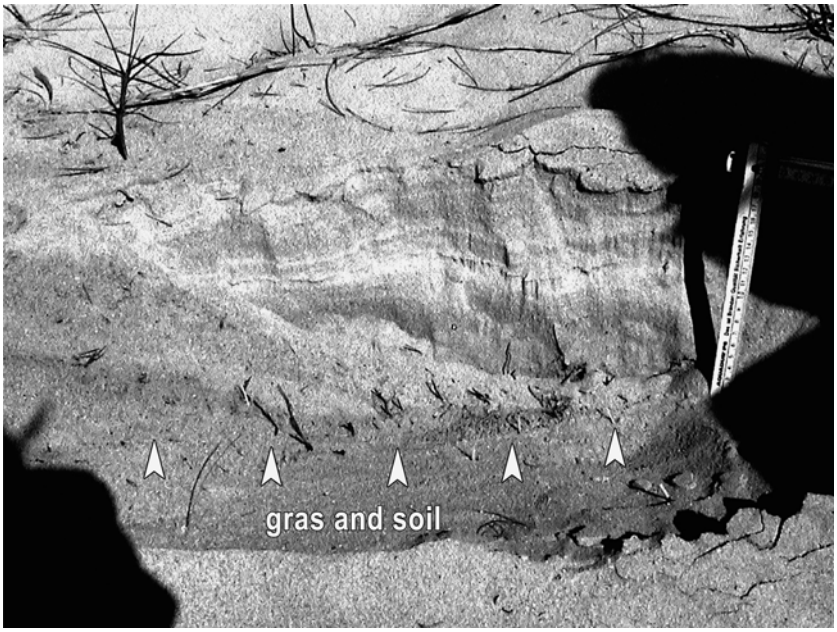


Figure 10
Stratified sand layers about 25 cm thick at Bang Thao Bay.

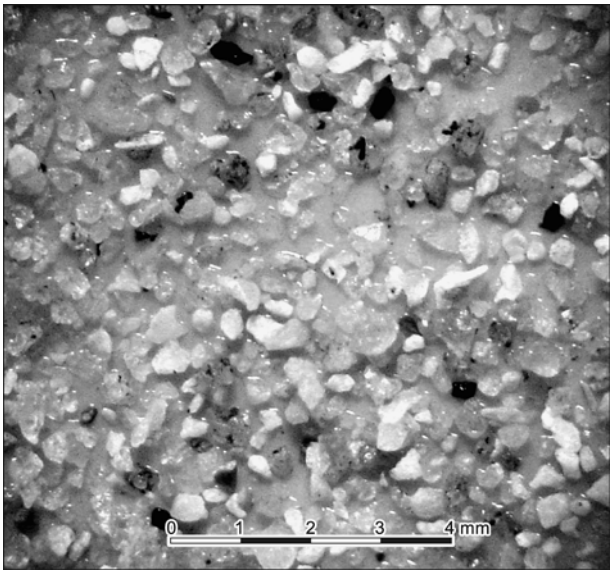


Figure 11
Fine angular sand grains from fresh tsunami deposits (Loc. of Fig. 10).

Figure 12
Pattern of bent grass leaves from a tsunami wave vortex in the northern part of Bang Thao Bay.

GELFENBAUM and JAFFE, 2003; KEATING *et al*., 2005; KELLETAT and SCHEFFERS, 2004; or SHI *et al*., 1995 ). However, no discordance and a very good stratification of sand deposits is corroborated by preliminary data from Sri Lanka (USGS, 2005a,b) or southern India (SOI, 2005). As has been discussed during the recent Tsunami Field Symposium on Bonaire in March, 2006 (Jaffe et al., 2006, compare also Moore et al., 2006) there is to date no clear differentiation between tsunami-deposited and storm-deposited sand layers, and most of these fine sediments show the characteristics of both processes. Whereas, as has been documented by USGS (2005 a,b), tsunami sand deposits may show perfectly fine stratigraphy with heavy mineral layers and good sorting, sandy storm sediments do not exhibit unsorted chaotic structure or thicker graded bedding. At some places as seen in the northern part of Bang Thao Beach even long grass has been bent down and formed into vortices without any destruction (Fig. 12).

*Coarse Sediment Transport*

Discussing coarse tsunami deposits may lead to some confusion using the normal terms for clast size. As we have worked on many sites with an extreme amount of decidedly large boulders (200 tons and more), we would like to call them mega-boulders in contrast to fragments of a size of more than 0.2 m which start to represent the boulder category. As mega-boulder is no set term, we have used it in relation to the individual situation: If normal tsunami boulders are around several tons, a 50 ton boulder may be called a mega-boulder, however, if the majority of tsunami boulders are beyond 50 tons (as in the north of the Bahamas or parts of Bonaire), the term mega-boulder should be restricted to the very largest ones.

One of our main aims of research was the comparison of the SE-Asian mega-tsunami with the sedimentary results of paleo-tsunami elsewhere, for which we do not know the exact energy or wave heights. Therefore we were surprised not to find larger amounts of coarse debris onshore such as boulder ridges or ramparts or single boulders far landward or high above the water level. One of the possible arguments for this circumstance can be clarified easily: Along the west coast of Thailand nearly everywhere boulders of different size (from less than one ton to more than 100 tons) are available, either from the living coral reefs, or from a former chemical deep weathering with woolsack formation. But these boulders have been moved only at very few sites and in a limited amount.

Coral debris deposits along the shoreline or on land are scarce. The same has been found by KEATING et al., (2005) and by KENCH et al. (2005) for the Maldives (where the largest fragment transported on land by the tsunami measured only 0.25 m!). The most extended area is a newly formed broad spit of coral rubble separating the southernmost sandy beach of Nai Yang from the open sea (Fig. 13), covered by water during mean water and high tide. The fragments have sizes up to 0.5 m and weights from several kg to about 100 kg. They are covered by mud and on first sight difficult to identify as fresh coral debris. The same can be observed along Kalim Beach north of Patong, where a coral rubble zone (about 500 m long and up to 80 m wide only visible at low water level) has been deposited (Fig. 14). In general, coarse debris is rarely transported against gravity.

From nearly all sites studied for Holocene paleo-tsunami, the authors have described large boulders transported as a prominent feature, and it was expected from this mega-tsunami, as well. However, the Sumatra-Andaman-Tsunami with

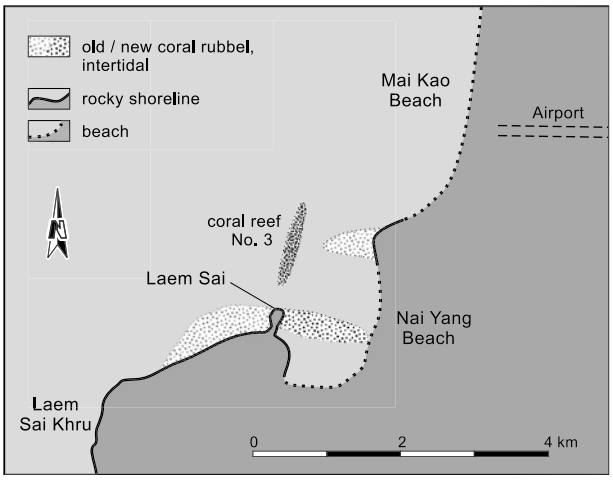


Figure 13
Sketch of the newly developed rubble spit in the southern section of Nai Yang Beach, Phuket.

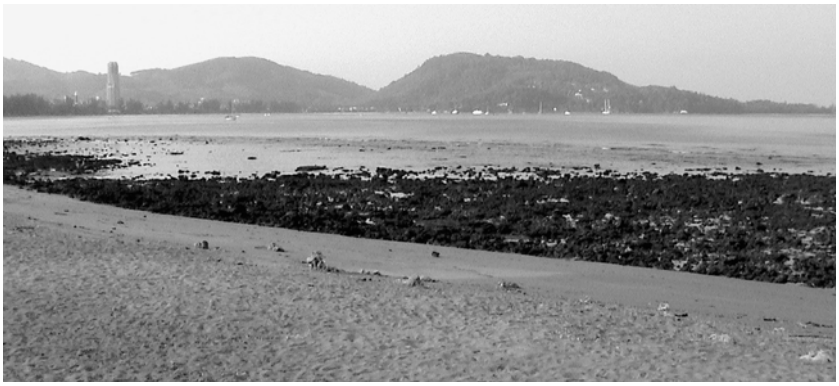

Figure 14
Coral rubble with mud covering at low tide in front of Kalim Beach north of Patong.

- quake force of 9.3 on the Richter scale,
- a horizontal movement of the ocean bottom of 13 m to the west and a vertical one of 2–3 m,
- affecting approximately 100.000 $km^2$ (GFZ: GeoForschungszentrum Potsdam, Germany, Infoblatt Tsunami, Version 05/05)
- 5000 km of deadly coverage,
- more than 30 m run-up along northwest Sumatra (TSUJI *et al.*, 2005) and more than 10 m run up 2000 km away at southeastern Sri Lanka (LIU *et al.*, 2005),
- with about 225, 000 victims (figure published by the International Red Cross disaster report for 2004),

was not able to dislocate large boulders against gravity in a significant amount—judged from the west Thailand field experience. There is no existing report to demonstrate the displacement of natural large boulders in any area affected by the 2004 tsunami. At Kalim Beach we found coral debris up to 0.5 tons at +2m and close to +4m, and at Khao Lak two large granite boulders (4 tons and approximately 10 tons) have been dislocated for a distance of less than 5 m. In the small bay south of Naiharn Beach (Nai Harn Noi) some large coral boulders were visible in the tidal area; one approximately 4 tons and the largest weighting of approximately 10 tons (Fig. 15). These boulders have been transported for more than 100 m and approximately 3–4 m against gravity, nonetheless their contact with the bottom and damage during transport is slight, indicating a strong swash process. Another boulder of approximately 3 tons nearby has been smashed and in the process is broken in 2 pieces.

The largest dislocated coral boulders could be found along the northern shore of the Phi Phi Don tombolo. Several of them could be clearly identified on satellite images, but are now covered by sand and mud. The largest live coral boulder moved has a weight of more than 40 tons (Fig. 16). This coral colony (*Porites lutea*) was

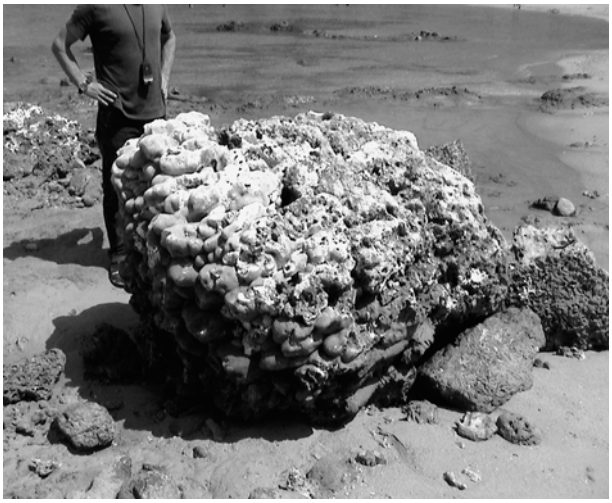

Figure 15
Boulder of nearly 10 tons from a coral pinnacle at Nai Harn Noi Beach in the tidal area.

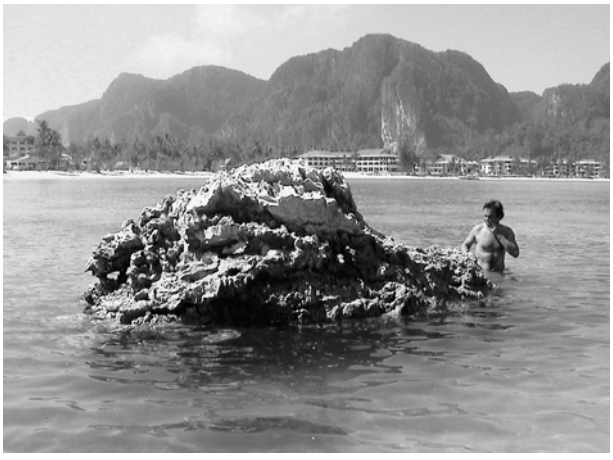

Figure 16
Boulder of about 40 tons dislocated from deeper water at a distance of at least 150 m into the eulitoral north of the Phi Phi Don tombolo at Loh Dalam Bay.

dislocated from approximately 5 m of water depth and transported against gravity over a distance of at least 150 m. Offshore in a water depth of 4 to 8 m many more coral colonies with even greater weight have been attacked by the tsunami waves, but are only tilted. At some places debris from the Phi Phi Don settlement has been caught under the boulders.

Even on pictures from fringing coral reefs uplifted during the large earthquake (8.7 on the Richter scale) of March, 28, 2005, from the island chain west of Sumatra (e.g., Nias or Simeulue) which have suffered from the December 26, 2004 tsunami, no sign of boulders or significant reef destruction is visible although situated very close to the epicenter.

*Changes in Geomorphology and Vegetation*

Transformation of the coastline by the tsunami can only be observed at certain places. Along rocky granite shorelines there are no signs of change. Sandy beaches mostly have configured a steeper profile, and a larger amount of sand has been transported onshore or to the foreshore. On the northern part of Bang Thao Beach the waves curving around Tha Island have abraded more than 20 m of a sandy shore platform at +1 m above the high water mark, and many Coconut trees have been uprooted (Fig. 17). Tidal creeks have been widened for about 1 m and deepened for about 20–30 cm. A similar picture, but with a smaller amount of tree cutting, can be seen along the southern shores of Khao Lak.

At the steep limestone coasts of Phang Nga Bay as well as on Phi Phi Don and Phi Phi Lae deep bio-erosive notches are characteristic of the tidal area. A bench of rock oysters up to more than 1 m wide and only 20–30 cm thick delicately reaches out into the sea over deep water at high water level. Over a stretch of many kilometers, we noticed only at 2 places that these benches have been recently broken off (for an extension of 2–3 meters).

In general, the impact of the Sumatra-Andaman-Tsunami of 2004 on coastal geomorphology was minimal along the west coast of Thailand compared with many

Figure 17
Abraded sandy cliff with uprooted coconut trees in the northern section of Bang Thao Bay.

paleo-tsunamis of unknown energy and wave height in the Atlantic region. However, along shorelines with artificial protection, damage to these constructions can be clearly detected. One of the reasons for the low impact on the coastal morphology of western Thailand is the rather slow speed of the tsunami waves crossing the shorelines, detected from video tapes being less than 8 m/s or less than 30 km/h. This resulted in transport energy too low for moving larger boulders.

Most of the higher vegetation survived the wave attacks. This is in striking contrast to the paleo-tsunami of Lisbon (1755 AD, compare SCHEFFERS and KELLETAT, 2005), or that of Cyprus about 250 to 300 years ago (KELLETAT and SCHELLMANN, 2001, 2002), where vegetation including roots was totally removed up to 16 and 50 m above sea level.

Run-up and inundation can easily be reconstructed by damage to trees and buildings, although this evidence will disappear in a short geological time. Sand deposits are limited to rather thin layers and will be transformed by bio-turbation or redistributed by heavy monsoon rain in years and decades as well as covered by dense vegetation. Boulders of significant size, which cannot be dislocated by a force other than a new strong tsunami, can only be found close to the shoreline in a very limited number. Calculating run-up values from the position of these boulders will give a totally wrong idea from the wave height of this tsunami, i.e., resulting in maximum run-up heights of 8–10 m lower than in fact have occurred. In our paleo-tsunami studies of the Intra-Americas Seas or southern Europe we often found mega-boulders from tsunami of unknown wave height and energy up to 10 or 20 m asl, which means that the run-ups have had at least these dimensions. Another way may be to calculate the tsunami wave heights by means of the boulder axes according to the equations of NOTT (2003), where the submerged and joint bound scenarios would be fitting best. However, this way will not lead to any information regarding the realistic tsunami wave height, because the NOTT equations are calculated to find wave heights "to overturn" a boulder, but the tsunami boulders of Thailand and other areas have been broken or moved from foreshore areas and dislocated for longer distances many meters against gravity, all of which is not included in the NOTT formulas and open to further discussion.

## *Conclusions*

Direction, strength, run-up and other parameters of paleo-tsunami are mostly identified in the field by specific deposits and coastal forms. Because of the extreme energy of the Sumatra-Andaman-Tsunami of 2004 one could expect, that it would at least surpass the signatures of many past tsunami. This is not the case, concerning effects on nature, which would leave behind signatures in the geological record like extended and thick sediment units, ridges or ramparts of coral debris onshore, large boulders surviving as landmarks for centuries or thousands of years. Furthermore, in

the area of highest run-up (around 35 m in W-Sumatra) no significant mega-boulder dislocation high and far inland has been reported. In contrary, the fringing reefs around Nias and Simeulue Islands west of Sumatra, which are situated very close to the epicenter of Dec. 26, 2004, with tsunami wave heights of approximately 30 m and uplifted by the 8.7 quake on March 28, 2005 show perfectly preserved coral colonies and no boulders or destruction for square kilometers, and the coastal vegetation along the beaches is intact, as well. It might be that at other coastlines affected, in particular along the northwest coast of Sumatra, the signatures of this mega-tsunami are much clearer and much more impressive, as may be shown by the vegetation-free inundation areas, or the mangrove destruction on Andaman and Nicobar Islands according to the earliest satellite images.

Now, about 15 months after the tsunami, we have not found any source describing spectacular boulder sizes or boulder fields, boulder ridges on land etc., as they have been demonstrated from paleo-tsunami of the Caribbean (ROBINSON *et al.*, 2006; SCHEFFERS, 2005) or Australia (BRYANT, 2001) from former tsunami. Therefore we will warn for taking this tsunami as a model for paleo-tsunami reconstruction or for modeling future events as a totally wrong picture from the real tsunami risk in this region can be deducted. The rather small impact of this tsunami on nature, possibly the result of shallow water along the west coast of Thailand (but not around the Maldives or Sri Lanka or parts of Sumatra!) and—maybe—a slow impulse of movement along the fracture zone—approximately 7 minutes duration along the 1200 km of the fault, moving from south to north (see also AMMON et al., 2005; KRÜGER and OHRNBERGER, 2005; or STEIN and OKAL, 2005)—can be the explanation, that strong tsunami in the northern part of the Indian Ocean were unknown so far. Maybe they have occurred, but their signatures might have been as weak as those from December 2004.

## *Acknowledgements*

This work was funded by a grant from the German Research Foundation (DFG, Ke 190/22-1), which we greatly appreciate.

## REFERENCES

AMMON, C.J., JI, C., THIO, H.-K., ROBINSON, D., NI, S., HJORLEIFSFOTTIR, V., KANAMORI, H., LAY, T., DAS, S., HEIMBERGER, D., ICHINOSE, G., POLET, J., and WALD, D. (2005), *Rupture Process of the 2004 Sumatra-Andaman Earthquake,* Science *308*, 1133–1135.

BRYANT, E. *Tsunami – The Underrated Hazard* (Cambridge University Press) (2001) 320 pp.

DAWSON, A.G. (1994), *Geomorphological effects of tsunami run-up and backwash*, Geomorphology *10*, 83–94.

DAWSON, A.G. (1996), *The geological significance of tsunami*, Zeitschrift für Geomorphologie NF Suppl. Bd *102*, 199–210.

DAWSON, A.G. and SHI, S.Z. (2000), *Tsunami deposits*, Pure Appl. Geophy. *157*(6–8), 875–897.

DAWSON, A.G., FOSTER, I.D.L., SHI., S., SMITH, D.E., and LONG, D. (1991), *The identification of tsunami deposits in coastal sediment sequences*, Science of Tsunami Hazards *9*(1), 73–82.

GELFENBAUM, G. and JAFFE, B. (2003), *Erosion and sedimentation from the 17 July, 1998 Papua New Guinea Tsunami*, Pure a Appl. Geophys. *160*, 1969–1999.

GFZ (2005), *GeoForschungszentrum Potsdam*, URL: http://www.gfz-potsdam.de.

GHOSH, S., HUYCK, C.K., ADAMS, B.J., EGUCHI, T., YAMAZAKI, F., and MATSOUKA, M. (2005), *Preliminary Field report: Post-tsunami Urban Damage Survey in Thailand, Using the VIEWS Reconnaissance System*, URL: http://mceer-nt4.mceer.buffalo.edu/research/tsunami/print.htm.

JAFFE, B.E., MORTON, R., GELFENBAUM, G., and RICHMOND, B.M. (2006), *Differentiating between tsunami and storm deposits*, Zeitschrift für Geomorphologie, NF, Suppl. Bd. *146* (in press).

KEATING, B., HELSLEY, C., WAFREED, Z., and DOMINEY-HOWES, D. (2005), *2004 Indian Ocean tsunami on the Maldives Islands: Initial observations*, Science of Tsunami Hazards *23*(2), 19–70.

KELLETAT, D. and SCHEFFERS, A. (2004), *Bimodal tsunami deposits—A neglected feature in paleo-tsunami research*, Coastline Reports *1*, 1–20.

KELLETAT, D. and SCHELLMANN, G. (2001), *Sedimentologische und geomorphologische Belege starker Tsunami-Ereignisse jung-historischer Zeitstellung im Westen und Südosten Zyperns*, Essener Geographische Arbeiten *32*, 1–74.

KELLETAT, D., and SCHELLMANN, G. (2002), *Tsunamis on Cyprus – Field evidences and $^{14}C$ dating results*, Zeitschrift für Geomorphologie NF *46*(1), 19–34.

KENCH, P.S., MCLEAN, R.F., BRANDER, W., NICHOL, S.L., SMITHERS, S.G., FORD, M.R., PARNELL, K.E., and ASLAM, M. (2005), *Geological effects of tsunami on mid-ocean Atoll Islands: The Maldives before and after the Sumatran tsunami*, Geology (in press).

KOWALIK, Z., KNIGHT, W., LOGAN, T., and WHITMORE, P. (2005), *Numerical modelling of the global tsunami: indonesian Tsunami of December 2004,* Science of Tsunami Hazards *23*(1), 40–56.

KRÜGER, F. and OHRNBERGER, M. (2005), *Tracking the rupture of the Mw = 9.3 Sumatra earthquake over 1,150 km at teleseismic distance,* Nature *435*(16), 937–939.

LAY, T., KANAMORI, H., AMMON, C.J., NETTLES, M., WARD, ST. N., ASTER, R.C., BECK, A.L., BILEK, S.L., BRUDZINSKI, M.R., BUTLER, R., DESHON, H.R., EKSTRÖM, G., SATAKE, K., and SIPKIN, S. (2005), *The Great Sumatra-Andaman earthquake of 26 December 2004*, Science *308*, 1127–1133.

LIU, P.L.-F., LYNETT, P., FERNANDO, H., JAFFE, B.E., FRITZ, H., HIGMAN, B., MORTON, R., GOFF, J., and SYNOLAKIS, C. (2005), *Observations by the International Tsunami Survey Team in Sri Lanka*, Science *308*, 1595.

MOORE, A., NISHIMURA, Y., GELFENBAUM, G., KAMATAKI, T., and TRIYONO, R. (2006), *Sedimentary deposits of the 26 December 2004 tsunami on the northwest coast of Aceh, Indonesia*, Earth Planets Space *58*, 253–258.

NGDC (2001): *Tsunami Database at National Geophysical Data Center*, URL: http://www.ngdc.noaa.gov/seg/hazard/tsu.shtml.

NOTT, J. (2003), *Waves, coastal boulders and the importance of the pre-transport setting*, Earth Planet. Sci. Lett. *210*, 269–276.

ROBINSON, E., ROWE, D-A., and KHAN, S. (2006), *Wave-emplaced boulders on Jamaica's rocky shores*, Zeitschrift für Geomorphology, NF, Suppl. Bd. 146 (in press).

SCHEFFERS, A. (2002a), *Paleo-tsunamis in the Caribbean: Field evidences and datings from Aruba, Curacao and Bonaire*, Essener Geographische Arbeiten, *33*, Essen 181 pp.

SCHEFFERS, A. (2002b), *Paleo-tsunami evidences from Boulder deposits on Aruba, Curacao and Bonaire,* Science of Tsunami Hazards *20*(1), 3–18.

SCHEFFERS, A. (2004), *Tsunami imprints on the Leeward Netherlands Antilles (Aruba, Curacao and Bonaire) and their relation to other coastal problems*, Quat. Internat. *120*(1), 163–172.

SCHEFFERS, A. (2005), *Coastal response to extreme wave events: Hurricanes and tsunami on Bonaire*, Essener Geographische Arbeiten *37*, 96 pp.

SCHEFFERS, A. and KELLETAT, D. (2003), *Sedimentologic and geomorphologic tsunami imprints worldwide – A review*, Earth Science Rev. *63*(1–2), 83–92.

SCHEFFERS, A. and KELLETAT, D. (2005), *Tsunami relics in the coastal landscape west of Lisbon, Portugal*, Science of Tsunami Hazards *23*(1), 3–16.

SCHEFFERS, A., SCHEFFERS, S.R., and KELLETAT, D. (2005a), *Paleo-tsunami relics on the southern and central Antillean Island arc (Grenada, St. Lucia and Guadeloupe)*, J. Coastal Res. *21*(2), 263–273.

SCHEFFERS, A., SCHEFFERS, S.R., and KELLETAT, D. (2005b), *Tsunami impacts on the Bahaman Islands of Long Island and Eleuthera*, Zeitschrift für Geomorphologie NF *48*(4), 519–540.

SHI, S., DAWSON, A.G., and SMITH, D.E. (1995), *Coastal sedimentation asociated with the December 12, 1992 tsunami in Flores, Indonesia*, Pure Appl. Geophy. *144*(3/4), 525–536.

SOI (Survey of India) 2005), *Preliminary report of tsunami observations*, URL: http://www.surveyofindia.gov.in/tsunami4.htm.

STEIN, S. and OKAL, E.A. (2005), *Speed and size of the Sumatra earthquake*, Nature *434*, 581–582.

TSUJI, Y., MATSUTOMI, H., TANIOKA, Y., NISHIMURA, Y., SAKAKIYAMA, T., KAMATAKI, T., MURAKAMI, Y., MOORE, A., and GELFENBAUM, G. (2005), *Distribution of the Tsunami Heights of the 2004 Sumatra Tsunami in Banda Aceh Measured by the Tsunami Survey Team*, URL: http://www.eri.u-tokyo.ac.jp/namehaya/sumatera/surveylog/eindex.htm.

USGS (UNITED STATES GEOLOGICAL SURVEY) (2005a), *The December 26, 2004 Indian Ocean Tsunami: Initial Findings on Tsunami Sand Deposits, Damage, and Inundation in Sri Lanka*, URL: http://walrus.wr.usgs.gov/tsunami/srilanka05/sand.html.

USGS (UNITED STATES GEOLOGICAL SERVICE) (2005b), *The December 26, 2004 Indian Ocean Tsunami: Survey Site Locations and Photos*, http://walrus.wr.usgs.gov/tsunami/srilanka05/Yala2_12.html.

(Received November 15, 2005, accepted September 11, 2006)

Pure appl. geophys. 164 (2007) 433–452
0033–4553/07/030433–20
DOI 10.1007/s00024-006-0167-2



Pure and Applied Geophysics

# Eyewitness Accounts of the Impact of the 1998 Aitape Tsunami, and of Other Tsunamis in Living Memory, in the Region from Jayapura, Indonesia, to Vanimo, Papua New Guinea

GORDEN N. JOKU,[1,2] JOCELYN M. DAVIES,[1] and HUGH L. DAVIES[1,*]

*Abstract*—Field investigations in 1999 confirmed that the tsunami that struck the Aitape coast of Papua New Guinea on 17 July, 1998 caused damage at points as far as 230 km to the west-northwest, particularly at locations where the coast is indented. Eyewitnesses saw the sea withdraw (in most cases), then surge to levels around 2 m higher than normal in a series of three waves. In some cases the time of arrival of the waves is known approximately by reference to the onset of darkness and to felt earthquakes. Seiche waves followed in some bays, notably in Yos Sudarso Bay, Indonesia, where waves persisted for 3–5 days. Damage was caused by the backwash from the waves. Bodies presumed to be those of Aitape victims were seen floating at sea off Jayapura five days after the tsunami. We record the recollections of people in the Yos Sudarso Bay area who experienced a number of tsunamis in the past 60 years; people that we interviewed on the Papua New Guinea side of the border recollected few or none.

**Key words:** Tsunami, Aitape, Papua New Guinea, Indonesia (Papua Province), seiche, tsunamis 1940–1999.

## *Introduction*

On the evening of 17 July, 1998 a destructive tsunami struck the coast west of Aitape, Papua New Guinea (PNG; Fig. 1; see papers in Pure and Applied Geophysics special volume 160 (2003)). The tsunami caused total destruction on a 14-km sector of coast centered on Sissano Lagoon (Fig. 1). Two villages were removed almost without trace, two other villages were partly destroyed, more than 1650 people died and an additional 1000 sustained major injuries, and 10,000 survivors were displaced to temporary shelters.

The shape and timing of the waves, as observed by survivors and deduced from damage mapping, were recorded by DAVIES *et al.* (2003). The tsunami

[1] Earth Sciences Division, University of Papua New Guinea, Box 414, University NCD, Papua New Guinea.
[2] Now at PT Minorco Services Indonesia, Jakarta, Indonesia.
* Corresponding author E-mail: hdavies@upng.ac.pg

comprised three waves that progressed westward along the coast and arrived some minutes apart. The waves were estimated at 4 m high as they approached observers on the beach, but were projected to heights of 10 and 15 m as they crossed the shoreline. The waves were preceded by a roaring sound that traversed east along the coast and then back to the west. Many described the water in the waves as unusually warm and smelly and at one locality survivors reported a smell of petroleum.

The waves were preceded by a shallow earthquake of $M_W$ 7.0 at 08:49 UT (6.49 p.m. local time); this was strongly felt in the villages that were subsequently affected by the tsunami. The initial shock was followed by two small aftershocks at 09:02:06 ($m_b$ = 4.4) and 09:06:03 (no magnitude reported), and then a doublet of stronger and widely felt aftershocks at 09:09:32 ($m_b$ = 5.6) and 09.10:02 ($m_b$ = 5.9) (SYNOLAKIS *et al.*, 2001; HURUKAWA *et al.*, 2003; OKAL, 2003). Epicenters for the 08:49, 09:09 and 09:10 events are shown in Fig. 1. T-wave signals from the 09:02:06 event have been interpreted as being generated by a submarine landslide which, in turn, may have caused the tsunami (SYNOLAKIS *et al.*, 2001; OKAL, 2003). Others deduced that the tsunami was caused by fault displacement of the sea floor (e.g., GEIST, 2000).

The time interval between the initial earthquake and the arrival of the tsunami at the coast was 10–15 minutes, when there was still sufficient daylight to see the waves approach, and before the arrival of shaking caused by the widely felt doublet of earthquakes (DAVIES *et al.*, 2003). The timing of arrival of the waves at the coast bears upon any interpretation of the source of the tsunami.

The earthquakes occurred beneath the inner wall of the New Guinea Trench (Fig. 1) and were triggered by movement either on a reverse fault dipping steeply to the north (GEIST, 2000), or on a thrust fault dipping 19° towards 236° (HURUKAWA *et al.*, 2003). A previous major earthquake beneath the inner wall of the New Guinea Trench, at a more westerly location (0.89°S, 136.95°E) on 17 February, 1996, caused a tsunami and loss of life on Biak Island in Indonesian Papua (IMAMURA *et al.*, 1997; OKAL, 1999; Biak Island is off the north coast of New Guinea at 136°E).

The first investigation of the Aitape tsunami was by an international team that entered the area on 1 August, 1998 and remained in the field for a week (KAWATA *et al.*, 1999). Other investigations followed, including a second visit by an international team in September 1998, and four major marine surveys. Results of the investigations have been presented by TAPPIN *et al.* (2001), SYNOLAKIS *et al.* (2001), LYNETT *et al.* (2003) and MATSUMOTO and TAPPIN (2003), amongst others.

In this paper we discuss the effect of the 1998 Aitape tsunami on the coast at distances of 100–230 km to the west. Others have recorded the effects at Wewak, 170 km to the east-southeast (LYNETT *et al.*, 2003); on western Manus Island, 500 km to the east-northeast (DAVIES, 1998); and in Japan where the tsunami was recorded on

two ocean bottom pressure gauges and six tide gauges (TANIOKA, 1999; SATAKE and TANIOKA, 2003); maximum amplitude recorded on the tide gauges was 10 cm.

Staff and students of the University of Papua New Guinea began a public awareness and information campaign in the area affected by the tsunami in August 1998 and continued until 2001. Useful information was gathered from survivors and eyewitnesses and by mapping the damage in the worst hit area; some of this information was published (DAVIES *et al.*, 2003). In 1999 field investigations were extended westward to the international border and beyond.

Our fieldwork began at Vanimo (Figs. 1, 2) in February and March 1999 (JMD, HLD) and at Jayapura and the adjacent coast (Figs. 1, 3, 4) in August 1999 (GNJ). We relied mostly on the recollections of eyewitnesses but also saw some physical evidence. For example, at some locations salt water inundation had caused vegetation to die and at others wave-washed debris and scour channels were preserved. Interviews in PNG were conducted in English and Tok Pisin, and in Indonesia, in Bahasa Indonesia. A standard questionnaire was adopted for the Indonesian survey (Appendix 1). Because of security concerns it was not possible to visit the Demta Bay area in Indonesia, but it was possible to interview eyewitnesses.

The questions that we sought to address, in particular, were the scale, shape and timing of the tsunami waves, the effect of the waves, and any unusual phenomena associated with the waves. We also enquired for any recollections of past tsunamis or any oral history of tsunamis, and for the level of awareness of tsunamis – did people know the warning signs and did they know what to do?

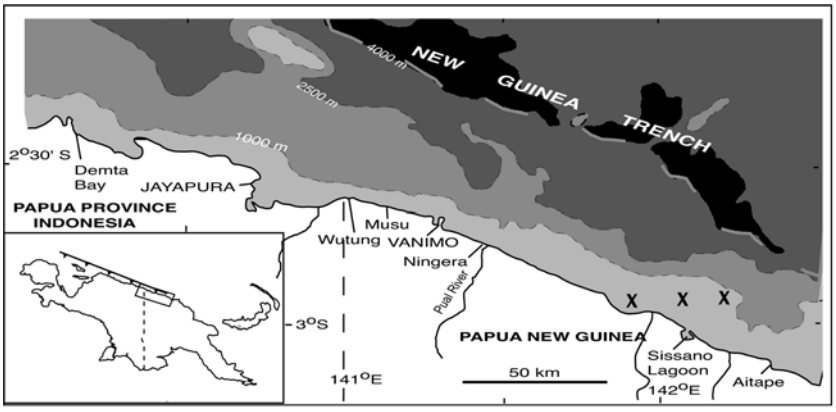


Figure 1
Map of the coast from Demta Bay, Indonesia, to Aitape, Papua New Guinea. X indicates epicenters of 06:49, 07:09 and 07:10 earthquakes of 17 July 1998, which progressed from left to right, locations from HURUKAWA *et al.* (2003). Isobaths east of 141°E and south of 2°S are from multibeam survey by RV Kairei in 1999 (MATSUMOTO and TAPPIN, 2003). Other isobaths are from spot depths on Marine Navigation Charts 3250 and Aus 389. Map drawn by R.M. Davies.

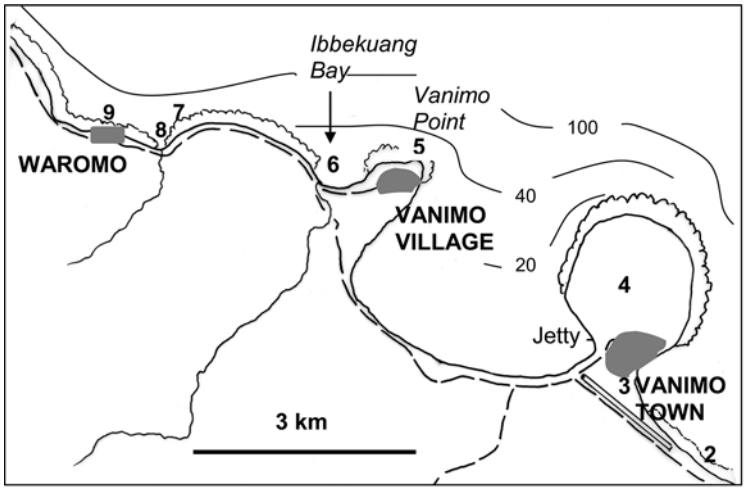


Figure 2
Map of the Vanimo area. Numbers are localities discussed in the text and Table 1. Isobaths in metres were derived from spot depths on navigation charts.

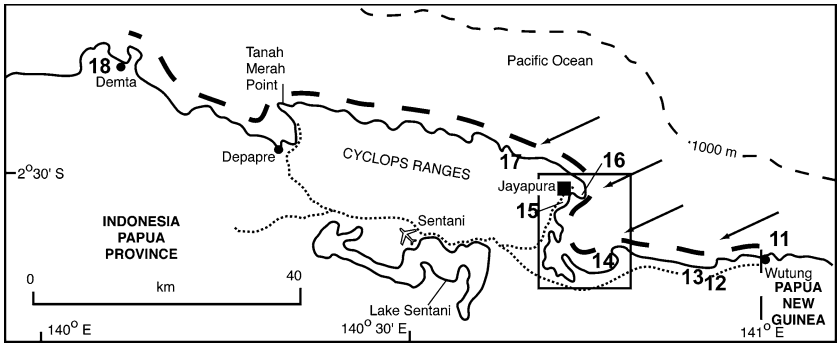


Figure 3
Map of the coast of Indonesian Papua from Demta Bay to the border. Numbers are localities discussed in the text and Table 2. The thick dashed line marks the shoreline that was affected by the tsunami. Where observed, the waves approached from the east-northeast, as indicated by the arrows. Rectangle marks area reproduced in Figure 4. Map drawn by R.M. Davies.

## *Coastal Geology and Relief*

The coast east of Vanimo to the Pual River and beyond (Fig. 1) is a prograding coastal plain, low-lying and partly swampy, and is backed by low hills of Plio-Quaternary sediments (NORVICK and HUTCHISON, 1980). From Vanimo

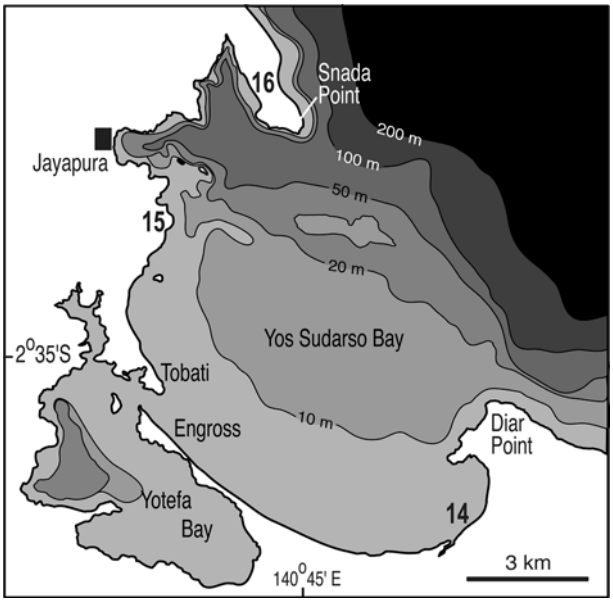


Figure 4
Map of Yos Sudarso Bay. Isobaths from spot depths on Marine Navigation Chart 2467, 1960 with corrections to 1964. Map drawn by R.M. Davies.

westward to the border the coastline is hilly and emergent and mostly comprises Quaternary raised coral reefs. The headland above Vanimo town (locality 4, Fig. 2) and the headland of Vanimo Point (locality 5, Fig. 2) both are raised patch coral reefs. Emergent fringing reef on both headlands indicates that uplift is continuing. The raised reefs further west, from Musu to Wutung (Fig. 1) are Plio-Pleistocene (NORVICK and HUTCHISON, 1980).

Much of the coast on the Indonesian side of the border is hilly and emergent. Coastal hills between the border and Diar Point (locality 14, Figs. 3, 4), and near Demta Bay (locality 18, Fig. 3), are Miocene limestone and sandy sediments (DOW *et al.*, 1986). High-grade metamorphic and ultramafic rocks form the steep mountains of the Cyclops Range (Fig. 3). The sand beaches and sand spits on the western and southern shores of Yos Sudarso Bay, and the sand spit that joins the rocky headland of Snada Point to the mainland are low lying and vulnerable to tsunamis (Figs. 4, 5, 6, 7).

Yos Sudarso Bay (previously known as Humboldt Bay) faces to the east and is bounded by the rocky headlands at Snada Point and Diar Point; these make an opening about 8 km across (Figs. 5, 6). The bay is generally shallow (less than 20 m depth; Fig. 4) with the exception of a deeper channel in the north that leads to Jayapura port.

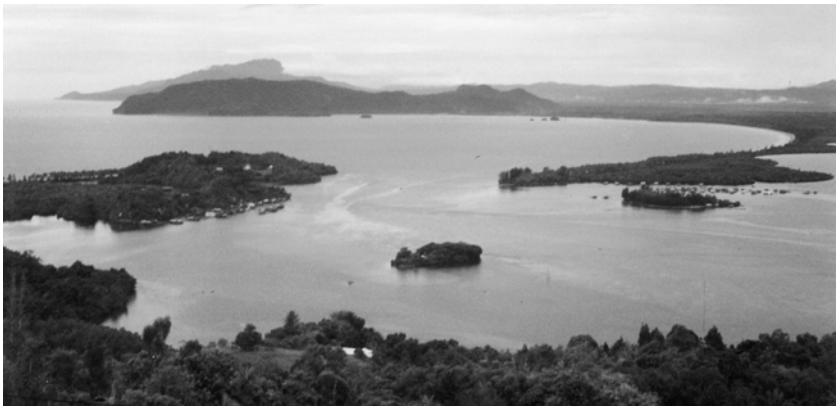

Figure 5
Photograph looks east across Yotefa Bay (foreground), and the peninsulas where Tobati and Engross villages are located, to the southern part of Yos Sudarso Bay, Holtekamp beach and Diar Point (middleground). Photograph G.N. Joku.

Figure 6
View east from above Jayapura to the hill that forms Snada Point. Base G Beach is on the ocean side of the lowlying peninsula to the left of the hill. Photograph G.N. Joku.

The slope of the sea floor immediately offshore from the rocky coast between Vanimo Point and the border is relatively steep. Further west the slope is gentler. In the east, east of Vanimo, the sea floor slopes gently to a depth of only 100 m at a distance of 3–4 km from the shore (Navigation Chart Aus389; Figs. 1, 2).

## *Results*

Results of interviews are summarized below and are given in more detail in Table 1 (Papua New Guinea) and Table 2 (Indonesia).

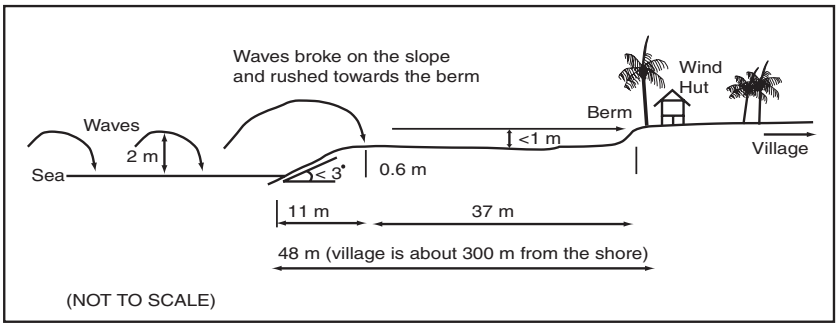


Figure 7
Sketch profile of the Beach at Skouw Saey village (not to scale).

*Height and Impact of the Tsunami Waves*

At all locations there were three main waves. On the Indonesian coast the waves swept in from the east-northeast, spaced some minutes apart, broke at the beach front where there were sandy beaches, and penetrated 10–50 m inland. Each wave receded before the next arrived. The backwash from the waves caused damage, carrying away canoes and logs that were stored for shipment, dragging boats from

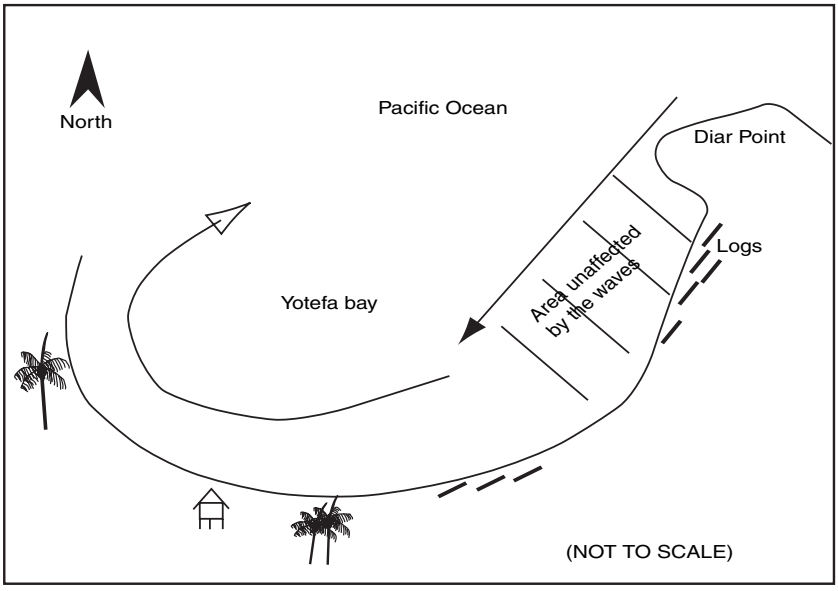


Figure 8
Sketch shows the behavior of the waves approaching Holtekamp Beach. The waves appeared like a whirlpool to observers. The shaded area was unaffected by the incoming waves.

Table 1

*Observations in Vanimo area of Papua New Guinea*

| LOCATION (Figs. 1,2) | REPORT includes sources and dates of interview where known |
|---|---|
| 1 | Ningera village, just west of mouth of Pual River, 142.45°E (Fig. 1), wave height 1.93 m, eyewitness and debris. KAWATA *et al.*, 1999. *5aug98*. |
| 2 | Waterstone, wave height 1.4 m, eyewitness. *KAWATA* et al., 1999. *5aug98*. |
| 3 | On east coast of Vanimo town. Marie Kafoa felt two earthquakes. They were stronger and longer-lasting than usual earthquakes, and made glassware and pottery shake. *Marie Kafoa.jmd.mar99*. |
| 4 | On Tower Hill above Vanimo town, at about 40 m elevation. Brother James felt one unusually strong earthquake that was longer-lasting than any he had experienced in 30 years in the area. *Br James Coucher.hld.* |
| 5 | At Vanimo Point on shoreline, below Vanimo (Lido) village.<br>**A.** Joseph Abi felt a normal earthquake and, about 15 minutes later, a weak earthquake. 15–20 minutes later heard a wave breaking, looked and saw it was breaking on a long front all along the reef. Usually waves break on a short front only. Reef was exposed because it was low tide. He related the wave to the earthquake. He did not see the sea recede before the waves came. There were three waves 5–6 minutes apart; the first wave approached directly from the north, light was good. The second wave came from the west, it was getting dark. The third came from the east. It was almost dark and he could only just see the third wave. The first wave filled space over the reef. The water did not recede and the following waves built on this to make a total height of 2–3 m. Previous tsunamis: Mr Abi recalled an occasion in about 1963 when the sea withdrew from the reef and minutes later a wave arrived. *Joseph Abi. jmd.28feb99*<br>**B.** James Nunakru and his brother Alfonz were on the beach 6.30–7 p.m. preparing to go fishing. It was low tide and their fishing gear was on the beach below high water mark ready to load into the boat. They felt one earthquake. Three to four minutes later a wave came in from the north. It was an unusual wave in that it reached as far as the eye could see, across the mouth of the bay to the west (Ibbekuang Bay), a distance of 1 km, and as far as the end of Vanimo Point to the east, a distance of 100 m. This was followed by a second wave, from the east, and a third wave, from the west. After the waves there was a strong current flowing from east to west. They decided to not go fishing and got help to pull their dinghy out of the water but even with four strong men pulling they had difficulty because of the current. *James Nunakru.jmd.28feb99*. |
| 6 | Ibbekuang Bay, west of Vanimo village. Raymond Apara and Bernard Mana were fishing in two canoes near a reef and close to the point, about 100 m offshore. They felt no earthquake. Raymond was facing out to sea and heard calls from the beach, then a sound like thunder or an aeroplane. He looked around and saw that the sea level had dropped and the reef was exposed, not just the top of the reef but all the way to the bottom of the reef. Both men were concerned, they had never seen anything like this, and decided to paddle back to the beach (to the south). [The first wave is thought to have arrived during this time – this is not clear from interview notes.] They could not paddle all the way because the water was so low so stopped on a sandbank about 30 m from the beach. They were there for 5–6 minutes before a wave (the second wave) carried them to the beach and to a point about 2 m above normal high water, to the grass and the trees that fringe the beach. The wave came from the east and receded to the east, carrying debris with it. A second big wave came from the west and receded back to the west carrying debris. They used this wave to move about 100 m along the shore to the east, to where they normally leave their canoes. The beach is narrower now, and vegetation has retreated about 30 m. *Raymond Apara and Bernard Mana.jmd.28feb99*. |

| | |
|---|---|
| 7 | Anton Alu's house, close to the shore and facing northwest. He felt an earthquake some minutes before the first wave. People called out and he looked to see the sea bubbling and boiling. This was at 6.57 p.m. by his wrist watch. The sea rose for a few seconds then dropped 3–4 m in a period of some minutes. Then the sea rose, water ran towards the beach and swept 10 m inland, then receded to reef. The sea welled up. There was no breaking wave. Then the sea humped up and swept to left and right, leaving his house untouched, then retreated. Then a third wave swelled up, the sea surface was shaking. There were three waves and the second was the biggest. It was all over by 8.07 p.m. The ground under Anton's house is 0.6 m above high water mark. It was low tide so the best estimate is that the sea level rose about 1.5 m. *Anton Alu. hldjmd.feb99.* |
| 8 | Maureen Soni was at the mouth of the small creek east of Waromo village. She felt an earthquake that shook for about 5 minutes. The sun was down but it was still daylight. About 5 minutes later a small wave, 15–30 cm, pushed in up the creek. Then the sea retreated for two minutes to 70 or 80 m from the shore. After 3–4 minutes the sea advanced again and reached her at chest height, with a strong current. Canoes and logs were carried in by the wave. Water flowed to the west. *Maureen Soni. hldjmd.feb99.* |
| 9 | At Waromo village the sea continued to advance and retreat for 3–4 hours, each cycle was 8–10 minutes, the waves getting smaller each time. *Ernest Nikengu. hldjmd.feb99.* |
| 10 | Musu? Listed as Musa by KAWATA *et al.* (1999) and given longitude 140.3° which is incorrect for Musu, so some uncertainty. Wave height 2.67 m. KAWATA *et al.* (1999) *5aug98* |
| 11 | Wutung, Bougainville Bay, PNG, 1.5 km east of International Border.<br>**A.** Dorothy Anton was sitting on the beach while her children swam in the estuary nearby. It was getting dark. She did not feel an earthquake. She saw the water recede about 100 m from the shore, much lower than a low tide. After 4–5 minutes the water returned, more like a tidal surge than a wave, and rose to the normal high water mark. A second wave followed within a few minutes and overtopped the HWM by about a meter to reach the grassy verge 10 m inland. The third wave was the highest and filled the estuary to reach the level of the bottom of the bridge, which is normally 3–5 m above water level. Fish were carried in with the wave. Between the second and third waves the sea receded, rolling the pebbles on the beach, and this made a lot of noise. It was dark enough that she could not see the wave effects at the point about 1 km away.<br>*Dorothy Anton jmd1mar99.*<br>A fiberglass dinghy belonging to police was slightly damaged when it was washed ashore and caught under the bridge. PNG Customs Officer at border post. *jmd1mar99*<br>**B.** Wave height 3.09 m at bridge and 1.79 m nearby, eyewitness account and debris. Arrival of wave was said to have coincided with second earthquake. Second earthquake was at 0909 hrs UT. (KAWATA *et al.*, 1999). *5aug98.* |

Table 2

*Observations in Papua Province*

| LOCALITY (Figs. 3,4) | REPORTS |
|---|---|
| 12 | Skouw Saey village is on a low-lying sandy coast a few km west of the international border. The village is 200–300 m from the water's edge behind a grove of coconut palms. The beach has a slope of less than three degrees. Eyewitness Nolita Palora, 36, was at her home near the beach on the afternoon of 17 July, 1998. She observed three waves about 2 m high approaching the coast from the east or east-northeast, and spaced about 1 minute apart. The waves broke on the slope at the front of the beach and progressed for 50 m, as far as the beachfront berm (Fig. 7), at which point the water was knee deep. The first wave receded to the sea before the second wave came ashore. A thunderous noise as of a strong wind and breaking waves accompanied the waves.<br>She estimated the time of arrival of the waves as between 5 and 6 p.m. local time (0800–0900 hours UT). A second eyewitness, Yowel Rolo, 69, male, said that the waves arrived at 7 p.m. local time (8 p.m. PNG time, 1000 hours UT). Neither of the witnesses felt any earth tremors. Both recalled that the waves breaking on the shore did not present a threat to the villagers but the force with which the water retreated back to the sea caused grave concern. The back-flow cut scour channels, uprooted some coconut trees, buried logs and carried debris out to sea. *GNJ7aug99*. |
| 13 | Skouw Mabo village is immediately west of Skouw Saey and shares the same gently sloping sandy waterfront. The village is less than 100 m from the water's edge. As with Skouw Saey, the villagers reported waves 2 m high breaking on the shore and progressing 50 m inland and, as at Skouw Saey, villagers were more concerned about the force of the back-flow, rather than the force of the incoming waves. The backwash scoured channels, uprooted coconut trees, buried logs and washed several canoes out to sea. No earth tremors were felt. *GNJ8aug99*. |
| 14 | Holtekamp Beach is within Yotefa Bay on a shoreline that faces northwest; it is protected by the hook-shaped headland of Diar Point (Fig. 4). The beach is 50–100 m wide and has a gentle slope. A logging company stores logs on the beach ready for transshipment.<br>Waves 2 m high approached the beach at an angle, broke about 20 m from the beach, and flowed 50 m inland. One eyewitness, Godlief Samallo, recalled hearing a sudden noise before the waves arrived. He saw a succession of many waves creating a whirlpool-like effect (Fig. 8). The waves or seiche continued for three days, each wave penetrating about 20 m inland. The waves uprooted trees, buried trees on the beach, and cut a scour channel. Some of the stacked logs were carried out to sea. Alfred Pattipeme commented about the earthquake on the evening of the tsunami. It was unusual in that it was at first strongly felt, then became weaker, then strongly felt again. *GNJ8aug99* |

| | |
|---|---|
| 15 | Hamadi market is on an east-facing promontory within Yos Sudarso Bay and is partly protected by Snada Point (Fig. 4). From this location, waves 2 m high were observed in the bay. The waves struck the beach and progressed 10–20 m inland. The backwash was sufficient to tear large canoes from their moorings. A seiche wave continued for several days. *GNJ8-9aug99* |
| 16 | Base G Beach faces eastward toward open ocean, northwest of Snada Point. Here waves 2 m high struck at an angle to the beach at 7–8 p.m. local time (1000–1100 hours UT) and progressed 20–30 m inland. The backwash from the waves was strong enough to uproot trees, and to carry canoes away from their moorings. An unusual sound, like that of a passing ship or noise of a helicopter (wop-wop sound) was said to have accompanied the waves. A weak earthquake was felt.<br>Yusup Makanuwey reported that on the southwest side of Snada Point a 2 m seiche wave developed and continued for more than an hour (10–11p.m. local time, 1300–1400 hours UT). The waves penetrated inland for 200 m, at which point the water was less than 1.5m deep. *GNJ9-10aug99*. |
| 17 | The Ormo coastline faces east and is on the east side of a small promontory. The tsunami waves reached this area at dusk while the eyewitness, Didimus Ireew, and friends were fishing on a reef. The sea receded, exposing the reef, then there were three waves, about 2 m high. The waves were accompanied by a sudden darkness and a thunderous sound. The waves flowed inland for a distance of about 12 m.<br>The fishermen had to hold fast to their aluminum motorised fishing canoes, and made their way to shore as quickly as they could, because the backflow from the waves threatened to pull them out to sea. Once they reached the shore there was what seemed an unusual or eerie calm. Water at the river mouth where they came ashore was unusually warm. They did not feel an earthquake. *GNJ10-11aug99*. |
| 18 | Demta Bay and headland, 70 km west of Jayapura, was not visited because of internal security problems at the time of survey. A Jayapura resident who visited Demta headland reported that waves about 2 m high reached the headland, probably on the evening of Friday 17 July. The waves approached the beach at an angle and were followed by a strong backwash. *GNJaug99* |

their moorings, uprooting coconut palms, and causing scour channels to develop. Fishermen trying to come ashore on the Ormo coast struggled to hold their boats against the rapidly retreating water. Within Yos Sudarso Bay and Yotefa Bay seiche waves were established that persisted for 3–5 days. The seiche waves were strong enough to uproot trees and moved sand so that logs on the beach were buried. The waves decreased in energy with time.

On the PNG coast two independent observers in the bay of Waromo village saw a small rise in sea level and then a pronounced drop of sea level, perhaps of the order of several meters, before the first significant wave arrived. In contrast to the Indonesian coast, the first wave reportedly approached on a line near parallel to the coast, more from the north-northeast rather than from east-northeast. The second wave built on the first to reach a maximum height of around 2 m above normal sea level. The second wave swept in from the east and the water retreated to the east, while the third wave came from, and retreated to, the west. The lateral flows of water along the shoreline were strong enough to test the strength of men pulling a dinghy ashore. Unlike the Indonesian coast, the waves had the form of a tidal surge, rather than a rolling or breaking wave, except on Vanimo Point where waves broke on the reef. The incoming surge at Wutung was confined by the narrow shape of the bay and rose to a height of 3 m above normal sea level — the maximum wave height recorded on these coasts. A seiche wave that continued for 3–4 hours was established in the bay of Waromo village.

### *Timing of the Waves*

In most cases observers reported that the first wave arrived while there was still sufficient daylight to see clearly. At Wutung (Locality 11) by the time the third wave arrived it was dark enough that the observer could not see clearly to the headland of the bay, 1 km away. At Ormo (Locality 17) the men who were fishing at dusk saw the water drain from the reef and the three waves arrive, at which time it suddenly became dark. From our observations at Sissano Lagoon, daylight in the month of July fades very quickly between 7.00 and 7.10 p.m. local time (09:00 to 09:10 UT) so that by 7.10 p.m. one would not see a wave approaching from the sea.

Making a correction for 1 degree of longitude (141°E at the border, 142°E at Sissano Lagoon) the daylight equivalent of 7.10 p.m. at Sissano Lagoon would be 7.14 p.m. at the border (09:14 UT or 6.14 p.m. Jayapura time). At Ormo, which is at longitude 140.6°E, the equivalent time would be around 09:15.5 UT. Based on those interviews where darkness is mentioned we can deduce that the waves reached the border region some time before 09:14 UT and perhaps as much as 5–10 minutes before that. One report (KATAWA *et al.*, 1999; source not given) was that the first wave arrived at Wutung at the time of the second main earthquake, which was 09:09 UT. These data are summarized in the following table.

| Location | Distance from Sissano Lagoon, km | Longitude | Calculated time when too dark to see (UT) | Conclusions |
|---|---|---|---|---|
| Wutung | 120 | 141 | 09:14 | Waves 1 and 2 arrived some minutes before 09:14 UT (and possibly at 09:09, the time of second earthquake) and wave 3 arrived near 09:14 UT. |
| Ormo | 170 | 140.65 | 09:15.5 | The waves arrived before 09:15.5 UT. |

Most of the observers did not have accurate timepieces. Only one observer, Anton Alu, near Waromo, recorded the arrival of the first wave by referring to his wristwatch. He gave the time of arrival of the first precursory small wave in the Waromo Bay as 6.57 p.m. Other observers gave estimates of time only.

*Noise*

In the Aitape area the wave was preceded by a noise that some described as a sound like a low-flying heavy aircraft and others as the woop-woop sound of the rotor blades of a large helicopter. Sister Margaret Conway at Malol, between Aitape and Sissano Lagoon, described the sound as that of an ocean liner close to the shore. Similar descriptions of a sound that preceded the wave were given by observers in the border region. At Base G Beach, before the waves arrived, Yusup Makanuwey heard the ''sound of a huge ship passing by, or the woop-woop of a helicopter''. More commonly, people in Indonesia described a sound of thunder or a thunderous sound as of waves breaking on cliffs or rocks (e.g., at localities 12, 13, 17). This was heard before and during the arrival of the waves. Our observers on the PNG side did not comment about any noise except for Dorothy Anton at Wutung who noted that as the second wave receded it rolled the pebbles on the beach and this made considerable of noise.

*Earthquakes*

Marie Kafoa at Vanimo felt two earthquakes that she described as stronger and longer lasting than normal, and which shook glassware and pottery. Brother James Coucher at Vanimo felt an earthquake that shook for longer than any he had felt in 30 years at Vanimo. Further west at Vanimo Point and at Anton Alu's house observers felt one or two earthquakes but did not comment that they were unusually strong. At Wutung and at most locations across the border no earthquake was felt by the people that we interviewed. However, at Holtekamp (Locality 14) clan chief Alfred Pattipeme recalled that the earthquake was prolonged, fluctuating between strongly and weakly felt. Two observers at Base G Beach recalled a weak earthquake that caused their houses to sway.

*Reports of Unusual Effects*

The fishermen at Ormo (Locality 17) described how it was a good evening for fishing but when the waves arrived it suddenly became dark. Afterwards there was a calm and an eerie feeling. When the fishermen came ashore at Ormo they noticed that the river entering the sea was warm, where usually it is cold. Other observers in the Vanimo-Jayapura area did not report warm water.

Villagers at Skouw Saey (Locality 12) reported that red bubbles, accompanied by a distinctive smell, appeared in the sea on Thursday 16 July, 1998 at about 8 p.m. local time, a day prior to the tsunami arriving at Aitape. The villagers have a customary belief that whenever red bubbles appear in the sea there will be some sort of unusual event, possibly but not necessarily a disaster, not necessarily in the local village but somewhere in the vicinity. At such times they take special care when going out fishing and do not let their children play by the sea.

*Bodies*

Fishermen from Hamadi and Skouw Mabo confirmed press reports (see Appendix 2) that bodies of tsunami victims were seen floating at sea. Fishermen from Skouw Mabo saw eight bodies on 22 July, five days after the tsunami. Fishermen at Hamadi recovered a skull with betel-nut-stained teeth from the stomach of a shark caught six days after the tsunami. A westward longshore drift is likely at this time of year because of the prevailing southeast trade winds.

There was an unconfirmed report that a body of a male youth, 16–18 years old, was found in a drifting canoe by villagers at Demta headland. He was wearing a traditional wristband made of beads and had in his possession a PNG two-kina plastic note. The youth is said to have been buried in the village.

*Tsunami Awareness*

Most interviewees did not understand the likely causes of tsunamis, but some knew from experience the warning signs of a tsunami: A strongly felt earthquake accompanied by the receding of the sea to expose the seabed. It is likely that the general level of tsunami awareness and understanding in the Jayapura area is poor. A program of visits to schools and villages in the Vanimo-Wutung area in late 2005 (GEDIKILE *et al.*, 2006) addressed tsunami awareness and education.

## *Past Tsunamis*

The following information was gathered in interviews.

*1941*: According to Yowel Rolo, the village of Skouw Saey (Locality 12) was swept away by a probable tsunami in the early hours of the night in 1941. He was 11

years old at the time. The story he told was that the alarm was raised by a man who went to the beach to relieve himself. All of the people in the village fled inland to safety and there was no loss of life. There were three closely spaced waves that seemed to hit the village all at once, in single sweep. The second village was built about 100 m inland from the first but had some houses destroyed by strong waves suspected to be tsunami-related. Since then, the village has moved inland twice after strong waves, waist deep, flowed under the houses. The houses are elevated above the ground on high posts. Dusk at Locality 12 would be at 6 p.m. local time or 0900 hours UT. Early evening might mean 1000–1200 hours UT.

*1950*: A tsunami destroyed Arop village on the margin of Sissano Lagoon (Fig. 1) in late 1949 or early according to the report of a government officer who visited the area towards the end of 1950 (MURPHY, 1950). No report of a 1950 event emerged from our survey in the Vanimo-Wutung area.

*1952*: A house in Engross village (Engross-Tobati area, Yos Sudarso Bay, Figs. 3, 4) was destroyed by waves in 1952. The waves were high and lasted through the night. Night time is 0900–2100 hours UT.

*1957*: Yowel Rolo described how in Skouw Mabo (Locality 13 in Fig. 3) in 1957 a body of swirling water, about 3-m high, which he described as a whirlpool, caught and drowned a man who was near the beach.

*1960s*: Yusup Makanuwey recalled that Engross and Tobati villages (Fig. 4) had been swept away twice in the 1960s, by tsunami waves that reached 10 m or higher. This was when he was a small boy.

In the Vanimo area, Joseph Abi recalled that in about 1963 the sea had drained from the reef (probably he was referring to Vanimo Point) and within minutes had returned. He said there was extensive damage at Wutung and dinghies were damaged.

*1970s*: Houses on stilts over the water at Base G (Locality 16, Fig. 3) were carried away by what were thought to be tsunami waves (Dores Awom of Base G Beach interviewed by GNJ on 10 August, 1999).

*1996*: The 1996 Biak tsunami caused seiche waves at Holtekamp (Locality 14, Fig. 3), just as the Aitape tsunami had done. Waves from the Biak tsunami also were observed at Base G Beach (Locality 16).

### *Discussion of Past Tsunamis*

We searched EVERINGHAM's (1977) catalogue of tsunamis in the New Guinea-Solomon Islands region for events that might match the historical record of tsunamis, and received advice on other possible matching events as recorded in the Integrated Tsunami Data Base for the Pacific (ITDB/PAC, 2004; written comm. G. L. Downes, 2006).

*1941 tsunami at Skouw Saey*: EVERINGHAM (1977:51) records tsunami effects on the Gazelle Peninsula of East New Britain on 13 January, 1941 for several hours

beginning at 16:28 UT and notes that there was a shallow M 7.0 earthquake at 4.5°S 152.5°E at 16:27 UT on 13 January, 1941. However, it is unlikely that this event would cause a major tsunami at a distance of almost 2000 km to the west.

*The tsunami at Arop in late 1949 or early 1950*: EVERINGHAM (1977, 51) records a 0.1 m periodic wave at Rabaul on 20 October, 1949 and a M 7.25 earthquake at 5.5°S 154°E at 21:00 UT on 19 October, 1949. It seems unlikely that this event would generate a damaging wave 2000 km to the west at Arop.

*The tsunami at Engross in Yos Sudarso Bay, Indonesia, in 1952*: Possibly this was caused by the great Kamchatka earthquake of 5 November, 1952, M 8.4. This caused waves higher than 2 m on the east coast of Bougainville Island, waves as high as a meter in Rabaul Harbour, and less than a meter in the Siassi Islands (6°S, 148°E). The tidal disturbance at Kokopo, near Rabaul, persisted for 48 hours (EVERINGHAM, 1977, 52–53).

*The tsunami in 1957 at Skouw Mabo*: This may have been linked to either a M 7.3 shallow earthquake at 1.5°S, 137°E (south of the New Guinea trench) on 22 June at 23:50 UT (EVERINGHAM, 1977, 54–55), or to the M 8.3 Aleutian Islands earthquake on 9 March (ITDB/PAC, 2004). The earthquake on the New Guinea Trench is thought to have been the cause of a 1.8 m tsunami at Seeadler Harbour on the north coast of Manus Island, PNG (EVERINGHAM, 1977, 55). Manus Island is at 2°S, 147°E.

*Two events at Engross and Tobati in the 1960s*: These tsunamis possibly originated with the great Chilean earthquake of 22 May, 1960 and the great Alaskan earthquake of 28 March, 1964. The Chilean earthquake caused tidal fluctuations of up to 1.8 m at Wewak and just over a meter on Manus Island, where tidal disturbances continued for almost 24 hours with a period of 45-75 minutes (EVERINGHAM, 1977, 58). The Alaskan earthquake caused only a small wave in Rabaul but oscillations were recorded on the Rabaul tide gauge for four days. There is no record of the impact of a tsunami from the great Alaskan earthquake on the Wewak coast.

*The damage at Base G Beach in 1970s*: The most likely cause is a M 7.0 earthquake on 31 October, 1970 at 17:53 UT at 4.9°S 145.5°E which caused waves up to 3 m high on the Madang coast. This earthquake triggered submarine slumping that severed the international communication cable offshore from Madang (EVERINGHAM, 1977, 60). Another possible source is a M 8.0 earthquake at 01:23 UT on 26 July, 1971 at 4.9°s 153.2°E (off southern New Ireland) which caused waves as high as 8 m in the Wide Bay area of New Britain (EVERINGHAM, 1977, 61).

## *Conclusions*

1. The Aitape tsunami was observed as a series of three main waves up to 2 m high on the north coast of New Guinea at locations as far as 230 km west of Aitape. The tsunami propagated more strongly in this direction than it did to the east-southeast, perhaps because of channeling of energy by the New Guinea Trench. In

the bay at Waromo (Locality 9) oscillations continued for hours and in Yos Sudarso Bay, Indonesia, for 3–5 days.

2. Damage from the tsunami within Yos Sudarso Bay, at Skouw Saey, Skouw Mabo and Holtekamp, where there was significant erosion by the backwash, was greater than on the PNG coast at points closer to Aitape, such as Wutung, Ibbekuang Bay, and Ningera.
3. In the past there may have been more damaging tsunamis on the Indonesian side of the border, in the Yos Sudarso Bay area, than on the PNG side of the border. People interviewed in the Yos Sudarso Bay area recollect a number of tsunamis in the past 60 years, whereas people interviewed on the PNG side recollect few or none. The probable reason is that Yos Sudarso Bay has served to focus the energy of any tsunami, even those of moderate scale, where the same tsunamis may have passed unnoticed on the more open and locally hilly PNG coast.
4. Other factors that may explain the discrepancy in tsunami history are population density and population distribution. In the Yos Sudarso Bay area population density is greater, and more people live at exposed sites.

## *Acknowledgements*

For fieldwork in Indonesia we thank Hosea Asmuruf (Sekolah Tinggi Teknik Jayapura), Connie Ohee and Reinhold Joku for maps; Harry Joku and Adolf Joku for assistance in the field; and Jacleana Zeydel, who provided invaluable finance and transport. This part of the survey was undertaken as an undergraduate research project of the Earth Sciences Division of the University of PNG. For fieldwork in PNG we thank Brother James Coucher and Arone and Marie Kafoa of Vanimo and the staff of Senta Bilong Halpim near Waromo for hospitality and support. We thank Fumihiko Imamura who assisted in the initial planning of the paper, and G.L. Downes for helpful critical comment.

## *Appendix* 1: Interview question sheet

*Basic information*

Date and time of interview:
Interviewee's name:
Location:
Where was the interviewee during the earthquake and the tsunami?

*Earthquake information*

Did the ground shake? How strong was it?

Describe the behavior and effect of the earthquake(s) or tremors? (e.g., spacing interval of each tremor)

How many tremor(s)? How long did it (they) last? Local time of occurrence:

Any other information

*Tsunami information*

Did the sea level drop and expose the reefs? Did this occur after the shaking of the ground? How far did the sea recede?

What was the behavior of the wind? Was it unusual at this time?

Describe any sounds or noise associated with the waves before, and at the time of their arrival?

Was it unusual to have this kind of rough seas at such time of the month?

Whereabouts was the first wave seen? How did they appear? How much time between each wave?

Which direction was the wave coming with respect to the shore? Oblique, perpendicular or parallel to coast.

How high were the incoming waves?

How strong did the waves strike the coast/village?

How far did the waves reach inland?

How deep was the water inland? ( < waistdeep)

How long did the waves stay inland?

Describe any changes the waves made in the land surface?

Were there any sightings of dead bodies? When and where were the bodies first seen? What was the appearance of the bodies?

*For those who were in boats*

Where were they before, during and after the tsunami?

What did the sea surface look like? How did the sea behave? Was the sea rough?

Was it unusual to have this kind of rough seas at such time of the month?

What was the behavior of the wind? Was it unusual at this time?

Did they notice any other unusual phenomenon?

Describe any sounds or noise associated with the waves before, and at the time of their arrival?

*Any other information*

What happened in the following days? (behavior of weather, wind, and sea)

Were there any casualties or injuries caused by the waves?

Were there any sightings of dead marine creatures?

Any deep sea or sediment deposits or unusual debris brought onshore by the waves?

Did this condition occur in the past? (date if possible)

*Awareness Campaign*

What do you know about tsunamis?

Recognizing the signs of tsunamis-earth tremors followed by sea receding.

What to expect or suspect?

What to do in the event of a tsunami? Run to higher grounds at the first signs.

The dangers of living near the coast, especially near active trenches such as the New Guinea trench.

Have you experienced any other events like this before in your lifetime, at this same place or another? and if so, when?

Do you know of stories/legends or experiences of such events that have been handed down?

## *Appendix 2: Press Report of Bodies*

200 bodies spotted by Irian Jaya fishermen

*Jakarta*: Fishermen in Irian Jaya, Indonesia, have spotted some 200 bodies believed to victims of the tsunami that smashed into neighbouring West Sepik province earlier this month, a news report said yesterday. The floating bodies were found by fishermen from Skouw Mabo and Skouw Sae villages near the Irian Jaya capital of Jayapura, the official Antara news agency said. Frightened by the sight, the fishermen left the bodies off the border area between Indonesia and Papua New Guinea, and stopped fishing in the area, Antara said. Meanwhile, authorities in the disaster area have dropped plans to destroy the lagoon where the bodies of thousands of people still lie as it is considered sacred by survivors, officials said. The decision came as an international team of doctors began winding down its operations in Vanimo, airlifting 24 survivors and their relatives to a government-run hospital in nearby Wewak. Less than 50 patients remained at the international field hospital in Vanimo yesterday and officials said the operation was likely to be shut down soon. –Agencies (Source: The National newspaper, Port Moresby, Wednesday July 29, 1998, p. 2).

## References

Davies, H.L. (1998): *Tsunami PNG 1998 - Extracts from Earth Talk*. Waigani, University of Papua New Guinea, 48 p.

Davies, H. L., Davies, J. M., Perembo, R. C. B., and Lus, W. Y. (2003), *Reconstructing the Aitape 1998 tsunami from interviews and field mapping*. Pure Appl. Geophys. *160*, 1895–1922.

Dow, D. B., Robinson, G. P., Hartono, U., and Ratman, N. (1986), *Geological map of Irian Jaya, Indonesia, scale 1:1,000,000*, Geological Research and Development Centre, Bandung.

EVERINGHAM, I. B. (1977), *Preliminary catalogue of tsunamis for the New Guinea / Solomon Islands region, 1968–1972,* Bureau of Mineral Resources, Australia, Report 180.

GEDIKILE, H., ILA'AVA, P., and DAVID, M. (2006), *Vanimo risk assessment project preliminary report,* Waigani, University of Papua New Guinea (unpublished).

GEIST, E. L. (2000), *Origin of the 17 July 1998 Papua New Guinea tsunami: Earthquake or landslide?* Seismol. Res. Lett. *71*, 344–351.

HURUKAWA, N., TSUJI, Y., and WALUYO, B. (2003), *The 1998 Papua New Guinea Earthquake and its fault plane estimated from aftershocks,*. Pure Appl. Geophys. *160*, 1829–1841.

IMAMURA, F., SUBNDONO, D., WATSON, G., MOORE, A., TAKAHASHI, T., MATSUTOMI, H., and HIDAYAT, R. (1997), *Irian Jaya earthquake and tsunami causes serious damage, EOS*, Transact. Am. Geophys. Union *78*(19), pp.197 and 201.

ITDB/PAC (2004), *Integrated Tsunami Data Base for the Pacific*, Version 5.1 of June 2004. CD-ROM, Tsunami Laboratory, ICDMMG SD RAS, Novosibirsk, Russia.

KAWATA, Y., TSUJI, Y., MATSUTOMI, H., IMAMURA, F., MATSUYAMA, M., and TAKAHASHI, T. (1999), *Field survey of the 1998 tsunami in the northwestern area of Papua New Guinea,* Report to Ministry of Education, Science, Sports and Culture, Japan.

LYNETT, P. J., BORRERO, J. C., LIU, P. L.- F., and SYNOLAKIS, C. E. (2003), *Field survey and numerical simulations: A review of the 1998 Papua New Guinea tsunami,* Pure Appl. Geophys. *160*, 2119–2146.

MURPHY, J. J. (1950), *District of Sepik (Aitape) Report no. 20/50/51, patrol conducted by JJ Murphy A/ADO Duration from 13/9/1950 to 1/10/1950,* Government of Papua New Guinea Archives.

MATSUMOTO, T. and TAPPIN, D. R. (2003), *Possible coseismic large-scale landslide off the northern coast of Papua New Guinea in July1998*, Pure Appl. Geophys. *160*, 1923–1943.

NORVICK, M. and HUTCHISON, D. S. (1980), *Aitape-Vanimo – 1:250,000 Geological Series – Explanatory Notes,* Geological Survey of Papua New Guinea SA/54-15, SA/54-11.

OKAL, E. A. (1999), *Historical seismicity and seismotectonic context of the great 1979 Yapen and 1996 Biak, Irian Jaya earthquakes*. Pure Appl. Geophys. *154*, 633–675.

OKAL, E. A. (2003), *T Waves from the 1998 Papua New Guinea earthquake and its aftershocks: Timing the tsunamigenic slump*. Pure Appl. Geophys. *154*, 633–675.

SATAKE, K. and TANIOKA, Y. (2003), *The July 1998 Papua New Guinea earthquake: Mechanism and quantification of unusual tsunami generation,* Pure Appl. Geophys. *160*, 2087–2118.

SYNOLAKIS, C., BARDET, J-P., BORRERO, J., DAVIES, H., OKAL, E., SILVER, E., SWEET, S., and TAPPIN, D. (2001), *The slump origin of the 1998 Papua New Guinea tsunami*. Proc. Royal Society London *458*, 763–789.

TANIOKA, Y. (1999), *Analysis of the far-field tsunamis generated by the 1998 Papua New Guinea earthquake*. Geophys. Res. Lett. *26*, 3393–3396.

TAPPIN, D. R., WATTS, P., MCMURTRY, G. M., LAFOY, Y., and MATSUMOTO, T. (2001), *The Sissano, Papua New Guinea tsunami of July 1998 — offshore evidence of the source mechanism*. Marine Geology *175,* 1–23.

(Received February 14, 2006, accepted September 22, 2006)
Published Online First: January 30, 2007

Pure appl. geophys. 164 (2007) 453–463
0033–4553/07/030453–11
DOI 10.1007/s00024-006-0168-1



Pure and Applied Geophysics

# Phases Representing Source Lengths of Tsunami in Tide Gauge Records

KUNIAKI ABE

*Abstract*—We identified a phase representing the source length of tsunami's in the tide gauge records around Japan. This phase was observed at tide stations, located in the direction of the long axis of the sources, for four large tsunamis: 1964 Niigata, 1968 Tokachi-oki, 1983 Nihonkaichubu, and 1993 Hokkaido-nanseioki. The phase consists of two continuous crests starting as the initial arrival and has a time length of 15–47 minutes. This is the time required to propagate across the source area along the long axis. Strong evidence that the phase is generated at the source is the good correlation between waveform observed at one side and time-inversed waveform at another side. The correlation results from the instantaneous generation of the source. The source lengths of 74–254 km were obtained under an assumption of sea depths at the sources and verified to coincide with ones within a relative error of 15% that were previously obtained by other methods.

**Key words:** Length phase, tsunami, tide gauge records, source length, undulation.

## *1. Introduction*

In Japan five hundred tide gauge stations were registered in May, 1989 (GEOGRAPHICAL SURVEY INSTITUTE, 1989). They are mainly constructed by the Japan Meteorological Agency (JMA), Japan Coast Guard, Port Construction office, Geographical Survey Institute and Prefecture Office. Most of them are settled in bays and ports. These stations have recorded many tsunamis including the 1896 Sanriku tsunami. In analyzing tsunamis we can point out two problems. One is a slow response of the tide gauges to a fast change of sea level and another is a problem of harbor resonance. The latter is an excitation of secondary undulation characteristic to enclosed regions at which tide stations are located. The tsunami excites the secondary undulation and it is difficult to separate the original tsunami from the sea-level waveform which consists of the tsunami. The first one became known at the 1983 Nihonkaichubu-oki earthquake tsunami. At that time, the tide gauges responded too slowly to rapid changes at sea level. The slow response of the tide gauges is due to an

Niigata Junior College, Nippon Dental University, Hamauracho 1-8, Niigata City, 951-8580, Japan. E-mail: abeku@ngt.ndu.ac.jp

intake pipe introducing water from the outer sea to the well. The discrepancy was related to recovery time of artificial pumping of water in the well and the recovery times of many tide stations in north Japan were measured by SATAKE *et al.* (1988). Secondly it is an essential problem relating to the amplification of a tsunami. The original meaning of a tsunami is port wave in Japanese and it suggests amplification of a tsunami at port and bay. Part of the amplification results from the resonance of a tsunami to port and bay. The development of secondary undulation results from the resonance. Regarding bay oscillation, NAKAMURA and WATANABE (1961) studied a forerunner observed at the 1960 Chilean tsunami. They attributed the forerunner to multiple reflection due to normal incidence of the tsunami to bays. The bay oscillation in Japan consists of short-period components with 10–30 minutes due to smallness of the bays. This fact suggests that we avoid the use of tsunamis that are normally incident to detect source information. We should use sea-level records obtained from gauges where the incidence of the tsunami is strongly oblique so that the effects of local resonance are damped.

## *2. Response Reduction*

We examined four tsunamis accompanied by earthquakes of 7.5 in magnitude or more originating in Japan. The earthquakes are Niigata Earthquake ($M$: 7.5) on June 16, 1964, Tokachi-oki Earthquake ($M$: 7.9) on May 16, 1968, Nihonkaichubu Earthquake ($M$: 7.7) on May 26, 1983 and Hokkaido Nansei-oki Earthquake ($M$: 7.8) on July 12, 1993. Among them the 1968 earthquake had an epicenter in the Pacific Ocean and the others occurred in the Japan sea as shown in Figure 1. These tsunamis were recorded at many tide stations around Japan. Their sources elongated in the north-south direction.

From the tide gauge records we selected ones which recorded waves propagating in the north direction from the sources and compared them propagating south for each tsunami. They have similar waveforms and are characterized by a long period in comparison with the ones observed at east-west directions of the sources. Thus, one pair of stations were picked for each tsunami: Matsugasaki, and Funakawa, for the 1964 Niigata tsunami, Urakami, and Tomakomai, for the 1968 Tokachi-oki tsunami, Niigata East Port, and Ishikari for the 1983 Nihonkaichubu tsunami, and Noshiro and Wakkanai for the 1993 Hokkaido Nansei-oki tsunami (Fig. 1). Response reductions were carried out for these records using method and data described by SATAKE *et al.* (1988). Recovery times applied to tide stations are 0 s for Ishikari because of the smallness (no reduction), 110 s (in) and 230 s (out) for Noshiro. Average recovery times of 269 s were used for other tide stations, which they did not visit (ABE, 2003). Sea levels, thus reduced and sampled at a time interval of 1 minute, were used for the analysis, which are shown in Figure 2. In the figure, the abscissa is the time elapsed from origin time of the earthquake and ordinate is sea level

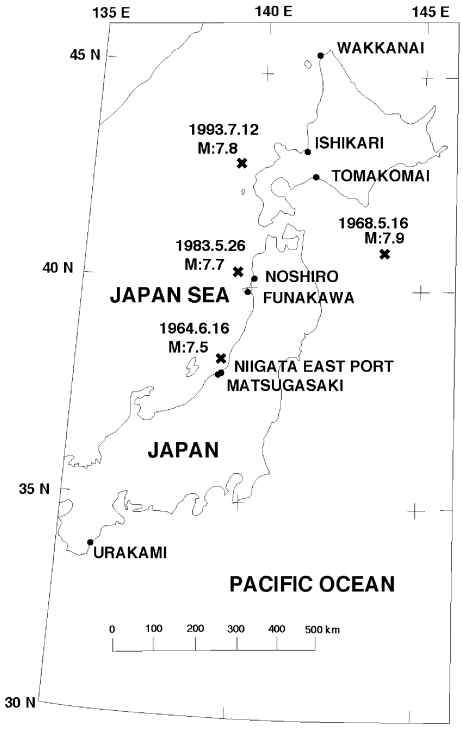


Figure 1
Epicenters of earthquakes generated tsunamis (solid cross) and tide stations (solid circle).

measured from the base line assumed for the digitizer, which was used for the A-D transform. The effect of the tide on the waveform is considered only in the case of the 1968 Tokachi-oki tsunami. The tide is removed from sea-level record using a linear formula applied to sea level before the arrival. Thus, the base line in this case is actually above the mean sea level for this station. For the other sea level records base lines are constant in time and used with no reduction.

## *3. Phases of Source Length*

Comparing initial upward motions observed at Matsugasaki with those at the Funakawa tide stations in the 1964 Niigata tsunami, we noticed a similarity of waveforms. The similarity is characterized by two crests and the same time lengths. Moreover, there is a significant feature of oblique incidences to coasts in the propagation paths. It is known that an oblique incidence prevents the excitation of secondary oscillations in a bay as described before. The propagation paths are satisfied with the condition of oblique incidence at shallow sea. Thus, this phase,

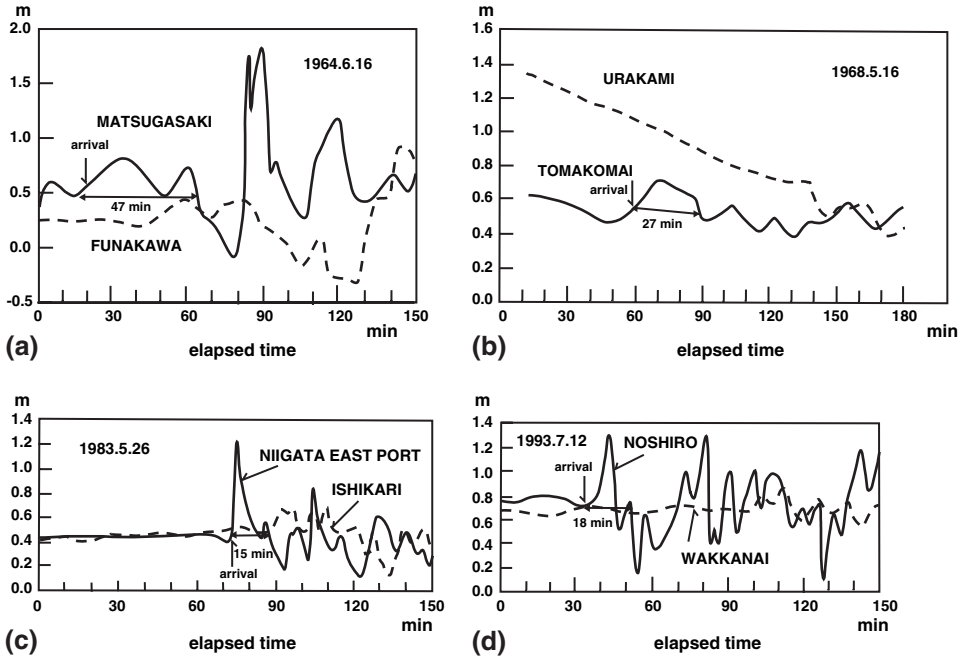


Figure 2
Response-reduced tide gauge records at Matsugasaki (solid line) and Funakawa (dotted line) for the 1964 Niigata earthquake tsunami (a), Tomakomai (solid line) and Urakami (dotted line) for the 1968 Tokachi-oki earthquake tsunami (b), Niigata East Port (solid line) and Ishikari (Ishikari shinkou, dotted line) for the 1983 Nihonkaichubu earthquake tsunami (c), Noshiro (solid line) and Wakkanai (dotted line) for the 1993 Hokkaidonansei-oki earthquake tsunami (d).

upward motion splitting into two, was concluded to be a phase having the origin in the source. To confirm this conclusion we calculated the correlation coefficient between the two. The process is shown in a block diagram of Figure 3. At station A we notice the sea level from the first arrival $T_1$ to zero cross followed from the second crest $T_2$. The sea level is sampled with a time interval of 1 minute. At station A inverse of the time history is taken. Another station is designated B. Correlation is computed from the inversed time profile at A and the time profile at B, and determined as a function of starting time $S_1$ moving the starting time in time profile of B. Similarity of the waveform is expressed by the correlation coefficient. From the maximum value the similarity is estimated. One expects the correlation coefficient to be maximized when the starting time is coincident with the arrival of the tsunami at station B. Thus, the correlation coefficient and the arrival time are obtained simultaneously. The process and result are shown in Figure 4. Arrival time dependence of the correlation coefficient is in the bottom and the correspondence of waveforms at the maximum is in the top. Correlation coefficients obtained are 0.43, 0.96, 0.82 and 0.52 for 1964, 1968, 1983 and 1993 tsunamis, respectively.

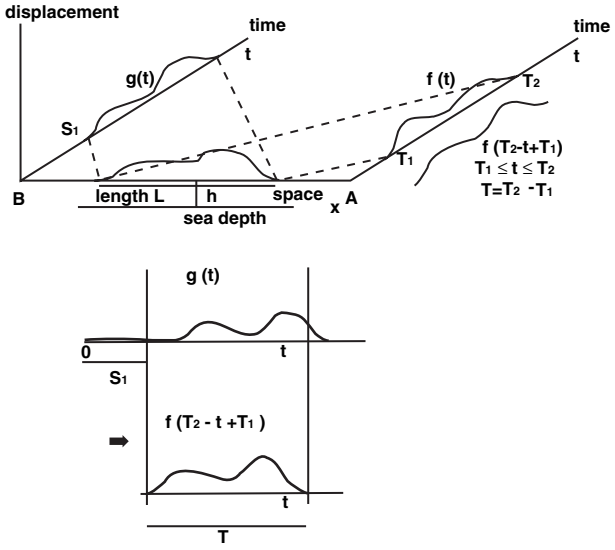


Figure 3
Block diagram of wave sampling at stations A and B (top). Correlation coefficient is obtained as a function of starting time, $S_1$, in $g(t)$ (bottom).

Collectively it is concluded that there are good correlations. It is concluded that time lengths of the particular phases assumed at A stations are applicable to those at B stations. Station's A and B are independent and equivalent to calculate the correlation coefficient. However it is convenient to define time length $T$ based on station A with larger amplitude between two.

## 4. Source Length

The time length of the noticeable phase $T$ results from travel time of the tsunami propagating across the source length $L$. The ideal model is a tsunami accompanied with instantaneous uplift at flat sea bottom. The same waveforms between the time inversed wave and normal wave will be observed at two stations in an opposite direction from the source. The velocity $v$ across the source length $L$ is one of the long wave expressed as the square root of the product of gravitational acceralation $g$ and sea depth $h$, that is

$$v = \sqrt{gh}, \tag{1}$$

and the source length $L$ is defined as

$$L = vT. \tag{2}$$

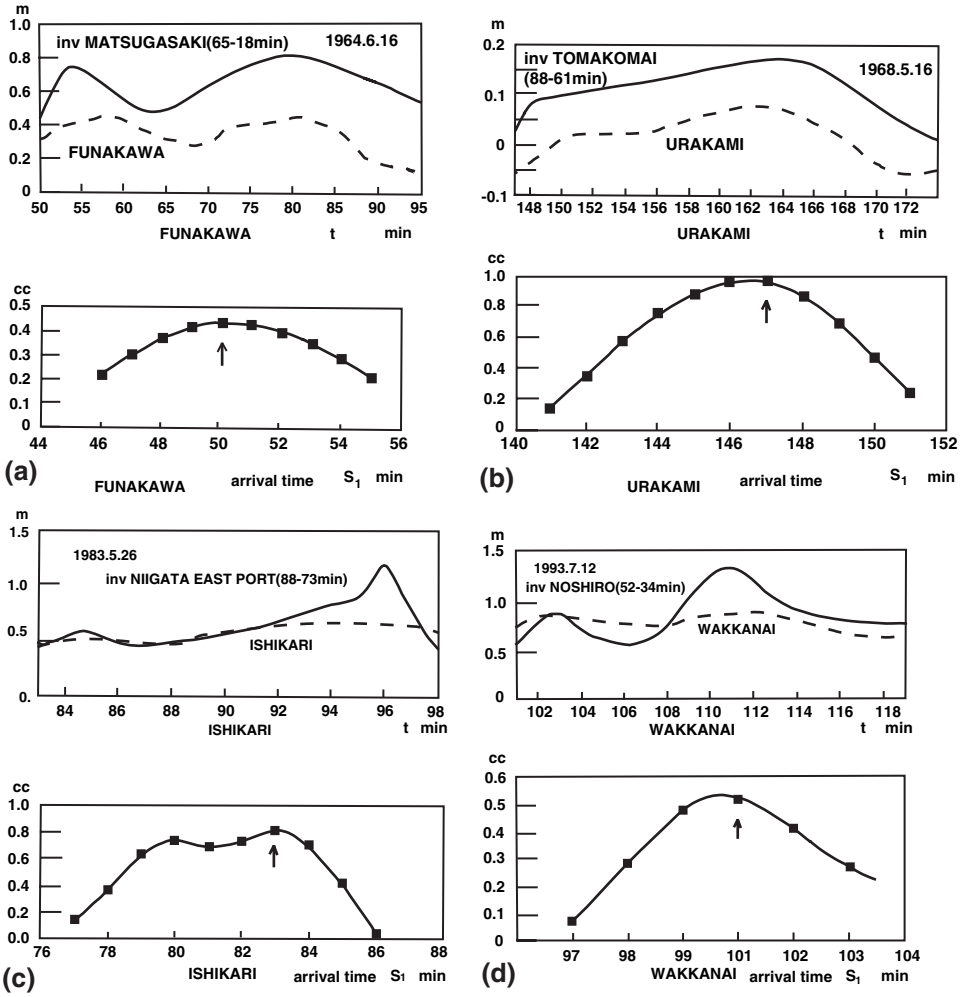


Figure 4
Waveform at Funakawa (dotted line in the top) of the maximum correlation (bottom) to time-inverse of the waveform at Matsugasaki (solid line in the top) (a). Same as at Tomakomai (b), at Ishikari (c), at Wakkanai (d). Arrows show the maxima.

Accordingly, source length $L$ also depends on the velocity $v$. It is not constant on the source because of the uneven bottom. Therefore we take a representative value in the meaning of average along the long axis in the source. Referring to sources previously obtained we approximated the sea depths to be 70 m (ABE, 1978), 2500 m (TSUNAMI RESEARCH GROUP, 1968), 2000 m (HATORI, 1983), and 2500 m (OKADA and NAKAMURA, 1994) for 1964, 1968, 1983 and 1993 tsunamis, respectively, The sources were obtained from inverse refraction diagrams that are shown in Figure 5:(a) (1964 tsunami), (b) (1968 tsunami), (c) (1983 tsunami), (d) (1993 tsunami).

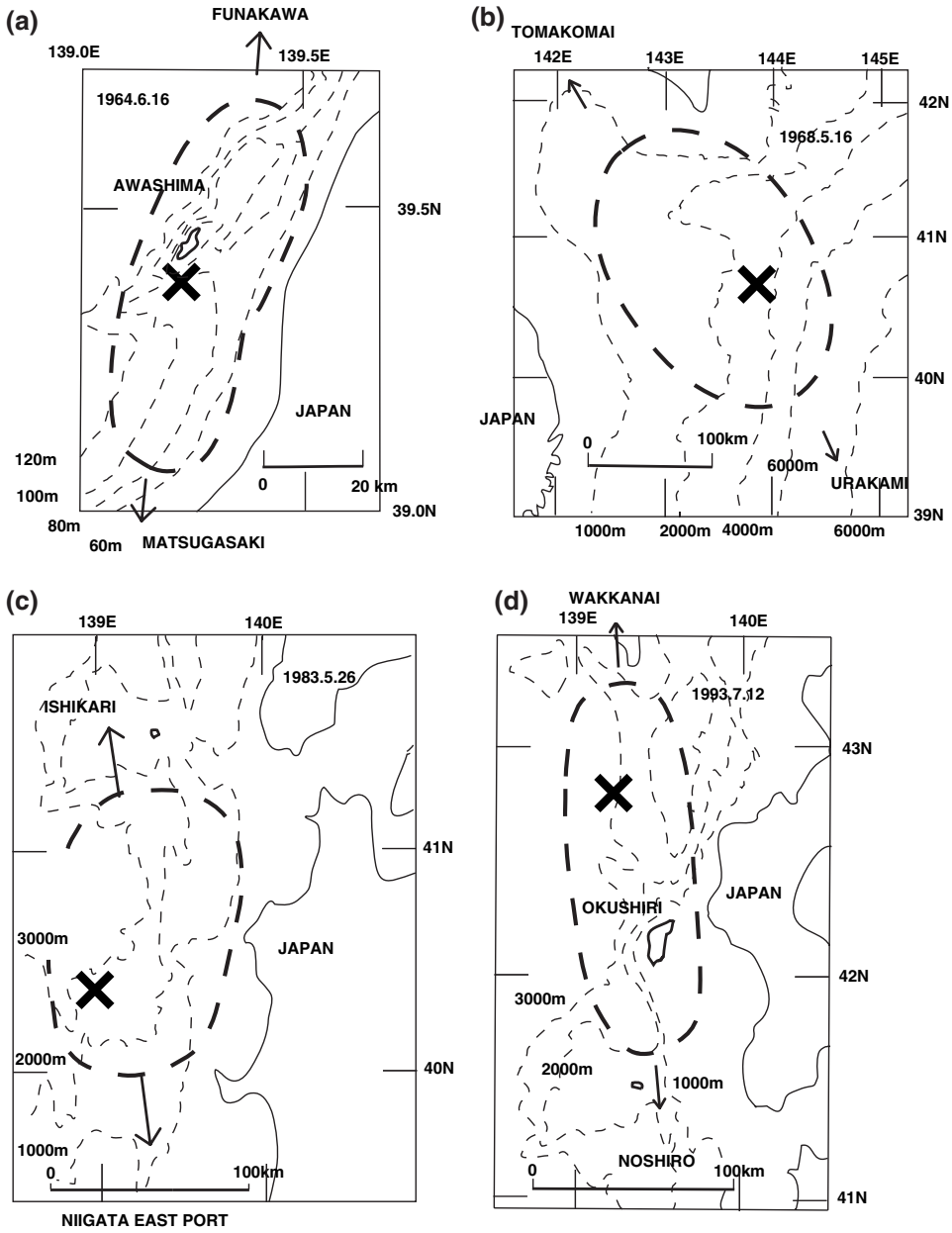


Figure 5

Tsunami source area (dotted line) reproduced for the 1964 tsunami (a), the 1968 tsunami (b), the 1983 tsunami (c) and the 1993 tsunami (d). Arrows show the approximated direction of wave radiation to referred stations. The sources of the original figures are shown in the text. Crosses are the epicenters.

By using time length $T$ and applying the average sea depth $h$ to formula (2) source length $L$ is obtained. They are 74, 254, 126 and 169 km for 1964, 1968, 1983 and 1993 tsunamis, respectively. This is summarized in Table 1. The lengths $L$ are expressed as a function of earthquake magnitude $M$ as shown in Figure 6. The relation is approximated by a linear curve in the semi-logarithmic graph shown with a dotted line. From the least-squares curve fitting we obtain a relation of

$$\mathrm{Log}\, L = 1.31\mathrm{M} - 7.99. \tag{3}$$

This relation was obtained neglecting the fault mechanism from four cases, but the deviation is quite small. Error bars were determined to use the propagation formula applied to formula (2). Error of the length $\Delta L$ results from the time length

Table 1

*Parameter list*

| Tsunami | Tide station A | Arrival time $T_1$ A(min) | Time length $T$ (min) | Tide station B | Arrival time $S_1$ B(min) | Correction coefficient | Sea depth $h$ (m) | Source length $L$ (km) |
|---|---|---|---|---|---|---|---|---|
| 1964 | Matsugasaki | 18 | 47 | Funakawa | 50 | 0.43 | 70 | 74 |
| 1968 | Tomakomai | 61 | 27 | Urakami | 147 | 0.96 | 2500 | 254 |
| 1983 | Niigata East Port | 73 | 15 | Ishikari | 83 | 0.82 | 2000 | 126 |
| 1993 | Noshiro | 34 | 18 | Wakkanai | 101 | 0.52 | 2500 | 169 |

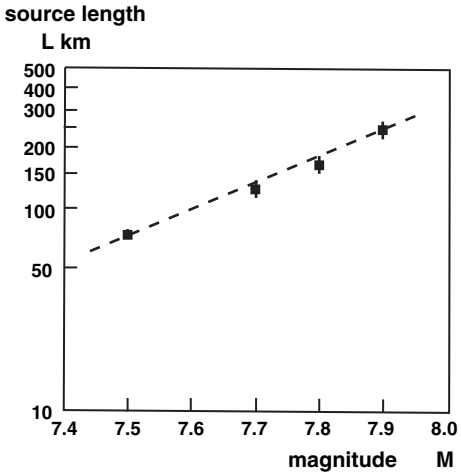


Figure 6
Relation of source length to earthquake magnitude.

of length phase $T$ and sea depth $h$. In a relative error the former is estimated to be 0.025 because of the smallness of error in reading the phase and the latter is estimated to be 0.20 from the unevenness. Since contribution to the result from the latter is half of it the total is less than 0.13. Thus, the obtained source length $L$ is expressed as

$$L \pm \Delta L = (1 \pm 0.13)L. \tag{4}$$

## 5. Discussion

The source lengths calculated from the length phases are compared with those obtained before by other methods. The lengths are 81 km by JMA (1965) for the 1964 Niigata tsunami. It was obtained from the refraction diagram of tsunami arrival times. Since the source mechanism is dip-slip type (HIRASAWA, 1965), the length is approximated to be one of an uplifted region as shown by MANSINHA and SMYLIE (1971). On the other hand the length phase leads us to obtain the length of 74 km. The difference of 7 km is 9% of the total length. In the second case the length obtained from the refraction diagram was 230 km by the TSUNAMI RESEARCH GROUP (1971). The mechanism is dip-slip including some strike-slip component (ABE, KA., 1973). Accordingly, the total length includes some subsided region. Our length phase does not correspond with the total length in this case. The time length of the phase is caused by an extension of the uplifting motion in the sea bottom. Our estimate is 254 km in the length under the sea depth of 2500 m and it is larger in comparison with the former one. The source area is in the continental slope. It is considered that the contribution of shallow sea was larger than that expected in a flat sea bottom of 2500 m. The third and fourth cases are both the pure dip-slip types (SATO, T., 1985; SATAKE and TANIOKA,1995) and the total lengths of the refraction diagram correspond with the uplifted region. From the refraction diagram by HATORI (1983), and OKADA and NAKAMURA (1994) the lengths are 147 and 180 km for the 1983 Nihonkaichubu and 1993 Hokkaido Nansei-oki tsunamis, respectively. In our estimation the former length is 126 km and the latter is 169 km. The relative differences are 14% and 6% for the former and latter cases, respectively. As the result our estimation moderately coincides with the source length estimated on the inverse refraction diagram.

In the case of pure dip-slip the estimated length is considered to be a good approximation of total fault length. However, the correlation between two waveforms is not so high. This result suggests that the length is stable in the propagation but the waveform is not stable. The time length reflects not only source length but also sea depth through the velocity. Since the longest one was found for the 1964 Niigata tsunami, which was the smallest in the earthquake magnitude among the four tsunamis, the time length is mostly affected by the sea depth.

Concluding, we will discuss the correlation coefficient between a waveform at one side and a time-inversed waveform at another side to the source. For lower values of the coefficient we can point out three reasons: (1) Applicability of the theoretical model of instant generation to the observed tsunami. In the 2004 Sumatra tsunami it was reported that the rupture propagated a distance of about 1200 km toward NNW direction unilaterally (e.g., AMMON et al., 2005). The unilateral rupture propagation is one cause of the lower value. A change of sea depth along the propagation paths also is included in this category. (2) Selection of pair stations. It is necessary for two tide stations to be located in the long-axis direction of the source. This condition depends on the density of stations. (3) Excitation of secondary undulation. The secondary undulation brings a disturbance to the length phase. Therefore, the excitation has a role to decrease the coefficient. Oblique incidence is effective to decrease the secondary undulation.

## 6. Conclusion

Phases representing source lengths were identified in tide gauge records of four large tsunamis in Japan. They were observed in the direction of the long axis of the source. The length of time corresponds to the travel time for the tsunami to propagate the source in the direction of the long axis. It was supported by the fact that a similar phase was also observed in the time inverse at another side for the long axis of the source. The source lengths were estimated under an assumption of constant sea depth. Thus were obtained source lengths, 74–254 km, approximate ones were obtained by other methods.

## 7. Acknowledgement

This work is much indebted to the tide gauge records of the tsunamis. Utilized tide gauge records were obtained at Japan Meteorological Agency, Port and River Offices under Government. We are grateful to many persons for keeping tide stations and permitting their use, and also to R.Wellensiek for critical reviewing.

## REFERENCES

ABE, Ka. (1973), *Tsunami and mechanism of great earthquakes*, Phys. Earth Planet. Inter. *7*, 143–153.

ABE, Ku. (1978), *A bending fault model of the 1964 Niigata Earthquake*, Bull. Nippon Dental Univ., General Education *7*, 59–68.

ABE, Ku. (2003), *Source model of a small tsunami accompanied with a volcanic earthquake at Kouzu-shima on July 1, 2000*, Zisin 2(56), 181–187 (in Japanese).

AMMON, J.C., JI, C., THIO, H., ROBINSON, D., NI, S., HJORLEIFSDOTTIR, V., KANAMORI, H., LAY, T., DAS, S., HELMBERGER, D., ICHINOSE, G., POLET, J. and WALD, D. (2005), *Rupture process of the 2004 Sumatra-Andaman earthquake*, Science *308*, 1133–1139.

GEOGRAPHICAL SURVEY INSTITUTE (1989), *List of tide stations in Japan*, pp. 1–127 (in Japanese).

HATORI, T. (1983),*Tsunami magnitude and source area of the Nihonkai-Chubu (the Japan Sea) earthquake in 1983*, Bull. Earthq. Res. Inst., Tokyo Univ., *58*, 723–734 (in Japanese).

HIRASAWA, T. (1965), *Source mechanism of the Niigata earthquake of June 16, 1964, as derived from body waves*, J. Phys. Earth *13*, 35–66.

JAPAN METEOROLOGICAL AGENCY (1965), *The report of the Niigata earthquake, 1964*, Technical report of JMA *43*, p. 211 (in Japanese).

MANSINHA, L. and SMYLIE, D.E. (1971), *The displacement fields of inclined faults*, B.S.S.A. *61*, 1433–1440.

NAKAMURA, K. and WATANABE, H. (1961), *Tsunami forerunners observed in the case of the Chile Tsunami of 1960, Rep. Chilean Tsunami of May 24,1960, as observed along the coast of Japan*, In (R. Takahashi *et al.*, eds) *The Chilean Tsunami of May 24,1960*, pp. 67–76.

OKADA, M. and NAKAMURA, K. (1994), *Okushiri tsunami and tide gauge records*, Kaiyo Monthly *7*, 123–131 (in Japanese).

SATAKE, K., OKADA, M., and ABE, Ku. (1988), *Tide gauge response to tsunamis: Measurements at 40 tide gauge stations in Japan*, J. Mar. Res. *46*, 557–571.

SATAKE, K. and TANIOKA, Y. (1995), *Tsunami generation of the 1993 Hokkaido Nansei-Oki earthquake*, Pure Appl. Geophys. *145*, 803–821.

SATO, T. (1985), *Rupture characteristics of the 1983 Nihonkai-Chubu(Japan Sea) Earthquake as inferred from strong motion accelerograms*, J. Phys. Earth *33*, 525–557.

TSUNAMI RESEARCH GROUP, Faculty of Sci.,Tohoku Univ. (1971), *Analyses of the tsunami accompanying the Tokachi-oki earthquake of 1968*. In *General Report on the Tokachi-oki earthquake of 1968*, *Keigaku,Tokyo*, 153–188.

(Received January 1, 2006, accepted September 27, 2006)

Pure appl. geophys. 164 (2007) 465–492
0033–4553/07/030465–28
DOI 10.1007/s00024-006-0169-0



Pure and Applied Geophysics

# Numerical Simulations of Tsunami Waves and Currents for Southern Vancouver Island from a Cascadia Megathrust Earthquake

Josef Y. Cherniawsky,[1] Vasily V. Titov,[2] Kelin Wang,[3] and Jing-Yang Li[4]

*Abstract*—The 1700 great Cascadia earthquake (M = 9) generated widespread tsunami waves that affected the entire Pacific Ocean and caused damage as distant as Japan. Similar catastrophic waves may be generated by a future Cascadia megathrust earthquake. We use three rupture scenarios for this earthquake in numerical experiments to study propagation of tsunami waves off the west coast of North America and to predict tsunami heights and currents in several bays and harbours on southern Vancouver Island, British Columbia, including Ucluelet, located on the west coast of the island, and Victoria and Esquimalt harbours inside Juan de Fuca Strait. The earthquake scenarios are: an 1100-km long rupture over the entire length of the subduction zone and separate ruptures of its northern or southern segments. As expected, the southern earthquake scenario has a limited effect over most of the Vancouver Island coast, with waves in the harbours not exceeding 1 m. The other two scenarios produce large tsunami waves, higher than 16 m at one location near Ucluelet and over 4 m inside Esquimalt and Victoria harbours, and very strong currents that reach 17 m/s in narrow channels and near headlands. Because the assumed rupture scenarios are based on a previous earthquake, direct use of the model results to estimate the effect of a future earthquake requires appropriate qualification.

**Key words:** Tsunami waves, Cascadia subduction zone, megathrust earthquake, numerical modelling.

## 1. Introduction

The Cascadia subduction zone (CSZ) is a convergent plate boundary off the west coast of North America where the Juan de Fuca Plate is subducted beneath the North America Plate (Fig. 1). The two plates move relative to each other at an average rate of about 4 cm year$^{-1}$, but are currently locked along a fault segment about 1100-km long and 100-km wide. The strain energy accumulating due to the locking of the subduction fault will be released in giant earthquakes. These great plate boundary earthquakes commonly cause large tsunamis. From various geological, paleoseismic and paleotsunami investigations spanning the last 7,000

[1] Institute of Ocean Sciences, Fisheries and Oceans Canada, P.O. Box 6000, Sidney, B.C., V8L 4B2, Canada. E-mail: cherniawskyj@pac.dfo-mpo.gc.ca
[2] NOAA/Pacific Marine Environmental Laboratory, Seattle, WA, U.S.A.
[3] Pacific Geoscience Centre, Geological Survey of Canada, Sidney, B.C., Canada.
[4] Department of Computer Science, University of Victoria, Victoria, B.C., Canada.

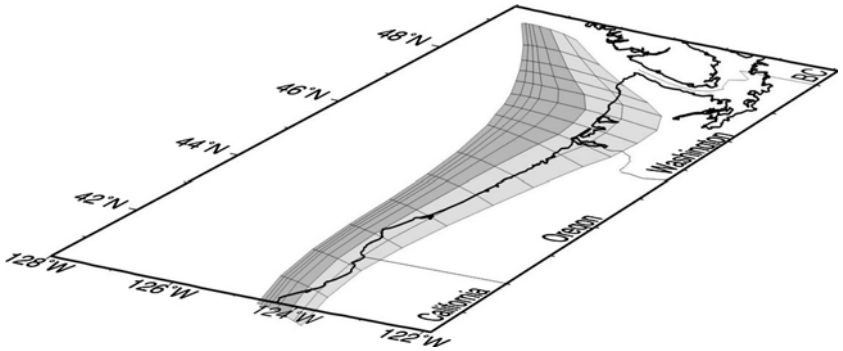


Figure 1
Fault geometry used to calculate coseismic deformation in the Cascadia subduction zone (CSZ). Dark-shaded fault area is the region of full rupture. Light-shaded area is the downdip transition zone over which slip decreases from full-rupture value to zero (modified from WANG *et al.*, 2003).

years (ATWATER, 1987; ADAMS, 1990; ATWATER and HEMPHILL-HALEY, 1997; CLAGUE, 1997; CLAGUE *et al.*, 2000; HUTCHINSON *et al.*, 2000; GOLDFINGER *et al.*, 2003; WITTER *et al.*, 2003; KELSEY *et al.*, 2005; WILLIAMS *et al.*, 2005), Cascadia megathrust earthquakes and associated tsunamis occur at irregular intervals, from a couple of hundred years to a thousand years, with an average interval of 500–600 years.

The last megathrust CSZ earthquake occurred in January 1700 and created tsunami waves that were observed and recorded in Japan (SATAKE *et al.*, 1996; 2003). ATWATER *et al.* (2005) describe in detail the detective work undertaken in the past 20 years on this event using numerous scientific clues from both Japan and North America. Records from Japanese villages pinpoint the tsunami date to January 26, 1700. Inverse model calculations of SATAKE *et al.* (2003), who used run-up and timing data at seven locations in Japan, suggest a rupture length of ~1100 km and moment magnitude $M_w \approx 9$.

There are certain paleo-observations of tsunami sediments from past CSZ megathrust earthquakes that can be used to estimate tsunami run-up on the west coast (CLAGUE *et al.*, 2000; HUTCHINSON *et al.*, 2000; PETERS *et al.*, 2003; KELSEY *et al.*, 2005). For example, marine sediment deposits at several nearshore lakes on Vancouver Island indicate *minimal* run-up heights between 1 and 4 m above mean sea level. However, from field studies of more recent events, a tsunami run-up usually extends at least twice as far inland as the sand layers deposited by such tsunami, which may indicate that run-up heights at these lakes could have been higher, as observed during the 2004 Sumatra tsunami (V. Barrie, personal communication, 2004). Given the paucity of such observations and the difficulty in interpreting the extent of marine sediments at few sites, another practical way to

derive estimates of maximum wave heights over a long coastline is by using numerical models.

There are a number of published numerical model results for tsunamis in this region, though many of them (e.g., MURTY and CREAN 1986; DUNBAR *et al.*, 1989; 1991) describe the 20th century tsunamis generated in other subduction zones. The potential impact of tsunamis from a CSZ megathrust earthquake on the west coast of North America has been investigated by several researchers (HEBENSTREIT and MURTY, 1989; MURTY and HEBENSTREIT, 1989; NG *et al.*, 1990; WHITMORE, 1993; MYERS *et al.*, 1999; PRIEST *et al.*, 2000). For example, NG *et al.* (1990) conducted a study of such tsunami using three finite-difference numerical models covering different areas: (a) a large-scale deep-ocean model with a 5-km grid for tsunami generation and propagation, (b) a 2-km grid model for propagation in the Juan de Fuca Strait and the Strait of Georgia, and (c) one-dimensional 2-km model for Alberni Inlet. They found the outer coast of Vancouver Island to be most affected, with maximum water levels in Barkley Sound and at the head of Alberni Inlet reaching 5 m and 16 m, respectively.

The 2-km grid in the NG *et al.* (1990) model is rather coarse, as are other finite-difference models listed above, and is not suitable for modelling waves in harbours and narrow channels. This may explain the relatively small maximum wave values for Victoria (2 m) and in the Strait of Georgia ($< 1$ m) and the overly high value for Sooke Basin (2 m), which is sheltered from Juan de Fuca Strait by a narrow and very shallow channel.

Most tsunami models for this region, and the model described here, are of the finite-difference type that use rectangular grid cells. The exception is the finite-element model used by MYERS *et al.* (1999; also in PRIEST *et al.*, 2000), which has variable spatial resolution and thus a more flexible representation of coastlines and smaller bathymetric features.

Finite-element models are commonly used for modelling barotropic tides in a spectral domain. These applications are very efficient as they do not require stepping in time (e.g., FOREMAN *et al.*, 2000, and references therein). Time-stepping finite-element models are also used, but due to various numerical approximations, such as the use of implicit solvers, they are prone to damping of high-frequency signals. They also tend to be technically more complex and have therefore received limited use in the tsunami modelling community.

The MYERS *et al.* (1999) CSZ tsunami model, as well as the more recent results from the NOAA National Tsunami Hazard Mitigation Program, Center for Tsunami Inundation Mapping Efforts (TIME)[1], are focused mainly on the bays and harbours in Oregon and Washington, with little attention paid to tsunami waves on Vancouver Island, which are the subject of this work.

[1] http://www.pmel.nooa.gov/tsunami/time

In the next section we present recently computed subduction scenarios that we used to simulate CSZ-generated tsunamis. The nested-grid finite-difference numerical model MOST-3, which has a very fine inner grid size (~10 m), is described in section 3, while modelled tsunami wave propagation and the properties of waves and currents in harbours are discussed in sections 4 and 5.

## 2. CSZ Earthquake Scenarios

An idealized geometry of the 1700 CSZ megathrust tsunami source is shown in Fig. 1 (Wang *et al.*, 2001, 2003). The coseismic slip distance in the full-slip area (dark shading) is assumed to be the plate convergence rate times 500 years, the approximate average recurrence interval of great Cascadia earthquakes. The coseismic slip has small along-strike variations, because the convergence rate and direction vary slightly along strike. The average slip distance in the full-slip zone is about 19 m. Downdip of the full-slip zone is the transition zone (light shading in Fig. 1), over which coseismic slip tapers linearly to zero.

The average coseismic fault slip of 19 m assumed in these models is equivalent to 500 years of plate convergence, that is, the earthquake is assumed to recover all slip deficit accumulated over 500 years of fault locking. If the next Cascadia megathrust earthquake were to occur now, just over 300 years since the 1700 event, the amount of slip is expected to be much less than 19 m, except for limited fault patches that may exhibit some "over shoot". The 19-m values may therefore represent an overestimate.

While this was a reasonable scenario for the 1700 earthquake (SATAKE *et al.*, 2003), the amplitude and geographical extent of the next CSZ megathrust earthquake are, of course, unknown. We therefore investigate here tsunami waves that may originate from three possible deformation scenarios, named in SATAKE *et al.* (2003) (a) *long-narrow*, (b) *short-north and* (c) *short-south*.

The *long-narrow* scenario is an 1100-km long rupture along the entire CSZ, from Cape Mendocino at ~40.5°N to the Nootka fracture zone near 49.5°N (Fig. 1). In the other two scenarios, the rupture is limited to either a northern or a southern portion of the CSZ. It is reasonable to assume that such partial ruptures can occur at different times. The *short-north* scenario extends north 670 km, from 44.3°N off central Oregon, whereas the *short-south* scenario extends from the same location 440 km south to Cape Mendocino. Earthquake magnitudes ($M_w$), equivalent uniform rupture widths and full-slip zone widths (in km) for these three scenarios are (a) 9.0, 74, 48, (b) 9.0, 87, 56, and (c) 8.8, 56, 37 (SATAKE *et al.*, 2003).

Our emphasis in this work is on the effects of tsunami waves on the British Columbia coast. We therefore placed the south boundary of the tsunami model at 43°N (Fig. 2), thus also reducing the southward extent of the *long-narrow* and *short-south* scenarios. As we shall see below, this restriction has little effect on tsunami

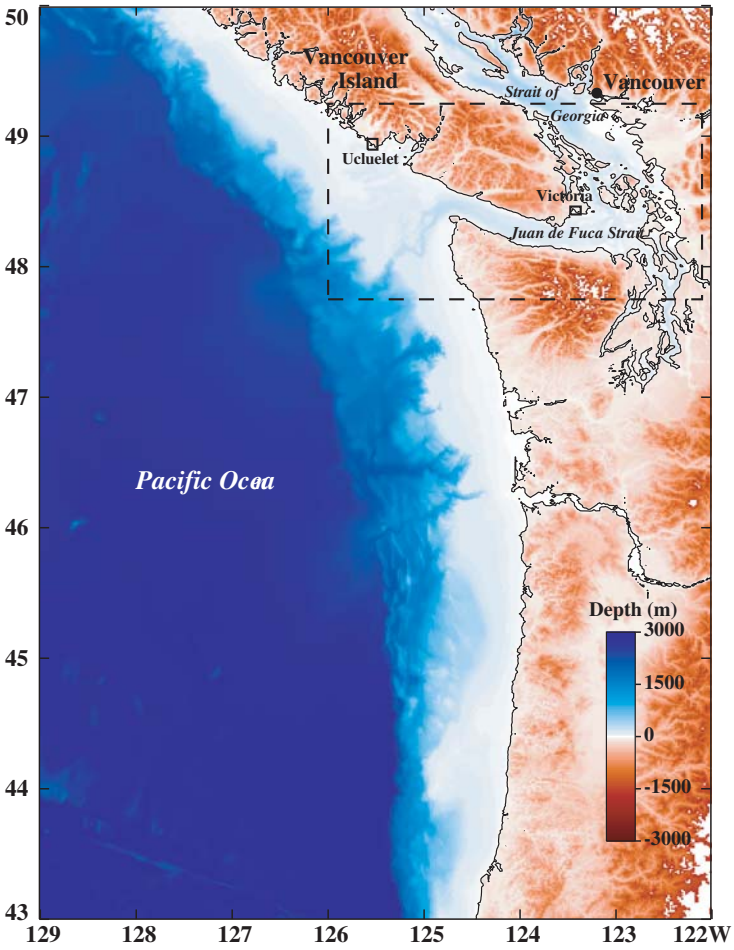


Figure 2
Numerical model domain and bathymetry. Dashed frame shows the medium-resolution grid, which includes Juan de Fuca Strait and the southern Strait of Georgia. Small rectangles mark two high-resolution grids for Ucluelet Inlet and Victoria and Esquimalt harbours.

waves in this region. However, if we were investigating the waves on California or southern Oregon coasts, the tsunami model domain would have to be extended farther south.

## 3. Numerical Model

The MOST-3 (Method Of Splitting Tsunamis, version 3) numerical model was described by TITOV and SYNOLAKIS (1997; 1998). It solves the nonlinear shallow-water wave equations

$$\frac{\partial h}{\partial t} + \nabla \cdot (\mathbf{u}h) = 0 \tag{1}$$

$$\frac{\partial \mathbf{u}}{\partial t} + \mathbf{u} \cdot \nabla \mathbf{u} + g\nabla h = g\nabla d - \mathbf{R} \tag{2}$$

where $h = \eta + d$, $\eta$ is the wave displacement, $d$ is the undisturbed water depth, $\mathbf{u} = (u, v)$, with $u$ and $v$ the depth-averaged east and north velocity components, g is the acceleration due to gravity, and $\mathbf{R} = (R_x, R_y)$ is the bottom friction term. The Coriolis force is not included here as its contribution in the wave equation is relatively small for tsunamis with typical wave periods of less than 100 minutes (TITOV and GONZÁLEZ, 1997; TITOV *et al.*, 2003).

The numerical procedure of solving this coupled set of partial differential equations was explained by TITOV and SYNOLAKIS (1997; 1998). This procedure is carried out on nested finite-difference grids, with free propagation of waves between the grids and out of the coarsest grid, using radiation conditions at its open boundaries.

The bottom friction $\mathbf{R} = C_f|\mathbf{u}|\mathbf{u}/h$ is used only in the fine-resolution grid. It requires specification of the friction coefficient $C_f$, which can be expressed in terms of Chezy's ($C$), or Manning's ($n$) coefficients, $C_f = g/C^2 = gn^2/h^{1/3}$ (e.g., RAMMING and KOWALIK, 1980; CHU and ABE, 1983; SATAKE, 1995). We used here a constant $n = 0.039$ m$^{-1/3}$s, which is comparable to shallow-water run-up values given in SATAKE (1995). Notably, this friction term becomes important only in very shallow water.

The nested grids used in this work are shown in Fig. 2 and described in Table 1, which lists relevant details, such as the number of grid points ($N_x$, $N_y$) and nominal horizontal grid size in meters ($\Delta x$, $\Delta y$). The three grids used in each simulation have coarse ("A" in Table 1), medium ("B") and fine ("C") horizontal resolution. The coarse and medium grids are the same in all experiments. Two fine grids were used for Victoria and Esquimalt harbours ("$C_{VE}$") and for Ucluelet Inlet ("$C_{Ucl}$").

The time step is subject to a numerical stability criterion: $\Delta t < \Delta_{\min}/\max(c + |\mathbf{u}|)$, based on smallest grid spacing $\Delta_{min} = \min(\Delta x, \Delta y)$ and maximum of tsunami phase speed and velocity in the fine grid. It was $\Delta t = 0.2$ sec for the Ucluelet fine grid and

Table 1

*Description of nested grids*

| Grid | $N_x$ | $N_y$ | Latitude range | Longitude range | $\Delta x \times \Delta y$ (m) |
|---|---|---|---|---|---|
| A | 351 | 700 | 43.000–50.000 | 122.000–129.000 | 1530×1100 |
| B | 1170 | 900 | 47.750–49.248 | 122.103–126.000 | 245×185 |
| $C_{VE}$ | 1200 | 675 | 48.400–48.461 | 123.368–123.476 | 6.6×10.1 |
| $C_{Ucl}$ | 738 | 889 | 48.897–48.979 | 125.486–125.588 | 10.0×10.3 |

0.15 sec for the Esquimalt and Victoria grid. Calculations on the medium and coarse grid were performed every 5 and 10 $\Delta t$, respectively.

The MOST-3 model includes moving boundary conditions to simulate onshore run-up and draw-down. These have been shown to work well when tested against actual observations of tsunami inundation (e.g., TITOV and SYNOLAKIS, 1997; TITOV *et al.*, 2005). However, high-resolution land topography data were not available for the nearshore areas surrounding the harbours. We therefore used vertical walls as land boundaries, albeit allowing draw-down when the waves retreat and subsequent run-up over the shallow areas in each fine-resolution grid.

## 4. Tsunami Wave Propagation

Underwater ground motion during a CSZ megathrust earthquake (Fig. 1) translates into water surface deformation that forms a long solitary surface wave over the source region, made of parallel positive and negative parts. As is the case for most subduction earthquakes, the positive part of this initial deformation is on the open ocean side, while the negative part, of smaller amplitude but wider extent, is close to and encroaches on land, causing subsidence of up to 1.9 m at the coast.

This initial surface wave disturbance splits into two long gravity waves. The westward wave moves across the Pacific Ocean and reaches Japan after about 10 hours (e.g., SATAKE *et al.*, 2003), while the eastward wave moves towards North America and its continental shelf. Theoretical descriptions of tsunami wave propagation and transformation over deep ocean, continental shelf and irregular coastlines are given in various monographs (e.g., MURTY, 1977; RABINOVICH, 1993) and are not repeated here. The following results from the MOST-3 model are consistent with the theory, showing how such waves are modified over variable bathymetry and propagate through nested model grids towards the two selected high-resolution areas, one located on the west coast of Vancouver Island and the other inside the Juan de Fuca Strait (Fig. 2).

### 4.1. West Coast of North America

We compare here wave propagation for the three CSZ earthquake scenarios described in section 2. The initial tsunami waves for each of these scenarios are shown in the left panels in Fig. 3. The other two panels show waves at 25 minutes and at 1 hour and 25 minutes after the earthquake. Model results from the higher-resolution medium grid (Fig. 2 and Table 1) were also included (interpolated) for display on this coarse grid. Note that snapshots of waves shown on Fig. 3 and in subsequent plots are relative to mean sea level (MSL), and hence effects of storm surges or tides are not included. Notably, MOFJELD *et al.* (1997) showed that low, neap tides were prevalent during the 1700 CSZ earthquake all along the West Coast.

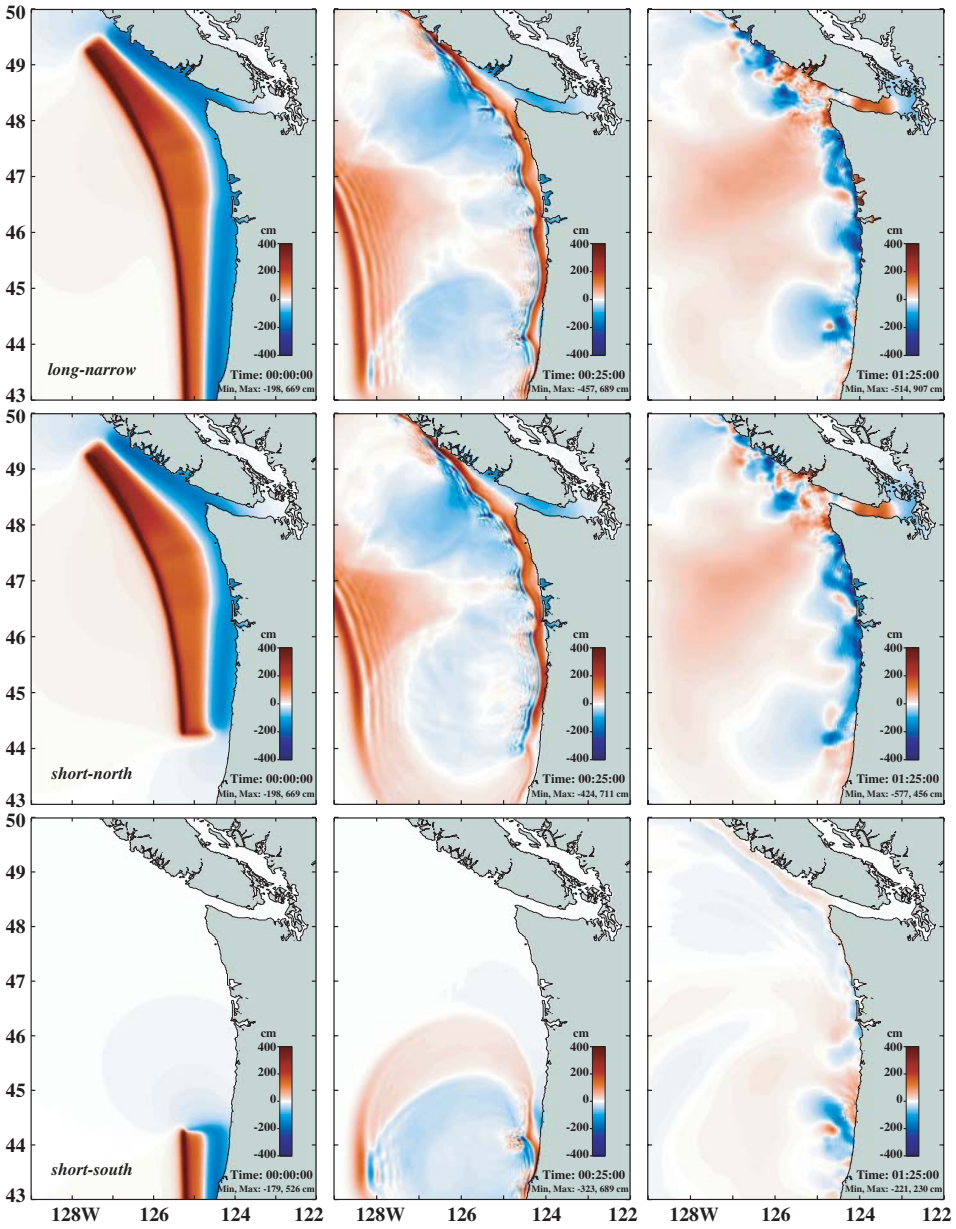


Figure 3
Model tsunami waves on coarse grid at 0:00, 0:25 and 1:25 (hour: minute) after CSZ earthquake for three deformation scenarios: *long-narrow*, *short-north* and *short-south*.

The resulting smaller tidal range has therefore diminished the importance of tides for this particular event.

Minimum and maximum values of the initial wave profiles are the same for the first two scenarios, −2.0 and 6.7 m, and somewhat smaller, −1.8 and 5.3 m, for the *short-south* scenario. Indeed, results for the *long-narrow* and *short-north* scenarios appear to be very similar for British Columbia, Washington and northern Oregon coasts. We therefore limit our discussion to the *long-narrow* and *short-south* initial deformation cases.

***Long-narrow scenario.*** The three snapshots for this case are displayed in the top panels of Fig. 3. Due to the shape of the initial deformation, and as is the case for similar subduction earthquakes elsewhere, the leading part of the wave approaching the coast is negative, causing a moderate drop in sea level and water withdrawal from shallow areas, before the arrival of a first positive wave. This wave front (left panel) splits into westward and eastward waves, with leading positive and smaller trailing negative wave profiles transformed within minutes (not shown) into nearly symmetrical (positive and negative) wave forms with an amplitude of ~4 m. Their deep-ocean group and phase speeds are essentially the same, $c_g \approx c = (gH)^{1/2}$. For a typical 4-km water depth, this speed is 200 m $s^{-1}$, or 720 km $hr^{-1}$.

At 25 minutes after the earthquake (middle panel), the westward positive wave front moves rapidly over deep water out of the model western boundary, followed by a train of shorter waves from numerical dispersion in the model. At the same time, the eastward positive wave front has already reached several locations along the coast where the continental shelf is narrower than elsewhere, such as the coast of northern California and the central west coast of Vancouver Island (Fig. 2).

The specified scenarios have a finite meridional extent, introducing end effects at their northern and southern boundaries. Thus circular wave fronts emanate from south and north ends of the initial deformation and move towards each other, forming extensive negative-elevation pools behind the zonally propagating plane waves (middle panels in Fig. 3).

The waves become slower, shorter and steeper, as they climb onto the shelf, and variable shelf and coast geometry lead to wave refraction and convergence, producing the irregular pattern of wave fronts (middle panel) and, somewhat later (right panel), surface signatures of edge waves that are generated by scattering of arriving waves by the irregular coastline. Edge waves have a discrete spectrum and are part of a family of coastal trapped waves, which includes shelf waves and shelf-slope-modified Kelvin waves (e.g., LeBlond and Mysak, 1978; Rabinovich, 1993). In addition to edge waves, a continuous spectrum of the so-called "leaky" waves (as opposed to trapped waves) radiate away from the shelf.

Edge-wave properties depend on the shape and dimensions of the continental shelf and slope. Edge waves move slowly along the shelf, as the group speed of their

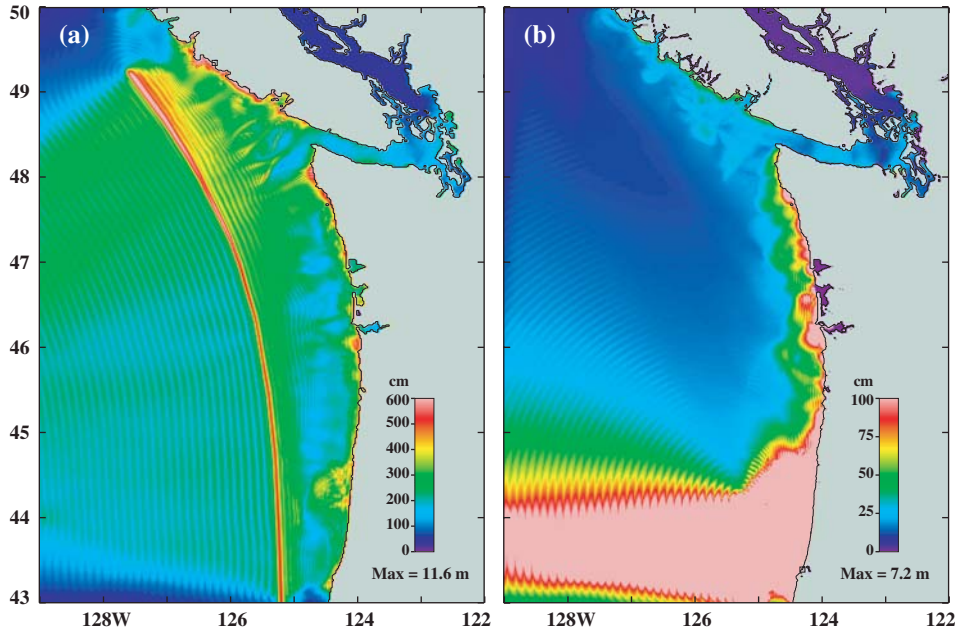


Figure 4
Maximum wave elevations on the coarse grid for (a) *long-narrow* and (b) *short-south* deformation scenarios computed from output data stored at a 1-minute interval. A different colour scale was used in (b) to display weak signals near Vancouver Island coast.

gravest mode is of the order of 10 m $s^{-1}$ (e.g., González *et al.*, 1995), which is slower than the speed of deep-ocean tsunami waves by a factor of about 20 and is also slower than gravity wave speed $\sqrt{gH}$ on the shelf by a factor of 2–4.

Kajiura (1972) derived analytical solutions to the shallow-water wave equation with a tsunami source near a shelf. His solutions for a step-like shelf profile, with $H_1/H_2 = 0.05$ ($H_1$ and $H_2$ are depths of the shelf and the deep ocean) and a relatively long source region ($a \geq l$, where $2a$ is the source length and $l$ shelf width) located mostly in the deep ocean (similar to CSZ), show that only a small fraction of initial wave energy is contained in edge waves, mainly in their leading mode. Most of the energy is in the "leaky" modes, either radiated directly to the open ocean or reflected away from the shelf. Our numerical model results (right panels of Fig. 3) and, in particular, tsunami model animations on the IOS website[2], show the trapped waves as height anomalies moving slowly along the coast, while "leaky" waves move west, away from the shelf.

The tsunami model was run for a duration of 12 hours of simulated time. Maximum wave elevations on the relatively coarse grid exceed 11 m at several

[2] http://www-sci.pac.dfo-mpo.gc.ca/osap/projects/tsunami/tsunamimodel_e.htm

locations on the west coast of Vancouver Island, both north and south of Ucluelet, at 33, 45 and 54 minutes. Fig. 4a shows maximum values from sea-level data every 1 minute, thus also displaying the offshore wave fronts at these time intervals. As expected from deep-ocean and shelf bathymetry (Fig. 2), the westward waves move faster than eastward waves. The latter are also more variable due to complex shelf topography, which includes deep canyons and shallow banks. These irregular coastlines cause wave refraction and convergence onto the banks, as will be seen in greater detail below, in section 4.2.

***Short-south scenario.*** This is a plausible scenario because many great earthquakes involve the rupture of limited segments of a subduction zone. The *short-south* deformation segment has a limited extent in our model domain. Because of the orientation of the source, most of the wave energy flux is towards the east and west, and only a small part of the initial wave energy is contained in semi-circular waves that move north and northwest (bottom panels in Fig. 3). While much of the eastward wave energy is reflected back into the open ocean, the remainder interacts with the variable coastline, producing trapped edge waves that move slowly north along the shelf, as was discussed above.

After about 1 hour and 20 minutes, tsunami waves arrive at the mouth of Juan de Fuca Strait. This arrival time is consistent with deep-ocean propagation of the initial wave front and its refraction onto the shelf. These incoming waves have a relatively small (generally, $<1$ m) amplitude on the Vancouver Island coast.

Such wave elevations may seem rather small for a large ($M_w = 8.8$) earthquake. However, most of the wave energy is in the ''leaky'' modes radiating into the open ocean away from the linear source, with relatively little energy directed to the north. The directional nature of the wave energy flux is quite evident in Fig. 4b, which shows the maximum wave elevations for this scenario. These were computed as in Fig. 4a, but are displayed with a 6-fold enhancement in the colour scale, allowing to discern the relatively weak signals along the Vancouver Island coast.

### *4.2. Southwest Coast of Vancouver Island, Juan de Fuca Strait and the Strait of Georgia*

Results of the model tsunami waves on the medium grid are presented here for the *long-narrow* scenario. The results from the *short-north* scenario are similar to those shown, whereas the waves from the *short-south* scenario are much smaller, as was discussed above (Fig. 3). The latter scenario will be discussed again in section 5.2, where we compare the waves from the two scenarios in Victoria and Esquimalt harbours.

Ocean depths and coastlines in the area covered by the model medium-resolution grid are complex (Figs. 2 and 5). The wide continental shelf contains several canyons

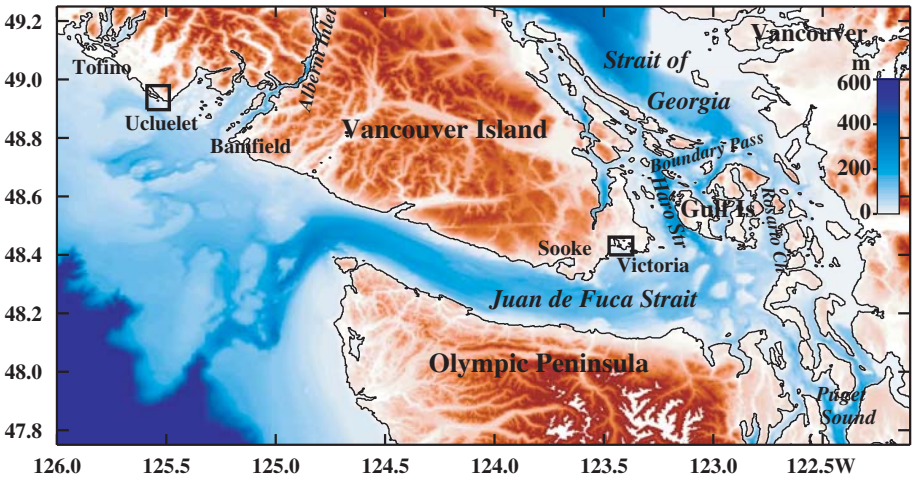


Figure 5
Ocean bathymetry and place names on the model medium grid. The two rectangles show the areas of high-resolution grids for Ucluelet Inlet and for Esquimalt and Victoria harbours.

and shallow banks, with the deep Juan de Fuca Canyon leading into the entrance of Juan de Fuca Strait.

Another relatively deep trough, with depths up to 150 m, called Barkley Sound, extends into Alberni Inlet (Fig. 5), whose 85-minute resonant period (HENRY and MURTY, 1995) is the likely cause of singularly large tsunami waves after the 1964

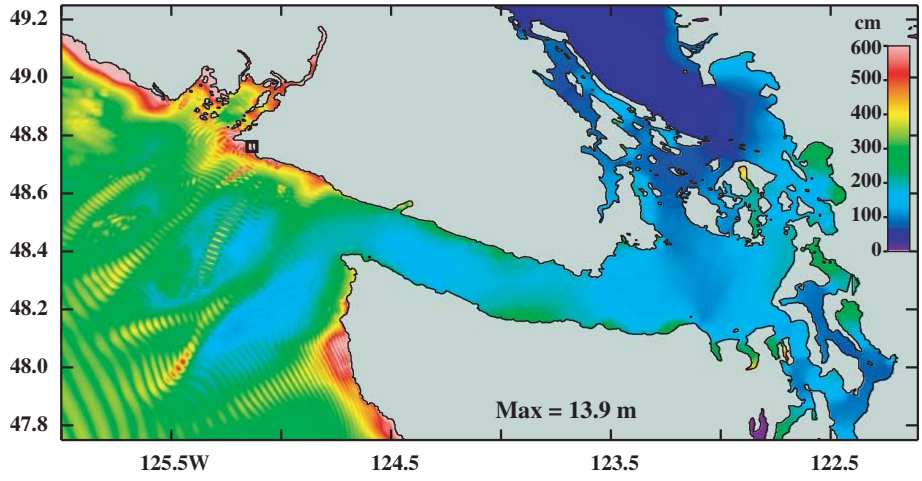


Figure 6
Maximum wave elevations on the model medium grid for the *long-narrow* deformation scenario computed from output data stored at 1-minute time interval.

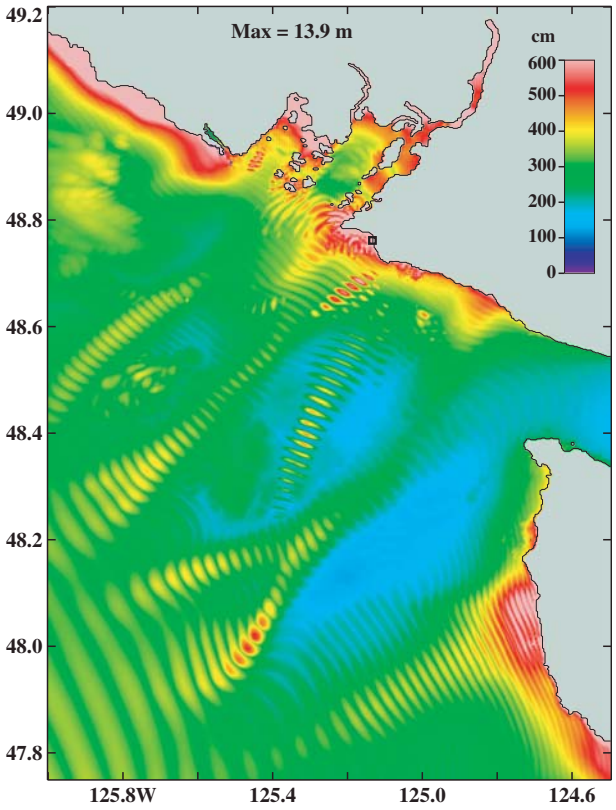


Figure 7
A detailed view of the western part of Figure 6.

Alaska $M_w$ = 9.2 earthquake (WIGEN and WHITE, 1964; DUNBAR *et al.*, 1989; NG *et al.*, 1990; HENRY and MURTY, 1995). The first wave in 1964 was about 3 m above MSL, at which point the tide gauge in Port Alberni, at the head of the inlet, was temporarily disabled. The third wave was considerably larger, about 5-m high, and caused most of the damage in this town.

We did not make high-resolution calculations for Alberni Inlet, but our results from the medium-resolution grid give us clues about the tsunami heights all along the coast, including this inlet. Figure 6 shows the maximum elevations of tsunami waves on the model medium grid, computed as in Figure 4, and therefore also showing the initial wavefronts at 1-minute intervals. Wave refraction and intensification on shallow banks is quite evident in this plot and, in greater detail, in Figure 7.

Maximum wave elevation on the medium grid is 13.9 m, located on the west coast southwest of Bamfield (marked by a small rectangle in Fig. 7). This value is not only higher but it is also about 50 km southeast of the coarse-grid maximum value of 11.6 m near Tofino (Fig. 4a), just outside of the northern boundary of the

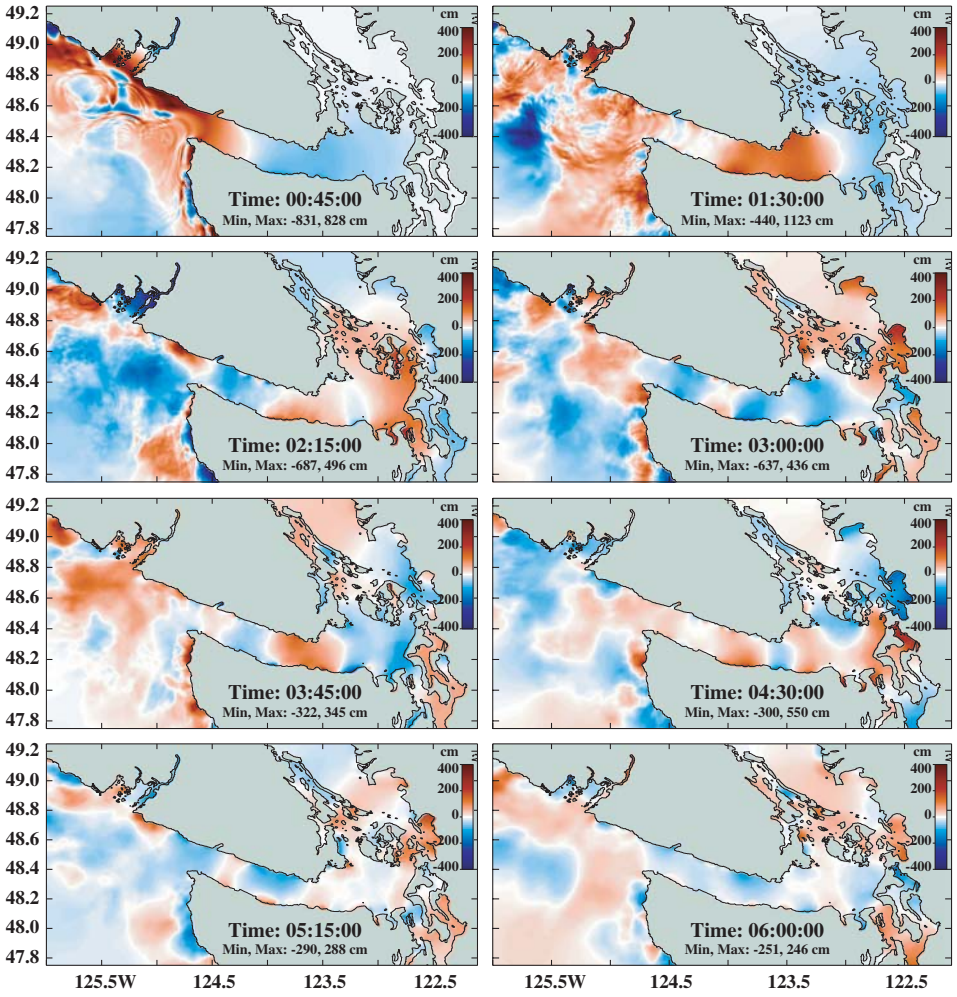


Figure 8
Model tsunami waves on the medium grid every 45 minutes from 0:45 to 6:00 (hour: minute) after the CSZ earthquake for the *long-narrow* deformation scenario.

medium grid. Such differences in heights are not surprising, as bathymetric details and wave propagation are somewhat different in these two grids, and isolated maxima are smoothed out when interpolating the nested medium-grid data onto the coarse grid.

Figure 8 displays the waves every 45 minutes, from 0:45 to 6:00 (hour:minute) after the earthquake. The first positive wave arrives at the outer coast near Ucluelet at 0:30 and is well inside Ucluelet Inlet by 0:45 (top-left panel in Fig. 8). Their amplitudes at the outer coast are 6 to 10 m. As these waves penetrate into Juan de Fuca Strait, their amplitude decreases to about 4 m. Some time later, after travelling

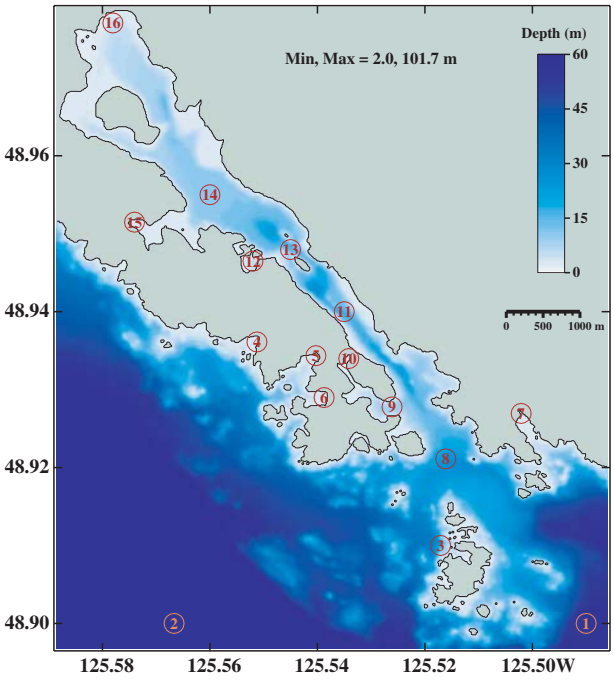


Figure 9
Bathymetry and site locations for Ucluelet Inlet fine-resolution grid.

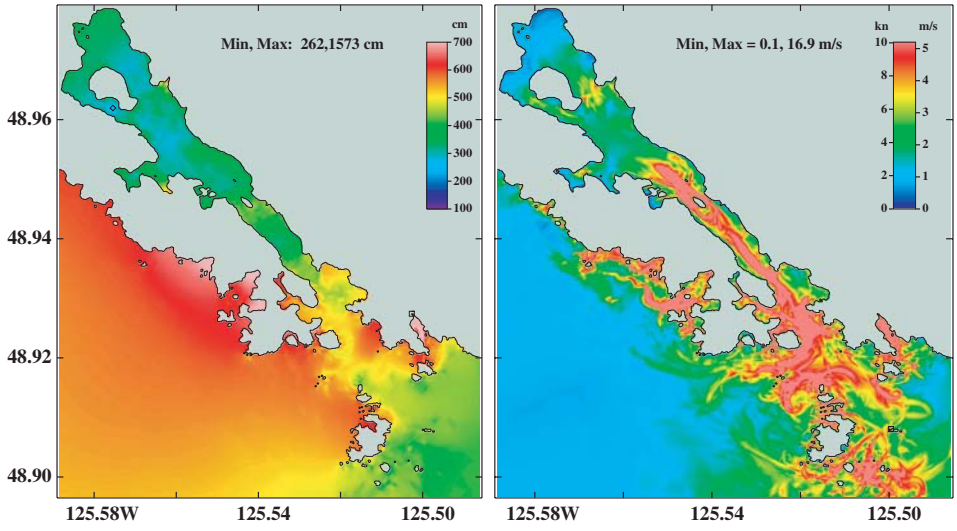


Figure 10
Maximum wave elevation (left) and water speed (right) in Ucluelet Inlet.

through the Gulf Islands via Haro Strait and Rosalio Channel (see Fig. 5 for place names), wave amplitudes in the Strait of Georgia decrease to less than 3 m.

It is important to reiterate that the main purpose of the coarse and medium-resolution grids is to propagate the waves towards the areas of high-resolution grids and that wave elevations in the former are likely underestimated due to inadequate horizontal resolution. For example, it is commonly assumed that the Strait of Georgia is sheltered from tsunamis originating in the open Pacific Ocean, but as we see from Figures 7 and 8, this is not entirely correct. Future higher-resolution simulations of CSZ tsunamis for various bays in this basin may show locations where wave elevations exceed the 3-m maximum reached on this medium-resolution grid.

## 5. Waves and Currents in Harbours

We now describe the numerical model results in areas covered by two high resolution grids: (1) Ucluelet Inlet and harbour and (2) Esquimalt and Victoria harbours.

### 5.1. Ucluelet Inlet and Surrounding Area

Water depths of the area enclosed by this high-resolution grid are shown in Figure 9. Numbered sites are where time series of sea-level heights were stored every 0.2-seconds (compared to grid data stored at 1-minute intervals). The maximum water depth in this grid is about 100 m, in the southwest corner. Three $\sim$20-m deep channels lead into Ucluelet Inlet, allowing waves to enter the inlet mouth from different directions.

Maximum wave elevations over the 12-hour time period are shown in Figure 10a. On the west coast of Ucluth Peninsula, which has several relatively shallow bays and bears the brunt of the initial tsunami waves in this area, the maximum elevation values are 6–9 m. However, the largest value in this grid is 15.7 m. This isolated maximum occurs in a narrow and shallow bay, an estuary of Itatsoo Creek southeast of Ucluelet Inlet, marked by a small square in Figure 10a (near 125.50°W, 48.92°N). In contrast, most of Ucluelet Inlet is partly protected by its relatively narrow entrance and the maximum wave amplitudes inside the inlet do not exceed 5 m.

The danger from tsunamis is not only from large waves, but also from very strong currents that may destroy ships and coastal structures, carry debris, and endanger the lives of those who were not able to escape to higher ground. Figure 10b shows the maximum water speeds on this grid during the 12-hour simulation. They range from less than 2 knots (1 knot $\approx$ 0.5 m $s^{-1}$) at the head of the inlet, or in the open ocean, to more than 20 knots in narrow channels and

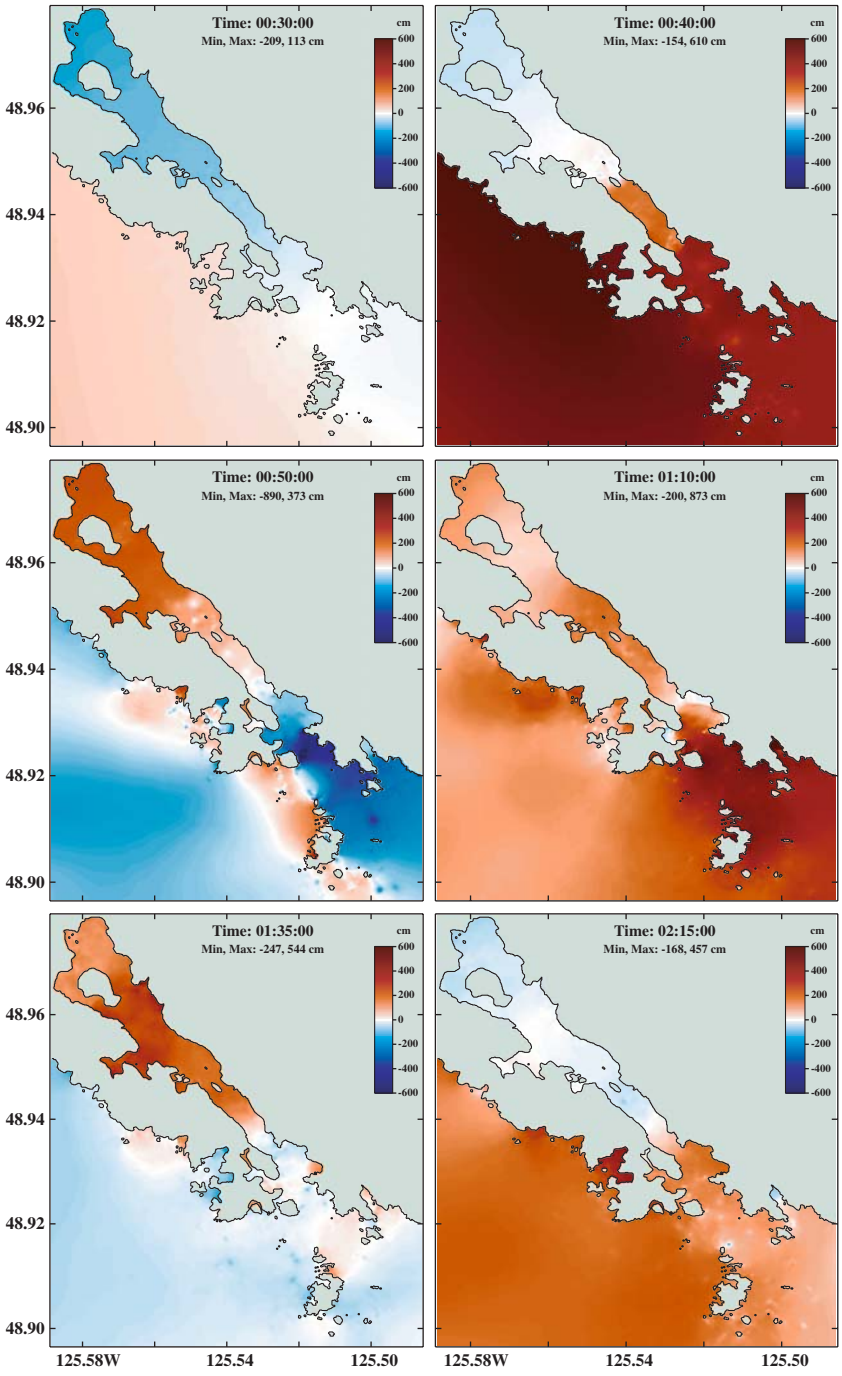


Figure 11
Tsunami waves in Ucluelet at 0:30, 0:40, 0:50, 1:10, 1:35 and 2:15 (hr: min).

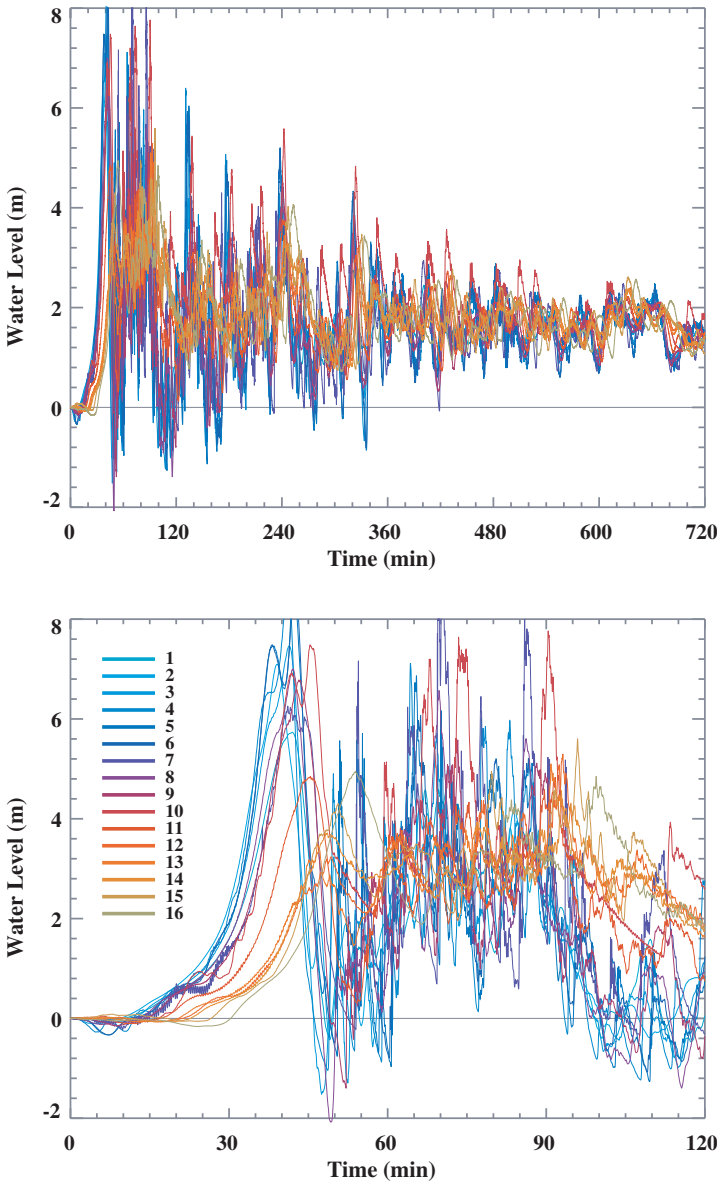


Figure 12
Simulated sea level records at numbered locations around Ucluelet (see Fig. 9) over time periods of 12 (top panel) and 2 (bottom panel) hours after the earthquake.

around headlands. The largest speed of $\sim$ 33 knots was near a small island in the southeastern part of this area, marked by a small rectangle in Figure 10b (near 125.50°W and 48.91°N).

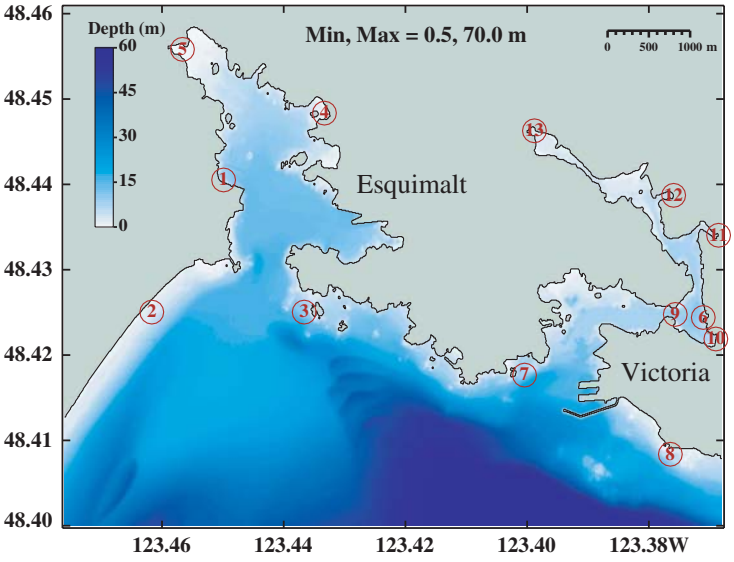


Figure 13
Bathymetry and site locations for the fine-resolution grid of Esquimalt and Victoria harbours.

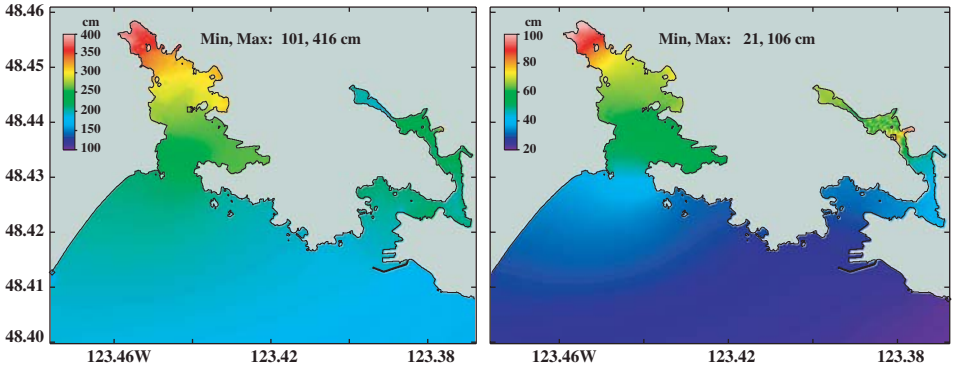


Figure 14
Maximum tsunami wave elevation in Esquimalt and Victoria harbours for *long-narrow* (left panel) and *short-south* (right, with different colour scale) deformation scenarios.

The six panels in Figure 11 show select snapshots of sea level on this grid during the first 2 hours and 15 minutes after the earthquake. Time intervals between the first three snapshots are only 10 minutes, showing how rapidly the flood changes to ebb and *vice versa*. This rapid development is also evident from sea-level time series shown in Figure 12 at 16 sites marked with numbers in Figure 9. This plot shows that tsunami wave periods are between 20 and 40 minutes and that the maximum

elevation of ~11 m at site 7 occurs near the 80-minute mark. This site is in the small bay southeast of Ucluelet Inlet, very close to the location of the large maximum wave elevation described above (Figure 10a).

The values on Figure 12 are relative to initial ($t = 0$) sea level after the earthquake, when land and water in this area have coseismically subsided by approximately the same amount of 1.7 m. These locations therefore do not experience the initial negative part of the wave, or withdrawal that occurs at locations farther away from the source. Because of this subsidence, any low-lying areas near the coast that were no higher than 1.7 m above mean sea level before the earthquake will remain below mean sea level long after the tsunami waves have died away—until these are elevated by subsequent postseismic uplift (WANG, 2006).

### *5.2. Esquimalt and Victoria Harbours*

Figure 13 shows water depths in the fine-resolution grid for Esquimalt and Victoria harbours. The deepest (close to 70 m deep) parts of this grid are east of the centre of its southern boundary. Therefore most of the incoming tsunami wave energy is expected to arrive from this direction. We mainly discuss here the results for the *long-narrow* deformation scenario, but also compare these to the results from the *short-south* scenario.

As this area is more distant from the CSZ source region and the incoming waves must first pass through Juan de Fuca Strait (Fig. 5), the maximum wave elevations in these two harbours, in the case of the *long-narrow* scenario (Fig. 14a), are smaller than on the West Coast by a factor of 2–3. The largest maximum elevations of over 4 m are in the northwestern shallow parts of Esquimalt Harbour, with isolated large values also in two small bays in Victoria Harbour.

The maximum wave elevations are smaller by a factor of 4–5 for the short-south scenario (Fig. 14b), but the overall patterns for the two scenarios are very similar, except that the north-south gradient is more distinct in the case of the *short-south* scenario. This similarity is due to the fact that the relative distribution of maximum wave elevations in a basin reflects the characteristics of local depths and geometry and is not sensitive to earthquake magnitude or distance to the tsunami source. Indeed, both scenarios produce amplifications of maximum elevations inside the harbours by a factor of 3–5 relative to their values outside.

The maximum water speeds in the two harbours are displayed in Figure 15, with the colour scale enhanced by a factor of 4 for the *short-south* case. As expected, the currents in the *long-narrow* deformation case are very strong, especially in the narrow channels and around capes, reaching at some instance 33 knots near a small island in the middle of Esquimalt Harbour. The speeds in the *short-south* case are considerably lower, but they are still well above the maximum tidal currents measured by AGES (1973) at several Victoria Harbour locations. His maximum current was 2 knots during ebb flow in the narrows under Johnson Street Bridge (123.37°W, 48.43°N in Fig. 15).

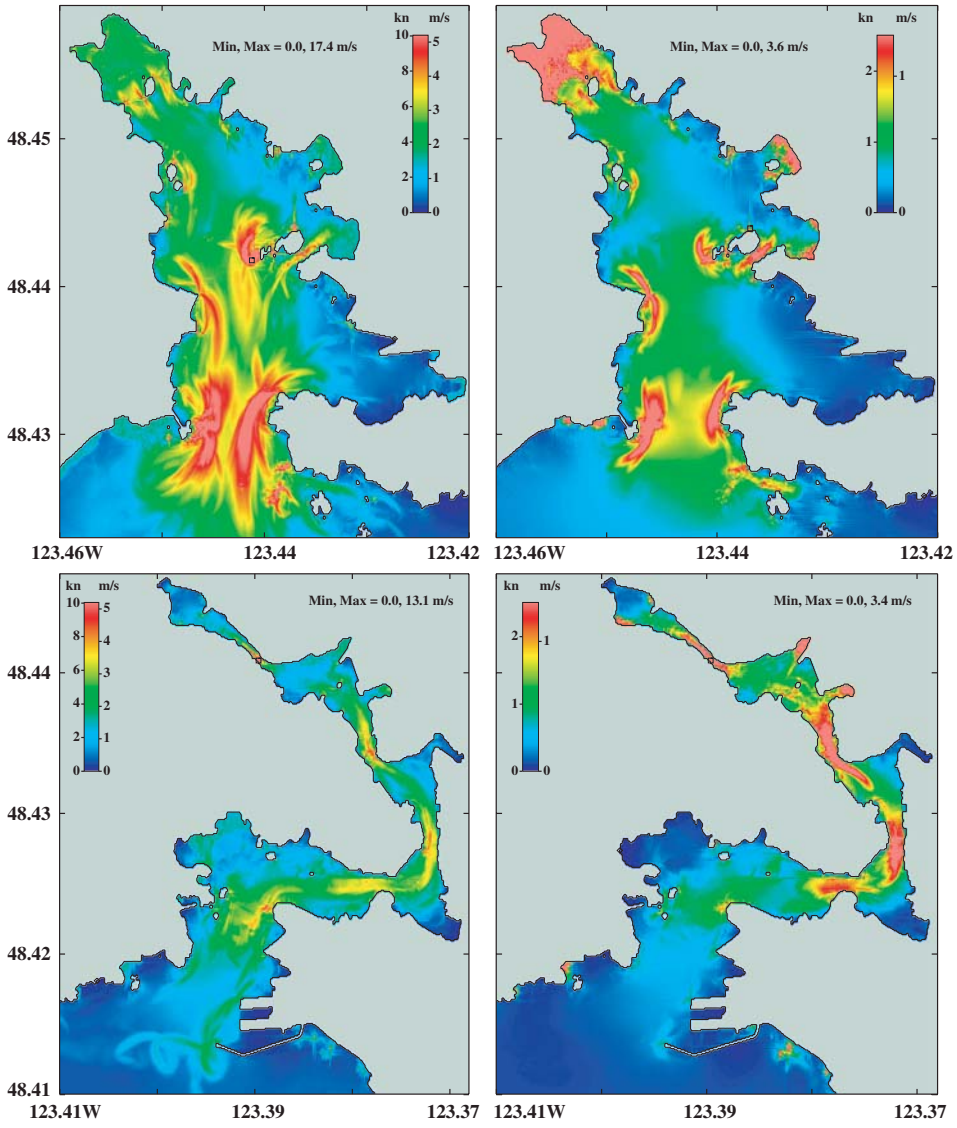


Figure 15
Maximum current speeds in Esquimalt Harbour (top panels) and in Victoria Harbour (bottom panels) for *long-narrow* (left panels) and *short-south* (right panels) deformation scenarios. Note that the colour scale for the two scenarios is different.

The spatial patterns of the two scenarios are similar. However, the differences in patterns for speeds (Fig. 15) are more pronounced than for maximum elevations (Fig. 14). For example, water speeds in small and very shallow bays around Esquimalt and Victoria harbours are only moderately lower in the *short-south* case, likely because these are limited there by bottom friction. Also, unstable features, such

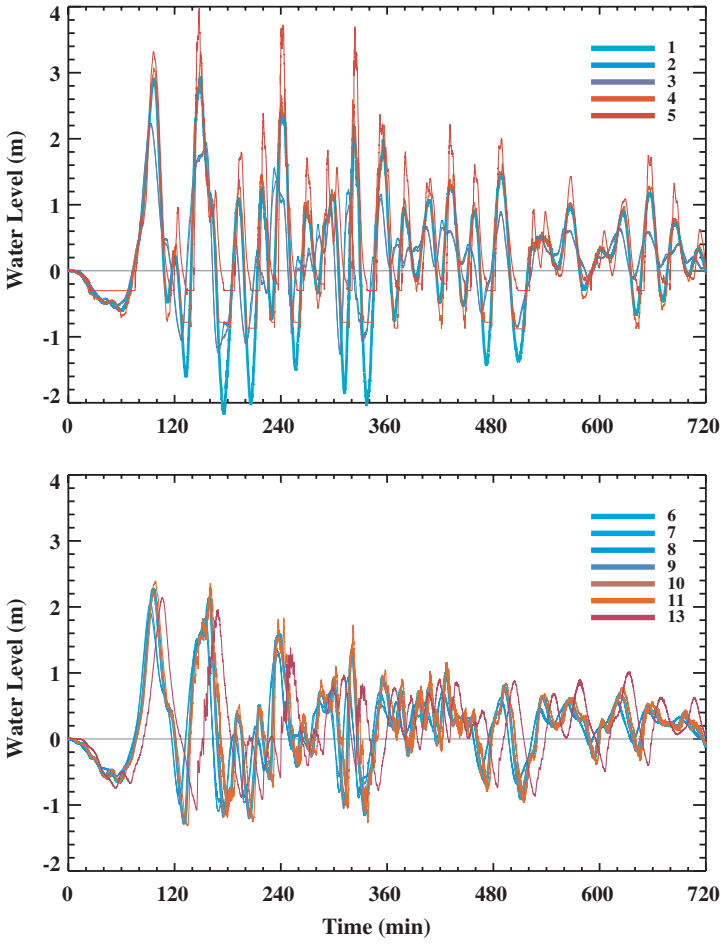


Figure 16
Simulated sea-level records in Esquimalt Harbour (top) and Victoria Harbour (bottom) for the *long-narrow* deformation scenario. The colour-coded curves are for sites shown in Figure 13.

as jets and eddies, exist in the more energetic *long-narrow* case, appearing as curved tracks in the left panels of Figure 15.

Time variations of water level at select sites in the two harbours are shown in Figure 16 for the *long-narrow* deformation scenario and in Figure 17 for the *short-south* scenario. Some of these sites are in very shallow water (e.g., site 5 at the head of Esquimalt Harbour; see Figure 13), completely emptied during ebb part of the tsunami cycle and therefore have their time series clipped at small negative values.

It is interesting to compare the timeseries for Ucluelet (Fig. 12) with that for Esquimalt and Victoria harbours (Fig. 16). The former shows much larger waves and

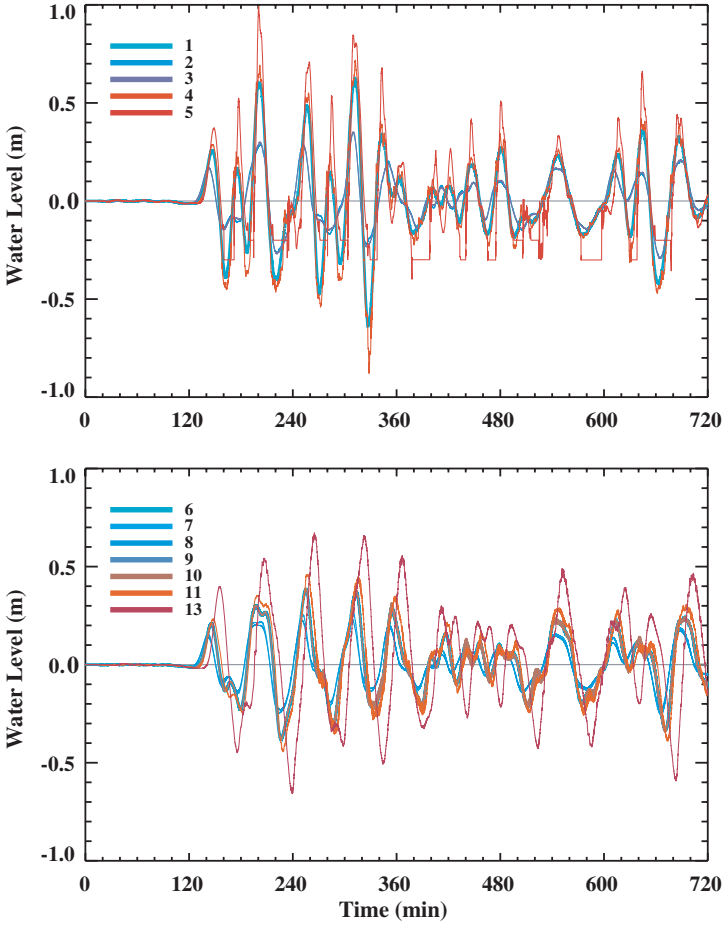


Figure 17
Simulated sea level records in Esquimalt Harbour (top) and Victoria Harbour (bottom) for the *short-south* deformation scenario. The colour-coded curves are for sites shown in Figure 13.

has more high-frequency content than the latter. These two harbours are farther from the source and may be more affected by additional scattering and filtering inside Juan de Fuca Strait.

Low-pass filtering of incoming waves is even more evident in time series from the more remote *short-south* scenario (Fig. 17), especially for the Victoria Harbour sites, which exhibit narrow-band (almost monochromatic) oscillations that decay very slowly with time.

Notably, the *long-narrow* scenario shows clearly leading negative waves and initial withdrawal of water (Fig. 16). Their absence in Ucluelet was explained in section 5.1 above. They are rather small (only a few centimetres) for the *short-south* case and thus almost invisible in Figure 17.

## 6. Discussion

Our numerical experiments have provided plausible and useful descriptions of CSZ tsunami waves propagation and their heights on the coast of southern Vancouver Island, as well as information on expected tsunami currents in Ucluelet Inlet and Esquimalt and Victoria harbours. Our results have also shown that there are areas of improvement, in particular in preparing the model grids, that can be addressed in future experiments.

The fine-resolution grids need to include nearshore land topography at comparable resolution, thus allowing simulations of run-up by the MOST-3 model. The resulting comparison between experiments with and without run-up would be instructive and useful for planning land use in areas covered by such grids and for projecting wave and run-up behaviour in other locations with similar bathymetry and beach characteristics. Although it may be possible to infer run-up values from tsunami waves at the coast, from bottom slopes and geometry of bays (e.g., ZAHIBO *et al.*, 2006), these values are likely to be in error and are poor substitutes for high-resolution modelling of fluid flow over complex basin topography.

Because of the north–south orientation of the subduction zone and thus predominantly east–west direction of initial tsunami energy flux, waves arriving at the Vancouver Island coast from the *short-south* subduction scenario are relatively small ($< 1$ m). However, resonances may lead to significant amplification and produce large waves in some inlets or harbours, as was the case in Alberni Inlet during the 1964 Alaska tsunami (WIGEN and WHITE, 1964; HENRY and MURTY, 1995). The $\sim$200-m grid size in our medium-resolution grid was inadequate to map this inlet and to capture such resonances. Therefore additional high-resolution grids and experiments, designed specifically for Alberni Inlet and for other bays and inlets on this coast, are in preparation and will be discussed elsewhere.

The issue of horizontal resolution in a model is also important when model results are used by civil authorities for planning tsunami preparedness and mitigation, or by engineers to design coastal structures. When the model grid is much larger than the scales of local bays and harbours, only gross behaviour of the waves can be inferred from numerical experiments, and important details remain unknown. This is quite evident in comparing the results for the same locations in the medium-and high-resolution grids. For example, the small bay southeast of Ucluelet (Itatsoo Creek Bay) had a 16-m wave, but this bay is less than 100 m wide and therefore does not even exist in the corresponding medium-resolution grid.

The effects of varying tidal heights and currents were not considered here, but are important and should also be included in future experiments. The tidal range in most of the coastal communities on Vancouver Island is about 4 m, making the tides significant contributors to wave heights and currents. The timing of the last Cascadia megathrust earthquake is known sufficiently well to be near 0500 UT January 27,

1700 (SATAKE *et al.*, 1996), allowing to hindcast the tides during and after this earthquake. MOFJELD *et al.* (1997) showed that low, neap tides were prevalent at the time all along the West Coast and their smaller range made the role of tides not as crucial. However, we do not know the timing of future Cascadia earthquakes. Hence, future experiments should include a full range of tidal scenarios.

We discussed above the differences in patterns for maximum speeds (Fig. 15) for two different earthquake scenarios which are more pronounced than for maximum elevations (Fig. 14). Such disparity between amplification of sea level and water speed were noted before (e.g., KOWALIK, 2001), as relative velocity range is greater than that for tsunami heights. Our nearshore results are likely incomplete, as the use of a simple friction rule in the model may not adequately address the effects of variable terrain, sediment transport and bottom scouring by the energetic flows. These effects can be investigated more fully in future experiments that include run-up.

Finally, it is useful to make a preliminary comparison between the model results and paleo-tsunami observations of run-up inferred from past CSZ great earthquakes, which include observations (or lack) of marine sediments in coastal marshes and lakes. Excluding very isolated maxima, which are not likely to be captured in field data, our simulated maximum wave amplitudes of 5–8 m on the southwest coast of Vancouver Island appear to be higher by a factor of 2 than the run-up heights inferred from paleo-tsunami data. Such disagreements may be due to a number of factors, as both model results and observations of paleo-tsunamis contain uncertainties.

The current model, with its coarse resolution (except for a few harbours) and no run-up, does not allow a precise point-by-point comparison with isolated field observations, while small bottom friction may lead to conservative (upper limit) results for wave amplitudes and currents near a coast. Furthermore, the assumed coseismic fault slip is equivalent to 500 years of plate convergence, which is longer than the time lapsed since the 1700 earthquake. The model results may therefore be somewhat conservative, i.e., err on the side of caution for present-day tsunami hazard.

However, the presence of marine sediments on the southwest coast of Vancouver Island points to a level of *minimal* run-up, as water is likely to move to a higher ground than where sediment is deposited. In other areas, such as the eastern Juan de Fuca Strait, modelled maximum wave amplitudes are generally (excluding isolated "hot-spots") between 1.5 and 3 m, which are closer to the values that can be inferred from sediment data from coastal marshes in this area (I. Hutchinson, personal communication, 2006).

## 7. Conclusions

We used three rupture scenarios for the CSZ earthquake as initial conditions in numerical ocean model experiments. These allowed us to study propagation of the

resulting tsunami waves off the West Coast and to predict tsunami heights and currents in several harbours on the west and south coasts of Vancouver Island, British Columbia. These locations include the inlet and harbour of Ucluelet, located on the west coast of the island, not far from the main subduction fault, and Victoria and Esquimalt harbours inside the Juan de Fuca Strait.

The earthquake scenarios considered here have an 1100-km long rupture over the entire length of the subduction zone, or separate ruptures of its northern or southern segments. As expected, the more remote southern *short-south* earthquake scenario has a limited effect over most of the Vancouver Island coast. The resulting waves in the harbours did not exceed 1 m. This however does not exclude the possibility of local resonances in harbours or inlets that were not covered by our high-resolution grids.

The other two scenarios, *long-narrow* and *short-north* had a very similar effect on the British Columbia coast. They produced very significant waves, up to 16 m in a small bay near Ucluelet and over 4 m in Esquimalt and Victoria harbours. They also carried very strong and dangerous currents, which reached maximum values near 17 m/s (33 knots) in narrow channels, or near headlands.

These numerical experiments also demonstrated the importance of high-resolution modelling of tsunami waves from megathrust earthquakes, of their behaviour at horizontal scales that are relevant for local tsunami preparedness and disaster mitigation planning.

## *Acknowledgments*

We are very grateful to Mr. Fred Stephenson and to the staff of the Canadian Hydrographic Service at the Institute of Ocean Sciences for providing digital bathymetric data sets that were used to generate high-resolution grids for the tsunami model. We also thank Drs. Alexander Rabinovich, Ian Hutchinson, Richard Thomson, Michael Foreman, Isaac Fine, Harold Mofjeld, Evgueni Kulikov and Garry Rogers for useful discussions and guidance. Detailed comments by the two reviewers enhanced this paper. This work was supported by the Canadian Coast Guard New Initiatives Fund and by Fisheries and Oceans Canada.

## References

Adams, J. (1990), *Paleoseismicity of the Cascadia subduction zone — Evidence from turbidities off the Oregon–Washington margins*, Tectonics *9*, 569–583.

Ages, A.B. (1973), *A numerical model of Victoria Harbour to predict tidal response to proposed hydraulic structures*, Pacific Mar. Sci. Rep. 73–3, Environment Canada, Pacific Region, 26 p.

Atwater, B.F. (1987), *Evidence for great Holocene earthquakes along the outer coast of Washington*, Science *236*, 942–944.

ATWATER, B.F. and HEMPHILL-HALEY, E. *Recurrence intervals for great earthquakes of the past 3500 years at northeastern Willapa Bay, Washington*, US Geological Survey Prof. Paper 1576 (USGS, Menlo Park, 1997).

ATWATER, B.F., MUSUMI-ROKKAKU, S., SATAKE, K., TSUJI, Y., UEDA, K., and YAMAGUCHI, D.K. *The orphan tsunami of 1700; Japanese clues to a parent earthquake in North America*, U.S. Geological Survey Prof. Paper 1707 (University of Washington Press, Seattle, 2005).

CHU, K.K. and ABE, T. *Tsunami run-up and back-wash on a dry bed*. In *Tsunamis: Their Science and Engineering* (eds. K.Iida and T.Iwasaki), pp. 453–466, (Terra Scientific Publishing Co., Tokyo, 1983).

CLAGUE, J.J. (1997), *Evidence for large earthquakes at the Cascadia subduction zone*. Rev. Geophys. *35*(4), 439–460.

CLAGUE, J.J., BOBROWSKY, P.T., and HUTCHINSON, I. (2000), *A review of geological records of large tsunamis at Vancouver Island, British Columbia, and implications for hazard*, Quatern. Sci. Rev. *19*, 849–863.

DUNBAR, D., LEBLOND, P. H., and MURTY, T.S. (1989), *Maximum tsunami amplitudes and associated currents on the coast of British Columbia*, Sci. Tsunami Hazards *7*, 3–44.

DUNBAR, D., LEBLOND, P.H., and MURTY, T.S. (1991), *Evaluation of tsunami amplitudes for the Pacific Coast of Canada*, Prog. Oceanogr. *26*, 115–177.

FOREMAN, M.G.G, CRAWFORD, W.R., CHERNIAWSKY, J.Y., HENRY, R.F., and TARBOTTON, M.R. (2000), *A high-resolution assimilating tidal model for the northeast Pacific Ocean*, J. Geophys. Res. *105*, 28,629–28,652.

GOLDFINGER, C., NELSON, C.H., and JOHNSON, J.E. (2003), *Holocene earthquake records from the Cascadia subduction zone and northern San Andreas fault based on precise dating of offshore turbidities*, Ann. Rev. Earth Planet. Sci. *31*, 555–577.

GONZÁLEZ, F.I., SATAKE, K., BOSS, E.F., and MOFJELD, H.O. (1995), *Edge wave and non-trapped modes of the 25 April 1992 Cape Mendocino tsunami*, Pure Appl. Geophys. *144*, 409–426.

HEBENSTREIT, G.T. and MURTY, T.S. (1989), *Tsunami amplitudes from local earthquakes in the Pacific Northwest region of North America, Part 1: The outer coast*, Mar. Geodesy, *13*(2), 101–106.

HENRY, R.F. and MURTY, T.S. *Tsunami amplification due to resonance in Alberni Inlet: Normal modes*. In *Tsunami: Progress in Prediction, Disaster Prevention and Warning* (eds. Y.Tsushiya and N.Shuto), pp. 117–128, (Kluwer, Dordrecht, 1995).

HUTCHINSON, I., GUILBAULT, J.-P., CLAGUE, J.J., and BOBROWSKY, P.T. (2000), *Tsunamis and tectonic deformation at the northern Cascadia margin: a 3000-year record from Deserted Lake, Vancouver Island, British Columbia, Canada* Holocene, *10*(4), 429–439.

KAJIURA, K. (1972), *The directivity of energy radiation of the tsunami generated in the vicinity of a continental shelf*, J. Oceanogr. Soc. Japan *28*, 260–277.

KELSEY, H.M., NELSON, A.R., HEMPHILL-HALEY, E., and WITTER, R.C. (2005), *Tsunami history of an Oregon coastal lake reveals a 4600-yr record of great earthquakes on the Cascadia subduction zone*, Geol. Soc. Am. Bull. *117*(7/8), 1009–1032.

KOWALIK, Z. (2001), *Basic relations between tsunami calculations and their physics*, Sci. Tsunami Hazards *19*(2), 99–115.

LEBLOND, P.H. and MYSAK, L.A. *Waves on the Ocean* (Elsevier, Amsterdam, 1978).

MOFJELD, H.O., FOREMAN, M.G.G., and RUFFMAN A. (1997), *West Coast tides during Cascadia subduction zone tsunamis*, Geophys. Res. Lett. *24*(17), 2215–2218.

MURTY, T.S., *Seismic Sea Waves — Tsunamis*, Bull. Fish. Res. Board Canada 198 (Fisheries and Oceans Canada, Ottawa, 1977).

MURTY, T.S. and CREAN, P.B. (1986), *Numerical simulation of the tsunami of June 23, 1946, in British Columbia, Canada*, Sci. Tsunami Hazards *4*(1), 3–14.

MURTY, T.S. and HEBENSTREIT, G.T. (1989), *Tsunami amplitudes from local earthquakes in the Pacific Northwest region of North America, Part 2: Strait of Georgia, Juan de Fuca Strait, and Puget Sound*, Mar. Geodesy *13*, 189–209.

MYERS, E.P., BAPTISTA, A.M., and PRIEST, G.R. (1999), *Finite element modelling of potential Cascadia subduction zone tsunamis*, Sci. Tsunami Hazards *17*, 3–18.

NG, M., LEBLOND, P.H., and MURTY, T.S. (1990), *Numerical simulation of tsunami amplitudes on the coast of British Columbia due to local earthquakes*, Sci. Tsunami Hazards *8*, 97–127.

PETERS, R., JAFFE, B., GELFENBAUM, G., and PETERSON, C. *Cascadia tsunami deposit database*, US Geological Survey Open-File Rep. 03-13, 24 pp. (USGS, 2003).

Priest, R.G., Myers, E., Baptista, A.M., Fleuck, P., Wang, K., and Peterson, C.D. (2000), *Source simulation for tsunamis: Lessons learned from fault rupture modelling of the Cascadia subduction zone, North America*, Sci. Tsunami Hazards *18*, 77–106.

Rabinovich, A.B., *Long Ocean Gravity Waves: Trapping, Resonance, Leaking* [in Russian], (Gidrometeoizdat, St. Petersburg, 1993).

Ramming, H.-G. and Kowalik, Z. *Numerical modelling of marine hydrodynamics* (Elsevier, Amsterdam, 1980).

Satake, K. (1995), *Linear and nonlinear computations of the 1992 Nicaragua earthquake tsunami*, Pure Appl. Geophys. *144*, 455–470.

Satake, K., Shimazaki, K., Tsuji, K., and Ueda, K. (1996), *Time and size of a giant earthquake in Cascadia earthquake inferred from Japanese tsunami records of January 1700*, Nature *379*, 246–249.

Satake, K., Wang, K., and Atwater, B.F. (2003), *Fault slip and seismic moment of the 1700 Cascadia earthquake inferred from Japanese tsunami descriptions*, J. Geophys. Res. *108*(B11), doi:10.1029/2003JB002521.

Titov, V.V. and González, F.I. *Implementation and testing of the Method of Splitting Tsunami (MOST) model*, NOAA Tech. Mem. ERL PMEL-112 (PMEL, Seattle, 1997).

Titov, V.V., González, F.I., Bernard, E.N., Eble, M.C., Mofjeld, H.O., Newman, J.C., and Venturato, A.J. (2005), *Real-time tsunami forecasting: Challenges and solutions*, Natural Hazards *35*, 41–58.

Titov, V.V., González, F.I., Mofjeld, H.O. and Venturato, A.J. *NOAA TIME Seattle Tsunami Inundation Mapping Project procedures, data sources and products*, NOAA Tech. Mem. OAR PMEL-124, (PMEL, Seattle, 2003).

Titov, V.V. and Synolakis, C.E. (1997), *Extreme inundation flows during the Hokkaido–Nansei–Oki tsunami*, Geophys. Res. Lett. *24*(11), 1315–1318.

Titov, V.V. and Synolakis, C.E. (1998), *Numerical modelling of tidal wave run-up*, J. Waterw. Port Coast. Ocean Eng. *124*(4), 157–171.

Wang, K., He, J., Dragert, H., and James, T.S. (2001), *Three-dimensional viscoelastic interseismic deformation model for the Cascadia subduction zone*, Earth Planets Space *53*, 295–306.

Wang, K., Wells, R., Mazzotti, S., Hyndman, R.D., and Sagiya T. (2003), *A revised dislocation model of interseismic deformation of the Cascadia subduction zone*, J. Geophys. Res. *108*(B1), doi:10.1029/2001JB001227.

Wang, K. (2006), *Elastic and viscoelastic models of subduction earthquake cycles*. In *The Seismogenic Zone of Subduction Thrust Faults* (eds. T. Dixon and J. C. Moore), Columbia University Press, in press.

Whitmore, P.M. (1993), *Expected tsunami amplitudes and currents along the North American coast for Cascadia subduction zone earthquakes*, Nat. Hazards *8*, 59–73.

Wigen, S.O. and White, W.R. *Tsunami of March 27–29, 1964, west coast of Canada* (Canada Department of Mines and Technical Surveys, Ottawa, 1964).

Williams, H.F.L., Hutchinson, I., and Nelson, A.R. (2005), *Multiple sources for late-Holocene tsunamis at Discovery Bay, Washington State, USA*, Holocene *15*(1), 60–73.

Witter, R.C., Kelsey, H.M., and Hemphill-Haley, E. (2003), *Great Cascadia earthquakes and tsunamis of the past 6700 years, Coquille River estuary, southern coastal Oregon*, Geol. Soc. Am. Bull. *115*(10), 1289–1306.

Zahibo, N., Pelinovsky, E., Golinko, V., and Osipenko, N. (2006), *Tsunami wave runup on coasts of narrow bays*, Int. J. Fluid Mech. Res. *33*(2).

(Received February 17, 2006, accepted June 8, 2006)

Pure appl. geophys. 164 (2007) 493–507
0033–4553/07/030493–15
DOI 10.1007/s00024-007-0179-y



Pure and Applied Geophysics

# Overview of Holocene Tsunami Deposits along the Nankai, Suruga, and Sagami Troughs, Southwest Japan

JUNKO KOMATSUBARA and OSAMU FUJIWARA

*Abstract*—Tsunami deposits provide a basis for reconstructing Holocene histories of great earthquakes and tsunamis on the Pacific Coast of southwest Japan. The deposits have been found in the past 15 years at lakes, lagoons, outcrops, and archaeological excavations. The inferred tsunami histories span 3000 years for the Nankai and Suruga Troughs and nearly 10,000 years for the Sagami Trough. The inferred histories contain recurrence intervals of variable length. The shortest of these —100–200 years for the Nankai Trough, 150–300 years for the Sagami Trough — resemble those known from written history of the past 1000–1500 years. Longer intervals inferred from the tsunami deposits probably reflect variability in rupture mode, incompleteness of geologic records, and insufficient research.

The region's tsunami history could be clarified by improving the geologic distinction between tsunami and storm, dating the inferred tsunamis more accurately and precisely, and using the deposits to help quantify the source areas and sizes of the parent earthquakes.

**Key words:** Holocene, Nankai Trough, Sagami Trough, Suruga Trough, tsunami deposit.

## 1. Introduction

Northeastern subduction margin of the Philippine Sea Plate, including the Nankai, Suruga and Sagami Troughs, is one of the most seismically active areas in the world. Several source areas are located along these troughs, each of which potentially excites M8-class earthquakes and large tsunamis. Earthquakes and tsunamis originating from these areas have repeatedly damaged the Pacific Coast of Japan, including Tokyo and Osaka metropolitan areas.

Estimated recurrence intervals of these great earthquakes and tsunamis from written records of each source area are about 100 to 200 years. However, even the oldest written earthquake in this area is AD 684 (USAMI, 2003) and younger than 1600 BP (USAMI, 2003) and it is too short to accurately evaluate the physical properties of earthquakes and tsunamis, such as recurrence intervals and rupture mode which occurred around the subduction zone.

Active Fault Research Center, AIST, GSJ. E-mail: J.komatsubara@aist.go.jp

Tsunami deposits provide long-term evidence of subduction-zone earthquakes and tsunamis, and produced an exceptional progress both in the geology and paleoseismology in the last 20 years as reviewed by FUJIWARA (2004) and NANAYAMA and SHIGENO (2004). Here we review the Holocene history of earthquakes and tsunamis in the Nankai, Suruga and Sagami Troughs mainly based on tsunami deposits, and prospect the direction of future research in relation to disaster mitigation.

## 2. Tsunami Deposits along the Nankai, Suruga and Sagami Troughs

### 2.1. Major Issues of Tsunami Deposits

The first discovery of tsunami deposits along the Nankai and Suruga Troughs was reported from an archeological site near Lake Hamanako (Fig. 1) and sand bar deposits at the lake inlet (NISHINAKA *et al.*, 1996). They reported sand layers which were transported by the AD 1707 Hoei earthquake tsunami. Subsequently, tsunami deposits correlated with historical tsunami events have been mainly discovered in cored samples from lake deposits in these areas (e.g., OKAMURA *et al.*, 1997, 2000; TSUJI *et al.*, 1998, 2002; NANAYAMA *et al.*, 2002).

Tsunami deposits from the coast of the Sagami Trough were firstly reported by FUJIWARA *et al.* (1997, 1999a,b). They discovered the tsunami sands from the Holocene buried valley sequences in the Boso and Miura Peninsulas (Fig. 1). These tsunami deposits were correlated to the emergence of Holocene marine terraces distributed along the southern Kanto District. Historical tsunami deposits also have been discovered on coastal plains along the Sagami Trough. Tsunami deposits attributed to the AD 1498 Meio earthquake, AD 1703 and 1923 Kanto earthquakes were reported from this area (FUJIWARA *et al.*, 2005a,b).

### 2.2. Distribution of Tsunami Deposits

Figure 1 shows localities where Holocene tsunami deposits have been discovered. Most of the tsunami deposits were reported from muddy and organic sediments in coastal lakes, lagoons, swamps and lowlands which were enclosed by barriers such as beach ridges during the Holocene (A, B, C, D, E, G, I in Fig. 1). Low-energy lake and lagoon environments have high preservation potential of tsunami deposits. Washover sand into the lakes and lagoons recorded as an abrupt facies change in stratigraphic record. Such event deposits are rapidly covered by a high sediment flax in the lakes and lagoons, and protected from subsequent erosion.

Most research is based on samples taken by piston cores from coastal lakes, or boring cores from coastal lowlands, excepting some examples from rapidly uplifting areas. The southern Boso Peninsula provides excellently exposed Holocene shallow marine successions intercalated by many tsunami deposits, because of its high uplifting rate during Holocene.

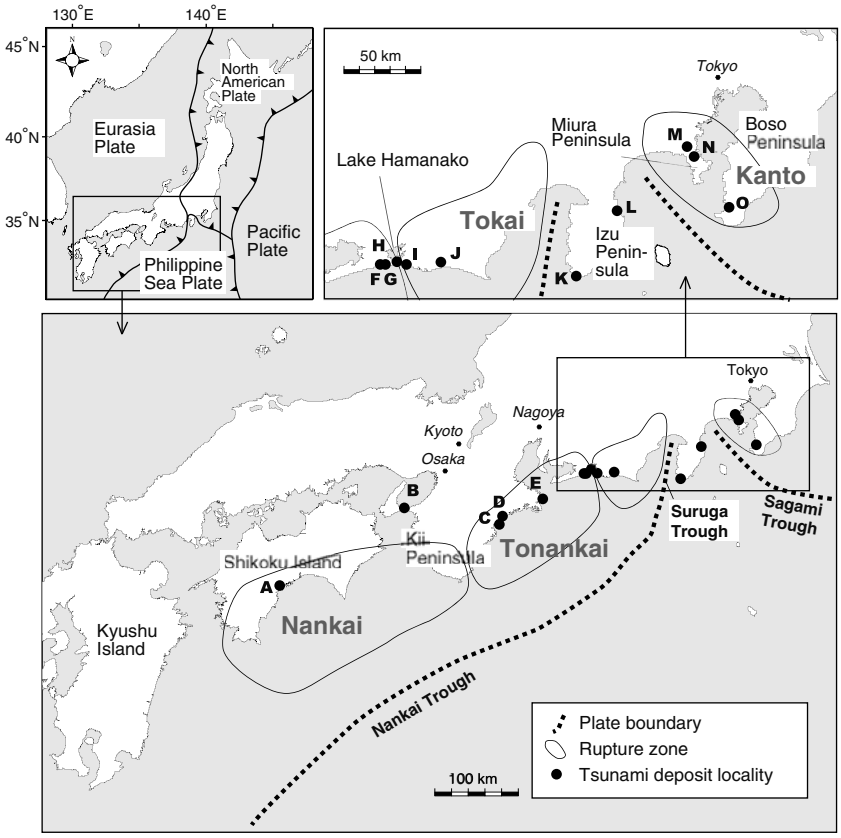


Figure 1
Localities of Holocene tsunami deposits. Subduction zone earthquakes which occured along the Nankai-Suruga Troughs are classified according to rupture areas; Nankai, Tonankai and Tokai Earthquakes, shown by the Headquarters for Earthquake Research Promotion, Japan. Those along the Sagami Trough are called Kanto earthquakes. See Table 1 for references.

Tsunami deposits are sometimes found in archeological excavation sites (F, H, K in Fig. 1). They are mainly represented as an unusual layer composed of clean, well-sorted marine sand, overspreading a ruin (e.g., KUMAGAI, 1999).

### *2.3. Sedimentological Characteristics of Tsunami Deposits*

Sedimentological characteristics of tsunami deposits reported along the Nankai, Suruga and Sagami Troughs are summarized in Table 1. Most of those deposits are recognized as unusual sedimentary layers composed of coarser grains compared with surrounding deposits. They generally have sharp erosional bases, sometimes with deformed contacts, implying a sudden increase in sedimentary load (FUJIWARA *et al.*, 2005a).

Table 1

*Group, observation method, characteristics and number of correlated historical earthquake of tsunami deposits discovered along the Nankai, Suruga and Sagami troughs.*

| | Locality | | Group | Normal deposits | Tsunami deposits | Inferred tsunami events | | | References |
|---|---|---|---|---|---|---|---|---|---|
| | | | | | | Number (Max) | pre-historical | historical | |
| A | Tadasuga-ike, Kochi Pref. | • | II · V | silt-sandy silt | sand | 7 | 5 | 2 | Okamura *et al.* (1997, 2000, 2003), Tsukuda *et al.* (1999) |
| B | Shinja-ike, Tomogashima Is., Wakayama Pref. | • | II | soil-clay | ms-cs | 4 | 0 | 4 | Nanayama *et al.* (2002) |
| C | Sugariura-oike, Owase Town, Mie Pref. | • | II · V | silt | fine sand | 10 | 8 | 2* | Tsuji *et al.* (2002) |
| D | Suwa-ike, Kii-Nagashima Town, Mie Pref. | • | II · V | no description | sand | 7 | 2–4 | 3–5* | Tsuji *et al.* (2002) |
| E | Osatsu Town, Owase City, Mie Pref. | •◯ | V | silt | vfs-gravelly vcs | 11 | 11 | 0 | Mitamura *et al.* (2001), Okahashi *et al.* (2001, 2002, 2005), Hirose *et al.* (2002) |
| F | Nagaya-Motoyashiki, Kosai City, Shizuoka Pref. | Δ | II · V | mud | sand | 3 | 0 | 3 | Kumagai (1999), Nishinaka *et al.* (1996) |
| | | | | mud-fs | fine sand | 8 | 0–2 | 6–8* | Kumagai (1999), Takada *et al.* (2002) |
| G | Shirasuka, Kosai City, Shuzuoka Pref. | ◯ | II · III | mud | ms, fs, clay | 4 | 0 | 4 | Komatsubara *et al.* (2006a) |
| H | Lake Hamanako, Shizuoka Pref. | • | II · V | sand | gravel, wood/ shell fragment | 5 | 2 | 3 | Tsuji *et al.* (1998), Okamura *et al.* (2000) |
| | | | II | sand | peat | 2 | 0 | 2 | Nishinaka *et al.* (1996) |
| I | Goten-ato, Arai Town, Shizuoka Pref. | Δ | II | organic sand | clean sand | 1 | 0 | 1 | Nishinaka *et al.* (1996) |
| J | Osuka Town, Shizuoka Pref. | ◯ | V | muddy deposit | sandy deposit | 1 | 1 | 0 | Uchida (2002) |
| K | Iruma, Minami-Izu Town, Shizuoka Pref. | ◯ | I | - | gravel, sand | 1 | 0 | 1 | Asai *et al.* (1998) |

| | | | | | | | | | |
|---|---|---|---|---|---|---|---|---|---|
| L | Usami, Ito City, Shizuoka Pref. | Δ | II | soil | gravel, sand, mud clast | 3 | 2 | 1 | FUJIWARA *et al.* (2005b) |
| M | Zushi City, Kanagawa Pref. | ■ | IV · V | mud | gravel, sand | 4 | 4 | 0 | FUJIWARA *et al.* (1999a, b) |
| N | Miura City, Kanagawa Pref. | ■ | IV · V | mud | gravel, sand | 7 | 7 | 0 | FUJIWARA *et al.* (1999a, b) |
| O | Tateyama City, Chiba Pref. | ■ | III · IV · V | mud | gravel, sand | 32 | 32 | 0 | FUJIWARA *et al.* (1997, 1999a, b, 2000), FUJIWARA and KAMATAKI (2003) |
| | | ○ | I · II | sand | gravel, sand | 2 | 0 | 2 | FUJIWARA *et al.* (2005a) |

* including an undescribed event in 13th century expected by recurrence interval.
• lake, pond.
○ coastal lowland.
Δ archeological site.
■ others.
vfs: very fine-grained sand.
fs: fine-grained sand.
ms: medium-grained sand.
cs: coarse-grained sand.
vcs: very coarse-grained sand.

It has been revealed that run-up tsunami currents sometimes leave characteristic sand layers thinning landward (DAWSON *et al.*, 1988). However there are few papers reporting an extent of tsunami deposits on the coastal plain along these troughs, because sample sites are often limited to small coastal lakes due to narrow coastal areas.

Tsunami deposits along these troughs are generally poorly- or well-sorted, coarse-grained deposits and, sometimes contain mud clasts of underlying strata origin (see Fig. 2 for example; KOMATSUBARA *et al.*, 2005). Some papers describe tsunami deposits only as ''sand'' intercalated with ''muddy'' deposits, without any sedimentological description. There has never been any study based on grain-size or grain composition analysis except for one example in the Boso Peninsula, along the Suruga Trough (FUJIWARA *et al.*, 2003b).

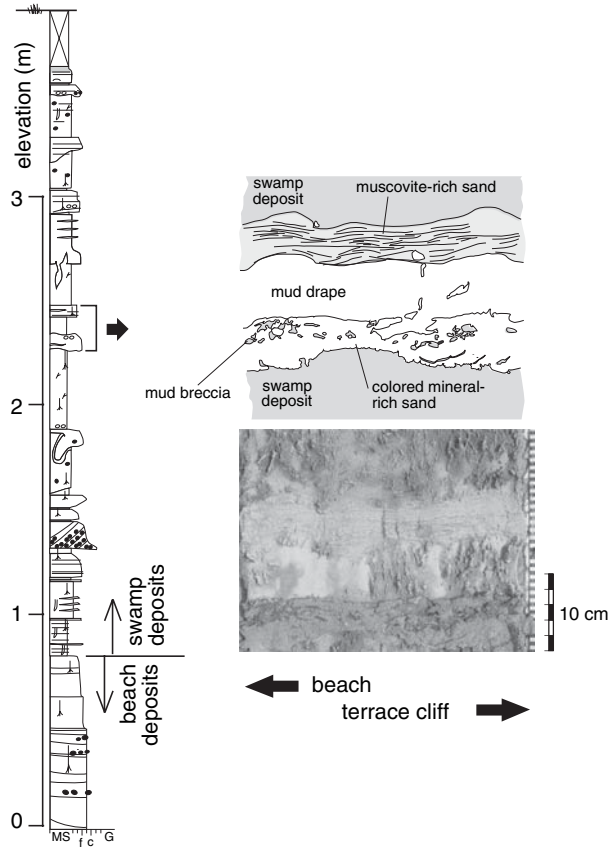


Figure 2

Possible tsunami deposits found in a coastal swamp succession at Shirasuka, locality G in Figure 1. One of them is composed of colored mineral-rich sand (from a beach), white draping mud and muscovite-rich sand (from a cliff behind) with seaward current ripples in an ascending order. These layers are attributed to a pair of run-up and return currents with a stagnant interval between them, possibly caused by a tsunami.

Note abundant mud breccias floating in the basal part. Revised from KOMATSUBARA *et al.* (2005).

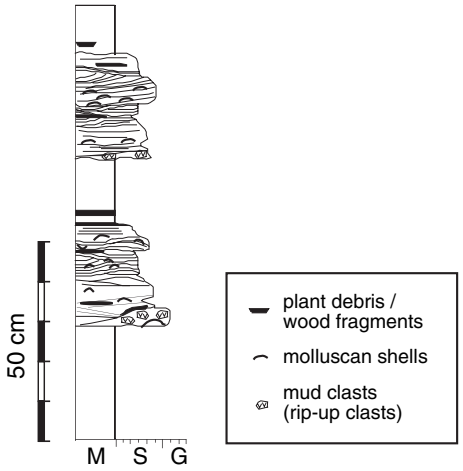


Figure 3
Two examples of tsunami deposits in Paleo-Tomoe Bay, Boso Peninsula. Note characteristics of tsunami deposits, such as a sharp erosional base, rip-up clasts, hummocky-cross stratifications, transported mulluscan shells, and plant debris overlying sand layers. Revised from FUJIWARA *et al.* (2003b).

Some of tsunami deposits yield various kinds of marine fossils, including mollusks (FUJIWARA *et al.*, 2003a), nanno planktons (OKAMURA *et al.*, 1997), foraminiferas (UCHIDA *et al.*, 2004) and ostracods (IRIZUKI *et al.*, 1999). They provide clues for the provenance of sediments and transport processes.

The thickness of reported tsunami deposits ranges from several centimeters to over 6 m (ASAI *et al.*, 1998). They commonly show a fining-upward trend and are sometimes covered by plant fragments (OKAMURA *et al.*, 1997; NANAYAMA *et al.*, 2002; FUJIWARA *et al.*, 2003a; OKAHASHI *et al.*, 2005).

Sedimentary structures reflecting the condition of source currents are sometimes observed in tsunami deposits. Parallel laminations, hummocky- and trough-cross stratifications, and current ripples are described as typical sedimentary structures (FUJIWARA *et al.*, 1997, 1999a,b, 2005a,b; NANAYAMA *et al.*, 2002; KOMATSUBARA *et al.*, 2006). Fig. 3 shows an example typically indicating these characteristics (FUJIWARA *et al.*, 2003b).

### *2.4. Classification of Tsunami Deposits*

There have been several criteria for identifying tsunami deposits because they show a wide variety of characteristics, such as thickness, components and sedimentary structures. Here we classify the tsunami deposits into five groups according to the types and nature of evidence for the identification. Types and nature of evidence control the accuracy of tsunami deposits. Group I is the most reliable and group V is doubtful as tsunami origin in some cases.

Group I includes the tsunami deposits which confidently correlate to historical tsunami events, based on historical records or eye witnesses, though they are very rare. FUJIWARA *et al.* (2005a) reported tsunami deposits attributed to the AD 1703 Genroku and AD 1923 Taisho Kanto earthquakes based on eyewitness evidence, from the southwestern coast of the Boso Peninsula near Tokyo. The tsunami layers are correlated with two coseismic uplifts of the depositional sites. They are obviously attributed to the two subduction zone earthquakes centered around the Sagami Trough.

Group II includes tsunami deposits correlated to historical earthquakes based on depositional ages only. The AD 1498 Meio earthquake tsunami deposit from the Izu Peninsula (FUJIWARA *et al.*, 2005b), the AD 1707 Hoei earthquake tsunami deposit from two archaeological sites near Lake Hamanako (TAKADA *et al.*, 2002; KUMAGAI, 1999) are the representatives. Figure 4 shows two layers of tsunami deposits correlated with historical earthquakes based on depositional ages (TAKADA *et al.*, 2002). However, we must note that they indicate vagueness resulting from the errors of age determinations. $^{14}C$ ages have an inevitable error range, from tens of years to over 100 years in some cases. There are two reasons for this error: one is a geologic error which represents the difference among the age dated on wood fragments or shells, the depositional age of those materials, and the age of the tsunami event. The other is the analytical errors in the process of age determination.

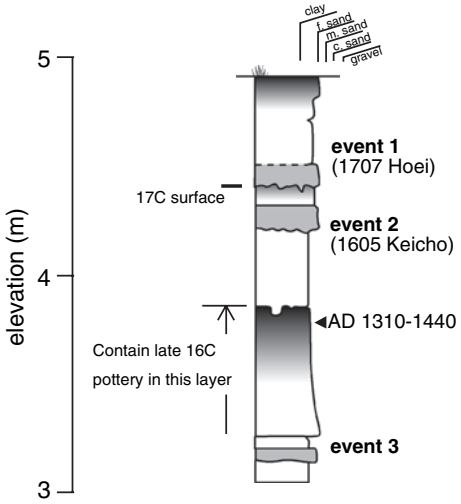


Figure 4

Tsunami deposits inferred from depositional age and correlation with historical tsunami events (group II), Nagaya-Motoyashiki, Kosai City, Shizuoka Prefecture. Locality F in Figure 1. Ages left of the column deduced from archaeological remains and those right from $^{14}C$ age. Event 1 is correlated with AD1707 Hoei earthquake and event 2 with AD 1605 Keicho earthquake. Revised from TAKADA *et al.* (2002).

Group III and IV are generally assigned to prehistorical deposits. Group III has certain sedimentary features indicating tsunami origin. FUJIWARA *et al.* (2003b) reported seven tsunami deposits that have unique sedimentary structures from a Holocene shallow bay deposit, in the southwestern Boso Peninsula. The tsunami deposits consist of alternation of sand sheets with hummocky cross-stratifications and mud drapes, and show the deposition from tsunamis that have long-wave periods. Repeated occurrence of sand sheets covered by mud drapes cannot be formed by short-period storm waves. KOMATSUBARA *et al.* (2005) also describe a distinctive event deposit attributed to a large single wave of a long period. The deposit implies the presence of running-up and returning currents separated by a complete stagnant phase (Fig. 2).

Storm waves cannot move sediments from deeper than 50–80 m except for very fine materials (SAITO, 1989), however, tsunamis can transport the large grains even in the deeper sea bottom. Tsunami deposits including fossils derived from the deep marine bottom are also included in Group III. OKAHASHI *et al.* (2002), FUJIWARA *et al.* (2003a) and UCHIDA *et al.* (2004) reported the tsunami deposits that included the fossils derived from the depth of 50–90 m or deeper sea bottom, from shallow bay and lake deposits.

Group IV includes the tsunami deposits which corresponds with tectonic movements suggested by marine terraces and emerged beach ridges. Few examples are known to date except for FUJIWARA *et al.*, (1999a, b).

Group V includes tsunami deposits which are not classified into group I to IV.

### *2.5. Temporal Distribution of Tsunami Deposits*

Figures 5 and 6 show temporal distribution of tsunami deposits and their classification (Group I - V), based on published data. Conventional ages listed in papers were corrected into calendar years by Calib 5.01 (STUIVER and REIMER, 1993) using Intcal04 dataset (REIMER *et al.*, 2004). Calibration data of $^{14}C$ ages are shown in KOMATSUBARA *et al.* (2006). Correlation between tsunami deposits and historical earthquakes are usually based on $^{14}C$ ages of strata integrated with stratigraphic evidence. As rare cases, magnetostratigraphy (OKAHASHI *et al.*, 2001) and archaeological remains (NISHINAKA *et al.*, 1996) have been used as age control. Dated material was taken from tsunami deposits themselves, just above them, or between event layers. Because in cases we cannot judge from previous researchers' descriptions what relationship their $^{14}C$ ages have with the time tsunami deposits settled, we adopt the tsunami ages the authors wrote in their paper without any discussion, if their ages are calibrated.

Temporal distribution of tsunami deposits ranges over nearly 10000 years long around the Sagami Trough, although only 3000 years along the Nankai and Suruga Troughs.

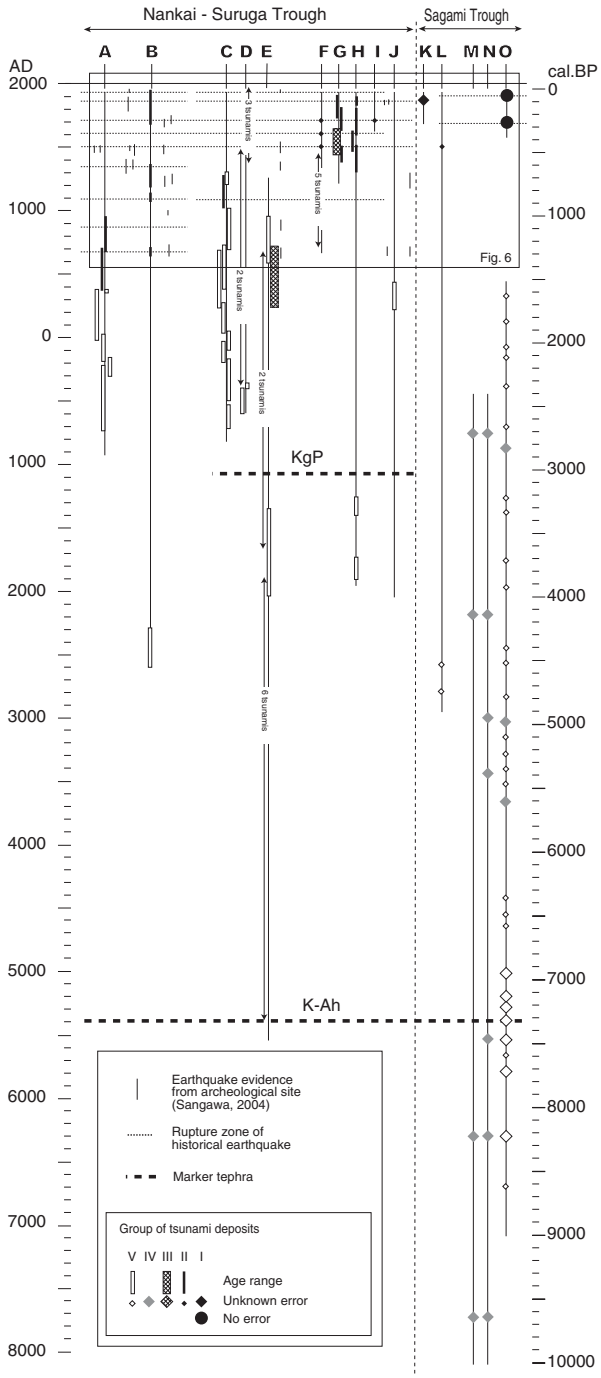
Nankai - Suruga Trough
Sagami Trough
A B C D E F G H I J K L M N O
AD
cal.BP
2000
1000
0
1000
2000
3000
4000
5000
6000
7000
8000
0
1000
2000
3000
4000
5000
6000
7000
8000
9000
10000
3 tsunamis
5 tsunamis
2 tsunamis
2 tsunamis
6 tsunamis
Fig. 6
KgP
K-Ah
Earthquake evidence from archeological site (Sangawa, 2004)
Rupture zone of historical earthquake
Marker tephra
Group of tsunami deposits
V IV III II I
Age range
Unknown error
No error

◀

Figure 5
Age distribution of tsunami deposits for each locality, showing recent 10,000 years. A - O are localities of discovered tsunami deposits (see Fig. 1). See text for classification of tsunami deposits. KgP: Kawagodaira Pumice, K-Ah: Kikai-Akahoya Tephra. A magnified diagram of recent 15,000 years (rectangle) is shown in Figure 6.

Along the Sagami Trough, tsunami records in the geologic successions are prehistorical with two exceptions attributed to historical earthquakes, the AD 1703 Genroku and 1923 Taisho Kanto earthquakes (Group I, FUJIWARA *et al.*, 2005a). Seven prehistorical tsunami deposits are correlated with seismically emerged marine terraces by $^{14}C$ ages (Group IV).

A period between 8200–6900 cal BP has the densest and reliable tsunami evidence represented by the Group III tsunami deposits. The shortest recurrence interval of tsunamis along the Sagami Trough that is calculated for this period is 150–300 years.

Other periods, though the reliability of data is relatively low (many of them are Group V tsunami deposits), also show similar recurrence intervals. This recurrence interval is remarkably shorter than that estimated from emerged shoreline topography, such as marine terraces and beach ridges (e.g., SHISHIKURA, 2003). SHISHIKURA (2003) identified two types of earthquakes around the Sagami Trough based on the distribution pattern of vertical displacement of emerged shoreline topography and estimated recurrence intervals of about 400 and 2000–2700 years for each type of earthquakes. Disagreement of recurrence intervals between tsunami deposits and emerged shoreline topography mainly resulted from the differences of preservation potential of geological and geomorphic evidence. Emerged shoreline topography is likely to wear off due to the coastal erosion. Tsunami deposits, in contrast, have relative high preservation potential under the coastal lowland including the shallow bay. On the other hand, tsunamis from the outer side of the

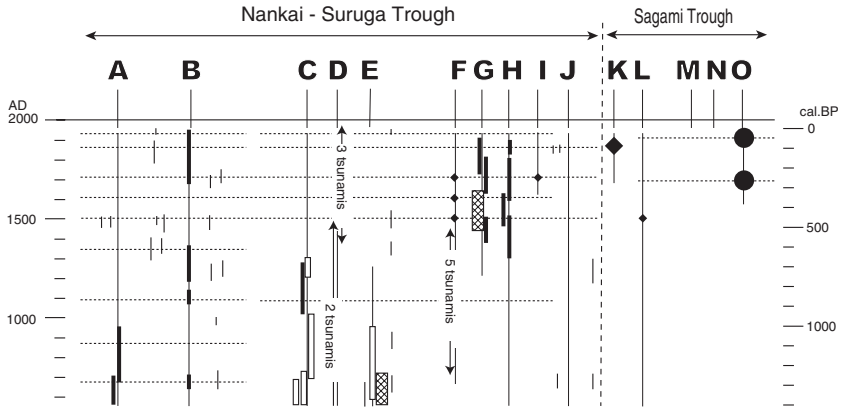


Figure 6
Age distribution of tsunami deposits for each locality, in recent 1,500 years.

Sagami Trough, e.g., from the Nankai Trough, may print their traces in the stratigraphic record along the Sagami Trough.

Along the Nankai and Suruga Troughs, written record of tsunamis can be retroactive to AD 684 (e.g., WATANABE, 1998). The reliable, shortest recurrence intervals from documents written during the last 400 years are 90–150 years. 60–90% of these historical tsunamis have their geological counterparts as deposits in the coastal sequences (Fig. 6). The number of reliable tsunami deposits rapidly diminishes in older ages. However, tsunami deposits, mainly Group V, provide the recurrence intervals which show good agreement with the value expected from the historical records, tracing back to ca. 2500 years BP. Before ca. 2500 years BP, the geological evidence of earthquakes and tsunamis had been barely discovered. The lack of data is attributed to the incompleteness of geological records of course, but also the insufficiency of field research.

## *3. Key Problems in Paleo-tsunami Studies*

BOURGEOIS and MINOURA (1997) and FUJIWARA *et al.* (2004) pointed out three key problems in paleo-tsunami studies: (1) positive identification of tsunami deposits, (2) dating and correlation of events, and (3) quantification of paleotsunami events. Their suggestions are also effective in the Nankai, Suruga and Sagami Troughs.

Reliability of the reconstruction of the tsunami histories strongly depends on the identification of tsunami deposits, though it is a difficult problem. Physical property of tsunamis may offer possible criteria for the identification. Tsunamis are characterized by extremely long wavelengths and periods compared with those of storm waves. FUJIWARA (2004) and FUJIWARA *et al.*, (2005c) proposed criteria for identifying the tsunami deposits in an inner bay, based on analyses of their sedimentary structures; 1) a cyclic succession of sand sheets, 2) mud drapes covering the sand sheets, and 3) repeated turnover of flow directions. Synthesis of these criteria suggests the deposition from tsunamis which have extremely long wavelengths and periods.

Dating and correlation of paleo-seismic events including tsunamis are closely related to the progress of age determination techniques. This problem was thoroughly discussed by FUJIWARA *et al.* (2004). We may correlate prehistorical tsunami deposits with each other if depositional age data increase both in number and accuracy in the future, and then confirm another subduction zone earthquake along the Nankai, Suruga and Sagami Troughs, currently unknown.

Quantitative evaluation of characteristics of ancient tsunamis is important, such as run-up heights and inundation areas. They can provide the clues for location and length of a rupture zone and dip and strike of a source fault. We may predict future events and prepare to encounter tsunami and earthquake disasters, based on this fundamental information.

## 4. Conclusions

The recent progress of paleo-tsunami studies along the Nankai, Suruga, and Sagami Troughs, based on tsunami deposits, is reviewed and compiled in a map showing temporal and spatial distribution. Temporal distribution of tsunami deposits ranges over nearly 10,000-years-long around the Sagami Trough, and 3000-years-long along the Nankai and Sagami Troughs. The shortest recurrence intervals of tsunamis were calculated as 150–300 years along the Sagami Trough and 100–200 years along the Nankai and Suruga Troughs. For future contribution to disaster mitigation our next objectives are: (1) discrimination of tsunami deposits, (2) precise age determination, and (3) estimation of tsunami characteristics.

## References


ASAI, D., IMAMURA, F., SHUTO, N., and TAKAHASHI, T. (1998), *Wave hight and sediment transportation of the Ansei Tokai Earthquake at Iruma, Izu Peninsula*, Proc. Coastal Engin. JSCE *45*, 371–375 (in Japanese).

BOURGEOIS, J. and MINOURA, K., *Paleotsunami studies contribution to mitigation and risk assessment*. In Tsunami Mitigation and Risk Assessment, Report of the International Workshop, Petropavlovsk-Kamchatsky, Russia, 1996, (ed. Gusiakov, V. K., 1997) 14 p.

DAWSON, A.G., LONG, D., and SMITH, D.E. (1988), *The Storegga Slides: Evidence from eastern Scotland for a possible tsunami,* Marine Geology *82*, 271–276.

FUJIWARA, O., *Sedimentological and paleontological characteristics of tsunami deposits*. In Earthquake-induced Event Deposits—From Deep Sea to on Land, Memoir of Geological Society of Japan, no. 58 (Fujiwara, O., Ikehara, K., and Nanayama, F. Eds.) (Geological Society of Japan, Tokyo 2004) pp. 35–44 (in Japanese).

FUJIWARA, O., HIRAKAWA, K., IRIZUKI, T., KAMATAKI, T., UCHIDA, J., ABE, K., HASEGAWA, S., TAKADA, K., and HARAGUCHI, T. (2005a), *Depositional structures of Historical Kanto Earthquake Tsunami Deposits from SW coast of Boso Peninsula, Central Japan*, Japan Earth and Planetary Science Joint Meeting 2005, Abstracts, J027–P023 (in Japanese).

FUJIWARA, O., HIRAKAWA, K., KANEKO, H., SUGIYAMA, H., and TAKADA, K. (2005b), *Tsunami (?) event deposits discovered from the Usami Ruins in northern Ito City, shizuoka Prefecture*, Japan Association for Quaternary Research, 2005 Annual Meeting, Abstract *35*, pp. 32–33 (in Japanese).

FUJIWARA, O., IKEHARA, K., and NANAYAMA, F., *Earthquake-induced event deposits: Importance and direction of future researches in relation to disaster mitigation*. In Earthquake-induced Event Deposits—From Deep Sea to on Land, Memoir of Geological Society of Japan, no. 58 (eds. Fujiwara, O., Ikehara, K., and Nanayama, F.) (Geological Society of Japan, Tokyo 2004) pp. 1–10 (in Japanese).

FUJIWARA, O. and KAMATAKI, T. (2003), *Tsunami depositional sequence model in bay sediments and tsunami potential of northeastern part of the Philippine Sea Plate*, Hokudan Internat. Symp. Active Faulting Conf. 2003, Abstract (in Japanese).

FUJIWARA, O., KAMATAKI, T., and FUSE, K. (2003a), *Genesis of mixed molluscan assemblages in the tsunami deposits distributed in Holocene drowned valleys on the southern Kanto Region, East Japan*, The Quat. Res. *42*, 389–412 (in Japanese).

FUJIWARA, O., KAMATAKI, T., and TAMURA, T. (2003b), *Grain-size distribution of tsunami deposits reflecting the tsunami waveform: An example from a Holocene drowned valley on the southern Boso Peninsula, East Japan*, The Quat. Res. *42*, 67–81 (in Japanese).

FUJIWARA. O., KAMATAKI, T., HIRAKAWA, K., IRIZUKI, T., UCHIDA, J., ABE, K., and HASEGAWA, S. (2005c), *Tsunami waveform of the AD1703 Kanto earthquake reconstructed from the deposit,* 2005 AGU Fall Meeting Program and Abstracts, T11A–0351.

FUJIWARA, O., MASUDA, F., SAKAI, T., FUSE, K., and SAITO, A. (1997), *Tsunami deposits in Holocene bay-floor muds and the uplift history of the Boso and Miura Peninsulas*, The Quat. Res. *36*, 73–86 (in Japanese).

FUJIWARA, O., MASUDA, F., SAKAI, T., IRIZUKI, T., and FUSE, K. (1999a), *Holocene tsunami deposits detected by drilling in drowned valleys of the Boso and Miura Peninsulas*, The Quat. Res. *38*, 41–58 (in Japanese).

FUJIWARA, O., MASUDA, F., SAKAI, T., IRIZUKI, T., and FUSE, K. (1999b), *Bay-floor deposits formed by great earthquakes during the past 1,000 yrs, near the Sagami Trough, Japan*, The Quat. Res. *38*, 489–501 (in Japanese).

FUJIWARA, O., MASUDA, F., SAKAI, T., IRIZUKI, T., and FUSE, K. (2000), *Tsunami deposits in Holocene bay mud in southern Kanto region, Pacific coast of central Japan*, Sedimentary Geol. *135*, 219–230.

HIROSE, K., GOTO, T., MITAMURA, M., OKAHASHI, H., and YOSHIKAWA, S. (2002), *Environmental change revealed by event deposits discovered from swamp deposits in Osatsu, Toba City, central Japan*, The Earth Monthly *24*, 692–697 (in Japanese).

IRIZUKI, T., FUJIWARA, O., and FUSE, K., *Taphonomy of fossil ostracode assemblages in Holocene deposits on the Miura Peninsula, central Japan*. In *Taphonomy and Sedimentary Process*, Memoir of Geological Society of Japan, no. 54 (eds. Ogasawara, K. and Kondo, Y.) (Geological Society of Japan, Tokyo 1999) pp. 99–116 (in Japanese).

KOMATSUBARA, J., FUJIWARA, O., and KAMATAKI, T. (2005), *Map of tsunami deposits along Nankai and Sagami Troughs, Japan*, AGU Fall Meeting, T11A–0352.

KOMATSUBARA, J., FUJIWARA, O., and KAMATAKI, T. (2006), *Tsunami deposits along the Nankai, Suruga and Sagami Troughs,* Historical Earthquakes *21*, 93–109 (in Japanese).

KUMAGAI, H. (1999), *Tsunami deposits of large earthquakes along the Nankai Trough: Investigation around Hamana Lake in central Japan*, J. Geography *108*, 424–432 (in Japanese).

MITAMURA, M., OKAHASHI, H., HIROSE, K., YOSHIKAWA, S., UCHIYAMA, M., NAKAMURA, T., and HARAGUCHI, T. (2001), *Event deposit and $^{14}C$ age preserved in coastal marsh in Osatsu, Toba, central Japan*, Proc. 11th Symp. Geo-Environm. Geo-Tech. 321–326 (in Japanese).

NANAYAMA, F., KAGA, A., KINOSHITA, H., YOKOYAMA, Y., SATAKE, K., NAKATA, T., SUGIYAMA, Y., and TSUKUDA, E. (2002), *Tsunami traces discovered in Tomogashima Island, Kitan Strait, central Japan*, Kaiyo Month. Symp. 123–131 (in Japanese).

NANAYAMA, F. and SHIGENO, K., *An overview of onshore tsunami deposits in coastal lowland and our sedimentological criteria to recognize them*. In *Earthquake-induced Event Deposits—From Deep Sea to on Land*, Memoir of Geological Society of Japan, no. 58 (eds. Fujiwara, O., Ikehara, K., and Nanayama, F.) (Geological Society of Japan, Tokyo 2004) pp. 19–33 (in Japanese).

NISHINAKA, H., KUMAGAI, H., OKUDA, Y., TORII, T., TAKANO, M., and NAKAMURA, T. (1996), *Search for paleoearthquakes along the eastern Nankai trough by the use of tsunami deposits*, Summaries of Research Using AMS at Nagoya University, 193–212 (in Japanese).

OKAHASHI, H., AKIMOTO, K., MITAMURA, M., HIROSE, K., YASUHARA, M., and YOSHIKAWA, S. (2002), *Event deposits preserved in coastal marsh at Osatsu, Toba, central Japan: Recognition of tsunami deposit on the basis of foraminifera analysis*, Chikyu Monthly, 698–703 (in Japanese).

OKAHASHI, H., YASUHARA, M., MITAMURA, M., HIROSE, K., and YOSHIKAWA, S. (2005), *Event deposits associated with tsunamis and their sedimentary structure in Holocene marsh deposits on the east coast of the Shima Peninsula, central Japan*, J. Geosci. Osaka City University *48*, 143–158.

OKAHASHI, H., YOSHIKAWA, S., MITAMURA, M., HYODO, M., UCHIYAMA, T., UCHIYAMA, M., and HARAGUCHI, T. (2001), *Tsunami deposits of Tokai earthquakes preserved in a coastal marsh sequence at Osatsu, Toba, central Japan, and their magnetochronological dates*, The Quat. Res. *40*, 193–202 (in Japanese).

OKAMURA, M., KURIMOTO, T., and MATSUOKA, H. (1997), *Coastal and lake deposits as a monitor*, Chikyu Monthly *19*, 469–473 (in Japanese).

OKAMURA, M., MATSUOKA, H., TSUKUDA, E., and TSUJI, Y. (2000), *Tectonic movements of recent 10000 years and observations of historical tsunamis based on coastal lake deposits*, Chikyu Month. Symp. 162–168 (in Japanese).

OKAMURA, M., TSUJI, Y., and MIYAMOTO, T. (2003), *Seismic activities along Nankai Trough recorded in coastal lake deposits*, Kaiyo Monthly *35*, 312–314 (in Japanese).

REIMER, P. J. (2004), *IntCal04 Terrestrial radiocarbon age calibration, 26–0 ka BP.*, Radiocarbon *46*, 1029–1058.

SAITO, Y. (1989), *Classification of shelf sediments and their sedimentary facies in the storm-dominated shelf: A review*, J. Geography *98*, 164–179 (in Japanese).

SHISHIKURA, M. (2003), *Cycle of interplate earthquake along the Sagami Trough, deduced from tectonic geomorphology*, Bull. Earthq. Res. Institute, University of Tokyo *78*, 245–254 (in Japanese).

STUIVER, M. and REIMER, P. J. (1993), *Extended C-14 data-base and revised Calib 3.0 C-14 age calibration program*, Radiocarbon *35*, 215–230.

TAKADA, K., SATAKE, K., SANGAWA, A., SHIMOKAWA, K., KUMAGAI, H., Goto, K., and Haraguchi, T. (2002), *Survey of tsunami deposits at an archaeological site along the eastern Nankai trough*, Chikyu Monthly *24*, 736–742 (in Japanese).

TSUJI, Y., OKAMURA, M., MATSUOKA, H., GOTO, T., and HAN, S. S. (2002), *Prehistorical and historical tsunami traces in lake floor deposits, Oike Lake, Owase City and Suwaike Lake, Kii-Nagashima City, Mie Prefecture, central Japan*, Chikyu Monthly *24*, 743–747 (in Japanese).

TSUJI, Y., OKAMURA, M., MATSUOKA, H., and MURAKAMI, Y. (1998), *Study of tsunami traces in lake floor sediment of the Lake Hamanako*, Historical Earthquake, 101–113 (in Japanese).

TSUKUDA, E., OKAMURA, M., and MATSUOKA, H. (1999), *Earthquakes of recent 2000 years recorded in geologic strata*, Chikyu Monthly Symp. 64–69 (in Japanese).

UCHIDA, C. (2002), *Event deposit in alluvium and its sedimentary environment in relation to paleo-topography in nearby Osuka town, Pacific coast area of Ensyu-nada*, Proc. General Meeting of the Assoc. of Japanese Geographers *61*, 135 (in Japanese).

UCHIDA, J., ABE, K., HASEGAWA, S., FUJIWARA, O., and KAMATAKI, T., *The depositional processes of tsunami deposits based on sorting of foraminiferal tests: A case study of tsunami deposits at Tateyama, southern part of the Boso Peninsula, central Japan*. In *Earthquake-induced Event Deposits—From Deep Sea to on Land*, Memoir of Geological Society of Japan, no. 58 (eds. Fujiwara, O., Ikehara, K., and Nanayama, F.) (Geological Society of Japan, Tokyo 2004) pp. 87–98 (in Japanese).

USAMI, T., *Materials for Comprehensive List of Destructive Earthquakes in Japan [416]–2001,* (Univ. Tokyo Press 2003), 605 pp. (in Japanese).

WATANABE, H., *Comprehensive list of tsunamis to hit the Japanese islands (second edit.)* (Univ. Tokyo Press 1998), 238 p. (in Japanese).

(Received March 30, 2006, accepted September 12, 2006)

Pure appl. geophys. 164 (2007) 509–525
0033–4553/07/030509–17
DOI 10.1007/s00024-006-0173-4



Pure and Applied Geophysics

# Micromorphological Analysis of Coastal Sediments from Willapa Bay, Washington, USA: A Technique for Analysing Inferred Tsunami Deposits

Aoibheann A. Kilfeather,[1] Jeffrey J. Blackford,[2] and Jaap J. M. van der Meer[1]

*Abstract*—Tsunami deposits are provisionally distinguished in the field on the basis of anomalous sand horizons, fining-up and fining-landward, coupled with organic-rich, fragmented 'backwash' sediments. In this paper, micromorphological features of a sediment sequence previously interpreted as being of tsunami origin are described. These characteristics are shown to be consistent with the macro-scale features used elsewhere, but show additional details not seen in standard stratigraphies, including possible evidence for individual waves, possibly wave-magnitude progression, organic fragment alignment and intraclast microstructures. Although replication and more complete studies are needed, this analysis confirms the identification of a tsunami in Willapa Bay in ca.1700 AD, while demonstrating a widely applicable technique for confirming or refuting possible tsunami deposits.

**Key words:** Tsunami, micromorphology, Cascadia subduction zone, Willapa Bay, Washington, thin sections.

## *Introduction*

One of the most important ways of estimating the risk of tsunami in coastal zones is to estimate the frequency and magnitude of past events (Nelson *et al.,* 1995; Fujiwara *et al*., 2000; Kelsey *et al*., 2005). Historical documents may record relatively recent events in some localities, but in many regions the records are incomplete, inconsistent or too short to record low-frequency, high impact events. Long-term ($10^2$–$10^4$ years) records can, however, be obtained from the recent geological record in coastal areas, particularly in incremental sedimentary contexts, such as estuarine environments or lakes close to the coast (Bondevik *et al.,* 1997; Fujiwara *et al*., 2000; Hutchinson *et al.,* 2000). Identifying palaeotsunami

[1] Department of Geography, Queen Mary, University of London, Mile End Road, London, E1 4NS, England. E-mail: a.a.kilfeather@qmul.ac.uk; j.meer@qmul.ac.uk
[2] Geography, School of Environment and Development, The University of Manchester, Oxford Road, Manchester, M13 9PL, UK. E-mail: jeffrey.blackford@manchester.ac.uk

sediments in the coastal zone is therefore an important part of an overall mitigation strategy. However, the certain identification of tsunami sediments is sometimes problematic (DAWSON *et al.*, 1991) as they are not always easy to distinguish from storm deposits (DAWSON and SHI 2000; GOFF *et al.*, 2004). Characteristics that may be visible close to the shore (NANAYAMA *et al.,* 2000) may become less clear with distance inland, with thinning of the sediment, and with post-depositional change.

Tsunami deposits are typically found in estuarine sediments and isolated coastal basins. Depositional sites include back-barrier lagoons (e.g., WILLIAMS and HUTCHINSON 2000), intertidal mud flats and salt marshes (SHENNAN *et al.,* 1996) and lakes (MINOURA *et al.*, 1994). Tsunami deposits are provisionally recognised in the field on the basis of anomalous sand horizons, often fining-up and fining-landward, coupled with organic-rich, fragmented 'backwash' sediments derived from landward sources and re-deposited as the water returns. In areas affected by tectonic deformation, such sand layers are also often associated with evidence for vertical displacement such as down-thrown saltmarsh sediments. This movement can be identified by organic remains, palaeosols or microfossil evidence of sea-water inundation (DAWSON and SHI, 2000; CLAGUE *et al.*, 2000; BRYANT 2001; ATWATER *et al.*, 2004). In some instances the interpretation of anomalous sand horizons in coastal zones as tsunami deposits can only be tentative. This uncertainty arises because other processes can lead to potentially similar deposits, particularly storm surges (GOFF *et al.,* 2004), i.e. extreme coastal flooding through high tides and wind action rather than seismic waves (NANAYAMA *et al.,* 2000). Past tsunamis may therefore be either under- or overestimated, resulting in the associated risk to coastal zones being wrongly assessed.

This paper uses thin section analysis to examine the characteristics of inferred tsunami deposits and tests the feasibility of using micromorphology as a diagnostic tool. The analysis of thin sections of undisturbed sediment samples has been used successfully to investigate structure and interpret processes of deposition in many other sedimentological applications including glacial sedimentology, slackwater flood sediments, alluvial soils and cave sediments (e.g., COURTY *et al.*, 1991; VAN DER MEER, 1997; WOODWARD *et al.*, 2001). The use of thin section analysis may reveal attributes of tsunamigenic sediments that can be used as diagnostic indicators.

## *Field Site*

The West Coast of North America has been the focus of much recent palaeoseismic research, especially following the impact of the Alaska 1964 Earthquake and the uncovering of geological evidence of large magnitude earthquakes and coincident tsunamis (ATWATER, 1987; CLAGUE, 1997; ATWATER and HEMPHILL-HALEY, 1997). The study area, in the southern part of Willapa Bay, Washington

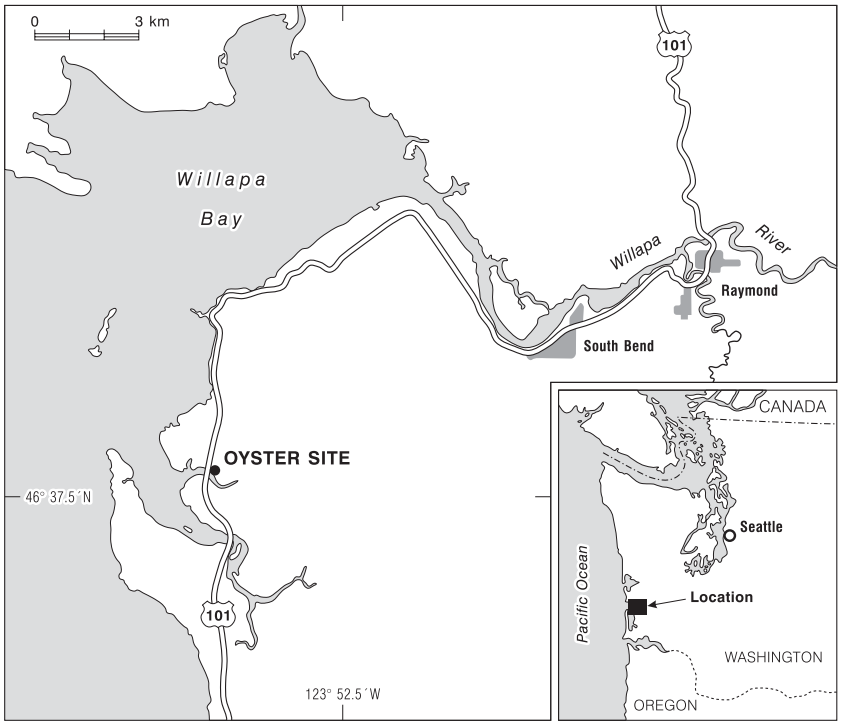


Figure 1
Locality map, Willapa Bay, Washington, USA.

(Fig. 1), has been shown to have been impacted by the ca. 1700 AD tsunami, recorded in Japan (SATAKE *et al.*, 1996, 2003) and thought to have originated from a large plate boundary rupture along the Cascadia subduction zone (NELSON *et al.*, 1995, ATWATER *et al.*, 2005). Estuarine sediments from the Niawiakum River valley, near the 'Oyster Site' of ATWATER and HEMPHILL-HALEY (1997) were re-sampled in September 2003 in order to extract material for thin-sectioning across the probable tsunamigenic sand inferred from earlier work. The site is representative of a number of exposures on the Washington coast where a sequence of buried soils demonstrates the occurrence of repeated plate boundary earthquakes. Associated with the most recent (ca. 1700 AD) event, coseismic subsidence caused an abrupt fall in relative sea level, shown clearly by diatom assemblages (HEMPHILL-HALEY, 1996). Immediately after subsidence, the soil horizon was overlain by a thin, tsunamigenic sand (ATWATER and HEMPHILL-HALEY, 1997) propagated by the earthquake. Photographs of the field site can be seen on the Access Washington website (http://apps.ecy.wa.gov/shorephotos/photos/Pacific/mediumres/PAC0185_mr.jpg) and the Quaternary Geoscience Research Centre, Simon Fraser University website (http://www.sfu.ca/~qgrc/people/jenn/willapabay.htm).

Figure 2 ▶
Thin section samples from inferred tsunami sediments, Willapa Bay, Washington. A) Flatbed scans of the thin sections. B) Flatbed scans with interpreted line-work and depositional units. Boxes indicate the locations of images in Figure 3.

## *Methods*

The field location, described and illustrated by ATWATER and HEMPHILL-HALEY (1997) and by ATWATER *et al.* (2004) was an exposed riverbank of estuary sediment cut parallel to the present river flow direction. The exact sampling point was an exposure of an organic-rich palaeosoil horizon with overlying sand representative of the site (ATWATER *et al.,* 2004). The sample included four main strata. From the base, these are: a) Estuarine sediments previously interpreted as being deposited high in the tidal range; b) an organic-rich 'peaty' palaeosoil previously considered to represent deposition close to, or above, the tidal range; c) banded, sand-rich inferred tsunamigenic sediments; and d) an estuarine mud layer. Undisturbed samples were collected from the cleaned face at low tide using 100 mm diameter plastic guttering, inserted into pre-cut slots. The samples were divided in two, with one half used to prepare three 80 mm wide thin sections over a 240 mm vertical interval spanning the thickness of the tsunami deposit.

The samples were dried in acetone and then impregnated with crystic resin in a vacuum chamber. After impregnation, the samples were left to harden for six weeks. They were then mounted on glass and ground to a thickness of approximately 25 μm (cf. MURPHY, 1986 for full details of the laboratory procedures). The thin sections were scanned on a high-resolution flatbed scanner to produce relatively low-magnification images of the thin sections in their entirety (Fig. 2). The samples were also examined, described and photographed using a petrographic microscope with magnifications of × 63 to × 320 with plain light conditions.

## *Results*

Figure 2A is a flatbed scan of the three thin section samples. The images and line-work (Fig. 2B) are described in the subsequent text. The micromorphological descriptions follow the format and terminology developed by pedologists (cf. BREWER, 1976).

### *Macroscopic Description*

Some of the structures in the thin sections are visible with the naked eye and these are described briefly in this section. The middle thin section contains the inferred tsunami deposits whereas the upper and lower ones contain finer grained sediments. The lowest thin section is a massive, fine, brown sediment that is organic in

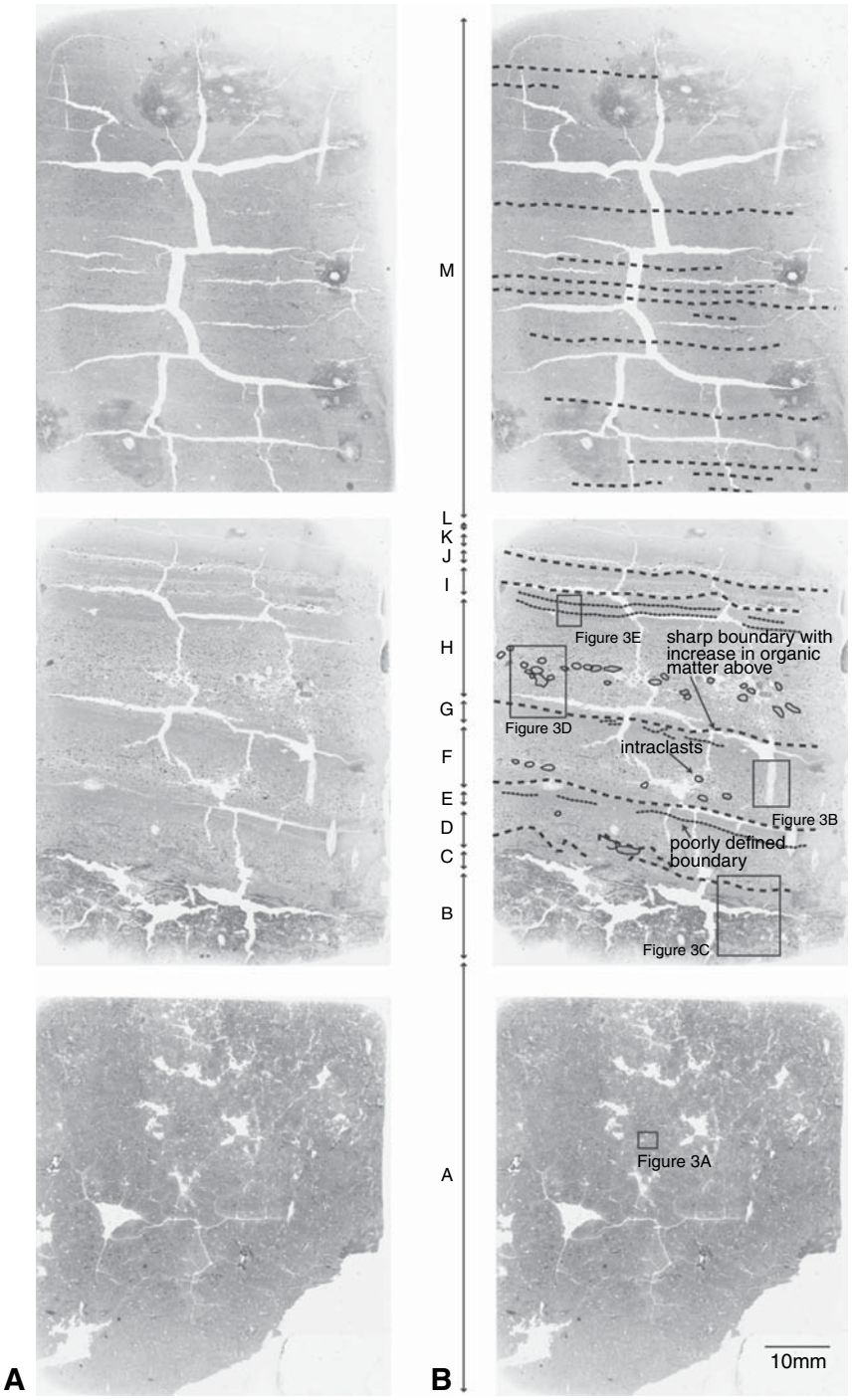
M
L
K
J
I
H
G
F
E
D
C
B
A
Figure 3E
sharp boundary with increase in organic matter above
Figure 3D
intraclasts
Figure 3B
poorly defined boundary
Figure 3C
Figure 3A
10mm
A
B

Figure 3 ▶
Photomicrographs in sediments from the Willapa Bay thin sections. A) Peat sediments in the lower thin section containing forams, cross sections of triglochin stems, wood fragments and framboid pyrite. B) Vertically oriented mollusc from unit F. C) The contact between the peat and the lower-most inferred tsunami deposits. D) Intraclasts and organic debris in unit H. E) Minor banding and changes of grain size in unit I.

appearance and contains organic skeleton grains and shell fragments. (Skeleton grains are large enough to be seen clearly in thin section; these thin sections are about 25 μm thick, so that individual grains of greater than about this diameter are described as skeleton grains. Finer grained material, not resolved in these thin sections, is described as plasma.) The base of the middle thin section is also a dark brown colour and is organic in appearance. Above this band, the remainder of the middle thin section is a fine-grained sediment containing five coarser grained bands of fine sand/coarse silt sized grains. All these structures dip gently to the right in the thin section. The upper thin section is a fine-grained grey-brown sediment, containing grains up to fine sand sized. Some poorly defined horizontal banding of dark brown grains are visible.

In all three thin sections there are planar voids (elongate and narrow voids) which formed due to differential drying rates and shrinkage of the thin sections prior to sediment impregnation. In the middle and upper thin sections these voids are mostly sub-horizontal, picking out planes of weakness along beds, whereas in the lower thin section they form chaotic patterns.

Parts of the upper thin section, and the right side of the middle thin section shows iron precipitate. The heaviest staining is around microfossils. It also appears to be in random patches within which non-stained areas at the centre contain voids. All three thin sections contain some framboid pyrite and manganese staining although they are mostly concentrated in the bottom thin section and in the organic material at the base of the middle thin section.

*Structure*

The following text should be read with reference to Figures 2 and 3.

Unit A: The lowest unit of the three thin sections comprises all of the lowest thin section and about 0.5 mm at the base of the middle thin section. The sediment is a massive brown slightly grainy plasma containing occasional tiny quartz skeleton grains (mostly less than 0.02 mm in diameter, or medium silt sized), organic plant pieces, microfossils including foraminifera, shell fragments and serated plant stems, probably *Triglochin* (Fig. 3A). The latter are seen in section as small rosette forms and in long section as banded elongated oval features. Some organic grains are aligned sub-horizontally but they appear mostly to be randomly oriented. Framboid pyrite is precipitated in places (Fig. 3A).

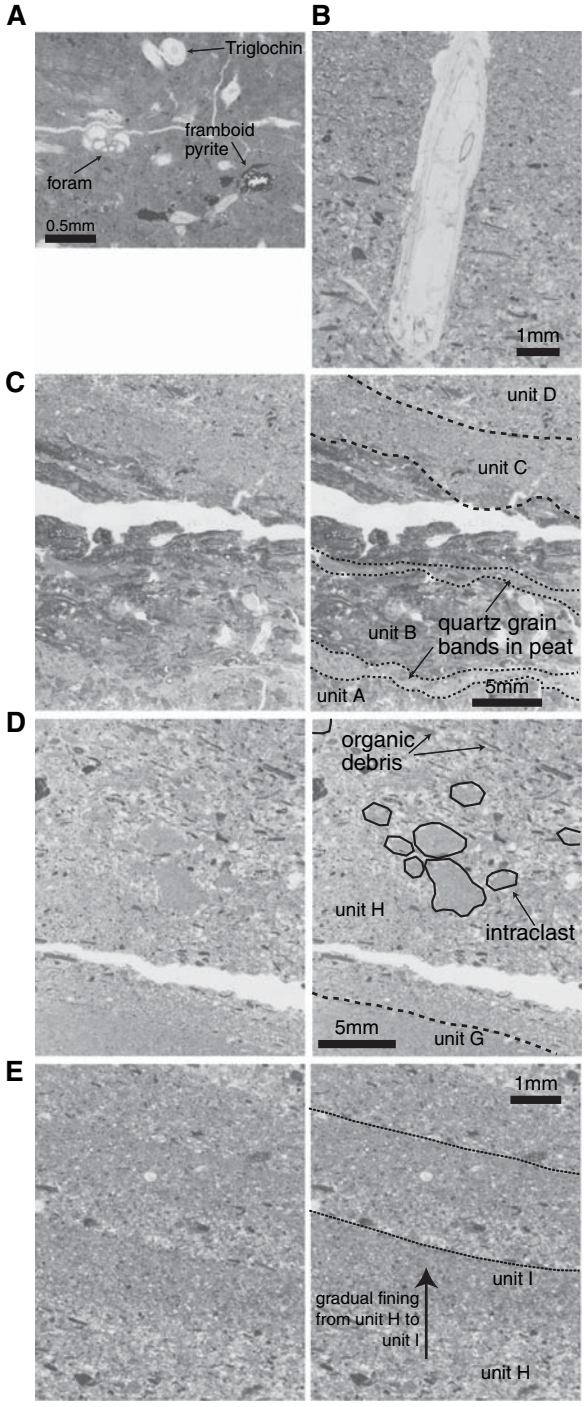
A
Triglochin
framboid pyrite
foram
0.5mm
B
1mm
C
unit D
unit C
unit B
quartz grain bands in peat
unit A
5mm
D
organic debris
unit H
intraclast
5mm
unit G
E
1mm
unit I
gradual fining from unit H to unit I
unit H

Unit B: This unit is composed largely of pieces of organic material including wood. Unit B is thickest on the left side of the slide, at 15 mm. The elongate pieces are almost all aligned sub-horizontally and some of the pieces are long (10–15 mm). Some very fine quartz grains occur amongst this material. Towards the right there is greater incorporation of mineral grains, with two discontinuous sub-horizontal bands of plasma and fine quartz grains on the right side of the sample (Fig. 3C) and one on the left.

Unit C: Above the predominantly organic band is a thin (2.1–3.8 mm), massive band of plasma-supported fine mineral grains and occasional elongate, sub-horizontal organic grains. The quartz grains are 0.05 mm in diameter (coarse silt) or less. The upper and lower boundaries are poorly defined. Towards the centre of the slide there is a poorly defined pocket of slightly coarser sediment.

Unit D: In unit D there is a change from a skeleton-grain dominated to skeleton grain supported band, composed mostly of coarser angular quartz grains, of approximately 0.2 mm (medium silt), and larger mostly elongate organic grains (A axes of up to 10 mm). Unit D is 4.6–7.9 mm thick. The boundary between this and the underlying unit C is diffuse and gradual. The elongate organic grains are mostly, although inconsistently, aligned sub-horizontally and follow the shape of the unit. Towards the centre of the slide there is a finer grained pocket. Almost all grains in the thin section have their long axes oriented sub-horizontally but at the right side of the slide there is a vertically oriented elongate shell (3.5 mm in length), and a second vertically oriented shell that penetrates from unit D into E and F. Figure 3B shows an elongate vertically oriented shell from unit F.

Unit E: Unit D rapidly fines upwards to a coarse plasma, containing very fine quartz skeleton grains (unit E). The organic particle content falls. The unit is 2.3–3.7 mm thick. Most quartz grains are $< 0.05$ mm in diameter (coarse silt) with many $< 0.01$ mm (medium silt). There is a slight coarsening to a poorly defined narrow horizon of fine quartz skeleton grains, a few grains thick. This band is barely perceptible on the left side of the slide; it has a relatively sharp boundary with the underlying sediment at the centre of the slide and there is a gradual coarsening upwards into this band on the right side of the slide, where it is best defined. The upper boundary is slightly sharper, with a change back to plasma-supported fine skeleton grains. There is a rounded, 3 mm long shell towards the left end of the unit.

Unit F: The boundary between units E and F is an abrupt change to a grain-rich sediment with an increase in organic particles. The sediment rapidly coarsens upward to coarser quartz and organic grains. Maximum mineral grain size in this band is about 0.3 mm (medium sand) with most being 0.1–0.2 mm (fine sand). The organic debris is more horizontally aligned than in unit D, with particles 1–5 mm long. Unit F contains small pockets of plasma towards its base (Fig. 2). Having coarsened upwards, the band then fines upwards, with a dramatic fall-off in the organic skeleton grain content. At the right side of the slide there are two vertically oriented elongate

shells, one of which is the longest in the sample at 5.6 mm. Unit F is 8.2–9.6 mm thick.

Unit G: There is no clear boundary between units F and G. The sediment gradually fines upwards and becomes dominated by a grainy brown plasma, supporting fine quartz grains < 0.05 mm diameter (coarse silt). At the centre of the thin section, towards the top of this band are discontinuous sub-horizontal bands and pockets in which there is a slight change to coarser material. The poorly defined horizons towards the top are just one grain thick and these grains are up to 0.2 mm in diameter (fine sand) (Fig. 2). This unit is 2.9–4 mm thick.

Unit H: As with the boundary between E and F, the boundary between bands G and H is marked by an abrupt but subtle change to a more grain-rich sediment with an increase in organic grains. Like unit F, unit H coarsens upwards. This unit contains many sub-rounded pockets of plasma supporting fine skeleton grains similar to the material in unit G (Fig. 3D), indicating that these are intraclasts from the underlying sediment. These intraclasts have a maximum length of 3 mm, and are more commonly 1–2 mm in diameter (coarse sand to fine gravel sized). They are confined to a restricted band between approximately 4.4 mm and 9.5 mm of the divide between units G and H. The band is coarsest above these pockets of plasma and remains coarse for a thickness of about 5 mm before gradually fining upwards again. There are many elongate organic grains in this band, as in units D and F, but also some considerably larger rounded pieces of organic material (up to 1.5 mm in diameter) in the zone in which the intraclasts are located, especially at the right end of the unit (Fig. 2). At the base of unit H, and up to where the intraclasts are located, the organic material is oriented in many directions. Only at the very base of unit H, and above the area containing intraclasts, is the organic debris oriented consistently horizontally (Fig. 3D). Unit H is 16.4–16.9 mm thick.

Unit I: The sediment fines upward in unit H and there is reduction in the organic grain content. There is a better-defined boundary between units H and I than between units F and G, with this boundary defined by a change from grain dominated sediment to matrix dominated sediment. Within unit I there are two thin bands of coarser grained material. The lower boundaries of these bands are relatively sharp; they then gradually fine upwards (Fig. 3E). These bands are mostly composed of quartz grains but they also contain occasional organic grains. The total thickness of unit I is 4.3–5.9 mm.

Unit J: Unit J is characterised by another abrupt change to matrix-supported, grain dominated sediment. The upper and lower parts of this band are mostly composed of quartz grains; the centre of the band contains mostly organic material. The elongate organic grains are all sub-horizontal. This unit is 2.3–2.7 mm thick.

Unit K: There is a clear transition from grain-dominated unit J to plasma-dominated unit K. The plasma contains mostly quartz grains and only very occasional small organic grains. There is one narrow discontinuous band of grain

dominated, matrix supported, quartz grains within unit K, which is just one to two grains thick. Unit K is 1.2–2.1 mm thick.

Unit L: The final coarse layer is again marked by a sudden change in grain size to grain supported and grain dominated quartz and elongate organic grain sediment, although there is less organic material in L than in other coarse grained units. At just 2.6 mm at its thickest, this band rapidly fines upwards into unit M.

Unit M: The sediment in Unit M is fine-grained grey-brown-stained plasma, supporting very fine skeleton grains of quartz and occasional elongate organic grains oriented sub-horizontally. It is largely massive, but there are thirteen poorly defined bands in the upper thin section in which there is a greater quantity of skeleton grains. Most of these bands contain a greater proportion of the sub-horizontal organic, elongate grains along them. Other bands, especially those towards the top of the thin section, are defined by a greater density of coarser plasma than in the rest of the sample. These features are poorly defined with diffuse boundaries, with the clearest having darker brown organic skeleton grains. Most bands span greater than half the width of the slide. The bands are not evenly distributed through the unit (Fig. 2). The first three bands are 13.6 mm, 15.35 mm and 16.8 mm from the base of unit M. The next two are more widely spaced at 24.9 mm and 35.3 mm from the base and a further cluster of five bands occurs at 39.9–47.3 mm. One more isolated band at 55.8 mm is followed by a pair at 74.9 mm and 77.4 mm. There are other very subtle changes in the unit M between phases with slightly denser or finer-grained material.

## *Interpretation*

It is clear from Figure 2 that the sand-rich band is composed of multiple layers. Although some banding has been described in this locality before, much more detail is revealed in the thin sections. The particle size, particle type, structure and thickness of the individual bands can be ascertained in a way that is not possible with the naked eye in the field or from the core samples.

### *Lower Marsh Sediments (Units A and B)*

The lowest unit (A) contains mostly organic material and fine plasma with microfossils. The presence of foraminifera and the halophytic *Triglochin* indicates a perimarine marsh setting. Unit B is composed of small pieces of non-decomposed vegetation, probably the surface of the marsh. It contains two discontinuous sub-horizontal bands of plasma and fine quartz grains. According to ATWATER and HEMPHILL-HALEY (1997) the marsh had a dense cover of vegetation that included the tufted grass *Deschampsia caespitosa* and *Potentilla pacifica* and leaf litter probably covered the marsh surface. A sudden change in

environment to one of marine deposition probably disturbed the leaf litter enough for the bands of plasma and quartz grains, like that in the overlying unit C, to be deposited within unit B. The abrupt change to banded silt, sand and organic skeleton grains (unit C upwards), indicates a sudden change in environment to one of cyclical sedimentation, with changes of energy which caused changes in the grain size of the bands.

*Banded Tsunami Sediments (Units C to L)*

Ten sorted sand and silt bands have been described (units C to L). Every second band is relatively coarse grained, containing fine quartz sand and sand-sized elongate organic grains. Between these bands there are finer grained quartz grain units with few organic fragments. The quartz grains are mostly angular. Sub-rounded intraclasts consisting of fine-grained sediment are incorporated into the lower parts of the coarse-grained organic rich bands. They are composed of the same sediment as the underlying fine-grained units.

The angularity of the quartz grains suggests that this sediment has not been worked over a long period of time. The sub-rounded intraclasts indicate reworking of the underlying sediment by turbulent flow. The changes in composition of the bands may indicate changes in direction of flow and hence source material, or may simply reflect a change of energy and thus particle size. The combination of an estuarine setting, high energy, turbulent deposition and the repeated cycles indicate that these sediments were deposited by wave action.

Vertically oriented shells on the right side of the banded sediments indicate that these mollusca were alive at the time of deposition and once deposited began to burrow downwards into the sediment. The largest mollusc, in band F, has a pore above it that originates in the coarsest part of band H. This indicates that the mollusc was deposited along with other coarse organic material in unit H, and then burrowed down into F leaving a roughly defined void and an area of bioturbated sediment in its track. Other shells also have bioturbated sediment above them.

Organic rich bands are cited as being characteristic of tsunami deposits (CLAGUE *et al*., 2000). The coarse organic-rich bands contain sub-horizontally oriented organic fragments that indicate non-turbulent flow of sediment-laden water at the sediment-water interface. The largest elongate organic grains are in the lowest coarse-grained band, unit D. The gradual reduction in organic grain size moving up the organic grain rich bands, with the exception of some large rounded organic grains on the right side of unit H, indicates that fewer large grains were mobilised or available during later wave cycles. This is possibly due to an initial burial of the peat, represented by unit B, by sediment from the first wave, represented by band C, reducing the availability of organic material for entrainment by subsequent waves. The extent to which the organic fragments are horizontally oriented increases from units D, to F, to H, suggesting that the passing water became progressively less

turbulent. However, in the area of band H that contains intraclasts from the underlying unit G, the organic fragments are oriented in many directions (Figs. 2 and 3D) indicating (together with the presence of the intraclasts), that this deposition was by more turbulent flow (perhaps brief or local). Intraclasts in units D and F also indicate some turbulent flow.

The lower contacts of the organic rich bands are the sharpest boundaries in this sample and are probably erosive. This supports the suggestion that the fine-grained intraclasts are derived from the underlying fine sediment bands. It also indicates that the organic-rich (in- or out-flowing) wave remobilised some of the sediment that had been deposited previously. The bands could therefore be described as pairs, in which units D and E form a continuous phase of sedimentation, as do F and G, H and I, J and K and unit L finally fines upwards and ends in unit M. Because of the uninterrupted fining-up sequence in each couplet, each pair probably represents a separate continuous depositional event, rather than two separate events. (Although the boundary between the largest organic-rich horizon (unit H) and the overlying fine-grained horizon (unit I) is relatively sharp and may be erosive.) In this case our interpretation would differ from those reported previously (e.g., NISHIMURA and MAYAJI, 1995; BONDEVIK *et al.*, 1997) because the lowest part of each couplet contains the most organic matter, which is usually interpreted as coming from the onshore to offshore returning wave (CLAGUE *et al.*, 2000; NANAYAMA *et al.*, 2000). However, previous studies have examined sediments close to the ocean shore, where there is a clear distinction between inorganic sources of material from offshore and organic sources from onshore. At this site it is known that a peaty upper marsh deposit (represented by unit B) and organic-rich forest soils lay between the site and the ocean (ATWATER and HEMPHILL-HALEY, 1997), as well as the Willapa Bay coastal barrier (Fig. 1). An incoming wave would therefore contain organic terrestrial and inter-tidal debris as well as minerogenic silts and sands. The incoming wave could therefore have deposited the coarse-grained organic debris. At the wane of the wave the finer grained material would have settled out, forming a fining-up sequence, which is almost all non-organic.

Alternatively, each pair of bands may represent deposition from the waves returning from onshore to offshore, and there may be no sedimentary record of the incoming waves. However, there are two arguments against a return-flow deposition hypothesis. First, return flows are often channelised, possibly cutting new channels but on other occasions using or remodelling existing ones (DAWSON, 1994; BRYANT, 2001), although extremely big tsunami waves can return across the entire valley floor. At the Niawiakum site, an estuary with a well defined river channel, it is possible that return flow followed the channel, with a lower discharge rate for a longer time as opposed to the rapid inflow for a short time that characterises an incoming wave. Second, an interpretation of deposition by the outgoing wave only is contrary to previous interpretations of tsunamigenic sediments, where the incoming wave is the dominant sand depositor (MCSAVENEY *et al.,* 2000). Also, ATWATER and HEMPHILL-HALEY (1997) present evidence for inflow deposition at the Niawiakum site,

including fold-over of plants rooted in the buried marsh. Given the potential sources of organic material between the site and the ocean, perhaps organic loading should not be considered diagnostic of return flow here.

The thickness of the pairs of bands differs. The pair D/E is 7.5–12.2 mm thick, F/G is 11.6–13.6 mm thick, H/I is 21.4–23.1 mm thick, J/K is 3.6–4.3 mm thick and L is 2.6 mm at its thickest where it fines upwards into unit M. The third band G/H is the thickest. The differing band thickness and particle size (or total mass) may be due to changes in wave velocity, wave volume, wave turbulence, direction of wave travel across the foreshore, availability of sediment, or the ability of subsequent waves to erode previously deposited material. The third wave (represented by units H and I) may have been the most energetic. Previous and subsequent depositional events left smaller grains in less abundance, implying reduced energy. Further sampling at the site would confirm whether or not these observed changes in band thickness were continuous across the site or were local changes. Tide level changes may also have been influential in determining the thickness and grain size of deposits. MOFJELD *et al.* (1997) demonstrated that the ca.1700 AD event probably occurred at or shortly after low tide during a neap tide phase, suggesting an exposed intertidal foreshore.

Grain size variations and faint stratification in the finer horizons (units E, G, I and K) suggest interrupted or changing flow pattern, perhaps as the waves peaked and ebbed or with reverse and lateral flows, or the return of the wave to flow from onshore to offshore. Stratification in units J to L could represent post-tsunami sedimentation, for example from river flow across a debris-laden valley floor, or tidal sequences redepositing material on a lowered surface, now within the tidal range.

The feint and irregular banding in unit M is consistent with tidal mud deposition, probably rapidly accumulating. ATWATER and HEMPHILL-HALEY (1997) recorded high percentages of tidal flat and subtidal diatoms in this phase, giving way to low marsh species within 0.2–0.3 m.

The sediments in Figure 2 could be interpreted in three ways: 1) 5 waves depositing couplets on the way inland with no sediments recording backflow, which was presumably channelised; 2) 5 waves depositing couplets on the way offshore, with no record of incoming waves due to either no deposition, or erosive returning flows; 3) 5 waves depositing fining-up sequences representative of both onshore and offshore flows. There also remains the possibility that the sequence shows a more complex pattern of sedimentation and erosion, or even a simpler one, with the sediments deposited by changing flow within a single flow (LOWE, 1982; 1988).

## *Discussion*

NANAYAMA *et al.* (2000) and GOFF *et al.* (2004) showed that there are differences between tsunami and storm surge sediments in the same depositional setting where

massive sands close to the shore are available for study. In the Niawiakum setting however, farther from the ocean and in an estuarine environment, the differences demonstrated by these previous studies are less evident, and other diagnostic features are therefore required. Previous research in Willapa Bay and in the wider region resulted in the interpretation of anomalous sand horizons in finer material as tsunami deposits (ATWATER and HEMPHILL-HALEY, 1997; ATWATER *et al.,* 2004). These interpretations were based on microfossil evidence, the position of the sand-rich horizons directly over a post-subsidence palaeosoil and correlation with similar deposits on a regional basis. The aim of this paper is to test the 'micromorphological signal' of these sediments interpreted as tsunamigenic in origin.

*Alternative Depositional Environments*

There are, however, other possible, non-tsunamigenic, interpretations of the microstratigraphy described above. To test the use of micromorphology as a means of determining the origin of these deposits the alternative modes of formation need to be considered. The alternatives include: 1) Sediment-laden floods from the Niawiakum River, 2) a coastal flood, or floods, including storm surge events and 3) other sources of sand including landslides and sediment shaking as discussed below.

The thin section analysis presented here is from a single site so it is not possible to assess whether there are upstream or altitudinal changes in the sediments deposited. However, evidence reported previously (ATWATER and HEMPHILL-HALEY, 1997; ATWATER *et al.,* 2004) describes landward tapering of inferred tsunami sands in the Niawiakum estuary, and landward tapering across individual meander bends as well, as marine sand-flat diatoms and folded-over plants, which, overall, overwhelmingly favour a seaward source for sedimentation. If thin section samples were taken at upstream and downstream locations they would also clearly show any upstream thinning or altitudinal change in the sediments deposited, and hence additionally test the river flood alternative.

The sequence shown here, with multiple events occurring over a short time period (shown by the lack of soil development and minimal bioturbation) suggests that a river flooding cause is unlikely.

The stratified, fining up couplets are similar to those recorded from known tsunami deposits (NISHIMURA and MIYAJI, 1995; SATO *et al.* 1995) and unlike the better sorted, overlapping sediments associated with storm sediments (SCHWARTZ, 1982; NANAYAMA *et al.*, 2000; GOFF *et al.*, 2004). Thin sections have revealed these couplets much more clearly.

There are other possible sources of the sequence of coarser layers, including re-working of a single sand sheet deposited by a tsunami, and an upstream origin in the Niawiakum catchment, for example landslides in the upland catchment east of the site, triggered by the inferred high magnitude earthquake at ca.1700 AD. In both cases, a post-subsidence sequence of sand deposition into the tidal prism would be

expected, with pulses of sand reactivated by either high tide or high river levels in the months following the earthquake.

Shaking of soft sediments in the coastal zone during the earthquake also seems likely, including the mud flats and near-shore shelf, again increasing the sediment supply for subsequent tidal in-wash. However, these alternatives cannot adequately explain the alternating organic-rich and organic-poor bands, the fining-up sequences, or critically, the 'rip-up' intraclasts. Despite the variability of tsunami deposits (NANAYAMA and SHIGENO, 2006) these features suggest that the use of thin sections can be diagnostic of tsunamigenic sediment in thin or fine-grained sediments where macro-scale structures are not evident. Seemingly simple, single sand layers could be analysed in this way to test for microscale diagnostic features.

## *Conclusion*

The examination of thin sections of inferred tsunami deposits has revealed much greater sedimentary complexity, in these anomalous sand horizons, than was visible in the field. A number of possibilities can be suggested as to how the horizon was formed, with a tsunami the most difficult to refute, and hence the most likely.

Only a single set of slides has been prepared from one site, but it is evident that sampling upstream and downstream from this site, and in adjoining estuaries would be beneficial. Replication of the 5-couplet sequence elsewhere along the same coast at the same stratigraphic level would strongly indicate that the 5 couplets represent a tsunami wavetrain, whereas inconsistency would weaken this hypothesis. The best way to test the alternative depositional hypotheses would be to study additional tsunami sediments, especially recently deposited sediments. Ideally these would be from a similar estuarine intertidal or supratidal setting and where real observations of either wave sequences or tidal gauges are available, such as Port Alberni on Vancouver Island and Crescent City, California in 1964, or in SE Asia following the 26/12/04 event. Estuaries along the west coast of Aceh Province, Sumatra, or along the Thai Peninsula may provide suitable analogues.

The aim of this study was to assess the use of micromorphology as a diagnostic tool to distinguish tsunamigenic sediments. The results presented here suggest that micro-rip-up clasts, millimetre-scale banding, organic entrainment, fining-up sequences and erosive contacts are all visible in thin section but not in field stratigraphy, and that the technique is of great potential for examining possible tsunami sediments.

## *Acknowledgements*

The authors would like to thank Brian Atwater for his very helpful comments on, and additions to, this project and his generosity with ideas and field data. Ms

B. Davenport (Washington Dept. Natural Resources) allowed access to the site. We would also like to thank the two anonymous referees for their helpful comments and suggestions.

## References

ATWATER, B. F. (1987), *Evidence for great Holocene earthquakes along the outer coast of Washington State*, Science *236*, 942–944.

ATWATER, B. F. and HEMPHILL-HALEY, E. (1997), *Recurrence intervals for great earthquakes of the past 3,500 years at northeastern Willapa bay, Washington*, US Geol. Survey Prof. Paper *1576*.

ATWATER, B. F., TUTTLE, M. P., SCHWEIG, E. S., RUBIN, C. M., YAMAGUCHI, D. K., and HEMPHILL-HALEY, E., *Earthquake recurrence inferred from paleoseismology*. In *The Quaternary Period in the United States* (eds. A. R. Gillespie *et al.*), (Elsevier, Amsterdam 2004) pp. 331–350.

ATWATER, B. F., MUSUMI-ROKKAKU, S., SATAKE, K., TSUJI, Y., UEDA, K., and YAMAGUCHI, D.K. (2005), *The orphan tsunami of 1700 — Japanese clues to a parent earthquake in North America,* U.S. Geol. Survey Prof. Paper *1707*, 133 pp. (published jointly by University of Washington Press, Seattle) (http://pubs.usgs.gov/pp/pp1707/).

BONDEVIK, S., SVENDSEN, J. I., and MANGERUD, J. (1997), *Tsunami sedimentary facies deposited by the Storrega tsunami in shallow marine basins and coastal lakes, western Norway*, Sedimentology *44*, 1115–1131.

BREWER, R., *Fabric and Mineral Analysis of Soils* (Kreiger, Huntington, New York 1976).

BRYANT, E., *Tsunami: The Underrated Hazard* (Cambridge University Press, Cambridge 2001).

CLAGUE, J. J. (1997), *Evidence for large earthquakes at the Cascadia Subduction Zone*, Rev. Geophys. *35*, 439–460.

CLAGUE, J. J., BOBROWSKY, P. T., and HUTCHINSON, I. (2000), *A review of geological records of large tsunamis at Vancouver Island, British Columbia, and implications for hazard*, Quat. Sci. Rev. *19*, 849–863.

COURTY, M.-A., GOLDBERG, P., and MACPHAIL, R. I., *Soils and Micromorphology in Archaeology*. (Cambridge University Press, Cambridge 1991).

DAWSON, A. G., FOSTER, I. D. L., SHI, S., SMITH, D. E., and LONG, D. (1991), *The identification of tsunami deposits in coastal sediment sequences*, J. Tsunami Haz. *9*, 73–82.

DAWSON, A. G. (1994), *Geomorphological effects of tsunami run-up and backwash*, Geomorphology *10*, 83–94.

DAWSON, A. G. and SHI, S. (2000), *Tsunami deposits*, Pure Appl. Geophys. *157*, 875–897.

FUJIWARA, O., MASUDA, F., SAKAI, T., IRIZUKI, T., and FUSE, K. (2000), *Tsunami deposits in Holocene Bay mud in southern Kanto region, Pacific coast of central Japan*, Sed. Geol. *135*, 219–230.

GOFF, J., MCFADGEN, B. G., and CHAGUÉ-GOFF, C. (2004), *Sedimentary differences between the 2002 Easter storm and the 15th-century Okoropunga tsunami, southeastern North Island*, New Zealand, Mar. Geol. *204*, 235–250.

HEMPHILL-HALEY, E. (1996), *Diatoms as an aid in identifying late-Holocene tsunami deposits*, Holocene *6*, 439–448.

HUTCHINSON, I., GUILBAULT, J-P., CLAGUE, J. J., and BOBROWSKY, P. T. (2000), *Tsunamis and tectonic deformation at the northern Cascadia margin: A 3000-year record from Deserted Lake, Vancouver Island*, Holocene *10*, 429–439.

KELSEY, H. M., NELSON, A. R., HEMPHILL-HALEY, E., and WITTER, R. C. (2005), *Tsunami history of an Oregon coastal lake reveals a 4600-yr record of great earthquakes on the Cascadia subduction zone*, Geol. Soc. Am. Bull. *117*, 1009–1032.

LOWE, D. R. (1982), *Sediment gravity flows; II, Depositional models with special reference to the deposits of high-density turbidity currents,* J. Sed. Petrology *52*, 279–297.

LOWE, D. R. (1988), *Suspended-load fallout rate as an independent variable in the analysis of current structures,* Sedimentology *35*, 765–776.

MCSAVENEY, M. J., GOFF, J. R., DARBY, D. J., GOLSMITH, P., BARNETT, A., ELLIOTT, S., and NONGKAS, M. (2000), *The 17 July 1998 tsunami, Papua New Guinea: Evidence and initial interpretation*, Mar. Geol. *170*, 81–92.

MINOURA, K., NAKAYA, S., and UCHIDA, M. (1994), *Tsunami deposits in a lacustrine sequence of the Sanriku coast, northeast Japan*, Sed. Geol. *89*, 25–31.

MOFJELD, H. O., FOREMAN, M. G. G., and RUFFMAN, A. (1997), *West coast tides during Cascadia subduction zone tsunamis*, Geophys. Res. Lett. *24*, 2215–2218.

MURPHY, C. P., *Thin Section Preparation of Soils and Sediments* (AB Academic Publishers, Berkhamstead, U.K 1986).

NANAYAMA, F., SHIGENO, K., SATAKE, K., SHIMOKAWA, K., KOITABASHI, S., MIYASAKA, S., and ISHII, M. (2000), *Sedimentary differences between the 1993 Hokkaido-nansei-oki tsunami and the 1959 Miyakojima typhoon at Taisei, southwestern Hokkaido, northern Japan*, Sed. Geol. *135*, 255–264.

NANAYAMA, F. and SHIGENO, K (2006), *Inflow and outflow facies from the 1993 tsunami in southwest Hokkaido*, Sed. Geol. *187*, 139–158.

NELSON, A. R., ATWATER, B. F., BOBROWSKY, P. T., BRADLEY, L-A., CLAGUE, J. J., CARVER, G. A., DARIENZO, M. E., GRANT, W. C., KRUEGER, H. W., SPARKS, R., STAFFORD, T. W., and STUIVER, M. (1995), *Radiocarbon evidence for extensive plate boundary rupture about 3000 years ago at the cascadia subduction zone*, Nature *378*, 371–374.

NISHIMURA, Y. and MIYAJI, N. (1995), *Tsunami deposits from the 1993 southwest Hokkaido earthquake and the 1640 Hokkaido Komagatake eruption, northern Japan*, Pure Appl. Geophys. *144*, 719–733.

SATAKE, K., SHIMAZAKI, K., TSUJI, Y., and UEDA, K. (1996), *Time and size of a giant earthquake in Cascadia inferred from Japanese tsunami record of January 1700*, Nature *379*, 246–249.

SATAKE, K., WANG, K. L., and ATWATER, B. F. (2003), *Fault slip and seismic moment of the 1700 Cascadia earthquake inferred from Japanese tsunami descriptions*, J. Geophys. Res.-Solid Earth *108*, 2535.

SATO, H., SHIMAMOTO, T., TSUTSUMI, A., and KAWAMOTO, E. (1995), *Onshore tsunami deposits caused by the 1993 southwest Hokkaido and 1993 Japan Sea earthquakes*, Pure Appl. Geophys. *144*, 693–717.

SCHWARTZ, R. K. (1982), *Bedform and stratification characteristics of some modern small-scale washover sand*, Sedimentology *29*, 835–849.

SHENNAN, I., LONG, A. J., RUTHERFORD, M. M., GREEN, F. M., INNES, J. B., LLOYD, J. M., ZONG, Y., and WALKER, K. J. (1996), *Tidal marsh stratigraphy, sea-level change and large earthquakes, I: a 5000 year record in Washington, USA,* Quat. Sci. Rev. *15*, 1023–1059.

VAN DER MEER, J. J. M. (1997), *Particle and aggregate mobility in till: Microscopic evidence of subglacial processes*, Quat. Sci. Rev. *16*, 827–831.

WILLIAMS, H. and HUTCHINSON, I. (2000), *Stratigraphic and microfossil evidence for two late Holocene tsunamis at Swantown marsh, Whidbey Island, Washington State*, Quat. Res. *54*, 218–227.

WOODWARD, J. C., HAMLIN, R. H. B., MACKLIN, M. G., KARKANAS, P., and KOTJABOPOULOU, E. (2001), *Quantitative sourcing of slackwater deposits at Boila Rocksheleter: A record of lateglacial flooding and Paleolithic settlement in the Pindus Mountains, northwest Greece*, Geoarchaeology *16*, 501–536.

(Received February 20, 2006, accepted July 30, 2006)

Pure appl. geophys. 164 (2007) 527–545
0033–4553/07/030527–19
DOI 10.1007/s00024-006-0178-z



Pure and Applied Geophysics

# Volcanogenic Tsunamis in Lakes: Examples from Nicaragua and General Implications

ARMIN FREUNDT,[1,2] WILFRIED STRAUCH,[3] STEFFEN KUTTEROLF,[1] and HANS-ULRICH SCHMINCKE[1,2]

*Abstract*—This paper emphasizes the fact that tsunamis can occur in continental lakes and focuses on tsunami triggering by processes related to volcanic eruptions and instability of volcanic edifices. The two large lakes of Nicaragua, Lake Managua and Lake Nicaragua, host a section of the Central American Volcanic Arc including several active volcanoes. One case of a tsunami in Lake Managua triggered by an explosive volcanic eruption is documented in the geologic record. However, a number of events occurred in the past at both lakes which were probably tsunamigenic. These include massive intrusion of pyroclastic flows from Apoyo volcano as well as of flank-collapse avalanches from Mombacho volcano into Lake Nicaragua. Maar-forming phreatomagmatic eruptions, which repeatedly occurred in Lake Managua, are highly explosive phenomena able to create hugh water waves as was observed elsewhere. The shallow water depth of the Nicaraguan lakes is discussed as the major limiting factor of tsunami amplitude and propagation speed. The very low-profile shores facilitate substantial in-land flooding even of relatively small waves. Implications for conceiving a possible warning system are also discussed.

**Key words:** Lake tsunami, volcanogenic tsunami, tsunami hazard, Nicaraguan lakes.

## *Introduction*

Tsunamis are widely recognized as disastrous waves in the ocean triggered by earthquakes, particularly since the Dec. 26, 2004 catastrophe in the Indian Ocean. This paper aims to draw attention to the facts that volcanic processes also trigger tsunamis, and that such disastrous waves do also occur in lakes on land. The best documented and most disastrous volcanogenic tsunami catastrophe in recorded history occurred during the 1883 eruption of the Krakatau Volcano in Indonesia. Almost 30,000 lives were taken along the Sunda Strait shores by tsunamis formed when voluminous pyroclastic flows entered the sea around the volcanic island of Krakatau (CAREY *et al.*, 2001). Pyroclastic flows also caused tsunamis at many

[1] SFB 574 at Kiel University, Wischhofstr. 1-3, D-24148, Kiel, Germany.
[2] IFM-GEOMAR, Wischhofstr. 1-3, D-24148, Kiel, Germany.
[3] Instituto Nicaragüense de Estudios Territoriales, INETER, Managua, Nicaragua.

other volcanoes such as Tambora in 1815 (SELF *et al.*, 1984; SIGURDSSON and CAREY, 1989), Aniakchak, Alaska (WAYTHOMAS and NEAL, 1998), Santorini, Greece (MCCOY and HEIKEN, 2000), most recently at Montserrat, Lesser Antilles (HART *et al.*, 2004; PELINOVSKY *et al.*, 2004), and at many other locations (DE LANGE *et al.*, 2001). Similar to pyroclastic flows, avalanches from collapsing flanks of stratovolcanoes can trigger tsunamis when entering water or when the debris masses move largely under water as on the flanks of volcanic ocean islands (e.g., KEATING and MCGUIRE, 2000). Such collapses can be triggered by volcanic or tectonic activity but also by climatic events (e.g., KERLE and VAN WYK DE VRIES, 2001; SCOTT *et al.*, 2005). In 1792, an earthquake-triggered collapse at Unzen, Japan, shed an avalanche into the Ariake Sea where it formed a tsunami; more than 14,000 lives were lost (SIEBERT, 2002). Apart from these two types of mass flows, volcanoes provide other potential trigger mechanisms of tsunamis such as caldera subsidence and other volcano-tectonic movements or underwater explosions (BEGET, 2000).

One type of tsunami has yet received little scientific attention although it can also be disastrous, albeit on a more local scale. This is tsunamis in continental lakes. A prominent volcanic example is the initial landslide of the May 18, 1980, Mount St. Helens eruption, which entered Spirit Lake and caused water run-up to 260 m above lake level (VOIGHT *et al.*, 1981). In 1999, a relatively small landslide caused a 15-m-high wave in the shallow crater lake of Kasu Tephra Cone, Papua New Guinea, injuring several people and killing one (WAGNER *et al.*, 2003). Underwater explosions in Lake Karymskoye, Kamchatka, in 1996 formed tsunamis with 2–30 m run-up heights at shore (BELOUSOV *et al.*, 2000). Naturally, non-volcanic landslides do also generate tsunamis in lakes. Fatal examples of landslide-triggered lake tsunamis occurred in 1971 in Lake Yanahuin, Peru (PLAFKER and EYZAGUIRRE, 1979), and 1987 in the Valtellina valley, Italian Alps (GOVI *et al.*, 2002). A 60-m-high wave formed by a landslide into the Vaiont reservoir, northern Italy, in 1967 drowned more than 2000 people (MÜLLER, 1964). Glacier falls can likewise trigger catastrophic tsunamis (SLINGERLAND and VOIGHT, 1979). Moreover, lake tsunamis may be triggered by earthquakes. Tectonic movement at a fault crossing a lake can form a tsunami and, if the lake is deep and has steep margins, also excite seiches which may flood the shores hours after the earthquake and tsunami (ICHINOSE *et al.*, 2000). Model results for the 500-m-deep Lake Tahoe (USA) indicate higher amplitudes for the seiches than the tsunami, and smaller seiches also form by resonance induced by earthquakes on faults 10-km away from the lake (ICHINOSE *et al.*, 2000). Fatal seiches destroyed villages at Taal Caldera Lake, Philippines, following a tectonic earthquake in 1749 (NEWHALL and DZURISIN, 1988). In 1878 and 1937, earthquakes associated with vertical ground motions triggered tsunamis in Rabaul caldera, Papua New Guinea, which forms a shallow bay (NEWHALL and DZURISIN, 1988).

In lakes as well as in largely enclosed bays and inlets the travel times of tsunamis to threatened shores are short. Early warnings will thus mainly depend on timely recognition of the potentially tsunami-triggering events.

## *Tsunamis in Nicaragua*

Since 1500, the number of 49 tsunamis is known to have occurred on the Central American Pacific and Atlantic Coasts (MOLINA, 1997); all generated by strong tectonic earthquakes. The largest and most destructive tsunami impacted on September 1, 1992, on the Nicaraguan Pacific Coast with wave heights up to 10 meters. The tsunami caused widespread destruction and killed more than 170 people. This event caused considerable interest in the Nicaraguan population on tsunami hazard, tsunami disaster prevention and mitigation, and was the starting point for the development of a National Tsunami Warning System for the Nicaraguan Pacific Coast. As Nicaragua has very large lakes the question arises whether tsunamis can occur in these lakes, which are the mechanisms to generate them, and whether early warning is possible for these events.

We have recently identified a tsunami deposit along the shore of Lake Managua that is related to a volcanic eruption (FREUNDT *et al.*, 2006a) and which we will briefly describe below. At both lakes, Lake Managua and Lake Nicaragua (Fig. 1), potentially tsunamigenic volcanic events have occurred in the past; we describe some of these below.

Tsunamis in these lakes would differ from those in the ocean mainly because shallow water depths (Table 1) limit tsunami speed, amplitude and wavelength. Like ocean coasts, however, lake shores in Nicaragua and elsewhere are densely populated and at high risk when a tsunami occurs. We will discuss some aspects of lake tsunamis using the two large lakes in Nicaragua as examples. Both lakes lie within the line of active arc volcanoes and within the Nicaraguan depression, a tectonic graben roughly parallel to the trench where the Cocos Plate subducts beneath the Caribbean Plate.

## *Tsunamigenic Events at the Nicaraguan Lakes*

### *The Mateare Eruption*

The subplinian to plinian Mateare eruption occurred between 3,000 to 6,000 years ago from a now hidden vent near the northwestern shore of Chiltepe Peninsula in Lake Managua (FREUNDT *et al.*, 2006a). Fossil shorelines found at Lake Managua (COWAN *et al.*, 2002) imply that the lake's water level dropped through the past several thousand years such that the proposed Mateare vent site would have been under water of several meters depth at the time of eruption. The eruption produced a

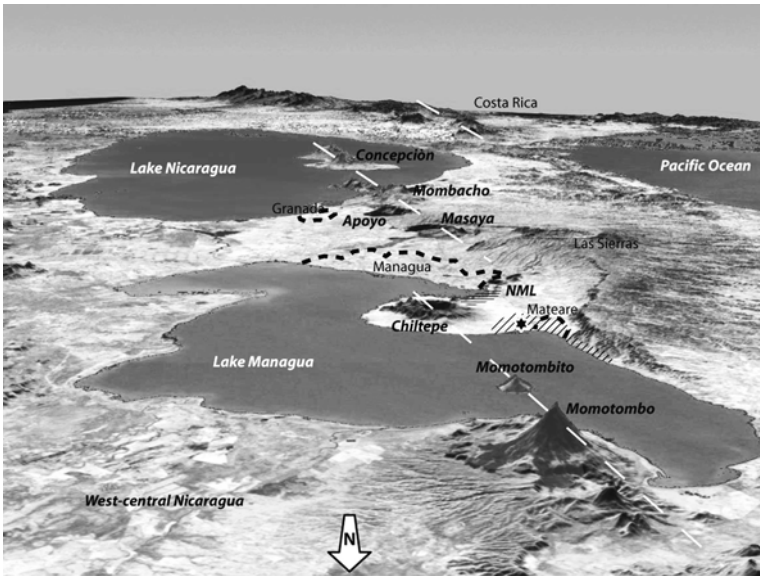


Figure 1

Oblique view, looking south, onto west-central Nicaragua with the two large lakes and chain of arc volcanoes. Modified from Google Earth. White dashed lines indicate linear segments of the volcanic front that are offset between Chiltepe Peninsula and Masaya volcano, and near the Nicaragua-Costa Rica frontier. NML is the Nejapa-Miraflores lineament, with the horizontally hatched area indicating the distribution of phreatomagmatic maar deposits. The diagonally hatched area around Mateare indicates the distribution of a tsunami deposit associated with a plinian eruption from a proposed vent site marked by the star.

dacitic to andesitic, compositionally zoned pumice lapilli fallout deposit—the Mateare Tephra—that is about 2-m thick and exposed along the shore of Lake Managua north of the town of Mateare over a distance of about 15 km (Fig. 1). We

Table 1

*Properties of the two large Nicaraguan lakes. Data from World Lakes Database (www.ilec.or.jp), 2004*

| Properties | Lake Nicaragua | Lake Managua |
|---|---|---|
| Length (km) | 160 | 58 |
| Width, W (km) | 70 | 22 |
| Area ($km^2$) | 8150 | 1016 |
| Volume ($km^3$) | 108 | 8 |
| Avg. depth (m) * | 13 | 8 |
| Max. depth, $D_{max}$ (m) | 70 ** | 26 |
| Avg. slope tan $\alpha = 2*D_{max}/W$ | 0.0020 | 0.0024 |
| Avg. wave celerity, c (m/s) | 11 | 9 |

* Volume divided by area.

** Note that low-resolution bathymetric data from Direccion Hidrografia de Instituto Nicaragüense de Estudios Territoriales (INETER), Managua, suggest a maximum depth of only $D_{max} < 30$ m.

have divided the deposit into four units (FREUNDT *et al.*, 2006a). Unit A is a well-stratified fallout of high-silica dacitic pumice with relatively high contents of ash and lithic fragments (Fig. 2). It is interpreted as the result of an early phase of eruption characterized by discrete explosions which appear to have been caused by both interaction with external water and temporary blocking of the vent by obsidian plugs. Unit B is a well-sorted, massive and lithic-poor light-gray dacitic pumice lapilli fallout that constitutes the major thickness of the deposit (Fig. 2). It represents the main, steady plinian phase of the eruption. Unit C is a continuation of unit B in terms of grain size and texture but is composed of black andesitic pumice. The change in composition occurs over a thin thickness interval. The rapid change in magma composition did not interrupt or significantly modify the continuing eruption. Unit D has a lapilli fallout layer at base composed of vesicle-poor andesitic scoria, some earlier erupted and entrained pumice lapilli, and lithic fragments. It is overlain by a stratified package of fallout ash rich in accretionary lapilli. Unit D represents fallout from the phreatomagmatic terminal eruption phase. The top of the Mateare Tephra has commonly been eroded, and basal unit A is missing in most outcrops along the lake shore.

A dark-gray sand layer, the Mateare Sand, lies stratigraphically between units A and B of the Mateare Tephra (Fig. 2); in the common absence of unit A, however, it lies at the base below unit B. This medium sand ($M_{d_\Phi} = 1.8$–$2.2$) is well sorted ($\sigma_\Phi = 0.95$–$1.85$) but contains outsized pumice lapilli either dispersed in the sand or forming pumice lenses. This light-gray pumice is mostly derived from the Mateare Tephra although there is a minor contribution of white pumice from the underlying, compositionally distinct Xiloa Tephra. The sand-size fraction contains angular vesicular through dense glassy fragments of Mateare dacite, rounded particles of Xiloa pumice, fragments of dacitic and basaltic lavas, and crystal fragments. Apart from the dominant Mateare dacite fraction, the composition of the sand is similar to that of modern beach sand at the shore of Lake Managua near Mateare. The Mateare Sand has wavy lower and upper contacts and is 5–20 cm thick in flat areas (Fig. 2) but locally forms thick fills of channels directed toward the lake. While mostly massive in the overbank facies, the channel fills show chaotic bedding with lenses of pumice lapilli. The sand layer can be traced to elevations up to 32 m above the present lake level. At the most elevated outcrops, molds from tree logs are surrounded by sediment aggradation structures interpreted to have formed as sand piled up against stranded driftwood poles.

The well-sorted sand is a water-lain deposit forming a widespread sheet along the shore of Lake Managua. It is not a beach sand because it reaches to elevations exceeding plausible beach levels even considering that the lake level was 9 m above present level ~6300 years ago (COWAN *et al.*, 2002), and underlying unit A of the Mateare Tephra was not emplaced in water but on dry land. Since the deposit formed during the Mateare eruption, we have interpreted it as a volcanogenic tsunami deposit. The timing of tsunami formation can be deduced from the composition of

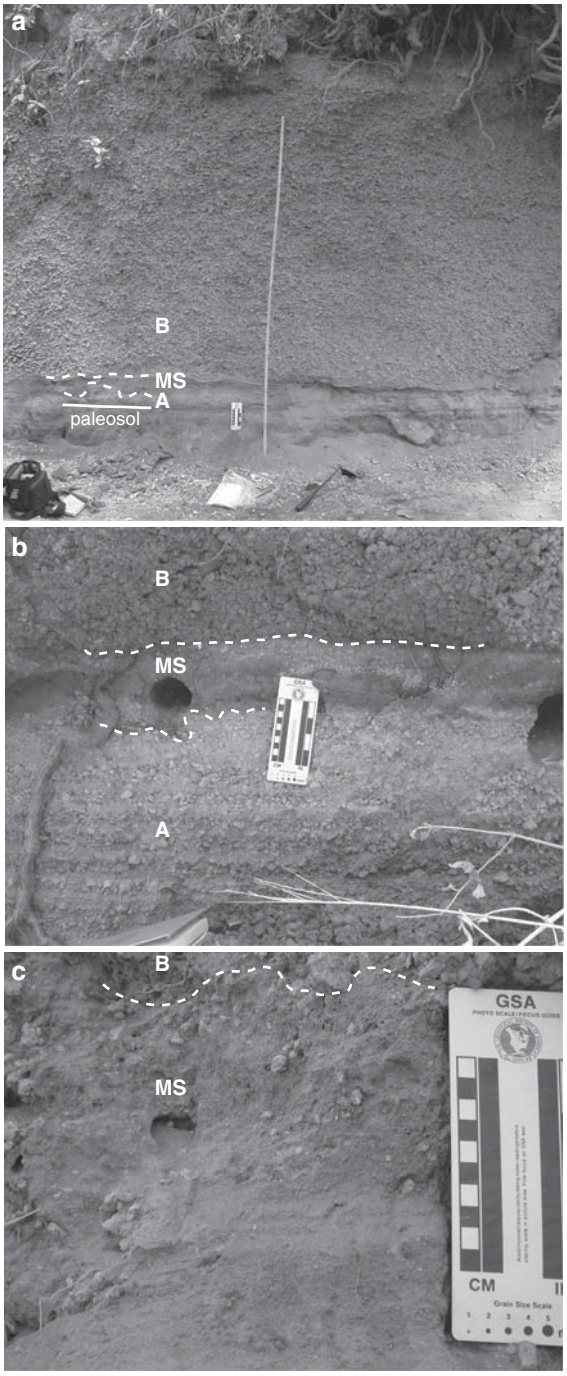
a
B
MS
A
paleosol
b
B
MS
A
c
B
MS
GSA
CM

◀

Figure 2

The Mateare Tephra including the Mateare Sand, a volcanogenic tsunami deposit. (a) Condensed tephra unit A erosively overlain by the sand (MS) which is covered by the massive pumice fallout unit B. Long scale is 2 m. Locality A71. (b) The thickest exposure of stratified fallout unit A, erosively overlain by the sand MS which contains molds from former driftwood logs. Massive unit B at top. Locality A114. (c) Detail of the massive sand with dispersed pumice lapilli. Locality A75. Localities and minimum distribution of sand layer are indicated in Figure 4.

the entrained Mateare pumice, making use of the chemical zonation of the deposit (FREUNDT *et al.*, 2006a). The composition of batches of pumice lapilli collected from the Mateare Sand is typically a mixture of unit-A and unit-B compositions, which are separated by a compositional gap in the primary fallout (Fig. 3a). The composition of pumice in the sand differs between outcrops such that the unit-B contribution decreases toward higher elevation above the lake (Fig. 3b). Hence, early tsunami waves mostly eroded unit A near shore and reached the highest run-up whereas closer to shore subsequent weaker tsunami waves lasted longer into unit-B eruption. The tsunami effect of inhibiting fallout emplacement of early unit-B pumice varied locally as shown by the variable composition of pumice at the very base of unit B (Fig. 3); this probably reflects topographic control on wave run-up and channeling. The late waves may have been separate tsunamis or waves reflected at the lake shores; we favor the first interpretation since the very gentle shore slopes would largely

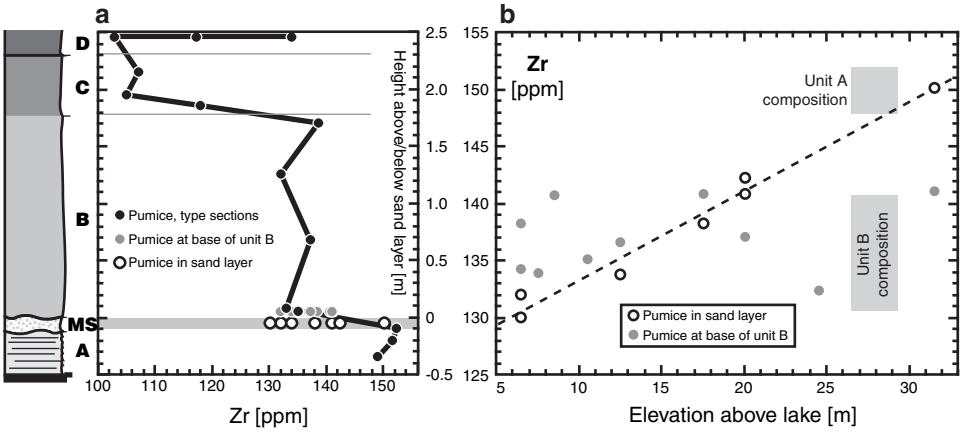


Figure 3

(a) Vertical chemical zonation of the Mateare Tephra using bulk-rock Zirconium content (black dots) as an example. The wide compositional range in phreatomagmatic unit D is due to re-entrainment of earlier erupted pumice. Composition at the exposed base of unit B (gray dots) differs between outcrops; the basal contact of B is thus not time-equivalent between outcrops. White dots are the bulk composition of batches of pumice lapilli collected from the sand layer; they bridge the gap between unit A and B compositions. (b) Composition at the base of unit B varies irregularly, but pumice in the sand systematically changes from unit B to unit A composition with elevation above the lake. Hence, more unit B material was entrained in the sand closer to shore.

dampen reflections. The interval of tsunami formation appears to be associated with the early unsteady phase of eruption, particularly when obsidian plugs blocked the vent and were violently disrupted, leaving abundant obsidian fragments in the deposit at this stratigraphic level. The detailed processes of tsunami formation remain unknown because the near-vent area is not exposed. There is no evidence that potentially tsunamigenic mass flows formed in this eruption, which occurred at a vent in flat land rather than from a volcanic cone. Subsidence at the vent is unlikely at a time when a stable plinian eruption column was forming and emplaced lithic-poor fallout. This leaves explosive processes as possible tsunami triggers. The Mateare Sand is the first documented tsunami deposit at a Nicaraguan lake and its importance is in showing that this type of volcanic hazard can occur and may affect significant areas along the gently sloping lake shores (Fig. 4).

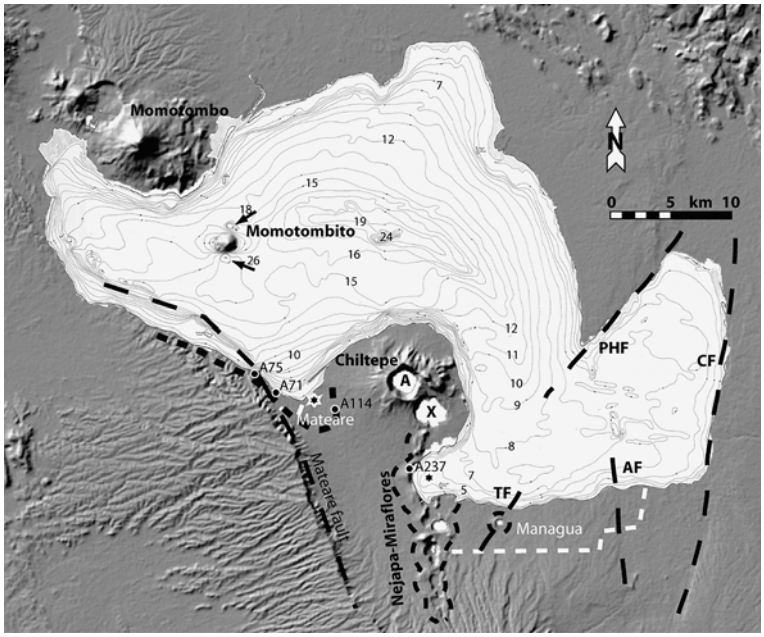


Figure 4

DEM of the area around Lake Managua. Superimposed bathymetry from 1979 map of INETER, Managua. Depths in meters. Note deep pits near Momotombito. The Mateare Fault is the western boundary of the Nicaraguan Depression; bathymetry suggests it curves westward within the lake. A = Apoyeque crater, X = Xiloa Maar. Bold dashed line near Mateare shows minimum distribution of Mateare Sand tsunami deposit; star marks proposed vent site of Mateare Tephra. A71, A75, A114, A237 are localities shown in Figures 2 and 5. Thin dashed lines along Nejapa-Miraflores lineament indicate distribution of phreatomagmatic maar deposits. Star in the SW bay of the lake suggests one or more vent sites on the lake floor. Major tectonic faults extending into the lake include the Punta Huete Fault (PHF), Cofradias Fault (CF), Aeropuerto Fault (AF), and Tiscapa Fault (TF) which was active during the 1972 earthquake (BROWN *et al.*, 1973). Numerous minor faults dissect the whole area.

*Phreatomagmatic Eruptions in Lake Managua*

The NW-SE trending linear volcanic front is offset between Chiltepe Peninsula and Masaya Volcano (Fig. 1), a region that corresponds to a segment boundary as defined by CARR (1984). The offset limbs of the front are connected by the N-S trending Nejapa-Miraflores lineament, a zone of numerous maars and cinder cones, that extends from west of Managua to the southern part of Chiltepe Peninsula, cutting across the southwestern bay of Lake Managua (Fig. 4). Within the thick pyroclastic succession, packages of phreatomagmatic deposits are separated by intercalated widespread dacitic tephra beds (Fig. 5), some of which we have dated.

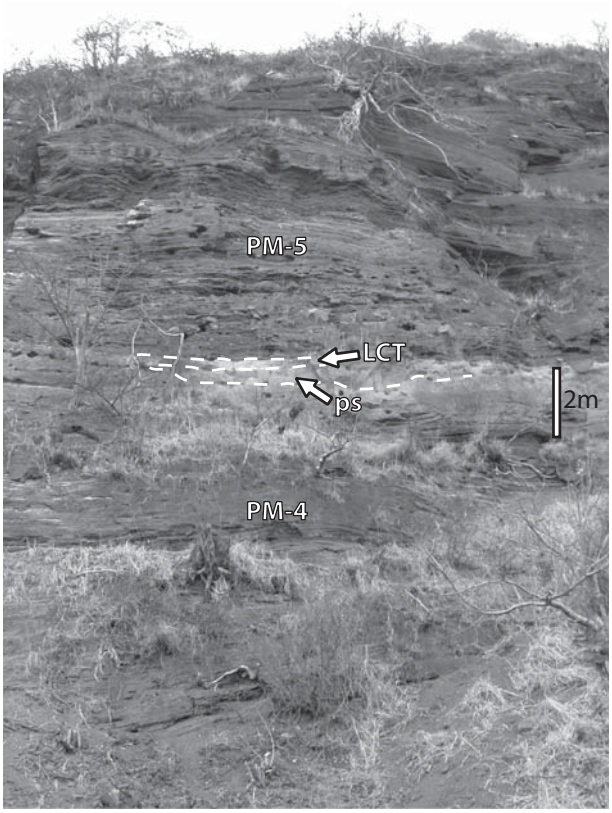


Figure 5
Phreatomagmatic deposits from maar-forming eruptions exposed in a cliff along the western shore of the SW bay of Lake Managua (Loc. A237 in Fig. 4). Pale band above massive paleosol (ps) is the Los Cedros Tephra (LCT), a dacitic pumice fallout that is approximately 2,500 years old. PM-4 and PM-5 are thick packages of well-stratified phreatomagmatic deposits that include major unconformities and are thus each the product of more than one maar eruption from vents on the floor of the SW bay of Lake Managua (Fig. 4).

Our stratigraphic investigations show that activity along the Nejapa-Miraflores lineament ranged from >13,000 to <2,000 years and is thus likely to continue (FREUNDT *et al.*, 2006b). A continuous cliff along the west shore of the SW bay of Lake Managua exposes thick successions of basaltic maar deposits that formed by numerous vigorous explosions when the hot magma encountered surface water (Fig. 5). Although a detailed study of the phreatomagmatic maar deposits is necessary yet, reconnaissance data suggest their source vents lie in the SW bay of the lake which is only < 7 m deep (Fig. 4). Phreatomagmatic eruptions in Lake Managua would be capable of producing hazardous tsunamis similar to those observed during the phreatomagmatic eruptions in Lake Karymskoye in 1996 (BELOUSOV *et al.*, 2000) or reported from the Taal Caldera Lake, Philippines, during phreatomagmatic eruptions in 1716, 1754 and 1911 (NEWHALL and DZURISIN, 1988).

The young volcanic cone of Momotombito in the northern part of Lake Managua has not yet been investigated but it is clearly a growing volcano. Its future eruptions and associated volcanotectonic movements could be tsunamigenic. The bathymetric map of Lake Managua shows two circular holes immediately north and south of the cone which might be craters from subaqueous explosions (Fig. 4). There is clear need for more detailed bathymetric and seismic studies to unravel volcanic vents and tectonic structures in the floor of Lake Managua.

*The Apoyo Ignimbrite*

Apoyo Caldera, 35 km southeast of Managua in Central Nicaragua (Fig. 1), is a large (6.5 km diameter), deep (*c.* ~600 m) circular volcanic subsidence basin (SUSSMAN, 1985). Two large-magnitude plinian eruptions in rapid succession formed the present caldera structure c. 24 ka ago and produced the Lower and Upper Apoyo Tephras. The c. 30 $km^3$ volume of the Upper Apoyo Tephra includes c. 8.5 $km^3$ of ignimbrite (SUSSMANN, 1985) exposed in the lowlands south and east of the caldera up to the shore of Lake Nicaragua. Average thickness is about 20 m but locally the ignimbrite is 55-m thick (Fig. 6). The city of Granada was built on these deposits which are unwelded but cemented by vapor phase mineralization and contain abundant degassing pipes, evidence that their depositing pyroclastic flows were hot.

Exposures of up to 20-m-thick ignimbrite along the shore show that the pyroclastic flows continued into the lake. The pyroclastic flows climbed 100 m high up the northern flank of Mombacho volcano at 5-km distance from Apoyo caldera, allowing SUSSMAN (1985) to estimate a velocity of 65 m/s (240 km/h). The ignimbrite is composed of several flow units (deposits from successive pyroclastic flows; Fig. 6a), each about 4-m thick at the lake shore. The flows entered the lake along a 15-km length of shore. The volume flux into Lake Nicaragua can thus be roughly estimated as $3*10^6$ $m^3/s$ although the total volume of tephra discharged into the lake remains unknown.

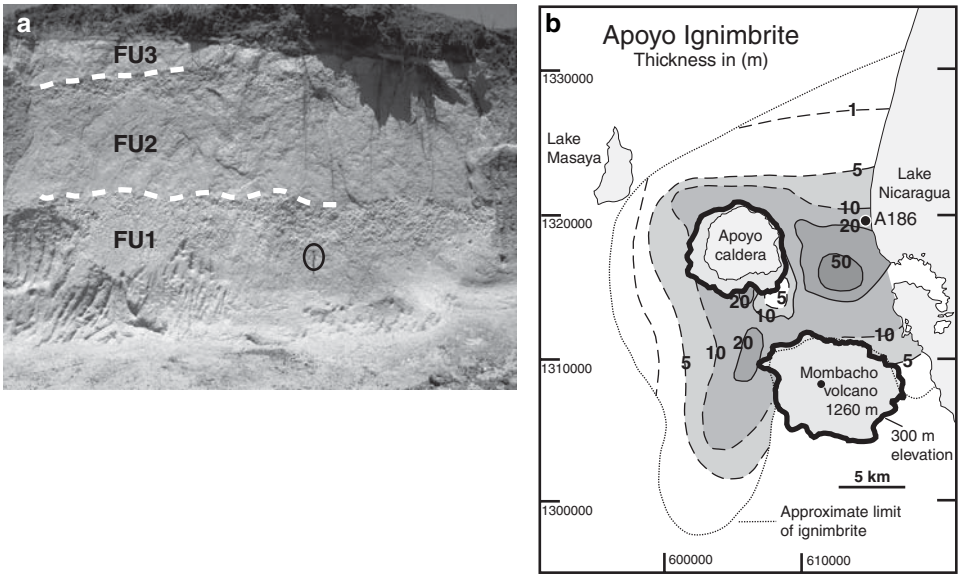


Figure 6
(a) Outcrops of three massive flow units (FU) of Apoyo Ignimbrite at the north rim of Granada City and close to the shore of Lake Nicaragua (Loc. A186 in b). Circle marks Hammer (40 cm) for scale. (b) Isopach map of the Apoyo Ignimbrite modified from SUSSMAN (1985). Major entrance of pyroclastic flows into Lake Nicaragua occurred along more than 15 km length of shore. The curved peninsula in the lake is composed of a debris avalanche from Mombacho volcano (cf. Fig. 7). Coordinates are UTM values.

*Volcano Flank Collapses and Mass-wasting Events*

Volcán Mombacho is located at the northern end of Lake Nicaragua near Granada (Figs. 1, 6), the second largest city in Nicaragua. Mombacho has erupted explosively in prehistoric times to form widespread ash-fall deposits, and repeated instability of the large cone also generated huge debris avalanches. Debris flow deposits at Mombacho volcano indicate that at least three large prehistoric flank collapses did occur (VALLANCE *et al.*, 2001a). The three massive debris avalanches extend about 10 km from the summit to the southeast, northeast and south. The large (20–30 $km^2$) hummocky debris lobes resulting from the final two events form small islands in Lake Nicaragua (Fig. 7; VALLANCE e*t al.*, 2001a). The last of these debris avalanches occurred at *c*. AD 450 (DULL *et al.*, 2005). Present-day Mombacho is a deeply dissected volcano and its interior is probably structurally weakened by alteration of rocks in its long-lived hydrothermal system. Strongly hydrothermally altered regions in a volcano substantially reduce edifice stability, control the location of failure and may result in more voluminous and mobile avalanches (REID *et al.*, 2001). Structural failure may be triggered by magmatic intrusions and eruptions but often is associated with external processes such as regional earthquakes, basal glide

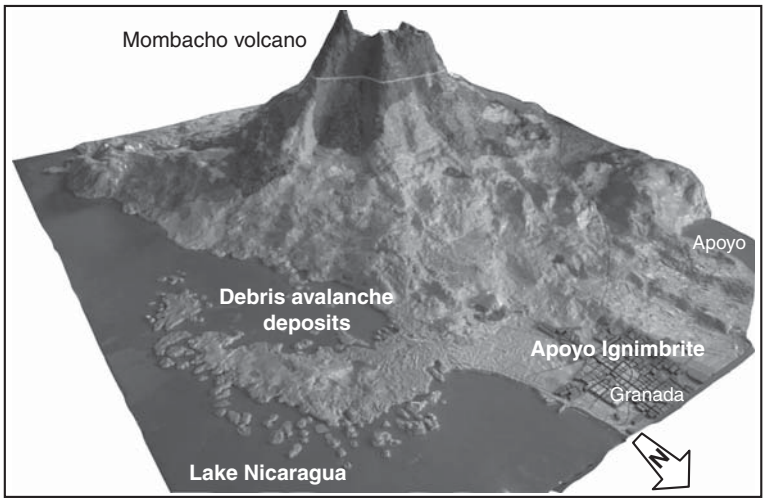


Figure 7
Model relief of Mombacho volcano showing the northwestern sector collapse scarp below the summit and debris avalanche deposits on the lower slopes and in Lake Nicaragua forming the curved peninsula and adjacent islets (which look very similar to the Tsukumo-shima islets formed by the 1792 landslide at Unzen volcano, Japan; Fig. 15 in SIEBERT, 2002). The City of Granada rests on the flat surface of the Apoyo Ignimbrite that filled the valley north of Mombacho. Modified photograph of a model displayed in the Mombacho tourist information center.

planes on which a volcanic edifice may spread laterally, and, particularly, heavy precipitation which increases pore pressure in the edifice and may liquify the debris (MC GUIRE, 2003). Heavy precipitation during hurricane Mitch in 1998 triggered the debris flows at Casita Volcano in Nicaragua (VALLENCE *et al.*, 2001b; SCOTT *et al.*, 2005). Debris avalanches from sector collapse can be particularly tsunamigenic when the collapse occurs in a catastrophic rather than piecemeal fashion. The intrusion of the Mombacho avalanches to at least 7 km into Lake Nicaragua (Fig. 7) most probably caused one or more tsunamis in the lake, although geologic evidence of such tsunamis has not yet been reported.

Concepción stratovolcano forms the northern half of Ometepe Island in Lake Nicaragua and rises 1600 m above the lake. Tectonic faults exposed on the shallower parts of the island indicate W-E extension and GPS measurements revealed radial but preferential westward spreading of the lower flanks. BORGIA and VAN WYK DE VRIES (2003) interpreted these data as gravitational spreading of the volcano under its own weight on the soft substrate of lake sediments. They concluded that such spreading would largely compensate stresses building up and thus reduce the risk of sector collapse but that, if a collapse were to occur, it would probably be on the western flank. There is only 10 km of lake water between the western shore of Ometepe and the city of Rivas on the west bank of Lake Nicaragua.

Of the large stratocones close to the lake, Mombacho and Concepción are known to have produced numerous rain-triggered lahars during historic and prehistoric times (VALLANCE *et al.*, 2001a, b). Both volcanoes are largely composed of pyroclastic material that is easily remobilized during torrential rains. Individual lahars may be small but can reach volumes of $10^6$ m$^3$ (VALLANCE *et al.*, 2001b). At Mombacho, a lahar similarly large as the one at Casita took 400 lives in 1570 (VALLANCE *et al.*, 2001a). If such a large lahar entered the lake it could be tsunamigenic.

## *Tsunamis in Lakes*

Tectonic faulting of the lake floor or intrusion of a mass flow displaces a volume of water from the area of movement. If the movement of such wavemakers is slow, the water can drain from the area relatively quietly. Conversely, if the wavemaking movement is fast, the water cannot drain quickly enough and a significant wave may build up (HAMMACK, 1973). The capacity of water to drain from the interaction area is limited by the long-wave celerity $c = \sqrt{gD}$, which depends on water depth $D$, with $g$ the gravitational acceleration. Considering the 2-D case and assuming the wavemaker has a length scale, $L$, then the time scale of water moving from the wavemaking region is $L/c$. Wavemaking operates over a time scale $t_w$. The ratio of the time scales, the Hammack number $Ha = t_w \cdot c/L$, must be Ha $< <$ 1 to produce a tsunami by impulsive wave formation (WATTS, 1998; WALDER *et al.*, 2003). These considerations show the important role in tsunami generation of the water depth, which is typically much shallower in lakes than in the ocean. For example, a wavemaker of $t_w = 60$ s and $L = 2000$ m in ocean water of $D = 1000$ m depth yields Ha $= 3$ whereas, in a lake of $D = 20$ m depth, the same wavemaker gives Ha $= 0.4$ and may impulsively form a tsunami. In this respect, shallow bays at ocean margins are similar to terrestrial lakes.

The energy of a wave is proportional to the square of its amplitude. The maximum wave amplitude is limited because higher waves break and dissipate their energy by turbulence. The breaking limit and the mode of breaking depend on the nature of the wave, its deep-water amplitude, and the slope of the bottom (DEAN and DALRYMPLE, 1991). Here we adopt the simple criterion that breaking occurs when wave amplitude exceeds 85% of the water depth. The shallow depth of lakes thus limits the energy that can be carried to greater distances by waves. The near-field wave amplitude generated by intruding mass flows has been investigated experimentally and theoretically. Early approaches mainly derived functions in which the dimensionless wave-crest amplitude $\eta = A/D$ is related to the Froude number $Fr = u/c$ and the total volume, $V_s$, of the landslide (e.g., SLINGERLAND and VOIGHT, 1979; see also review in FRITZ, 2002); $A$ is absolute amplitude and $u$ the slide velocity. In long flows, however, only the frontal portion acts to form a wave rather than the

total volume. More recently, FRITZ (2002) has identified dimensionless wave amplitude as $\eta = nFr^m\sigma^p$, where the ratio $\sigma = S/D$ of slide thickness, $S$, to water depth, $D$, is a dimensionless slide thickness, and $n = 0.25$, $m = 1.4$ and $p = 0.8$ are constants from regression of experimental data. This solution treats landslide velocity, Fr, and depth, $\sigma$, independantly. WALDER *et al.* (2003) combined both parameters in the dimensionless slide volume flux per unit width, $q = Q/cD$, where $Q = u \cdot s$ is the 2-D volume flux and $cD$ is the limiting volume flux of water. Their experimental data is well regressed by the function $\eta = a \cdot q^b$ with the constants $a = 1.32$ and $b = 0.68$. WALDER *et al.* (2003) used solid boxes to simulate a landslide and identified $Q$ as the maximum volume flux. In experiments using granular flows intruding water (FREUNDT, 2003), waves formed and escaped from the region of interaction while the mass flow was still coming in. Using the initial volume flux as the relevant value of $Q$, observed wave amplitudes followed the power-law function of WALDER *et al.* (FREUNDT, 2006). Moreover, modelling the flows as intruding granular jets yields the same form of function with the constants $1 < a < 1.2$ and $b = 2/3$, providing a physical explanation of the above regression (FREUNDT, 2006).

The 2-D volume flux, $Q_{0.85}$, at which dimensionless amplitude reaches the limiting value $\eta = 0.85$, depends on water depth, D, as $\mathbf{Q}_{0.85} = 2.13 \cdot \mathbf{D}^{3/2}$. The limiting volume flux would be only $Q_{0.85} = 190$ m$^2$/s in a 20-m-deep lake. Using the Apoyo Ignimbrite as an example, we obtain a volume flux per unit width of $Q = 260$ m$^2$/s by dividing the bulk volume flux estimated above by the shore length of entry into Lake Nicaragua. Considering the average depth $D = 13$ m of Lake Nicaragua (Table 1), the volume flux of the Apoyo Ignimbrite was 2.5 times above the condition for formation of breaking waves. The average depth of Lake Managua is even lower at $D = 8$ m (Table 1); hence, a landslide descending, for example, from Momotombo volcano would only need a volume flux of 46 m$^2$/s to reach the breaking-wave condition. For comparison, a 2-D volume flux of 100 m$^2$/s can be estimated for the 1998 Casita debris flow that had a bulk volume flux of approximately 100,000 m$^3$/s and was 1 km wide on the plain below Casita volcano (SCOTT *et al.*, 2005). With the low average bottom slopes (Table 1) on which mass flows would intrude, the average water depth is reached at 3 to 6 km distance from shore in Lakes Managua and Nicaragua, respectively. When modelling the spreading of a tsunami in shallow lakes such as those in Nicaragua, the breaking-wave limit appears to be a reasonable starting point without the need to be more specific on the size of the triggering mass flow. In small lakes, however, where the intruding debris constitutes a significant fraction of the resident water volume and waves quickly reach opposing shores before much dissipation can occur, wave heights may well exceed the breaking-wave limit. Possible examples are the 15-m-high wave formed when a landslide intruded the crater lake of Kasu Tephra Cone, Papua New Guinea, which is mostly only 5 m deep with a maximum depth of 20–30 m but is also only 350 m long (WAGNER *et al.*, 2003), and the 60-m-high wave formed by a non-volcanic landslide into the Vaiont Reservoir, Italy (MÜLLER, 1964).

Using wave celerities based on the average depths (Table 1), a tsunami triggered at Momotombito would reach Mateare within 25 mins and Managua after 70 mins; a tsunami due to an avalanche from Mombacho would reach Granada almost immediately and take about 90 mins to reach the eastern shores. Although waves travel relatively slowly in the shallow lakes, and the Nicaraguan lakes are quite large, warning times after a tsunamigenic event has started are very short, particularly for communities close to the site of tsunami formation. The flat, scarcely vegetated slopes along most of the lake shores offer little resistance to tsunami run-up.

## *Conclusions*

### *Population under Risk by Lake Tsunamis*

The population at the shores of Lake Managua is mainly concentrated in Managua itself, the capital of Nicaragua. Several thousand inhabitants of Managua could be affected by tsunamis triggered by volcanic explosions on or near Chiltepe Peninsula or by tectonic activity at the numerous active faults that dissect the lake bottom. Parts of the small town of Mateare could also suffer from tsunamis related to explosions at Momotombito volcanic island, or to explosions or flank-collapse avalanches at Momotombo volcano. At Mateare, the tsunami hazard would add to the volcanic hazards mainly arising from pyroclastic fallout dispersed in generally westerly directions by the prevailing winds. In comparison, the small village of San Francisco Libre on the northern shore of Lake Managua has only a minor hazard due to direct volcanic phenomena. But, as the beach has a very low profile, even a relatively weak tsunami could generate heavy damage.

Granada is the largest city on the shores of Lake Nicaragua. The city's shores and especially the hundreds of little islands of the "Isletas" —many of them populated — would be heavily affected by a tsunami generated anywhere in Lake Nicaragua. Another landslide from Mombacho volcano may cause extreme water run-up close to source as observed for the 1958 Lituya Bay, Alaska, event (MILLER, 1960). The island of Ometepe is another threatened place with respect to tsunamis because many people live nearby the lake on beaches with very shallow profile. Even the relatively large town of San Carlos, situated at the San Juan River on the southeastern shore of Lake Nicaragua, can be considered as endangered by tsunamis because the beaches are very low and population density is relatively high.

We mention that fast dangerous inundations similar to tsunamis could occur on the coasts of the large Nicaraguan lakes also due to meteorological effects (storm swells, especially if the meteorological disturbance passes the lake with a velocity similar to the average wave celerity) and seismic effects (seiches) due to near or distant very large earthquakes which generate oscillations of the water body with periods similar to the eigen-period of the lake. Seiches possibly occurred in 1844 in

Lake Nicaragua (MOLINA, 1997; FERNANDEZ *et al.*, 2000) and were observed in April 1991 in Escondido River, Nicaraguan Atlantic Region, caused by the M = 7.1 El Limon earthquake in Costa Rica. Several major tectonic faults extend into Lake Managua (Fig. 4) which were active during Holocene to recent times (BROWN *et al.*, 1973; COWAN *et al.*, 2002).

Future work in Nicaragua should include: (a) geological studies to identify fossil tsunami deposits around the lakes, (b) high-resolution bathymetry of the lakes as a prerequisite to apply numerical models of tsunami propagation (e.g., TINTI *et al.*, 1999), and (c) shallow seismic study of the lake bottoms to identify tectonic structures and distribution of intruded mass flows. Such data will allow identification of possible source areas, spreading paths, and run-up heights of tsunamis which are needed for a useful tsunami hazard map.

*Possible Tsunami Warning System*

The efficiency of a tsunami warning system for the Nicaraguan Lakes depends much on the forewarning time span possibly available to people. To estimate this time we use wave celerities based on the average depths (Table 1). In Lake Managua: A tsunami triggered at Momotombito volcano would reach Mateare within 25 minutes and Managua after 70 minutes. In Lake Nicaragua: A tsunami due to an avalanche from Mombacho volcano would reach Granada almost immediately but would take about 90 minutes to reach the eastern shores. A tsunami generated by an avalanche at Concepción volcano on Ometepe Island would affect immediately the nearest beaches of the island but the wave would travel some tens of minutes to reach the opposite side of the island. We see that although tsunami waves travel slowly in the shallow lakes and the Nicaraguan lakes are rather large, warning times after a tsunamigenic event are short, particularly for communities close to the site of tsunami formation. Nevertheless, the times are quite comparable to those for tsunamis which threaten the towns on the Pacific coast of Nicaragua after very strong local earthquakes in the Nicaraguan subduction zone. In case of the 1992 tsunami at the Nicaraguan Pacific coast the first destructive wave impacted the beach about 45 to 60 minutes after the earthquake occurred. In recent years, the Nicaraguan geosciences institute (INETER) and Nicaraguan Civil Defense developed a tsunami warning for the Pacific coast of Nicaragua. Though tsunami hazard in the Pacific Ocean is certainly much higher, it might also make sense to think about tsunami warning for the shores of the large Nicaraguan lakes. For the tsunami warning in the Pacific Ocean, seismic stations are used as primary data sources pertaining to the occurrence of a large earthquake beneath the ocean which possibly could generate a tsunami. This method produces false alarms as not all large earthquakes generate tsunamis and it might fail completely for volcano and landslide-induced tsunamis in the lakes.

Given the short tsunami travel times in the lakes, early warning mainly depends on timely recognition of possible trigger events. Though problematic with earthquakes, adequate monitoring can provide timely warning of volcanic eruptions and flank failure. Telemetric sea gauges may make use of the confined lake volume leading to a rise in lake level as a volcanic edifice in the lake inflates prior to eruption (or collapse). The problem of false alarms remains since it cannot be predicted with certainty if any of these events will actually produce a tsunami. A critical element in mitigating tsunami hazard at the lakes is public education. To quickly escape from near-shore areas, people must be aware that earthquakes and volcanic eruptions, which will be felt and seen by many of the population, may cause tsunamis.

In summary, tsunami hazard in the large Nicaraguan lakes exists due to manifold possible tsunami generation mechanisms related to volcanic eruptions and volcanic edifices. The risk level for the population might be relatively small in comparison with the risk due to direct effects of earthquakes, volcanic eruptions, and landslides or in comparison to tsunami risk on the Pacific coast of Nicaragua. Nevertheless, during ongoing volcanic eruptions the tsunami hazard might increase considerably and can be considered as the prevailing hazard for areas that would remain unaffected by other volcanic hazards. A tsunami warning system for the large lakes of Nicaragua might be developed as a part of a multi-purpose information and alert system on volcanic, meteorological and seismic phenomena. Public education, however, is crucial to achieve adequate response to such alerts.

## *Acknowledgements*

Constructive comments from two referees helped to improve this paper. We thank the Direccion Hidrografia of INETER, Managua, for supplying bathymetric data of the lakes. This publication is contribution no. 95 of the Sonderforschungsbereich 574 on *Volatiles and Fluids in Subduction Zones* at Kiel University.

## References

Beget, J.E. *Volcanic tsunamis*. In (Sigurdsson H. *et al*. eds) *Encyclopedia of Volcanoes*. (Academic Press: 2000) pp. 1005–1014.

Belousov, A., Voight, B., Belousova, M., and Muravyev, Y. (2000), *Tsunamis generated by subaquatic volcanic explosions: Unique data from 1996 eruption in Karymskoye Lake, Kamchatka, Russia,* Pure Appl. Geophys. *157,* 1135–1143.

Borgia, A. and van Wyk de Vries, B. (2003), *The volcano-tectonic evolution of Concepcion, Nicaragua,* Bull. Volcanol. *65,* 248–266.

Brown, R.D., Ward, P.L., and Plafker, G. (1973), *Geologic and seismologic aspects of the Managua, Nicaragua, earthquakes of December 23, 1972,* US Geol. Surv. Prof. Paper *838,* 34 p.

Carey, S., Morelli, D., Sigurdsson, H., and Bronto, S. (2001), *Tsunami deposits from major explosive eruptions: An example from the 1883 eruption of Krakatau,* Geology *29*, 347–350.

CARR, M.J. (1984), *Symmetrical and segmented variation of physical and geochemical characteristics of the Central American volcanic front,* J. Volcanol. Geotherm. Res. *20,* 231–252.

COWAN, H., PRENTICE, C., PANTOSTI, D., DE MARTINI, P., STRAUCH, W., and WORKSHOP PARTICIPANTS (2002), *Late Holocene earthquakes on the Aeropuerto Fault, Managua, Nicaragua,* Bull. Seismol. Soc. Am. *92,* 1694–1707.

DE LANGE, W.P., PRASETYA, G.S., and HEALY, T.R. (2001), *Modelling of tsunamis generated by pyroclastic flows (ignimbrites),* Natural Hazards *24,* 251–266.

DEAN, R.G. and DALRYMPLE, R.A. *Water wave mechanics for engineers and scientists,* Adv. Ser. Ocean Engin. vol. 2 (World Scientific, Singapore, New Jersey 1991), pp. 1–353.

DULL, R., STANSELL, N., ABBOTT, M., and LACAYO, M.R. (2005), *Lahar hazards and late Holocene paleoecology from Volcan Mombacho, Nicaragua*, Abstract Paleobiogeography II.

FERNANDÉZ, M., MOLINA, E., HAVSKOV, J., and Atakan, K. (2000), *Tsunamis and tsunami hazards in Central America*, Natural Hazards *22,* 91–116.

FREUNDT, A., KUTTEROLF, S., WEHRMANN, H., SCHMINCKE, H.-U., and STRAUCH, W. (2006a), *Eruption of the dacite-to andesite-zoned Mateare Tephra, and associated tsunamis in Lake Managua, Nicaragua.* J. Volcanol. Geotherm. Res. *149,* 103–123.

FREUNDT, A., KUTTEROLF, S., SCHMINCKE, H.-U., HANSTEEN, T.H., WEHRMANN, H., PEREZ, W., STRAUCH, W., and NAVARRO, M. (2006b), *Volcanic hazards in Nicaragua: Past, present, and future*, GSA Spec. vol. *412* (in press).

FREUNDT, A. (2003), *Entrance of hot pyroclastic flows into the sea: Experimental observations,* Bull. Volcanol. *65,* 144–164.

FREUNDT, A. (2006), *Entrance of hot pyroclastic flows into the sea: Experimental tsunami formation,* Bull. Volcanol. (in review).

FRITZ, H.M. (2002), *Initial phase of landslide generated impulse waves,* Ph.D. Thesis, ETH Zürich, Switzerland, ETH No. 14'871, 249 p.

GOVI, M., GULLA, G., and NICOLETTI, P.G. (2002), *Val Pola rock avalanche of July 28, 1987 in Valtellina (Central Italian Alps)*. In (Evans, S.G., DeGraff, J.V. eds.) *Catastrophic Landslides: Effects, Occurrence and Mechanisms,* Reviews in Engineering Geology *15,* 71–89.

HAMMACK, J.L. (1973), *A note on tsunamis: Their generation and propagation in an ocean of uniform depth,* J. Fluid Mech. *60,* 769–799.

HART, K., CAREY, S., SIGURDSSON, H., SPARKS, R.S.J., and ROBERTSON, R.E.A. (2004), *Discharge of pyroclastic flows into the sea during the 1996–1998 eruptions of the Soufriere Hills Volcano, Montserrat,* Bull. Volcanol. *66,* 599–614.

ICHINOSE, G.A., ANDERSON, J.G., SATAKE, K., SCHWEICKERT, R.A., and LAHREN, M.M. (2000), *The potential hazard from tsunami and seiche waves generated by large earthquakes within Lake Tahoe, California – Nevada,* Geophys. Res. Lett. *27*, 1203–1206.

KEATING, B.H. and MCGUIRE, W.J. (2000), *Island edifice failures and associated tsunami hazards,* Pure Appl. Geophys. *157,* 899–955.

KERLE, N. and VAN WYK DE VRIES, B. (2001), *The 1998 debris avalanche at Casita Volcano, Nicaragua — Investigation of structural deformation as the cause of slope instability using remote sensing*, J. Volcanol. Geotherm. Res. *105,* 49–63.

MCCOY, F.W. and HEIKEN, G. (2000), *Tsunami generated by the Late Bronze Age eruption of Thera (Santorini), Greece,* Pure Appl. Geophys. *157,* 1227–1256.

MCGUIRE, W.J. (2003), *Volcano instability and lateral collapse,* Revista *1,* 33–45.

MILLER, D.J. (1960), *Giant waves in Lituya Bay, Alaska,* US Geol. Surv. Prof. Paper *354*-C, 1–86.

MOLINA, E. (1997), *Tsunami catalogue for Central America 1539–1996*, Report No. II 1-04, Institute of Solid Earth Physics, University of Bergen, Norway.

MÜLLER, L. (1964), *The rockslide in the Vaiont Valley,* Rock Mech. Eng. Geol. *2,* 148–212.

NEWHALL, C.G. and DZURISIN, D. (1988), *Historical unrest at large calderas of the world*, US Geol. Surv. Bull. *1855* (2 vol), 1108 p.

PELINOVSKY, E., ZAHIBO, N., DUNKLEY, P., EDMONDS, M., HERD, R., TALIPOVA, T., KOZELKOV, A., and NIKOLKINA, I. (2004), *Tsunami generated by the volcano eruption on July 12–13, 2003 at Montserrat, Lesser Antilles,* Sci. Tsunami Hazards *22,* 44–57.

PLAFKER, G. and EYZAGUIRRE, V.R. *Rock avalanche and wave at Chungar, Peru*. In (Voight, B. ed) *Rockslides and Avalanches,* vol. 2, Developments in Engineering Geology 14B (Elsevier, NL: 1979) 269–279.

REID, M.E., SISSON, T.W., and BRIEN, D.L. (2001), *Volcano collapse promoted by hydrothermal alteration and edifice shape, Mount Rainier, Washington,* Geology *29,* 779–782.

SCOTT, K.M., VALLANCE, J.W., KERLE, N., MACIAS, J.L., STRAUCH, W., and DEVOLI, G. (2005), *Catastrophic precipitation-triggered lahar at Casita Volcano, Nicaragua: Occurrence, bulking and transformation,* Earth Surf. Process. Landforms *30,* 59–79.

SELF, S., RAMPINO, M.R., NEWTON, M.S., and Wolff, J.A. (1984), *Volcanological study of the great Tambora eruption of 1815,* Geology *12,* 659–663.

SIEBERT, L. (2002), *Landslides resulting from structural failure of volcanoes*. In (Evans, S.G. and DeGraff, JV eds.) *Catastrophic Landslides: Effects, Occurrence and Mechanisms,* Rev. Engig. Geol. *15,* 209–235.

SIGURDSSON, H. and CAREY, S.N. (1989), *Plinian and co-ignimbrite tephra fall from the 1815 eruption of Tambora volcano,* Bull. Volcanol. *51,* 243–270.

SLINGERLAND, R.L. and Voight, B. *Occurrences, properties and predictive models of landslide–generated tsunami waves*. In (Voight, B., ed) *Rockslides and avalanches*, vol. 2, Developments in Engig. Geol. *14B* (Elsevier, NL: 1979) pp.317–397.

SUSSMAN, D. (1985), *Apoyo Caldera, Nicaragua: A major Quaternary silicic eruptive center,* J. Volcanol. Geotherm. Res. *24,* 249–282.

TINTI, S., BORTOLUCCI, E., and ARMIGLIATO, A. (1999), *Numerical simulation of the landslide-induced tsunami of 1988 on Vulcano Island, Italy,* Bull. Volcanol. *61,* 121–137.

VALLANCE, J.W., SCHILLING, S.P., and DEVOLI, G. (2001a), *Lahar hazards at Mombacho Volcano, Nicaragua,* USGS Open File Report 01-455, 14 p.

VALLANCE, J.W., SCHILLING, S.P., DEVOLI, G., and HOWELL, M.M. (2001b), *Lahar hazards at Concepción Volcano, Nicaragua,* USGS Open File Report 01-457, 13 p.

VOIGHT, B., GLICKEN, H., JANDA, R.J., and DOUGLASS, P.M. (1981), *Catastrophic rockslide avalanche of May 18*. In (P.W. Lipman and D.R. Mullineaux, eds), *The 1980 eruptions of Mount St. Helens, Washington,* US Geol. Survey Prof. Paper *1250,* 347–377.

WAGNER, T.P., MCKEE, C.O., KUDUON, J., and KOMBUA, R. (2003), *Landslide-induced wave in a small volcanic lake: Kasu Tephra Cone, Papua New Guinea,* Int. J. Earth Sci. *92,* 405–406.

WALDER, J.S., WATTS, P., SORENSEN, O.E., and JANSSEN, K. (2003), *Tsunamis generated by subaerial mass flows,* J. Geophys. Res. *108,* 2236, doi: 10.1029/2001JB000707.

WATTS, P. (1998), *Wavemaker curves for tsunamis generated by underwater landslides,* J. Waterway Port Coastal and Ocean Engrg. *124,* 127–137.

WAYTHOMAS, C.F. and NEAL, C.A. (1998), *Tsunami generation by pyroclastic flow during the 3500-year B.P. caldera-forming eruption of Aniakchak Volcano, Alaska,* Bull. Volcanol. *60,* 110–124.

(Received February 22, 2006, accepted July 30, 2006)

Pure appl. geophys. 164 (2007) 547–564
0033–4553/07/030547–18
DOI 10.1007/s00024-006-0166-3



Pure and Applied Geophysics

# Estimation of Tsunami Hazard in New Zealand due to South American Earthquakes

WILLIAM POWER, GAYE DOWNES, and MARK STIRLING

*Abstract*—We develop a probabilistic model for estimating the tsunami hazard along the coast of New Zealand due to plate-interface earthquakes along the South American subduction zone. To do this we develop statistical and physical models for several stages in the process of tsunami generation and propagation, and develop a method for combining these models to produce hazard estimates using a Monte-Carlo technique. This process is largely analogous to that used for seismic hazard modelling, but is distinguished from it by the use of a physical model to represent the tsunami propagation, as opposed to the use of empirical attenuation models for probabilistic seismic hazard analysis.

**Key words:** Tsunami, New Zealand, probabilistic, hazard model, Monte Carlo.

## *Introduction*

The location of New Zealand on the Pacific rim exposes it to a high risk of tsunami generated by great earthquakes located along the numerous subduction zones around the Pacific rim. This includes the Hikurangi-Kermadec subduction zone off the east coast of the North Island of New Zealand, and the Fiordland and Puysegur subduction zones in the southwest of the country. Tsunamis may also be locally generated by volcanoes or landslides on the continental shelf. However, for the initial development of the methodology of our probabilistic tsunami hazard analysis (PTHA) model we consider only distant source events; specifically those generated by South American earthquakes. Historically, these have been the most frequently occurring distant source of damaging tsunami in New Zealand, and therefore provide data against which to check the accuracy of the PTHA models. Three such tsunamis have had a significant, widely distributed and damaging impact along the east coast of New Zealand and on the offshore Chatham Islands (1000 km east of the main islands of New Zealand) in the last 150 years.

Probabilistic seismic hazard analysis (PSHA: CORNELL, 1968; MCGUIRE, 2004) is a well-established technique, of great value for developing appropriate hazard

GNS Science, 1 Fairway Drive, Avalon, PO Box 30368, Lower Hutt, New Zealand.

mitigation strategies. It is frequently used to determine the structural design specifications needed to withstand a specified return period ground-shaking, and indeed to determine whether a site is suitable for a particular application (e.g., a nuclear power plant). The destructive power of tsunamis so graphically demonstrated by the Sumatra tsunami of 26 December 2004 (BORRERO, 2005; GHOBARAH *et al.*, 2006), has drawn attention to the desirability of being able to apply similar probabilistic techniques to estimate tsunami hazard and so recognise the potential for events not experienced historically.

Until recently tsunami hazard has been regarded as very difficult to estimate in a probabilistic manner with sufficient accuracy to be of practical benefit. This is in large part due to the diversity and complexity of tsunami sources and the complexity of source-site propagation, which for the most part does not allow simple empirically derived attenuation relationships such as are used in seismic hazard analysis (for example, relationships describing the dependence of ground motions on distance from an earthquake source, and parameters of the earthquake such as magnitude and source mechanism) to be used without large uncertainties. Numerical models of tsunami propagation provide a means to approach the problem of PTHA by directly calculating the source-to-site relationship. RIKITAKE and AIDA (1988) estimated tsunami hazard probability for the east coast of Japan using numerical models of tsunamis originating from characteristic earthquake sources off the Pacific Coast of the Japanese Islands. ANNAKA *et al.* (2004; this issue) used a logic tree approach to estimate tsunami hazard at specific locations along the Japanese coast, incorporating a mixture of numerically modelled tsunami from local and distant earthquake sources. THIO *et al.* (2005; this issue) have estimated tsunami hazard in the Indian Ocean due to earthquakes off the coast of Sumatra, using an approach that allows for non-uniform slip on the earthquake rupture surface.

In this paper we present a new methodology for PTHA, which we illustrate with reference to the impact in New Zealand of tsunami from a particular group of tsunami sources, but which we believe can be extended to all distant and local earthquakes. Extension of the method to cover landslide sources is likely to be challenging, one key reason being that, in general, suitable magnitude/frequency relations for underwater landslides are difficult to establish. Volcanic and bolide sources can in principle be included, provided suitable physical models of tsunami initiation are available.

The methodology we describe is based on the use of Monte-Carlo simulations; MUSSON (2000) has made a comparison of conventional PSHA (as described in CORNELL, 1968; MCGUIRE, 2004) and the Monte-Carlo method of seismic hazard analysis, and his study of the relative pros and cons of each technique is equally applicable to tsunami hazard analysis. Monte-Carlo techniques have previously been used to study landslide tsunami hazard off Southern California (WATTS, 2004), and to evaluate the tsunami risk to New Zealand cities from local and distant earthquakes using empirical attenuation relationships (BERRYMAN, 2005).

## *Historical Background*

The written historical record of tsunami in New Zealand covers less than two centuries, which is short compared to many similar countries bordering the Pacific, such as Japan (1500 years: IIDA *et al.*, 1967) and the South American states (500 years: LOCKRIDGE, 1985). Consequently events with long recurrence intervals will not be fully represented. Further, the historical record is likely to be incomplete (missing events, or missing data on known events) even over the time it spans due to the sparse population distribution in the early days of European settlement and due to the inhospitable nature of some regions (POWER *et al.*, 2005).

The historical record is supplemented by investigating tsunami recorded in the oral history of New Zealand's indigenous population, the Māori, and in the geological record. There are a number of events that could be interpreted as tsunami in Māori history and legends (MCFADGEN, pers. comm.), many of which were documented by early European missionaries, but it is difficult to attach specific dates to these events and to establish whether or not particular stories relate to the same event. Paleo-tsunami studies (for example, COCHRAN *et al.*, 2005; GOFF *et al.*, 2000; NICHOL *et al.*, 2003) have identified a number of large tsunami inundation events in the pre-historical period, but their sources are not always clear. What is clear is that New Zealand has a significant tsunami hazard problem that the shortness of the historical record may not adequately represent.

Nevertheless, the historical record indicates the important contribution of trans-Pacific tsunamis to New Zealand's tsunami hazard and risk, and the importance of fully understanding the tsunami risk from distant sources. For example, three well-documented historical trans-Pacific tsunami caused significant and widespread damage throughout the east coast of New Zealand. These were generated by the 1868 $M_w$ 9.1 southern Peru, 1877 $M_w$ 9.0 northern Chile, and 1960 $M_w$ 9.5 southern Chile earthquakes, respectively (magnitudes from ITDB/PAC, 2004); details of these events are described in Appendix 1. Some very minor damage was caused by the tsunami generated by the 1946 $M_w$ 7.9 Aleutian earthquake (OKAL *et al.*, 2002).

Not all events that caused damaging tsunami to propagate around the Pacific affected New Zealand. Only minor impact in New Zealand was experienced from tsunamis caused by the 1933 $M_w$ 8.6 Japan, 1952 $M_w$ 9.0 Kuril, 1957 $M_w$ 8.7 Aleutian, 1964 $M_w$ 9.5 Alaska, 1906 $M_w$ 8.7 Columbia-Ecuador and the 1919 $M_w$ 8.4 Tonga trench earthquakes (Fig. 1, magnitudes from ITDB/PAC, 2004). This is not unexpected given the orientation of these subduction zones and the large-scale radiation pattern for earthquake-generated tsunami that can be estimated using the techniques of BEN-MENAHEM and ROSENMAN (1972) (for a more recent perspective on this approach see OKAL (2003)). However bathymetric features can also have a significant impact on the propagation and affect the directivity in the

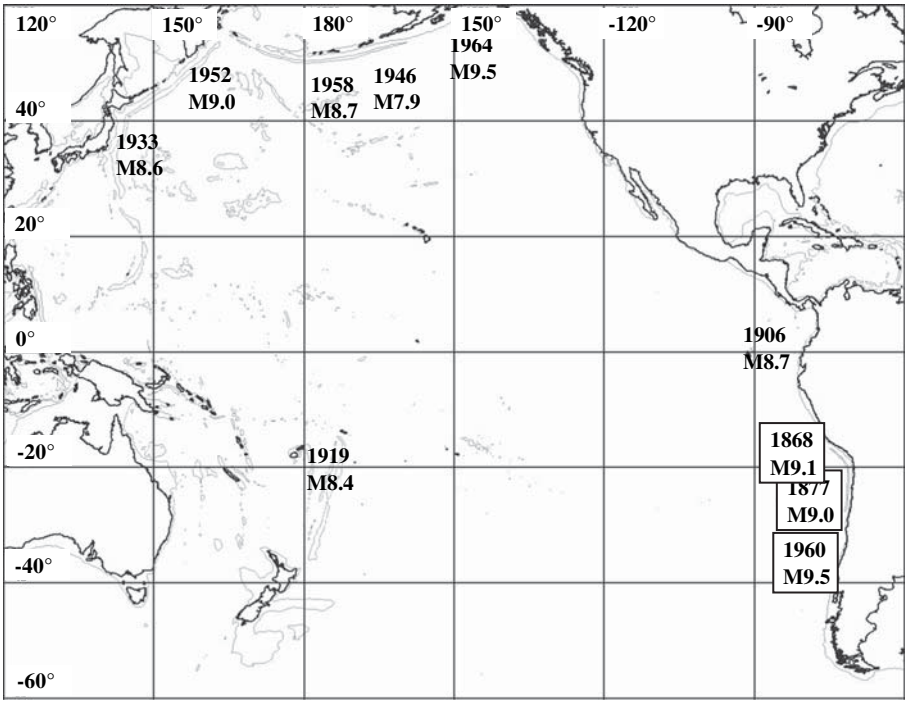


Figure 1
Locations of selected great earthquakes around the Pacific, boxes indicate that the earthquake had a significant impact on New Zealand. Magnitudes and outline map from Integrated Tsunami Database for the Pacific (ITDB/PAC, 2004).

far-field, as was apparent following the 2004 Sumatra tsunami (TITOV *et al.*, 2005). For this reason, the possibility of damage being caused by larger tsunamis originating from less-than-optimally oriented regions cannot be excluded without some investigation using numerical models. This is particularly important for areas which have not been the source of great earthquakes in the last 200 years, such as Central America, Cascadia, the Kermadec trench and the Southern Ocean.

Investigation of the magnitude/frequency distribution of large subduction zone earthquakes, numerical modelling of tsunami and the development of PTHA has the potential to identify the level of threat that goes beyond the historical record, and allows estimation of the hazard in terms of return periods commonly used for analysis of natural hazards, such as 100, 500, and 2,500 years. As with PSHA, the historical and pre-historical records are useful for validating the source-to-site relationships (tsunami propagation models in PTHA, attenuation relations in PSHA), and for checking the reliability of the hazard estimates.

*Methodology*

In principle there is the potential for many different tsunamigenic earthquakes to occur on the South American subduction zone. Rupture dimensions and distributions of slip on the plate interface differ in space and in time. For example, the 2001 Peru earthquake ruptured a smaller area of the interface than the 1868 earthquake which occurred in the same general area. Our PTHA methodology assumes that this variability can be approximately represented by a set of modelled scenarios for which the key parameters for impact at great distances from the source are the source location (specifically the midpoint of the rupture zone), and the seismic moment (TITOV *et al.*, 2001).

We establish a range of source locations (32 equally spaced source locations along the length of the Peru-Chilean subduction zone) – and seismic moments (corresponding to $M_w$ 8.5 to 9.5 in increments of 0.1 magnitude units) that encompass the set of possible tsunamigenic earthquakes affecting New Zealand. For each combination of location and magnitude we estimate a credible slip distribution and surface deformation using appropriate scaling relationships (Fig. 2). This deformation is used as the initial input to a trans-Pacific tsunami propagation model and nested-grid model of impact on New Zealand. The estimates of maximum wave-heights from this set of model calculations, combined with a statistical model of the occurrence of each of the different source events, is then used to create a synthetic catalogue of source events and subsequent impacts on New Zealand using the Monte-Carlo technique (Fig. 3). This synthetic catalogue is generated in such a way that the modelled events have the same statistical properties as those estimated for the real events over an appropriately long time-scale. The synthetic catalogue of

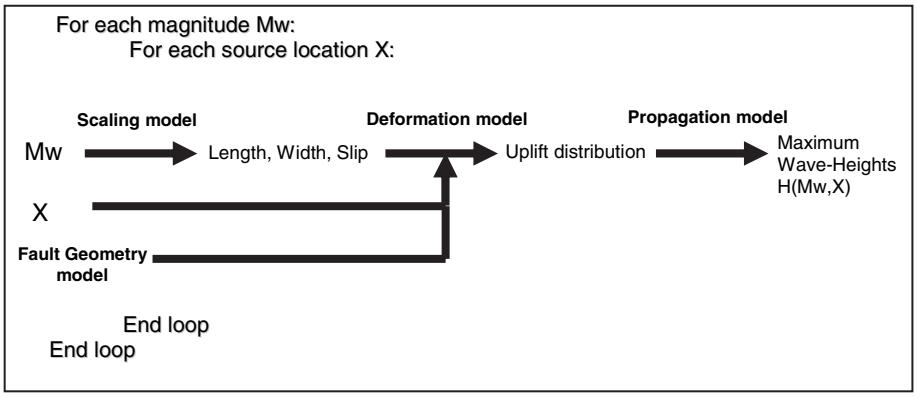


Figure 2
Outline procedure for estimating maximum wave heights for each combination of source location and moment magnitude. The maximum wave heights are stored for every point on the New Zealand nested grid.

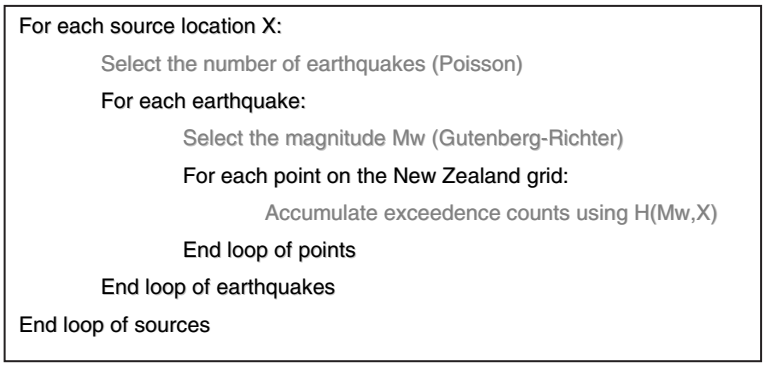


Figure 3
Outline Monte-Carlo procedure for generating synthetic catalogue of tsunami-generating events and subsequent impacts around New Zealand.

sources and impacts can then be used to estimate the hazard for any location of interest around the New Zealand coastline.

The procedure we have developed for PTHA requires the combination of several distinct models, each of which is described below.

*Fault Geometry Model*

The trough or trench was manually digitised with the assistance of the Integrated Tsunami Database software (ITDB/PAC, 2004). This is taken to represent the approximate up-dip extent of the plate interface at 2 km depth as shown in Figure 4. Based on analysis of deformation following the 1960 Chile earthquake BARRIENTOS and WARD (1990) have derived estimates of the cross section of the fault plane. Their modelling suggests an average dip on the fault plane of 20°, and an average width of 130 km, over the area of the 1960 rupture. As a first approximation for the purpose of developing the methodology, we have assumed that this cross section can be extended, at least approximately, along the full length of the subduction zone.

*Scaling Model*

The range of source magnitudes covered by this study initially ran from $M_W$ 8.0 to 9.5. To estimate the deformation and fault length over this magnitude range, two different scaling models (Fig. 5) were used. From $M_W$ 8.0 to 8.5 the relations of ABE (1975) were used to estimate typical rupture length, width and displacement for these magnitudes. Above magnitude 8.6 the rupture width extends for the full width of the fault plane (to the brittle-ductile boundary where fault locking no longer occurs). For these magnitudes we assume that the displacement continues to scale proportionately with the fault length; this is known as the L-model (SCHOLZ, 1982; HANKS and BAKUN, 2002). We found this model to give a better match to historical events on the

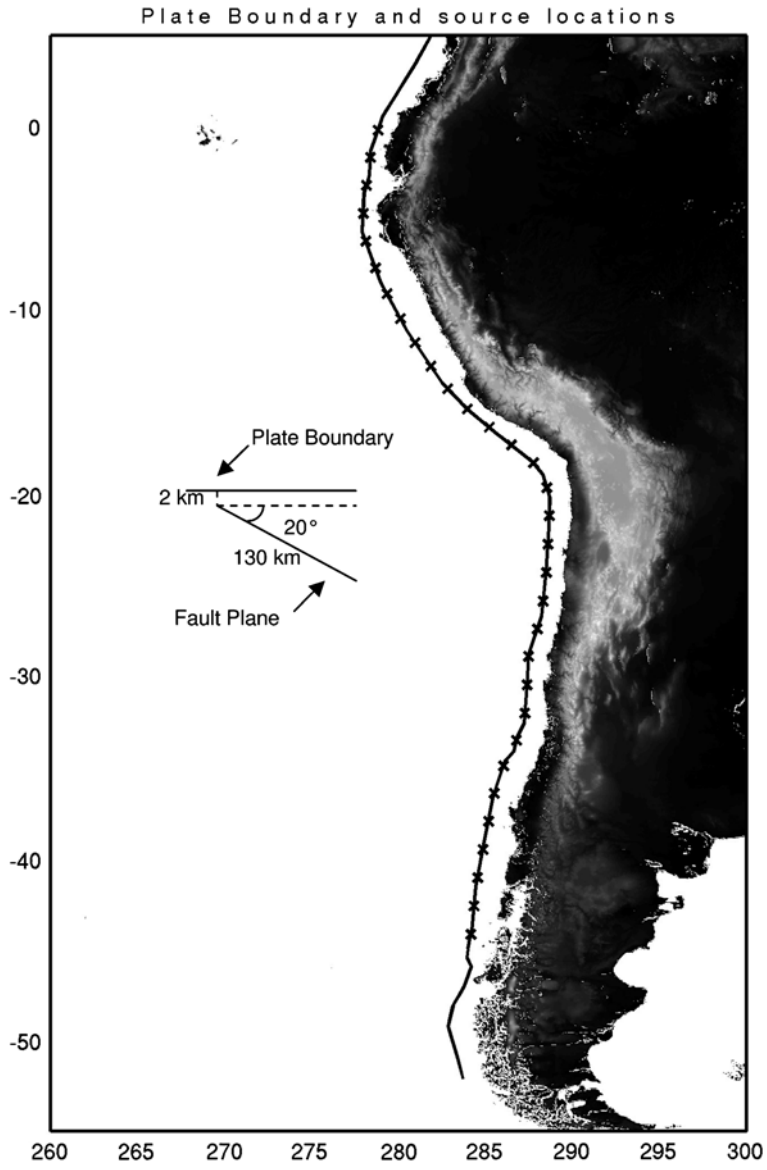


Figure 4
Digitised fault trace and assumed cross section for the plate interface. The crosses show the 32 source locations.

South American plate interface than the alternative W-model (ROMANOWICZ, 1992, 1994).

After initial trials, it was found that in general only earthquakes larger than about 8.5 were sufficient to produce tsunamis that were likely to cause damage in

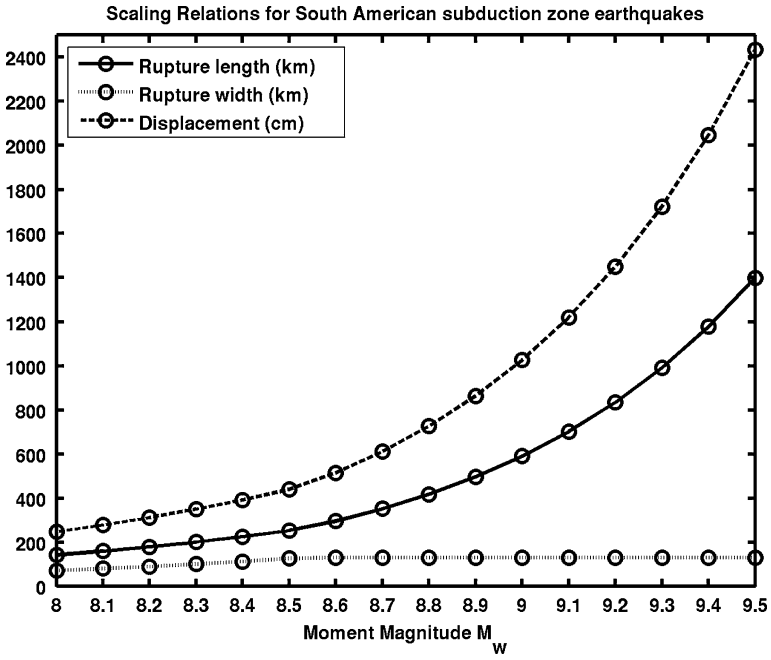


Figure 5
Scaling relations for rupture parameters as a function of moment magnitude.

New Zealand[1]. This is consistent with the historical record. Subsequently only sources in the range from 8.5 to 9.5 were included in our hazard calculations presented here.

*Deformation Model*

The deformation model is based on Okada's formula for deformation of an elastic half space (OKADA, 1985). Given the source location, rupture dimensions and geometrical model of the fault plane, a series of rectangular fault segments is calculated that collectively represent the rupture surface. It is assumed that the displacement is uniform over this compound surface. On each segment of the rupture surface it is assumed that the rupture is described by a pure 'thrust' mechanism with none of the moment taken up in strike-slip movement (for a discussion of slip-partitioning see MCCAFFREY, 1992, 1996).

[1] There remains the possibility that 'tsunami-earthquakes' (first recognised by KANAMORI, 1972) of magnitude less than M 8.5 could cause damaging tsunami in New Zealand, but these are not considered in this study. Some apparent 'tsunami earthquakes' may be due to underestimation of the true moment.

*Propagation Model*

The propagation of the tsunami, from its initiation by the deformation model uplift to its impact at the New Zealand shoreline, is calculated by using the MOST tsunami model (TITOV and GONZALEZ, 1997). Two modelling grids were used: The first covering the entire southern Pacific from 160°E–300°E and 65°S–5°N at a resolution of four minutes, and a one-minute nested grid allowing finer scale modelling of the tsunami at the New Zealand coastline.

The Pacific scale grid is based upon the one minute grid developed by Smith which blends the SMITH and SANDWELL (1997) gravity-derived dataset (accurate in deeper waters) with the GEBCO bathymetry database (more accurate in shallower waters). Around the New Zealand landmass the NZ National Institute for Water and Atmospheric Research contributed bathymetry data to the GEBCO dataset.

The finer nested grid, at one minute resolution, was derived by blending Smith's one-minute grid described above, with data gridded from C-MAP digital bathymetry supplied by Seabed Mapping of Nelson. This later dataset provides good resolution at shallow depths, particularly in the vicinity of ports and harbours. The one-minute nested grid covers the range from 165.6°E–179.5°E and 48.5°S–33.5°S.

The model treats the 10 m water depth contour as a reflecting boundary condition. The addition of finer grids and inundation calculations will be a future extension to this work. An empirical run-up factor can be used to relate the peak wave height at the 10 m contour to the on-land run-up height (see Results section).

*Statistical Model*

The statistical model describes the magnitude-frequency relationship for each source location. In this model the magnitude-frequency relationship is assumed to follow a truncated Gutenberg-Richter relationship with parameters $a$ and $b$ and maximum magnitude $M_{\max}$.

$$\begin{aligned} \frac{dN}{dM_W} &= 10^{a-bM_w} \qquad M_W < M_{\max} \\ &= 0 \qquad\qquad M_W \geq M_{\max} \end{aligned}$$

$$N(M > M_W) = \frac{10^a}{b\ln(10)}\left(10^{-bM_W} - 10^{-bM_{\max}}\right).$$

The values for these parameters are based upon those used by BERRYMAN (2005). Following this reference a $b$-value of 1 is assumed (Fig. 6)[2], as is a maximum

[2] Figure 6 is notable for the extent to which the global average $b$-value of 1 (WESNOUSKY, 1999) appears to hold even for the largest magnitude earthquakes; however some caution needs to be exercised as the sample size is small (8 events greater than magnitude 8.5 over 200 years).

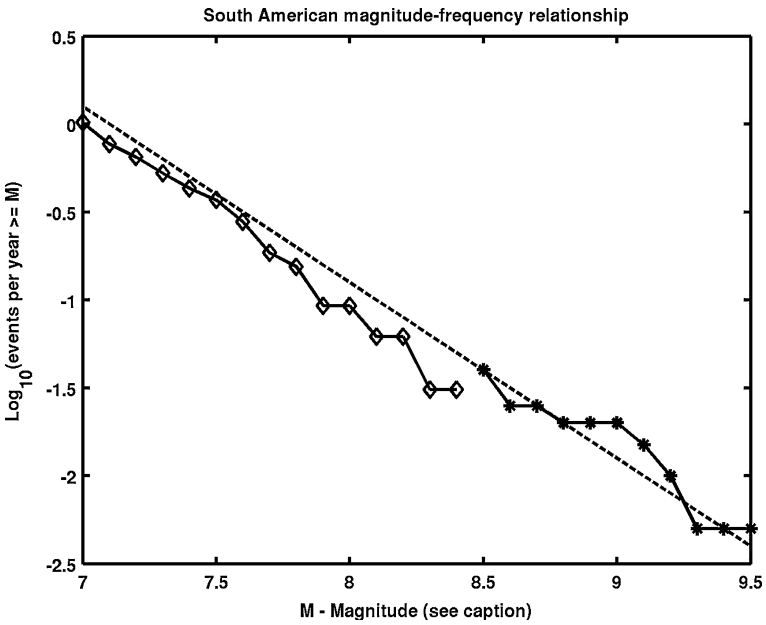


Figure 6
Magnitude-frequency relationship for the west coast of South America between 45°S and the equator. The data used to plot the diamonds are taken from the USGS/NEIC catalogue and spans from 1973 to May 2005. The data used to plot the asterisks are taken from the ITDB/PAC (2004) catalogue of tsunamigenic earthquakes (years 1803 to 2003, magnitudes ≥ 8.5), and the magnitude used is the first quoted value in the sequence: $M_w$, $M_t$, $M_s$. The two datasets are plotted as independent cumulative distributions. The dashed line represents a Gutenberg-Richter magnitude-frequency relationship with *b*-value of 1 and a recurrence interval of 25 years for $M \geq 8.5$, corresponding to 75% of the relative plate motion being released seismically.

magnitude of 9.5, corresponding to the upper limit of estimates of the moment of the 1960 Chile earthquake. This maximum magnitude is taken to apply throughout the length of the plate boundary. The *a*-values have been estimated assuming that 75% of the relative plate motion (perpendicular to strike) is released seismically on the plate interface. For this purpose the plate boundary has been divided into two types; between 19°S and 9°S where convergence is oblique, and the remaining locations where convergence is approximately orthogonal to the strike.

For the purpose of the Monte-Carlo method it is convenient to convert the *a*-values into recurrence intervals for earthquakes exceeding the threshold $M_{\min} = 8.5$. This leads to recurrence intervals of 9*110 = 990 years for the 9 source locations between 19°S and 9°S, and 23*32 = 736 years for the remaining 23 source locations. For the South American subduction zone as a whole the recurrence interval for exceeding $M_{\min}$ is then $1/(110^{-1} + 32^{-1}) \approx 25$ years (see comparison with the historical record in Fig. 6).

*Monte-Carlo Generation of Synthetic Catalogue*

The procedure for generating the synthetic catalogue of earthquake sources and tsunami impacts is outlined in Figure 3.

First a time span is chosen for the synthetic catalogue; this needs to be significantly longer than any of the time scales in the magnitude-frequency statistics to ensure that all possible events are sampled several times. Here we have used 500,000 years. For each source we then calculate the number of earthquakes exceeding $M_{\min}$ by sampling from a Poisson distribution, and for each of these earthquakes we calculate a magnitude by sampling from a truncated Gutenberg-Richter distribution. In this way the synthetic catalogue of sources is developed.

For the purpose of estimating tsunami hazard it is necessary to count the number of occasions when a given wave height is exceeded. This is done by incrementing an array of exceedence-counts, defined at all locations in the nested grid, after each event in the catalogue using the pre-calculated arrays $H(M_w, X)$. As our measure of hazard we use the double-amplitude H2, in this case estimated by doubling the maximum wave elevation over the ambient sea-level. The result is a count of the number of times that H2 exceeded 1 m, 2 m,…, 20 m at each point around the New Zealand coastline greater than 10 m deep over the period of the synthetic catalogue. From this information we can estimate the recurrence time for a given H2, and convert this information into a plot of H2 for a given return period using conventional PSHA techniques.

## *Results*

The results shown below represent the tsunami hazard due to only one type of source, namely South American subduction zone earthquakes. The parameterisation of our model is preliminary and is used to illustrate the Monte-Carlo technique; future refinements are discussed in the following section.

In order to make the results more clearly visible on the printed page we have applied a technique described in Appendix 2.

The reason for plotting the tsunami double amplitude is to enable a link to the tsunami run-up height. KAJIURA (1983, 1986) showed that the double amplitude as measured from peak to trough by a tide gauge was a good estimate of the median run-up height measured in the vicinity of the tide gauge[3]. This is equivalent to assuming a run-up factor of 2 (see GEIST, 1998 and SATAKE, 1994 for discussion of run-up factors).

[3] However, some of this apparent amplification may be due to underestimation of the true waveheight due to filtering of the signal by the tide-gauge (SATAKE *et al.*, 1988). The association of modelled H2 with run-up should be regarded as tentative pending further calibration or more detailed modelling.

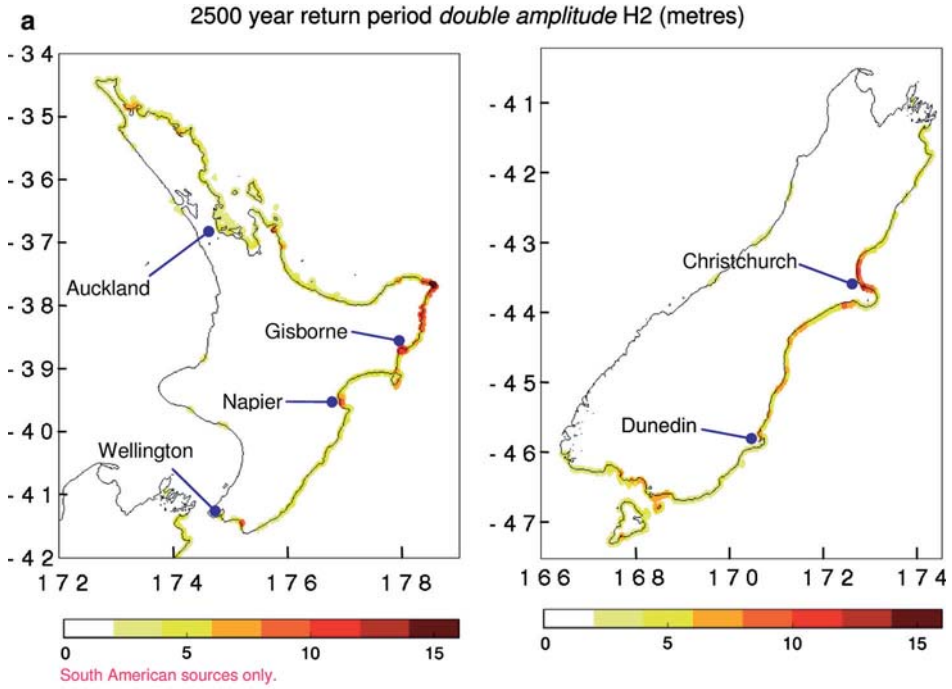
a
2500 year return period *double amplitude* H2 (metres)
-34
-35
-36
-37
-38
-39
-40
-41
-42
172
174
176
178
Auckland
Gisborne
Napier
Wellington
-41
-42
-43
-44
-45
-46
-47
166
168
170
172
174
Christchurch
Dunedin
0
5
10
15
South American sources only.

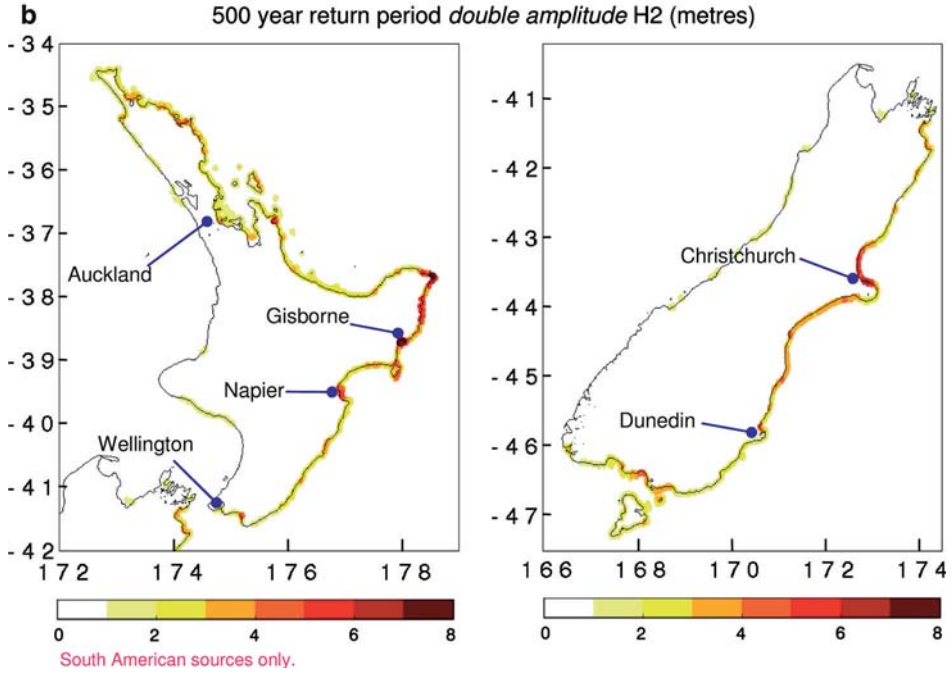
b
500 year return period *double amplitude* H2 (metres)
-34
-35
-36
-37
-38
-39
-40
-41
-42
172
174
176
178
Auckland
Gisborne
Napier
Wellington
-41
-42
-43
-44
-45
-46
-47
166
168
170
172
174
Christchurch
Dunedin
0
2
4
6
8
South American sources only.

◀

Figure 7
**a.** Double amplitude H2 in metres for the 2500-year return period South American tsunami at each location around the New Zealand coastline. H2 can be used as a first estimate of the median run-up within the surrounding area. **b.** Double amplitude H2 in metres for the 500-year return period South American tsunami at each location around the New Zealand coastline. H2 can be used as a first estimate of the median run-up within the surrounding area.

The results in Figures 7a and 7b show the values of H2 estimated for return periods of 2500 and 500 years, respectively. The general pattern of hazard is similarly distributed in both cases, and largely matches expectations based on the historical records of the 1868, 1877 and 1960 tsunamis. In particular we see high hazard around Banks Peninsula (immediately south of Christchurch) due to the wave-guiding effect of the Chatham rise (which extends east from Banks Peninsula to the Chatham Islands), and along the coast north of Gisborne, as has been observed historically. The hazard on Banks Peninsula appears historically to vary significantly from bay to bay, probably due to local resonances, an effect which is not apparent in our model due to the limited resolution of our nested grid. The elevated hazard level around the southern part of the South Island was not anticipated, and some important future work will be to disaggregate the hazard here to identify which sources are contributing.

*Limitations and Future Refinements*

We expect to make further refinements to the statistical and physical models of the earthquake sources. Our statistical model is relatively simple and based on the assumption that the plate-boundary is seismically homogeneous (except for the change in recurrence interval between 19°S and 9°S due to oblique convergence). A detailed study of the seismic characteristics of different sections of the plate-boundary will be a necessary step in the refinement of our model.

Our physical model of the sources assumes a uniform displacement over the rupture surface. It is known that slip distribution plays a significant role in the near-field (GEIST, 1998), and the far-field sensitivity to slip distribution is an area for future study.

The method shown here can be extended to include further levels of nested grid, and to include inundation modelling of specific key sites.

The addition of tides to the Monte-Carlo model is expected to be relatively straightforward in the first approximation: At any particular site the effect of tides on the median run-up height (estimated by H2) can be modelled by randomly sampling for the phase of the tide at which the peak wave arrives. It should be noted that for distant-source tsunami the time-envelope of the arriving wave-train may stretch over several wave-periods; in this case the highest combination of wave and tide may not

necessarily occur at the moment of the peak wave, and more careful modelling is required.

Most practical uses of PTHA will require the inclusion of all hazardous tsunami sources affecting New Zealand, in particular earthquakes on the plate boundary which pass through New Zealand.

## *Conclusions*

We conclude that a PTHA for distant source tsunami is feasible, using techniques similar to those used for PSHA. The Monte-Carlo approach presented here is relatively simple to use, though moderately demanding of computer time. The model we present produces results consistent with the historical record of South American tsunamis, and should be extended to include all known tsunami sources likely to be hazardous in New Zealand.

## *Acknowledgements*

We gratefully acknowledge the assistance of: Warwick Smith, Phil Scadden and John Beavan at GNS Science; Vasily Titov, Harold Mofjeld and Frank Gonzalez at NOAA PMEL; and Jose Borrero at ASR Limited.

## *Appendix 1 Major Historical Trans-Pacific Tsunami*

### *1868*

In 1868 a great earthquake of magnitude 9.1 (ITDB/PAC, 2004) occurred along the southern coastline of Peru and northernmost area of Chile. The rupture area is estimated to have extended for at least 500 km northwest from Arica in Chile (COMTE and PARDO, 1991), although recent results suggest it may have extended significantly further than this (OKAL *et al.*, 2006). Locally run-ups of 15 m were reached (ITDB/PAC, 2004).

Numerical modelling developed for this paper shows that tsunami sourced from plate interface events in this region are orientated in such a way that a large proportion of the wave energy is directed towards New Zealand. Unsurprisingly then, the impact of this tsunami on New Zealand was significant, though somewhat lessened by the good fortune of arriving near low-tide in many parts of the country.

Maximum run-ups on the East Coast were widely distributed in the range between 1 and 2 metres, but were significantly higher in a number of specific locations, notably Banks Peninsula (3–4 m), the Canterbury coast (4 m ), the Bay of

Plenty (3 m) and the Chatham Islands (10 m) (Downes, unpublished New Zealand Tsunami Database).

*1877*

The 1877 great earthquake in northern Chile is estimated to have had a magnitude of approximately 8.8, and to have ruptured along a length of about 400 km extending south from Arica (the southernmost limit of the 1868 rupture zone) (COMTE and PARDO, 1991). Local run-up heights for this event exceeded 20 metres. This area of South American coastline is less effective at directing tsunami waves towards New Zealand. More energy was directed to the north with run-up heights of 4–5 m observed in Hawaii and Japan.

Around New Zealand run-up heights were again widely observed in the 1–2 m range, though typically lower than for the 1868 event at the same locations. The highest maximum wave height observations were in the 3–4 m range (Downes, unpublished New Zealand Tsunami Database).

*1960*

The magnitude 9.5 Chile earthquake of 1960 (KANAMORI and ANDERSON, 1975) is well-known for being the largest earthquake to be instrumentally recorded (OKAL and TALANDIER, 1991). The rupture zone extended for approximately 1000 km south from the Arauco Peninsula (CIFUENTES, 1989). The subsequent tsunami caused great damage locally, with peak run-up heights of about 25 metres. The orientation of the rupture zone directed the tsunami energy towards the north, and large run-up heights were recorded in Hawaii (up to 12 m) and Japan (up to 6.4 m); severe damage and loss of life occurred in these locations.

Many locations on the New Zealand east coast observed peak run-up heights in the range from 0.5 to 1.5 m. Largest observations were in Gisborne and Napier (4–5 m), and around Banks Peninsula (3–4 m). As in 1868, the impact was reduced by the largest waves occurring near low tide over a significant part of the coast (Downes, unpublished New Zealand Tsunami Database).

## *Appendix 2 Processing of Results for Representation on a Small Map*

When a one minute grid is used for estimating tsunami hazard we encounter the problem that the hazard values (in our case H2 wave heights) at points closest to the coast form a strip which is too small to see clearly on the printed page. To resolve this issue we apply the following procedure:

All points within a 3.5-grid cell distance of the 10 m isobath are selected. For each of these points the colour used to represent the wave height is chosen based on the highest wave height at any point within a 3.5-grid cell radius.

This process therefore emphasises the largest hazard within the vicinity of a particular location. Although this procedure is principally intended to improve legibility, it also represents a conservative assumption regarding the uncertainties in propagating from the 10 m isobath to the shoreline.

## References


Abe, K. (1975), *Reliable estimation of the seismic moment of large earthquakes*, J. Phys. Earth. *23*, 381–390.

Annaka, T., Satake, K., Shuto, N., Sakayima, T., and Yanagisawa, K. (2004), *Logic-tree approach for Probabilistic Tsunami Hazard Analysis and its applications to the Japanese Coasts*, Eos Trans. AGU, 85(47), Fall Meet. Suppl., Abstract OS23D-1349.

Barrientos, S.E. and Ward, S.N. (1990), *The 1960 Chile earthquake; inversion for slip distribution from surface deformation*, Geophys. J. Internat. *103*(3), 589–598.

Ben-Menahem, A. and Rosenman, M. (1972), *Amplitude patterns of tsunami waves from submarine earthquakes,* J. Geophys. Res. *77*, 3097–3128.

Berryman, K. (compiler) (2005), *Review of tsunami hazard and risk in New Zealand*, Institute of Geological and Nuclear Sciences client report 2005/104. http://www.civildefence.govt.nz/memwebsite.nsf/wpg_URL/For-the-CDEM-Sector-Publications-Tsunami-Risk-and-Preparedness-in-New-Zealand?OpenDocument.

Borrero, J.C. (2005), *Field survey of Northern Sumatra and Banda Aceh, Indonesia after the Tsunami and earthquake of 26 December 2004*, Seismol. Res. Lett. *76*(3), 312–320.

Cifuentes, I.L. and Silver, P.G. (1989), *Low-frequency source characteristics of the great 1960 Chilean earthquake*, J. Geophys. Res. *94*(B1), 643–663.

Cochran, U.A., Berryman, K.R., Mildenhall, D.C., Hayward, B.W., Southall, K., and Hollis, C.J. (2005), *Towards a record of Holocene tsunami and storms for Northern Hawke's Bay, New Zealand.* New Zealand J. Geol. Geophys. *48*, 507–515.

Comte, D. and Pardo, M. (1991), *Reappraisal of great historical earthquakes in the northern Chile and southern Peru seismic gaps*, Natural Hazards *4*, 23–44.

Cornell, C.A. (1968), *Engineering seismic risk analysis*, Bull. Seismol. Soc. Am. *58*(5), 1583–1606.

Ghobarah, A., Saatcioglu, M., and Nistor, I. (2006), *The impact of the 26 December 2004 earthquake and tsunami on structures and infrastructure,* Eng. Struct. *28*(2), 312–326.

Geist, E.L. (1998), *Local tsunamis and earthquake source parameters*, Advan. Geophys. *39*, 117–209.

Goff, J.R., Rouse, H.L., Jones, S.L., Hayward, B.W., Cochran, U., McLea, W., Dickinson, W.W., and Morley, M.S. (2000), *Evidence for an earthquake and tsunami about 3100–3400 yrs. ago, and other catastrophic saltwater inundations recorded in a coastal lagoon, New Zealand,* Marine Geology *170*, 231–249.

Hanks, T.C. and Bakun, W.H. (2002), *A bilinear source-scaling model for M-log A observations of continental earthquakes*, Bull. Seismol. Soc. Am. *92*(5), 1841–1846, illus. incl. 1 table, 28 refs.

Iida, K., Cox, D. and Pararas-Carayannis, G. (1967), *Preliminary Catalogue of Tsunamis occurring in the Pacific Ocean*, Data Report N 5, HIG 67-10, Hawaiian Inst. of Geophysics, University of Hawaii, 274 p.

ITDB/PAC (2004), *Integrated Tsunami Database for the Pacific*, Version 5.1 of June 2004. CD-ROM, Tsunami Laboratory, ICDMMG SD RAS, Novosibirsk, Russia.

KAJIURA, K. (1983), *Some statistics related to observed tsunami heights along the coast of Japan*, In (K. Iida and T. Iwasaki, eds.), *Tsunamis – Their Science and Engineering* (Terra. Sci. Publ., Tokyo, 131–145.

KAJIURA, K. (1986), *Height distribution of the tsunami generated by the Nihonkai-Chubu (Japan Sea Central Region) Earthquake*, Science of Tsunami Hazards *4*(1), 3–14.

KANAMORI, H. (1972), *Mechanism of tsunami earthquakes*, Phys. Earth Planet. and Inter. *6*, 346–359.

KANAMORI, H. and ANDERSON, D.L. (1975), *Amplitude of the Earth's free oscillations, and long-period characteristics of the earthquake source*, J. Geophys. Res. *80*, 1075–1078.

LOCKRIDGE P.A. (1985), *Tsunamis in Peru-Chile*, Report SE-39, Boulder, WDC-A for Solid Earth Geophysics, 97 p.

MCCAFFREY, R. (1992), *Oblique plate convergence, slip vectors, and forearc deformation*, J. Geophys. Res. *97*, B6, 8905–8915.

MCCAFFREY, R. (1996), *Estimates of modern arc-parallel strain rates in fore arcs*, Geology *24*(1), 27–30.

MCGUIRE, R. (2004), *Seismic hazard and risk analysis*, MNO-10 (Earthquake Engineering Research Institute, USA).

MUSSON, R.M.W. (2000), The use of Monte Carlo simulations for seismic hazard assessment in the U.K., Annali di Geofisica *43*(1), 1–9.

NICHOL, S.L., LIAN, O.B., and CARTER, C.H. (2003), *Sheet-gravel evidence for a late Holocene tsunami run-up on beach dunes, Great Barrier Island*, New Zealand, Sediment. Geol. *155*, 129–145.

OKADA, Y. (1985), *Surface deformation due to shear and tensile faults in a half-space*, Bull. Seismol. Soc. Am. *75*(4), 1135–1154.

OKAL, E.A., SYNOLAKIS, C.E., FRYER, G.J., HEINRICH, P., BORRERO, J.C., RUSCHER, C., ARCAS, D., GUILLE, G. and ROUSSEAU, D. (2002), *A field survey of the 1946 Aleutian tsunami in the far field*, Seismol. Res. Lett. *73*, 490–503.

OKAL, E.A., BORRERO, J.C. and SYNOLAKIS, C.E. (2006), *Evaluation of tsunami risk from regional earthquakes at Pisco, Peru*, Bull. Seismol. Soc. Am. (in press).

OKAL, E.A. (2003), *Normal mode energetics for far-field tsunamis generated by dislocations and landslides*, Pure Appl. Geophys. *160*, 2189–2221.

OKAL, E.A. and TALANDIER, J. (1991), *Single-station estimates of the seismic moment of the 1960 Chilean and 1964 Alaskan earthquakes, using the mantle magnitude* $M_m$, Pure Appl. Geophys. *136*, 103–126.

POWER, W., DOWNES, G., MCSAVENEY, M., BEAVAN, J., and HANCOX, G. (2005), *The Fiordland earthquake and tsunami, New Zealand, 21 August 2003*. In *Tsunamis: Case Studies and Recent Developments*, vol. 23 of the series *Advances in Natural and Technological Hazards Research*, (Springer, New York, VIII).

RIKITAKE, T. and AIDA, I. (1988), *Tsunami hazard probability in Japan*, Bull. Seismol. Soc. Am. *78*(3), 1268–1278.

ROMANOWICZ, B. (1992), *Strike-slip earthquakes on quasi-vertical transcurrent faults: Inferences for general scaling relations*, Geophys. Res. Lett. *19*, 481–484.

ROMANOWICZ, B. (1994), *Comment on 'A reappraisal of large earthquake scaling' by C. Scholz*, Bull. Seismol. Soc. Am. *84*, 1675–1676.

SATAKE, K., OKADA, M., and ABE, K. (1988), *Tide gauge response to tsunamis: Measurements at 40 tide gauge stations in Japan*, J. Marine Res. *46*, 557–571.

SATAKE, K. (1994), *Mechanism of the 1992 Nicaragua tsunami earthquake*, Geophys. Res. Lett. *21*, 2519–2522.

SCHOLZ, C.H. (1982), *Scaling laws for large earthquakes; consequences for physical models*, Bull. Seismol. Soc. Am. *72*(1), 1–14.

SMITH, W.H.F. and SANDWELL, D.T. (1997), *Global sea floor topography from satellite altimetry and ship depth soundings*, Science *277*(5334), 1956–1962.

THIO, H.K., I., G. and SOMMERVILLE, P. (2005), *Probabilistic tsunami hazard analysis,* IASPEI General Assembly, Abstract 636.

TITOV, V.V. and GONZALEZ, F.I. (1997), *Implemenation and testing of the method of splitting tsunami (MOST) model,* NOAA Technical Memorandum ERL PMEL-112.

TITOV, V.V., MOFJELD, H.O., GONZÁLEZ, F.I., and NEWMAN, J.C. (2001), *Offshore forecasting of Alaskan tsunamis in Hawaii*, In (G.T. Hebenstreit, ed.), *Tsunami Research at the End of a Critical Decade* (Kluwer, Netherlands, pp.75–90).

TITOV, V.V., RABINOVICH, A.B., MOFJELD, H.O., THOMSON, R.E., and GONZÁLEZ, F.I. (2005), *The global reach of the 26 December 2004 Sumatra tsunami*, Science *209*, 2045–2048.

WATTS, P. (2004), *Probabilistic predictions of landslide tsunamis off Southern California*, Marine Geology *203*, 281–301.

(Received February 5, 2006, accepted June 26, 2006)
Publised Online First: January 30, 2007

Pure appl. geophys. 164 (2007) 565–576
0033–4553/07/030565–12
DOI 10.1007/s00024-006-0176-1



Pure and Applied Geophysics

# Tsunami Assessment for Risk Management at Nuclear Power Facilities in Japan

Ken Yanagisawa,[1] Fumihiko Imamura,[2] Tsutomu Sakakiyama,[3] Tadashi Annaka,[4] Tomoyoshi Takeda,[1] and Nobuo Shuto[5]

*Abstract*—The present study focuses on evaluation of the maximum and minimum water levels caused by tsunamis as risk factors for operation and management at nuclear power facilities along the coastal area of Japan. Tsunamis generated by submarine earthquakes are examined, basing literature reviews and databases of information on historical tsunami events and run-up heights. For simulation of water level along the coast, a numerical calculation system should be designed with computational regions covering a particular site. Also the calculation system should be verified by comparison of historical and calculated tsunami heights. At the beginning of the tsunami assessment, the standard faults, their locations, mechanisms and maximum magnitudes should be carefully estimated by considering historical earthquake-induced tsunamis and seismo-tectonics at each area. Secondly, the range of errors in the model parameters should be considered since earthquakes and tsunamis are natural phenomena that involve natural variability as well as errors in estimating parameters. For these reasons, uncertainty-induced errors should be taken into account in the process of tsunami assessment with parametric study of the tsunami source model. The element tsunamis calculated by the standard fault models with the errors would be given for the design. Then, the design tsunami can be selected among the element tsunamis with the most significant impact, maximum and minimum water levels, on the site, bearing in mind the possible errors in the numerical calculation system. Finally, the design tsunami is verified by comparison with the run-up heights of historical tsunamis, ensuring that the design tsunami is selected as the highest of all historical and possible future tsunamis at the site.

**Key words:** Tsunami assessment, design tsunami, standard fault model, nuclear power facility.

## 1. Introduction

Earthquakes of magnitude 8 would periodically occur in and around Japan, resulting in large tsunamis hitting the coast A tsunami event must be taken into account in the design of Nuclear Power Facilities (NPFs) in Japan in order to operate

[1] Tokyo Electric Power Company, 1-3, Uchisaiwai-cho 1-chome, Chiyoda-ku, Tokyo 100-8560, Japan. E-mail: yanagisawa.ken@tepco.co.jp
[2] Disaster Control Research Center, Tohoku University, Aoba 06, Aramaki, Aoba-ku, Sendai, 980-8579, Japan.
[3] Central Research Institute of Electric Power Industry, 1646, Abiko, Abiko 270-1166, Japan.
[4] Tokyo Electric Power Services Co., Ltd., 3-3, Higashi-ueno 3-chome, Taito-ku, Tokyo, 110-0015, Japan.
[5] Advanced Research Institute for the Sciences and Humanities, Nihon University, 12-5, Goban-cho, Chiyoda-ku, Tokyo, 102-8251, Japan.

the system including intake-cooling water and to discuss the location and safety level of each facility. The standard code and method for the ground motion due to the earthquake have been developed and authorized (NUCLEAR SAFETY COMMISSION OF JAPAN, 1990); nevertheless, there has yet been no standard method to assess the tsunami risk to NPFs. To date specific tsunami evaluation for NPFs has been carried out site by site. A new method for tsunami evaluation available for any region in Japan is required in order to enhance the safety and reliability of coastal power facilities including nuclear power plants. The design tsunami assessment method should be based on the newest findings through the most recent studies of tsunamis and earthquakes. This paper proposes a practical standard method to estimate standard fault model, element tsunamis and design tsunamis at NPFs in Japan (TSUNAMI EVALUATION SUBCOMMITTEE, JSCE, 2002; TANAKA *et al.*, 2003).

The impact that a tsunami affects on a site should include the several tsunami related phenomena such as water's rise and fall, sand movement and floating material. For NPF assessment, evaluation of water rise and fall is the most significant one among them, because the water rise and run-up of a tsunami may damage buildings and facilities on land, and water receding for long time cause the problem of intake water systems. Therefore, the present study focuses on the evaluation of water rise and fall.

A tsunami can be generated by an earthquake, volcanic eruption, collapse of a volcano, a landslide or meteorite. But volcano- and meteorite-induced tsunamis are infrequent events in comparison with earthquake-induced ones (IMAMURA, 1998). As most landslide-induced tsunamis would be triggered by earthquakes, such tsunamis should be included in the earthquake-induced category. Therefore, only earthquake-induced tsunamis are focused in this paper.

## 2. Overview of the Method

To ensure the safety of coastal power facilities, the design tsunami should be the highest one at the site among all historical and possible future tsunamis that can be estimated with the seismo-tectonics (HAGIWARA, 1991). The design tsunami should also have the most significant impact on the target site in terms of maximum and minimum water levels. We face a serious problem that the data of historical and possible tsunamis at the site is limited (WATANABE, 1998). How can we estimate the tsunami at the site? The answer is that the value of the time history of tsunamis can be obtained by the numerical simulation once we know the fault model. Therefore, a kind of standard faults must be modeled beforehand. In the modeling process, seismo-tectonics and historical earthquakes/tsunamis should be referred. The standard faults are considered to be those in the region of neighboring plate boundaries, the eastern margin of the Sea of Japan, active submarine faults and more distant plate boundaries. Here we should remind that we still have limitation of data to model them and some errors in their parameters could be contained fatefully.

A flow chart to evaluate the historical tsunamis, element tsunamis and design tsunamis for the NPF assessment is shown in Figure 1. The procedure can be divided into two main parts. The first is 'Verification of the fault model and the numerical

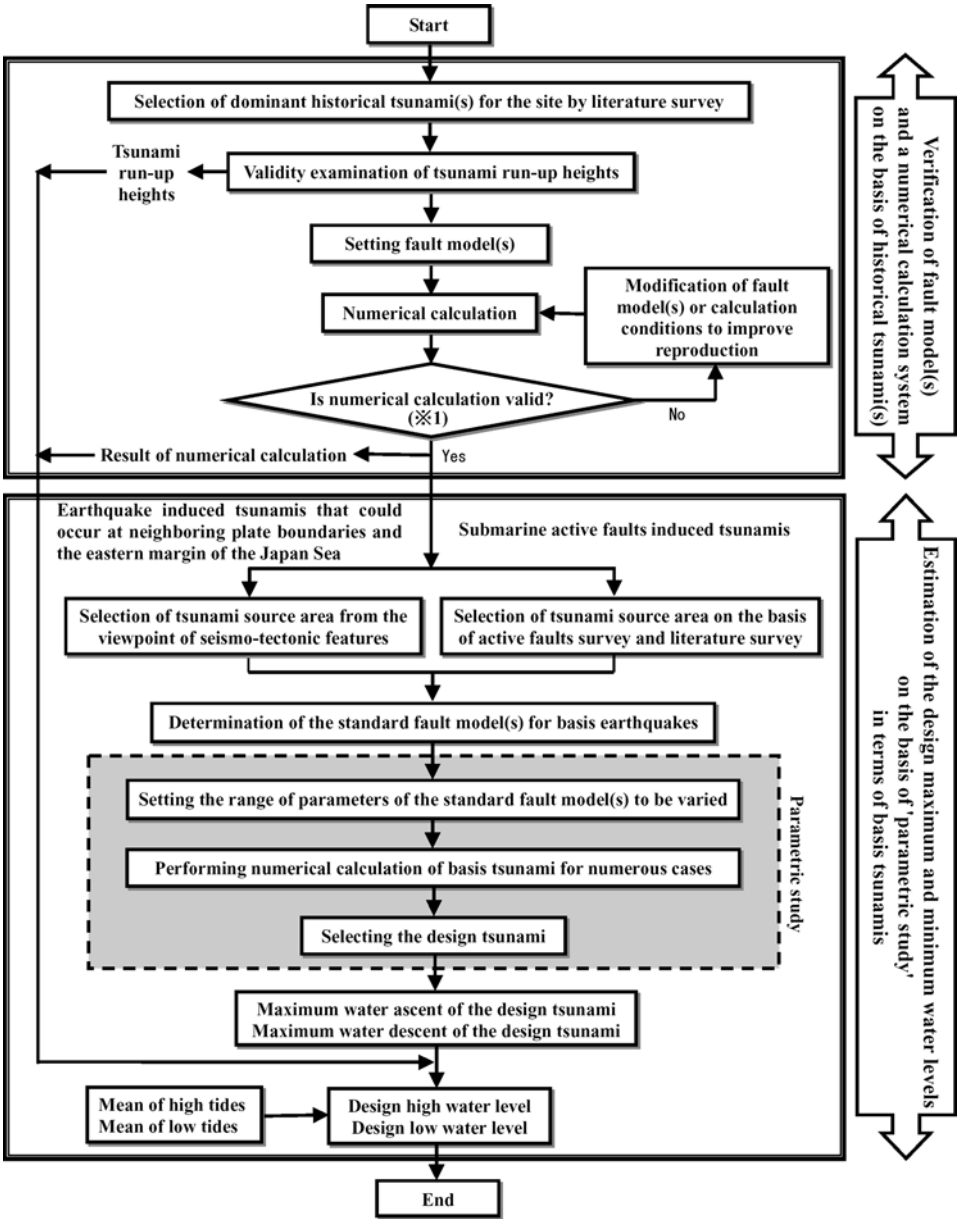


Figure 1
Flow chart for evaluation of the design tsunami.

calculation system' and the second is 'Determination of the design high and low water levels'.

## 3. Verification of the Fault Model and the Numerical Calculation System

Documented historical tsunamis are reviewed and a geological study is carried out to select typical tsunamis for the NPF site. Tsunami run-up heights are entered in the database. Not only local tsunamis but also distant tsunamis are listed. Before performing numerical calculations, the listed tsunami run-up heights are examined for validity. In Japan, old tsunami records documented before the 1896 Meiji-Sanriku tsunami are less reliable because of misreading, misrecording, and the low technology available for the measurement itself. The data can be compared with that from other documents and plotted on the map. Tsunami run-up records that appear unreliable should be excluded.

For appropriate tsunami evaluation, careful selection of the fault model parameters, bathymetry data, and the numerical calculation system are essential. Once these are selected, we can compare documented/recorded tsunami heights and calculated tsunami heights. In the present study, nonlinear long-wave theory is used in the calculations (GOTO, and OGAWA, 1982; TANAKA, 1985). When we discuss the reliability of the numerical calculation system, AIDA's indexes (1977) $K$ and $\kappa$, geometric average and variance are introduced, and the appropriate numerical model should satisfy the following conditions.

$$0.95 < K < 1.05, \quad \kappa < 1.45$$

$$\log K = \frac{1}{n}\sum_{i=1}^{n} \log K_i, \quad \log \kappa = \left[\frac{1}{n}\left\{\sum_{i=1}^{n}(\log K_i)^2 - n(\log K)^2\right\}\right]^{1/2},$$

where n: number of data points for evaluation, $K_i = R_i/H_i$, $R_i$: documented/recorded tsunami height for instance $i$, $H_i$: calculated tsunami height for instance $i$.

If $K$ and $\kappa$ do not satisfy the above conditions, fault model or calculation conditions should be modified to improve reproduction.

## 4. Estimation of the Design Maximum and Minimum Water Levels

### 4.1. Standard Fault

First the standard fault model for the element earthquake is selected. For earthquake-induced tsunamis that may occur at neighboring plate boundaries and the eastern margin of the Sea of Japan (see Fig. 2), the tsunami source area is estimated from seismo-tectonics. Neighboring plate boundaries for Japan are the

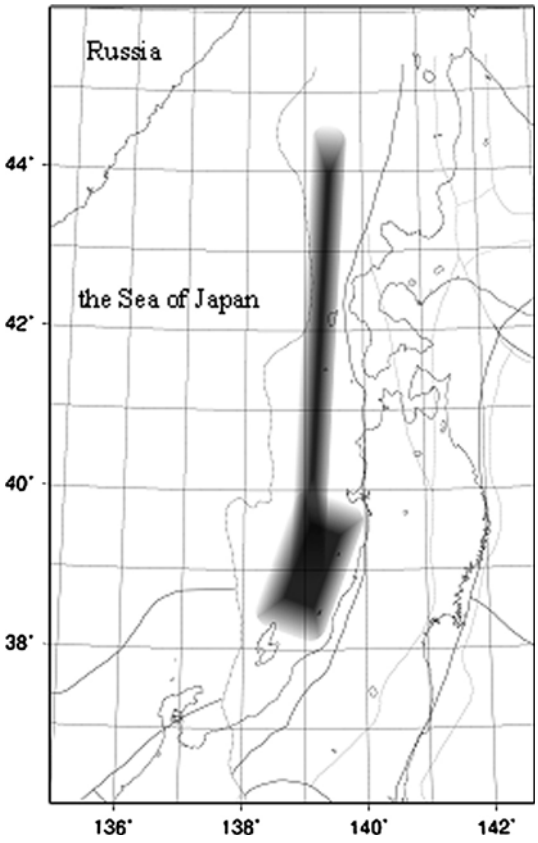


Figure 2
Tsunami source region on the eastern margin of the Sea of Japan.

Japan Trench, southern Kurile Trench (see Fig. 3) and Nankai Trough (see Fig. 4). For tsunamis induced by active submarine faults, the relevant area is estimated from a survey of the active faults and the literature. In addition, more distant plate boundaries with the greatest potential impact on the Japanese coast should be included, such as those off the west coast of South America.

The characteristics of earthquakes and fault models are as follows. The standard fault model parameters concerning fault position and magnitude $M_w$ need to be set in such a way that the numerical model reproduces historical tsunami run-up heights. When there are multiple historical tsunamis from the same fault region, a historical tsunami that has the maximum magnitude is selected. The standard fault models should be used in numerical calculations involving the nonlinear long-wave theory.

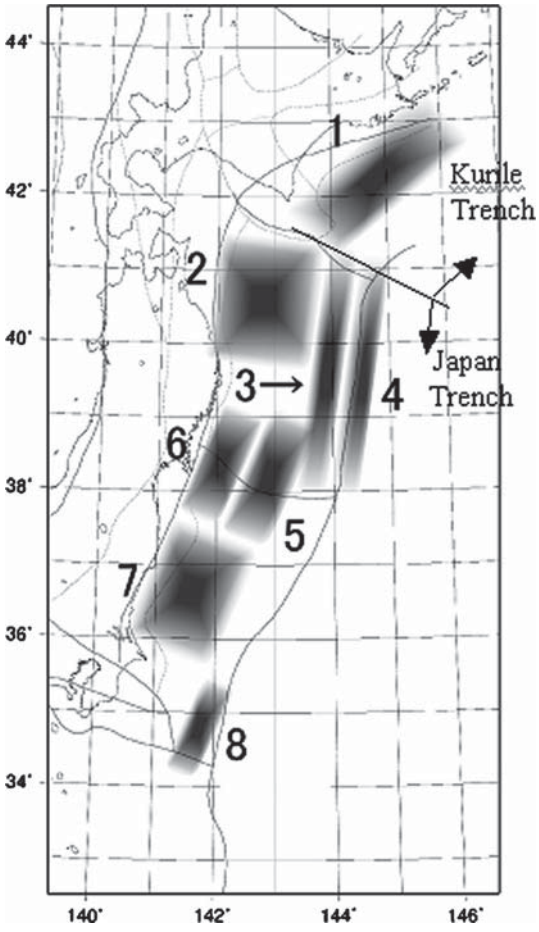


Figure 3
Tsunami source regions in the Japan Trench and southern Kurile Trench.

### *4.2. Taking Uncertainties and Errors into Account*

As earthquakes and tsunamis are natural phenomena, their variable and uncertain aspects should be considered. In the process of tsunami assessment, uncertainties and errors in many important parameters are unavoidable, including the tsunami source, fault position, depth of the upper edge of the fault plane, strike direction, dip angle, dip direction, slip angle and combination of segments. In the numerical simulation, the governing equations, boundary conditions, initial conditions, grid division, modeling of bathymetry data and reliability of run-up heights may also involve uncertainties. However, it is rather difficult to estimate those uncertainties quantitatively and to deal with them one by one. Consequently, only

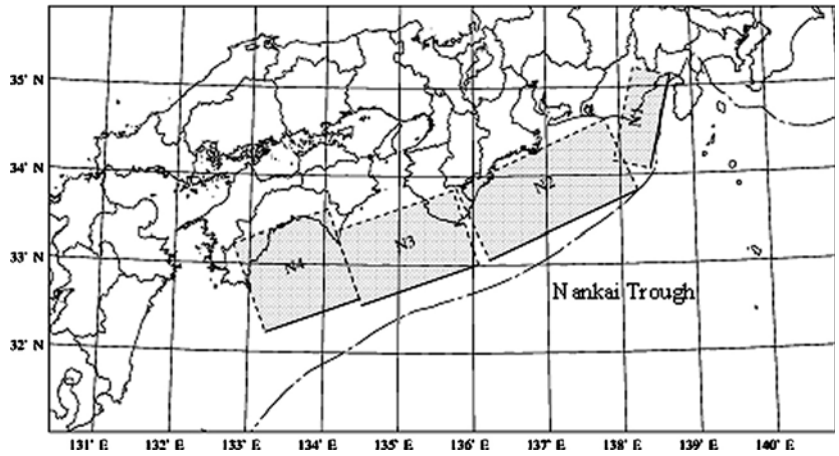


Figure 4
Fault positions in the Nankai Trough.

uncertainties concerning the tsunami source are dealt with in this study, because they can significantly influence tsunami assessment (see the Table 1).

Parametric study, which is a way to take into account the uncertainties about tsunami sources, is performed as described below.

1) Setting the range of variation of the parameters of the standard fault model(s). As a rule, the range of parameters is determined within its standard deviation.
2) Performing a numerical calculation of the element tsunamis for numerous cases based on a standard fault with errors.
3) Selecting the design tsunami among element tsunamis in each area as the one with the most impact on the target site (see the Fig. 5). The fault model for the highest water level and that for the lowest water level may be different.

After verification of the design tsunami, as described below, tides should be considered. For example, when numerical calculation is carried out based on the mean tide, the mean of high tides and the mean of low tides should be added in the determination of maximum water rise and fall.

## *5. Verification of the Design Tsunami*

When run-up height record or other data for the site are available, the adequacy of the design tsunami is verified by satisfying the following two points. At the site, the design tsunami heights exceed the recorded run-up heights of historical tsunamis. In the vicinity of the site the envelope of the element tsunami heights obtained by parametric study exceeds all recorded run-up heights of historical tsunamis.

Table 1

*Parameters of the standard fault model*

| Name of sea area | Type of earthquakes | Parameters of the standard fault model | | | | | | |
|---|---|---|---|---|---|---|---|---|
| | | Fault position | Depth of upper edge of the fault plance (d) | Strike direction ($\theta$) | Dip angle ($\delta$) | Dip direction | Slip angle ($\lambda$) | Combination of segments |
| along the Japan trench | typical inter-plate earthquakes | ○ | ○ | ○ | ○ | – | ○ #3 | – |
| | T sunami earthquakes (slow earthquakes) | ○ | ○ | ○ | ○ | – | ○ #3 | – |
| | normal fault earthquake in the subducting plate | ○ | ○ | ○ | ○ | – | be fixed at 270 degree | – |
| along the Nankai trough | typical inter-plate earthquakes | ○ | ○ | ○ | ○ | – | ○ #3 | ○ |
| Eastern margin of the Sea of Japan | earthquakes which occur within upper crust | ○ | ○ | ○ | ○ | ○ west dip east dip | - be fixed at 90 degree | – |
| submarine active faults | earthquakes which occur within upper crust | – | ○ #1 | – | ○ #1 | ○ #2 | ○ #4 | |

#1: When this is known by survey, it can be fixed.
#2: When this is unknown, both directions have to be set.
#3: Slip angle is to be set in conjuction with strike direction taking variation of slip direction into account.
#4: Slip angle is to be set in conjuction with dip angle taking variation of stress field into account.
○: ○ is an item that should be taken into consideration in 'parameter study'.

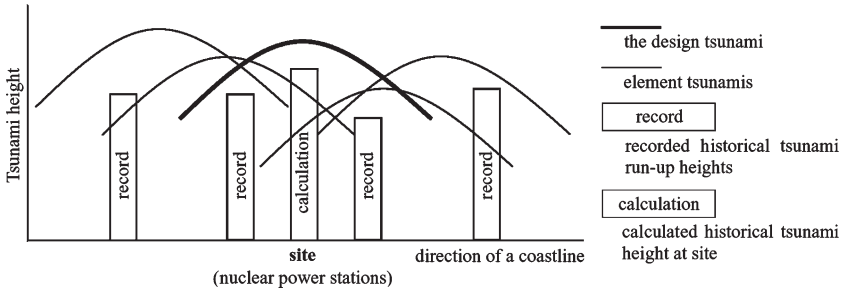


Figure 5
Selecting the highest tsunami at NPF.

There are two reasons why run-up heights are selected for confirmation. One reason is that run-up height includes all uncertainties regarding tsunami sources irrelevant. The other reason is that the number of tsunamis recorded on the coast of Japan is sufficient for usage of comparison with numerical calculation results.

The design tsunami heights finally obtained by the above-mentioned parametric study exceed recorded historical tsunami heights at 185 imaginary NPF sites on the Japanese coast. The geometric mean of design tsunami heights is about double that of recorded historical tsunami heights. The significance of this is not that this method may overestimate tsunami heights, but that from the viewpoint of safety for NPFs, it can be assumed that the design tsunami is higher than any possible future tsunamis at the site.

If no run-up height record or data for the site are available, reliability is verified by satisfying the following two points. First, the design tsunami heights at the site should exceed reproduced calculation heights of historical tsunamis. Second, in the vicinity of the site, the envelope of the element tsunami heights should exceed all run-up heights of recorded historical tsunamis.

## *6. Example of a Parametric Study*

An example of a parametric study on the eastern margin of the Sea of Japan is as follows. First, a general parametric study is carried out. Magnitude is fixed at $M_w = 7.8$ based on the maximum historical magnitude in this region, which is the 1993 Southwest Hokkaido earthquake. The fault plane is 131 km long and 15 km wide, as shown in Figure 6(a). The fault model is placed at the 15 positions shown in Figure 6(a), and at each location the parameters can take on eight patterns due to permutations of fault position, dip angle and dip direction as shown in Figure 6(b). This is because the trench axis is not clear in the eastern margin of the Sea of Japan, for other neighboring plate boundaries not all eight patterns are needed. As a result

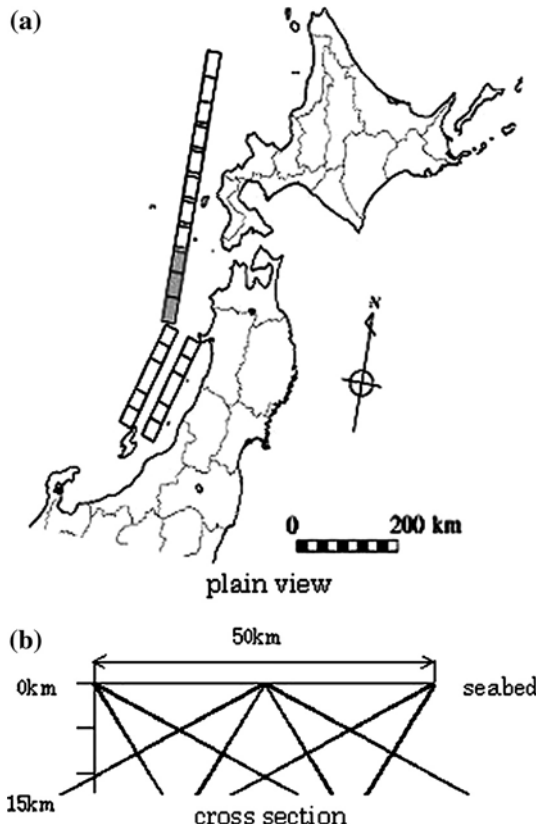


Figure 6
Fault positions and direction of dip: Eastern margin of the Sea of Japan.

of the general parametric study, historical run-up heights are still higher than element tsunamis at some points in this example case.

Second, a detailed parametric study is carried out. The fault model places the depth of the upper edge of the fault plane ($d$) at $d = 0$, 2.5, and 5 km, the dip angle ($\delta$) at $\delta = 45$, 52.5, and 60 degrees, and the strike direction ($\theta$) at $\theta = \pm 10$ degrees. For some points, the size of the grid is subdivided to evaluate the coastal region more thoroughly.

As a result of the general and detailed parametric studies, the heights of the element tsunamis are higher than all historical tsunamis, as shown in Figure 7. Here it is shown that the design tsunami is higher than all historical tsunamis, and moreover the design tsunami is higher than any possible future tsunamis at the site. It can be considered that uncertainties and errors can be taken into account with parametric study in the process of tsunami assessment.

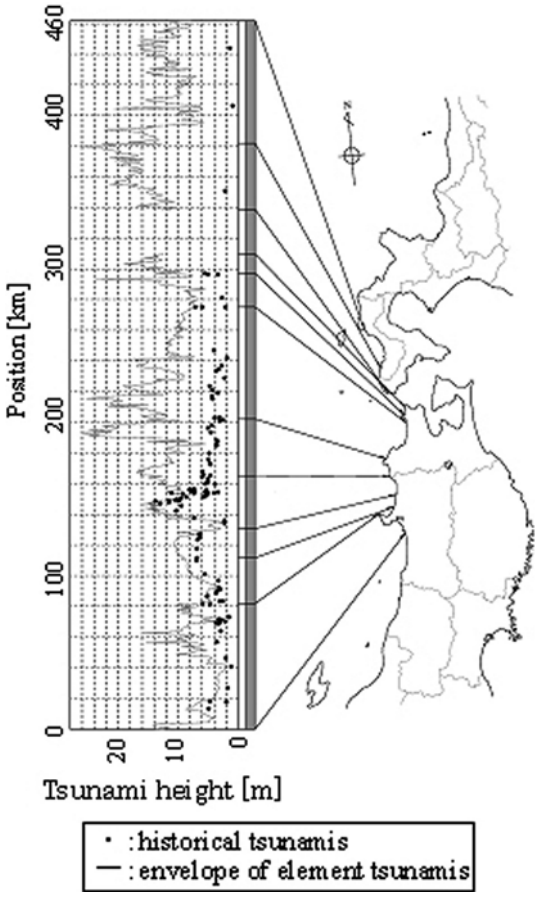


Figure 7
Results of parametric study: Eastern margin of the Sea of Japan.

## 7. Conclusions

A method of tsunami risk evaluation and assessment of design tsunamis at nuclear power facilities in the coastal area of Japan is described. Characteristics of this method are summarized as follows.

1) Uncertainties and errors of the standard fault can be taken into account in the process of tsunami assessment with parametric study of the tsunami source model.
2) The element tsunamis can be calculated by numerical simulation using the standard faults.
3) The design tsunami is selected among the element tsunamis with the greatest influence on the site.

4) The design tsunami is verified by comparison with run-up heights of historical tsunamis. To ensure the safety of coastal power facilities, the design tsunami is selected as the highest among all historical and possible future tsunamis at the site.

*Acknowledgements*

The present study is part of the research work by the Tsunami Evaluation Subcommittee (Chair: Dr. Shuto) of the Nuclear Civil Engineering Committee of the JSCE (Japan Society of Civil Engineers), which was supported by Japanese electric power companies. The authors would like to express their deepest gratitude to the members of the subcommittee.

## References

Aida, I. (1977), *Simulation of large tsunamis occurring in the past off the coast of the Sanriku District*, Report of Earthquake Research Institute, Tokyo University, Vol. 52, pp. 71–101 (in Japanese).

Goto, C. and Ogawa, Y. (1982), *Numerical calculation method using the Leapfrog Method*, Data of Civil Engin. Department, School of Engin. Tohoku University, 52 p. (in Japanese).

Hagiwara, T., *Seismicity of the Japanese Arc—Earthquake Engineering and Regional Seismicity Evaluation* (Kajima Institute Publishing Co., Tokyo 1991), 215 p. (in Japanese).

Imamura, F. (1998), *Development of tsunami numerical simulation in the latest 15 years and its future,* Kaiyou *15*, 89–98 (in Japanese).

Nuclear Safety Commission of Japan (1990), *Guideline about Safety Design for Light Water Nuclear Power Generating Facilities* (in Japanese).

Tanaka, H. (1985), *Development of mathematical models for tsunami behavior on coastal zones*, Abiko Research Laboratory Report of Central Research Institute of Electric Power Industry, No. 385017, 46 p. (in Japanese).

Tanaka, H., Takao, M., and Annaka, T. (2003), *Establishment of a tsunami assessment manual for nuclear power facilities*, IUGG2003, Abstract No.1700–047.

Tsunami Evaluation Subcommittee, Nuclear Civil Engineering Committee, Japan Society of Civil Engineers (2002), *Tsunami assessment method for nuclear power plants in Japan*, Japan Society of Civil Engineers (in Japanese). (http://www.jsce.or.jp/committee/ceofnp/Tsunami/eng/tsunami_eng.html)

Watanabe, H., *List of Damaging Japanese Tsunami,* (2nd edition) (Tokyo University Publishing 1998), 238 p. (in Japanese).

(Recevied February 17, 2006, accepted August 31, 2006)

Pure appl. geophys. 164 (2007) 577–592
0033–4553/07/030577–16
DOI 10.1007/s00024-006-0174-3



Pure and Applied Geophysics

# Logic-tree Approach for Probabilistic Tsunami Hazard Analysis and its Applications to the Japanese Coasts

Tadashi Annaka,[1] Kenji Satake,[2] Tsutomu Sakakiyama,[3]
Ken Yanagisawa,[4] and Nobuo Shuto[5]

*Abstract*—For Probabilistic Tsunami Hazard Analysis (PTHA), we propose a logic-tree approach to construct tsunami hazard curves (relationship between tsunami height and probability of exceedance) and present some examples for Japan for the purpose of quantitative assessments of tsunami risk for important coastal facilities. A hazard curve is obtained by integration over the aleatory uncertainties, and numerous hazard curves are obtained for different branches of logic-tree representing epistemic uncertainty. A PTHA consists of a tsunami source model and coastal tsunami height estimation. We developed the logic-tree models for local tsunami sources around Japan and for distant tsunami sources along the South American subduction zones. Logic-trees were made for tsunami source zones, size and frequency of tsunamigenic earthquakes, fault models, and standard error of estimated tsunami heights. Numerical simulation rather than empirical relation was used for estimating the median tsunami heights. Weights of discrete branches that represent alternative hypotheses and interpretations were determined by the questionnaire survey for tsunami and earthquake experts, whereas those representing the error of estimated value were determined on the basis of historical data. Examples of tsunami hazard curves were illustrated for the coastal sites, and uncertainty in the tsunami hazard was displayed by 5-, 16-, 50-, 84- and 95-percentile and mean hazard curves.

**Key words:** Logic-tree approach, probabilistic tsunami hazard analysis, tsunami hazard curve, epistemic uncertainty, aleatory uncertainty.

## *1. Introduction*

A probabilistic approach is necessary for evaluating tsunami hazard, because many uncertainties exist in a process of estimating coastal tsunami heights from tsunami source models. However, a probabilistic tsunami hazard analysis (PTHA) is not common (Power *et al.*, 2005; Thio *et al.*, 2005) in comparison with a

[1] Tokyo Electric Power Services Co., Ltd., 3-3, Higashi-ueno 3-chome, Taito-ku, Tokyo, 110-0015, Japan. E-mail: annaka@tepsco.co.jp
[2] Geological Survey of Japan, AIST, Site 7, 1-1-1, Higashi, Tsukuba 305-8567, Japan.
[3] Central Research Institute of Electric Power Industry, 1646, Abiko, Abiko 270-1166, Japan.
[4] Tokyo Electric Power Company, 1-3, Uchisaiwai-cho 1-chome, Chiyoda-ku, Tokyo 100-8560, Japan.
[5] Advanced Research Institute for the Sciences and Humanities, Nihon University, 12-5, Goban-cho, Chiyoda-ku, Tokyo 102-8251, Japan.

probabilistic seismic hazard analysis (PSHA). The PSHA is a methodology for estimating the probability that specified levels of earthquake ground motions will exceed at a given location in a given future time period by combining the probabilistic models of earthquake occurrence and earthquake-caused ground motion (CORNELL, 1968; WGCEP, 1995). The objective of the present study is to develop a model for PTHA in Japan based on the significant achievement in the field of the PSHA.

For developing the PTHA model in Japan, only tsunami sources induced by earthquakes are considered because most of historical tsunamis in Japan were caused by large shallow earthquakes. Other tsunami sources such as volcanogenic processes, submarine landslides, and meteorites are excluded because the probabilities of tsunami-generation are assumed to be lower than those by earthquakes and the evaluation of the probabilities is difficult.

Although an empirical attenuation equation is generally used for estimating ground motion parameters in case of the PSHA, it is very difficult to develop an empirical equation for estimating tsunami heights from a supposed tsunami source because the effects of submarine topography and coastline geometry on tsunami heights are significant. Therefore a numerical simulation based on a finite-difference method is used for estimating tsunami heights from a rectangular fault plane of a supposed tsunami source.

The result of the PTHA is represented by a tsunami hazard curve (relationship between tsunami height and probability of exceedance). For a practical engineering judgment it is more important to evaluate the uncertainty in the tsunami hazard curve rather than obtaining a 'best-estimated' hazard curve. This can be performed by a logic-tree approach (e.g., PACIFIC GAS AND ELECTRIC COMPANY, 1988). We propose a model based on the logic-tree approach to estimate tsunami hazard curves and present examples for Japan. The proposed method consists of a tsunami source model and coastal tsunami height estimation. The result of the PTHA will be used for quantitative tsunami risk assessment for important coastal facilities.

## 2. Logic-tree Approach

The logic-tree approach can be used for evaluating uncertainty in tsunami hazard. Two kinds of uncertainty, aleatory and epistemic, are generally distinguished in the PSHA (SENIOR SEISMIC HAZARD ANALYSIS COMMITTEE (SSHAC), 1997). Aleatory uncertainty is due to the random nature of earthquake occurrence and its effects. The variation in tsunami heights from earthquakes with similar source characteristics is treated as aleatory uncertainty in the same way as the variation in ground motions from earthquakes with similar magnitude, focal depth and distance. Its nature can be determined from the variation in the ratios of observed to numerically calculated tsunami heights for historical tsunami sources. Epistemic

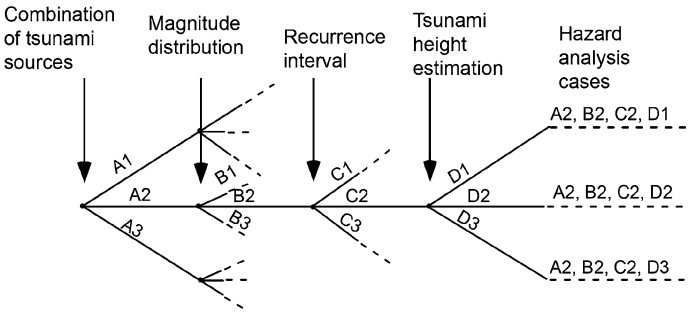


Figure 1
Outline of the logic-tree approach used in the present research. The logic-tree consists of the branches for the combination of tsunami sources, magnitude distribution of characteristic tsunamigenic earthquakes, their recurrence interval, and tsunami height estimation procedure based on a numerical simulation. Each path of the logic-tree generates a tsunami hazard curve.

uncertainty is due to incomplete knowledge and data about the earthquake process. Uncertainties in various model parameters and various alternatives about the PTHA model are treated as epistemic uncertainty. A hazard curve is obtained by integration over the aleatory uncertainties. A large number of hazard curves are obtained for different branches of logic-tree representing epistemic uncertainty.

Figure 1 shows an outline of the logic-tree approach used in the present research. The logic-tree consists of the branches for the combination of tsunami sources, magnitude distribution of characteristic tsunamigenic earthquakes, their recurrence interval, and tsunami height estimation procedure based on a numerical simulation. The logic-tree models were set up based on the principle of mutually exclusive branching, which means that if one branch is correct, the other branches are not correct. Each path of the logic-tree generates a tsunami hazard curve. Accordingly many hazard curves can be systematically obtained by the logic-tree approach.

## *3. Tsunami Source Model*

We developed the logic-tree models for local tsunami sources around Japan and for distant tsunami sources along the South American subduction zones (Fig. 2). The islands of Japan lie mainly on the Eurasia and Okhotsk plates. The Pacific and Philippine Sea plates subduct beneath the islands towards the west-northwest and northwest, respectively. The seismic activities in and around Japan are controlled by the interaction of the four plates. The tsunami source zones in Figures 2(a), (b), and (c) are mainly identified from the fault models of historical large earthquakes that generated significant tsunamis along the Japanese coasts. For distant tsunami sources, South America was selected because their impacts on the Japanese coasts are predominant among the circum-Pacific distant tsunami sources (WATANABE, 1988).

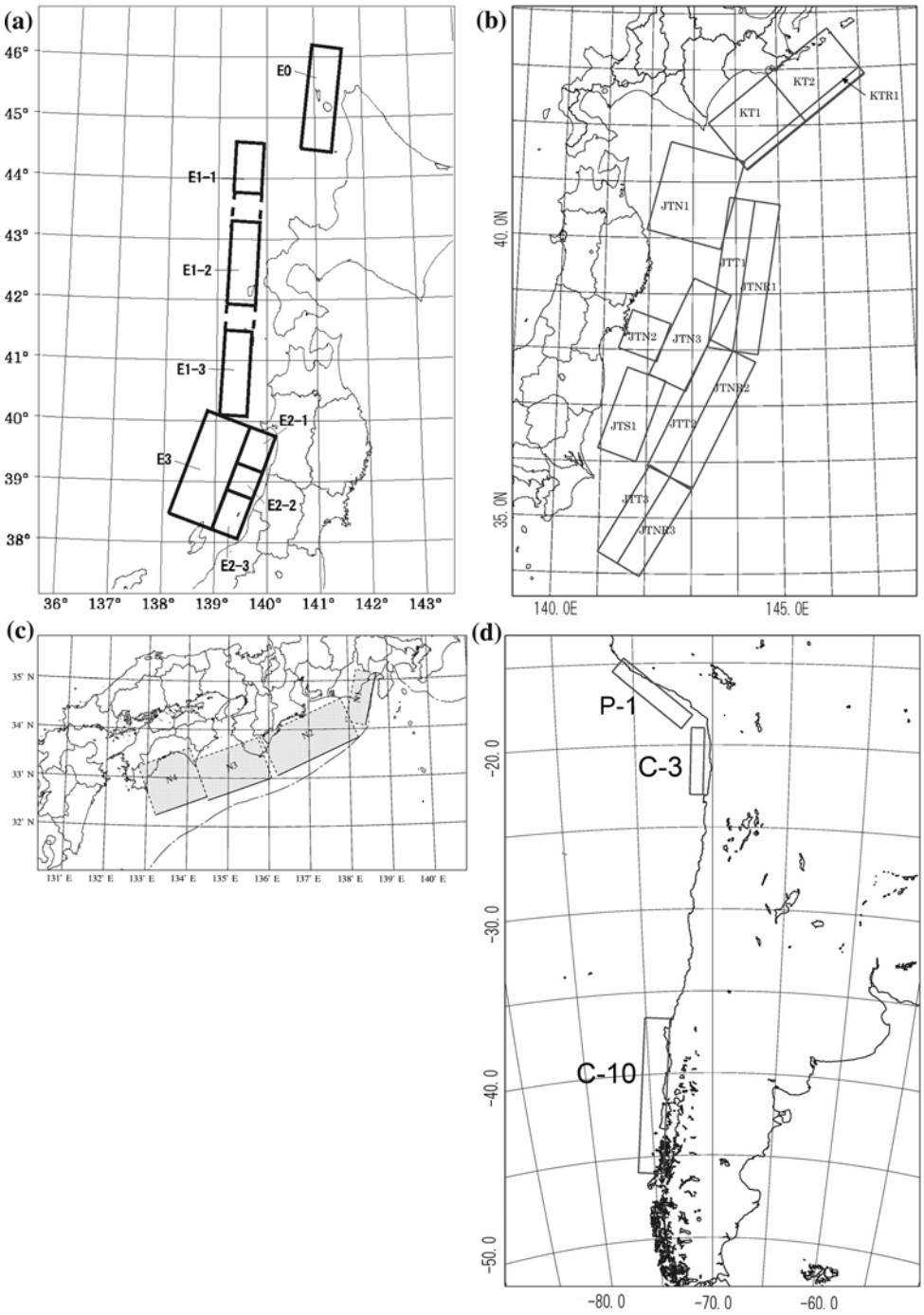
(a)
46°
45°
44°
43°
42°
41°
40°
39°
38°
E0
E1-1
E1-2
E1-3
E2-1
E2-2
E2-3
E3
36° 137° 138° 139° 140° 141° 142° 143°
(b)
KT1
KT2
KTR1
JTN1
JTT1
JTNR1
JTN2
JTN3
JTNR2
JTS1
JTT2
JTT3
JTNR3
40. 0N
35. 0N
140. 0E
145. 0E
(c)
35° N
34° N
33° N
32° N
131° E 132° E 133° E 134° E 135° E 136° E 137° E 138° E 139° E 140° E
(d)
P-1
C-3
C-10
-20. 0
-30. 0
-40. 0
-50. 0
-80. 0
-70. 0
-60. 0

◀

Figure 2

Distribution of tsunami source zones identified from historical tsunami data. (a) Tsunami source zones along the eastern margin of the Japan Sea which are the plate boundaries between the Eurasia and Okhotsk plates. (b) Tsunami source zones along the Japan and southern Kurile Trenches where the Pacific plate subducts beneath the Okhotsk plate. (c) Tsunami source zones along the Nankai Trough where the Philippine Sea plate subducts beneath the Eurasia plate. (d) Tsunami source zones along the west coast of South America where the Nazca plate subducts beneath the South American plate.

Tsunamigenic earthquakes around Japan are restricted to the large shallow earthquakes along the boundaries of the above four plates. Occurrences of these large earthquakes can be represented by a characteristic earthquake model rather than a b-value model based on a Gutenberg-Richter relationship (WESNOUSKY *et al.*, 1984). In the characteristic earthquake model, large earthquakes with a characteristic magnitude in each source zone occur periodically with a characteristic recurrence interval. The other moderate and small earthquakes, which can be represented by the b-value model, hardly generate significant tsunamis and their contributions to tsunami hazard can be neglected.

Tsunamigenic earthquakes in each tsunami source are represented by the characteristic earthquake model. The magnitude-frequency distribution of characteristic earthquakes is assumed to be uniform in a specified magnitude range (YOUNGS and COPPERSMITH, 1985). Moment magnitude ($M_W$) scale is used because it is considered to be most appropriate for tsunami generation. The width of magnitude range is assumed to be either 0.5 or 0.3 based on the variation in magnitudes of characteristic earthquakes in the past.

For evaluating two kinds of tsunami hazards, long-term stationary and instantaneous tsunami hazards, different recurrence models for earthquake occurrences were used. The long-term stationary tsunami hazard, or the average hazard for the very long-term period, is represented by the relation between tsunami height and average annual exceeding frequency of tsunami height. The annual frequency can be converted to the annual probability by assuming a Poisson process for earthquake occurrences. Instantaneous tsunami hazard, the hazard during the coming $t$ years from the present, is represented by the relation between tsunami height and the probability of exceedance during the coming $t$ years. The probabilities of earthquake occurrences during the coming $t$ years can be evaluated by a renewal model with a BPT (Brownian Passage Time) distribution (ELLSWORTH *et al.*, 1999; MATTHEWS *et al.*, 2002). The BPT distribution is considered to be most appropriate for evaluating the long-term probability of earthquake occurrence (EARTHQUAKE RESEARCH COMMITTEE, 2001) and it is in close agreement with a log-normal distribution.

The logic-tree models were made for the combination of tsunami source zones and the size and frequency of characteristic earthquakes for each zone. Some examples of branches in the logic-tree are illustrated in Figure 3. The number for

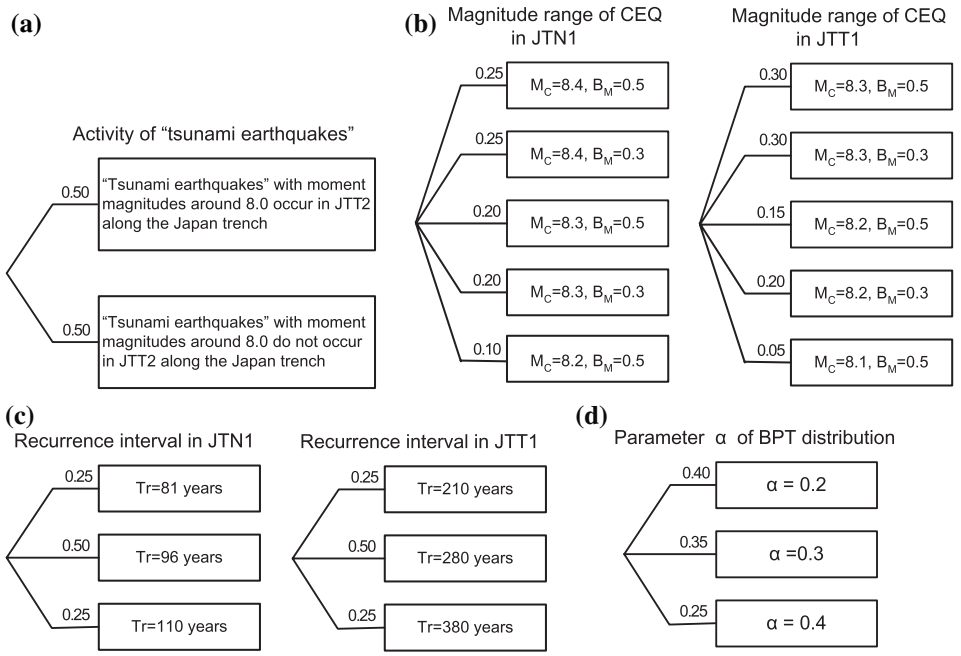


Figure 3

Examples of branches in the logic-tree used in the present research. The number for each branch denotes the weight of the branch. (a) Branches for the activity of Tsunami Earthquakes in JTT2 along the Japan Trench. (b) Branches for magnitude ranges of characteristic earthquakes (CEQ) in JTN1 and JTT1. Parameters for determining the magnitude ranges of CEQ are central magnitude ($M_C$) and magnitude bandwidth ($B_M$). Maximum moment magnitudes determined from historical tsunami data for JTN1 and JTT1 are 8.3 and 8.2, respectively. (c) Branches for average recurrence intervals in JTN1 and JTT1 along the Japan Trench. These branches were selected based on the error evaluation of the average recurrence interval from the data. Three branches are average – standard error, average, and average + standard error. (d) Branches for the value of parameter $\alpha$ for BPT (Brownian Passage Time) distribution. Parameter $\alpha$ represents the variation in recurrence intervals of characteristic earthquakes. The three branches are set on the basis of $\alpha$ values estimated from historical data in Japan.

each branch denotes the weight of the branch. Weights of discrete branches that represent alternative hypotheses and interpretations were determined by the questionnaire survey of tsunami and earthquake experts (maximum 35), whereas those that represent the error of estimated value were determined based on the error evaluation.

Figure 3(a) represents the branches for the activity of ''tsunami earthquakes'' along the Japan Trench. ''Tsunami earthquakes'' are those earthquakes that produce much larger tsunamis than expected from seismic waves (KANAMORI, 1972). The effect of ''tsunami earthquakes'' on tsunami hazard is significant. The mechanisms and locations of ''tsunami earthquakes'' are still controversial; some propose that ''tsunami earthquakes'' occur at particular locations of subduction zones, while

others argue that they can occur anywhere near trenches (SATAKE and TANIOKA, 1999; SENO, 2002). The 1896 Sanriku "tsunami earthquake" (TANIOKA and SATAKE, 1996) occurred in JTT1, and the 1677 Boso "tsunami earthquake" (ABE, 1999; ISHIBASHI, 2003) occurred in JTT3 (Fig. 2(b)). Historically, no "tsunami earthquakes" have occurred in JTT2. Two alternative hypotheses are selected; one is that "tsunami earthquakes" occur in JTT2, and the other is that "tsunami earthquakes" do not occur in JTT2.

Figure 3(b) represents the branches for magnitude range of characteristic earthquakes. In our model, the parameters for determining the magnitude ranges of characteristic earthquakes are central magnitude ($M_C$) and magnitude band-width ($B_M$). One of the five alternatives will be proved correct in future. The bandwidth for the magnitude range is either 0.3 ($M_C \pm 0.1$) or 0.5 ($M_C \pm 0.2$) around the central magnitude. The central magnitudes were selected based on the maximum moment magnitude ($M_w$) of historical tsunamigenic earthquakes in the source zone. The maximum $M_w$ for JTN1 and JTT1 are 8.3 and 8.2, respectively. The maximum $M_w$ was determined from a fault model that numerically produces coastal tsunami heights compatible with the historical tsunami run-up data. This type of branch was applied for all source zones.

Figure 3(c) represents the branches for the average recurrence interval in JTN1 and JTT1 (Fig. 2(b)). These branches were selected based on the error evaluation of the average recurrence interval from the data assuming the log-normal distribution of recurrence intervals. Four characteristic earthquakes have occurred in JTN1 in 1677, 1763, 1856 and 1968 and two characteristic earthquakes have occurred in JTT1 in 1611 and 1896 (USAMI, 2002; EARTHQUAKE RESEARCH COMMITTEE, 2002). The average recurrence intervals estimated from the data for JTN1 and JTT1 are about 96 and 280 years, respectively. Three branches were set to correspond to average – standard error, average, and average + standard error.

Figure 3(d) represents the branches for parameter $\alpha$ of the BPT distribution. Parameter $\alpha$ represents the variation in recurrence intervals of characteristic earthquakes. The three branches are set on the basis of $\alpha$ values estimated from historical data in Japan (EARTHQUAKE RESEARCH COMMITTEE, 2001). The $\alpha$ values were estimated from about 0.2 to about 0.4.

## *4. Tsunami Height Estimation Model*

Numerical simulation rather than empirical relation is used for estimating the median tsunami heights. Fault models used for numerical simulation are determined by scaling relations from the optimal fault models of the historical tsunamigenic earthquakes (KANAMORI and ANDERSON, 1975; TAKEMURA, 1998). The optimal models used as a reference for scaling relations along the Japan and southern Kurile Trenches are shown in Table 1. The optimal fault models were determined by

Table 1

*Optimal fault models for historical tsunamigenic earthquakes*

| Zone | L (km) | W (km) | D (m) | $\delta$ (°) | $\lambda$ (°) | $M_W$ | Year (A.D.) |
|---|---|---|---|---|---|---|---|
| KT1 | 130 | 100 | 3.5 | 20 | 115 | 8.2 | 1952 |
| KT2 | 60 | 100 | 2.2 | 27 | 115 | 7.8 | 1973 |
| JTN1 | 150 | 100 | 6.0 | 20 | 80 | 8.4 | 1968 |
| JTN2 | 26 | 65 | 2.0 | 20 | 85 | 7.5 | 1978 |
| JTN3 | 210 | 70 | 4.0 | 15 | 85 | 8.2 | 1793 |
| JTS1 | 100 | 60 | 2.3 | 10 | 85 | 7.8 | 1938 |
| JTT1 | 210 | 50 | 9.7 | 20 | 75 | 8.3 | 1896 |
| JTT3 | 200 | 50 | 6.5 | 20 | 95 | 8.2 | 1677 |
| JTNR1 | 185 | 50 | 6.6 | 45 | 270 | 8.4 | 1933 |

L: fault length, W: fault width, D: average slip, $\delta$: dip angle, $\lambda$: slip angle, $M_W$: moment magnitude.

numerical tsunami simulation so that the calculated tsunami heights are best fitted to the observed tsunami heights (YANAGISAWA *et al.*, 2007).

The logic-tree for tsunami height estimation is shown in Figure 4. Two models, the unique fault model and the variable fault model, are used for numerical simulation. The difference of the two models is whether the fault parameters for the magnitude and the same location are uniquely assigned (unique model) or whether variability of fault parameters exists (variable fault model). For the unique fault model, a reference fault model is used for a given location and magnitude, assuming that all the fault parameters are uniquely estimated and there is no variability. For the variable fault model, on the other hand, multiple fault models with variable parameters such as fault strike are used, assuming that the variability of fault models actually exists.

The distribution of tsunami heights around the median value is assumed to be log-normal based on the previous research on the distribution of the ratios between observed and numerically calculated tsunami heights (e.g., AIDA, 1978). The variance parameter $\beta$, standard deviation of log-normal distribution, is related with $\kappa$, an error factor often referred to as Aida's $\kappa$ in Japan, as $\kappa = \exp(\beta)$ (AIDA, 1978). While parameter $\beta$ is introduced for taking account of the aleatory uncertainty of tsunami heights, the value of $\beta$ is treated as epistemic uncertainty. Four values are selected as the branches for $\beta$. The three branches ($\kappa = 1.35, 1.45,$ and$1.55$) are selected based on the $\kappa$ data determined from a numerical simulation for the optimal fault models of eleven tsunamigenic earthquakes with many historical run-up data based on ergodic hypothesis. The $\kappa$ values determined in this study are shown in Table 2. The value of $\kappa$ ranges from 1.35 to 1.60. The branch of $\kappa = 1.25$ is introduced by considering the possibility that ergodic hypothesis is not true. The log-normal distribution is truncated at either $\pm 2.3\beta$ or $\pm 10\beta$ (actually no truncation). These two branches are selected as extremes.

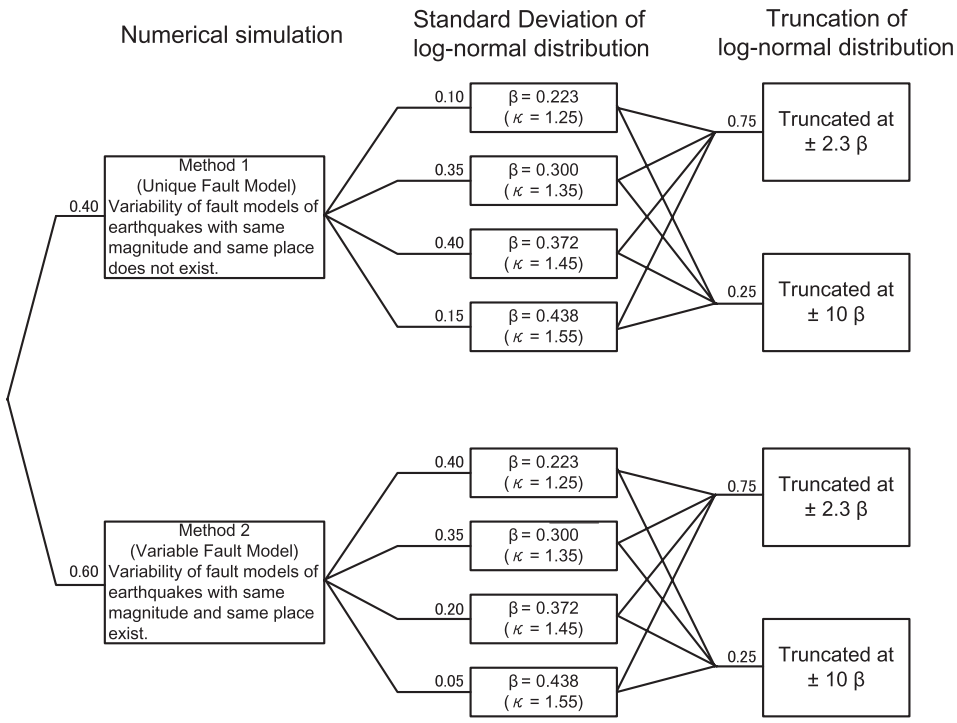


Figure 4
Logic-tree for tsunami height estimation. Two models, the unique fault model and variable fault model, are used for numerical simulation. The difference of the two models is whether the variability of fault models of earthquakes with the same magnitude and the same place exists or not. Variance parameter $\beta$, or standard deviation of log-normal distribution, is introduced for consideration of the aleatory uncertainty of tsunami heights. But the value of $\beta$ is treated as epistemic uncertainty. The log-normal distribution is truncated at either $\pm 2.3\beta$ or $\pm 10\beta$ (actually no truncation). These two branches are selected as extremes.

## 5. Tsunami Hazard Calculation

By combining the tsunami source model and the tsunami height estimation above, we calculate tsunami hazard curves. Both long-term stationary tsunami hazard and instantaneous tsunami hazard are evaluated.

For evaluating long-term stationary tsunami hazard, the annual frequency $\lambda$ of tsunami heights exceeding $h$ is written as

$$\lambda = \sum_{k=1}^{n} v_k p_k \qquad [H \geq h | \text{one tsunami}],$$

where $v_k$ is the annual frequency of tsunamis evaluated from the mean recurrence interval in zone $k$ and $p_k$ $[H \geq h | \text{one tsunami}]$ is the probability exceeding one

Table 2

*Values of κ and β for 11 historical tsunamigenic earthquakes*

| Name | Number of run-up data | $\kappa$ | $\beta$ |
|---|---|---|---|
| 1707 Hoei | 61 | 1.35 | 0.300 |
| 1854Ansei Tokai | 89 | 1.47 | 0.385 |
| 1854 Ansei Nankai | 60 | 1.42 | 0.351 |
| 1896 Meiji Sanriku | 257 | 1.45 | 0.372 |
| 1933 Showa Sanriku | 572 | 1.40 | 0.336 |
| 1944 Tonankai | 43 | 1.58 | 0.457 |
| 1946 Nankaido | 159 | 1.60 | 0.470 |
| 1960 Chile | 764 | 1.37 | 0.315 |
| 1968 Tokachi-oki | 273 | 1.41 | 0.344 |
| 1983 Nihonkai-chubu | 209 | 1.48 | 0.392 |
| 1993 Hokkaido-nansei-oki | 216 | 1.47 | 0.385 |

tsunami in zone $k$. Assuming the Poisson process, the exceeding probability during $t$ years can be written as

$$p\ [H \geq h; t] = 1 - \exp(-\lambda t).$$

For evaluating instantaneous tsunami hazard, recurrence of a tsunami is principally modeled by using the renewal process (BPT model). But the Poisson process is used for a zone where the repetition of characteristic earthquakes is undefined. For zone $k$ modeled by the BPT distribution, the exceeding probability during $t$ years is written as

$$p_k[H \geq h; t] = 1 - \sum_{n=0}^{\infty} P_k[n; t](1 - P[H \geq h|\text{one tsunami}])^n$$

where $P_k[n, t]$ is the probability that $n$ tsunamis occur during $t$ years and $P[H \geq h|\text{one tsunami}]$ is the probability exceeding one tsunami in zone $k$. The exceeding probability during $t$ years for all the zones modeled by the BPT distribution can be obtained by

$$p_C[H \geq h; t] = 1 - \prod_k (1 - p_k[H \geq h; t]).$$

The exceeding probability during $t$ years for all the zones modeled by the Poisson process can be written by the annual frequency $\lambda_B$ of tsunami heights exceeding $h$ as

$$p_B[H \geq h; t] = 1 - \exp(-\lambda_B t).$$

Total exceeding probability during $t$ years can be obtained combining the above two results as follows:

$$p[H \geq h; t] = 1 - (1 - p_C[H \geq h; t])(1 - p_B[H \geq h; t]).$$

In the logic-tree approach, a tsunami hazard curve is obtained for each path of the logic-tree. Then the total number of tsunami hazard curves that can be calculated is equal to that of all paths in the logic-tree. Uncertainty in the tsunami hazard can be displayed by fractile hazard curves.

Figure 5 schematically shows the process for obtaining fractile hazard curves. Figure 5(a) shows the composite of 72 tsunami hazard curves obtained for one tsunami source by the logic-tree. The scatter of the hazard curves was caused mainly

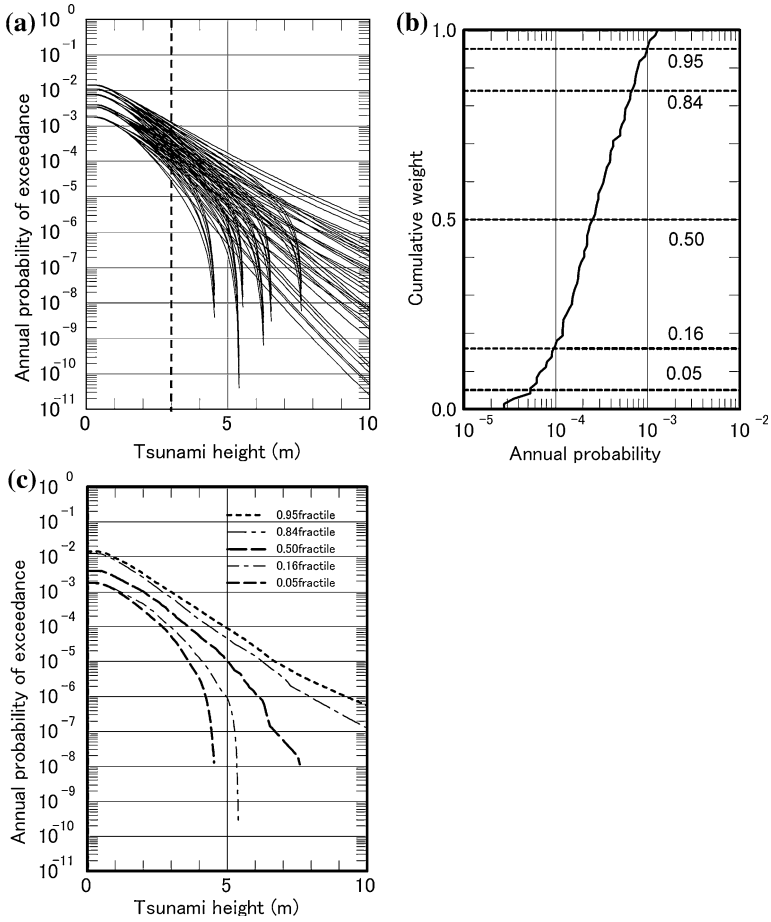


Figure 5

Process for obtaining fractile hazard curves. (a) Distribution of 72 tsunami hazard curves obtained for one tsunami source by the logic-tree. The vertical broken line indicates a tsunami height of 3 m, along which the cumulative weight curve in (b) is calculated. (b) Relationship between annual probability and cumulative weights at a tsunami height of 3.0 m. Dashed horizontal lines indicate five fractile levels (0.05, 0.16, 0.50, 0.84 and 0.95) that will be used to draw curves in (c). (c) Fractile hazard curves obtained by connecting the probabilities with the same fractile values for different tsunami heights. Five fractile values from 0.05 to 0.95 shown here are usually used.

Figure 6 ▶

Examples of the results by probabilistic tsunami hazard analysis. (a) Location of the site (Yamada in Iwate prefecture) and the numerical calculation area. Horizontal and vertical axes are grid numbers in I and J directions, respectively. Rectangles with numbers represent areas where finer-grids are adopted. Grid intervals are changed from 4320 m to 240 m. Bathymetry contours for determining grid partition are 120 m, 1080 m, and 4320 m. (b) Long-term stationary fractile and mean hazard curves obtained from local and distant tsunami sources for Yamada. Mean and five curves for fractile levels between 0.05 and 0.95 are shown. The horizontal and vertical broken lines denote the probability level corresponding to 400 years (the length of available historical data) and 7 m (maximum historical run-up height), respectively. (c) the same as (b) except that only distant tsunami sources are considered. (d) Comparison of fractile hazard curves between the long-term stationary (thin curves) and the instantaneous tsunami hazards for 50 years (thick curves) at Yamada. Only three levels of fractiles are shown here.

by the branches for $\beta$ in Figure 4. The effect of $\beta$ on tsunami hazard is significant, especially in the lower probability level. The weight of each hazard curve is given by the product of the weights of all branches in the path. Figure 5(b) shows the relationship between annual probability and cumulative weights at a tsunami height of 3.0 m. The cumulative weight curve can be obtained by summing the weights of tsunami hazard curves from lower probability to higher probability along the section of 3.0 m in Figure 5(a). Fractile values from 0.05 to 0.95 shown here are usually used in the PSHA. The probability level for each fractile value can be determined by the cumulative weight curve. By connecting the probabilities with the same fractile value for different tsunami heights, the fractile hazard curves can be obtained as shown in Figure 5(c). If the number of hazard analysis cases in the logic-tree becomes very large, over ten million, a Monte Carlo approach can be used to simulate a distribution of tsunami hazard curves (e.g., CRAMER *et al.*, 1996).

Tsunami heights along the coast are affected by a tidal stage at tsunami arrival. Therefore it is necessary to allow for variation of tidal stage in the PTHA. Variation of tidal stage can be incorporated into the calculation by the convolution of tsunami height distribution. Variation of tidal stage, the probabilistic density distribution of tidal stage, can be determined from observed sea-level data.

## 6. Examples of Tsunami Hazard Curves

As a demonstration of the proposed model, tsunami hazard curves were evaluated for a coastal site as shown in Figure 6. Uncertainty in the tsunami hazard was displayed by 0.05-, 0.16-, 0.50-, 0.84- and 0.95-fractile and mean hazard curves.

The location of the site (Yamada in Iwate prefecture) and the numerical calculation area are shown in Figure 6(a). The nine local tsunami source zones, JTN1, JTN2, JTN3, JTT1, JTT2, JTT3, JTNR1, JTNR2, and JTNR3, and the three distant tsunami source zones, C-3, C-10, and P-1, were considered. For distant tsunami sources, input tsunami waves at the open sea boundary were calculated from

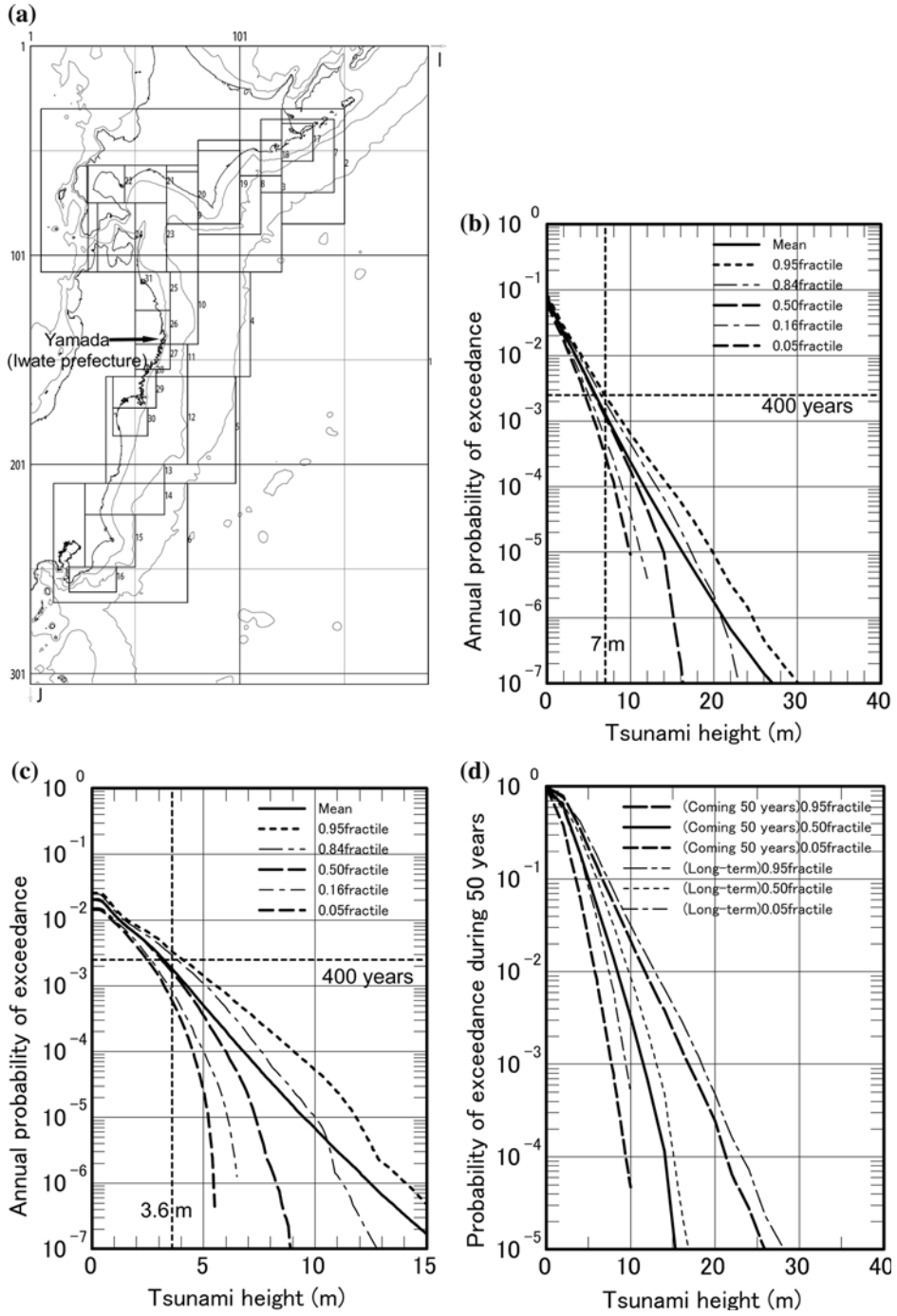
(a)
Yamada
(Iwate prefecture)
(b)
Annual probability of exceedance
Mean
0.95fractile
0.84fractile
0.50fractile
0.16fractile
0.05fractile
400 years
7 m
Tsunami height (m)
(c)
Annual probability of exceedance
Mean
0.95fractile
0.84fractile
0.50fractile
0.16fractile
0.05fractile
400 years
3.6 m
Tsunami height (m)
(d)
Probability of exceedance during 50 years
(Coming 50 years)0.95fractile
(Coming 50 years)0.50fractile
(Coming 50 years)0.05fractile
(Long-term)0.95fractile
(Long-term)0.50fractile
(Long-term)0.05fractile
Tsunami height (m)

the numerical simulation of the tsunami propagation over the Pacific Ocean. The numerical tsunami simulation cases for local and distant tsunami sources were 540 and 75, respectively.

The long-term stationary fractile and mean hazard curves obtained from local and distant tsunami sources for Yamada are shown in Figure 6(b) and those obtained from distant tsunami sources only are shown in Figure 6(c). The Monte-Carlo approach was used for the local tsunami sources because the number of hazard analysis cases in the logic-tree becomes about ten billion. The recorded maximum run-up heights for local and distant tsunamis during the recent roundly 400 years are about 7 m and 3.6 m, respectively. The horizontal and vertical broken lines in Figures 6(b) and (c) denote the probability level corresponding to 400 years and the recorded maximum run-up height, respectively. The intersection points of the horizontal and vertical broken lines for Figures 6(b) and (c) lie near 0.95-fractile and 0.84-fractile lines, respectively. These results of comparison can be recognized considering that the maximum-scale tsunamigenic earthquakes in the source zones, the 1611 Keicho Sanriku and 1960 Chilean earthquakes, occurred during the 400 years and it suggests that the obtained fractile hazard curves are reasonable.

Comparison of fractile hazard curves between the long-term stationary and the instantaneous tsunami hazards for 50 years is shown in Figure 6(d). The probability levels for the coming 50 years are lower than those for the long-term mean. This result is plausible because the two large tsunamigenic earthquakes, the 1896 Meiji Sanriku and 1933 Showa Sanriku earthquakes, along the Japan Trench occurred recently in their recurrence intervals.

## *7. Conclusions*

In the present study, we made an effort to prepare a probabilistic tsunami hazard analysis model for important coastal facilities in Japan by constructing the logic-trees for tsunami sources induced by earthquakes and coastal tsunami height estimation.

Tsunami sources were identified for three local tsunami areas around Japan and one distant tsunami area off the west coast of South America. A characteristic earthquake model, whose magnitude-frequency distribution is assumed to be uniform in a specified magnitude range, is applicable for tsunami sources.

Uncertainties in activities of tsunami sources and those in model parameters of characteristic earthquakes in each source, such as magnitude band-width, central magnitude, and mean and variation of recurrence intervals, were represented by the logic-tree format. Weights of discrete branches were determined either by the questionnaire survey of tsunami and earthquake experts or by the error evaluation. The determination of the weights by the questionnaire survey is tentative and the

manner in which expert opinions are elicited and interpreted should be selected more carefully in case of assessing tsunami hazard for a specified important facility.

The logic-tree for tsunami height estimation based on numerical simulation using a fault model was also constructed. The variance parameter $\beta$, standard deviation of log-normal distribution, is introduced for taking account of the aleatory uncertainty of tsunami heights. However, uncertainty in the value of $\beta$ is treated as epistemic uncertainty. The effect of $\beta$ on tsunami hazard is significant. Therefore it is very important to investigate the nature of $\beta$.

As a demonstration, tsunami hazard curves were evaluated for a coastal site, Yamada in Iwate prefecture. The results are considered plausible and reasonable judging from the comparison with the recorded maximum run-up heights for local and distant tsunamis during the recent approximately 400 years.

## *Acknowledgements*

The present study is the result of activity by the Tsunami Evaluation Subcommittee (Chair person: Dr. Shuto) of the Nuclear Civil Engineering Committee in the Japan Society of Civil Engineers, which was supported by Japanese electric power companies. We would like to express our deepest gratitude to the members of the subcommittee.

## References

ABE, K. (1999), *Quantification of historical tsunamis by the Mt scale*, Zisin, ser. 2, *52*, 369–377 (in Japanese).

AIDA, I. (1978), *Reliability of a tsunami source model derived from fault parameters*, J. Physics Earth *26*, 57–73.

CORNELL, C.A. (1968), *Engineering seismic risk analysis*, Bull. Seismol. Soc. Am. *58*, 1583–1606.

CRAMER, C.H., PETERSEN, M.D. and REICHLE, M.S. (1996), *A Monte Carlo approach in estimating uncertainty for a seismic hazard assessment of Los Angeles, Ventura and Orange Counties, California*, Bull. Seismol. Soc. Am. *86*, 1681–1691.

EARTHQUAKE RESEARCH COMMITTEE, *Regarding Methods for Evaluating Long-term Probability of Earthquake Occurrence* (Publications of Earthquake Research Committee for 2000, 2001), pp. 511–590 (in Japanese).

EARTHQUAKE RESEARCH COMMITTEE, *Long-term Evaluation of Seismicity along the Japan Trench from off Sanriku to off Boso* (Publications of Earthquake Research Committee for 2001, 2002), pp. 541–604 (in Japanese).

ELLSWORTH, W.L., MATTHEWS, M.V., NADEAU, R.M., NISHENKO, S.P., REASENBERG, P.A., and SIMPSON, R.W., *A Physically-based Earthquake Recurrence Model for Estimation of Long-term Earthquake Probabilities* (Workshop on Earthquake Recurrence: State of the Art and Directions for the Future, Istituto Nazionale de Geofisica, Rome, Italy, 22–25 February, 1999).

ISHIBASHI, K. (2003), *The 1677 Empo off Boso tsunami earthquake studied from historical documents*, Chikyu Monthly *25*, 382–388 (in Japanese).

KANAMORI, H. (1972), *Mechanism of tsunami earthquakes*, Phys. Earth Planet. Inter. *6*, 246–259.

KANAMORI, H. and ANDERSON, D.L. (1975), *Theoretical basis of some empirical relations in seismology*, Bull. Seismol. Soc. Am. *65*, 1073–1095.

MATTHEWS, M.V., ELLSWORTH, W.L., and REASENBERG, P.A. (2002), *A Brownian model for recurrent earthquakes*, Bull. Seismol. Soc. Am. *92*, 2233–2250.

PACIFIC GAS AND ELECTRIC COMPANY, *Final Report of the Diablo Canyon Long-Term Seismic Program* (U.S. Nuclear Regulatory Commission, 1988), 50–275 and 50–323.

POWER, W.L., DOWNES, G.L., and STIRLING, M (2005), *Estimating the tsunami hazard in New Zealand from earthquakes on the interface of the South American and Nazca Plates*, abstract for International Workshop *Tsunami hazard Mitigation and Risk Assessment* (submitted to Pure Appl. Geophys.).

SATAKE, K. and TANIOKA, Y. (1999), *Source of tsunami and tsunamigenic earthquakes in subduction zones*, Pure Appl. Geophys. *154*, 467–483.

SENIOR SEISMIC HAZARD ANALYSIS COMMITTEE (SSHAC), *Recommendations for Probabilistic Seismic Hazard Analysis: Guidance on Uncertainty and Use of Experts* (U.S. Nuclear Regulatory Commission, NUREG/CR-6372, Washington, DC., 1997).

SENO, T. (2002), *Tsunami earthquakes as transient phenomena*, Geophys. Res. Lett. *29*, doi: 10.10129/2002GL014868.

TAKEMURA, M. (1998), *Scaling law for Japanese intraplate earthquakes in special relations to the surface faults and damages,* Zisin, ser. 2, *51*, 211–228 (in Japanese).

TANIOKA, Y. and SATAKE, K. (1996), *Fault parameters of the 1896 Sanriku tsunami earthquake estimated from tsunami numerical modeling*, Geophys. Res. Lett. *23*, 1549–1552.

THIO, H.K., ICHINOSE, G., and SOMERVILLE, P. (2005), *Probabilistic tsunami hazard analysis*, IASPEI 2005, abstract Mo. 636.

USAMI, T., *Historical earthquakes in Japan,* In *International Handbook of Earthquake and Engineering Seismology* (eds. Lee, W.H.K., Kanamori, H., Jennings, P.C. and Kisslinger, C.), pp. 799–802 (Academic Press, 2002).

WATANABE, H., *Comprehensive List of Tsunamis to Hit the Japanese Islands* (2nd ed.), (Univ. Tokyo Press, 1988).

WESNOUSKY, S.G., SCHOLZ, C.H., SHIMAZAKI, K., and MATSUDA, T. (1984), *Integration of geological and seismological data for the analysis of seismic hazard: A case study of Japan*, Bull. Seismol. Soc. Am. *74*, 687–708.

WGCEP (WORKING GROUP ON CALIFORNIA EARTHQUAKE PROBABILITIES) (1995). *Seismic hazards in southern California: Probable earthquakes, 1994 to 2024,* Bull. Seismol. Soc. Am. *85*, 379–439.

YANAGISAWA, K., IMAMURA, F., SAKAKIYAMA, T., ANNAKA, T., TAKEDA, T., and SHUTO, N. (2007), *Tsunami Assessment Method for Nuclear Power Facilities in Japan*, Pure. Appl. Geophys. this volume.

YOUNGS, R.R. and COPPERSMITH, K.J. (1985), *Implications of fault slip rates and earthquake recurrence models to probabilistic seismic hazard estimates*, Bull. Seismol. Soc. Am. *75*, 939–964.

(Received January 31, 2006, accepted August 17, 2006)

Pure appl. geophys. 164 (2007) 593–603
0033–4553/07/030593–11
DOI 10.1007/s00024-006-0170-7



Pure and Applied Geophysics

# Conditional Probability Approach of the Assessment of Tsunami Potential: Application in Three Tsunamigenic Regions of the Pacific Ocean

K. Orfanogiannaki and G. A. Papadopoulos

*Abstract*—We develop stochastic approaches to determine the potential for tsunami generation from earthquakes by combining two interrelated time series, one for the earthquake events, and another for the tsunami events. Conditional probabilities for the occurrence of tsunamis as a function of time are calculated by assuming that the inter-arrival times of the past events are lognormally distributed and by taking into account the time of occurrence of the last event in the time series. An alternative approach is based on the total probabilitiy theorem. Then, the probability for the tsunami occurrence equals the product of the ratio, $r$ (= tsunami generating earthquakes/total number of earthquakes) by the conditional probability for the occurrence of the next earthquake in the zone. The probabilities obtained by the total probability theorem are bounded upwards by the ratio $r$ and, therefore, they are not comparable with the conditional probabilities. The two methods were successfully tested in three characteristic seismic zones of the Pacific Ocean: South America, Kuril-Kamchatka and Japan. For time intervals of about 20 years and over the probabilities exceed 0.50 in the three zones. It has been found that the results depend on the approach applied. In fact, the conditional probabilities of tsunami occurrence in Japan are slightly higher than in the South America region and in Kuril-Kamchatka they are clearly lower than in South America. Probabilities calculated by the total probability theorem are systematically higher in South America than in Japan while in Kuril-Kamchatka they are significantly lower than in Japan. The stochastic techniques tested in this paper are promising for the tsunami potential assessment in other tsunamigenic regions of the world.

**Key words:** Tsunami potential, stochastic approaches, Pacific Ocean.

## *Introduction*

The stochastic forecasting of strong tsunami occurrences in tsunamigenic seismic zones is of great importance for the development of reliable tsunami hazard assessment and risk mitigation strategies. However, no standard methodologies have been developed so far to forecast tsunami occurrences. Nevertheless, some statistical and probabilistic methods have been proposed and two main types of approaches can be recognized. The first focuses on the estimation of the recurrence of tsunami

Institute of Geodynamics, National Observatory of Athens, 11810 Athens, Greece.
E-mails: korfanogiannaki@freemail.gr; g.papad@gein.noa.gr

wave generation in particular tsunamigenic sources or zones. A classic effort of this type was presented by SOLOVIEV (1970) for the tsunami recurrence in the Pacific in terms of statistical parameters and probabilities based on relations of magnitude-frequency for earthquakes and tsunamis. The magnitude-frequency statistics for earthquakes combined with the conversion of earthquake occurrence estimates in tsunami probabilities was introduced by TINTI (1993) for the tsunami hazard assessment in Italy. The tsunami intensity-frequency statistics was used by PAPADOPOULOS (2003) to calculate mean recurrence and probabilities of occurrence of tsunamis of different intensity levels in the Corinth Gulf, Greece.

The second type of approach emphasizes the estimation of the recurrence of tsunami wave height in particular coastal sites. LIN and TUNG (1982) combined seismological and hydrodynamic models and analyzed tsunami hazard as the probability of the event that the water elevation at a site exceeds an arbitrary but specified level. Similarly, combining the wave height estimate from a numerical experiment with the probability evaluation of tsunami occurrence in Japan, RIKITAKE and AIDA (1988) evaluated probabilities of a site being hit by a tsunami, of which the wave height exceeds certain levels. According to GO *et al.* (1985), tsunami recurrence for tsunami hazard assessment is described by two parameters: Frequency of occurrence of large tsunamis and coefficient of wave amplification near the shore. The joint probability method was applied by several authors (e.g., SANCHEZ and FARRERAS, 1987; RABINOVICH *et al.*, 1992) for the calculation of expected runup height due to tsunamis and other rapid sea-level changes, like astronomical tides and storm surges.

Very recently, GEIST and PARSONS (2006) developed probabilistic tsunami hazard analysis (PTHA) from the standpoint of integrating computational methods with empirical analysis of past tsunami runup. PTHA is derived from probabilistic seismic hazard analysis, with the main difference being that PTHA must account for far-field sources.

In this paper we introduce the concept of *tsunami potential* which is defined as the probability for the generation of one or more tsunami waves, of a prescribed magnitude or intensity range, in a particular tsunamigenic zone within a particular time window. This definition implies that the approach developed here is of the first type since it does not describe probabilities of tsunami occurrence in coastal sites but probabilities for tsunami generation in tsunami sources. The definition of tsunami potential proposed here is similar to that introduced by NISHENKO (1985) for seismic potential.

## *Methodology*

Postulate that in a seismic zone one or more seismic sources are capable of producing tsunamis and that the tsunami generation in the zone is a point process in time. Subsequently, the tsunami potential of the zone could be approached by

considering a probability model for the tsunami generation process in time. As explained in the introductory section, however, such an approach is not new. On the other hand, the calculation of the tsunami probability depends on the data completeness. For very strong events the tsunami catalogues may be complete for the last 100 years or more. However, for strong or moderate tsunamis the catalogues are complete only for the last few decades, which implies that the number of tsunami events available is relatively low, even in the most active seismic zones of the Pacific Ocean, and that the assessment of tsunami potential in probabilistic terms may suffer from reduced reliability. In addition, a hiatus in the high magnitude tsunamis has been observed at least in some regions, like in Sanriku, NE Japan (ADAMS, 1972a,b), which implies that in the existing catalogues the number of high magnitude tsunamis is underestimated due to long repeat time.

To overcome these difficulties of tsunami statistics for the assessment of tsunami potential one may rely on earthquake statistics and calculate the probability that the next earthquake in the zone, whenever it occurs, will be a tsunamigenic one. This implies that the calculation of probabilities is based on the earthquake time series. Tsunami catalogues possibly are more complete than the earthquake catalogues in the last 100 years or so although the total number of events inserted in the complete parts of the catalogues is certainly higher in the earthquake catalogues than in the tsunami catalogues. This is because only a fraction of earthquakes is tsunamigenic.

For the application of probabilistic approaches we implement the total probability theorem, hereafter called TPT for reasons of brevity, combined with a model of conditional probabilities. It is assumed that tsunami generation due to non-seismic sources in the zone, like landslides or earth slumps, is negligible, that is tsunamis are produced only by earthquakes.

Let $E$, $E^c$ be a partition of the sample space $\Omega$, where $E$ is an earthquake event and $E^c$ is the complementary event of $E$. Then, according to TPT the probability, $P(T)$, of occurrence of a tsunami event $T$ becomes

$$P(T) = P(E) \cdot P(T|E) + P(E^c) \cdot P(T|E^c), \tag{1}$$

where $P(T/E) = r$ is the ratio of tsunami generating earthquakes over the total number of earthquakes, and $P(E^c)$ is the probability of tsunami occurrence, given that no earthquake has occurred. $P(T/E^c)$, however, equals zero since the assumption has been made that only earthquakes and no other causes generate tsunami waves in the zone. As a consequence the expression (1) is reduced to

$$P(T) = r \cdot P(E), \tag{2}$$

which is the probability of tsunami generation in association with the next earthquake $E$ in the zone; $P(E)$ is the probability for the occurrence of the next earthquake within time interval from $t_0$ to $t_0 + t$. Probability $P(E)$ becomes simple Poissonian by assuming that the time distribution of earthquakes in the zone is random. The random model implies that the probability for the occurrence of an

earthquake is independent of the time of occurrence of the last earthquake. However, other probability models could be adopted as well. We selected to follow the model of conditional probability for the earthquake occurrence as it was introduced by the WORKING GROUP ON CALIFORNIA EARTHQUAKE PROBABILITIES (1988). This model introduces some memory in the system by means of considering the time elapsed since the last earthquake occurrence in the zone.

The assumption is made that the interarrival time, $\tau$, of successive earthquake events follows a lognormal distribution, that is log $\tau$, is distributed normally. The probability density function of $\tau$ is

$$f(\tau) = \frac{1}{\sqrt{2\pi\sigma\tau}} \exp\left[-(\ln \tau - \mu)^2 / 2\sigma^2\right], \tag{3}$$

where $\mu$ = mean of ln $\tau$, $\sigma$ = standard deviation of ln $\tau$. The probability that the recurrence interval is shorter than $\tau$ is

$$F(\tau) = \int_0^{\tau} f(\tau')\, \tilde{d}\tau'. \tag{4}$$

The conditional probability that the next earthquake will occur within the time interval from $t_0$ to $t_0 + t$ equals to

$$P(E_c) = \frac{F(t_0 + t) - F(t_0)}{1 - F(t_0)}. \tag{5}$$

From equation (5) one may calculate the conditional probability, $P(E_c)$, to observe one earthquake, *Eq1*, in a time interval from $t_0$ to $t_0 + t$ under the condition that no earthquake occurred after the last earthquake event, *Eq0*, in the seismic zone; where $t_0$ is a prescribed date after the occurrence of the last event. Then inserting $P(E_c)$ in formula (2) we get the probability, $P(T)$, for the next earthquake to generate a tsunami. In this approach the probability for more than one earthquake event can be calculated. However, for reasons of simplicity one may consider that the calculation is updated after the occurrence of the earthquake *Eq1* by inserting in the data set the time interval from *Eq0* to *Eq1*, and updating the values of $\mu$ and $\sigma$. Then, the time interval $(t_0, t_0 + t)$ is renewed given that $t_0$ counts from the origin time of *Eq1* instead of *Eq0*.

The conditional probability, $P(T_c)$, for the tsunami generation in the time interval from $t_0$ to $t_0 + t$ can be independently determined from (5) by considering only the tsunami time series in the zone. This is also the conditional probability for the generation of tsunamigenic earthquakes. However, as mentioned this approach suffers in that the numbers of tsunami events in the catalogues usually are relatively low.

## *Data and Application*

Three characteristic zones of high seismicity and tsunamicity were selected for the application of the methodology described above. They are the regions of South

America, Kuril-Kamchatka and Japan (Fig. 1). Earthquake and tsunami events occurring in these regions were selected from the database of GUSIAKOV (2001) for the time interval from 1900 to 2000. This database indicates that the tsunamis listed in the three regions were produced by strong ($M_s \geq 7.0$), shallow ($h < 50$ Km) earthquakes, where $M_s$ and $h$ are the surface-wave magnitude and focal depth, respectively. Therefore, in our analysis we consider only strong, shallow earthquakes that occurred in the time interval from 1900 to 2000. Completeness analysis based on the magnitude-frequency or Gutenberg-Richter relationship showed that in the three earthquake data sets the completeness magnitude threshold is well below 7.0.

In the database used the tsunami size is quantified in terms of tsunami intensity, $I$, following the scale introduced by SOLOVIEV (1970)

$$I = \log_2 \sqrt{2}(H), \tag{6}$$

where $H$ (in m) is the mean tsunami height in the coast. Completeness analysis based on the intensity-frequency relationship demonstrated that the tsunami data are complete for $I \geq 0$, $I \geq 2$ and $I \geq -2$ for the regions of South America, Kuril-Kamchatka and Japan, respectively (Fig. 2). Only tsunami complete data sets were introduced in our calculations. The number of earthquake and tsunami events inserted in the data sets are shown in Table 1. As one may expect in the three regions, the number of earthquakes exceeds significantly the number of tsunamis. On the other hand, the

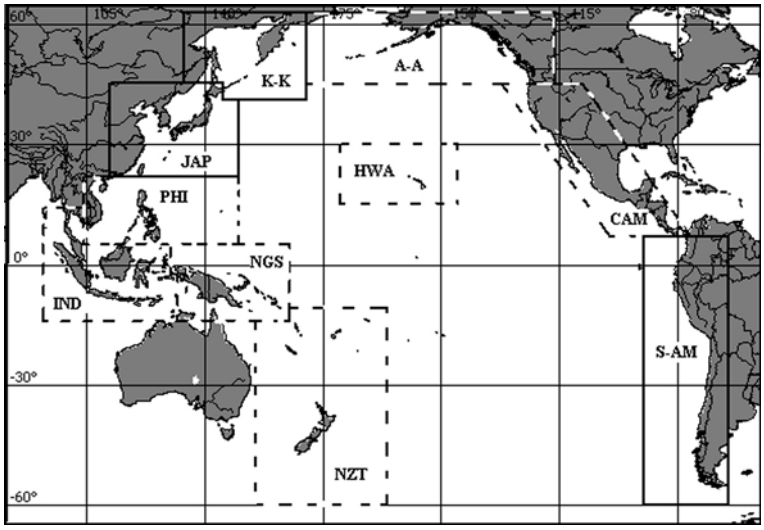


Figure 1
The ten tsunamigenic regions in the Pacific as defined by GUSIAKOV (2001). The solid lines show boundaries of the three regions examined in this paper, while the dashed lines show the boundaries of the remaining regions. *Key*: S-AM = South America, K-K = Kuril-Kamchatka, JAP = Japan, A-A = Alaska-Aleutians, CAM = Central America, NZT = New Zealand-Tonga, NGS = New Guinea-Solomon I., IND = Indonesia, PHI = Philippines, HAW = Hawaii.

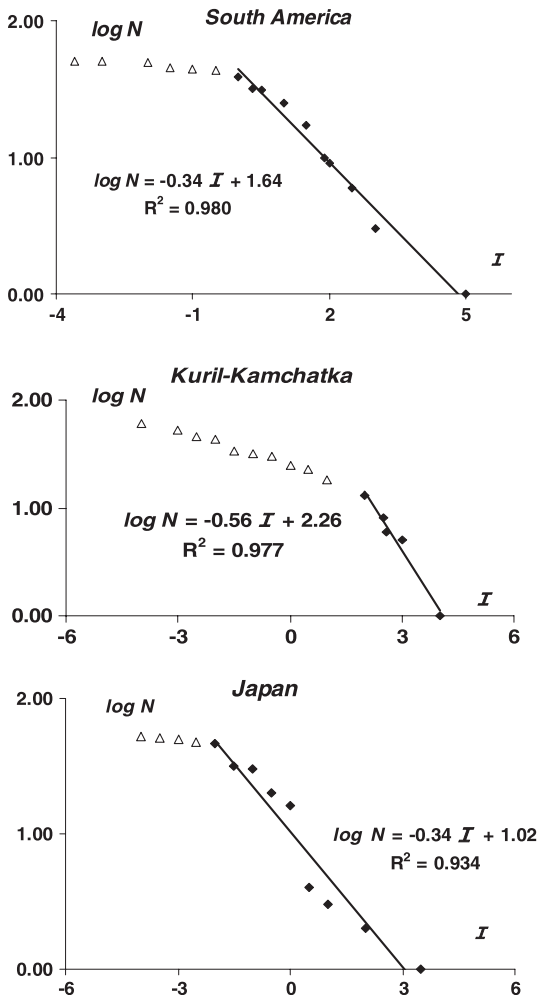


Figure 2
Intensity-frequency relationships for tsunamis occurring in the three zones examined. *Key*: $N$ = cumulative number of events in the time interval from 1900 to 2000, $I$ = tsunami intensity in the SOLOVIEV (1970) scale, $R$ = correlation coefficient. The intensity cut-off for the completeness of tsunami reporting has been determined by the linear regression best-fit at the right side of the diagram. Solid diamond and open triangle indicate the complete and incomplete parts of the data set, respectively.

ratio, $r$, of tsunami generating earthquakes over the total number of earthquakes varies from 0.39 in South America to 0.12 in Kuril-Kamchatka to 0.26 in Japan.

## *Results*

For each one of the three regions examined, Table 2 lists the conditional probabilities for the occurrences of (i) strong, shallow earthquakes and (ii) strong,

Table 1

*Numbers of strong ($M_s \geq 7.0$), shallow ($h < 50$ Km) earthquakes and tsunamis inserted in the data sets analyzed for the time interval 1900–2000. Tsunami intensity ($I$) completeness threshold varies*

| Region | Number of earthquakes | Number of tsunamis |
|---|---|---|
| South America | 77 | 30 ($I \geq 0$) |
| Japan | 116 | 30 ($I \geq -2$) |
| Kuril-Kamchatka | 85 | 10 ($I \geq 2$) |

shallow tsunamigenic earthquakes, which is also the conditional probability for the tsunami occurrence, as well as the probability for the tsunami occurrence as calculated by the total probability theorem. The parameters of the log-normal distribution used for the evaluation of the conditional probabilities of earthquake and tsunami occurrence are shown in Table 3.

Tsunami probabilities concern tsunami events with minimum tsunami intensity as shown in Table 1. The conditional probabilities for the occurrence of the next tsunami are systematically smaller than the respective probabilities for the earthquake occurrence (Fig. 3) since earthquakes occur more frequently than tsunamis. However, the difference in probabilities is not significant for long-time intervals. In the three regions examined, the conditional probabilities for the

Table 2

*Parameters introduced and results obtained*

| Region | $t_E$ | $t_{Ts}$ | $d_E$ | $d_{Ts}$ | $t$ | $P(E_c)$ | $P(T_c)$ | $P(T)$ |
|---|---|---|---|---|---|---|---|---|
| South America | 31.3.1999 | 21.02.1996 | 5.52 | 8.63 | 1 | 0.14 | 0.07 | 0.05 |
| | | | | | 5 | 0.46 | 0.27 | 0.18 |
| | | | | | 20 | 0.80 | 0.61 | 0.31 |
| | | | | | 50 | 0.93 | 0.81 | 0.36 |
| | | | | | 100 | 0.97 | 0.91 | 0.38 |
| Kuril-Kamchatka | 04.8.2000 | 04.10.1994 | 4.17 | 10.0 | 1 | 0.11 | 0.05 | 0.01 |
| | | | | | 5 | 0.39 | 0.20 | 0.05 |
| | | | | | 20 | 0.76 | 0.48 | 0.09 |
| | | | | | 50 | 0.92 | 0.68 | 0.11 |
| | | | | | 100 | 0.97 | 0.81 | 0.12 |
| Japan | 06.1.1995 | 28.12.1994 | 9.75 | 9.78 | 1 | 0.15 | 0.10 | 0.04 |
| | | | | | 5 | 0.48 | 0.37 | 0.13 |
| | | | | | 20 | 0.80 | 0.74 | 0.21 |
| | | | | | 50 | 0.92 | 0.91 | 0.24 |
| | | | | | 100 | 0.97 | 0.97 | 0.25 |

*Key*: $t_E$ = date of the last earthquake, $t_{Ts}$ = date of the last tsunami, $d_E$ = time interval (in years) since the occurrence of the last earthquake, $d_{Ts}$ = time interval (in years) since the occurrence of the last tsunami, $t$ = time window for the occurrence of the next event (in years), $P(E_c)$ = conditional probability to observe one earthquake in $t$ years from $t_E$ given that no earthquake occurred after the last event, $P(T_c)$ = conditional probability to observe one tsunami in $t$ years from $t_{Ts}$ given that no earthquake occurred after the last event, $P(T)$ = probability by the total probability theorem.

Table 3

*Parameters of the log-normal distribution used for the evaluation of the conditional probabilities of earthquake and tsunami occurrence*

| *Regions* | *Earthquake data* | | *Tsunami data* | |
|---|---|---|---|---|
| | $\mu$ | $\sigma$ | $\mu$ | $\sigma$ |
| South Amerika | 5.18 | 1.93 | 6.43 | 1.62 |
| Kuril-Kamchatka | 4.96 | 2.09 | 6.60 | 2.44 |
| Japan | 4.18 | 1.99 | 6.18 | 2.03 |

occurrence of the next tsunami exceed 0.5 when the time interval exceeds 20 years. The conditional probabilities of tsunami occurrence in Japan are slightly higher than in the South America region. Although the number of events in the data sets of both regions is equal ($n=30$), in Japan the last tsunami occurred earlier than in South America. On the contrary, in Kuril-Kamchatka the conditional probabilities of tsunami occurrence are clearly lower than in Japan and South America due to the relatively low number ($n=10$) of tsunami events inserted in the data set.

The probabilities, $P(T)$, obtained by the total probability theorem are not comparable to the conditional probabilities calculated for a particular time interval. This is because the maximum value these probabilities can attain is not 1, as for conditional probabilities, but $r$, the ratio of tsunami-generating earthquakes. For instance, in the Kuril-Kamchatka region the probability of tsunami occurrence in the next 20 years based on the total probability theorem is only 0.09. This value appears very low as compared to 1, but is actually high enough with respect to 0.12, the value of $r$ in that region. It is worthnoting, however, that the variation of probabilities $P(T)$ calculated by this method follows the variation of the ratio $r$ from one region to another. In fact, probabilities $P(T)$ are systematically higher in South America than in Japan because the ratio $r$ is higher in South America ($r=0.39$) than in Japan ($r=0.26$). Contrastingly, $P(T)$ are significantly higher in Japan than in Kuril-Kamchatka because in this region $r$ is only equal to 0.12.

## *Conclusions*

The stochastic description of the potential for tsunami generation in a seismic zone has been approached by two probabilistic techniques. The first calculates conditional probabilities for the occurrence of tsunamigenic earthquakes as a function of time by assuming that the inter-arrival times of the past earthquake events are lognormally distributed and by taking into account the time of occurrence of the last event in the time series. Because of the relatively low number of tsunamis in the complete parts of the existing tsunami catalogues, this approach suffers reduced reliability, particularly for short time windows. The second approach is

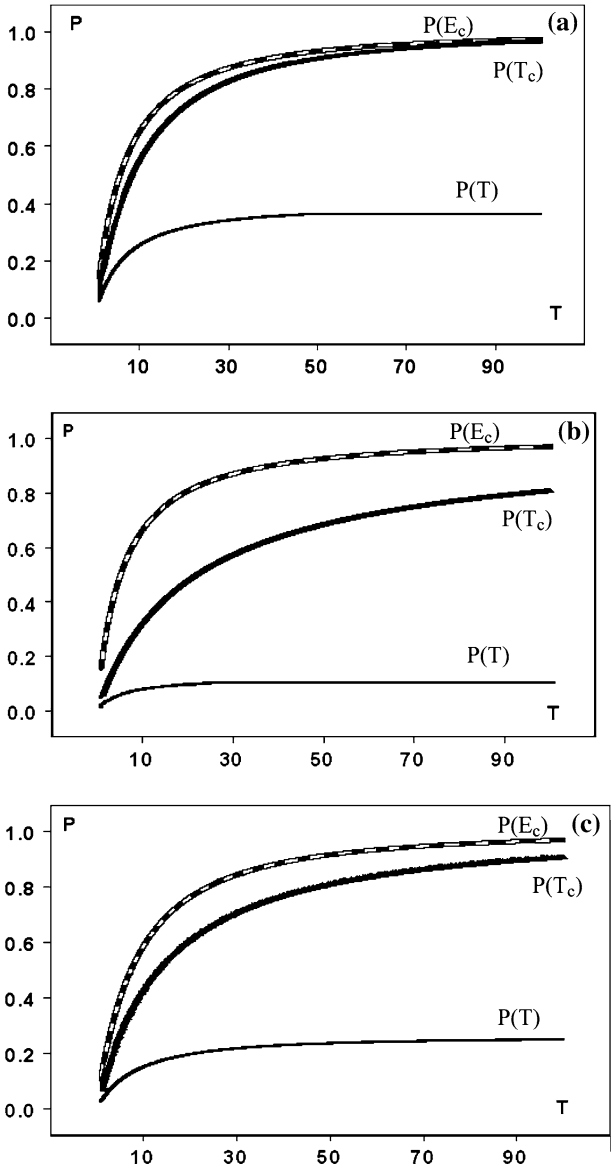


Figure 3

Probabilities, P, for the occurrence of earthquakes and tsunamis in South America (a), Kuril-Kamchatka (b) and Japan (c) as a function of time T (in years). Time starts at the time of occurrence of the last event in each of the zones examined. *Key*: $P(E_c)$ (dashed line) = the conditional probability to observe one earthquake given that no earthquake occurred after the last event, $P(T_c)$ (thick solid line) = the conditional probability to observe one tsunami given that no tsunamigenic earthquake occurred after the last event, $P(T)$ (thin solid line), = probability to observe one tsunami calculated by the total probability theorem.

based on the total probability theorem. Then, the probability for the tsunami occurrence equals the product of the ratio, $r$, of tsunami-generating earthquakes over the total number of earthquakes, by the conditional probability for the occurrence of earthquakes. The probabilities obtained by the total probability theorem are bounded upwards by the ratio $r$ and, therefore, they are not comparable with the conditional probabilities.

The two methods were successfully tested in three characteristic seismic zones of the Pacific Ocean: South America, Kuril-Kamchatka and Japan. For time intervals of about 20 years and more the probabilities become high in the three zones. However, it has been found that the results depend on the approach applied. Factually, conditional probabilities of tsunami occurrence in Japan are slightly higher than in the South America region, and in Kuril-Kamchatka they are clearly lower than in South America. Probabilities calculated by the total probability theorem are systematically higher in South America than in Japan, and in Kuril-Kamchatka they are significantly lower than in Japan. The stochastic techniques tested in this paper are promising for the tsunami potential assessment not only in the rest of the Pacific Ocean but also in other tsunamigenic regions of the world.

## *Acknowledgement*

This is a contribution to the EU TRANSFER tsunami research project, contract n, 037058–2006.

## References

Adams, W.M. (1972a), *A hiatus in the energy range of tsunamis generated off Northeastern Honshu*, Bull. IISEE *9*, 11–25.

Adams, W.M. (1972b), *Statistical significance of the energy gap observed for tsunamis generated off the Sanriku coast*, Bull. IISEE *9*, 137–141.

Geist, E.L. and Parsons, T. (2006), *Probabilistic analysis of tsunami hazards*, Natural Hazards *37*, 277–314.

Go, C.N., Kaistrenko, V.M., and Simonov, K.V. (1985), *A two-parameter scheme for tsunami hazard zoning, Marine Geodesy 9,* 469–476.

Gusiakov, V.K. (2001), *Basic Pacific tsunami catalogs and database, 47 BC – 2000 AD: results of the first stage of the project*, Proc. Internat. Tsunami Symp. August 7–9, 2001, Seattle, USA, PMEL/NOAA, pp. 263–272.

Lin, I.-C. and Tung, C.C. (1982), *A preliminary investigation of tsunami hazard*, Bull. Seismol. Soc. Am. *72*, 2323–2337.

Nishenko, S.P. (1985), *Seismic potential for large and great interplate earthquakes along the Chilean and Southern Peruvian margins of South America: A quantitative reappraisal*, J. Geophys. Res. *90*, 3589–3615.

Papadopoulos, G.A. (2003), *Tsunami hazard in the Eastern Mediterranean: Strong earthquakes and tsunamis in the Corinth Gulf, Central Greece*, Natural Hazards *29*, 437–464.

RABINOVICH, A.B., SHEVCHENKO, G.V., and SOKOLOVA, S.E. (1992), *An estimation of extreme sea levels in the northern part of sea of Japan*, Proc. 6th Japan and East China Seas Study Workshop, 22–27 April 1991, Fukuoka, Japan, 30, pp. 179–190.

RIKITAKE, T. and AIDA, I. (1988), *Tsunami hazard probability in Japan*, Bull. Seismol. Soc. Am. *78*, 1266–1278.

SANCHEZ, A.J. and FARRERAS, S.F. (1987), *Tsunami flooding extension for coastal zones of Mexico*, Marine Geodesy *11*, 127–135.

SOLOVIEV, S.L., *Recurrence of tsunamis in the Pacific*. In *Tsunamis in the Pacific Ocean* (ed. Adams, W.M.) (Honolulu, East-West Center Press 1970) pp. 149–163.

TINTI, S., *Evaluation of tsunami hazard in Calabria and eastern Sicily, Italy, Tsunamis in the World*. In (ed. Tinti, S.) *Advances in Natural and Technological Hazards Research* (Kluwer Academic Publishers, Dordrecht 1993) pp. 141–157.

WORKING GROUP ON CALIFORNIA EARTHQUAKE PROBABILITIES, Probabilities of Large Earthquakes Occurring in California on the San Andreas Fault (ed. U.S. Government Printing Office) (U.S.Geological Survey Open-File Report, Washington, D.C. 1988) pp. 88–398.

(Received March 10, 2006, accepted June 20, 2006)

Pure appl. geophys. 164 (2007) 605–616
0033–4553/07/030605–12
DOI 10.1007/s00024-006-0175-2



Pure and Applied Geophysics

# Steps Towards the Implementation of a Tsunami Detection, Warning, Mitigation and Preparedness Program for Southwestern Coastal Areas of Mexico

SALVADOR FARRERAS, MODESTO ORTIZ, and JUAN I. GONZALEZ

*Abstract*—The highly vulnerable Pacific southwest coast of Mexico has been repeatedly affected by local, regional and remote source tsunamis. Mexico presently has no national tsunami warning system in operation. The implementation of key elements of a National Program on Tsunami Detection, Monitoring, Warning and Mitigation is in progress. For local and regional events detection and monitoring, a prototype of a robust and low cost high frequency sea-level tsunami gauge, sampling every minute and equipped with 24 hours real time transmission to the Internet, was developed and is currently in operation. Statistics allow identification of low, medium and extreme hazard categories of arriving tsunamis. These categories are used as prototypes for computer simulations of coastal flooding. A finite-difference numerical model with linear wave theory for the deep ocean propagation, and shallow water nonlinear one for the near shore and interaction with the coast, and non-fixed boundaries for flooding and recession at the coast, is used. For prevention purposes, tsunami inundation maps for several coastal communities, are being produced in this way. The case of the heavily industrialized port of Lázaro Cárdenas, located on the sand shoals of a river delta, is illustrated; including a detailed vulnerability assessment study. For public education on preparedness and awareness, printed material for children and adults has been developed and published. It is intended to extend future coverage of this program to the Mexican Caribbean and Gulf of Mexico coastal areas.

**Key words:** Tsunamis, coastal flooding, vulnerability assessment, warning system instrumentation, mitigation and preparedness, middle-America trench off Mexico.

## *1. Introduction*

The southwest coast of Mexico has been heavily affected by local tsunamis generated by large earthquakes in the adjacent Middle America Trench, where the Cocos Plate collides with and subsides underneath the North American Plate. In addition, the Pacific coast of Central America and Colombia encompass a source of regional tsunamis, while the colliding tectonic plate borders, called the ''Ring of

Oceanology Division, Center for Scientific Research and Higher Education of Ensenada, Ensenada, Baja California, 22860 Mexico. E-mail: sfarrera@cicese.mx

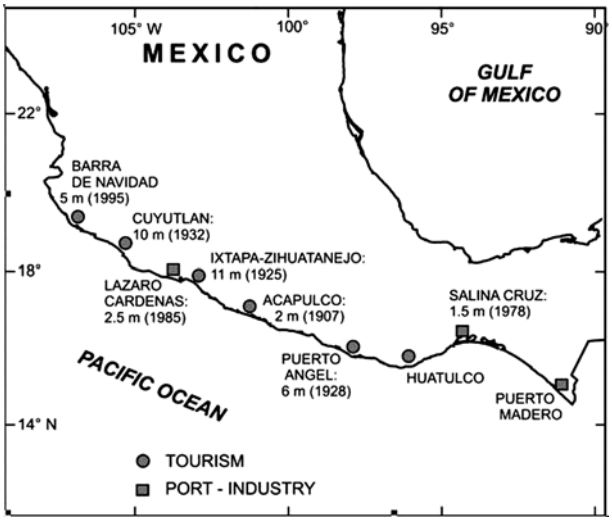


Figure 1
Port, industry, urban developments and tourist resorts in the Pacific ocean coast of Mexico. Dates and wave heights of destructive tsunamis.

Fire'', all around the coasts of the Pacific ocean constitute a source of distant ones for Mexico. Different travel times from their source to the arrival sites for each case, gives from a few minutes to a few hours to half a day or more, to issue effective early tsunami warning messages to the affected communities.

This coast is highly vulnerable due to the presence of an extensive industrial port, tourism, fisheries and densely populated urban developments. Figure 1 shows the 1000 km vulnerable coastal corridor scenario and the maximum wave heights and dates of the largest past tsunami occurrences.

It is intended to extend future coverage of this study to the Caribbean plate colliding border zones, which present a tsunami threat to the southeast coast of Mexico.

## *2. History and Prototypes*

Statistics of 56 tsunamis affecting the Mexican West Coast in a 272-year period, roughly one every 5 years, (SÁNCHEZ and FARRERAS, 1993), show that, besides the smaller and very frequent ones with less than 1 meter wave height, two categories which represent low and medium hazard with 3 and 5 meters maximum wave heights and an average return time of a quarter and half a century, respectively, are prevalent. These categories can be used as prototypes for computer simulations of coastal flooding.

In addition, high hazard extreme tsunamis with 10 meter estimated wave heights have materialized only twice in contemporary times, 16 November 1925 and 22 June, 1932. Their reccurrence time cannot be estimated at the present time. SINGH *et al.* (1998) ruled out a local earthquake shock as the cause of the 1925 tsunami, and indicated a sea-floor slumping as the possible source. The 1932 singular event is extensively described in SOLOVIEV and GO (1975) and SÁNCHEZ and FARRERAS (1993), among others.

The most recent low and medium hazard category events were the 19 September, 1985 and the 9 October, 1995 tsunamis with maximum wave heights of 2.5 and 5 meters respectively, which produced widespread damage in several communities along the coast (FARRERAS and SÁNCHEZ 1987, BORRERO *et al.*, 1997).

## 3. Strategy

Although Mexico presently has no national tsunami warning system in operation, important steps are taking place towards its development. A pannel of scientific expert advisors to the Civil Protection National System from the Secretary of the Interior, issued a recommendation to implement a National Program on Tsunami Detection, Monitoring, Warning and Prevention (SINAPROC, 1998). Key elements of this program are:

- operational infrastructure for detection, monitoring, and early warning message dissemination capabilities,
- training of personnel, managers and decision makers,
- zoning of expected inundation area extensions with water depth estimations,
- vulnerability studies and land use regulations,
- public outreach education for preparedness and awareness, and
- emergency response plans.

Early in 2005, after the devastating experience of the 26 December, 2004 Indian Ocean tsunami, several research institutions and local civil protection agencies from Mexico agreed on the need to share responsibilities and start the implementation of these tsunami program key elements.

## 4. Accomplishments

### 4.1. Operational

For distant tsunamis, where travel times could be of half a day or more, Mexico relies entirely on Pacific Tsunami Warning Center (PTWC) information. Since 1990, the federal Scientific Research and Higher Education Center of Ensenada (CICESE)

in cooperation with the Mexican Navy installed and mantains in Manzanillo, Isla Socorro and Cabo San Lucas, three sea-level gauge stations equipped with real-time signal transmitters to the GOES satellite, for the PTWC network.

PTWC watch and warning bulletins are curently received at the Mexican National Weather Service via dedicated WMO circuits, and at CICESE via Internet, where they are redistributed to federal and local civil protection agencies.

For travel times of less than 4 hours for regional tsunamis, and no more than one hour and a half for the local ones we cannot rely entirely on PTWC remote network information, but we must establish a system for rapid detection and analysis of our own local or nearby seismic and sea-level data to issue early warnings in time.

The National Research Institute for Earth Science and Disaster Prevention (NIED) from Japan, under an agreement with CICESE, provided partial financial support to develop this aspect of the operational program. A robust and low-cost high frequency sea-level tsunami gauge, sampling every minute and equipped with 24 hours real-time transmission to the Internet, was designed and installed. The signals from a bottom pressure sensor are carried to the ground by a hydrographic cable, and all the ground components of the system (solar panel, transmitter, antenna) are located at the top of a 10 meter height strong pole, to make it capable of withstanding the tsunami attack (Fig. 2). The prototype of this instrument is

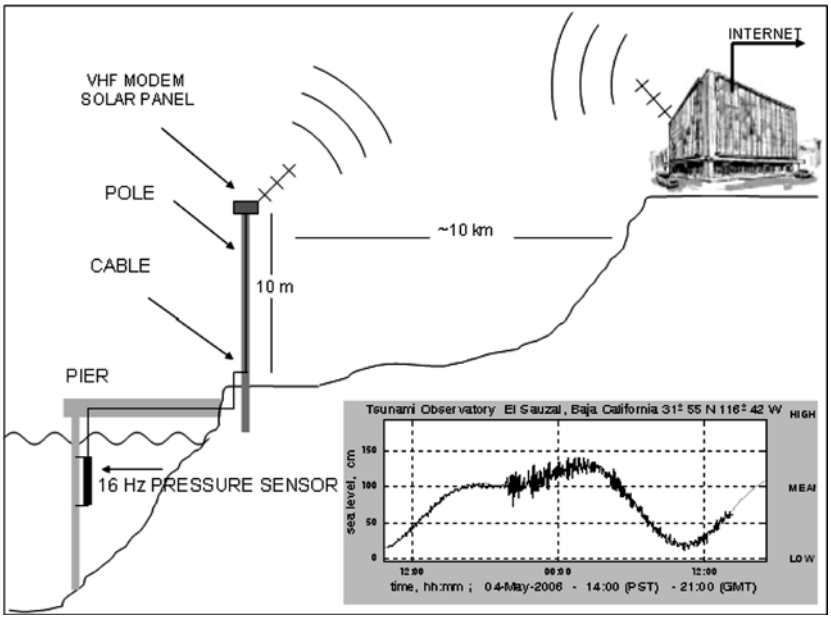


Figure 2
High frequency sea-level tsunami gauge, sampling every minute, equipped with real time transmission to the Internet; and actual sea-level record updated every minute, as can be seen at http://observatorio.cicese.mx

currently in operation at the port of El Sauzal, Baja California (31°55′N, 116°42′W) and the signal can be viewed permanently at the http://observatorio.cicese.mx Internet site.

It is intended to establish a network of these real-time sea-level sensors with one instrument installed every 100 kilometers covering the Pacific Ocean coast of Mexico, the Central American countries and Colombia.

Simultaneously, to increase the effectiveness and reliability of this early warning system for regional and local tsunamis, a database of forecast estimated arrival heights and times were computed from wave forms of synthetic tsunamis. These tsunamis, numerically computed by solving the shallow water long-wave equations, were generated from groups of impulse functions of a collection of segmented rupture area sources of prototype earthquakes along the Pacific coast of Mexico, Central and South America. The predicted height and time arrivals were so obtained from a linear superposition of the specific group of Green's functions corresponding to the segments of the rupture areas (ASTE, 2003). In a real case, for a rapid estimation of a tsunami occurrence, the magnitude of the coseismic dislocation and the location of the rupture has to be evaluated from early determinations of the earthquake parameters (i.e., USGS, Harvard) and/or from an inverse analysis of early observations of the tsunami in the vicinity of the generation area, adjusted as time progresses.

### *4.2. On Prevention and Planning*

To reduce the loss of life and property, and minimize the socioeconomic disruption caused by tsunamis, microzonation risk analysis and vulnerability assessment studies are being performed. At this initial stage, the following sites are included in this study: Manzanillo (19°03.2′N, 114°19.8′W), Lázaro Cárdenas (17°57.5′N, 102°11.5′W), Zihuatanejo (17°36.5′N, 101°33.0′W), Acapulco (16°50.4′N, 99°55.0′W) and Salina Cruz (16°09.6′N, 95°12.2′W). An important element for the analysis and studies is the determination of probable tsunami wave elevations and expected inundation limits at each location. Presently, the best alternative to determine these parameters is through numerical simulation of wave generation and propagation from the source to the shoreline and inland areas (FARRERAS and SÁNCHEZ, 1991).

With the financial support of the Japanese International Cooperation Agency (JICA), the University of Tohoku under the Tsunami Inundation Modeling Exchange (TIME) program transferred tsunami numerical modelling technology to Mexico to produce tsunami inundation maps for prevention purposes.

The TIME model consists of the shallow-water nonlinear vertically integrated equations of motion (1 and 2) and the equation of continuity (3), without Coriolis effect term (GOTO *et al.*, 1997):

$$\frac{\partial M}{\partial t}+\frac{\partial}{\partial x}\left(\frac{M^2}{D}\right)+\frac{\partial}{\partial y}\left(\frac{MN}{D}\right)+gD\frac{\partial \eta}{\partial x}+\frac{gn^2}{D^{7/3}}MQ=0 \tag{1}$$

$$\frac{\partial N}{\partial t}+\frac{\partial}{\partial x}\left(\frac{MN}{D}\right)+\frac{\partial}{\partial y}\left(\frac{N^2}{D}\right)+gD\frac{\partial \eta}{\partial y}+\frac{gn^2}{D^{7/3}}NQ=0 \tag{2}$$

$$\frac{\partial \eta}{\partial t}+\frac{\partial M}{\partial x}+\frac{\partial N}{\partial y}=0 \tag{3}$$

where $\eta$ = vertical displacement of the water surface above the still water level, $D = (\eta + h)$ instantaneous total water depth, $h$ = average depth of the water column, $M$ and $N$ = vertically integrated components of the horizontal and vertical transport per unit width (flow flux), $g$ = acceleration of gravity, $Q = (M^2 + N^2)^{1/2}$ = transport magnitude, and $n$ = 0.025 Manning's roughness parameter, considered constant.

The above set of equations are solved by finite differences in an explicit rectangular staggered leap-frog scheme in a set of interconnected grids that allows the use of the linearized set of equations in deep water, and the conservation of the nonlinear and friction terms in the inner higher resolution grid for the selected coastal regions. One of the most important capabilities of this model is the inclusion of wave run-up estimates in the inner higher resolution grid, where the nonlinear field acceleration terms and bottom friction are kept. Whether a computation cell is dry or submerged is judged in terms of the total water depth, as follows:

$$\begin{aligned} &D=\eta+h>0, \quad \text{then the cell is submerged, and}\\ &D=\eta+h<0, \quad \text{the cell is dry.} \end{aligned} \tag{4}$$

For a wave front located between the dry and submerged cells, the discharge across the boundary between the two cells is computed if the ground height in the dry cell is lower than the water level in the submerged cell. In other cases, discharge is considered zero. The boundary conditions at the seaside of the inner grid are taken from the intermediate resolution grid, whereas the radiation condition at the offshore boundary in the low-resolution grid is taken from the characteristic solution of the wave equation

$$(M,N)=\pm\eta\sqrt{gh}, \tag{5}$$

where the sign is taken in such manner that the wave will propagate outward from the computational domain.

For the initial condition, the model assumes that the instantaneous topography of the sea-surface deformation approximates the vertical deformation of the sea floor produced by the earthquake. This deformation is determined from analytical expressions for the internal deformation of a continuous media due to shear and tensile faulting (e.g., MANSINHA and SMYLIE, 1971). It considers a simple rupture geometry and uniform slip distribution on the fault plane.

Prototype tsunamis, as defined early above, were simulated with this model in a computer by CICESE to produce inundation maps indicating flooding extensions and expected wave heights, for several industrial ports and coastal cities.

An illustrative example is the heavily industrialized port of Lázaro Cárdenas in the state of Michoacán. This port is located on the sand shoals of the Balsas River delta along a 6-km-wide strip parallel to the coast, in a region where numerous marshes, ponds, coastal lagoons and estuarine branches were land-filled, raised and leveled up to 2 or 4 meters above sea level. The industrial zone includes two steel mill plants producing 4.4 million tons/year, a fertilizer factory producing 2.9 million tons/year, a container port, metal and mineral docks, grain storage silos with 80,000 tons capacity, a Navy base and a marine oil terminal capable of storing 541 million barrels of gasoline, diesel, jet fuel and fuel oil. One thermoelectric and two hydroelectric power plants provide 2,340 mega watts to this mega port-industrial-naval complex. Most of the port facilities, structures, services, roads and utility lines are settled on the low flat sedimentary coastal terraces of the river delta shoals, and are vulnerable to tsunami attack. The estimated population is presently 250,000. Figure 3 shows the location and distribution of the port and industrial structures, and the urban area in a topographic map. Not all the sites considered for this study have topographies available with a resolution as detailed as Lázaro Cárdenas.

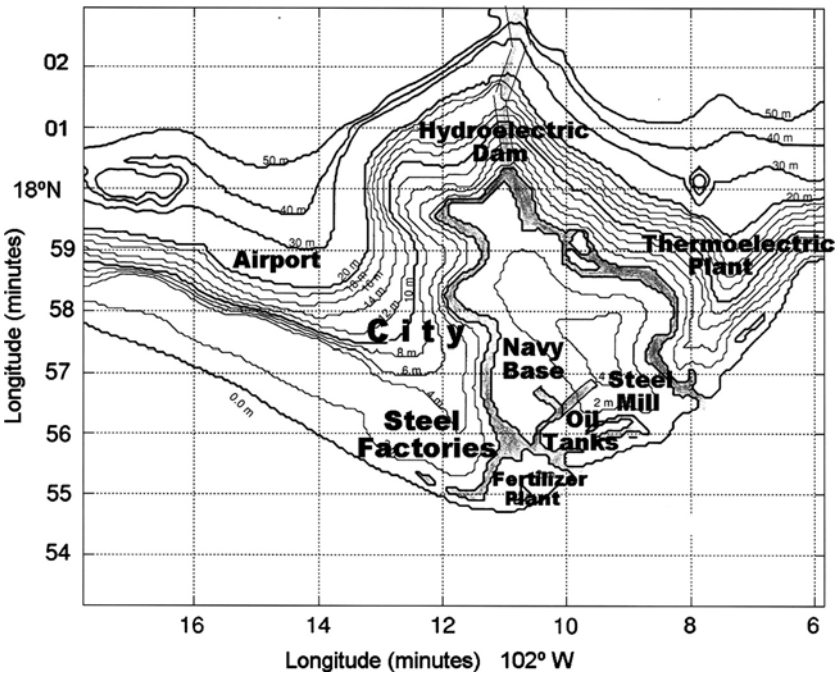


Figure 3
Port of Lázaro Cárdenas industrial installations and urban area, in the River Balsas delta.

On 19 September, 1985 an 8.1 Ms earthquake (ANDERSON *et al.*, 1986) occurred in a subduction zone segment of the Middle America Trench northwest of Lázaro Cárdenas. Waves of 2.5 meters maximum height from the generated tsunami reached the port and flooded a horizontal distance of approximately 500 meters inland. Major damage was attributable to the inundation. Approximately 1.5 km of railroad tracks were destroyed because the bank under the tracks was eroded. An earth embankment bridge providing access to the fertilizer plant was also washed out. Beach configuration changes attributable to approximately 2 m vertical piling of sand were also observed. Results of a survey with detailed damage patterns were presented elsewhere by FARRERAS and SÁNCHEZ (1987) and URBAN REGIONAL RESEARCH (1988). This tsunami stands as slightly lower than a low hazard category event as defined above.

For the computer simulations the following two cases, similar to those which have occurred, so that their recurrence could be reasonably expected, were selected:

- a slightly larger than a low hazard category event, with maximum wave heights of 3.5 m (40% higher wave heights than the 19 September, 1985 tsunami), and
- a medium hazard category event, with maximum wave heights of 5.0 m (similar to the 9 October, 1995 tsunami).

The rupture zone was assumed in the Middle America Trench in front of Lázaro Cárdenas, with earthquake fault parameters derived from the preliminary Harvard Moment Tensor solution and adjusted by trial-and-error method constrained by the analytical relation defining the seismic moment. ETOPO-2 digital bathymetry was used for the offshore wave propagation, and Mexican Navy bathymetric charts for the near shore propagation and coastal interaction. A reverse fault of 40 km width by 100 km length along the strike for the first case and 50 km width by 120 km length for the second case were used. Four and six meter dislocations along a constant dip-slip angle of 15 degrees were assumed for each case, respectively.

Figure 4 shows in an aerial photograph the boundaries of the inundation areas determined by the numerical simulations of each category event. The coastal strip flooded by the 19 September, 1985 tsunami, as surveyed, is also indicated.

A vulnerability assessment study (FARRERAS *et al.*, 2003) indicates that the shallow small island in the middle of the delta, where the container docks and the fertilizer factory sit, is the most vulnerable area to tsunami inundation. Both category events will completely flood the structures, with extensive damage and casualties to be expected. About 15 to 25% of the total area of the two main steel factories can be affected, according to the severity of the tsunami. The oil storage tanks, steel mill and coal yard sitting in the coastal strip of the main island of the delta may experience slight to severe damage from tsunami flooding in about 30 to 60% of their installations. The Mexican Navy base, the grain silos, the urban

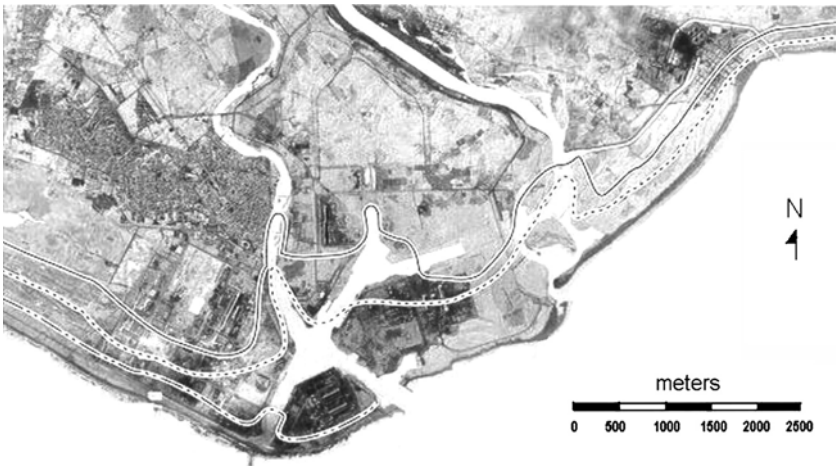


Figure 4
Boundaries of tsunami inundation for Lázaro Cárdenas: – —— – coastal strip flooded by the 19 September, 1985 tsunami, maximum wave heights = 2.5 m (survey), - - - - - slightly larger than a low hazard category event, maximum wave height = 3.5 m (simulation), ———— medium hazard category event, maximum wave height = 5.0 m (simulation).

area of the city and the hydroelectric and thermoelectric power plants are estimated not to be at risk of inundation by these two categories of tsunami. Secondary damage and destruction may happen by the impact of floating objects and ships carried by the tsunami waves, against fixed coastal structures like storage tanks. Fires, explosions, and contamination from oil and chemical spills in the inside harbor can cause severe damage and toxic effects to the population and the marine flora and fauna. Some liquid fertilizers, nitrogen solutions, sodium nitrate and hydroxide, sulfuric acid and urea are water reactive and could give off toxic fumes.

Additional recommendations on urban development to minimize the loss of life, and reduce the damage to property, include: Relocation of the steel factory railroad tracks and roads further inland, protect the most vulnerable industrial port installations and storage facilities, and establish evacuation routes and open space buffer zones for the population to evacuate promptly to emergency shelters at higher elevations or far inland from the risk area.

Similar inundation maps for the Mexican ports of Ensenada, Zihuatanejo and Salina Cruz, produced by numerical simulations as described above, are published elsewhere (CENAPRED, 2001).

### *4.3. On Preparedness and Awareness*

Public education is a key element for preparedness, awareness, the effective application of civil protection measures and the adequate response from the


Figure 5
Awareness/educational tsunami publications: Children book and adult booklet.

population to an early warning system. CICESE altogether with the National Center for Disaster Prevention from the Mexican Secretary of the Interior, developed, published and distributed a Spanish translation and adaptation of the Intergovernmental Oceanographic Commission of UNESCO Children's book on tsunamis (FARRERAS *et al.*, 2002), a 40-page booklet called *Fasciculo on Tsunamis* (FARRERAS *et al.*, 2005), brochures and several other printed materials for the general public (Fig. 5).

## 5. Conclusions

Three steps to create a tsunami-resistant community are to (BERNARD, 1999):

- Produce tsunami hazard maps to identify areas susceptible to tsunami flooding
- Implement and maintain an awareness/educational program on tsunami dangers
- Develop early local warning systems to alert coastal residents that danger is imminent.

Mexico has recognized that at least these three steps are important key elements for a National Program on Tsunami Detection, Monitoring, Warning and Mitigation. Efforts are taking place to successfully accomplish this objective.

*Acknowledgments*

The present study was partially supported by research Grant #G34601-S/2000 from Consejo Nacional de Ciencia y Tecnología (CONACyT) of México.

The National Research Institute for Earth Science and Disaster Prevention (NIED) from Japan, provided financial support to develop the prototype of a high frequency sea-level tsunami gauge.

With the financial support of the Japanese International Cooperation Agency (JICA), the University of Tohoku under the Tsunami Inundation Modeling Exchange (TIME) program transferred tsunami numerical modelling technology to Mexico to produce the tsunami inundation maps.

## References

Anderson, J.G., Bodin, P., Brune, J.N., Prince, J., Singh, S.K., Quaas, R., and Oñate, M. (1986), *Strong ground motion from the michoacan-mexico earthquake*, Science *233* (4768), 1043–1049.

Aste, A. (2003), *Optimización del Sistema Regional de Alerta de Tsunamis en Perú mediante la Detección Temprana y la Simulación Numérica*, Tesis de Maestría, División de Oceanología, CICESE, Ensenada, BC, México, 81 p.

Bernard, E. (1999), *Tsunami*. In *Natural Disaster Management*, United Nations, Tudor Rose Holdings (J. Ingleton editor) 320 p.

Borrero, J., Ortiz, M., Titov, V., and Synolakis, C. (1997), *Field survey of Mexican tsunami produces new data, unusual photos*, EOS *78* (8), 85–88.

Cenapred (2001), *Diagnóstico de Peligros e Identificación de Riesgos de Desastres en México: Atlas Nacional de Riesgos de la República Mexicana*, México, D.F., 225 p.

Farreras, S.F., and Sánchez, A.J. (1987), *Generation, wave form and local impact of the September 19, 1985 Mexican tsunami,* Science of Tsunami Hazards *5*, 3–13.

Farreras, S.F., and Sánchez, A.J. (1991), *The tsunami threat on the Mexican west coast: A historical analysis and recommendations for hazard mitigation*, Natural Hazards *4*, 301–316.

Farreras, S.F., Domínguez, R., and Gutiérrez, C.A. (2005), *Tsunamis*, Fascículo, 2ª Edición, Centro Nacional de Prevención de Desastres, Secretaría de Gobernación, México, D.F., 39 p.

Farreras, S., Ortiz, M., and Alcalá, G. (2003), *Riesgo de Maremotos en Ciudad Lázaro Cárdenas, Michoacán: Medidas de Prevención*. Serie: Linderos de la Costa, vol. 3, El Colegio de México, CICESE, y El Colegio de Michoacán, México, D.F., 100 p.

Farreras, S.F., and Pararas-Carayannis, G. *et al.* (2002), *Alerta de Tsunami (Maremoto): Qué Hacer* (librito infantil). El Colegio de Michoacán, El Colegio de México, Centro de Investigación Científica y Educación Superior de Ensenada, y Centro Nacional de Prevención de Desastres (Sec. de Gobernación), Lázaro Cárdenas, Michoacán, México, 32 p.

Goto, C., Ogawa, Y., Shuto, N., and Imamura, F. (1997), *IUGG/IOC time project: Numerical method of tsunami simulation with the leap-frog scheme*, Intergovernmental Oceanographic Commission of UNESCO, Paris, France, 19 p.

Mansinha, L., and Smylie, D.E. (1971), *The displacement field of inclined fault,* Bull. Seismol. Soc. Am. *61*, 1433–1440.

Sánchez, A.J., and Farreras, S.F. (1993), *Catalog of tsunamis on the western coast of Mexico*, World Data Center, NOAA, Boulder, Colorado, USA, 27 p.

Sinaproc (1998), *Detección, Monitoreo, Alerta y Prevención de Tsunamis en México*, Recomendación RG/04/98, Comité Científico Asesor sobre Fenómenos Perturbadores de Origen Geológico, México D.F., 10 p.

SINGH, S.K., PACHECO, J.F., and SHAPIRO, N. (1998), *The earthquake of 16 November, 1925 (Ms = 7.0) and the reported tsunami in Zihuatanejo, Mexico,* Geofísica Internacional *37*(1), 49–52.

SOLOVIEV, S.L., and GO, C.N., *A Catalogue of Tsunamis on the Eastern Shore of the Pacific Ocean (1513–1968)*, (Nauka Pub. House, Moskow, USSR, 1975) 204 p.

URBAN REGIONAL RESEARCH (1988), *Planning for risk: Comprehensive planning for tsunami hazard areas*, prepared for the National Science Foundation, Seattle, Washington, USA, 246 p.

(Received February 16, 2006, accepted September 10, 2006)

Pure appl. geophys. 164 (2007) 617–631
0033–4553/07/030617–15
DOI 10.1007/s00024-006-0177-0



Pure and Applied Geophysics

# A Study of Tsunami Wave Fission in an Undistorted Experiment

Masafumi Matsuyama,[1] Masaaki Ikeno,[1]
Tsutomu Sakakiyama,[1] and Tomoyoshi Takeda[2]

*Abstract*—To study tsunami soliton fission and split wave-breaking, an undistorted experiment was carried out which investigated tsunami shoaling on a continental shelf. Three models of the continental shelf were set up in a 205-m long 2-dimensional flume. Each shelf model was 100 m, long with slopes of either 1/100, 1/150, or 1/200. Water surface elevations were measured across the flume, including a dense cluster of wave gages installed around the point of wave-breaking. We propose new methods for calculating wave velocity and the wave-breaking criterion based on our interpretation of time series data of water surface elevation. At the point of wave-breaking, the maximum slope of water surface is between 20 to 50 deg., while the ratio of surface water particle horizontal velocity to wave velocity is from 0.5 to 1.2. The values determined by our study are larger than what has been reported by other researchers.

**Key words:** Tsunami, shoaling, soliton fission, wave-breaking, an undistorted experiment.

## 1. Introduction

On May 26 in 1983, an earthquake of magnitude 7.7 occurred in the Japan Sea, generating a large tsunami, known as the 1983 Nihonkai-Chubu earthquake tsunami. During that event, 'tsunami soliton fission' was observed on the gentle seabed slope in the shallow water along the coast (Shuto, 1985). This phenomena occurs when short waves split from the tsunami crest due to nonlinearity and dispersion. When soliton fission occurs, the new leading wave height increases and breaks. It is therefore important to investigate the characteristics relative to breaking of tsunami soliton fission.

Shaffer *et al.* (1993) and Madsen *et al.* (1997) used the local slope ($\theta$) of a wave profile as a breaking criteria for wind waves. Shaffer *et al.* (1993) found that acceptable results could be obtained by using the value $\theta_b = 20$ deg. for spilling breakers, and $\theta_b = 25$ deg. for plunging breakers.

Sato (1996) and Iwase *et al.* (2004) used the parameter $(u_s/c)$ as a breaking criteria. This number relates the ratio of surface water particle horizontal velocity $u_s$

[1] Central Research Institute of Electric Power Industry, Japan.
[2] Tokyo Electric Power Company, Tokyo, Japan.

to wave velocity $c$. SATO (1996) defined a breaker limit $u_s/c = 0.4$ based on experiments for wind waves in the surf zone. SATO (1996) carried out a numerical simulation of 1993 Southwest Hokkaido tsunami and was able to reproduce tsunami soliton fission offshore of Aonae Cape on Okushiri Island by using a finite-difference method based on Boussinesq-type equations with wave-breaking term. In this study he let $c = \sqrt{g(h+\eta)}$ where $g$ is gravitational constant, $h$ is water depth, and $\eta$ is water surface elevation.

IWASE *et al.* (2004) carried out experiments investigating wave soliton fission on a flat bottom to develop a wave-breaking model. By using the velocity of a stable solitary wave he proposed a breaker limit $u_s/c = 0.59$. These breaking criteria however were not based on a long wave such as a tsunami. In this study the breaking criteria is investigated by simulating tsunami shoaling across a continental in an undistorted model in a two-dimensional flume.

## 2. Hydraulic Model Experiment

### 2.1. Flume and Model

The Large Wave Flume located at Central Research Institute of Electric Power Industry, Japan (CRIEPI) is shown in Figure 1. The dimensions are 205 m long, 3.4 m wide, and 6 m deep in the 115 m-long generator-side flat section. The wave generator is the piston type blade, with a maximum stroke of 2.2 m. Three different types of continental shelf models were set up in the flume at an undistorted 1/200 scale. Each model had a different seabed slope, 1/200, 1/150, and 1/100, as shown in Figure 2.

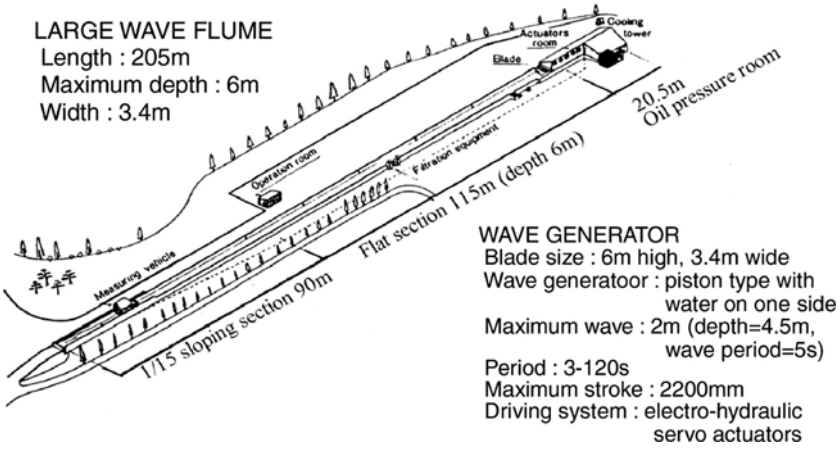


Figure 1
The CRIEPI Large Wave Flume.

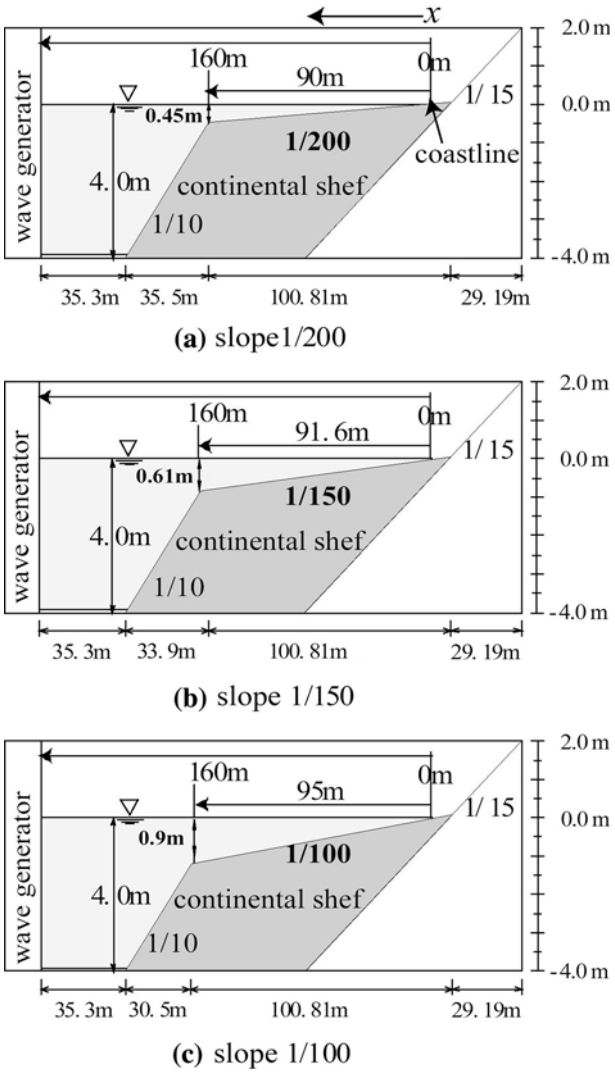


Figure 2
Three models of the continental shelf in the wave flume.

### *2.2. Data Acquisition System*

Water surface elevations were measured by capacitance-type wave gages. Ten gages were arranged across the model at intervals of 5, 10, or 20 m (Fig. 3). We first checked where wave-breaking appeared for each wave condition. Ten more gages were then set up at the breaking point with either a 20 or 40 cm interval to resolve the

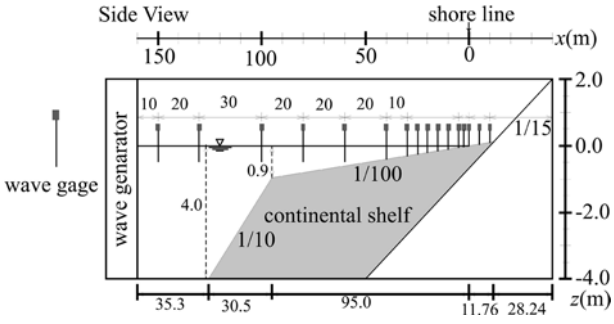


Figure 3
An example of the arrangement of fixed wave gages on the slope 1/100.

wave shape around the breaking point. Water surface elevation was recorded at a time interval of 0.01 sec (100 Hz).

### *2.3. Incident Wave Condition*

Table 1 lists the input wave cases. Input wave profile $\eta_I$ is a sinusoidal wave shape of only one cycle as shown in Figure 4.

$$\begin{aligned} \eta_{\mathrm{I}} &= A \sin\left(\frac{2\pi}{T} t\right) \quad 0 \le t \le T \\ &= 0 \quad t > T \end{aligned}, \tag{1}$$

Table 1

*Incident wave condition*

| No. | Period(sec) | Amplitude(m) |
|---|---|---|
| 021 | 20 | 0.005 |
| 022 | | 0.01 |
| 023 | | 0.02 |
| 024 | | 0.03 |
| 041 | 40 | 0.01 |
| 042 | | 0.02 |
| 043 | | 0.03 |
| 044 | | 0.04 |
| 045 | | 0.09 |
| 061 | 60 | 0.005 |
| 062 | | 0.01 |
| 063 | | 0.02 |
| 064 | | 0.03 |
| 065 | | 0.04 |
| 121 | 120 | 0.01 |
| 122 | | 0.02 |

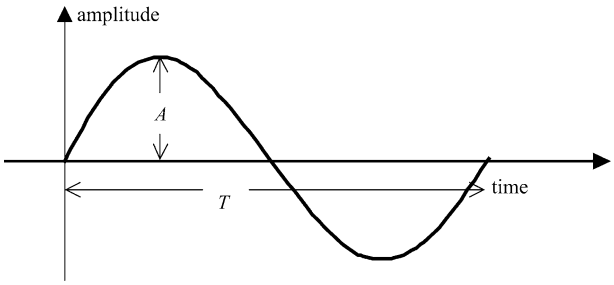


Figure 4
Incident wave shape.

where $\eta_I$ is water surface elevation, $A$ is wave amplitude, $T$ is period, and $t$ is time. Input waves ranged in amplitude and period from 0.005 m to 0.09 m and from 20 sec to 120 sec (Table 1). In actual scale, wave periods ranged from 282 s (4.7 min) to 1690 s (28.3 min), which is long enough to reproduce tsunami shoaling on the continental shelf.

Since the aim of this experiment is to keep track of split wave deformation at wave-breaking point and because wave-breaking is a sensitive phenomena, each experimental test was carried out two or more times for each incident wave condition to check for consistency and repeatability.

## 3. Experimental Results

### 3.1. Outline of Wave Shoaling

Figure 5 shows time histories of water surface elevation for Case 024 ($T = 20$ sec, $A = 0.03$ m, slope $= 1/200$). Wave height increased and wavelength decreased during propagation across the continental shelf. The soliton fission was observed as a split wave with new short waves appearing. Three short waves appeared with approximately 1 second between subsequent crests. These short waves amplified remarkably just before breaking. The new wave height at the point of breaking is about 0.14 m, which is twice as big as the wave height at the beginning of soliton fission. As shown in Photo 1**,** plunging breakers were produced. After wave-breaking, the height of the split wave decreased through energy dissipation. When converted to actual scale, the period of short waves is approximately 14 sec., which is similar to observations of wave fission during the 1983 Nihonkai-Chubu Earthquake Tsunami (SHUTO, 1985).

Figure 6 shows the time histories of water surface elevation for Case 063 ($T = 60$ sec, $A = 0.02$ m, slope $= 1/200$). In this case, a new wave crest is not observed at the tsunami peak, but rather on the wavefront. That is, wave split point has moved forward relative to the tsunami crest. The tendency increased in frequency, as the period of incident wave exists longer.

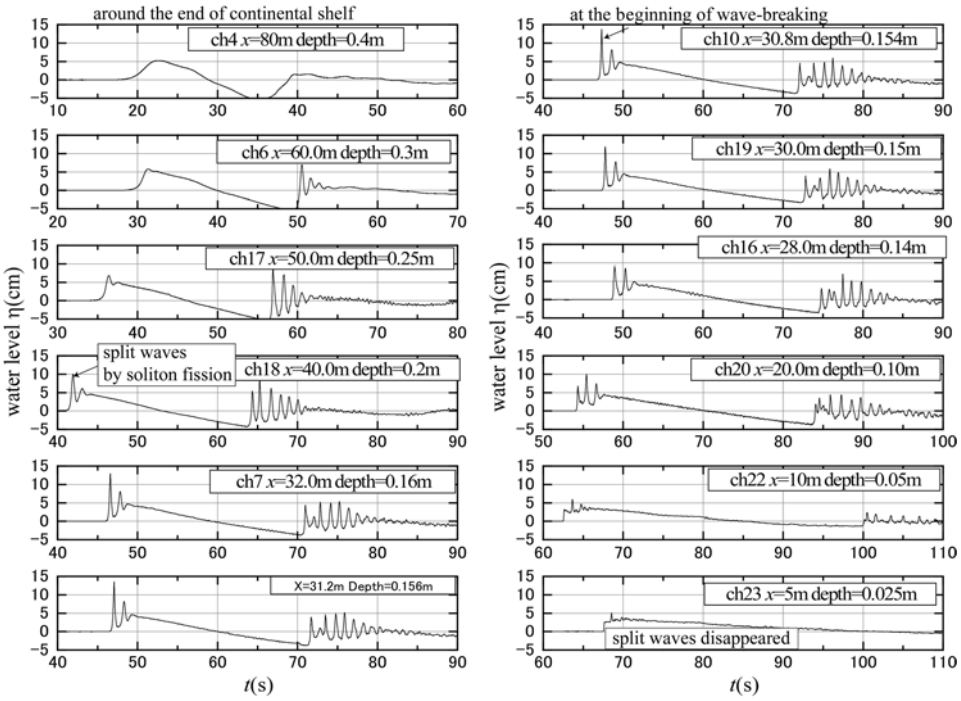


Figure 5
Time histories of water surface elevation for Case 024 ($T$ = 20 sec., $A$ = 0.03 m, slope = 1/200).

### *3.2. Wave-breaking*

#### *3.2.1. Breaking wave height and water depth*

Figure 7 shows the time histories of water surface elevation at the moment of wave-breaking for two different incident wave conditions on seabed slopes of 1/100, 1/150, and 1/200. These figures show differences in wave shape and deformation at wave-breaking for different seabed slopes. For Case 024, the breaking height for the first split wave is 0.144 m on 1/200 slope, 0.148 m on 1/150 slope, and 0.142 m on 1/100 slope. For Case 063 the values are 0.064 m on 1/200, 0.061 m on 1/150, and 0.053 m on 1/100. Thus, breaking-wave heights on three slopes are comparable. On the other hand, as seabed slope increases, the water depth at breaking is smaller, i.e., 0.150 m on 1/200, 0.148 m on 1/150, and 0.128 m on 1/100 for Case 024. As a result, $\varepsilon_b$, which is the ratio of maximum wave surface level $\eta$ of the first split wave to water depth $h$ at the wave-breaking point, is larger, as the seabed slope increases. Figure 8 shows $\varepsilon_b$ for all plotted against water depth at wave-breaking. The range of $\varepsilon_b$ was from 0.7 to 1.4. Average values of $\varepsilon_b$ with respect to each seabed slope are 0.87 for 1/200, 1.00 for 1/150, and 1.23 for 1/100.

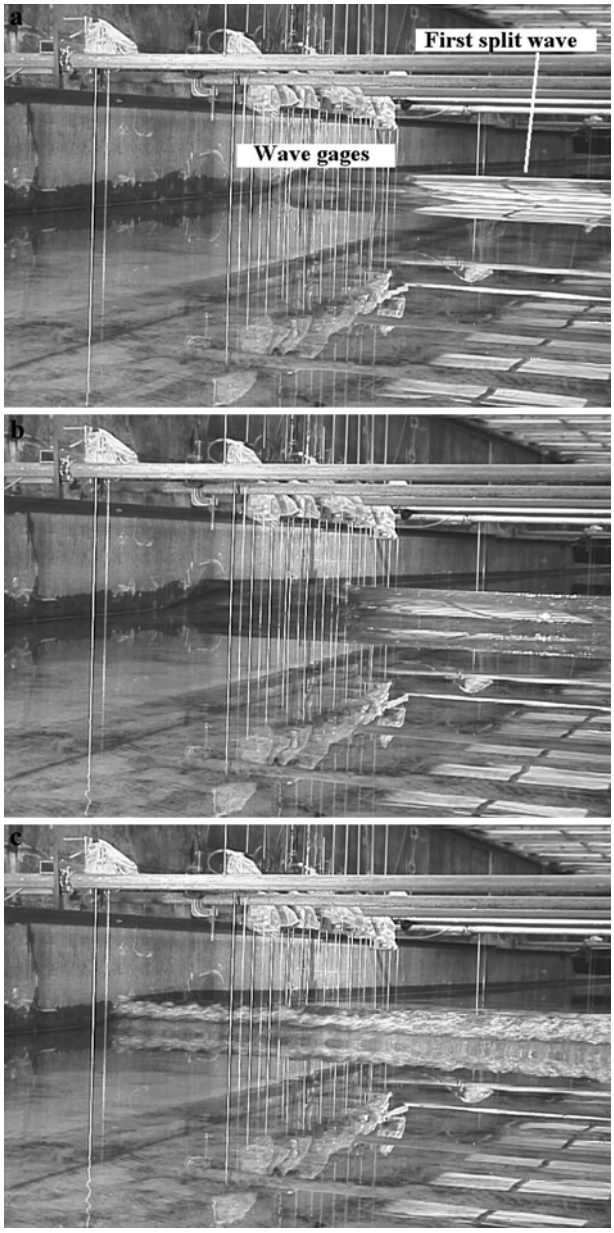


Photo 1
Snapshots around the break point for Case No. 024. (a) Before wave-breaking, (b) At wave-breaking, (c) After wave-breaking.

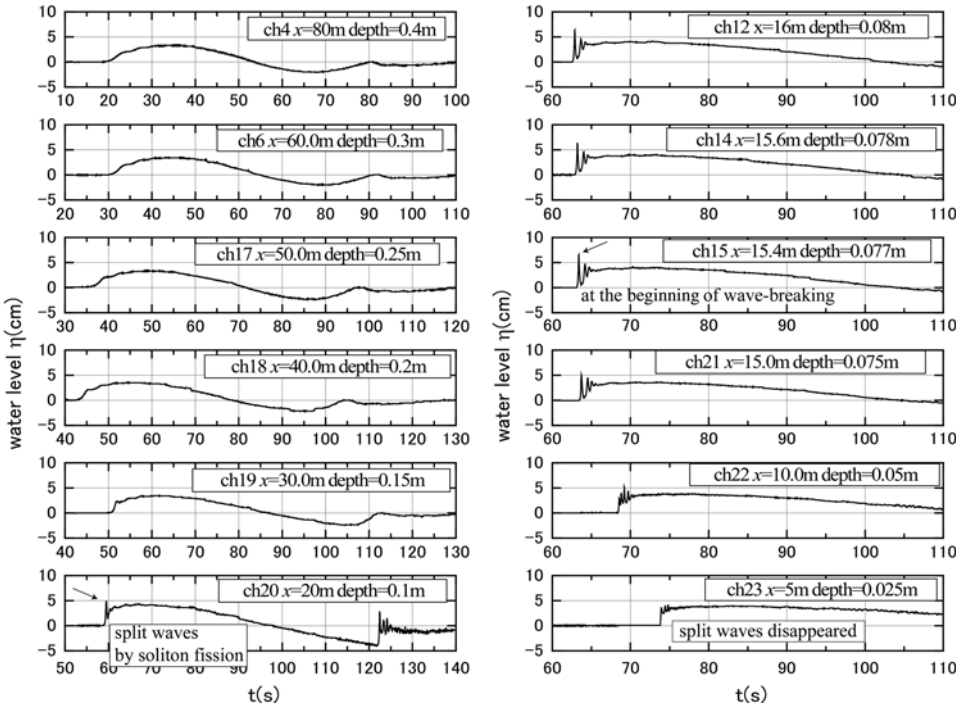


Figure 6
Time histories of water surface elevation for Case 063 ($T$ = 60 sec., $A$ = 0.02 m, slope = 1/200).

### *3.2.2. Breaking criterion*

Two parameters related to the breaking criterion were investigated. One is local slope $\theta$ of the water surface and the other is the ratio of water surface particle velocity $u_s$ to wave horizontal velocity $c$ ($u_s/c$).

#### *(1) Wave velocity*

Wave velocity $c$ is necessary to convert time histories of water surface elevation to spatial wave shape. Thus a new method is proposed, which is based on nonlinear dispersion wave theory. For shallow water waves with dispersion over gentle slope, one-dimensional Boussinesq equation is expressed as

$$\frac{\partial \eta}{\partial t} + \frac{\partial M}{\partial x} = 0 \tag{2}$$

$$\frac{\partial M}{\partial t} + \frac{\partial}{\partial x}\left(\frac{M^2}{D}\right) + gD\frac{\partial \eta}{\partial x} = \frac{1}{3}h^3\frac{\partial^3 \bar{u}}{\partial t \partial x^2}, \tag{3}$$

where $M$ is flux, $h$ is still water depth, $D$ is $\eta + h$, $\bar{u}$ is horizontal velocity averaged vertically. Assumed wave profile is not deformed in small time $\Delta t$, progressive wave velocity $c$ is defined as follows:

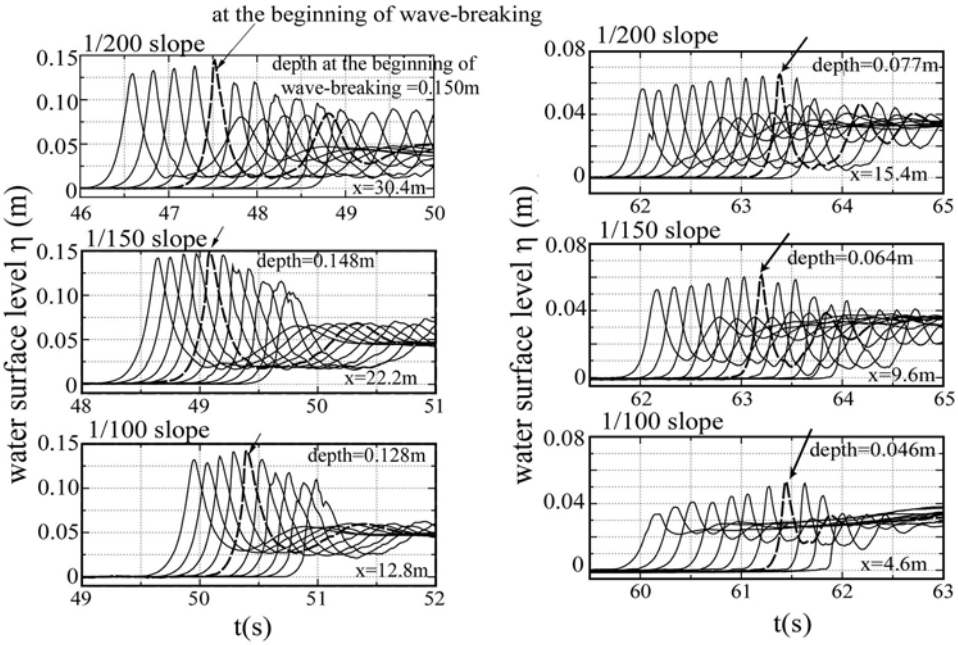


**(a)** No.024
period 20 sec, amplitude 0.03 m

**(b)** No.063
period 60 sec, amplitude 0.02 m

Figure 7
Time histories of the first split wave at the wave-breaking point.

$$\frac{\partial}{\partial t} = -c\frac{\partial}{\partial x}. \tag{4}$$

Equations (2) and (4) are combined to give

$$M = c\eta. \tag{5}$$

Equations (4) and (5) to (3) reduced to

$$c\eta - \frac{c\eta^2}{D} - \frac{gD}{c}\eta - \frac{1}{3}\frac{h^3}{c}\left[\frac{1}{(h+\eta)^3}\left\{h(h+\eta)\frac{\partial^2\eta}{\partial t^2} - 2h\left(\frac{\partial\eta}{\partial t}\right)^2\right\}\right] = 0. \tag{6}$$

Wave velocity $c$ can be evaluated by using time series data of water surface elevation accordingly, as follows:

$$c_t = \sqrt{gh}\sqrt{(1+\varepsilon)^2 + \frac{1}{3gh\varepsilon(1+\varepsilon)^2}\left\{D\frac{\partial^2\eta}{\partial t^2} - 2\left(\frac{\partial\eta}{\partial t}\right)^2\right\}}, \tag{7}$$

where $\varepsilon = \eta/h$.

Figure 9 shows the wave profile and a ratio of wave velocity $c_t$ by equation (7) to $c_p$, which is calculated by phase delay based on a time lag between wave crests of

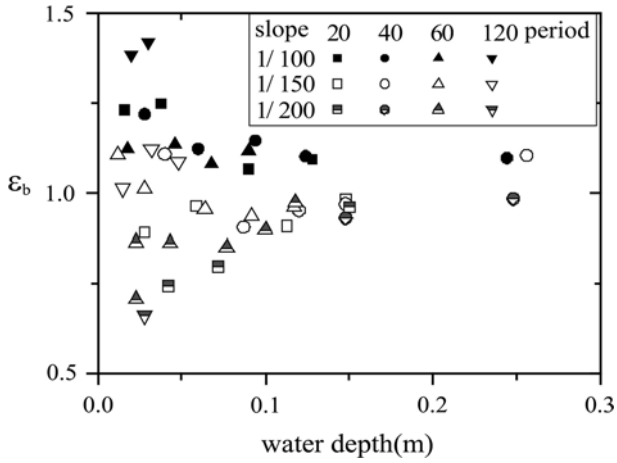


Figure 8
$\varepsilon_b(\eta/h)$ versus water depth at the wave-breaking point.

adjacent wave gages. The ratio is almost 1.0 except for both edges of the split wave. This result indicates the adequacy of equation (7) at least for progressive waves.

*(2) Local slope θ of water elevation*

The local slope of water surface $\theta$, is obtained from time series data for $\eta$ and wave velocity $c$ by the following equation.

$$\theta = \tan^{-1}\left(-\frac{1}{c_t}\frac{\partial \eta}{\partial t}\right). \tag{8}$$

Figure 10 shows time histories of water surface elevation $\eta$ and local slope $\theta$ at the wave-breaking point for the first split wave on the 1/100 slope. In each case, wave-breaking began when $\theta$ exceeded 30°.

Figure 11 shows the maximum local slope $\theta(=\theta_b)$ at the breaking point for all cases. $\theta_b$ ranges from 20 to 50 deg., and increases with wave velocity. As shown in Photo 1, the waves are breaking in a plunging fashion. According to Figure 11, the breaker limit seems to be at $\theta_b = 30$ deg. for plunging breakers. We assumed that for cases $\theta_b$ is more than 30 deg., wave-breaking has already begun and the wave is beginning to lose shape. Bottom slope is not related to breaker limit $\theta_b$.

*(3) Ratio of surface water particle horizontal velocity to wave velocity $u_s/c$*

FUJIMA *et al.* (1986) examined the accuracy of nonlinear dispersive long-wave equations by higher order approximation. They derived an equation for $u_s$ under the condition of $\varepsilon \sim 1$ and $\sigma \gg 1$ ($\sigma = (L/h)^2$). When the bottom slope is gentle, the equation is expressed as below.

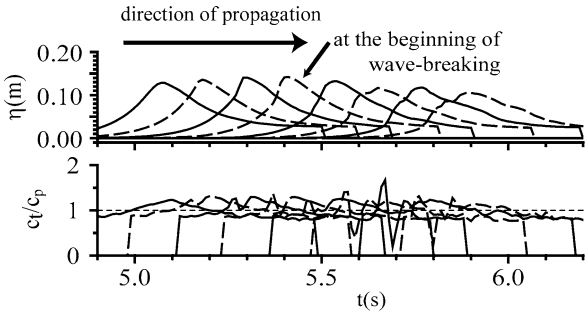


**(a)** Case.024: $T=20$ sec, $A=0.03$ m, slope$=1/100$

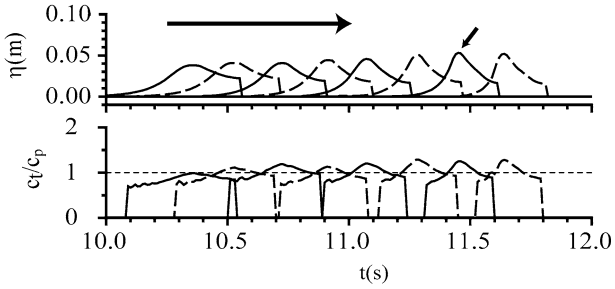


**(b)** Case.063: $T=60$ sec, $A=0.02$ m, slope$=1/100$

Figure 9
Wave profile, ratio $c_t/c_p$ around the point of wave-breaking.

$$u_S = \bar{u} - \frac{D^2}{3}\frac{\partial^2 \bar{u}}{\partial x^2}. \tag{9}$$

If equations (4) and (5) are applied to equation (9), we obtain equations of $u_s/c$ for the progressive wave.

$$\frac{u_S}{c} = \frac{\eta}{D} - \frac{h}{3D}\left\{ D\frac{\partial^2 \eta}{\partial x^2} - 2\left(\frac{\partial \eta}{\partial x}\right)^2 \right\} \tag{10}$$

and

$$\frac{u_S}{c} = \frac{\eta}{D} - \frac{h}{3Dc^2}\left\{ D\frac{\partial^2 \eta}{\partial t^2} - 2\left(\frac{\partial \eta}{\partial t}\right)^2 \right\}, \tag{11}$$

where $D$ is $\eta + h$. In equation (10) the values of $u_s/c$ are expressed by wave shape and water depth $h$. On the other, $u_s/c$ is expressed by time histories of water surface elevation, wave velocity $c$, and water depth $h$ in equation (11). According to equations (7) and (11) we are able to estimate the values of $u_s/c$ from time histories data of water surface elevation $\eta$ and water depth $h$.

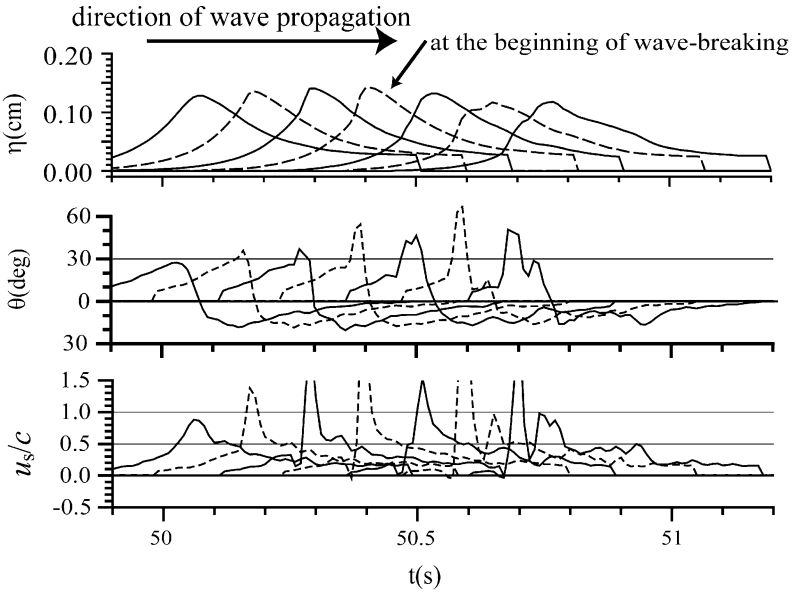


**(a)** Case.024: $T=20$ sec, $A=0.03$ m, slope$=1/100$

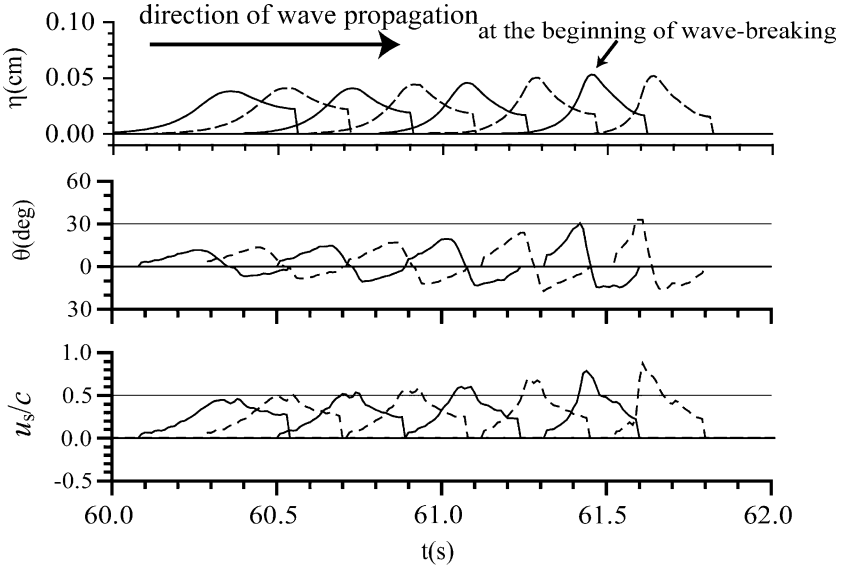


**(b)** Case.063: $T=60$ sec, $A=0.02$ m, slope$=1/100$

Figure 10
Time histories for water surface elevation and parameters $\theta$ and $u_s/c$ near the wave-breaking point for the first split wave.

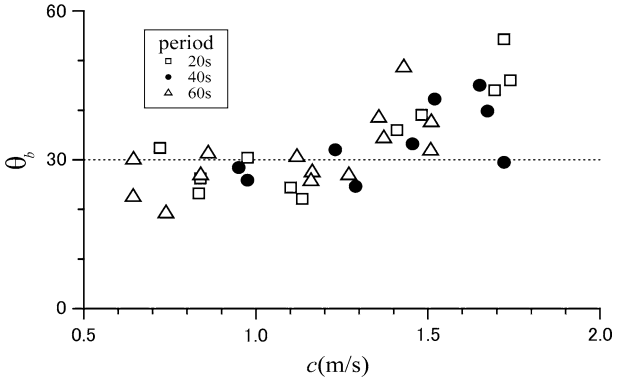


Figure 11
The maximum slope $\theta_b$ of water surface elevation at the point of wave-breaking.

Figure 10 shows time histories of $\eta$ and $u_s/c$ around the wave-breaking point for cases 024 and 063. The maximum value for $u_s/c$ was not observed at the wave crest, but rather at a point slightly ahead of the crest in both cases. Peak values of $u_s/c$ at peak increased toward the wave-breaking point. $u_s/c$ exceeded 1.5 for Case 024 and reached 0.8 for Case 063.

Figure 12 shows $\gamma$, which is maximum $u_s/c$ at the wave-breaking point. This value generally ranges between 0.5 to 1.2 except for a few cases and increases with wave velocity. We therefore suggest that the wave-breaking limit $u_s/c$ should be set to 0.9 so as not to underestimate the maximum wave height and wave force. The values for $\lambda$ determined here are larger than values reported in previous studies, i.e., $\gamma = 0.59$ in IWASE *et al.* (2004).

Differences in model bathymetry may explain the discrepancy between the two studies. IWASE (2004) experiments used considerably steeper slopes which resulted in less stable split waves than in the present experiment, resulting in a smaller value for $\gamma$.

## 4. Conclusions and Future Work

An undistorted experiment was carried out to study tsunami soliton fission and split wave-breaking. We obtained time series data of water surface elevations around the wave-breaking point after tsunami shoaling and soliton fission on a continental shelf.

The major conclusions of the present study can be summarized as follows:

1) The wave split point has moved forward to the tsunami crest, as the period of incident wave is longer.

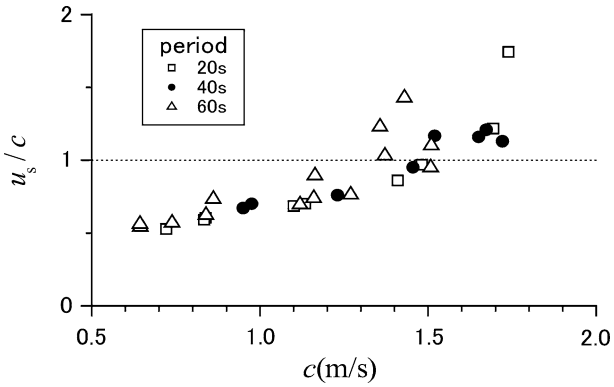


Figure 12
Values for $u_s/c$ at the point of wave-breaking.

2) Wave height of split waves at breaking is not related to the bottom slope on a continental shelf. On the other hand, as the bottom slope increases, the water depth $h$ at wave-breaking is smaller and consequently $\eta/h$ of the first split wave at wave-breaking is larger.
3) We proposed new methods, which are based on a nonlinear dispersion wave theory, to estimate wave velocity and wave-breaking criterion for a progressive wave. Then its capability was demonstrated by applying it to experiment results.
4) $\lambda$, which is the maximum $u_s/c$ of split waves at wave-breaking, ranges 0.5 to 1.2 on a continental shelf. The values are larger than values reported in previous studies.

The next step is to integrate the results from this study into numerical models for wave-breaking.

## *Acknowledgements*

The present study results from the activity of the Tsunami Evaluation Subcommittee (Chair person: Dr. Shuto) of the Nuclear Civil Engineering Committee in JSCE (Japan Society of Civil Engineers), which was supported by Japanese electric power companies. The authors would like to express their deepest gratitude to the members of the subcommittee.

## References

Fujima, K., Goto, T., and Shuto, N. (1986), *Accuracy of nonlinear dispersive long-wave equations*, J. Japan Society of Civil Engineers, JSCE *369*, II-5, 223–232 (in Japanese).

Iwase, H. and Imamura, F. (2004), *A new tsunami numerical simulation with Boussinesq-Type equations applied for the 1983 Nihonka-Chubu Earthquake tsunami*, Proc. APAC2003 Makuhari, Japan, pp. 12–13.

MADSEN, P.A., SØRENSEN, O.R., and SCHÄFFER, H.A. (1997), *Surf zone dynamics simulated by a Boussinesq type model. Part I: Model description and cross-shore motion of regular waves*. Coastal Engin. *32,* 255–287.

SHÄFFER, H.A., MADSEN, P.A., and DEIGAARD, R. (1993), *A Boussinesq model for waves breaking in shallow water*, Coastal Engin. *20*, 185–202.

SATO, S. (1996), *Numerical simulation of 1993 Southwest Hokkaido earthquake tsunami around Okushiri Island*, J. Waterway, Port, Coastal, and Ocean Engin. ASCE, *122*(5), 209–215.

SHUTO, N (1985), *The Nihonkai-Chuubu earthquake tsunami on the north Akita coast*, Coastal Engin. Japan, JSCE *28*, Tokyo, Japan, 255–264.

(Received February 20, 2006, accepted October 28, 2006)